

SPRINGER PROCEEDINGS IN PHYSICS

- 79 **Nonlinear Dynamics and Pattern Formation in Semiconductors and Devices**
Editor: F.-J. Niedernostheide
- 80 **Computer Simulation Studies in Condensed-Matter Physics VIII**
Editors: D.P. Landau, K.K. Mon, and H.-B. Schüttler
- 81 **Materials and Measurements in Molecular Electronics**
Editors: K. Kajimura and S. Kuroda
- 82 **Computer Simulation Studies in Condensed-Matter Physics IX**
Editors: D.P. Landau, K.K. Mon, and H.-B. Schüttler
- 83 **Computer Simulation Studies in Condensed-Matter Physics X**
Editors: D.P. Landau, K.K. Mon, and H.-B. Schüttler
- 84 **Computer Simulation Studies in Condensed-Matter Physics XI**
Editors: D.P. Landau and H.-B. Schüttler
- 85 **Computer Simulation Studies in Condensed-Matter Physics XII**
Editors: D.P. Landau, S.P. Lewis, and H.-B. Schüttler
- 86 **Computer Simulation Studies in Condensed-Matter Physics XIII**
Editors: D.P. Landau, S.P. Lewis, and H.-B. Schüttler
- 87 **Proceedings of the 25th International Conference on the Physics of Semiconductors**
Editors: N. Miura and T. Ando
- 88 **Starburst Galaxies Near and Far**
Editors: L. Tacconi and D. Lutz
- 89 **Computer Simulation Studies in Condensed-Matter Physics XIV**
Editors: D.P. Landau, S.P. Lewis, and H.-B. Schüttler
- 90 **Computer Simulation Studies in Condensed-Matter Physics XV**
Editors: D.P. Landau, S.P. Lewis, and H.-B. Schüttler
- 91 **The Dense Interstellar Medium in Galaxies**
Editors: S. Pfalzner, C. Kramer, C. Straubmeier, and A. Heithausen
- 92 **Beyond the Standard Model 2003**
Editor: H.V. Klapdor-Kleingrothaus
- 93 **ISSMGE Experimental Studies**
Editor: T. Schanz
- 94 **ISSMGE Numerical and Theoretical Approaches**
Editor: T. Schanz
- 95 **Computer Simulation Studies in Condensed-Matter Physics XVI**
Editors: D.P. Landau, S.P. Lewis, and H.-B. Schüttler
- 96 **Electromagnetics in a Complex World**
Editors: I.M. Pinto, V. Galdi, and L.B. Felsen
- 97 **Fields, Networks, Computational Methods and Systems in Modern Electrodynamics**
A Tribute to Leopold B. Felsen
Editors: P. Russer and M. Mongiardo
- 98 **Particle Physics and the Universe**
Proceedings of the 9th Adriatic Meeting, Sept. 2003, Dubrovnik
Editors: J. Trampetić and J. Wess
- 99 **Cosmic Explosions**
On the 10th Anniversary of SN1993J (IAU Colloquium 192)
Editors: J. M. Marcaide and K. W. Weiler
- 100 **Lasers in the Conservation of Artworks**
LACONA V Proceedings, Osnabrück, Germany, Sept. 15–18, 2003
Editors: K. Dickmann, C. Fotakis, and J.F. Asmus
- 101 **Progress in Turbulence**
Editors: J. Peinke, A. Kittel, S. Barth, and M. Oberlack
- 102 **Adaptive Optics for Industry and Medicine**
Proceedings of the 4th International Workshop
Editor: U. Wittrock

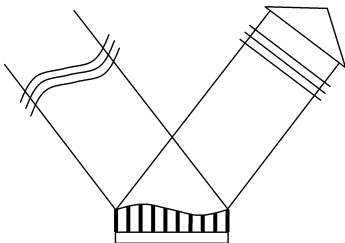
Volumes 50–78 are listed at the end of the book.

U. Wittrock (Ed.)

Adaptive Optics for Industry and Medicine

Proceedings
of the 4th International Workshop
Münster, Germany, Oct. 19–24, 2003

With 283 Figures



 Springer

Professor Dr. Ulrich Wittrock

University of Applied Sciences Münster, Dept. of Applied Physics, Photonics Laboratory
Stegerwaldstr. 39, 48565 Steinfurt, Germany
E-mail: wittrock@fh-muenster.de

ISSN 0930-8989

ISBN-10 3-540-23978-2 Springer Berlin Heidelberg New York

ISBN-13 978-3-540-23978-9 Springer Berlin Heidelberg New York

Library of Congress Control Number: 2004115731

This work is subject to copyright. All rights are reserved, whether the whole or part of the material is concerned, specifically the rights of translation, reprinting, reuse of illustrations, recitation, broadcasting, reproduction on microfilm or in any other way, and storage in data banks. Duplication of this publication or parts thereof is permitted only under the provisions of the German Copyright Law of September 9, 1965, in its current version, and permission for use must always be obtained from Springer-Verlag. Violations are liable to prosecution under the German Copyright Law.

Springer is a part of Springer Science+Business Media.

springeronline.com

© Springer-Verlag Berlin Heidelberg 2005

Printed in Germany

The use of general descriptive names, registered names, trademarks, etc. in this publication does not imply, even in the absence of a specific statement, that such names are exempt from the relevant protective laws and regulations and therefore free for general use.

Typesetting and production: PTP-Berlin, Protago-TeX-Production GmbH, Berlin

Cover concept: eStudio Calamar Steinen

Cover production: *design & production* GmbH, Heidelberg

Printed on acid-free paper SPIN: 11362708 57/3141/YU 5 4 3 2 1 0

Preface

The *4th International Workshop on Adaptive Optics for Industry and Medicine* took place in Münster, Germany, from October 19 to October 24, 2003. The series of *International Workshops on Adaptive Optics for Industry and Medicine* began with the first workshop in Shatura/Russia in 1997, the second workshop took place in Durham/England in 1999, and the third workshop was held in Albuquerque/USA in 2001. The workshop series started out as a true grassroots movement and kept an informal spirit throughout all four workshops. Many personal friendships and scientific collaborations have been formed at these meetings.

This fourth workshop was supposed to be held in Beijing, China. However, the program committee decided in May 2003 to move the workshop to Münster due to the general perception that the SARS (Severe Acute Respiratory Syndrome) cases reported in China could lead to a large epidemic. Despite this rather short notice the workshop in Münster was attended by about 70 people. Incidentally, the workshop coincided with the 50th anniversary of adaptive optics, because it was October 1953 when Horace Babcock published his famous paper “The possibilities of compensating astronomical seeing” in the *Publications of the Astronomical Society of the Pacific*.

For years, adaptive optics has been synonymous for correction of atmospheric aberrations, but many more applications have emerged in recent years. Examples of fairly novel applications are imaging of the retina, confocal microscopy, laser resonators, dispersion compensation in ultrafast lasers, and free space optical communication. At the same time, significant progress has been made in reducing the cost of adaptive optics components such as deformable mirrors, driver electronics, or wavefront sensors. These factors are expected to lead to much more widespread applications of adaptive optics in the near future.

The workshops have never been associated with any of the big scientific societies. While this kept the cost for attendees low, it also meant that a lot of work had to be done by the local organizing committee. I’m very grateful to Agnes Frieling, Ivo Buske, Hagen Zimer, Hans Heuck, and Petra Welp for their great enthusiasm in organizing this workshop.

VI Preface

The attendees at the workshop in Münster voted to hold the *5th International Workshop on Adaptive Optics for Industry and Medicine* in Beijing in 2005. I wish the organizers well in their undertakings and look forward to meeting many old and new friends in Beijing!

Münster, May 2005

Ulrich Wittrock



Contents

Part I Wavefront Correctors and Mirror Control

1 Micromachined Membrane Deformable Mirrors <i>G. Vdovin</i>	3
2 The Development and Optimisation of High Bandwidth Bimorph Deformable Mirrors <i>D. Rowe, L. Laycock, M. Griffith, N. Archer</i>	9
3 Deformable Mirrors with Thermal Actuators <i>G. Vdovin, M. Loktev</i>	17
4 Technology and Operation of a Liquid Crystal Modal Wavefront Corrector <i>M. Loktev, G. Vdovin</i>	25
5 Aberration Compensation Using Nematic Liquid Crystals <i>S. Somalingam, M. Hain, T. Tschudi, J. Knittel, H. Richter</i>	35
6 Wireless Control of an LC Adaptive Lens <i>G. Vdovin, M. Loktev, X. Zhang</i>	45
7 Summary of Adaptive Optics at Stanford <i>P. Lu, Y.-A. Peter, E. Carr, U. Krishnamoorthy, I.-W. Jung, O. Solgaard, R. Byer</i>	53
8 Control of a Thermal Deformable Mirror: Correction of a Static Disturbance with Limited Sensor Information <i>M. de Boer, K. Hinnen, M. Verhaegen, R. Fraanje, G. Vdovin, N. Doelman</i>	61
9 A Novel Microprocessor-Controlled High-Voltage Driver for Deformable Mirrors <i>H.-M. Heuck, I. Buske, U. Buschmann, H. Krause, U. Wittrock</i>	73
10 Preliminary Investigation of an Electrostatically Actuated Liquid-Based Deformable Mirror <i>E.M. Vuelban, N. Bhattacharya, J.M. Braat</i>	83

11 Interferometer-Based Adaptive Optical System
O. Soloviev, G. Vdovin 91

Part II Wavefront Sensors

12 Extended Hartmann–Shack Wavefront Sensor
B. Schäfer, K. Mann, M. Dyba 103

13 High Resolution Wavefront Sensing
J.E. Oti, V.F. Canales, M.P. Cagigal..... 111

14 Distorted Grating Wavefront Sensing in the Midwave Infrared
D.M. Cuevas, L.J. Otten, P. Harrison, P. Fournier 119

15 Comparative Results from Shack–Hartmann and Distorted Grating
 Wavefront Sensors in Ophthalmic Applications
*P. Harrison, G.R.G. Erry, P. Fournier, D.M. Cuevas, L.J. Otten,
 A. Larichev* 129

16 Shack–Hartmann Sensors for Industrial Quality Assurance
J. Pfund, M. Beyerlein, R. Dorn..... 141

17 Single-Chip Neural Network Modal Wavefront Reconstruction
 for Hartmann–Shack Wavefront Sensors
*T. Nirmaier, G. Pudasaini, C. Alvarez Diez, J. Bille,
 D.W. de Lima Monteiro* 151

18 CMOS Technology in Hartmann–Shack Wavefront Sensing
D.W. de Lima Monteiro and T. Nirmaier 163

19 Generalised Phase Diversity Wavefront Sensor
A.H. Greenaway, H.I. Campbell, S. Restaino 177

20 Generalised Phase Diversity: Initial Tests
S. Zhang, H.I. Campbell, A.H. Greenaway 187

21 Prime Microlens Arrays for Hartmann–Shack Sensors:
 An Economical Fabrication Technology
D.W. de Lima Monteiro, O. Akhzar-Mehr, G. Vdovin 197

22 A Proposal for Wavefront Retrieval from Hartmann Test Data
*V.M. Duran-Ramírez, D. Malacara-Doblado, D. Malacara-Hernandez,
 D.P. Salas-Peimbert, G. Trujillo-Shiaffino*..... 207

Part III Laser Resonators and Laser Amplifiers

23 Use of Intracavity Adaptive Optics
in Solid-State Lasers Operation at 1 μm
W. Lubeigt, P. van Grol, G. Valentine, D. Burns 217

24 Intracavity Use of Membrane Mirrors in a Nd:YVO₄ Laser
P. Welp, I. Buske, U. Wittrock 229

25 Adaptive Optics for High-Power Laser Beam Control
*A. Kudryashov, V. Samarkin, A. Alexandrov, A. Rukosuev,
V. Zavalova* 237

26 Aberrations of a Master-Oscillator-Power-Amplifier Laser
with Adaptive Optics Correction
I. Buske, H.-M. Heuck, P. Welp, U. Wittrock 249

27 Dynamic Aberrations Correction in an ICF Laser System
Y. Zhang, Z. Yang, C. Guan, H. Wang, P. Jiang, B. Xu, W. Jiang ... 261

28 Adaptive Shaping of High-Power Broadband Femtosecond
Laser Pulses
*T. Witting, G. Tsilimis, J. Kutzner, H. Zacharias, M. Köller,
H. Maurer* 273

29 Wavefront Measurement and Adaptive Optics
at the PHELIX Laser
*H.-M. Heuck, U. Wittrock, C. Häfner, S. Borneis, E. Gaul, T. Kühl,
P. Wiewior* 283

30 ISTC Projects from RFNC-VNIIEF
Devoted to Improving Laser Beam Quality
F. Starikov, G. Kochemasov 291

Part IV Medical Applications

31 Adaptive Optical System
for Retina Imaging Approaches Clinic Applications
N. Ling, Y. Zhang, X. Rao, C. Wang, Y. Hu, W. Jiang, C. Jiang 305

32 Adaptive Optics to Simulate Vision
with a Liquid Crystal Spatial Light Modulator
S. Manzanera, P.M. Prieto, J. Salort, E.J. Fernández, P. Artal 317

33 Confocal Scanning Retinal Imaging with Adaptive Optics
I. Iglesias, B. Vohnsen, P. Artal 325

34 A High-Resolution Adaptive Optics Fundus Imager
G.R.G. Erry, L.J. Otten, A. Larichev, N. Irochnikov 333

35 Perceived Image Quality Improvements
from the Application of Image Deconvolution
to Retinal Images from an Adaptive Optics Fundus Imager
P. Soliz, S.C. Nemeth, G.R.G. Erry, L.J. Otten, S.Y. Yang 343

36 Adaptive Aberrometer
for Acuity Measurements and Testing
A. Larichev, N. Irochnikov, S. Gorbunov 353

Part V Atmospheric Propagation

37 Adaptive Optics with Strong Scintillation
and Optical Vortices for Optical Communication
C. Paterson, C.R. Walker 365

38 Wavefront Measurement over an Extended Horizontal Path
Using a Wavefront Curvature Sensor
J. Burnett, S. Woods, A. Turner, A. Scott 377

39 The Detection of Atmospheric Tip-Tilt
and its Program Construction in Lunar Laser Ranging
G. Rui, X. Yaoheng 389

Author Index 397

List of Contributors

O. Akhzar-Mehr

Delft University of Technology
EEMCS
Electronic Instrumentation
Laboratory
Mekelweg 4, 2628 CD Delft
The Netherlands
o.mehr@gmx.de

A. Alexandrov

Russian Academy of Sciences
ILIT
Adaptive Optics for Industrial and
Medical Applications Group
Svyatoozerskaya 1
Shatura 140700, Russia

N. Archer

BAE Systems
Product Assurance Group
West Hanningfield Road
Chelmsford, England
nick.archer@baesystems.com

P. Artal

Universidad de Murcia
Laboratorio de Óptica
Campus de Espinardo Ed. C.
30071 Murcia, Spain
pablo@um.es

M. Beyerlein

Optocraft GmbH Optical Metrology
Hofmannstraße 118
91052 Erlangen, Germany

N. Bhattacharya

Delft University of Technology
Department of Imaging Science and
Technology
Optics Research Group
Lorentzweg 1, Delft
The Netherlands

J. Bille

University of Heidelberg
Kirchhoff Institute of Physics
Im Neuenheimer Feld 227
69120 Heidelberg, Germany

M. de Boer

Delft University of Technology
Delft Center of Systems and Control
Mekelweg 2, 2628 CD Delft
The Netherlands

S. Borneis

Gesellschaft für
Schwerionenforschung mbH
Planckstr. 1, 64291 Darmstadt
Germany

J.M. Braat

Delft University of Technology
Department of Imaging Science and
Technology
Optics Research Group
Lorentzweg 1, Delft
The Netherlands

J. Burnett

QinetiQ Ltd.
Malvern Technology Centre
St Andrews Road
Malvern, Worcs WR14 3PS, UK
jgburnett@QinetiQ.com

D. Burns

University of Strathclyde
Institute of Photonics
106 Rottenrow
Glasgow G4 0NW, Scotland

U. Buschmann

Münster University
of Applied Sciences
Photonics Laboratory
Stegerwaldstr. 39
48565 Steinfurt, Germany

I. Buske

Münster University
of Applied Sciences
Photonics Laboratory
Stegerwaldstr. 39
48565 Steinfurt, Germany
buske@fh-muenster.de

R. Byer

Stanford University
Ginzton Laboratory
450 Via Palou
Stanford, CA 94305-4088, USA

M.P. Cagigal

Universidad de Cantabria
Departamento de Física Aplicada
Avda. Los Castros S/N
39005 Santander, Spain

H.I. Campbell

Heriot-Watt University
Department of Physics
Riccarton
Edinburgh, EH14 4AS, UK
H.I.Campbell@hw.ac.uk

V.F. Canales

Universidad de Cantabria
Departamento de Física Aplicada
Avda. Los Castros S/N
39005 Santander, Spain

E. Carr

Stanford University
Ginzton Laboratory
450 Via Palou
Stanford, CA 94305-4088, USA

D.M. Cuevas

Kestrel Corporation
3815 Osuna Road NE
Albuquerque, NM 87109, USA
dcuevas@kestrelcorp.com

C. Alvarez Diez

University of Heidelberg
Kirchhoff Institute of Physics
Im Neuenheimer Feld 227
69120 Heidelberg, Germany

N. Doelman

TNO TPD
Stieltjesweg 1
2628 CK Delft
The Netherlands
doelman@tpd.tno.nl

R. Dorn

Optocraft GmbH Optical Metrology
Hofmannstraße 118
91052 Erlangen, Germany
dorn@optocraft.de

V.M. Duran-Ramirez

Centro de Investigaciones en Optica
Loma del Bosque 115
Leon, Gto, Mexico
vicdur@cio.mx

M. Dyba

MPI für Biophysikalische Chemie
Am Fassberg 11
37077 Göttingen, Germany
mdyba@gwdg.de

G.R.G. Erry

Kestrel Corporation
3815 Osuna Road NE
Albuquerque, NM 87109, USA
gerry@kestrelcorp.com

E.J. Fernández

Universidad de Murcia
Laboratorio de Óptica
Campus de Espinardo Ed. C.
30071 Murcia, Spain
enriquej@um.es

R. Fraanje

University of Twente
Faculty of Applied Physics, Enschede
The Netherlands

P. Fournier

Kestrel Corporation
3815 Osuna Road NE
Albuquerque, NM 87109, USA

E. Gaul

Gesellschaft für
Schwerionenforschung mbH
Planckstr. 1, 64291 Darmstadt
Germany

S. Gorbunov

IPLIT RAS
Pionerskaya 2
Troick, Moscow region 142092
Russia

A.H. Greenaway

Heriot-Watt University
Department of Physics
Riccarton
Edinburgh, EH14 4AS, UK
a.h.greenaway@hw.ac.uk

M. Griffith

BAE Systems
Advanced Technology Centre
West Hanningfield Road
Chelmsford, England

P. van Grol

University of Strathclyde
Institute of Photonics
106 Rottenrow
Glasgow G4 0NW, Scotland

C. Guan

Chinese Academy of Sciences
Institute of Optics and Electronics
PO Box 350, Shuangliu
Chengdu 610209, PR China

C. Häfner

Gesellschaft für
Schwerionenforschung mbH
Planckstr. 1, 64291 Darmstadt
Germany

M. Hain

Technische Universität Darmstadt
Hochschulstr. 6
64289 Darmstadt, Germany

P. Harrison

Kestrel Corporation
3815 Osuna Road NE
Albuquerque, NM 87109, USA
pharrison@kestrelcorp.com

H.-M. Heuck

Münster University
of Applied Sciences
Photonics Laboratory
Stegerwaldstr. 39
48565 Steinfurt, Germany
heuck@fh-muenster.de

K. Hinnen

Delft University of Technology
Delft Center of Systems and Control
Mekelweg 2
2628 CD Delft
The Netherlands
k.j.g.hinnen@dcsc.tudelft.nl

Y. Hu

Chinese Academy of Sciences
Institute of Optics and Electronics
PO Box 350, Shuangliu
Chengdu 610209, PR China

I. Iglesias

Universidad de Murcia
Laboratorio de Óptica
Campus de Espinardo Ed. C.
30071 Murcia, Spain
iic@um.es

N. Irochnikov

M.V. Lomonosov Moscow State
University
Faculty of Physics
Leninskiye Gory
Moscow 119992, Russia

C. Jiang

E&ENT Hospital
of Fudan University
Shanghai, PR China

P. Jiang

Chinese Academy of Sciences
Institute of Optics and Electronics
PO Box 350, Shuangliu
Chengdu 610209, PR China

W. Jiang

Chinese Academy of Sciences
Institute of Optics and Electronics
PO Box 350, Shuangliu
Chengdu 610209, PR China

I.-W. Jung

Stanford University
Ginzton Laboratory
450 Via Palou
Stanford, CA 94305-4088, USA

M. Köller

Westfälische Wilhelms-Universität
Münster
Institut für Numerische und
instrumentelle Mathematik
Einsteinstr. 62
48149 Münster, Germany
kollerma@math.uni-muenster.de

J. Knittel

Deutsche Thomson Brandt GmbH
Hermann-Schwer-Str. 3
78048 Villingen-Schwenningen
Germany
joachim.knittel@thomson.net

G. Kochemasov

Russian Federal Nuclear Center –
VNIIEF
Sarov, Nizhny Novgorod
Reg. 607190, Russia

H. Krause

Münster University
of Applied Sciences
Photonics Laboratory
Stegerwaldstr. 39
48565 Steinfurt, Germany

U. Krishnamoorthy

Stanford University
Ginzton Laboratory
450 Via Palou
Stanford, CA 94305-4088, USA

T. Kühl

Gesellschaft für
Schwerionenforschung mbH
Planckstr. 1, 64291 Darmstadt
Germany

A. Kudryashov

Russian Academy of Sciences
 ILIT
 Adaptive Optics for Industrial and
 Medical Applications Group
 Svyatoozerskaya 1
 Shatura 140700, Russia
 kud@laser.ru

J. Kutzner

Westfälische Wilhelms-Universität
 Münster
 Physikalisches Institut
 Wilhelm-Klemm-Str. 10
 48149 Münster, Germany

A. Larichev

M.V. Lomonosov Moscow State
 University
 Center of Medical Physics
 Leninskiye Gory
 Moscow 119992, Russia
 larichev@optics.ru

L. Laycock

BAE Systems
 Advanced Technology Centre
 West Hanningfield Road
 Chelmsford, England

D.W. de Lima Monteiro

Delft University of Technology
 EEMCS
 Electronic Instrumentation
 Laboratory
 Mekelweg 4, 2628 CD Delft
 The Netherlands
 davies@titus.et.tudelft.nl

N. Ling

Chinese Academy of Sciences
 Institute of Optics and Electronics
 PO Box 350, Shuangliu
 Chengdu 610209, PR China

M. Loktev

Delft University of Technology
 EEMCS
 Electronic Instrumentation
 Laboratory
 Mekelweg 4, 2628 CD Delft
 The Netherlands
 m.loktev@ewi.tudelft.nl

P. Lu

Stanford University
 Ginzton Laboratory
 450 Via Palou
 Stanford, CA 94305-4088, USA
 patlu@Stanford.EDU

W. Lubeigt

University of Strathclyde
 Institute of Photonics
 106 Rottenrow
 Glasgow G4 0NW, Scotland
 walter.lubeigt@strath.ac.uk

D. Malacara-Doblado

Centro de Investigaciones en Optica
 Loma del Bosque 115
 Leon, Gto, México
 dmalacdo@cio.mx

D. Malacara-Hernandez

Centro de Investigaciones en Optica
 Loma del Bosque 115
 Leon, Gto, México
 dmalacara@cio.mx

K. Mann

Laser Laboratorium Göttingen
 Hans-Adolf-Krebs-Weg 1
 37077 Göttingen, Germany
 kmann@llg.gwdg.de

S. Manzanera

Universidad de Murcia
 Laboratorio de Óptica
 Campus de Espinardo Ed. C.
 30071 Murcia, Spain
 silmanro@um.es

H. Maurer

Westfälische Wilhelms-Universität
Münster
Institut für Numerische und
instrumentelle Mathematik
Einsteinstr. 62
48149 Münster, Germany

S.C. Nemeth

Kestrel Corporation
3815 Osuna Road NE
Albuquerque, NM 87109, USA

T. Nirmaier

University of Heidelberg
Kirchhoff Institute of Physics
Im Neuenheimer Feld 227
69120 Heidelberg, Germany
nirmaier@kip.uni-heidelberg.de

J.E. Oti

Universidad de Cantabria
Departamento de Física Aplicada
Avda. Los Castros S/N
39005 Santander, Spain
otije@unican.es

L.J. Otten

Kestrel Corporation
3815 Osuna Road NE
Albuquerque, NM 87109, USA
ljotten@kestrelcorp.com

C. Paterson

Imperial College
The Blackett Laboratory
London, SW7 2BW, UK
carlp@imperial.ac.uk

Y.-A. Peter

Stanford University
Ginzton Laboratory
450 Via Palou
Stanford, CA 94305-4088, USA

J. Pfund

Optocraft GmbH Optical Metrology
Hofmannstraße 118
91052 Erlangen, Germany

P.M. Prieto

Universidad de Murcia
Laboratorio de Óptica
Campus de Espinardo Ed. C.
30071 Murcia, Spain
pegrito@um.es

G. Pudasaini

University of Heidelberg
Kirchhoff Institute of Physics
Im Neuenheimer Feld 227
69120 Heidelberg, Germany
gopal@kip.uni-heidelberg.de

X. Rao

Chinese Academy of Sciences
Institute of Optics and Electronics
PO Box 350, Shuangliu
Chengdu 610209, PR China

S. Restaino

Naval Research Laboratory
Remote Sensing Division, Code 721
Kirtland Airforce Base
Albuquerque, NM, USA

H. Richter

Deutsche Thomson Brandt GmbH
Hermann-Schwer-Str. 3
78048 Villingen-Schwenningen
Germany

D. Rowe

BAE Systems
Advanced Technology Centre
West Hanningfield Road
Chelmsford, England
duncan.rowe@baesystems.com

G. Rui

National Astronomical Observatories
CAS
Yunnan Observatory
gr806@tom.com

A. Rukosuev

Russian Academy of Sciences
ILIT
Adaptive Optics for Industrial and
Medical Applications Group
Svyatoozerskaya 1
Shatura 140700, Russia

D.P. Salas-Peimbert

Instituto Tecnológico de Chihuahua
31310 Chihuahua, Chih., Mexico
dsalas@itchihuahua.edu.mx

J. Salort

Universidad de Murcia
Laboratorio de Óptica
Campus de Espinardo Ed. C.
30071 Murcia, Spain
salort@um.es

V. Samarkin

Russian Academy of Sciences,
ILIT
Adaptive Optics for Industrial and
Medical Applications Group
Svyatoozerskaya 1
Shatura 140700, Russia
samarkin@laser.ru

B. Schäfer

Laser Laboratorium Göttingen
Hans-Adolf-Krebs-Weg 1
37077 Göttingen, Germany
bschae@llg.gwdg.de

A. Scott

QinetiQ Ltd.
Malvern Technology Centre
St Andrews Road
Malvern, Worcs WR14 3PS, UK

O. Solgaard

Stanford University
Ginzton Laboratory
450 Via Palou
Stanford, CA 94305-4088, USA

P. Soliz

Kestrel Corporation
3815 Osuna Road NE
Albuquerque, NM 87109, USA
psoliz@kestrelcorp.com

O. Soloviev

Delft University of Technology
Electronic Instrumentation
Laboratory
Mekelweg 4, 2628 CD, Delft
The Netherlands
O.Soloviev@EWI.TUdelft.nl

S. Somalingam

Technische Universität Darmstadt
Hochschulstr. 6
64289 Darmstadt, Germany
somalin@
prp.physik.tu-darmstadt.de

F. Starikov

Russian Federal Nuclear Center –
VNIIEF
Sarov, Nizhny Novgorod Reg.
607190, Russia
starikov@otd13.vniief.ru

T. Tschudi

Technische Universität Darmstadt
Hochschulstr. 6
64289 Darmstadt, Germany

G. Trujillo-Shiaffino

Instituto Tecnológico de Chihuahua
31310 Chihuahua, Chih., Mexico

G. Tsilimis

Westfälische Wilhelms-Universität
Münster
Physikalisches Institut
Wilhelm-Klemm-Str. 10
48149 Münster, Germany

A. Turner

QinetiQ Ltd.
Malvern Technology Centre
St Andrews Road
Malvern, Worcs WR14 3PS, UK
ajturner2@qinetiq.com

G. Valentine

University of Strathclyde
Institute of Photonics
106 Rottenrow
Glasgow G4 0NW, Scotland
garth.valentine@
strath.ac.uk

G. Vdovin

Delft University of Technology
EEMCS
Electronic Instrumentation
Laboratory
Mekelweg 4, 2628 CD Delft
The Netherlands
gleb@ei.et.tudelft.nl
and
OKO Technologies
PO Box 581
2600 AN Delft
The Netherlands
gleb@okotech.com

M. Verhaegen

Delft University of Technology
Delft Center of Systems and Control
Mekelweg 2, 2628 CD Delft
The Netherlands

B. Vohnsen

Universidad de Murcia
Laboratorio de Óptica
Campus de Espinardo Ed. C.
30071 Murcia, Spain

E.M. Vuelban

Delft University of Technology
Department of Imaging Science and
Technology
Optics Research Group
Lorentzweg 1, Delft
The Netherlands
e.vuelban@tnw.tudelft.nl

C.R. Walker

Imperial College
The Blackett Laboratory
London, SW7 2BW, UK

C. Wang

Chinese Academy of Sciences
Institute of Optics and Electronics
PO Box 350, Shuangliu
Chengdu 610209, PR China

H. Wang

Chinese Academy of Sciences
Institute of Optics and Electronics
PO Box 350, Shuangliu
Chengdu 610209, PR China

P. Welp

Münster University
of Applied Sciences
Photonics Laboratory
Stegerwaldstr. 39
48565 Steinfurt, Germany
petrawelp@fh-muenster.de

P. Wiewior

Julius Maximilian Universität
Würzburg
97703 Würzburg, Germany

T. Witting

Westfälische Wilhelms-Universität
Münster
Physikalisches Institut
Wilhelm-Klemm-Str. 10
48149 Münster, Germany
twitting@nwz.uni-muenster.de

U. Wittrock

Münster University
of Applied Sciences
Photonics Laboratory
Stegerwaldstr. 39
48565 Steinfurt, Germany
wittrock@fh-muenster.de

S. Woods

QinetiQ Ltd.
Malvern Technology Centre
St Andrews Road
Malvern, Worcs WR14 3PS, UK
scwoods@taz.qinetiq.com

B. Xu

Chinese Academy of Sciences
Institute of Optics and Electronics
PO Box 350, Shuangliu
Chengdu 610209, PR China

X. Yaoheng

National Astronomical Observatories
CAS
Yunnan Observatory
yozsx@public.km.yn.cn

S.Y. Yang

Texas Tech University
Lubbock, TX, USA
gzsyayang@yahoo.com

Z. Yang

Chinese Academy of Sciences
Institute of Optics and Electronics
PO Box 350, Shuangliu
Chengdu 610209, PR China
zpyang@ioe.ac.cn

H. Zacharias

Westfälische Wilhelms-Universität
Münster
Physikalisches Institut
Wilhelm-Klemm-Str. 10
48149 Münster, Germany
hzach@uni-muenster.de

V. Zavalova

Russian Academy of Sciences
ILIT
Adaptive Optics for Industrial and
Medical Applications Group
Svyatoozerskaya 1
Shatura 140700, Russia

S. Zhang

Heriot-Watt University
Department of Physics
Riccarton
Edinburgh, EH14 4AS, UK
sijiong.zhang@hw.ac.uk

X. Zhang

Delft University of Technology
EEMCS
Electronic Instrumentation
Laboratory
Mekelweg 4, 2628 CD Delft
The Netherlands

Y. Zhang

Chinese Academy of Sciences
Institute of Optics and Electronics
PO Box 350, Shuangliu
Chengdu 610209, PR China
ydzhang@ioe.ac.cn

Part I

Wavefront Correctors and Mirror Control

1 Micromachined Membrane Deformable Mirrors

G. Vdovin

Delft University of Technology, EEMCS, Electronic Instrumentation Laboratory
Mekelweg 4, 2628 CD Delft, The Netherlands

and

OKO Technologies

PO Box 581, 2600 AN Delft, The Netherlands

Summary. Development of adaptive optics, initiated 50 years ago with the article of Babcock [1], resulted in impressive technical and scientific results in military and astronomical applications. These results were obtained on a high price using custom-developed complex adaptive optical systems. Adaptive optics has a great potential to be applied in a range of optical systems, including imaging, ophthalmic, laser, optical communications and information processing. These systems are marketed widely and use relatively inexpensive parts with high performance. This article presents a fragmentary analysis of the current state and possible future development of inexpensive deformable mirrors for the industry and medicine. The analysis is mainly based on the results obtained by the author and his colleagues at the TU Delft and OKO Technologies during 1993–2003.

1.1 Design and Parameters

A Micromachined Membrane Deformable Mirror (MMDM) [2] consists of a thin stretched membrane suspended over an array of electrostatic electrodes. The membrane is fabricated by LPCVD deposition of a thin $\approx 0.5\ \mu\text{m}$ layer of tensile stressed silicon nitride Si_nN_m , followed by anisotropic etching of bulk silicon to release the membrane. Pure nitride membranes are sufficiently strong for mirrors with a diameter of up to 25 mm, larger membranes – up to 50 mm – can be fabricated by sandwiching a relatively thick – up to $10\ \mu\text{m}$ – layer of epitaxial polysilicon between two nitride layers.

In the simplest case the membrane is coated by a thin layer of metal – aluminum or gold – providing sufficiently reflective broadband coatings in the visible (Al) and infrared (gold) regions. In case a higher reflectivity is required (for instance for laser intracavity applications), the membrane can be coated with Cr/Ag composition followed by up to 12 dielectric layers, resulting in reflectivity of up to 99.8% in a narrow spectral region. Multilayer coated mirrors reported to work with laser loads of up to 550 W in a 5 mm circular beam at $\lambda = 1.06\ \mu\text{m}$. The typical parameters of a standard MMDM produced by OKO Technologies are shown in Table 1.1.

The initially flat membrane can be deformed only towards the electrostatic actuators because the electrostatic force can be only attractive. This limits

Table 1.1. MMDM technical data

Parameter	Value
Aperture shape	approximately circular
Mirror coating	Al, Au, HR ($R \approx 99.9\%$)
Aperture	diameter 15–50 mm
Number of electrodes	37–79
Control voltages V_c	0 . . . 300 V
Initial rms deviation from plane	less than 0.3 μm
Main initial aberration	1 fringe at 630 nm
Frequency range	1000 Hz
Maximum deflection of the mirror center	9–30 μm

the possible optical figures of the MMDM to be always concave. Since most of the applications require both convex and concave operation of the mirror, the initial mirror figure is electrically biased to take a concave parabolic shape, median with respect to zero and maximum deflection. From this position, the mirror can correct both concave and convex aberrations with relation to the parabolically biased figure. The typical response time is ~ 1 ms, making the mirror suitable for real-time control of turbulence-induced aberrations.

1.2 Limitations

Technology of MMDM has certain limitations. The technology is suited for membranes with diameters in the range of 0.4–5.0 cm. It is difficult to fabricate larger or smaller mirrors. The effective number of electrodes is also limited. Electrostatic actuators can be easily integrated in very dense grids, resulting in small area per actuator. The maximum response per actuator is proportional to the actuator area. Practically it does not make sense to have actuators that produce maximum response of less than $\lambda/4$, which limits the maximum number of actuators to several hundreds for a 5 cm mirror. In practice, the mirror substrate should have voids, that are necessary for reduction of the air damping of the membrane movement. These voids should be uniformly spaced and they occupy a considerable area, even more reducing the possible number of uniformly spaced actuators.

The mirror membrane is fixed along its edges. To eliminate the influence of fixed boundary conditions, the light aperture should occupy approximately the central 50% of the mirror surface. For example, if a membrane mirror has an aperture of 15 mm, only the central area of 10 mm in diameter can be used for functional correction of wavefront aberrations. To ensure best spatial resolution, the array of electrostatic actuators is also placed under the central area of the membrane, occupying only about 60% of the membrane area.

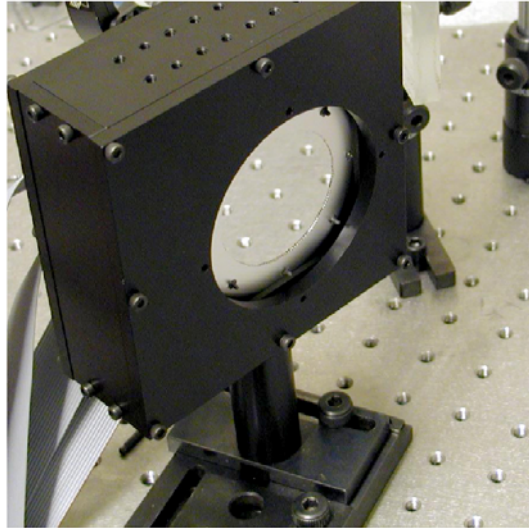
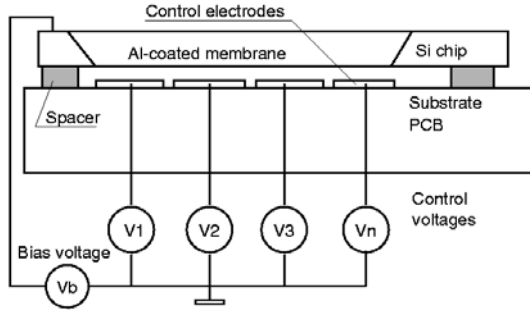


Fig. 1.1. A simplified cross-section of a MMDM (*top*) and complete 79-ch 50-mm MMDM coated for 1060 nm wavelength (*bottom*)

The design of a micromachined deformable mirror allows deflection of the mirror surface only in the direction of the control electrodes, corresponding to a positive curvature of the mirror surface. To be able to correct an aberration that has both positive and negative curvature, the mirror surface should be pre-deformed to a concave spherical shape, having a weak positive optical power in the biased “zero” position. The surface displacement of the biased mirror surface limits the amplitude of the corrected aberration, moreover the correction amplitude and precision depends on the characteristic size of the aberration to be corrected.

The bias curvature $C_b = 1/R_b$, where R_b is the radius of biased surface, should be equal to the half of the maximum achievable curvature $C_{\max} = 1/R_{\max} = 2/(R_b)$. The range of curvature control is limited by the curvature of the biased membrane. The shape of the membrane $s(x)$ – that is needed

to correct for a hypothetical harmonic aberration – can be described by a harmonic function with a period T and amplitude A : $s(x) = A \sin(2\pi x/T)$ – for simplicity we consider a one-dimensional case. The curvature of the membrane $C(x) = 4\pi^2 A/T^2 \sin(2\pi x/T)$ is limited by the value of $4\pi^2 A/T^2$. This value (positive or negative) cannot exceed the absolute value of the bias curvature given by $|1/R_b|$. The amplitude of achievable harmonic deformation of the membrane mirror is given by

$$A_m = \frac{T^2}{4\pi^2 R_b}, \quad (1.1)$$

where T defines the characteristic size of the aberration to be corrected. Finally the achievable P - V correction amplitude in terms of wavefront deformation will be four times larger (P - V amplitude of a harmonic function is two times larger than its amplitude, further the phase deformation equals to doubled mirror surface deformation), yielding for P - V amplitude of wavefront correction:

$$A_{\text{wf}} = \frac{T^2}{\pi^2 R_b} = \frac{1}{\pi^2 f R_b}, \quad (1.2)$$

where f is the spatial frequency of the surface deformation. For aberrations with a spatial period smaller than the mirror aperture, the membrane corrector represents a low-frequency filter, with a maximum amplitude of corrected aberration decreasing with aberration spatial frequency by 40 dB per decade or 12 dB per octave. For the typical values of our system $T = 1$ cm and $R_b = 4$ m – aberration over the whole aperture – the maximum amplitude of correction equals $2 \mu\text{m}$ while for a local aberration with $T = 5$ mm the maximum amplitude of correction is almost an order of magnitude lower and equals only $0.5 \mu\text{m}$.

Equation 1.2 defines the maximum amplitude of the wavefront that can be corrected as a function of the aberration period T . A is the maximum amplitude of a wavefront with a spatial period of T_{\min} , that still can be corrected by the mirror. Wavefronts with larger amplitude and/or smaller periods cannot be corrected.

$$T_{\min} = \pi \sqrt{R_b A}. \quad (1.3)$$

Assuming the mirror diameter is D and we need at least 4 actuators to correct an aberration with a spatial period T , the total number of actuators providing correction with amplitude precision A and period T_{\min}

$$N = \frac{16D^2}{\pi^2 R_b A}. \quad (1.4)$$

For a deformable mirror with light aperture of $D = 10$ mm, $R_b = 5$ m and $A = 10^{-7}$ m we have $T_{\min} \approx 2$ mm and $N \approx 300$. For comparison, the real device has only $N = 37$ actuators. For a mirror with $D = 35$ mm, $R_b = 20$ m and $A = 10^{-7}$ m we obtain $T_{\min} \approx 4.5$ mm and $N \approx 1000$.

As we made no assumption about the nature of the deformable mirror response, this analysis is valid in general for any curvature-limited deformable mirror device.

1.3 Applications

Since the technology of MMDM is based completely on inorganic materials, devices were demonstrated to work in vacuum at cryogenic temperatures down to $T = 78\text{ K}$ [3], which makes them potentially suitable for space-based adaptive optics.

MMDM is reported to be successfully used for real-time correction of phase aberrations in laboratory and in a one meter telescope at Apache Point, New Mexico [4]. In particular, the Strehl ratio was improved in average from 0.08 to 0.48 for simulated turbulence in the laboratory, and from 0.04 to 0.1 in a 10-exposure field experiment with Altair image.

Small size, quick response, high density of actuators, smooth modal response and hysteresis-free operation make MMDM highly suitable for feed-forward correction using control approach based on a combination of optimization with program control. In the beginning, the voltage vector applied to the mirror electrodes is optimized to obtain the maximum of the appropriate quality parameter – brightness for laser systems, sharpness and image quality for imaging systems, pulse duration for ultrafast lasers. The optimization process can take up to several thousand iterations and usually results in significant improvement of the quality of the optical system. The control vector is written in the memory of the computer and can be recalled every time the control situation repeats.

Based on this approach, a wide field correction of scanning optical microscope was demonstrated in [5]. The scanning beam quality was individually optimized for each point in the field of view and the lookup table of MMDM control vectors was stored in the computer. In the operation mode, the scanning beam was corrected “on the fly” for each scan position, resulting in drastic improvement of the microscope resolution over the whole field.

Another example of the optimization approach combined with a lookup table is given in [6] – where the authors report on a $1 \times N$ optical switch with MMDM used to improve coupling efficiency in each switch channel of a fiber switch by pre-setting the mirror shape in accordance with the lookup table.

Optimization approach proved very efficient in numerous experiments with compression and optimization of ultrafast optical pulses. A special MMDM was developed for one-dimensional correction of phase aberrations along a single line. These devices are usually used in a stretcher of ultrafast laser to balance phase delays of spectral components. Optimization of the spectral phase resulted in efficient compression of femtosecond pulses and even in improvement of the efficiency of a EUV plasma source [7–9].

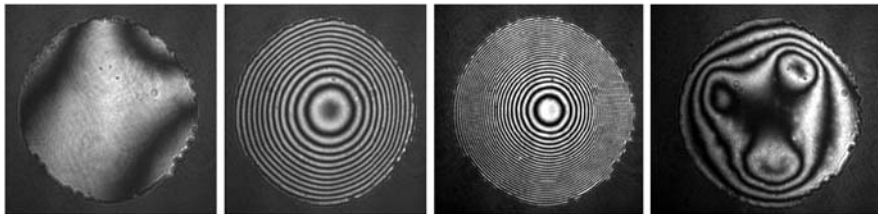


Fig. 1.2. Typical interferometric pattern of a 37-ch 15 mm MMDM: zero voltage applied, control byte 180 applied to all actuators, control byte 255 applied to all and to some actuators (*left to right*)

MMDMs were also successfully used for wavefront correction in terawatt lasers [10] and for intracavity control of high-power industrial lasers [11, 12].

Finally, MMDM are suitable for real-time correction of the aberrations of the human eye, making possible “electronic spectacles” for real-time improvement of the visio nactuity [13].

Compactness, simplicity and high optical quality make MMDM the device of choice for a number of optical applications in the laser optics, imaging, optical testing and astronomy.

References

1. H.W. Babcock: The possibility of compensating astronomical seeing. Publications of the astronomical society of Pacific **65**, 229 (1953)
2. G.V. Vdovin, S. Middelhoek, P.M. Sarro: Opt. Eng. **36**, 1382 (1997)
3. H.M. Dyson, R.M. Sharples, N.A. Dipper, G.V. Vdovin: Opt. Express **8**(1) (2001)
4. D. Dayton, S. Restaino, J. Gonglewski, J. Gallegos, S. McDermott, S. Browne, S. Rogers, M. Vaidyanathan, M. Shilko: Opt. Comm. **176**, 339 (2000)
5. O. Albert, L. Sherman, G. Mourou, T.B. Norris, G. Vdovin: Opt. Lett. **25**(1), 52 (2000)
6. F. Gonte, A. Courteville, R. Dandliker: Opt. Eng. **41**(5), 1073 (2002)
7. E. Zeek, R. Bartels, M.M. Murnane, H.C. Kapteyn, S. Backus, G. Vdovin: Opt. Lett. **25**(8), 587 (2000)
8. A. Baltuska, T. Fuji, T. Kobayashi: Opt. Lett. **27**(5), 306 (2002)
9. R. Bartels, S. Backus, E. Zeek, L. Misoguti, G. Vdovin, I.P. Christov, M.M. Murnane, H.C. Kapteyn: Nature **406**, 164 (2000)
10. F. Druon, G. Cheraux, J. Faure, J. Nees, M. Nantel, A. Maksimchuk, G. Mourou, J.C. Chanteloup, G. Vdovin: Opt. Lett. **23**, 1043 (1998)
11. G. Vdovin, V. Kiyko: Opt. Lett. **26**(11), 798 (2001)
12. W. Lubeigt, G. Valentine, J. Girkin, E. Bente, D. Burns: Opt. Express **10**(13), 550 (2002)
13. E. Fernandez, I. Iglesias, P. Artal: Opt. Lett. **26**(10) 746 (2001)

2 The Development and Optimisation of High Bandwidth Bimorph Deformable Mirrors

D. Rowe¹, L. Laycock¹, M. Griffith¹, and N. Archer²

¹ BAE Systems Advanced Technology Centre
West Hanningfield Road, Chelmsford, England

² BAE Systems Product Assurance Group
West Hanningfield Road, Chelmsford, England

Summary. Our first mirror designs were based on a standard bimorph construction and exhibited a resonant frequency of 1 kHz with a maximum stroke of $\pm 5 \mu\text{m}$. These devices were limited by the requirement to have a “dead space” between the inner active area and the mirror boundary. This was necessary to ensure that the requirements for both the stroke and the static boundary conditions at the edge of the mirror could be met simultaneously, but there was a significant penalty to pay in terms of bandwidth, which is inversely proportional to the square of the full mirror diameter. In a series of design iteration steps, we have created mounting arrangements that seek not only to reduce dead space, but also to improve ruggedness and temperature stability through the use of a repeatable and reliable assembly procedure. As a result, the most recently modeled mirrors display a resonance in excess of 5 kHz, combined with a maximum stroke in excess of $\pm 10 \mu\text{m}$. This has been achieved by virtually eliminating the “dead space” around the mirror. By careful thermal matching of the mirror and piezoelectric substrates, operation over a wide temperature range is possible. This paper will discuss the outcomes from the design study and present our initial experimental results for the most recently assembled mirror.

2.1 Introduction

The BAE SYSTEMS Advanced Technology Centre has been involved in a systems study to investigate the use of deformable mirrors to correct for distortions in atmospheric imaging and laser beam propagation. Typical applications include thermal imaging and laser remote sensing.

For correcting atmospheric distortions, the bandwidth required for the control system is typically 1 kHz. This means that the deformable mirror’s resonant frequency needs to be $> 1 \text{ kHz}$. In terms of stroke, the correction of moderate turbulence ($D/r_0 = 10$, where D is the diameter of the aperture and r_0 is the coherence length), requires the capability to provide a movement of $0.5 \mu\text{m}$ ($\lambda = 1 \mu\text{m}$) over the mirror’s active surface. We have used these two basic parameters as the target requirements in the development of a number of prototype bimorph mirrors.

2.2 1st Iteration Flexure

2.2.1 Design and Fabrication

The first bimorph mirror fabricated was based on the standard scheme where a glass/PZT sandwich is supported rigidly around its edge. While this scheme is robust, the total substrate diameter is typically twice that of the required active area. Since the resonant frequency of this device is inversely proportional to the square of the mirror diameter, reducing the “dead” space at the periphery of the mirror was regarded as a prime objective. One way that this has been achieved in the past is to support the periphery of the mirror with an o-ring. This prevents any vertical displacement at the edge, but does enable a non-zero gradient. However, achieving an even pressure over the entire o-ring is difficult and requires careful adjustment of the clamping screws to avoid introducing mirror distortions. For this reason, we devised the 1st iteration flexure mount as an alternative mounting scheme. The flexures create a robust support which nevertheless enables a non-zero gradient at the mirror edge. This reduces the proportion of the mirror which is outside the main pupil.

Analytical modeling [1] was used to provide an initial estimate of the required substrate thickness. The trade off between the mirror stroke and resonant frequency is shown in Fig. 2.1.

The mirror was then drawn in Pro-Engineer, and transferred to Pro-Mechanica for finite element analysis. The electrode pattern chosen was based on the work carried out by Edric Mark Ellis in his thesis [1]. A photograph of the back of the mirror showing the flexures and electrode pattern, along with a picture of the fully assembled mirror is given in Fig. 2.2.

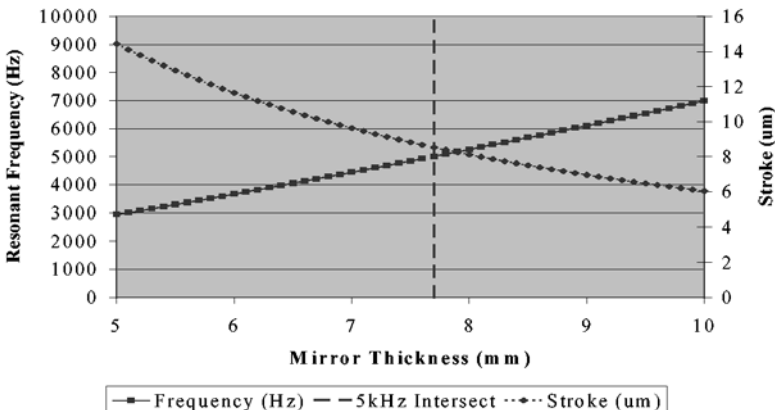


Fig. 2.1. Analytical plot of mirror resonance and maximum displacement as a function of mirror substrate thickness

Table 2.1. Comparison of modelled and measured results

	Stroke (300 V pk-pk)	Resonant Frequency
Modelled ^{a)}	$\pm 7.3 \mu\text{m}$	3.37 kHz
Final Mounted Mirror	$\pm 5 \mu\text{m}$	2.7 kHz
% Achieved	62	80

^{a)} The glue layer has not been taken into account in the modelled performance

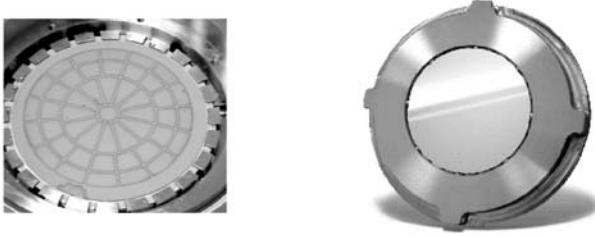


Fig. 2.2. Photographs of the back of the mirror, showing the flexures and electrode pattern, and the fully assembled mirror

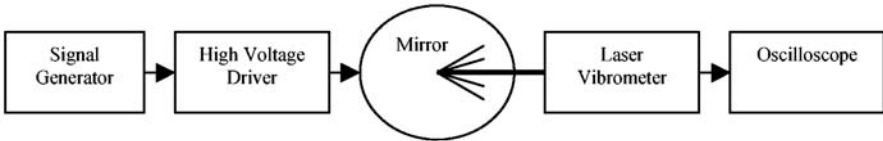


Fig. 2.3. Schematic of laser vibrometer test set-up

2.2.2 Performance

A laser vibrometer (see Fig. 2.3 for schematic) was used to determine the resonant frequency and maximum stroke of the assembled device. A comparison of the modelled and measured results is given in Table 2.1.

From the table it can be seen that the measured resonant frequency is close to that predicted. The stroke achieved is only 60% of that predicted, but the model does not include the glue layer between the mirror substrate and PZT elements.

2.3 2nd Iteration Flexure

2.3.1 Design

While the 1st iteration flexure enabled a non-zero gradient at the mirror periphery, the unused portion of the mirror could be reduced even further if some vertical (piston) displacement were also possible. The 2nd iteration flexure is designed to provide this.

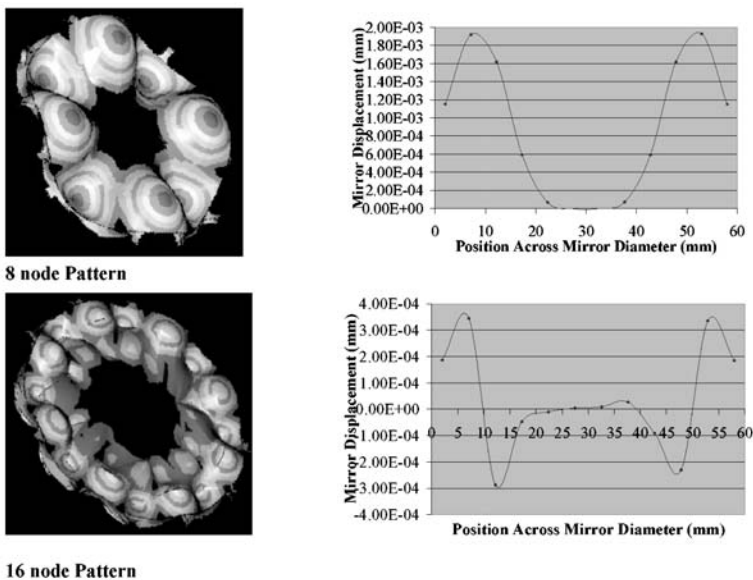


Fig. 2.4. Exaggerated 3D plots, and plots of mirror displacement for the 8 node and 16 node cases

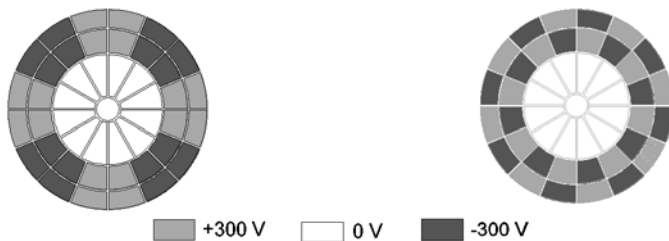


Fig. 2.5. Bias voltages used to generate the 8 and 16 node patterns

Again, the mirror was drawn in Pro-Engineer, and transferred to Pro-Mechanica for finite element analysis, and the same 45 element electrode pattern was employed. This mirror was smaller than the 1st iteration design, and the substrate was fabricated from borosilicate glass. The PZT chosen matches the thermal expansion of the glass to within 0.25 ppm/°K. If you assume that no more than 10% of the maximum stroke should be used to compensate for thermal distortions, then the effective temperature range for the bimorph is $\pm 64^\circ\text{C}$. This, in conjunction with suitable choice of epoxies and a PZT Curie temperature of $> 200^\circ\text{C}$, gives the mirror a potential operating temperature range of between -40°C and $+80^\circ\text{C}$.

Figure 2.4 shows the results of modelling the mirror, while Fig. 2.5 shows the bias voltages used to create the nodal patterns.

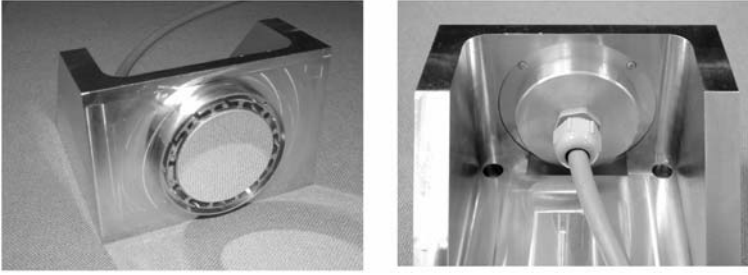


Fig. 2.6. Photographs of the fully assembled 2nd iteration mirror

As expected, the total levels of movement are reduced for the finer patterns. The plots also show that vertical movement is achieved at the mirror periphery. Photographs of the front and back of the assembled mirror are shown in Fig. 2.6.

2.3.2 Performance

The resonant frequency and deformation profile (focus mode) were measured with the laser vibrometer. In Fig. 2.7, the normalised profile of the 2nd iteration mirror is plotted together with those for the 1st iteration mirror and an unsupported, or totally free, mirror. The measured stroke and resonance are compared to the modelled results in Table 2.2.

From Fig. 2.7, it can be seen that the 2nd iteration profile provides a closer fit to the ideal, unsupported case.

From Table 2.2 it can be seen that the resonant frequency is below that predicted. The two more likely reasons for this are:

1. The effect of the adhesive is more significant than we expected, and is causing a lower resonance.
2. The “easy” fit into the mount has meant that less support is being supplied than expected to the mirror.

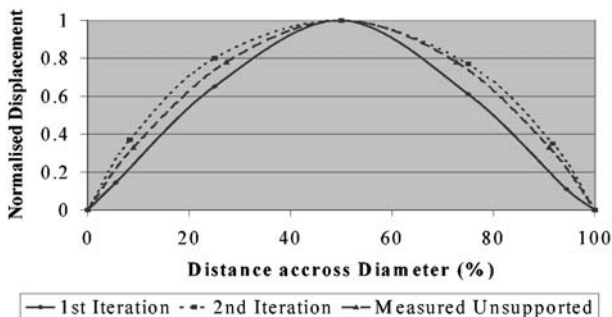


Fig. 2.7. Normalised focus mode profiles

Table 2.2. Test Results Summary for 2nd Iteration Mirror

Task	Stroke (300 V pk-pk)	Resonant Frequency
Modelled	$\pm 22.4 \mu\text{m}$	5 kHz
Measured	$\pm 25 \mu\text{m}$	2.7 kHz
% Achieved	112	54

2.4 New Concept Mirror

The latest design concept considered exploits support flexures located underneath the bimorph mirror, rather than at its edge. This increases the value of the lowest resonance, and the thickness of the mirror substrate can therefore be reduced. In the example modelled, the mirror substrate thickness is 1 mm, compared to 2.5 mm for the 2nd iteration mirror, which has the same diameter. This, in conjunction with a simplified flexure arrangement, should reduce the manufacturing cost of this option. Because of the reduction in weight, the new concept design could utilise compliant epoxy or rubber to hold the mirror in place.

Figure 2.8 shows the results of modelling the 8 and 16 node cases for this mirror.

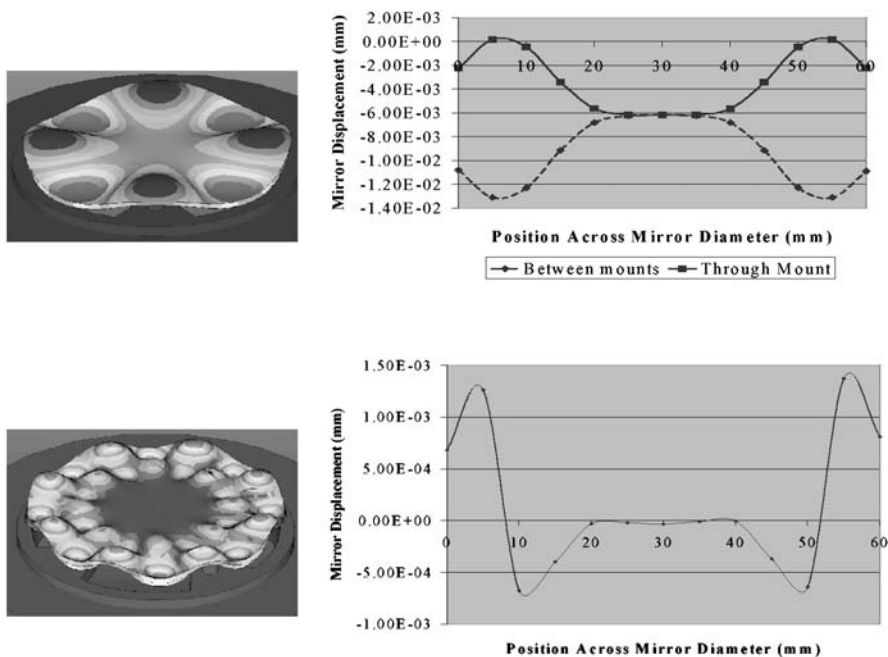


Fig. 2.8. Modelled Results: Exaggerated 3D plots, and plots of mirror displacement for the 8 and 16 node cases

As expected, the mirror sensitivity is higher in-between the mounts. In instances where the mirror is to be used in a closed loop system, this difference can be registered via the mirror's influence function. The maximum stroke and resonant frequency modelled for the mirror are $\pm 60\mu\text{m}$ and $> 11\text{ kHz}$ respectively. This performance is a significant improvement on the 2nd iteration flexure, but issues associated with the variation in mirror sensitivity, and with the increased reliance on an external tip-tilt system will need to be fully addressed before the design is taken further.

2.5 Conclusions

The 1st iteration flexure design provided an improvement over the standard rigid mounting scheme, which should nevertheless be rugged enough for military applications. The modelling enabled the assembled mirror to be close to our requirements.

The 2nd iteration flexure design provided some piston movement at the edge of the mirror, which reduced the unusable mirror area further. The profile of this mirror is very close to the unsupported case. The PZT and substrate are matched thermally to within $0.25\text{ ppm}/^\circ\text{K}$.

The new concept mirror offers the potential for a further marked improvement in performance. However, this design is at a very early stage and there are issues that will need to be addressed before further progress can be made towards a practical mirror.

Acknowledgements

Aspects of the work reported here have been carried as part of the Smart Optics Faraday Partnership entitled *A Complete Toolkit for Adaptive Optics*. The aim of the programme is to develop low cost solutions to promote the use of Adaptive Optics. The other collaborators are: Imperial College, Davin Optronics, and Optisense.

References

1. E.M. Ellis: Low-Cost Bimorph Mirrors in Adaptive Optics. PhD Thesis, IPL

3 Deformable Mirrors with Thermal Actuators

G. Vdovin^{1,2} and M. Loktev¹

¹ Delft University of Technology, EEMCS, Electronic Instrumentation Laboratory
Mekelweg 4, 2628 CD Delft, The Netherlands

² OKO Technologies
PO Box 581, 2600 AN Delft, The Netherlands

Summary. Adaptive optics is applied in lasers, scientific instrumentation, ultra-fast sciences, ophthalmology and material processing. For successful use in these applications, the deformable mirrors must be simple, inexpensive, reliable and efficient. Most of the currently used technologies based on piezoelectric, electrostrictive, electromagnetic and electrostatic actuation are rather expensive. We report on a novel type of ultra-low-cost deformable mirror with actuators based on thermal expansion. The 19-channel one inch deformable mirror has response time of ≈ 15 s, actuator stroke of about $6\ \mu\text{m}$, temporal stability of about $\lambda/10$ rms in the visible range. The mirror has shown good correction ability for low-order Zernike polynomials, therefore it can be used for correction of rather large aberrations with slow changing amplitudes in both temporal and spatial domains.

3.1 Introduction

Many scientific [1–3], industrial [4] and medical [5] applications of low-cost adaptive and active optics developed recently, require high quality wavefront correction on a slow time scale. Existing technologies of continuous faceplate deformable mirrors, bimorph mirrors [6], Liquid Crystal [7, 8] and MEMS [9, 10] devices bear certain low-cost potential [11] but are still relatively expensive, mainly due to the high price of modern materials used for fabrication. In many cases the application of fast and expensive mirrors is not justified, therefore we decided to investigate thermal actuation as an alternative technology for low-cost active optics.

3.2 Design of a Thermal Mirror

We used standard resistors used for through-the-hole-mountage as the first thermal actuators. These resistors are formed by a ceramic cylinder coated with a thin resistive layer of carbon or metal. Typical size of the ceramic cylinder are 2.2×6.6 mm with copper leads having diameter of 0.6 mm and length of up to 40 mm. The power dissipated by such a resistor can reach 0.6 W, the temperature of the resistor can be up to $100\ \text{K}^\circ$ higher than the ambient temperature. The heat is easily transferred from the ceramic body to the copper leads, and the thermal expansion of the leads will cause the

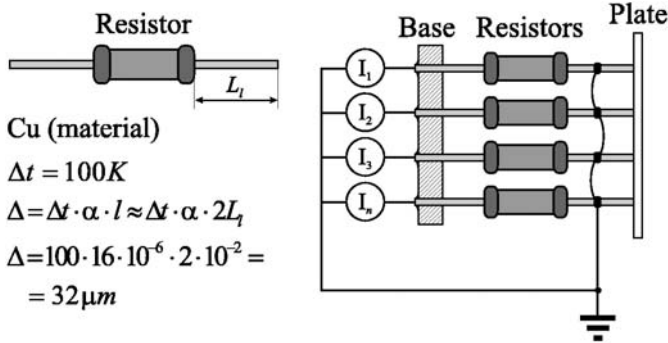


Fig. 3.1. Estimated elongation Δ of a resistor with copper leads under assumption of $\Delta t = 100 K^\circ$ change of the lead temperature. Here $L_l = 1$ cm is the lead length, $\alpha = 16 \cdot 10^{-6}$ is the coefficient of thermal expansion of copper. The right picture shows simplified schematic of a thermal deformable mirror

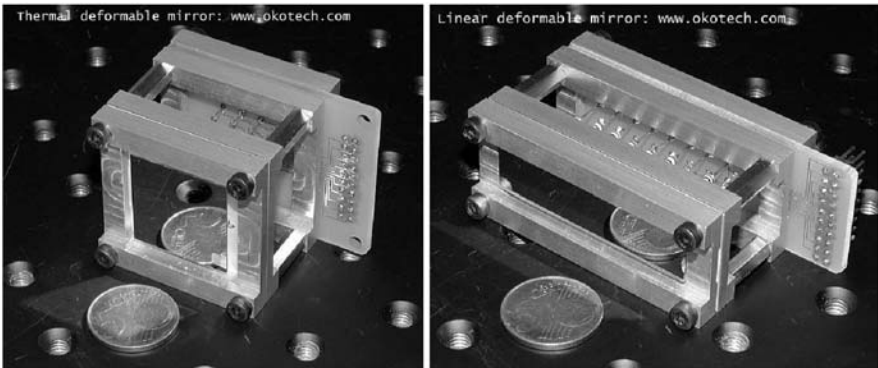
change of the length of a resistor. An example of the expected elongation is given in Fig. 3.1.

The main advantage of the resistor as a thermal actuator is its very low cost. The price of a resistor can be as low as one cent, and it can provide elongation of tens of micrometers. Piezo-ceramic actuators with comparable elongation would be priced in the range of tens to hundreds of US dollars. Naturally, thermal actuators do not demonstrate any considerable hysteresis and can be driven by a very simple current sources. Low stiffness and slow response are the main disadvantages and the design of the deformable mirror should compensate for these disadvantages.

We fabricated a deformable mirror demonstrator, formed by a 1-inch 0.75 mm-thick glass wafer supported by 19 thermal actuators placed in a hexagonal grid with a pitch of 7 mm. To achieve thermal actuation, we used SFR 16S-220R resistors. The length of the resistor depends on the resistor temperature, which can be controlled by the resistor current. Resistors chosen demonstrated up to $20 \mu m$ elongation at nominal power dissipation. To drive the deformable mirror, the resistors were soldered directly to the mirror base and glued with their leads to the back of the mirror wafer (see Fig. 3.2). The temperature of each of the 19 resistors was controlled by an individual current source with all 19 drivers occupying 100×100 mm printed board – and powered with a standard $\pm 15 V/0.5 A$ laboratory supply with total dissipation not exceeding 8 W for 19 channels. All 19 drivers were controlled using a 20-ch 8-bit DAC board installed in a PC running FrontSurfer wavefront control system (OKO Technologies). The technical data of the thermal mirrors are summarized in Table 3.1 and the interferometric patterns in Fig. 3.3. We are glad to note that the initial optical quality of our recent mirrors (one fringe) is much improved in comparison with reported in our first publication [14].

Table 3.1. Technical data of thermal mirrors

One-inch 19-ch mirror	
Aperture shape	circular
Aperture dimensions	25 mm dia
Number of actuators	19
Control voltages V_c	0...10 V
Initial RMS deviation from reference sphere	1 fringes
Same after active flattening	0.5 fringe
Main initial aberration	
response time 90%	20 s
Maximum deflection per actuator	5 μ m
Maximum optical load	10 W in a 25 mm beam
Linear mirror	
Aperture shape	rectangular
Aperture dimensions	10 \times 45 mm
Number of actuators	18
Control voltages V_c	0...10 V
Initial RMS deviation from reference sphere	up to 4 fringes
Main initial aberration	astigmatism/random
response time 90%	20 s
Maximum deflection per actuator	5 μ m
Maximum optical load	10 W in a 25 mm beam

**Fig. 3.2.** One-inch 19-ch mirror and linear mirror

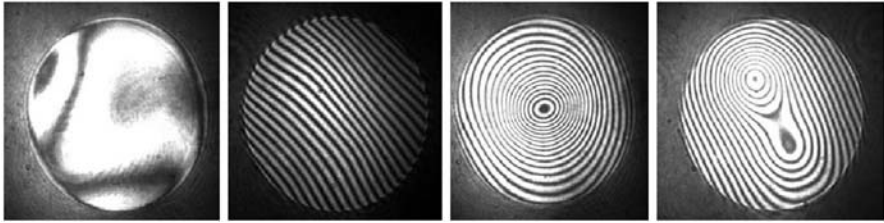


Fig. 3.3. Interferometric patterns of a one-inch 19-channel thermal deformable mirror registered in a Twyman–Green interferometer with a flat reference. The initial optical figure (zero fringe and tilted) same with central actuator on and with two actuators on (*left to right*)

3.3 Optical Performance of a Thermal Mirror

The mirror was tested in a closed-loop AOS with Hartmann wavefront sensor (see Fig. 3.4). The reference arm, normally blocked, was used for calibration of the Hartmann sensor and also provided an independent method of mirror testing by observing live interferometric patterns obtained by removing the mask and by shifting the CCD forward into the image plane.

The ability to correct low-order aberrations with large amplitude is the primary parameter, characterizing the quality of a deformable mirror. We tested the 19-ch thermal mirror as a corrector of low-order Zernike aberrations.

In the experiment we did not introduce any aberrations into the closed loop system. We followed a simple procedure:

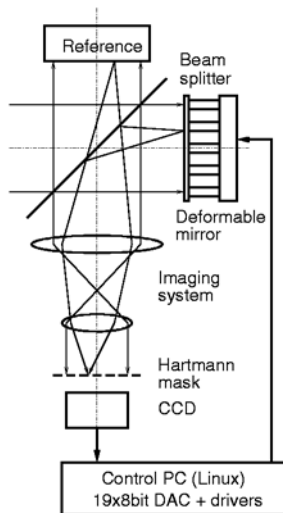


Fig. 3.4. Testing set-up with Hartmann sensor

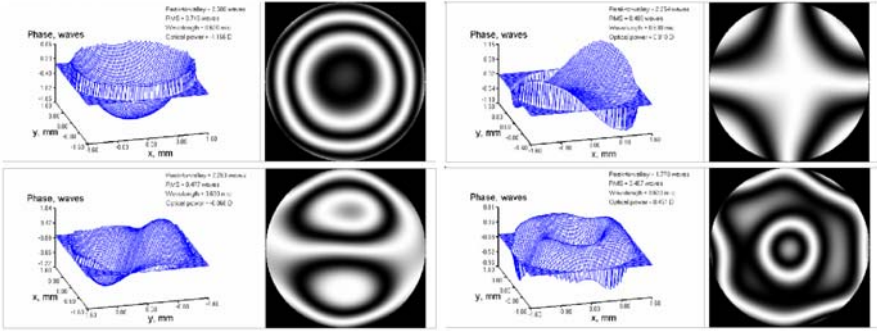


Fig. 3.5. Hartmann test reconstruction of primary aberrations formed by the thermal deformable mirror

- In the first step the mirror was planarized and the correspondent response of the Hartmann sensor was stored in the computer.
- In the second step this “target” response was modified to include the response, corresponding to the chosen aberration, and the feedback was closed to compensate for this modification. As a result, the chosen aberration was formed by the deformable mirror.
- We could measure the quality of the aberration using the Hartmann sensor and also independently, observing the interferometric pattern. The result of our measurements are shown in Fig. 3.5.

Deformable mirror demonstrated a very good ability to correct aberrations with relatively large amplitude. This ability can be explained by a large amplitude of response corresponding to any individual actuator. For example, the typical amplitude of single actuator response of a micromachined membrane deformable mirror (MMDM) does not exceed $1\ \mu\text{m}$, the amplitude of single actuator response of a thermal mirror can reach $6\ \mu\text{m}$.

The results of mode analysis is shown in Fig. 3.6. As expected, the mirror can robustly form at least 18 linearly independent modes. The last mode is rather illconditioned. We suggest the last mode corresponds to piston movement of the mirror surface, which cannot be measured by the Hartmann sensor.

To test the mirror ability of dynamic correction, we have measured the convergency time of the adaptive optical system, after static aberration was abruptly introduced in the mirror plane. The results are shown in Fig. 3.7. The typical correction time was of the order of 1 min and several aberrations were needed to achieve the optimal correction.

We have also achieved some very preliminary results using correction with feedback coefficients much larger than one and the loop period much shorter than the response time of the mirror. In this case the actuators are controlled by very short pulses with maximum amplitude, providing for very quick response of the mirror. We observed dynamically stable correction of low-order

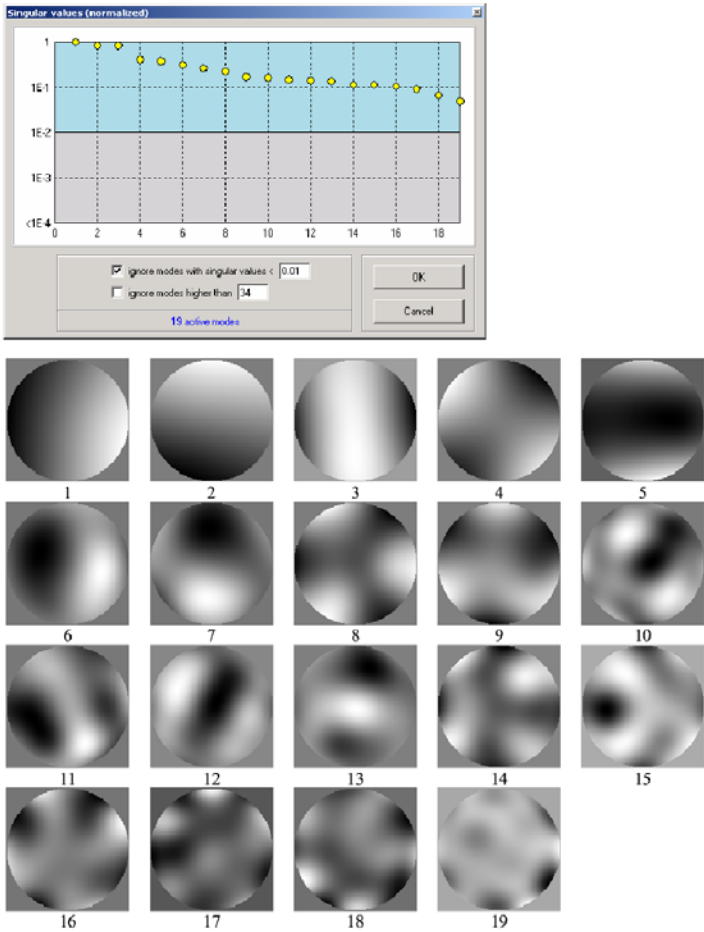


Fig. 3.6. SVD modes of the AOS with 91-subaperture Hartmann sensor and 19-ch thermal mirror

aberrations with relatively short correction times – of the order of 10 s. We observed a very interesting difference between the two approaches:

- In the case of stable correction with the feed back coefficient smaller than unity and with long delays between iterations, the convergency was rather slow, but the system remained in the right positions after the feedback loop was stopped. This can be explained by the fact that in such a mode, the control signals applied to the mirror correspond to the ones that are necessary to correct the aberration.
- In the case of quick correction with large feedback coefficients, the convergency is rather quick, but the system can remain stable only with feedback loop running. If the feedback loop is stopped, the very large control sig-

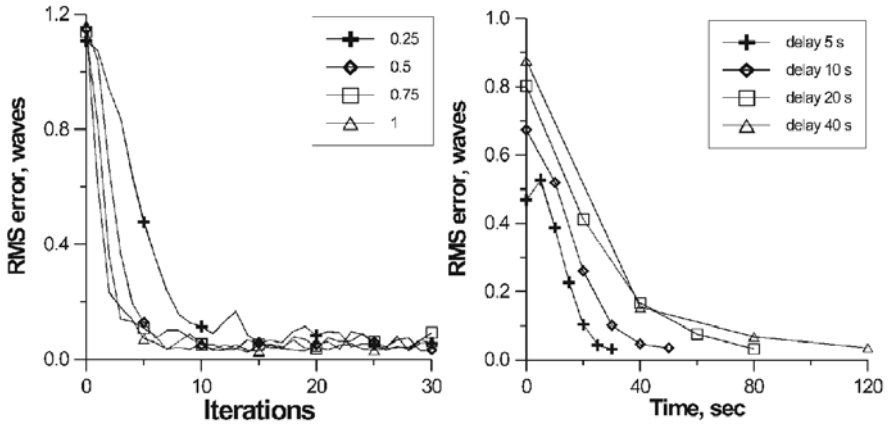


Fig. 3.7. Approximation error as a function of the feedback coefficient (*left*) and iteration delay (*right*). Best correction of a static aberration is achieved in less than 1 min

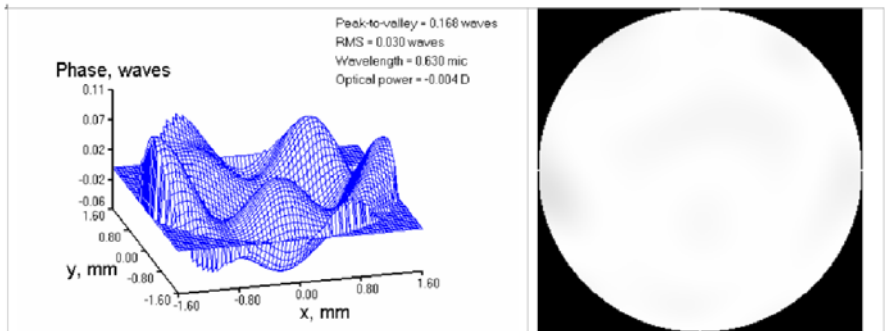


Fig. 3.8. Hartmann test reconstruction of the planarized surface of the thermal deformable mirror

nals applied to the mirror actuators for a long time will completely spoil the mirror figure. This control system can be operating only in dynamics, constantly “pushing” and “pulling” the actuators in the direction of right positions with forces that are much higher than ultimately necessary to reach these positions.

3.4 Conclusions

Thermal mirrors represent a useful alternative to more expensive mirrors based on piezoelectric and electrostatic drive. They demonstrate low hysteresis, simple control and can be fabricated on a very low expense. Naturally, the applicability of these mirrors is limited to set-ups with low correction

speed and large aberration amplitude. A good performance can be achieved by combining the thermal mirror (to correct slow large aberrations) with a faster mirror with smaller amplitude of response, to correct quick aberrations with higher spatial frequency.

References

1. M.R. Armstrong, P. Plachta, E.A. Ponomarev, R.J.D. Miller: Versatile 7-fs optical parametric pulse generation and compression by use of adaptive optics. *Opt. Lett.* **26**, 1152 (2001)
2. O. Albert, L. Sherman, G. Mourou, T.B. Norris, G. Vdovin: Smart microscope: an adaptive optics learning system for aberration correction in multiphoton confocal microscopy. *Opt. Lett.* **25**, 52 (2001)
3. R. Bartels, S. Backus, E. Zeek, L. Misoguti, G. Vdovin, I.P. Christov, M.M. Murnane, H. Kapteyn: Shaped-pulse optimization of coherent emission of high harmonic soft x-rays. *Nature* **406**, 164 (2000)
4. G. Vdovin, V. Kiyko: Intracavity control of a 200-W continuous-wave Nd: YAG laser by a micromachined deformable mirror. *Opt. Lett.* **26**, 798 (2001)
5. E.J. Fernandez, I. Iglesias, P. Artal: Closed-loop adaptive optics in the human eye. *Opt. Lett.* **26**, 746 (2001)
6. J.C. Dainty, A.V. Koryabin, A.V. Kudryashov: Low-order adaptive deformable mirror. *Appl. Opt.* **37**, 4663 (1998)
7. A.V. Kudryashov, J. Gonglewski, S. Brownie, R. Highland: Liquid crystal phase modulator for adaptive optics. Temporal performance characterization. *Opt. Comm.* **141**, 247 (1997)
8. A.F. Naumov, G. Vdovin: Multichannel liquid crystal-based wavefront corrector with modal influence functions. *Opt. Lett.* **23**, 1550 (1998)
9. M.C. Roggemann, V.M. Bright, B.M. Welsh, W.D. Cowan, M. Lee: Micro-electro-mechanical deformable mirrors for aberration control in optical systems. *Opt. Quantum Electr.* **31**, 451 (1999)
10. G. Vdovin, P.M. Sarro: Flexible mirror micromachined in silicon. *Appl. Opt.* **34**, 2968 (1995)
11. C. Paterson, I. Munro, J.C. Dainty: A low cost adaptive optics system using a membrane mirror. *Opt. Express* **6**, 175 (2000)
12. S.P. Timoshenko, S. Woinowsky-Krieger: *Theory of Plates and Shells* (McGraw-Hill, 1989)
13. J.P. Holton: *Heat Transfer* (McGraw-Hill, 1997)
14. G. Vdovin, M. Loktev: Deformable mirror with thermal actuators. *Opt. Lett.* **27**, 677 (2002)

4 Technology and Operation of a Liquid Crystal Modal Wavefront Corrector

M. Loktev and G. Vdovin

Delft University of Technology, EEMCS, Electronic Instrumentation Laboratory
Mekelweg 4, 2628 CD Delft, The Netherlands

Summary. Possibilities for implementation of a reflective-type liquid crystal modal wavefront corrector (LC-MWC) based on the silicon technology are discussed. Two possible corrector's configurations are considered; the first one is based on a continuous thin-film resistive layer, and the second one uses a network of discrete IC resistors. Technological issues of the manufacturing of silicon-based LC-MWC are discussed. Results of analysis of correction efficiency and various operation modes are presented.

4.1 Introduction

Operation of liquid crystal (LC) phase modulators is based on change of the birefringence of a thin LC layer under applied electric field. Most of the commercially available nematic LC phase modulators use pixelated structure of actuators, which allows piston-like phase correction, similar to that of piston-type segmented mirrors [1, 2]. Using of a distributed voltage divider in the design of a liquid crystal phase modulator allows realization of a wavefront corrector with modal influence functions [3]. The advantage of the modal approach is that low-order wavefront aberrations can be compensated in a continuous way using relatively small number of actuators. Recently the results of a liquid crystal modal wavefront corrector (LC-MWC) manufactured using glass-based technology were reported [4, 5]. Another technological option is represented by silicon technology; we discuss it in this paper.

Silicon technology allows to form the required structure of actuators on the surface of a silicon chip using standard integrated circuit (IC) manufacturing processes. An important advantage is provided by the possibility to integrate an optical part of the device and a part of control electronics in a single chip. In particular, it allows reducing the number of inputs of the chip relative to the number of actuators, making the technology scalable in that way.

Design and technology of the reflective-type LC-MWC with silicon backplane are discussed in this paper. We show that the voltage divider can be realized either as a continuous thin-film resistive layer or as a network of discrete IC resistors. An advantage of the second approach is that it can be implemented using standard processes, resulting in a pixelated device with much higher optical performance than that of ordinary piston-type LC modulators with the same number of control channels. Numerical simulation has

shown that relatively poor matching of resistors (10% standard deviation of the mismatch) is sufficient for proper operation of the device. We also show that optical performance of the modulator can be optimized by proper choice of the number of pixels and adjustment of individual resistances.

Previous theoretical and experimental study of LC-MWC has shown that control of additional parameters of the driving AC voltage signals, namely, frequencies and electrical phases, can be used for further improvement of performance of the device. Later it was found that the best performance and flexibility can be achieved by independent control of amplitudes and phases of driving AC voltages for all actuators, whereas amplitude-only control allows application of linear control algorithms similar to those developed for deformable mirrors, which is an important feature for using in practical adaptive optical system.

4.2 Design and Technology

4.2.1 LC-MWC with Continuous Resistive Layer

Modal principle can be implemented by introduction of a highly resistive layer into the design of standard sandwich-type LC cell (see Fig. 4.1). This layer plays an essential role in formation of the local voltage profile that controls the phase distribution across the corrector's aperture due to electro-optic S-effect. We shall refer to it as the control electrode (CE). The device is driven by AC voltages applied through the set of point-like contacts connected to the

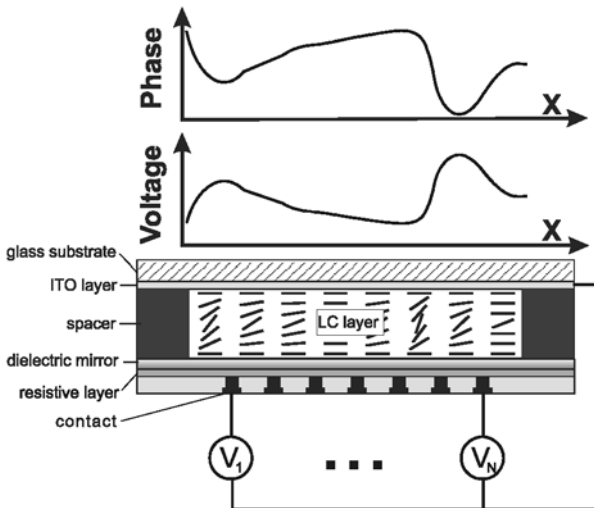


Fig. 4.1. Design and principle of operation of the liquid crystal modal wavefront corrector (LC-MWC) with continuous resistive layer

CE, which ensures smooth voltage variation across the aperture. The dielectric mirror covers the high-resistance electrode improving the LC corrector's reflectivity. Thin layer of nematic LC is sandwiched between the dielectric mirror and a transparent low-resistance electrode made of indium-tin oxide (ITO), which is placed on the top substrate. Aligning coatings deposited on the dielectric mirror and ITO electrode determine the initial homogeneous alignment of the LC molecules. The thickness of the LC layer is preset by calibrated dielectric spacers.

For single-harmonic control signal with frequency ω the distribution of complex amplitude of the voltage V over the aperture is described by the following equation, which was derived in the theory of liquid crystal adaptive lenses [7]

$$\nabla_s^2 V = \rho_s(g - i\omega c)V, \quad (4.1)$$

where ρ_s is the sheet resistance of control electrode, c and g are capacitance and conductivity of the LC layer per unit area, respectively. The voltage distribution in LC-MWC is determined by boundary conditions at the contacts, i.e., by contact voltages, but it is also influenced by capacitive and conductive properties of the LC layer. As it follows from (4.1), this influence can be minimized by appropriate reduction of the value of ρ_s ; in this case, the voltage distribution will be described by Laplace's equation

$$\nabla_s^2 V = 0. \quad (4.2)$$

The value of ρ_s should be kept high enough to prevent the CE from heating, which can affect its resistivity and properties of the LC. Our practical experience shows that it is relatively safe to keep it in the range of $0.1 \dots 10 \text{ M}\Omega/\text{sq}$.

Standard silicon microfabrication processes (bipolar and CMOS) usually include at least two layers of metallization and a silicon dioxide layer. It makes easy to manufacture the structure of contacts and connecting wires. Manufacturing of the control electrode represents the main technical challenge because standard processes do not include layers with that high sheet resistance. Recently the required properties were demonstrated for thin films of silicon carbide (SiC), which were deposited using PECVD technology and then annealed with an excimer laser [8]. We used this material in the design of a 39-channel LC-MWC.

The design is shown in Fig. 4.2. It includes two metallization layers (Al/Si alloy), one insulating silicon dioxide layer and one laser annealed silicon carbide layer, which is used for making of the CE. Contacts and contact pads are formed in the upper metallization layer, whereas the lower metal provides wiring between them. In order to provide more reliable connection between the contacts and the CE, contacts should be placed on top of the CE. It is especially important because only a thin (less than 100 nm) top layer of the SiC becomes conductive after laser annealing, whereas bulk of the material remains an insulator. Silicon dioxide layer is added to ensure reliable isolation between the wires and the CE. In order to provide connection between the

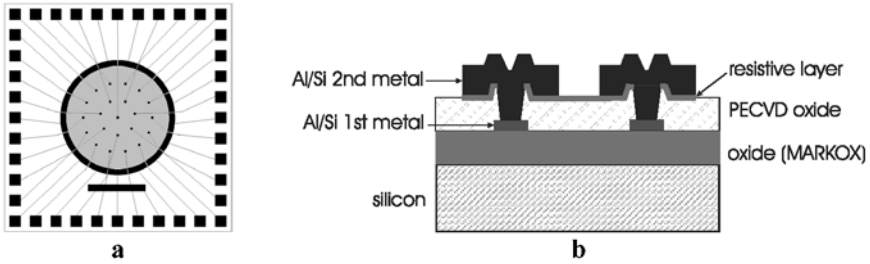


Fig. 4.2. Design of the backplane of 39-channel LC-MWC with continuous resistive layer. (a) View from top, (b) cross section

wires and the contacts, vias should be etched through both the oxide and the carbide layers.

One of the difficult issues in processing of this design is patterning of the second metal layer, as it should be done with no damage to conductive properties of the CE. At the moment the solution is not found yet. Significant roughness of the surface of SiC after annealing (10 nm rms and 80 nm peak-to-valley) represents another problem, as it may result in deterioration of quality of the dielectric mirror and LC alignment. This problem can be solved by deposition of a thick oxide layer over the whole structure and its subsequent planarization using ion beam polishing technique.

4.2.2 LC-MWC Based on Discrete IC Resistors

As we see from the previous section, manufacturing of the LC-MWC with continuous resistive layer cannot be accomplished in the framework of standard bipolar and CMOS processes; it requires additional technological steps that can increase the processing costs. Practical implementation of the proposed approach, however, can be done indirectly. In particular, it is possible to replace the continuous resistive layer by a matrix of pixels connected in a network by discrete IC resistors, as shown in Fig. 4.3. Driving signals should be applied only to some pixels in this network; we can call them *active* and other pixels *passive*. The network of resistors provides gradual voltage variation between the pixels. Such a combination of zonal and modal approaches should result in a modulator with large amount of pixels driven by much smaller number of control channels.

In case when all resistors have the same resistance, distribution of voltage in this modulator can be described by finite-differential equivalent of (4.1), where ρ_s should be replaced by the resistance of a single resistor. To take into account possible variation of individual resistances, we have performed numerical simulation using the system of equations, which consists of Kirchhoff's rules defined for all nodes of the network. The nodes, for which Kirchhoff's rules were defined, corresponded to the positions of pixels.

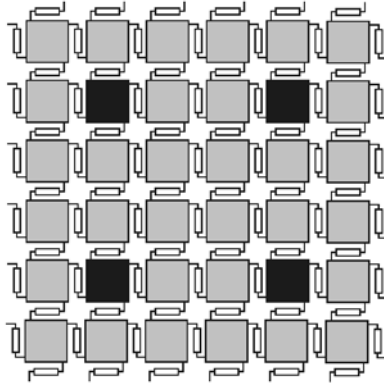


Fig. 4.3. LC-MWC based on discrete IC resistors; active pixels (those connected to the control unit) are marked *black*

To estimate how many intermediate passive pixels should be placed between two adjacent active pixels to obtain reasonable correction quality, we calculated electrical and optical responses of a modulator with 36 (6×6) active pixels and variable number of passive pixels. In this simulation we calculated influence functions of the modulator and used them for approximation of various wavefront aberrations. We assumed linear dependency of phase response of the LC from the rms voltage; for real nematic LCs it corresponds to approximately half of the total phase delay variation range.

To evaluate average optical performance of the wavefront corrector, we need to apply it to the whole class of optical fields. Earlier [9] we have developed a method, which allows evaluating statistically average efficiency of the wavefront corrector. This method used the Kolmogorov statistical model of random wavefront aberrations produced by atmospheric turbulence. Modal wavefront correction is usually described in terms of complete orthogonal sets of functions, such as Zernike polynomials or Karhunen–Loève functions. The last one is a special set of functions, best fit for representation of random wavefronts with statistics described by the Kolmogorov theory. In our method, the correction efficiency was evaluated as equivalent number of Karhunen–Loève modes resulting in the same fitting error. We also evaluated the rms error of correction in percents to the rms initial aberration.

Using this method we evaluated correction efficiency of 36-channel modulator for different numbers of passive pixels placed between two adjacent active pixels; the results are presented in Fig. 4.4. Zero number of passive pixels corresponds to the well-known case of piston corrector. The results show that the efficiency of 36-channel piston corrector is equal to 5 Karhunen–Loève modes, whereas using of passive pixels allows increasing it up to 19.7 modes, reducing the rms correction error in approximately 2 times. To demonstrate the possibility for improvement of the correction efficiency by adjustment of

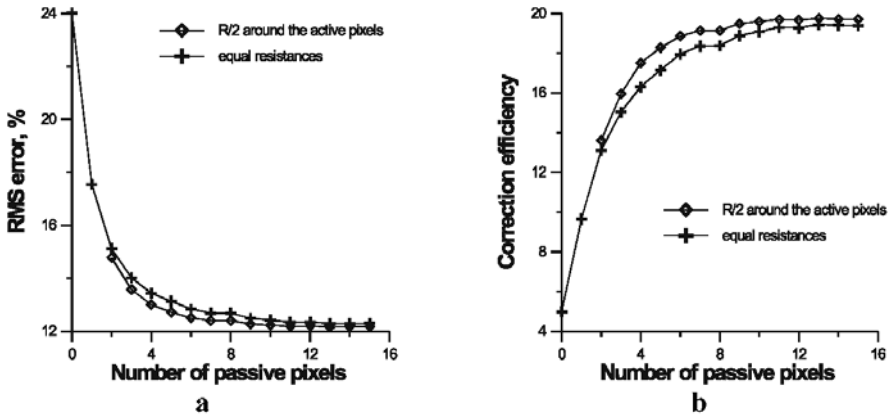


Fig. 4.4. Rms correction error (a) and correction efficiency (b) of 36-channel LC-MWC based on discrete IC resistors vs number of passive pixels placed between two adjacent active pixels

individual resistances, we have performed simulations for two different configurations of resistors. In the first case we assumed all resistances to be equal; in the second case resistances of those resistors connected to the active pixels were two times smaller than those of other resistors. Improvement in the second case is clearly seen in Fig. 4.4. To find an optimum configuration of the resistances, a special investigation can be undergone in the future.

It is seen from the graph that the correction efficiency saturates at 19.7 Karhunen–Loève modes for approximately 12 intermediate passive pixels. At the same time, for two times lower resolution (6 intermediate passive pixels) the efficiency is not significantly lower and is equal to 18.9 modes. Total amount of pixels in this case is 1296 (36×36); we used this configuration of pixels in our further simulations.

In practical IC manufacturing processes tolerances of minimum size resistors reach $\pm 30\%$, whereas different resistors in the same chip can be matched by better than 0.1% by using of special matching techniques [10]. In order to determine the type and the optimum layout of the resistors it is important to know how precisely they should be matched. With this purpose we calculated how the correction efficiency depends on the resistance error. For our calculation we used a randomly generated array of resistances with Gaussian distribution having 100 kOhm average and given standard deviation. The results presented in Fig. 4.5a show that even very large resistance variations do not seriously affect of the correction efficiency, and at 10% mismatch this effect can be neglected. We also simulated the situation when a certain amount of resistors does not function, i.e., has infinite resistance. The results in Fig. 4.5b show that 1–2% of non-functioning resistors can be tolerated. It means that the behavior of the resistive network as a whole can compensate defects of its separate elements.

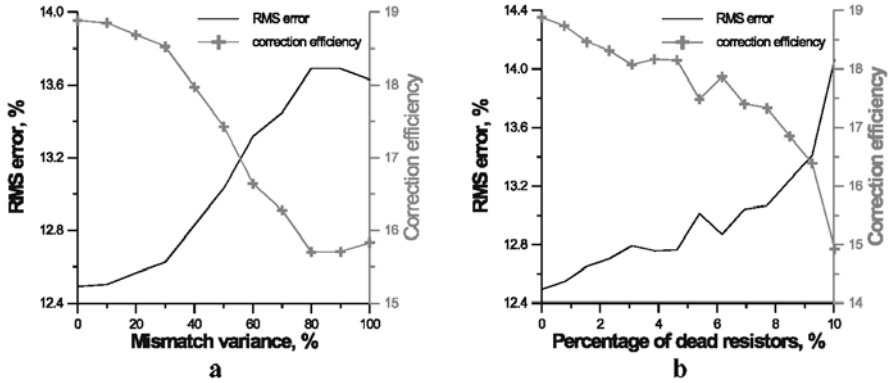


Fig. 4.5. Rms correction error and correction efficiency of 36-channel LC-MWC vs resistors' mismatch variance (a) and percentage of dead resistors (b)

Silicon processes offer many options in constructing of resistors, where polysilicon resistors represent the most preferred choice for CMOS processes and diffusion resistors for bipolar ones [10]. Diffusion resistors are preferred for this particular application as they have two important advantages. First of all, they are formed by doping of certain areas of the silicon substrate, which operation does not affect flatness of the substrate. It facilitates placement of the resistors under the layer of pixels, thus keeping fill factor of the LC modulator high; for polysilicon resistors it is much more difficult to provide. In the second place, poly resistors are more susceptible to overheating because they are usually surrounded by the oxide, which does not conduct heat well. On the contrary, monocrystalline silicon substrate material, which makes up the diffusion resistor and its surrounding, is a good heat conductor. Design of LC-MWC based on discrete diffusion-type resistors is actually at the development stage.

4.3 Control Modes of LC-MWC

The modal LC wavefront corrector is unique among other types of modal correctors in that it can be operated with several degrees of freedom per actuator. Each of the driving AC voltages is characterized by several parameters; namely, amplitude, frequency, phase and harmonic structure of the wave. It is shown that variation of any of these parameters for a given contact changes either its electro-optic response or the result of its interaction with neighboring contacts [11]. It is necessary to realize which set of control parameters provides maximum flexibility in control of the device and maximum correction quality.

With this purpose we performed investigation of several methods of control using numerical simulation and analytic approach. Some of the results

were verified experimentally using a prototype; the details are given in [6]. Two methods were found to be the most useful; they are shortly described below.

1. *Amplitude-only control*, under which means that all contacts are driven with AC voltages of the same frequency and phase, provides the correction quality close to that of deformable mirrors; efficiency of 37-channel corrector with hexagonal arrangement of contacts is estimated as 22 Karhunen–Loève modes. Due to quasi-linear behavior of the device in this mode, linear control algorithms can be implemented, which is already proved to work in experimental adaptive optical system [5].
2. *Amplitude and phase control*, which includes additional optimization of phase shifts between the voltages, can be used for further improvement of the results obtained by the 1st method. Simulations have shown that the reduction of residual aberrations due to optimization of phase shifts can reach 65%. However, this method requires using of nonlinear optimization algorithms.

The maximum flexibility of control can be achieved by combination of these two methods. Optimization can be accomplished in two stages: optimization by amplitudes using linear algorithm allows to get the first approximation in a short time; further, these results can be improved using optimization by both voltages and phase shifts. Although the major conclusions were made based on consideration of LC-MWC with continuous resistive layer, they are also applicable to the corrector’s modification based on discrete IC resistors.

4.4 Conclusion

We report on progress in development of a modal LC wavefront corrector based on silicon technology. Feasibility of the proposed approach was demonstrated in our previous publications by results of numerical simulation and experimental investigation of glass-based devices, including their operation in real adaptive optical system. In this paper we describe two possible ways of realizations of the modal LC corrector in silicon, considering arising technological problems and ways of their solution.

We show that the configuration of LC-MWC based on a continuous resistive layer requires development of additional processing steps, whereas the configuration based on a network of discrete IC resistors can be realized with no extensions to standard silicon processes. For the second case we perform analysis of the correction efficiency and investigate the influence of the resistors’ mismatch; we show that rather poor matching and even non-functioning of some resistors can be tolerated.

Finally, we discuss possibilities for using of additional degrees of freedom of driving AC voltages. In particular, simultaneous adjustment of amplitudes and electric phases provides better correction quality than amplitude-only

control; however, the latter method is more practical because it allows application of linear control algorithms.

Acknowledgements

We thank Prof. P.M. Sarro from DIMES (Delft, The Netherlands) and Dr. I.R. Guralnik from Samara State University (Samara, Russia) for useful discussions, Dr. H.T.M. Pham and J. Slabbekoorn (DIMES) for the manufacturing of resistive SiC films. This work was supported by the Dutch Technical Foundation STW, project DOE.5490.

References

1. D. Dayton, S. Browne, J. Gonglewski, S. Restaino: Characterization and control of a multielement dual-frequency liquid crystal device for high-speed adaptive optical wavefront correction. *Appl. Opt.* **40**, 2345 (2001)
2. D.J. Cho, S.T. Thurman, J.T. Donner, G.M. Morris: Characteristics of a 128×128 liquid crystal spatial light modulator for wavefront generation. *Opt. Lett.* **23**, 969 (1998)
3. A.F. Naumov, G.V. Vdovin: Multichannel LC-based wavefront corrector with modal influence functions. *Opt. Lett.* **23**, 1550 (1998)
4. S.P. Kotova, M.Y. Kvashnin et al.: Modal liquid crystal wavefront corrector. *Opt. Express* **10**, 1258 (2002), <http://www.opticsexpress.org/abstract.cfm?URI=OPEX-10-22-1258>
5. S.P. Kotova, P. Clark et al.: Technology and electro-optical properties of modal liquid crystal wavefront correctors. *J. Opt. A: Pure Appl. Opt.* **5**, S231 (2003)
6. M. Loktev, G. Vdovin, I. Guralnik: Operation modes of a liquid crystal modal wavefront corrector. *Appl. Opt.* **43**, 2209 (2004)
7. G.V. Vdovin, I.R. Guralnik, S.P. Kotova, M.Y. Loktev, A.F. Naumov: Liquid crystal lenses with programmable focal distance. Part I: Theory. Part II: Experiment. *Quant. Electr.* **29**, 256 (1999)
8. H.T.M. Pham, T. Akkaya, C.R. de Boer, P.M. Sarro: Electrical characteristics of plasma-enhanced chemical vapor deposited silicon carbide thin films. *Materials Science Forum* **433**, 451 (2002)
9. M. Loktev, D.W. De Lima Monteiro, G. Vdovin: Comparison study of the performance of piston, thin plate and membrane mirrors for correction of turbulence-induced phase distortions. *Opt. Comm.* **192**, 91 (2001)
10. A. Hastings: *The Art of Analog Layout* (Prentice-Hall, Saddle Brook, NJ 2001)
11. M. Loktev, G. Vdovin, A. Naumov, C. Saunter, S. Kotova, I. Guralnik: Control of a modal liquid crystal wavefront corrector. In: S.R. Restaino, S.W. Teare (eds.): *Adaptive Optics for Industry and Medicine* (Starline Printing 2002), pp. 145–153

5 Aberration Compensation Using Nematic Liquid Crystals

S. Somalingam¹, M. Hain¹, T. Tschudi¹, J. Knittel², and H. Richter²

¹ Technische Universität Darmstadt
Hochschulstr. 6, 64289 Darmstadt, Germany

² Deutsche Thomson Brandt GmbH
Hermann-Schwer-Str. 3, 78048 Villingen-Schwenningen, Germany

Summary. We have developed a novel transmissive nematic liquid crystal device which is capable of compensating spherical wavefront aberration that occurs during the operation of optical pickup systems. In order to increase the storage capacity, next generation optical data storage systems beyond CD and DVD will use according to the Blu-Ray specification (BD) blue laser light and an objective lens with high numerical aperture (N.A.) of 0.85. However, such high N.A. systems have an inherent higher sensitivity on aberrations. For example spherical aberration is inversely proportional to the wavelength and grows with the fourth power of N.A. of the objective lens. In an optical pickup system there are two sources for spherical aberration: The first one is the variation of the substrate thickness due to manufacturing tolerances under mass production conditions. The second one concerns disks with multiple data-layers, which cause spherical aberration when layers are switched, as the objective lens can only be optimized for a single layer thickness. We report a method for effective compensation of spherical aberration by utilizing a novel liquid crystal device, which generates a parabolic wavefront profile. This particular shape makes the device highly tolerant against lateral movement. A sophisticated electrode design allows us to reduce the number of driving electrodes down to two by using the method of conductive ladder mashing. Further evaluation in a blue-DVD test drive has been carried out with good results. By placing the device into an optical pick-up we were able to readout a dual-layer ROM disk with a total capacity of 50 gigabytes (GB). A data-to-clock jitter of 6.9% for the 80 μm and of 8.0% for the 100 μm cover layer could be realized.

5.1 Introduction

Using liquid crystal (LC) devices for aberration compensation which occurs for example in the next generation of optical pickup systems, has distinct advantages compared to alternative solutions like mechanical compensators [1, 2]. Adaptive aberration compensation by means of varying the voltage makes any moving parts unnecessary. Furthermore the power consumption of an LC device is very low and the planar construction of the LC device enables low cost mass production.

The increase of spherical aberration that occurs in the next generation BD-type pickups is a result of reduced laser wavelength from 650 nm down to 405 nm and an increased N.A. of the readout objective lens from 0.6 to

0.85. Thereby the track pitch is reduced from currently $0.74\mu\text{m}$ down to $0.32\mu\text{m}$ and the minimum pit length is reduced from $0.4\mu\text{m}$ down to $0.15\mu\text{m}$ compared to a DVD.

This enables the BD-type disk to store up to 27 GB per layer on a standardized disk of 12 cm diameter, which is five times more than the recording capacity of a current DVD. According to the following formula spherical aberration increases by the fourth power of N.A. of the objective lens and is in addition inversely proportional to the wavelength [1]. It is to remark that this approximation is good for paraxial limit by use of high N.A. lenses and short wavelengths. S is the sensitivity of the system and d denotes the cover layer thickness.

$$s = \left(\frac{d}{\lambda}\right) (\text{N.A.})^4.$$

In a BD-system spherical aberration occurs once because of mass-production limited waviness of the surfaces of the disks. A nominal waviness of $\pm 2\mu\text{m}$ on the surface requires an active correction [3, 4].

The second source for spherical aberration in a BD-system results from the optical path differences of the axial and periphery rays when switching between the data layers. The BD-type disk uses two data layers with cover layer thicknesses of typically $80\mu\text{m}$ and $100\mu\text{m}$, respectively and by focusing through the first semi-transparent data layer onto the second fully reflective data layer light passes through a spacing layer of around $20\mu\text{m}$ consisting of polycarbonate. Consider the objective lens could only be corrected to focus on one data layer perfectly. A mechanical repositioning of the lens is not favorable because of abrasion, inertia, complexity and the limited space in a pickup system.

5.2 Our Approach

One method to compensate spherical aberration is to introduce inverse spherical wavefront by placing an adequate LC device into the beam path. This operation changes the effective working distance of the objective lens and can partially compensate the spherical aberration caused by the cover layer thickness variation. The effect of the LC device in this mode of operation is similar to placing a variable telescope optic into the beam path.

Our LC device consists of concentric ring electrodes to generate parabolic phase profiles to deform the wavefront that enters the objective lens. Simulations were made using the software ZEMAX to evaluate the extent of spherical aberration in a BD-system with dual data layers and to study the effect of compensation using the LC device. It could be simulated that an 0.85 N.A. objective lens system which focuses perfectly on the $100\mu\text{m}$ data layer, shows spherical aberration in the order of $550\text{m}\lambda$ (RMS) when focusing on the $80\mu\text{m}$ layer. The tolerance limit for spherical aberration in a

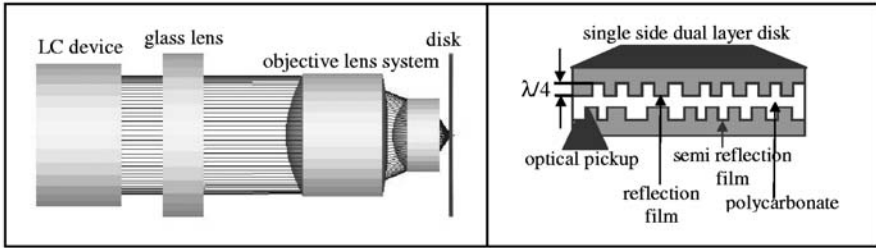


Fig. 5.1. Simulation set-up of a BD-type pickup and disk to calculate spherical aberration. The additional glass convex lens with a calculated focal length of 316 mm is necessary to generate the correct wavefront. By evaluation of the LC device in a BD test drive with 50 GB data capacity distributed on two layers, we achieved better results with a glass convex lens with $f = 400$ mm than with $f = 300$ mm

BD-system is below $20\text{ m}\lambda$ (RMS). By using the LC device a reduction down to $3\text{ m}\lambda$ (RMS) could be achieved on the $80\text{ }\mu\text{m}$ layer. For the particular simulation an objective with a double lens configuration of 0.85 N.A. and a laser diode with 405 nm were used. In Fig. 5.1 the simulation set-up contains an additional glass convex lens to inverse the wavefront profile of the LC device. The focal length of this lens was set to 316 mm. This is necessary because our LC device can only function as a concave lens. The reason will be explained later.

5.3 Working Principle and Design of the LC Device

5.3.1 Conductive Ladder Mashing (CLM)

By this method a narrow stripe lateral electrode is connected at both ends to broad driving electrodes. The whole electrode structures consist of the same ITO layer with a homogeneous sheet resistance. However the broad geometry of the driving electrodes leads to a smaller total net resistance compared to the narrow shaped lateral electrode. The resistance ratio can be adapted through admeasurements of the electrode's geometry.

Figure 5.2 illustrates the working principle of CLM. Addressing a potential difference to the driving electrodes a linear potential drop across the lateral electrode appears. Additional tapping electrodes acquire the local potential. Changing the initial potential results in changing the potential of the tapping electrodes. This method allows to vary the voltage of a huge number of tapping electrodes by varying the potential of just two driving electrodes. Otherwise the number of driving electrodes might be the same as the number of tapping electrodes to enable individual driving.

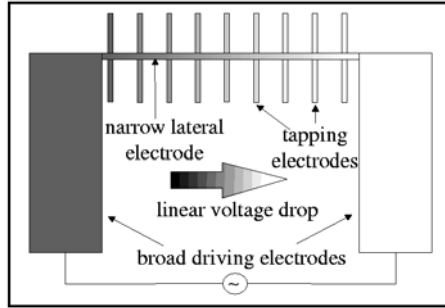


Fig. 5.2. Working principle of conductive ladder mashing

5.3.2 Electrode Design

Our LC device consists of two glass plates whose inner surfaces are coated with indium tin oxide (ITO). One of the surfaces is coated homogeneously to provide a uniform potential distribution. The second surface is provided with an electrode structure. The cell gap is filled with nematic LCs which are aligned planar through a polyimide layer. Depending on the local electric field distribution the effective birefringence Δn_{eff} , which is defined as the retardation caused by the LC molecules divided by the cell gap, changes because of the realignment of the LC molecules and therefore the local phase of the incident linear polarized light changes. This could be used to tailor the wavefront by using adequate electrode design and changing the local electric field.

The electrode structure of the second substrate consists of 33 equidistant ring electrodes with $47\ \mu\text{m}$ width and $6\ \mu\text{m}$ spacing which are conjoint with the narrow lateral stripe electrode of $20\ \mu\text{m}$ width (see Fig. 5.3). The rings are open at the opposite side where they would normally cross the lateral electrode again. These prevent a current flow. Both ends of the lateral electrode are connected to the two broad driving electrodes. The whole electrode structure was etched out of the same ITO layer of around $100\ \Omega/\text{sq.}$ sheet resistance. Because of the difference in width, the driving electrodes have a 1 : 2.5 times smaller total resistance than the narrow lateral stripe electrode. This causes the potential drop along the lateral electrode.

The conjoint spots of the rings on the lateral electrode acquire the particular local potential. And the potential changes linearly from ring to ring. In combination with the homogeneous electrode on the second substrate a spherical voltage distribution inside the cell cavity appears.

5.3.3 Driving Method

For the following measurements an LC device with a cell gap of $24.5\ \mu\text{m}$ filled with the LC mixture BL 006 from Merck Inc. was used and illuminated with a laser diode of $405\ \text{nm}$ wavelength from Nichia Inc.

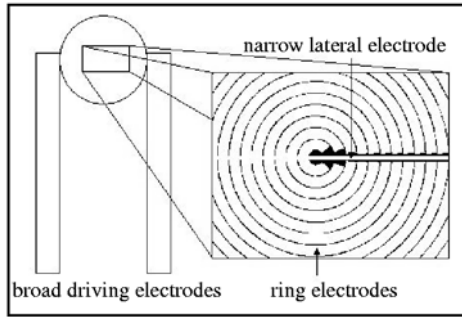


Fig. 5.3. The electrode design of the LC device using CLM technique

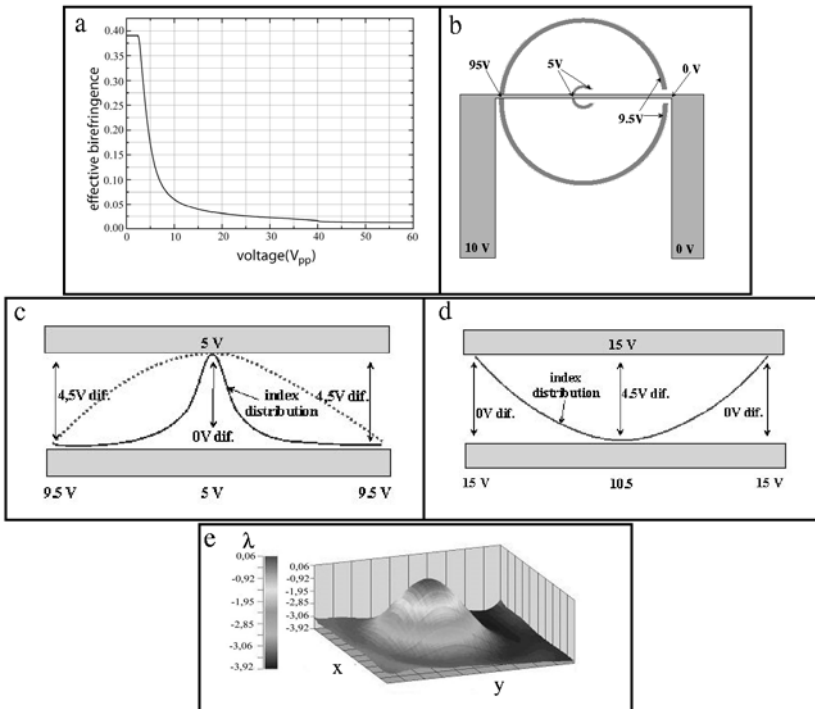


Fig. 5.4. The effective birefringence vs. voltage characteristic and a schematical driving method of the LC device is depicted. Figure 5.4e shows a measured wave-front using a Shack–Hartmann sensor

As already known the effective birefringence is a nonlinear function of the applied voltage. For our planar oriented LC device the measured dependence is depicted in Fig. 5.4a. The effective birefringence is maximal when there is no voltage applied to the cell. By increasing the voltage Δn_{eff} decreases.

The used driving scheme is depicted in Fig. 5.4b. The driving electrodes are provided with e.g. 10 and 0 V, respectively. Therefore the outer rings are provided with higher voltages than the inner rings. If the homogenous electrode is addressed e.g. with 0 V a minimum potential difference occurs in the center of the cell. Hence the phase shift in this region is maximal and it decreases towards the outer rings. According to the radial symmetry of the electrodes and the shape of the birefringence vs. voltage characteristic a narrow bell-like refractive index distribution arises, which is not sufficient for optimal focusing of the incoming beam (Fig. 5.4c). For sufficient focusing the dashed index profile is necessary. Figure 5.4e shows the measured wavefront using a Shack–Hartmann wavefront sensor, where the bell-like wavefront could be confirmed.

By reversing the applied voltages so that a higher potential difference exists in the center of the cell (Fig. 5.4d), a proper spherical index distribution arises. Nevertheless this configuration produces a concave lens. To compensate spherical aberration in a BD-system an inverse wavefront has to be generated. This was realized using an additional glass convex lens in combination with the LC device.

5.4 Implementation of the LC Device in a BD-System

For a BD-system it is important to control the spherical aberration which occurs when switching between the layers. The following solution was developed and evaluated successfully: The objective lens itself was matched to focus perfectly on one data layer, in this case on the 100 μm layer. In addition the glass convex lens and the objective lens have been adjusted to focus perfectly on the 80 μm layer when the LC device is switched off. By focusing on the 100 μm layer under this condition (objective lens + convex glass lens, LC element is not switched on) a spherical aberration of several hundreds of $\text{m}\lambda$ (RMS) originates which prevents a proper readout of the information on the disk. At the same time when the LC element is switched on, this causes collimation of the beam by degrading the power of the convex glass lens and the objective lens could focus perfectly onto the 100 μm layer. In order to quantify the performance of our LC device we measured the eye pattern and quantified the corresponding jitter value using a limit equalizer [5]. Figures 5.5 and 5.6 show the measured eye patterns for the 80 μm layer and 100 μm layer, respectively. The data-to-clock jitter values for 80 μm and 100 μm layers have been 6.9% and 8.0% (14% was measured when the LC device was switched off). These jitter values were in the range of BD-system requirements of 6.5% and 8.5% for the 80 μm and 100 μm layer and hence could be implemented in consumer BD-pickups.

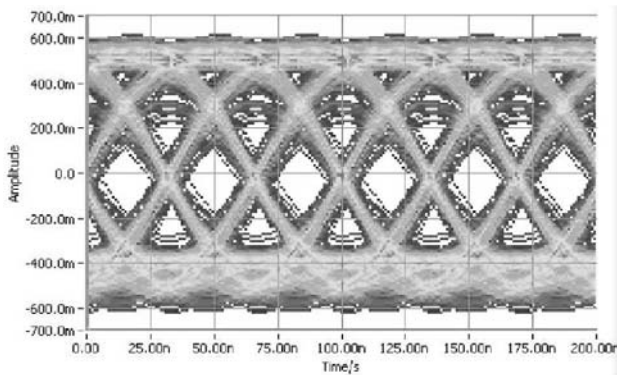


Fig. 5.5. Measured eye pattern of the 80 μm layer using limit equalizer

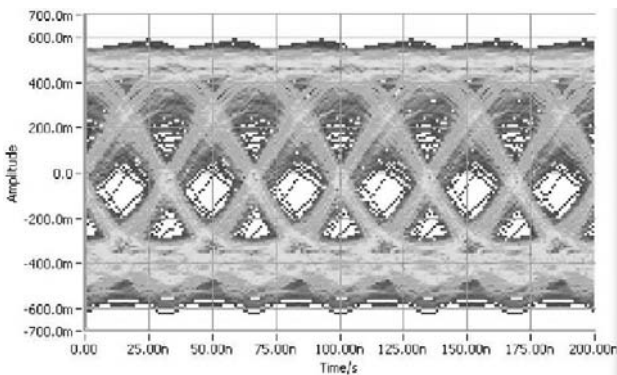


Fig. 5.6. Eye pattern of the 100 μm layer

5.5 Coma

Based on the CLM technique we have developed another LC device to compensate coma aberration that occurs in BD-type pickups when the disk tilts. Among other aberrations coma aberration dominates at small tilt angles up to 0.5° [2]. As depicted in Fig. 5.7 the phase profile of coma shows a higher and a lower phase shift level and a plateau in between. To compensate this profile an inverse phase profile is required. Therefore we divided the electrode's area according to the cross section of the laser spot into several sub domains (see Fig. 5.8a–b) and connected each domain to the tapping electrodes from the lateral electrode.

When applying appropriate voltages to the driving electrodes, the first tapping electrodes and therefore the connected sub domains will be addressed with low voltages which leads to high phase shift in this area. The last tapping electrodes are provided with high voltages and therefore the last sub domains generate low phase shifts. The comparatively large central plateau is realized

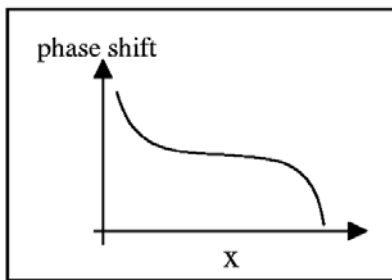


Fig. 5.7. Phase profile of coma aberration

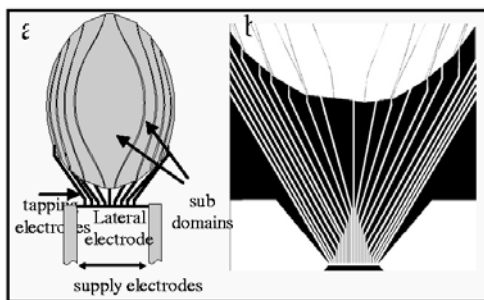


Fig. 5.8. Electrode design of the LC device to compensate coma aberration

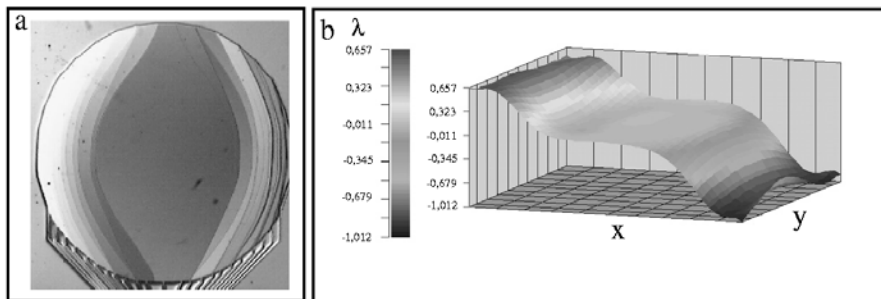


Fig. 5.9. Visualized phase shift under two crossed polarizers and the measured phase profile using a Shack–Hartmann sensor

using an appropriate large sub domain, which is provided with a medial voltage. Figure 5.9a visualizes the different phase shifts under two crossed polarizers when illuminated with white light. Figure 5.9b shows a preliminary measurement of the wavefront when LC device was switched on. One can see clearly the typical phase profile of coma. Changing the initial voltage distribution results in a variation of the total phase shift. Evaluations in a BD-type pickup have not been taken place yet.

5.6 Conclusion and Outlook

We have demonstrated two types of LC devices based on enhanced conductive ladder meshing technique to compensate spherical and coma aberration that occurs in the next generation of optical data storage systems like the Blu-Ray standard. The compensation of spherical aberration in a test drive with a total capacity of 50 GB could be demonstrated with data-to-clock jitter values of 6.9% and 8.0% for the 80 μm and 100 μm data layer, respectively.

The low switching performance of our LC devices in the range of 4–10 Hz leaves room for improvements. Also the concept of multifunctional LC devices could be considered for the compensation of higher order aberrations.

Acknowledgements

The authors would like to thank BMBF for financial support in this research under the project “Blue Spot” (FZ: 01BS050A).

References

1. S. Stallinga, J. Vreken, J. Wals, H. Stapert, E. Versteegen: Liquid crystal aberration compensation devices. Optical storage and optical information processing. Proc. SPIE **4081**, 50 (2000)
2. S. Ohtaki, N. Muraio, M. Ogasawara, M. Iwasaki: The applications of a liquid crystal panel for the 15 GByte optical disk system. Jpn. J. Appl. Phys. **38**, 1744 (1999)
3. J. Braat: Influence of substrate thickness on optical disk readout. Appl. Opt. **36**, 8056 (1997)
4. J. Knittel, H. Richter, M. Hain, S. Somalingam, T. Tschudi: A liquid crystal lens for spherical aberration compensation in a blu-ray disc system. To be published
5. S. Miyanabe, H. Kuribayashi, K. Yamamoto: New equalizer to improve signal-to-noise ratio. Jpn. J. Appl. Phys. **38**, 1715 (1999)

6 Wireless Control of an LC Adaptive Lens

G. Vdovin^{1,2}, M. Loktev¹, and X. Zhang¹

¹ Delft University of Technology, EEMCS, Electronic Instrumentation Laboratory
Mekelweg 4, 2628 CD Delft, The Netherlands

² OKO Technologies
PO Box 581, 2600 AN Delft, The Netherlands

Summary. We consider using liquid crystal adaptive lenses to correct the accommodation loss and higher-order aberrations of the human eye. In this configuration, the adaptive lens is embedded into the eye lens implant and can be controlled through a wireless inductive link. In this work we experimentally demonstrate a wireless control of a liquid crystal adaptive lens in a wide range of its focusing power by using two coupled coils with the primary coil driven from a low-voltage source through a switching control circuit and the secondary coil used to drive the lens.

6.1 Introduction

The aberrations of the human eye can significantly contribute to the loss of the visual acuity [1]. The resolution of the retina can be higher than the resolution of the human eye [2] optic. Traditional correction with spectacles and contact lenses is useful for only two aberrations – defocus and astigmatism [3, 4]. To correct the higher-order aberrations, the corrector should be optically conjugated to the eye pupil. To achieve such a conjugation, an imaging optical system is used to make the image of the corrector co-incident with the eye. Breadboard adaptive optical set-ups based on this principle demonstrate the feasibility of high-order correction [5–7]. These breadboard set-ups cannot be converted into wearable devices due to their bulkiness and complexity.

Another ophthalmic problem that can be corrected with adaptive optics is the age-related or post-surgery loss of accommodation. Attempts were made to develop a corrector for presbyopia [8] with moderate practical success.

Here we present the first results of our experiments with inductive wireless control of a liquid crystal wavefront corrector, proving the technical feasibility of dynamic correction of human-eye aberrations by placing the wavefront corrector directly into the pupil of the human eye.

6.2 Liquid Crystal Wavefront Correctors

Liquid crystal (LC) lenses, demonstrated recently [9–11], are well suited for wavefront correction in the human eye because of their small size – several

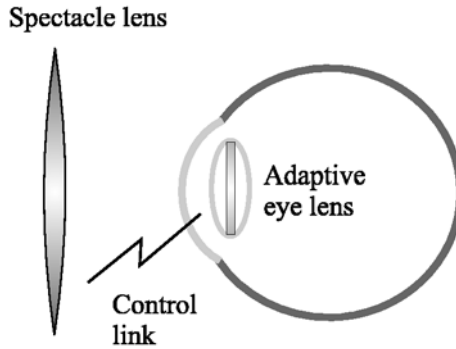


Fig. 6.1. Implantable adaptive eye lens

mm in diameter, with the thickness limited ultimately by the thickness of the LC layer which is 10–50 μm , low power consumption – of the order of tens of microwatts, low control voltages – in the range of 0–10 V and a wide range of optical power: up to $\approx 3\text{D}$ – which corresponds to infinity to $\approx 30\text{ cm}$, translated into the accommodation depth of the human eye.

The modal liquid crystal lens [9] consists of two electrodes with an oriented layer of nematic LC between them. The amplitude and spectral composition of the applied bipolar *ac* voltage can be used to control the optical power and radial aberrations of the modal LC lens [12]. Azimuthal components can be realized by splitting the annular control ring into sectors with independent control signal applied to each sector.

Although technically challenging, all optical and electrical parts of the liquid crystal modal corrector, including wireless control, can be integrated between two thin sheets of transparent plastic with a total thickness of the order of tens of micrometers using a “Silicon-on-anything” technology [13].

In case the LC lens is implanted into the human eye or used as a contact lens, it should satisfy the following requirements:

- The corrector should combine adaptive optics with the receiving of external control signals. In addition, some kind of feedback – either psychophysical or objective – should be present to generate the control signals. In the simplest case, manual control of the focusing power and spherical aberration of the corrector can be implemented.
- Both the LC material and the lens optics should be biologically compatible. Not all LC materials satisfy these requirements [14]. Merck’s data sheets declare liquid crystal materials “not acutely toxic”, moreover according to tests conducted on 224 liquid crystal substances [15], 215 compounds did not have any acute toxic potential. Eye irritation tests performed with 14 LC compounds proved all 14 compounds to be non-irritant.

- A simple LC lens acts only on one polarization state of light. There are two ways to use the lens with randomly polarized light: to combine it with a linear polarizer – resulting in a light loss of 50%, or to combine two lenses acting on orthogonal polarization states.
- While the implantable lens dimensions should not exceed 4 mm in thickness and 9 mm in diameter – about the size of the eye lens [16], the adaptive contact lens thickness should be limited to several tens of micrometers – the typical thickness of an ordinary soft contact lens.

6.3 Wireless Control

The adaptive lenses described above can easily be fabricated to match the size of the human eye lens. However, it is much more difficult to organize the wireless control, as, we believe, no wires can be used in the human eye and no battery can be embedded into the lens.

The wireless link to the intra-ocular lens should supply the necessary power and at the same time it should carry the information about the optical parameters of the corrector, such as the optical power and the aberration terms. In the case of an adaptive lens with an analog ac drive, the focusing power will correspond to the amplitude of the signal, while the radial aberrations can be controlled by the signal spectrum [12].

The typical power required to drive the lens is in the range of $50\ \mu\text{W}$ to $1\ \text{mW}$ (see Fig. 6.2), depending on the control frequency and the parameters of the coating and the liquid crystal. This power should be transferred to the lens through the wireless link.

As a control principle, we consider an inductive link using linked coils (see Fig. 6.2). The transmitter coil is integrated into the frame of the spectacles,

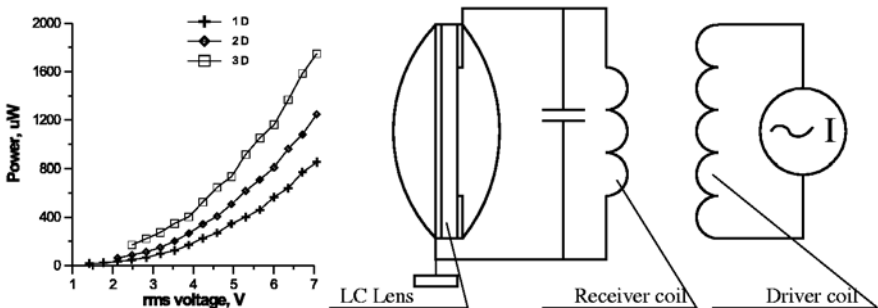


Fig. 6.2. Experimentally measured reactive power required to drive the LC lens as a function of the driving voltage and the focusing power. Since the lens is a reactive load, the active power dissipated in the lens is considerably smaller than shown in this graph. The right figure shows the schematic of inductive control of an LC lens

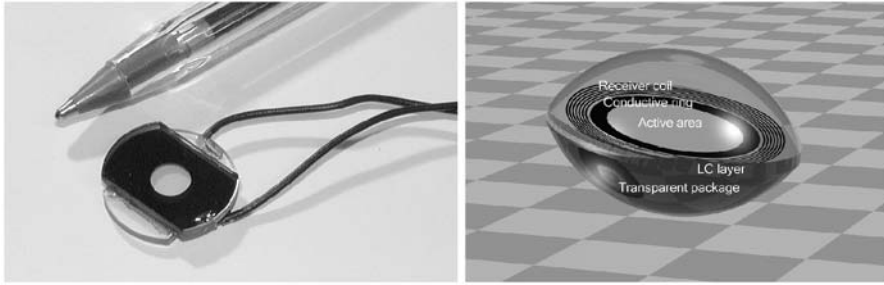


Fig. 6.3. Adaptive LC lens fabricated for experiment with wireless control (*top*) and 3D model of a wireless implantable LC corrector with integrated receiver coil for remote control (*bottom*)

while the receiver coil is integrated in the adaptive LC lens, around the optically active area (see 3D model in Fig. 6.3).

6.4 Experimental Results

We have fabricated a number of adaptive LC lenses with a diameter of 15 mm and thickness of 4 mm, with a clear light aperture of 5 mm and the LC layer thickness of 25 and 50 μm (see Fig. 6.3). These dimensions were dictated by the ease of manufacture. Nevertheless, the optical parameters of the lens are close to those required for intra-ocular application; the main difference is the overall size and the lack of integrated control electronics and a wireless link.

For a wireless control driving system, a two-coil apparatus controlled and driven by a switching circuit has been designed and fabricated. A schematic diagram of the wireless control driving system for LC optical component, which consists of a electronic switch, an oscillator coil generating the driving voltage and an inducting coil connected with the LC lens, as illustrated in Fig. 6.4. The electronic switch was designed to have the ability of driving the power MOSFET (BUZ11) in a relatively low operating frequency of a few KHz. The typical diameters of the primary coil were in the range of 16–50 mm and the windings of the coils were in the range of 5–40 turns. The secondary coils were fabricated with 10–100 turns. The effective distance between the primary and the secondary coils were varied in the range of about 0–60 mm. The voltage, used to drive the switching circuit was adjustable in the range of 0–30 V, with maximum primary coil current of 1 A.

We tested the optical performances of the LC device driven by the coupled-coil system. The images were obtained with a CCD camera attached to a computer to demonstrate the optical interference behaviors of LC device used. The pictures indicating the corresponding optical performance are shown in Fig. 6.5.

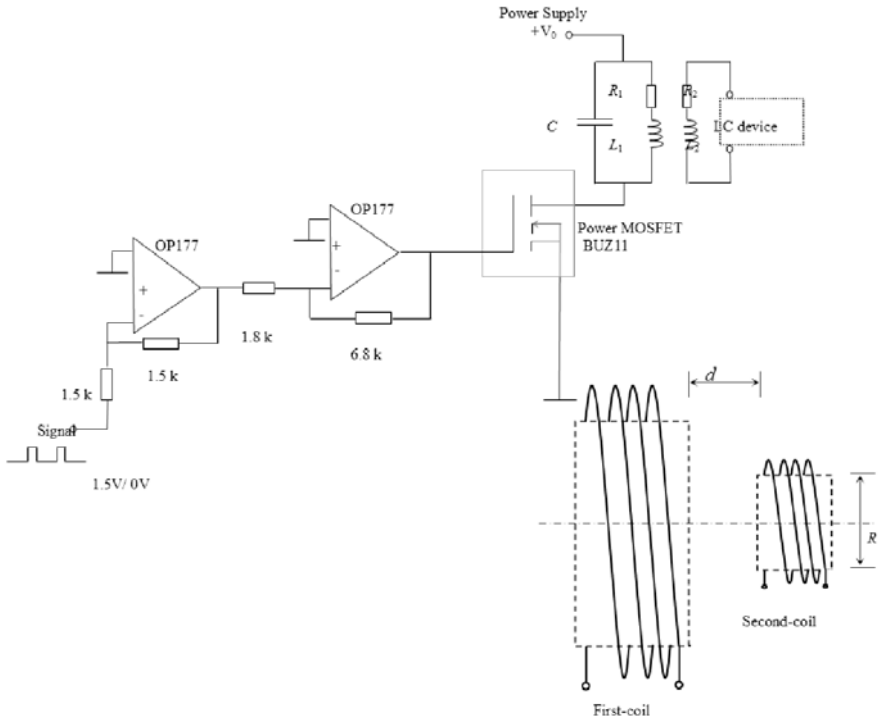


Fig. 6.4. Switching circuit used to drive the LC lens

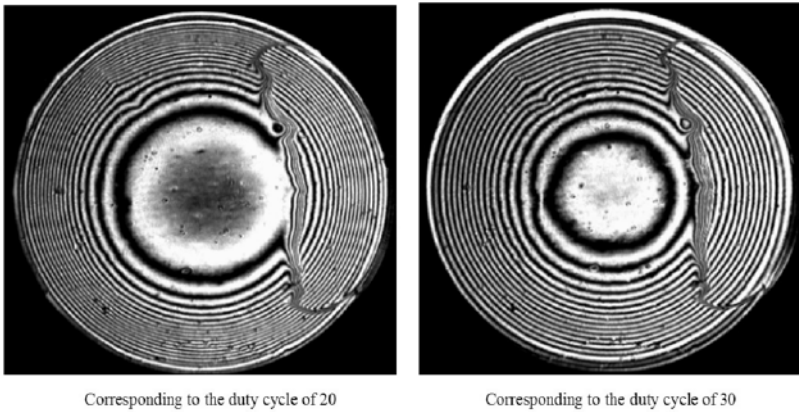


Fig. 6.5. Interferometric patterns obtained with wireless control of the LC lens. The lens was fabricated with a defect in the right side, which did not influenced the efficiency of control

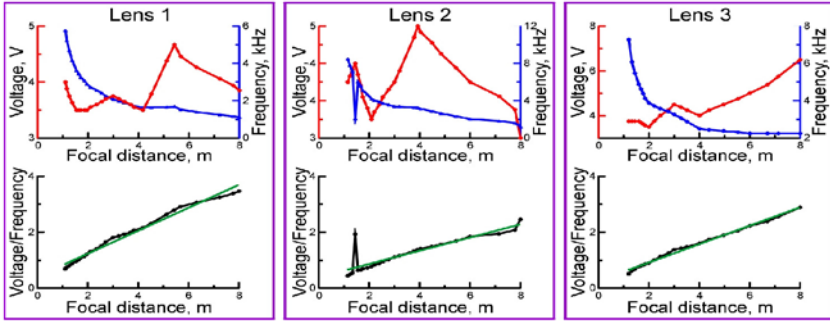


Fig. 6.6. Voltage-frequency calibration curves for three different LC lenses

Our experiments resulted in a reliable control of the optical power in the whole range of the adaptive LC lens (see Fig. 6.5). Figure 6.6 gives an impression of the combination of the control voltage and frequency that should be applied to the LC lens to control only defocus. Deviations from these values normally result in additional radial aberrations that can be also calibrated and used to correct the aberrations of the eye. In the case of switching control the driving voltage has a very special shape, therefore a special calibration of the driver is necessary to provide predictable and aberration-free behavior of the lens.

6.5 Conclusions

As published recently [2, 5, 6] the resolution of the human eye can be improved by correcting the eye lens aberrations. Compensation of high-order aberrations is possible only if the corrector is optically conjugated with the eye lens.

We have proposed and implemented a wireless inductive control circuit, enabling efficient wireless control of an LC modal lens. In the future, such a lens can be implanted into the human eye for correction of accommodation loss.

Based on the results of our preliminary experiments, it seems possible to develop a wireless-controlled adaptive contact lens or eye lens implant for correction of accommodation loss and also, in the future, multichannel correctors for dynamic correction of high-order aberrations of the human eye.

References

1. J. Liang, B. Grimm, S. Goelz, J.F. Bille: Objective measurement of wave aberrations of the human eye with the use of a Hartmann–Shack wavefront sensor. *J. Opt. Soc. Am.* **11**, 1949 (1994)

2. K.N. Ogle: On the resolving power of the human eye. *J. Opt. Soc. Am.* **41**, 517 (1951)
3. R. Navarro, E. Moreno-Barriuso, S. Bara, T. Mancebo: Phase plates for wave aberration compensation in the human eye. *Opt. Lett.* **25**, 236 (2000)
4. M.P. Cagigal, V.F. Canales, J.F. Castejon-Mochon, P.M. Prieto, N. Lopez-Gil, P. Artal: Statistical description of wavefront aberration in the human eye. *Opt. Lett.* **27**, 37 (2002)
5. N. Doble, G. Yoon, L. Chen, P. Bierden, S. Oliver, D.R. Williams: Use of a microelectromechanical mirror for adaptive optics in the human eye. *Opt. Lett.* **27**, 1537 (2002)
6. F. Vargan-Martin, P.M. Prieto, P. Artal: Correction of the aberrations in the human eye with a liquid crystal spatial light modulator: limits to performance. *J. Opt. Soc. Am. A* **15**, 2552 (1998)
7. E.J. Fernandez, I. Iglesias, P. Artal: Closed-loop adaptive optics in the human eye. *Opt. Lett.* **26**, 746 (2001)
8. C.W. Fowler, E.S. Pateras: Liquid crystal lens review. *Ophthalm. Physiol. Opt.* **10**, 186 (1990)
9. A.F. Naumov, M.Y. Loktev, I.R. Guralnik, G. Vdovin: Liquid crystal adaptive lenses with modal control. *Opt. Lett.* **23**, 992 (1998)
10. A.F. Naumov, G. Vdovin: Multichannel liquid crystal based wavefront corrector with modal influence functions. *Opt. Lett.* **23**, 1550 (1998)
11. S.P. Kotova, M.Y. Kvashnin, M.A. Rakhmatulin, O.A. Zayakin, I.R. Guralnik, N.A. Klimov, P. Clark, G.D. Love, A.F. Naumov, C.D. Saunter, M.Y. Loktev, G.V. Vdovin, L.V. Toporkova: Modal liquid crystal wavefront corrector. *Opt. Express* **22**, 1258 (2002), www.opticsexpress.org/abstract.cfm?URI=OPEX-10-22-1258
12. A.F. Naumov, G.D. Love, M.Y. Loktev, F.L. Vladimirov: Control optimization of spherical modal liquid crystal lenses. *Opt. Express* **4**, 344 (1999), www.opticsexpress.org/abstract.cfm?URI=OPEX-4-9-344
13. J. Bruines: Process outlook for analog and rf applications. *Microelectronic Engineering* **54**, 35 (2000)
14. B. Simon-Hettich, W. Becker: Toxicological investigations of liquid crystals. In: 28th Freiburg Workshop on Liquid Crystals. Freiburg 1999
15. W. Becker, B. Simon-Hettich, P. Hnicke: Toxicological and ecotoxicological investigations of liquid crystals and disposal of lcds. Merck brochure, Merck KGaA, Liquid Crystals Division and Institute of Toxicology. Darmstadt 2001
16. E. Hecht: *Optics*. 3rd edn. (Addison Wesley, Longman 1998), Chap. 5, pp. 203–205
17. R.E. Bedford, G. Wyszecki: Axial chromatic aberration of the human eye. *J. Opt. Soc. Am.* **47**, 564 (1947)
18. L. Llorente, L. Diaz-Santana, D. Lara-Saucedo, S.L. Marcos: Aberrations of the human eye in visible and near infrared illumination. *Optometry and Vision Science* **80**, 26 (2003)
19. T.L. Kelly, A.F. Naumov, M.Y. Loktev, M.A. Rakhmatulin, O.A. Zayakin: Focusing of astigmatic laser diode beam by combination of adaptive liquid crystal lenses. *Opt. Commun.* **181**, 295 (2000)

7 Summary of Adaptive Optics at Stanford

P. Lu, Y.-A. Peter, E. Carr, U. Krishnamoorthy, I.-W. Jung, O. Solgaard, and R. Byer

Stanford University, Ginzton Laboratory
450 Via Palou, Stanford, CA 94305-4088, USA

Summary. The status of adaptive optics at Stanford is summarized. Particular focus is given to the fabrication and testing of segmented, micro-mirror SLMs developed under the CCIT (Coherent Communications, Imaging, and Targeting) project [1]. Square and hexagonal “ 5×5 ” and “ 32×32 ” arrays have been fabricated using MEMS technology, and “ 5×5 ” arrays have been characterized.

7.1 Introduction

For the past two years, the development of wavefront correction technology at Stanford has supported the CCIT (Coherent Communications, Imaging, and Targeting) project [1]. Funded by DARPA, its main objective is to develop a million-pixel mirror array capable of piston and tip/tilt motions and associated packaging and electronics. The principal participants in this project are the Lawrence Livermore National Laboratory (electronics and testing), MicroAssembly Technologies (packaging), Lucent Technologies (packaging and testing), Boston University (fabrication and testing), Boston Micromachines (fabrication and testing), and Stanford University (fabrication and testing).

Potential applications of these mirror-based spatial light modulators include secure free space communication, aberration correction for lasers, astronomy, ophthalmology, nano-scale manipulations of particles, projection displays, and maskless photolithography.

Table 7.1 summarizes the requirements of the CCIT project.

7.2 History of CCIT Mirror Development at Stanford

The program milestones included the development of piston-only mirrors prior to the fabrication of mirrors capable of piston motion in combination with rotation on two orthogonal axes (tip/tilt motion). The first generation micro-mirror piston SLMs developed for the CCIT project at Stanford [2] used a commercial MEMS process called MUMPs[®] [3, 4]. Mirror and electrode chips were made in parallel and integrated via flip-chip bonding. This permits separate optimization of mirrors and electrodes and prevents print-through of electrode patterns on the mirror surface.

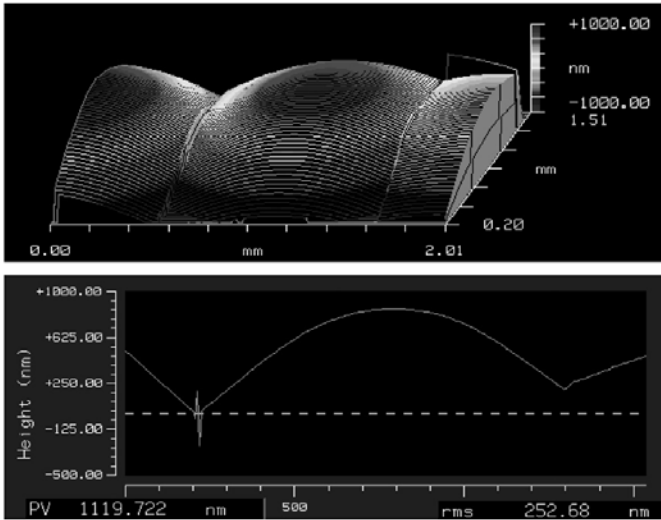


Fig. 7.1. One MUMPs mirror measured using an interferometric profilometer. The height between the center and the edge due to stress is greater than one micron

Though the convenience of having a commercial foundry complete most of the fabrication steps offers a compelling reason to use MUMPs, the flatness requirements of the project were not met. Under MUMPs, mirror surfaces were made of polysilicon, which was deposited with small but finite stress gradients. After an HF release, these mirrors became highly curved. Figure 7.1 shows measurements made of an array completed using this process. The difference in mirror height between the center of a pixel and its edge is over one micron, which exceeds the target actuation depth of $0.75\ \mu\text{m}$.

Table 7.1. CCIT project requirements

Category	Requirement
Pixel size	$100\ \mu\text{m} \times 100\ \mu\text{m}$
Pixel count	10^6
Pixel flatness	$\lambda/50$ at $1.5\ \mu\text{m}$, or $30\ \text{nm}$
Piston response time	$\leq 10\ \mu\text{s}$, or resonant frequency $> 100\ \text{kHz}$
Tip/tilt response time	$\leq 100\ \mu\text{s}$, or a resonant frequency $> 10\ \text{kHz}$
Fill factor	$> 98\%$
Piston stroke depth	$\lambda/2$ at $1.5\ \mu\text{m}$
Piston resolution	≥ 8 bits or 256 levels, or $3\ \text{nm}$
Tip/tilt max deflection	$\pm 10^\circ$ mechanical, or $\pm 20^\circ$ optical
Tip/tilt resolution	≥ 10 bits or $200\ \mu\text{rad}$
Operating voltage	$\approx 100\ \text{V}$

7.3 SOI Process: Fabrication

An alternate process was developed to address mirror flatness based on SOI technology, which previously has been shown to yield devices with high surface quality [5, 6]. SOI wafers typically consist of a 500 μm silicon substrate and a 5–10 μm device layer separated by a micron of thermal oxide. Under this process, the device layer, composed of bulk silicon, becomes the mirror surface. This leads to improved pixel flatness values that exceed the program specifications.

Like the MUMPs process, this new process involves flip-chip bonding. The procedure for fabricating mirror chips is as follows:

- Discrete mirror elements, or pixels, are patterned onto the device layer of an SOI wafer using a Deep Reactive Ion Etch (DRIE) based on the Bosch process (Fig. 7.2).
- A one micron layer of low-temperature oxide is then deposited using Low-Pressure Chemical Vapor Deposition (LPCVD). This is a sacrificial layer which must be removed later.
- Next, a wet etch, using a 6 : 1 Buffered Oxide Etch (BOE), creates holes in the oxide directly over the center of each pixel.
- Then a 2 μm layer of amorphous silicon is deposited with another LPCVD. This layer will eventually become the actuator, or spring which bends and flexes to allow mirror motions.
- The actuator needs to be conductive, so 0.4 μm of phosphorous-doped oxide is deposited onto this layer, annealed for an hour, and then stripped. This allows for the diffusion of dopants into the amorphous silicon layer.
- Then, spring structures are patterned onto the amorphous silicon layer using a RIE (Fig. 7.3).
- Following this, gold bond pads are deposited at specific sites on the actuator. The gold bond pads of the mirror chip are then aligned to the gold pads of the electrode chip, and the two chips are pressed together at 100 MPa and heated to 300°C.
- Next, the silicon substrate is removed using either a XeF_2 or Bosch etcher.
- Then, 49% hydrofluoric acid (HF) is used to remove the sacrificial oxide layers, and a critical point drying procedure is performed.
- Finally, the array is wire-bonded (Fig. 7.5).

7.4 SOI Process: Fabrication Results

Arrays composed of hexagonal and square pixel elements were both fabricated. Hexagonal arrays had sizes of 19 and 1027 elements, and square arrays of 25 and 1024 elements. For convenience, the smaller arrays will be referred to as “5 \times 5” and the larger ones as “32 \times 32”. The “5 \times 5” arrays have been assembled and tested. Figure 7.6 shows that single pixels on a “5 \times 5”

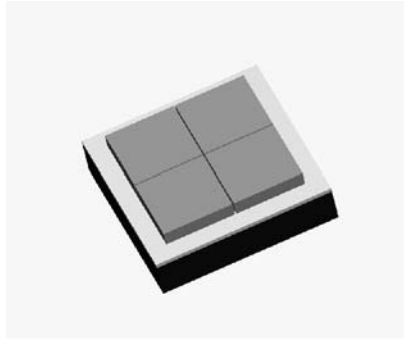


Fig. 7.2. *Top and bottom:* silicon device layer patterned with mirrors, oxide, silicon substrate



Fig. 7.3. Patterned actuators. The sacrificial oxide layer not shown

array were flat to within 2 nm as measured by a white-light interferometer, with 30 nm rms of roughness and one meter of curvature for the entire array. Figure 7.7 shows a static actuation measurement made of a square “5 × 5” array. A half-wavelength of displacement was achieved at 80 V. Based on the observed spring constant, the resonant frequency is calculated to be 80 kHz. Square pixels are 200 μm in size while hexagonal pixels are 300 μm. The gap between mirrors is 2 μm. This corresponds to a fill factor of over 99%.

The “32 × 32” arrays have been fabricated, though with less reliability than the “5 × 5” arrays. Frequently, the mirror and electrode chips become debonded after the substrate is removed, possibly because of stress between the Si and SiO₂ layers producing lateral shear forces on the gold to gold bond junction. This stress does not cause problems in “5 × 5” arrays, but becomes increasingly significant when array sizes are scaled upwards.

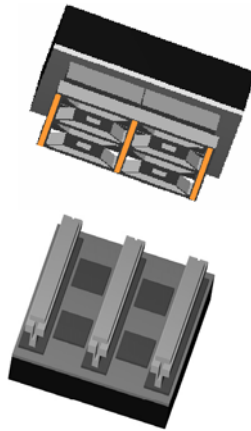


Fig. 7.4. Top and bottom chips ready for bonding

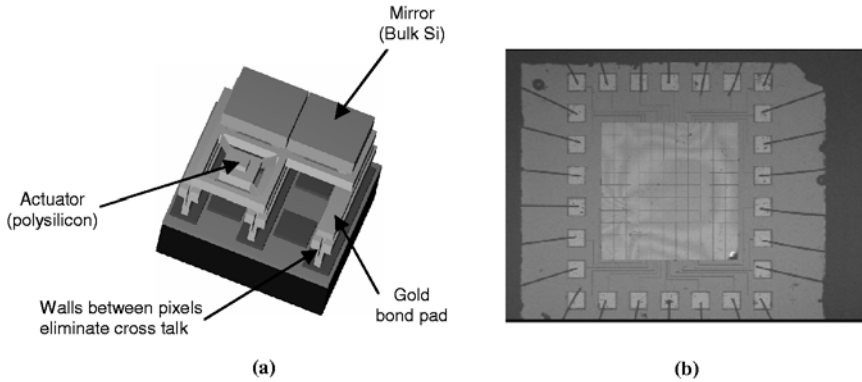


Fig. 7.5. (a) 3-D model of completed array. (b) Square “5 × 5” array–wire-bonded and surrounded by dummy pixels (total 11 × 11)

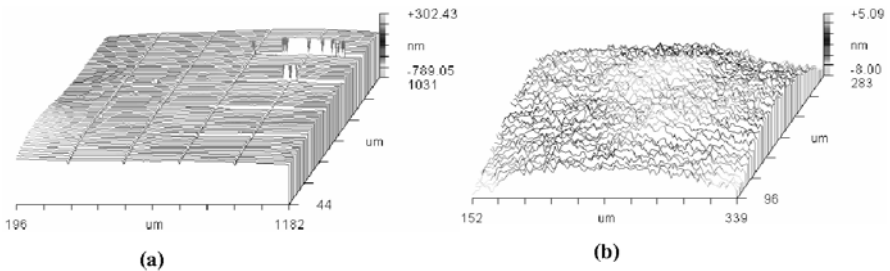


Fig. 7.6. (a) Flatness measurements of an SOI-process array. (b) Measurements of a single pixel

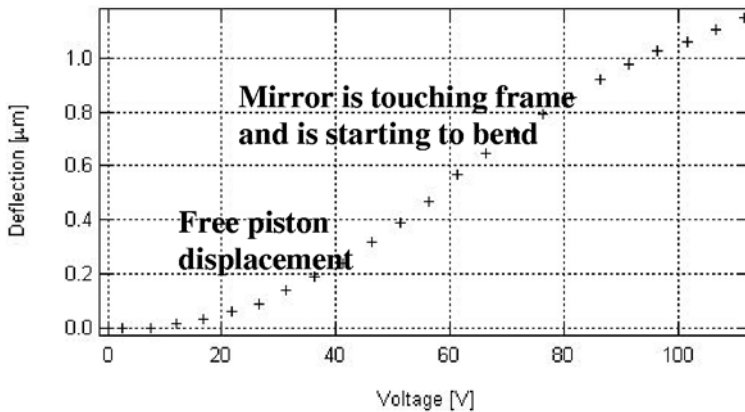


Fig. 7.7. Static actuation measurement of a pixel in a “5 × 5” array

7.5 Future Work

Work pertaining to the “32 × 32” arrays involves increasing fabrication reliability and characterizing previously fabricated devices. A possible solution to the debonding problem mentioned above is to partially remove the substrate prior to performing the HF release, leaving behind a grid pattern. This would lend structural support to the mirrors on the opposing side of the oxide membrane. Investigations of this approach are in progress.

The next major thrust of CCIT is the fabrication of mirrors capable of tip, tilt, and piston motions. Designs and simulations for these mirrors, based on a dual-gimbaled vertical comb drive structure, have been completed.

Another area of future work would be the inclusion of piston-only mirrors in laser-power scaling experiments. For these, segmented mirrors will be placed in a laser Master Oscillator Power Amplifier (MOPA) configuration where the phase of a beam is pre-corrected prior to sending it through slab amplifiers. Since the incident power on these mirrors will be on the order of watts, power absorbed in the gaps between the mirrors will not be significant.

Another application for these segmented mirrors is to create a supermode from a phased array of laser beamlets. The phase of each beamlet in the supermode is to be independently controlled by a pixel in the array. This will permit coherent far-field adding of the beamlets and active beam steering.

7.6 Conclusion

Using the MUMPs process for fabricating micro-mirror arrays produced curved mirrors where peak to valley distortions exceeded the target stroke depth of 0.75 μm . Another flip-chip bonding process, involving SOI technology, was developed to solve this problem. Square and hexagonal “5 × 5” arrays

were assembled using the SOI process in Stanford clean rooms and characterized. These mirrors, made from the device layer of SOI wafers, have individual pixels which are flat to within 2 nm. The fabrication of “ 32×32 ” arrays is being optimized, and existing “ 32×32 ” devices will soon be characterized. Finally, tip/tilt/piston mirrors have been designed and their fabrication is underway.

Acknowledgements

We would like to acknowledge funding from the DARPA CCIT Program through the Lawrence Livermore National Laboratory under program number B517092-6-7.

References

1. Coherent communications, imaging and targeting. More information at <http://www.darpa.mil/tto/PROGRAMS/ccit.html>
2. Y.A. Peter, E. Carr, O. Solgaard: Segmented deformable micro-mirror for free-space optical communication. IEEE/LEOS International Conference of Optical MEMS. Lugano, Switzerland, 2002, pp. 197–198
3. MUMPs[®] (Multi-User MEMS Processes) is offered by MEMSCAP (formerly Cronos Integrated Microsystems)
4. K.W. Markus, D.A. Koester, A. Cowen, R. Mahadevan, V.R. Dhuler, D. Robertson, L. Smith: MEMS infrastructure: The multi-user MEMS processes (MUMPs). In: K.W. Markus (ed): Micromachining and Microfabrication Process Technology. Proc. SPIE **2639**, Austin, TX 1995, pp. 54–63
5. R. Conant, J. Nee, K. Lau, R. Muller: A fast flat scanning micromirror. Solid-State Sensor and Actuator Workshop, Hilton Head, SC 2000, pp. 6–9
6. U. Krishnanmoorthy, O. Solgaard: Self-aligned vertical comb drive actuators for optical scanning micromirrors. Proceedings of Optical MEMS Conference, Okinawa, Japan 2001

8 Control of a Thermal Deformable Mirror: Correction of a Static Disturbance with Limited Sensor Information

M. de Boer¹, K. Hinnen¹, M. Verhaegen¹, R. Fraanje², G. Vdovin³, and
N. Doelman⁴

¹ Delft University of Technology, Delft Center of Systems and Control
Mekelweg 2, 2628 CD Delft, The Netherlands

² University of Twente, Faculty of Applied Physics, Enschede, The Netherlands

³ Delft University of Technology, EEMCS, Electronic Instrumentation Laboratory
Mekelweg 4, 2628 CD Delft, The Netherlands

⁴ TNO TPD, Stieltjesweg 1, 2628 CK Delft, The Netherlands

Summary. This research considers the control of a Thermal Deformable Mirror (TDM), which is used to correct a static aberration in a light beam. The TDM is a cheap, but relatively slow, deformable mirror suited for the correction of static and thermal aberrations. Correction of quasi-static disturbances can, for example, be used to enhance microscope images, or to improve the quality of femto-second light wave packages.

The control objective is to maximize the light power that drops through a pinhole after focusing of the beam in a minimal time span. Only the light power behind the pinhole is available for feedback. The slow dynamics of the mirror and the lack of measurement information complicate the control task.

The optimization algorithm (OA) used to maximize the light power is based on consecutive line searches in the direction of several Zernike modes. The OA operates on the surface shape of the mirror, rather than the mirror input voltages. To speed up and to improve the performance of the algorithm, model predictive control (MPC) is used to adjust the mirror shape to the shape provided by the OA.

The effectiveness of using MPC has been experimentally validated. The disturbance in the experiments consists of a focus and tilt misalignment, and the zero-input shape of the TDM. Without MPC, the light power reaches 40% of the maximum light power within 3000 iterations. When applying the MPC controller, 40% of the maximum intensity is obtained within 700 iterations, and 50% within 2200 iterations.

8.1 Introduction

In applications where adaptive optics are used, there is a need to correct a distortion in a beam of light. This can be accomplished by deformable mirrors which are available in several different designs. A well-known deformable mirror is the Micro-machined Membrane Deformable Mirror (MMDM). An MMDM consists of a thin reflective surface which can be deformed by electrostatic actuators. It is used for fast corrections of aberrations in optical systems, but the device is not low-cost, and the voltages used to drive the

mirror are high. A cheaper alternative for the MMDM is the thermal deformable mirror (TDM) [2]. A TDM consists of a reflective surface with several resistors glued to the back side. The elongation of the resistors is dependent on their temperature which is controlled by the resistor current. This results in a low-cost deformable mirror with low driver voltages, a large dynamic range, but with slow dynamic properties.

To measure the distortion of the light beam, a Shack–Hartmann wavefront sensor could be used. However, these types of wavefront sensors are, like the MMDM, expensive. An alternative method for determining the quality of the beam is with the use of a lens, pinhole and photodiode. The light beam is then focused on the pinhole that is situated in the focal plane of the lens. The power of the light that passes through the pinhole is measured by the photodiode and indicates the quality of the light beam. If the pinhole is the size of the Airy disk, the light power reaches its global maximum when the light beam is perfectly corrected [5]. The equipment for this type of measurement is low-cost, but the measurement information is severely limited. The distortion of the light beam cannot be determined from the measurement directly, and therefore the desired surface shape is not known in advance. It should also be taken into account that the intensity measurement is a highly non-linear function of the mirror surface shape.

Summarizing, when correcting a light beam with the use of a TDM and using the light intensity as the distortion measurement, there are two main problems that have to be solved:

- slow mirror dynamics,
- limited sensor information.

Section 8.2 considers the control problem and describes the experimental set-up. Section 8.3 explains the solution to this problem in the form of a controller for the TDM. The model used by the controller is described in Sect. 8.4. The experimental results are presented in Sect. 8.5 and conclusions are discussed in Sect. 8.6.

8.2 Problem Formulation

The laboratory set-up used to control the TDM is illustrated in Fig. 8.1. The light source is the laser on the left side. With a microscope objective (lens 1a) the laser beam is focussed on pinhole 1. This pinhole will act as a point source without any aberration. Lens 1b converts the point light source to a beam.

After the creation of this undistorted light beam, a static distortion ϕd is introduced. This statically distorted light beam will travel through the beam splitter and reflect on the TDM. The TDM corrects the beam, and the beam reflects on the beam splitter again and is focussed on the photodiode. Pinhole 2 is the size of the Airy disk and guarantees that, if the light beam is perfectly focused, the intensity measured by the photodiode is at a maximum.

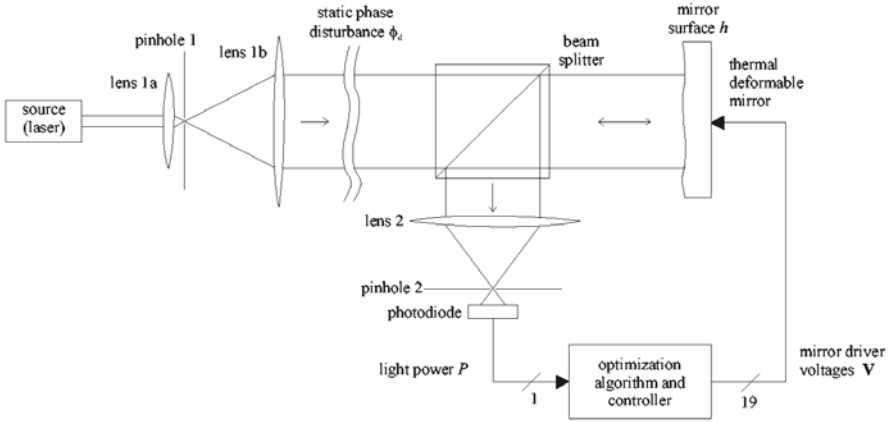


Fig. 8.1. Test set-up of the thermal deformable mirror

The power of the light beam P that passes pinhole 2 is measured by the photodiode. This measurement is the input of the optimization algorithm and controller. The controller’s outputs are 19 voltages \mathbf{V} which drive the mirror actuators.

The disturbance ϕ_d that is used in the experimental set-up consists of a misalignment of the pinhole and the initial surface shape of the mirror. The misalignment of the pinhole in the x - and y -direction is equivalent to a tilt disturbance (Zernike mode 1 and 2). Misalignment in the z -direction is equivalent to a focus (Zernike mode 4) disturbance. The zero-input surface shape of the TDM is not flat, and therefore causes a disturbance as well. This disturbance is approximately equal to an astigmatism (Zernike mode 6) disturbance.

The optimization problem is summarized by the following equation

$$\max_{\mathbf{V} \in [0,5] \times \dots \times [0,5]} P(h(\mathbf{V}), \phi_d) ,$$

where \mathbf{V} are the 19 actuator voltages, $P(h(\mathbf{V}), \phi_d)$ is the light power collected by the photodiode and $h(\mathbf{V})$ is the height of the reflective surface of the mirror with respect to a plane perpendicular to the beam. The voltages are constrained, since a voltage below 0 V would heat up the resistor again, and over 5 V is above its physical limitation. The light power $P(h(\mathbf{V}), \phi_d)$ is proportional to

$$P(h(\mathbf{V}), \phi_d) \propto \iint_{\text{pinhole}} \left| f \left\{ A_0(x, y) e^{i(\phi_d - \frac{4\pi}{\lambda} h(\mathbf{V}))} \right\} \right|^2 ,$$

where $F\{\cdot\}$ is the 2-dimensional Fourier transform, $A_0(x, y)$ is the light amplitude which is assumed to be constant, ϕ_d is the static disturbance of the light beam and λ is the laser wavelength.

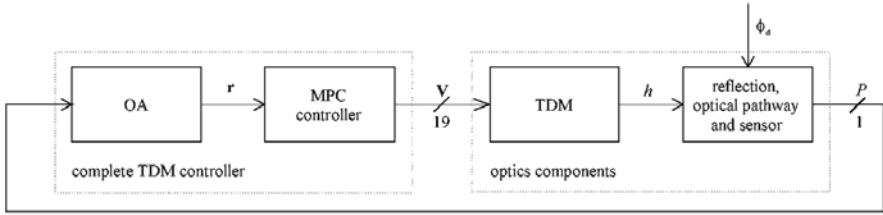


Fig. 8.2. Configuration of the controller and the optics set-up

8.3 Controller

Figure 8.2 illustrates the configuration of the controller in the optics set-up. The optimization algorithm (OA) is defined as a search method which optimizes the light power, by evaluating input and output values in a structured manner. This OA is used to deal with the limited sensor information. In the case of the optics set-up, the evaluation of the function $P(h, \phi_d)$ is a measurement of the light power. The light power is dependent on the surface shape of the mirror h , and the static phase disturbance of the light beam ϕ_d . The phase disturbance ϕ_d is unknown and the intensity measurement of the light beam can only be influenced by the mirror surface shape h . Because the adjusting of the TDM is a dynamic process, and the TDM has slow dynamic properties, we define a desired reference surface height \mathbf{r} . The reference is the input for the MPC controller, which will calculate mirror input voltages \mathbf{V} . These control inputs make sure that the surface height of the TDM approximates the reference \mathbf{r} as fast as possible. When the mirror is set-up, the light power is measured and the OA calculates a new input value \mathbf{r} .

8.3.1 Optimization Algorithm

We have chosen to use a Zernike modes direction line search OA. This is a search method that uses the Zernike modes basis to find a useful optimum because the Zernike basis is associated with the disturbance used in the optics set-up. The algorithm only uses function evaluations and no derivative information. Because the OA performs a line search, the function evaluations require a smooth deformation of the mirror. This is advantageous because it reduces the influence of the dynamics. The following text describes the initialisation and one iteration of the algorithm.

0 Initialisation

Define the initial guess \mathbf{r}_0 and set the Zernike mode i to 1. Define the maximum number of Zernike modes used in the optimization m and the range over which a line search is conducted as ν .

1 Direction Determination

Determine the search direction

$$\mathbf{d}_i = \frac{1}{\|\mathbf{z}_i\|_2} \mathbf{z}_i,$$

where

$$\mathbf{z}_i = \begin{bmatrix} Z_i(x_1, y_1) \\ Z_i(x_2, y_2) \\ \vdots \\ Z_i(x_n, y_n) \end{bmatrix}$$

and $Z_i(x_n, y_n)$ is the value of Zernike mode i at the position of actuator n .

2 Line Search

Perform the line search optimization

$$\max_s P(\mathbf{r}_k + \mathbf{d}_i s, \phi_d) \quad s \in \left[-\frac{\nu}{2}, \frac{\nu}{2}\right].$$

The starting point of the next iteration is then given by

$$\mathbf{r}_{k+1} = \mathbf{r}_k + \mathbf{d}_i s_k^*,$$

where

$$s_k^* = \arg \max_s P(\mathbf{r}_k + \mathbf{d}_i s, \phi_d).$$

3 Stopping Criteria

If the Zernike mode i is equal m , terminate the optimization.

8.3.2 MPC Controller

The controller used to set-up the mirror to the reference surface is a Model Predictive Control (MPC) controller [4]. The structure of the MPC controller is shown in Fig. 8.3a. The principle of operation is shown in Fig. 8.3b. The controller receives the reference surface height at the actuator positions \mathbf{r} . The MPC controller calculates an optimal control value \mathbf{q} that minimizes a performance index $J(\mathbf{q}, k)$ subject to constraints. It does so by computing a sequence of future control signals by means of an internal model of the TDM. The TDM model returns a prediction of the surface height \mathbf{h} . The controller

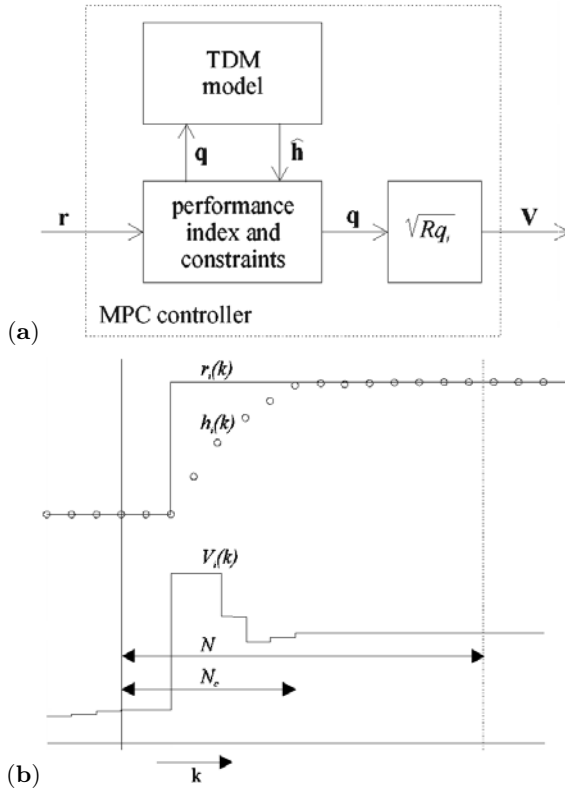


Fig. 8.3. Structure of the MPC controller (a). Principle of operation of the MPC controller (b)

minimizes the performance index

$$J(q_i, k) = \sum_{i=1}^{19} \sum_{j=0}^{N-1} \left(\hat{h}_i(k+j|k) - r_i(k+j|k) \right)^2, \quad (8.1)$$

where N is the prediction horizon and $\hat{h}_i(k+j|k)$ is the prediction of $h_i(j+k)$ based on the knowledge up to time k . This performance is a function of the difference between the reference surface height, and the predicted surface height at the actuator positions. The MPC controller calculates control values that will minimize the performance index. With these control values, the difference between reference and predicted surface height will be made as small as possible in a least squares sense over the prediction horizon. The control signal q is converted to TDM input voltages by $V_i = \sqrt{Rq_i}$ where R is the actuator resistance.

The performance index is minimized under equality and inequality constraints. The equality constraint is motivated by the controller and is de-

defined as

$$q_i(k+j) = q_i(k+N_c-1) \quad \text{for } j \geq N_c, \quad i \in \{1, \dots, 19\}, \quad (8.2)$$

where N_c is the control horizon. The constraint guarantees stability, because the output of the mirror (the mirror surface) is forced to its steady-state after N_c .

The inequality constraint is motivated by the physical limitations of the actuators and is defined as

$$0 \leq q_i(k+j) \leq 0.125 \quad \text{for } i \in \{1, \dots, 19\}. \quad (8.3)$$

It ensures that the output is within the bounds of the physical limitations of the actuators. This means the mirror driver voltages are between 0 and 5 V. Equations (8.1), (8.2) and (8.3) along with the TDM model are transformed into the standard predictive control problem [4]. The calculated control action is then the solution to a quadratic programming problem.

8.4 Dynamic Mirror Model

The model that is used by the MPC controller is based only on input–output data sets of the TDM and includes no physical parameters. It is therefore called a black-box model. This black-box model is a Linear Time Invariant (LTI) model.

8.4.1 Mirror Model

The essential parts of the mirror are shown in Fig. 8.4 and the structure of the TDM is shown in Fig. 8.5. The mirror [1,2] consists of a thin reflective surface h , with 19 resistors glued to the back side. Every resistor has its own voltage source V connected to it. A voltage over a resistor will cause the resistor to dissipate the energy q . The heat flows through the copper wires which will therefore elongate with a certain length Δl . Different currents through the resistors will result in different elongations, thus making various surface shapes possible. Physical insights show that the relation between q and h is approximately linear time invariant (LTI).

The input of the black-box model (see Fig. 8.5) is the dissipated power in the resistors \mathbf{q} , the output is the surface height at the actuator positions \mathbf{h} . Every actuator responds slightly different to an equal input and these differences are difficult to model into a physical model. The black-box model includes all actuator dynamics and can cope with these differences as well.

The method used for determining this black-box model is the subspace model identification (SMI) method N4SID of the MATLAB system identification toolbox. The algorithm is described in [3]. This method is suited for

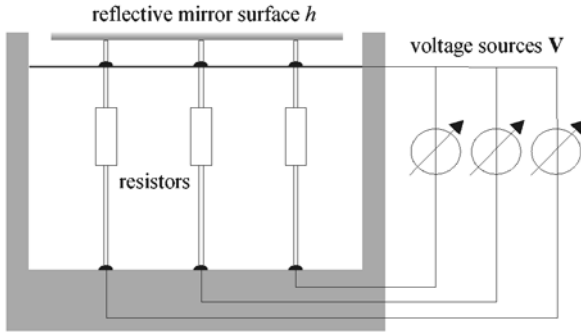


Fig. 8.4. Schematic of the TDM

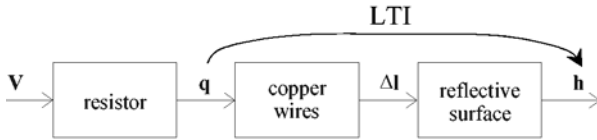


Fig. 8.5. Structure of the TDM model

large scale problems, and is based on well known concepts of linear algebra, like the QR-decomposition, the singular value decomposition and the linear least squares problem. The input is straightforward, since the only input is the input–output data set and the order of the calculated system.

The output data of the TDM consist of measurements of the surface height at the actuator positions \mathbf{h} (this measurement was done on a separate experimental set-up, with an optical profiler). The input of the TDM is a block voltage V which is high (5 V) for 50 time-samples ($t_s = 2.4$ s) and low (0 V) for another 50 time-samples. This input is applied on every single actuator consecutively, while keeping the others zero. The input voltage V is converted to dissipated power \mathbf{q} by $q_i = V_i^2/R$, which is used as the input data of the algorithm. This conversion is necessary because the mirror has got a linear response to the dissipated power, and not to the voltage.

The input–output data set, along with the order of the system, is the input for the subspace identification algorithm. The result is an LTI model of the TDM which maps the dissipated power \mathbf{q} to the mirror surface height at the actuator positions \mathbf{h} . Every actuator shows a first order response (see Sect. 8.4.2 and Fig. 8.6b), and since the TDM contains 19 actuators, the order of the black-box model is 19.

8.4.2 Model Validation

For validation of the model, several separate aspects of the mirror are examined. For these experiments, the surface of the mirror was measured with a Veeco Instruments WYKO 400 optical surface profiler. An example of such

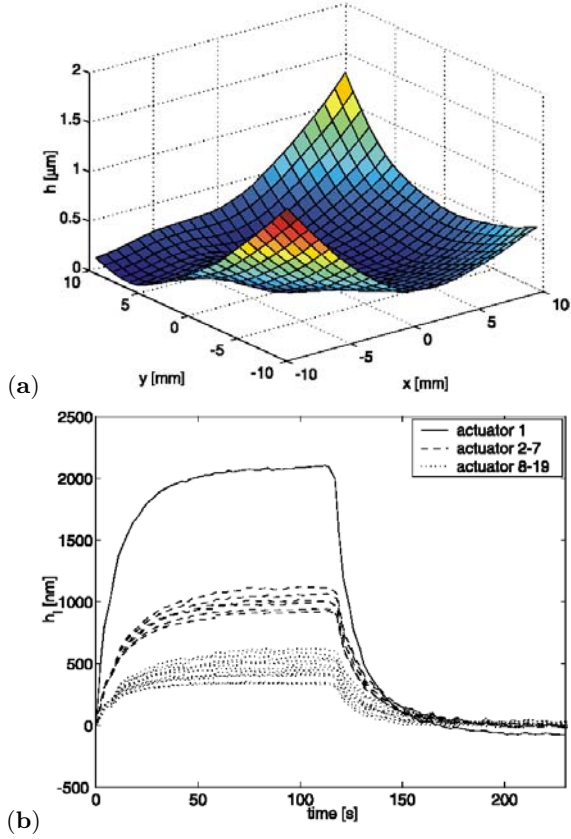


Fig. 8.6. Example of a measured surface profile: the zero-input surface (a). Response of the actuators to a voltage step of 5 V on actuator 1 (b)

a measurement is shown in Fig. 8.6a. The different aspects include the zero-input surface shape, the dynamics of the actuators, the linearity of the actuators and surface shape properties.

Figure 8.6b shows the surface shape height at the positions of the actuators h . The actuator shows a first order response with a time-constant of 12.8 s.

Actuators 2–7 form the middle ring and actuators 8–19 form the outer ring of the actuator structure. When only actuator 1 is excited, the differences between the surface heights in the middle ring are up to 200 nm, in the outer ring up to 300 nm. The reason for these differences can be the variable thickness in the reflective surface, differences in the resistor values of the actuators, the alignment of the actuators, the actuator to surface connection et cetera.

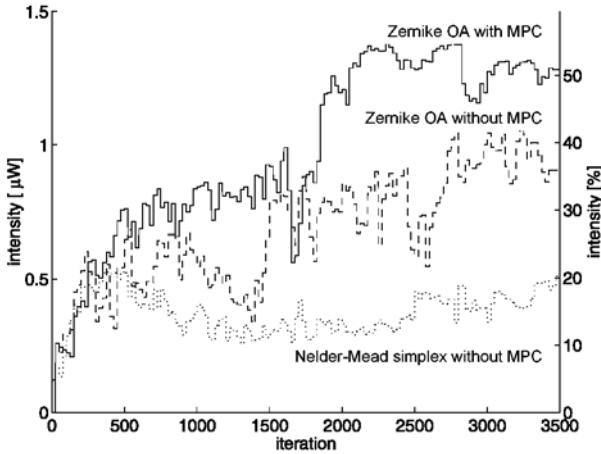


Fig. 8.7. Experimental results of the Zernike mode direction search OA with and without MPC control, and the reference experiment. The reference experiment is the Nelder–Mead simplex OA without MPC control. The time per iteration is 5 s for the Zernike modes OA and 10 s for the Nelder–Mead simplex OA

To analyze the accuracy of the black-box model, the model is used in a simulation. The output of the simulation \mathbf{h}^{sim} is then compared to the measurements \mathbf{h}^{data} for every actuator i with the following fit function:

$$\text{fit}(i) = 100 \left(1 - \frac{\|h_i^{\text{sim}} - h_i^{\text{data}}\|_2}{\|h_i^{\text{data}} - h_i^{\text{data}}\|_2} \right) \% \quad \text{for } i \in \{1, \dots, 19\},$$

where $\overline{h_i^{\text{data}}}$ is the mean of h_i^{data} . The calculated fit is the percentage of the measured output that is explained by the model. The mean fit for all actuators is 91.9%, with a minimum of 87.4% and a maximum of 95.3%. It is therefore concluded that this model is accurate for the MPC controller and can be used for the controller in the experiments.

8.5 Experimental Results

The Zernike modes direction search (with and without MPC control) is compared to a reference experiment. The reference experiment is the Nelder–Mead simplex OA without control [5]. Figure 8.7 shows the results. The intensity in μW is the light power received by the photodiode. The intensity in % is the light power in relation to the maximum correction.

The time per iteration is 5 s for the Zernike modes OA and 10 s for the Nelder–Mead simplex OA. Without using the MPC controller, the Nelder–Mead simplex OA results in 15% of the maximum possible light power. When

using the Zernike modes direction OA without MPC control, 40% of this maximum is reached. Using the Zernike modes direction OA with MPC control, 50% of this maximum is reached in 67% of the time. The Zernike modes direction search finds a higher optimum either with or without the MPC controller. The MPC controller speeds up the convergence of the optimization and the performance achieved is also better than without MPC control.

8.6 Conclusions

It is concluded that without MPC control, both the Nelder–Mead simplex and the Zernike modes OA can compensate for the limited sensor information. However, the Zernike modes direction OA results in a higher light intensity. The use of an additional MPC controller, which compensates the slow dynamics, increases the performance of the Zernike mode OA significantly. The MPC controller is responsible for a reduction of the mismatch between the actual surface shape and the shape calculated by the OA. This results in an even higher light intensity (thus better correction of the light beam) and a faster convergence to this intensity.

References

1. G. Vdovin: Thermal deformable mirror technical data. Flexible Optical B.V.
2. G. Vdovin, M. Loktev: Deformable mirror with thermal actuators. *Opt. Lett.* **27**, 677 (2002)
3. L. Jung: System Identification: Theory for the User. 2nd edn. (PTR Prentice Hall, Upper Saddle River, NJ 1999)
4. T.J.J. van den Boom, T.C.P.M. Backs: Model Predictive Control – Lecture Notes 2001
5. G. Vdovin: Optimization based operation of micro-machined deformable mirrors. Conference on Optical Systems Technologies. Proc. SPIE 902–909 (1998)

9 A Novel Microprocessor-Controlled High-Voltage Driver for Deformable Mirrors

H.-M. Heuck, I. Buske, U. Buschmann, H. Krause, and U. Wittrock

Münster University of Applied Sciences, Photonics Laboratory
Stegerwaldstr. 39, 48565 Steinfurt, Germany

Summary. Genetic algorithms have found widespread use in adaptive optics. One important advantage compared to the matrix inversion method is that it is not necessary to measure the wavefront of the optical beam on which the deformable mirror acts. Instead, any signal, that is monotonic increasing with the quality of the desired wavefront, is sufficient as a feedback signal. Often, this signal derives from a power-in-the-bucket measurement in the far-field of the beam. In coherent control of chemical reactions with temporally shaped femtosecond laser pulses the signal derives from the rate at which the desired chemical is produced. In our adaptive optics experiments we use micro-machined silicon membrane mirrors with up to 59 electrostatic actuators. We have developed a microprocessor-controlled high-voltage driver for up to 60 channels because we could not find a suitable driver on the market. The driver is a fully self-contained unit that only needs input power and communicates with a personal computer via a USB interface. It is especially suited for controlling adaptive mirrors with a genetic algorithm. The driver can store up to 100 voltage patterns, apply them sequentially to the mirror, store up to 4 feedback signals for each voltage pattern, and relay these feedback signals back to the host computer. We will discuss performance issues and tradeoffs like speed, bit resolution, and number of electrodes in our presentation.

9.1 Introduction

The development of low-priced adaptive mirrors during the last years, like micromachined membrane mirrors and bimorph adaptive mirrors, allows use of adaptive optics for many new applications like ophthalmology, free space communication, and a wide range of laser applications.

We use membrane mirrors from Flexible Optical [1] to compensate for aberrations in a master oscillator power amplifier (MOPA) laser and to optimize laser resonators. Contrary to ophthalmic or free space applications we can reach a time-independent state where the laser gives us the best beam quality at the maximum output power. This allows us to renounce a matrix inversion algorithm and to use a search algorithm to optimize the laser. The main advantage of a search algorithm is to reduce the costs of the system because only one signal related to the beam quality is required to find the right surface of the mirror.

Figure 9.1 is a general example of the pre-compensation of aberrations [2, 3]. A master oscillator delivers a laser beam with good beam properties.

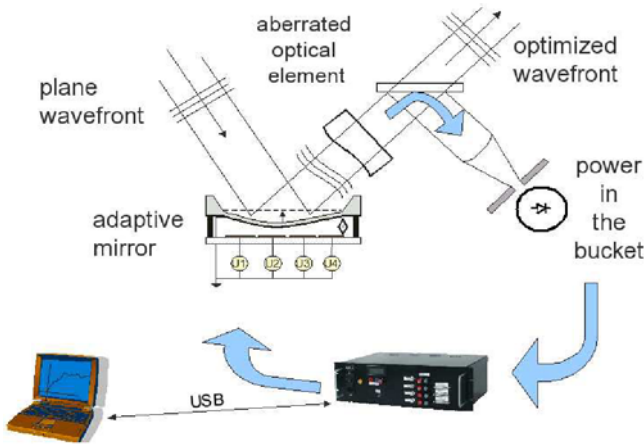


Fig. 9.1. Pre-compensation for aberration using a genetic algorithm

The beam comes from the top-left in Fig. 9.1 and is reflected by an adaptive mirror to an aberrating element. In our case, the aberrations are induced by the power amplifier laser rod. Behind this element the phase of the laser is distorted. To correct the wavefront with a genetic algorithm it is necessary to measure a signal of quality of our laser. This could be done with a power in the bucket signal where the laser is focused on a diffraction limited pinhole and the power is measured with a photodiode. If the laser has some aberrations, a part of the signal is cut off and we get a reduced signal. The photodiode signal is measured with our a new high-voltage driver and controlling device HVD-1. A computer reads out the signals and calculates the best voltage pattern with a genetic search algorithm.

During the last years our laboratory grew up and we have had the need to buy additional voltage drivers for our adaptive mirrors. For a typical driver suitable for our applications, we would have had to buy and assemble three single high-voltage amplifier boards, three analog-to-digital PC-card boards, a high-voltage source and, especially for our applications, an analog-to-digital board and a photodiode amplifier. This is why we decided to develop a new all-in-one mirror driver.

9.2 Requirements

In addition to a low-cost adaptive mirror, the parts needed to drive a mirror should not be much more expensive than the adaptive mirror itself. The mirror driver should also be as flexible as possible. In this chapter, the requirements for such a driver device for low-cost adaptive optics are discussed.

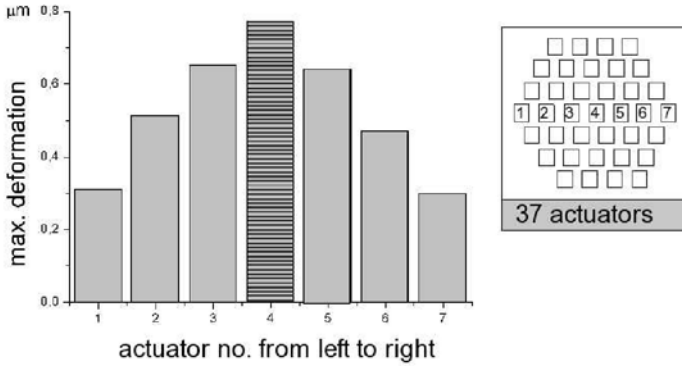


Fig. 9.2. Maximum deformation when applying voltage to a single actuator, the HVD-1 reaches a 12 nm accuracy by dividing the center-actuator in 64 steps

9.2.1 Voltage and Number of Channels

The hardware has to drive both, electrostatic membrane mirrors [1] and optionally bimorph adaptive mirrors. The required maximum voltage for an electrostatic membrane mirror depends on the gap between the electrodes. For a membrane mirror an uni-polar voltage in a maximum voltage range between 170 V to 300 V is required. Bimorph adaptive mirrors must be driven bi-polar. The required voltage depends on the thickness and material property of the piezo disks. For a low-voltage piezo bi-morph mirror a range between ± 150 V is suitable. Today, low-cost adaptive mirrors with 79 channels are available; our largest membrane mirror has 59 channels.

For technical reasons we have limited the number of channels to 60 and have implemented a uni-polar user adjustable voltage of 400 V maximum. In the bi-polar mode the voltage range is user-adjustable between ± 175 V. Due to the higher capacitive load of a piezo disk compared to a membrane, the driver must be driven about 10 times slower compared to the uni-polar mode.

9.2.2 Resolution and Accuracy

The resolution of each actuator is limited by the digital-to-analog converter in the HVD-1. For technical reasons we have implemented a conversion depth of 6 bit. To characterize how precise the membrane mirrors can be controlled, the deformation of every single actuator of a membrane mirror was measured. In Fig. 9.2 the deformation due to a single actuator is shown. With a 6 bit (64 steps) resolution an accuracy of 12 nm on the middle actuator is reached. For electrodes in the outer ring the precision is much higher because the absolute stroke of the single electrodes is lower. The maximum deformation when applying voltage to all electrodes of this mirror was 6 μm . But the question is how precise the mirror can correct defocus, astigmatism, etc. In [4] Enrique J. Fernandez and Pablo Artal have characterized the reachable Zernike modes of

a membrane mirror with a specified maximum stroke of $8\ \mu\text{m}$. The resolution to compensate defocus and astigmatism reaches an absolute stroke of about $2\text{--}3.5\ \mu\text{m}$. When interpolating the voltage pattern to a 6 bit resolution the stroke of this modes can be controlled with an accuracy of $0.05\ \mu\text{m}$. For higher modes the maximum stroke is less than $1\ \mu\text{m}$, which means that the accuracy is better than $0.015\ \mu\text{m}$.

9.2.3 Handling

The HVD-1 should be easily connected and controlled by a computer. This is realized with an USB 1.1 interface. The device can be connected to any computer or laptop by using the Plug'n Play standard. To control the device we have written a driver DLL for C++ and a library for Lab-View.

9.2.4 Feedback Signals

To optimize a wavefront two different ways are applicable: A direct optimization with a wavefront sensor or a search algorithm, e.g. a genetic algorithm or a hill-climbing algorithm. The HVD-1 is optimized for a genetic algorithm. Therefore an optimization signal, e.g. the power-in-a-bucket signal from a photodiode, is needed. In the HVD-1 four feed-back channels for photodiodes are implemented. A transimpedance converter amplifies the current from a photodiode by an adjustable amplification of about $10^6\ \text{V/A}$. Then the voltage signal is digitized by an 8 bit analog-to-digital converter and can be read out via the USB interface.

9.2.5 Speed

The speed of the device should be as fast as possible. The cut-off frequency of a membrane mirror is about $1\text{--}2\ \text{kHz}$. The speed of the HVD-1 is limited by the speed of the USB and by the speed of the internal digital-to-analog conversion. To provide the fastest way to control the mirror with the matrix inversion method and with a genetic algorithm, the HVD-1 has two operating modes, the direct-control and the genetic-algorithm mode. In the direct-control mode the driver can control all 60 channels at $70\ \text{Hz}$, in the genetic-algorithm mode at $90\ \text{Hz}$.

9.3 Optimization with a Genetic Algorithm

Some applications do not need a very high control speed or do not have a linear solution. In this case a genetic algorithm could be a favorable and simple solution. The advantage is the replacement of an expensive SHS or the use in set-ups where the resulting wavefront is not linear correlated to the

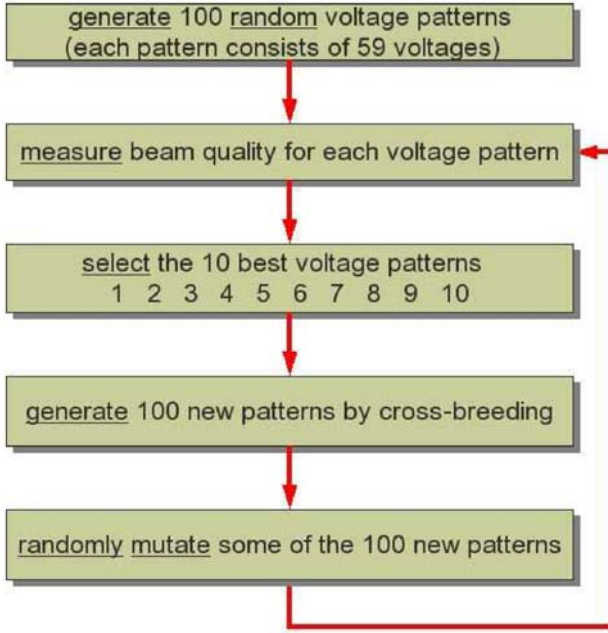


Fig. 9.3. Flow chart of the genetic algorithm

mirror surface, e.g. when using an adaptive mirror inside a laser resonator and measuring the wavefront outside.

The genetic algorithm is a try-and-error optimization routine which imitates the “survival of the fittest” mechanism of nature. The advantage of a genetic algorithm compared to a simplex or hill-climbing algorithm is that it can handle a lot of degrees of freedom.

To start the algorithm, an initial population G^0 has to be defined. This is done by creating a random set of voltage pattern $\vec{I}_i, i = 0 \dots j$, e.g. $j = 100$. Each voltage pattern represents an individual \vec{I}_i ; the actuators are the genes where the voltage value is the phenotype (property) of the gene $p_{i,n}$

$$\begin{aligned}
 \vec{I}_i &= \begin{pmatrix} p_{i,0} \\ \vdots \\ p_{i,n-1} \end{pmatrix} & j &= \text{No. of individuals} \\
 & & n &= \text{No. of parameter} \\
 & & p_{i,n} &= (0, \dots, U_{\max}) \\
 & & k &= \text{Age of generation}
 \end{aligned}$$

$$G^k = \left\{ \vec{I}_0, \dots, \vec{I}_j \right\} . \tag{9.1}$$

Every individual \vec{I}_i is applied to the adaptive mirror and a signal σ_i of the wavefront quality σ is measured. This quality signal is called “fitness”. Like in nature, only the fittest individuals will survive, get children and build a

new generation. To realize the process in the algorithm, 100 new individuals are built from the ten best individuals G_{Best}^k (9.2). The new individual is built with the help of a randomly filled matrix \mathbf{Z} by crossing over the genes from two randomly chosen individuals $\vec{I}_{q1}, \vec{I}_{q2}$ (9.3). The fitness signal equals the probability to select the individuals for the creation of the new generation

$$G_{\text{Best}}^k \subset \{G^k \cap \sigma_B | \sigma_B > \sigma_{\text{selection}}\}, \quad (9.2)$$

$$\mathbf{Z} = \begin{pmatrix} z_{11} & & \\ & \ddots & \\ & & z_{nn} \end{pmatrix} \quad \text{randomly filled matrix,} \quad (9.3)$$

\mathbf{E} = identity matrix,

$$z_{xy} = \begin{cases} x = y & z \in [0, 1] \\ x \neq y & z = 0 \end{cases},$$

$$I_{i,\text{new}} = \mathbf{Z} \times I_{q1} + (\mathbf{E} - \mathbf{Z}) \times I_{q2},$$

$$I_q \in G_{\text{Best}}^k, \quad I_{i,\text{new}} \in G^{k+1}.$$

In order to prevent the convergence from going towards a local maximum, the genes are changed in a small range. This could be done by randomly changing the voltage of one or two genes in the voltage pattern (9.5) or by switching neighborhood actuators. This process is similar to mutations in nature

$$M = \begin{pmatrix} m_{11} & & \\ & \ddots & \\ & & m_{nn} \end{pmatrix} \quad \text{randomly filled matrix,} \quad (9.4)$$

$$m \in \{\mathbb{R} \cap m | m_{\min} < m < m_{\max}\},$$

$$I_{i,\text{mutated}} = M \times I_i.$$

This new generation must be tested on the mirror. Afterwards, the process, the selection, inheriting, and mutation, begins again (Fig. 9.3).

For the example described in the introduction the fitness signal is generated with a power-in-the-bucket measurement. After an iteration of 4–5 generations the laser reaches 80% of the maximum in the optimization process. Therefore only 500 individuals have to be tried out, which is a very small fraction of the $2^{637} = 6.7^{66}$ possibilities.

9.4 Operating Modes

Due to a communication overhead in the USB protocol two operating modes are implemented. The USB-Controller uses 1 ms frames to communicate with the client device. When a single pattern is applied to the HVD-1 there is only a small advantage of the speed of the 10 Mbits/s fast USB, because for the next pattern the controller has to wait for the next communication frame. The first

operating mode is the direct-control or wavefront-sensing mode (WS-mode), the second is a special mode for operating with the genetic algorithm.

9.4.1 Wavefront-Sensing Mode

To control a mirror with a matrix inversion algorithm the phase of the aberrated beam is measured with a wavefront sensor. Then a computer calculates the optimal deformation and applies the voltage pattern to the mirror. In the WS-mode only one voltage pattern is sent via USB to the HVD-1 applied by a micro-controller. This can be done very fast, in 13 ms for all 60 actuators, but for the next transfer the device has to wait for the next communication frame.

9.4.2 Genetic Algorithm Mode

To optimize the mirror surface with a genetic algorithm in the WS-mode costs a lot of unnecessary time. During the optimization, hundreds of voltage patterns have to be tested and a quality signal has to be read out. If this is done step after step, the USB has to use a 1 ms communication frame for every single operation. At first, the data are sent in 3 ms to the micro-controller, secondly, the controller applies the voltages in 11 ms on all actuators and thirdly, the computer must read out the data from the photodiodes in 4 ms. In a special genetic algorithm mode (GA mode) 100 voltage patterns are transferred at once to the HVD-1 and applied step by step by an internal micro-controller. The photodiode signals are read out and stored in an internal memory. After applying all 100 patterns, the results can be read out at once (see Fig. 9.4). This procedure saves time for reading and writing communication because all 100 patterns can be transferred in nearly the same time as only one pattern.

In the next development stage of the HVD-1 a new communication controller with USB 2 will be used. The controller speeds up also the HVD-1 internal data communication. With this interface the speed of the HVD-1 is increased by a factor of two.

9.5 HVD-1

The HVD-1 uses the internal micro-controller Cypress an2135sc with 8 kbytes internal memory for the data communication via USB and to control the hardware. The microprocessor communicates over an I²C-bus with eight eightfold digital-to-analog converters. The analog signal is then amplified by three 20 channel high-voltage amplifier boards. Each board is connected by a sub-d port. This allows the use of three separate 19 channel mirrors, or

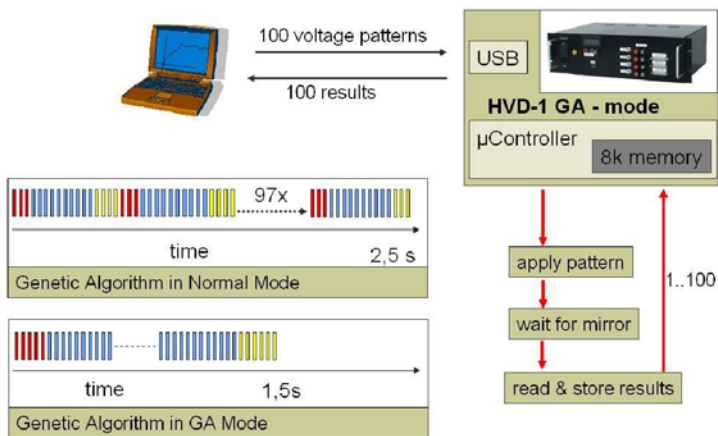


Fig. 9.4. Comparison between the two data-transfer modes for optimization with a genetic algorithm. Explanation in Sect. 9.4.2

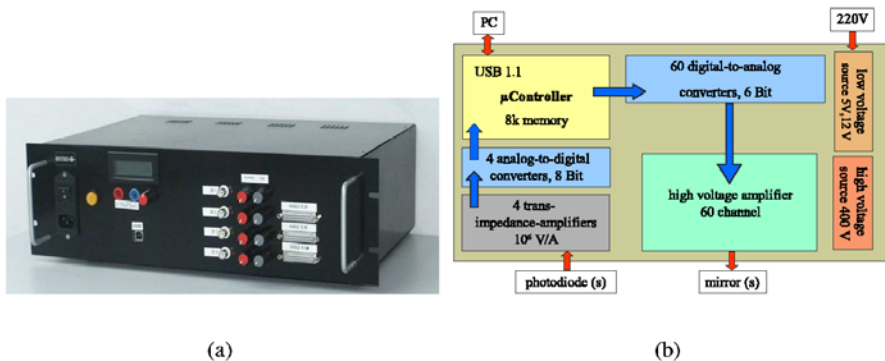


Fig. 9.5. High-Voltage Driver HVD-1, (a) frontview, (b) schematic overview

one 60 channel mirror, or any suitable combination. Our HVD-1 has implemented four trans-impedance amplifiers for direct connection of four photodiodes. The photodiodes can be connected to the HVD-1 by BNC-connectors. The transimpedance amplifiers are shielded with a metal to reduce the noise caused by the high-voltage amplifier. The photodiode signal can be digitized by four 8 bit analog-to-digital converter. These converters are read out by the I²C-bus and the data are stored in the internal memory of the micro-controller. The memory of the micro-controller is accessible by the USB interface. All voltage sources are internally implemented, so there is no need for any extra hardware (see Fig. 9.5). With an internal jumper the HVD-1 can be switched to the bi-polar mode.

Table 9.1. Specifications of HVD-1

High Voltage		Interface	
High voltage uni-polar	50 ... 400 V	Software	C++, Labview
High voltage bi-polar	± 174 V	Hardware	USB 1.1
Voltage resolution	6 bit	High voltage output	3 \times sub-D
HV supply	internal 30 W	Feedback input	3 \times BNC
Feedback		Dimensions	
A/D channels	4	Type	19" Rack
Amplification	$\approx 10^6$ V/A	Dimensions	480 \times 290 \times 140 mm ³
Noise	20 mV	Weight	4 kg
Resolution	8 bit	Input	240 V, 50 Hz, 0.5 A
Bandwidth	5 kHz		

References

1. Flexible Optical B.V., PO Box 581, 2600 AN, Delft, The Netherlands, www.okotech.com
2. I. Buske, H.-M. Heuck, J. Hüve, U. Wittrock: Master-Oscillator-Power-Amplifier laser with adaptive aberration correction. In: OSA Trends in Optics and Photonics (TOPS), Vol. 73. Conference on Lasers and Electro-Optics, OSA Technical Digest, Postconference Edition. Optical Society of America, Washington 2002, pp. 22–23
3. I. Buske, H.-M. Heuck, U. Wittrock: Adaptive aberration control in laser amplifiers and laser resonators. In: Proceedings of Photonics West. San Jose, CA 2003, pp. 4969–4936
4. E.J. Fernandez, P. Artal: Membrane deformable mirror for adaptive optics: performance limits in visual optics. *Opt. Express* **11** (2003)

10 Preliminary Investigation of an Electrostatically Actuated Liquid-Based Deformable Mirror

E.M. Vuelban, N. Bhattacharya, and J.M. Braat

Delft University of Technology, Optics Research Group, Department of Imaging Science and Technology, Lorentzweg 1, Delft, The Netherlands

Summary. Adaptive optics is essential to offset the effect of wavefront distortions introduced by the aberrating media between the object and the imaging optics. Efficient adaptive optics systems can improve the resolution and image quality by suitably correcting these wavefront distortions. One of the crucial components of an adaptive optics system is the deformable mirror. Several types of deformable mirrors based on liquids are currently under investigation. Several groups have demonstrated magnetic actuation of a liquid deformable mirror. Our research is focused on the design and construction of a low cost electrostatically actuated liquid-based deformable mirror, which would exhibit higher spatio-temporal bandwidth compared to the current mechanically driven deformable mirrors. Preliminary simulation shows that stroke requirements for astronomical application are easily met while complying with low power demands.

10.1 Introduction

The correction for atmospheric distortion was first proposed by Horace Babcock in 1953 using the Eidophor projection system [1]. The Eidophor consists, along with other important optical components, of a thin oil film covering a reflecting mirror. An electron beam bombards electric charges onto the surface of the oil and through electrostatic force a controlled film deformation is achieved [2]. However, Babcock's proposed set-up for atmospheric turbulence correction has not been implemented and reported in the literature.

As far as we know, only two liquid-based deformable mirrors have been demonstrated so far. In 1994, Ragazzoni and Marchetti have successfully demonstrated electromagnetic actuation of a thin layer of mercury [3]. In their set-up, an electrical current flow through the liquid while another current passes through an actuator coil situated underneath the liquid. The two current-carrying media, in consequence, experience a repulsive or attractive force depending on the direction of the two currents. A liquid surface deformation is achieved as a result of this repulsion or attraction. However, mercury poses some drawbacks especially when used as a magnetic liquid. These drawbacks motivated Borra and his team to use water or oil based ferrofluid coated with a reflective metal liquid-like film, instead of mercury, which serves as the reflective surface [4].

Liquid-based deformable mirrors (LDM) offer several advantages. The fabrication of a low cost deformable mirror with a large number of actuators can be easily realized using liquid. Aside from this, the scalability of such a liquid-based deformable mirror would not pose any serious manufacturing problem. LDMs are free from mechanical constraints such as resonance and structural coupling. Achieving an optical flat surface, without any need of polishing, is easy with LDMs. LDMs would exhibit a high spatio-temporal bandwidth comparable to the existing high bandwidth deformable mirrors [4].

10.2 Statement of the Problem

The determination of the mirror's influence function is one of the important issues in the design of a deformable mirror [5]. The influence function is basically the shape of the mirror surface when one actuator is actuated. For a continuous deformable mirror, such as the liquid deformable mirror, the influence function is commonly modeled using Gaussian functions, polynomials and trigonometric functions.

We want to determine the influence function of the liquid-based deformable mirror when subjected to an electrostatic field. We are also interested on the maximum permissible values for the deformation and applied voltage. We consider the static case. The system considered is that of a thin conducting liquid situated on top of a solid substrate. The liquid is connected to an external voltage source. A solid transparent electrode, also connected to the voltage source, is situated at a certain distance above the liquid. We consider air as the dielectric medium in between the two electrodes. The set-up is illustrated in Fig. 10.1.

For adequately large lateral dimension, the liquid will initially assume a flat surface. At thermodynamic equilibrium and in the absence of an electrostatic field the shape of the surface can be determined using the given equation,

$$\Delta p = p_1 - p_2 = \gamma \left[\frac{1}{R_1} + \frac{1}{R_2} \right], \quad (10.1)$$

where p_1, p_2 are the pressures in the conducting liquid and in air respectively, γ is the liquid surface tension and R_1, R_2 are the principal radii of curvature

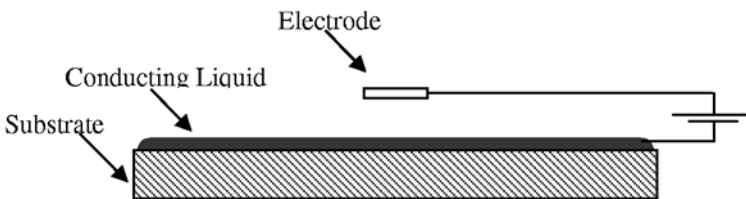


Fig. 10.1. Set-up for determining the influence function of the liquid-based deformable mirror

at a given point of the surface. We assume that the deformation is much smaller than the dimension of the liquid and, hence, the term in the bracket can be simplified into

$$\left[\frac{1}{R_1} + \frac{1}{R_2} \right] = \frac{\partial^2 z}{\partial x^2} + \frac{\partial^2 z}{\partial y^2}, \quad (10.2)$$

where x , y , z are the Cartesian coordinates. Substituting (10.2) into (10.1), we obtain a differential equation for the surface shape as

$$\gamma \left(\frac{\partial^2 z}{\partial x^2} + \frac{\partial^2 z}{\partial y^2} \right) - g(\rho_1 - \rho_2)z = 0, \quad (10.3)$$

where g is the acceleration due to gravity, ρ_1 and ρ_2 are the densities of the conducting liquid and air respectively. When an electrostatic field is introduced, (10.3) is modified to account for the perturbing field. The electrostatic pressure is just given by

$$P_e = \frac{\varepsilon E^2}{2}, \quad (10.4)$$

where ε is the permittivity of air. In general, the influence of an external perturbing field, such as electromagnetic, acoustic and optical fields, on the surface shape can be written as

$$\gamma \left(\frac{\partial^2 z}{\partial x^2} + \frac{\partial^2 z}{\partial y^2} \right) - g(\rho_1 - \rho_2)z = P_{\text{external}}, \quad (10.5)$$

where P_{external} is the pressure term of the external perturbing field.

10.3 Modeling

We used the finite element method to solve for (10.5), together with the corresponding expression for the electrostatic pressure. The electric field, E , given in (10.4) is not a constant term but follows a certain distribution. Before we calculate for the profile of the deformation $z(x, y)$, it is first necessary to determine the electric field distribution. For simplicity, we consider only the two dimensional case; along the z - x plane. Figure 10.2 shows the electric field distribution of the system shown in Fig. 10.1. For the model, the size of the electrode is 5 mm and a lateral dimension of the liquid is 40 mm. It is important to note that as preliminary work we calculated the final state of the deformation that is solving directly the differential equation without considering the intermediate steps. Other works [6, 7] have considered the iterative approach, where the electric field distribution is calculated given the shape of the deformation and reintroducing it into the equation for the deformation, until the solution converges to the final shape of the deformation.

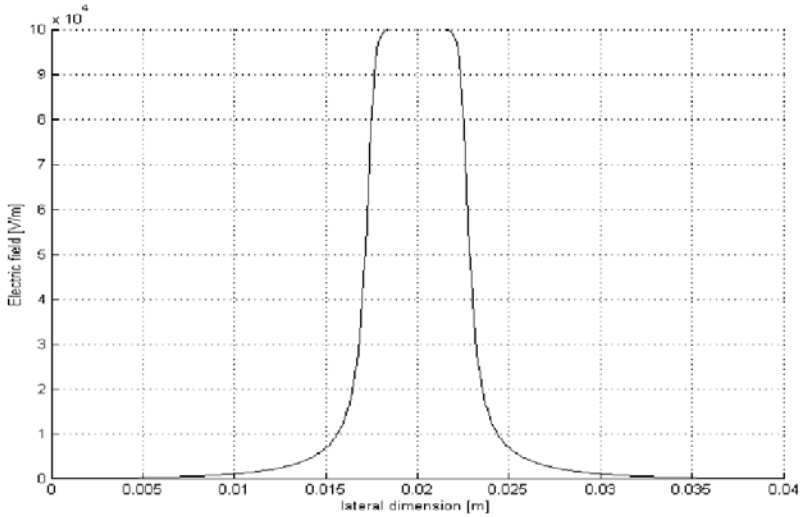


Fig. 10.2. The electric field distribution of the set-up considered

We approximate the above electric field distribution with the equation

$$E(x) = \frac{E_0}{(1 + (x/x_c)^2)}, \quad (10.6)$$

where E_0 is the magnitude of the field applied, x_c is the dimension of the electrode.

10.4 Results and Discussion

Using the approximation [6]

$$\Delta Z = \frac{\varepsilon E^2}{2g(\rho_1 - \rho_2)},$$

we obtain the dependence of the deformation on the applied electric field. This dependence is shown in Fig. 10.3. We just considered some representative liquids (water, mercury and gallium). The three vertical lines depicted in the figure are the critical electrical fields for each representative liquid respectively. This critical field indicates the maximum electric field we can apply before instabilities of the surface occur. It can be seen from the graph that the maximum deformation we can obtain before the onset of surface instabilities is in the order of millimeter, which is far greater than the typical stroke requirements for atmospheric turbulence correction in astronomy. The electric field required to achieve a deformation of 10 microns is of the order of hundred kilovolts per meter. If we have a gap of 1 mm between the

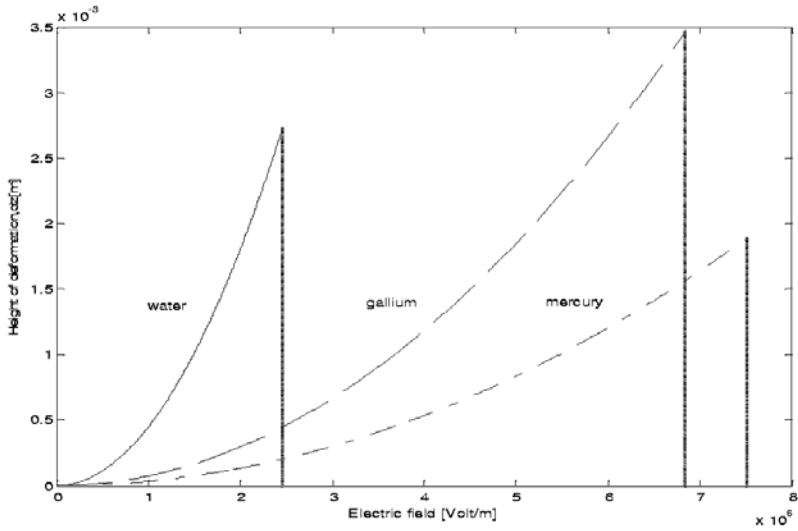


Fig. 10.3. Dependence of the deformation on the applied field

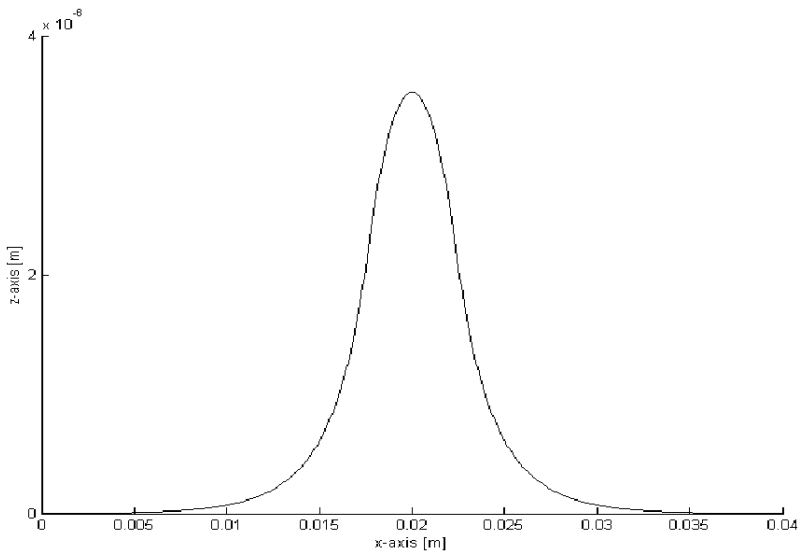


Fig. 10.4. Profile of the deformation. Size of the electrode is 5 mm

liquid surface and the upper electrode, the voltage required for a 10 micron deformation is a few hundred volts. Such voltage requirement can easily be met with existing voltage sources. The profile of the surface deformation is shown in Fig. 10.4. In the simulation we use a voltage of 75 V with a gap of 0.5 mm in between the electrode and the liquid surface.

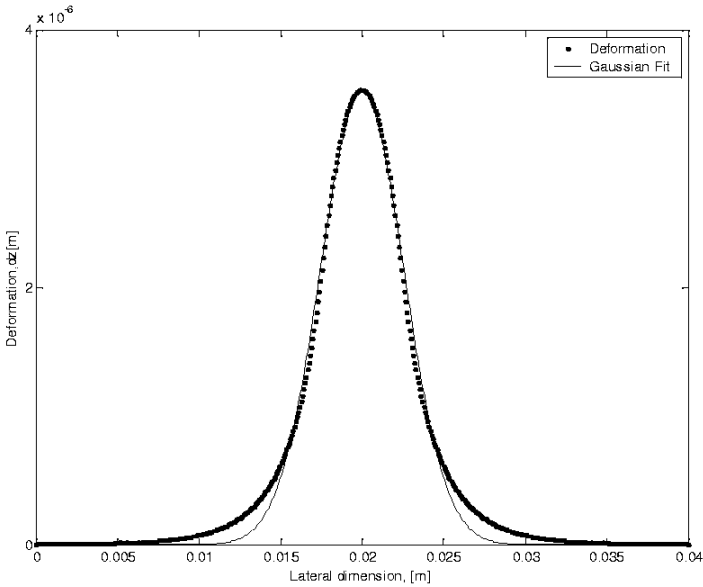


Fig. 10.5. Curve fitting of the profile obtained

A curve fitting for the profile shown in Fig. 10.4 is depicted in Fig. 10.5. The profile obtained closely follows a Gaussian distribution, with a modified variance. It can be seen from the figure that the tail of the profile is somewhat larger than the Gaussian fit. This might be due to the fact that the electric field distribution has been modeled using (10.6) and edge effects are not completely accounted for.

10.5 Conclusion

We have determined the deformation of the liquid surface under the influence of an electrostatic field. The influence of an external perturbing field on the surface deformation can be determined using (10.5). The maximum allowable value for the deformation of some representative liquids is of the order of millimeters, far greater than what is required for atmospheric correction in astronomy. The voltage required to achieve a stroke of 10 microns is in the order of few hundred volts. The profile of the deformation closely resembles that of a Gaussian profile.

An experimental verification of the results obtained is being planned. Further improvement of the model, to account for the influence of other thermodynamics parameters such as temperature and viscosity, will be made as well. Other future work involves the modeling of the dynamic behavior of the system.

Acknowledgement

This project is being funded by the Netherlands Organization for Applied Scientific Research, TNO-TPD, for the Knowledge Center for Optical Aperture Synthesis TUD-TNO.

References

1. H.W. Babcock: *Pub. Astron. Soc. Pacific.* **65**(386), 229 (1953)
2. V.F. Fischer, H. Thiemann: *Schweiz. Arch. Angew. Wiss. Tech.* **7**(1 and 2) (1941)
3. R. Ragazzoni, E. Marchetti: *Astron. Astrophys.* **283**, L17 (1994)
4. P.R. Laird, et al.: *Proc. SPIE* **4839**, 733 (2003)
5. R. Tyson: *Principles of Adaptive Optics* (Academic, New York 1991), pp. 200
6. G.I. Taylor, A.D. McEwan: *J. Fluid Mech.* **22**, 1 (1965)
7. G.H. Joffree, M. Cloupeau: *J. Electrostatics* **18**, 147 (1986)
8. R. Cade: *Proc. Phys. Soc.* **86**, 939 (1965)

11 Interferometer-Based Adaptive Optical System

O. Soloviev¹ and G. Vdovin^{1,2}

¹ Delft University of Technology, EEMCS, Electronic Instrumentation Laboratory
Mekelweg 4, 2628 CD Delft, The Netherlands

² OKO Technologies
PO Box 581, 2600 AN Delft, The Netherlands

Summary. Interferometer-based adaptive optics has an advantage of direct measurement of the wavefront profile. Nevertheless the majority of adaptive optical systems, realized so far, use other types of wavefront sensors, such as Hartmann sensors. Interferometric sensors have two problems: (1) a source of a coherent reference wave should be present and (2) in many cases it is impossible to reconstruct the wavefront unambiguously from a single interferogram, due to the ill-posed nature of the phase unwrapping problem. In the case of an adaptive optical system with a limited number of degrees of freedom, one can expect that the ambiguity of the solution will be partly or even completely eliminated by looking for the wavefront reconstruction only in the existing basis. We report on the expected performance of interferometric adaptive optical system with a 37-channel membrane deformable mirror, based on a computer model of a complete system.

11.1 Introduction

Wavefront sensor is the key element of any adaptive optical system. It provides the information about the wavefront which is necessary to make the appropriate correction with an adaptive element. There are two requirements to the wavefront sensor: the information should be as complete as possible for every measurement (high spatial resolution) and the processing by the system should be as quick as possible (high update rate, or temporal resolution). The last demand is especially crucial for a *real-time* AO system. There are methods [1] of wavefront sensing which try to combine both the high speed and the high resolution. These methods can be divided into two groups: indirect and direct. Indirect methods reconstruct the wavefront and then obtain the correction commands. Direct methods skip the wavefront representation and obtain corrector commands from the wavefront measurements directly. Since the knowledge about the wavefront shape is not very important in a real-time adaptive optical system, the majority of the methods skip the wavefront representation and produce direct conversion of sensor data into the corrector control signals.

In this article, we consider the possibility of using an interferometer as a direct wavefront sensor in an AO system. Interferometry compared with,

for instance, Hartmann method, has two advantages: higher accuracy of the wavefront measurement (all the data are wavelength related only), and a high spatial resolution (which is limited only by the camera resolution). Despite this interferometry is seldom used in AO, mainly due to some potential problems of the interferometry. Obtaining an interferogram could pose a problem due to the lack of coherent reference wave. Phase extraction and unwrapping also belong to the class of ill-posed problems. However, in some practical cases these problems can be solved approximately with good practical precision. In the following sections we dwell on some of these cases and examine the effects of reconstruction error on an interferometer-based adaptive optics system with a model written in *Mathematica*[®].

11.2 General Flowchart

In general, any AO system with an interferometer as a wavefront sensor, should operate as follows (see Fig. 11.1). After some initial steps, the system goes into the main loop:

1. obtain interferogram,
2. get phase,
3. modal or zonal decomposition for a corrector,
4. correction.

Every step in this flowchart can be done by a number of ways, but to build a real-time working system, we should minimize the time needed for every step. It can be considered as a criterion for algorithm choosing. In addition,

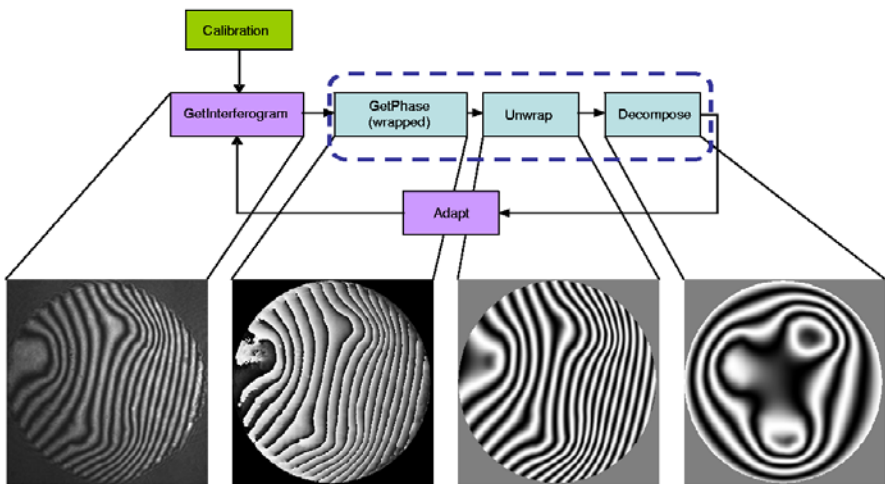


Fig. 11.1. General flowchart of an AO system with an interferometer as a direct wavefront sensor

the method chosen for a step affects the applicability of any method for the next steps. For instance, zonal phase decomposition is preferable for a zonal adaptive element. Let us look in detail at every step.

The first step, interferogram obtaining, takes no computational time, but the way it encodes the phase information affects the whole loop. We do not discuss here the interferometric methods one can use in AO (they are described in the literature, see [2] for instance), but remind only that we can choose between encoding the profile information (by means of interference with a well-known wavefront) or the slope information (shearing interferometer).

After the information about the wavefront is encoded in the fringes pattern of the interferogram, it should be extracted. There are a lot of methods described in the literature (see, for instance, [3, 4]). Most of them are based on multiple measurements, but have such advantages as computational simplicity and sometimes increased accuracy due to insensitivity to some error sources. A single-measurement method, based on Fourier transform (e.g. [5–7]), usually require a linear or circular carrier. Another price for a single-measurement phase extraction is an increased computational complexity and thus increased time, which remains moderate with modern computer speed and FFT implementations, however. Analysis of an arbitrary interferogram, including those with closed fringes, by means of genetic algorithms or phase regularization technique [8–11] requires usually minutes of computation. Therefore, Fourier-transform algorithm with a linear carrier seems to be the most appropriate for the moment.

Unfortunately, the phase values obtained by Fourier method is wrapped, i.e. instead of ϕ varying in the real number range, we get only $\mathcal{W}\phi$ varying from $-\pi$ to π

$$\mathcal{W}\phi = \phi + 2\pi k, \quad k \in \mathbb{Z}, \quad k : \mathcal{W}\phi \in (-\pi, \pi]. \quad (11.1)$$

In ideal case (no noise, no scintillation and Nyquist condition) the phase can be restored (unwrapped). The method to unwrap is simple: by the Itoh [12] lemma wrapped difference of the wrapped phase is equal to the difference of the original phase:

$$\mathcal{W}\Delta\mathcal{W}\phi[\mathbf{x}] = \Delta\phi[\mathbf{x}], \quad \text{if } |\Delta\phi[\mathbf{x}]] < \pi. \quad (11.2)$$

So if the obtained vector field of wrapped differences in x - and y -directions, so-called “quasigradient” field $(\mathcal{W}\Delta_x\mathcal{W}\phi[\mathbf{x}], \mathcal{W}\Delta_y\mathcal{W}\phi[\mathbf{x}])$ is a consistent gradient field, it can be integrated. In practice, however, that happens not so often. Obtained vector field can contain so-called residues, so that the integral around these points are not zero. They can appear due to different factors, not only because of the noise, sometimes the residues are present in the wavefront itself. The task of unwrapping becomes thus nontrivial. A number of methods exist to obtain the real, unwrapped phase (see [13] for an overview). Every method usually makes an assumption about the initial “real” phase.

We will discuss this in the following section in regard with decomposition by the influence functions.

Suppose we have unwrapped the phase. Now we should extract from this information the wavefront corrector signals, i.e. approximate the wavefront by a linear combination of the set of influence functions of the adaptive element. Again, there is a number of ways to do this. We can chose that the linear combination should have the same slope in some points, as with the Hartman–Shack sensor. Or the global modal decomposition via approximation in the least square sense, which is also frequently used.

At the last step in the loop, the correction signals obtained on the previous step are sent to the adaptive element, sometimes with a non-unity gain. A new interferogram containing the information about the incident wavefront plus correction is obtained and processed and so on.

The speed and accuracy of the interferometer-based AOS can be estimated with a model based on the methods chosen for each step implementations. We have programmed the main loop as a *Mathematica*[®] package. In the next section we present some simulated results and discuss some theoretical points concerning phase unwrapping via modal decomposition.

11.3 Examples and Discussion

11.3.1 Unwrapping via Modal Decomposition

We can merge two steps (unwrapping and decomposition) from the general flowchart on Fig. 11.1 in one, and approximate the inconsistent gradient field, obtained with Itoh algorithm, with a linear combination of the gradients of the influence functions of the adaptive mirror, thus skipping the most time-expensive and ambiguous step of phase unwrapping (see an example on Fig. 11.3). Moreover, we will show now that direct decomposition of quasi-gradient field over the gradients of some basis function is equivalent to unwrapping the phase with the least square algorithm and then approximation of the unwrapped phase by the weighted sum of the basis functions.

Let us recall that by Helmholtz's theorem any vector field may be written as the sum of an irrotational part (gradient of some scalar field) and a solenoidal part

$$\mathbf{f} = \nabla\phi + \nabla \times \mathbf{A}.$$

All gradient fields possible in our image dimensions form a linear subspace G in the space of all vector fields F (see Fig. 11.2). Any phase unwrapping algorithm finds a point in G , $\nabla\phi_a$, close enough to initial inconsistent gradient field \mathbf{f} . The proximity criterion defining how close or how far the unwrapped phase gradient $\nabla\phi_a$ could be from the quasigradient field is chosen by the algorithm and usually is based on some additional suppositions about the initial phase, desired noise robustness and so on. According to a particular

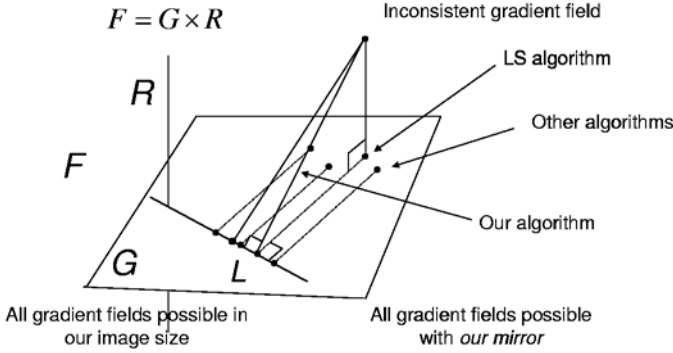


Fig. 11.2. Schematic representation of the phase unwrapping problem

algorithm, the point $\nabla\phi_a$ in G could be far enough from the irrotational component $\nabla\phi$ of the field \mathbf{f} , which is always provided by the least square algorithm, but could be closer to the original, noise-free phase gradient $\nabla\phi_0$.

Gradients of all phase corrections that may be made with an adaptive mirror's influence functions form in turn another linear subspace L in G . Again any decomposition of the unwrapped phase ϕ_a finds a close enough to $\nabla\phi_a$ point $\nabla\phi_a = \sum \lambda_i \nabla f_i$ in L .

There is a possibility to find immediately close enough to \mathbf{f} point in L , fulfilling thus unwrapping and decomposition tasks. It seems to be natural approach as far as we can apply wavefront correction only with weighted sum of the influence functions. The number of algorithms here is moderate, to our knowledge. Genetic algorithm [8] provides good noise robustness but is very slow. So up to now the only candidate is a modal decomposition of the inconsistent gradient \mathbf{f} by gradients of the influence functions in the least square sense.

It can be shown that the result of this “quasigradient by gradients” decomposition coincides with the decomposition of the irrotational component of \mathbf{f} over the same gradients. Indeed, if we introduce a dot product (f, h) for $f = (f_x[\mathbf{x}], f_y[\mathbf{x}])$ and $h = (h_x[\mathbf{x}], h_y[\mathbf{x}])$ defined on \mathcal{S} as

$$(f, h) = \sum_{\mathbf{x} \in \mathcal{S}} (f_x[\mathbf{x}]h_x[\mathbf{x}] + f_y[\mathbf{x}]h_y[\mathbf{x}]),$$

and thus the distance as

$$\|f\| = \sqrt{(f, f)}, \quad (11.3)$$

then the irrotational component $\nabla\phi$ is an orthogonal projection (the closest point) of \mathbf{f} on G , and further decomposition over gradients of the basis is an orthogonal projection of $\nabla\phi$ on L . By the theorem on three perpendiculars it gives the same point as an orthogonal projection of \mathbf{f} on L .

This algorithm can be regarded as a generalization of the least square unwrapping algorithm. All the drawbacks of the L_2 unwrapping algorithm

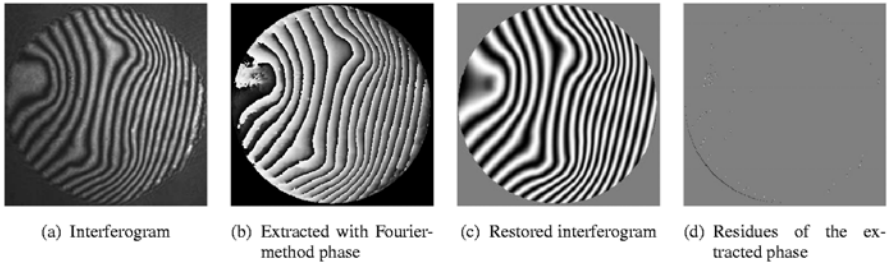


Fig. 11.3. Real-world interferogram obtained with an adaptive mirror. A spatial carrier allows extracting the phase with the Fourier-transform method. The extracted phase is unwrapped via demodulation by the simulated response functions and is shown as an interferogram for clearness. Though the response functions were not obtained from the same mirror, the two interferograms demonstrate a sufficient similarity

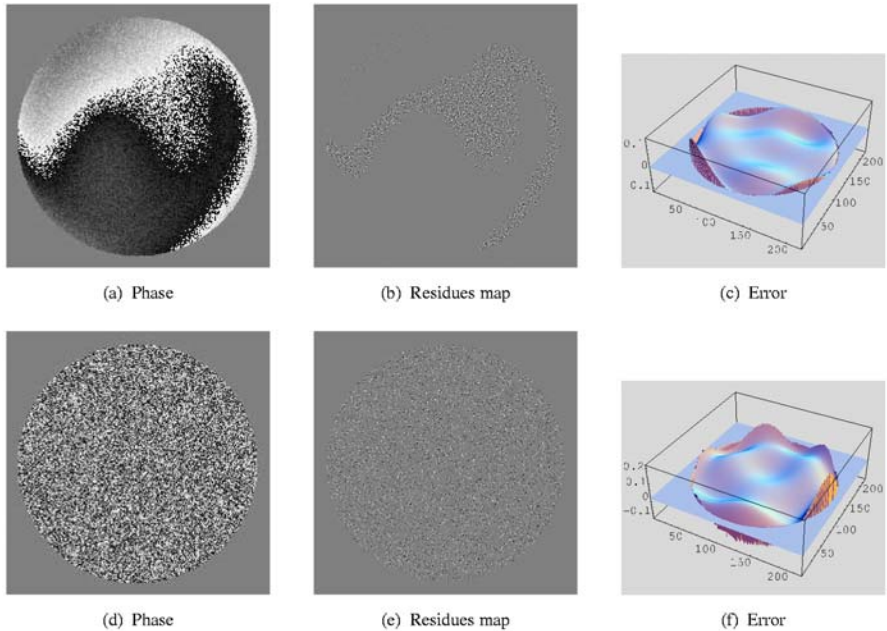


Fig. 11.4. Examples of computer generated interferograms where small noise creates a wrapped phases with a lot of residues. The second line shows how the phase consisting only from noise term, with residues almost in every point, is wrongly decomposed in terms of Zernike polynomials

are thus transferred – noise sensitivity is high, for instance. Even small noise can create a large number of residues that seriously change the irrotational component, and thus change the decomposed phase. See the examples on

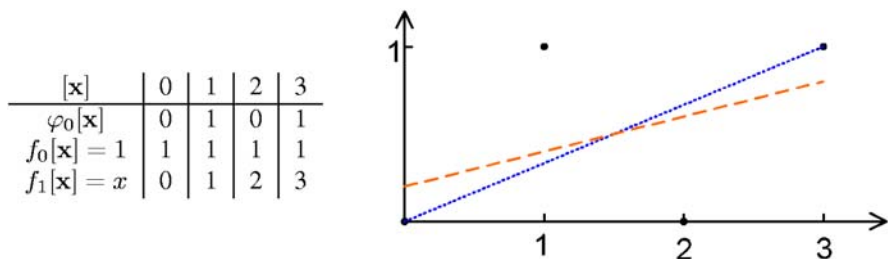


Fig. 11.5. Simple example that demonstrates the difference between usual and gradient approximations. By approximating $\phi_0[\mathbf{x}]$ with functions $a + bx$ in the least square sense we get $1/5 + x/5$, and $x/3$ by approximating $\nabla\phi_0[\mathbf{x}] = (1, -1, 1)$ with functions $a\nabla f_0[\mathbf{x}] + b\nabla f_1[\mathbf{x}] = b(1, 1, 1)$

Fig. 11.4, where just pure noise is approximated not with zero function, but with some large variance.

Another disadvantage – we approximate gradients by gradients in L_2 , not the phase by the influence functions. If a set of decomposition functions $\{f_i\}$ forms a full basis in the space of scalar fields on \mathcal{S} (e.g. all one-pixel characteristic functions), then these two approaches give the same result. This is not the case in the general situation. E.g. consider the example on Fig. 11.5, where \mathbf{x} we choose to be one-dimensional and \mathcal{S} to consist only from 4 points for clarity. Then in case of approximation by f_0 and f_1 in least-squares sense we will get $(x + 1)/5$ as the solution, and $x/3$ in case of gradient over gradient approximation.

11.3.2 Closed Loop Behaviour

The considerations from the previous subsection can prevent from using of the unwrapping via demodulation algorithm for a single interferogram analysis. But fortunately, in closed loop systems the situation can be improved by following iterations (see the examples on Fig. 11.6). If we look at the coefficients values at every step of the closed loop, we can see that during first steps large aberration is canceled, so the rest contains less residues (if they are not intrinsic to the phase), and then unwrapping algorithm provides the phase more accurately, with the error mainly due to the decomposition.

We can also roughly estimate the speed of the interferometer-based AO system. A discrete Fourier transform of an average image size can be performed at rate from several Hz to 1kHz, depending on CPU type and a total number of the image pixels N (see www.fftw.org for reference). During the unwrapping/decomposition operation a $2n \times 2n$ -matrix is multiplied with a $2n$ -vector, where n is a number of influence functions. The matrix contains information about the slopes of the influence functions and can be calculated during the initialization step, thus not decreasing the speed of the main loop. The vector calculation requires about $2nN$ operations, which also

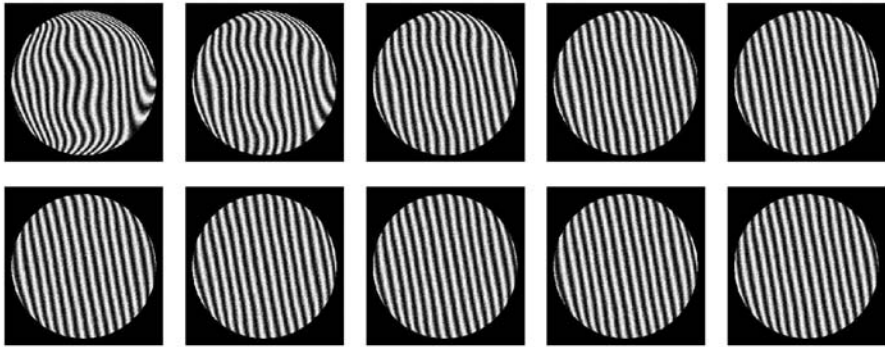


Fig. 11.6. Ten iterations of simulated closed-loop behaviour. The incoming wavefront was a randomly chosen combination of the first 30 Zernike polynomials with a linear carrier and remained constant through all the iterations. The normally distributed noise was added both to phase and interferogram and was updated every iteration. The phase was extracted with Fourier method and unwrapped via decomposition over a set of the influence functions of an adaptive mirror. The feedback gain was chosen empirically equal to 0.7. We can see that the system stabilizes itself after about 4 iterations

can be performed with the modern computers at kHz speed (at least with the fixed-point numbers). Therefore, we can expect from the whole system the update rate about several tens of hertz, or about several kHz in case of hardware-performed FFT.

11.4 Conclusion

Numerical simulations provide a strong evidence that an interferometric sensor can be used in a stable adaptive optical system with good performance. In such a system, the phase is extracted using the Fourier transform method. The control signals for the adaptive mirror are generated by direct decomposition of the wrapped phase over the influence functions of the adaptive mirror. Numerical simulations show that the errors introduced by the decomposition do not affect the system performance if the registered interferograms have a low noise contents. The speed is limited by the speed of Fourier transform. Hardware-based FFT processors can be used to build high performance systems.

References

1. R.K. Tyson: Principles of adaptive optics. 2nd edn. (Academic Press 1998)
2. T. Shirai, T.H. Barnes, T.G. Haskell: Adaptive wavefront correction by means of all-optical feedback interferometry. *Opt. Lett.* **25**, 773 (2000)
3. D. Malacara, M. Servín, Z. Malacara: Interferogram Analysis for Optical Shop Testing (Marcel Dekker, New York Basel Hong Kong 1998)
4. Y. Surrel: Photomechanics (Springer, Berlin Heidelberg New York 1987) pp. 55–102
5. M. Takeda. Temporal versus spatial carrier techniques for heterodyne interferometry. in: *Proc. SPIE* **813**, 329–330 (1987)
6. T. Kreis: Digital holographic interference-phase measurement using the fourier-transform method. *J. Opt. Soc. Am. A* **3**, 847 (1986)
7. Z. Ge, F. Kobayashi, S. Matsuda, M. Takeda: Coordinate-transform technique for closed-fringe analysis by the fourier-transform method. *Appl. Opt.* **40**, 1649 (2001)
8. F.J. Cuevas, J.H. Sossa-Azuela, M. Servín: A parametric method applied to phase recovery from a fringe pattern based on a genetic algorithm. *Opt. Commun.* **203**, 213 (2002)
9. J.L. Marroquin, R. Rodríguez-Vera, M. Servín: Local phase from local orientation by solution of a sequence of linear systems. *J. Opt. Soc. Am. A* **15**, 1536 (1998)
10. M. Servín, J.L. Marroquin, F.J. Cuevas: Fringe-follower regularized phase tracker for demodulation of closed-fringe interferograms. *J. Opt. Soc. Am. A* **18**, 689 (2001)
11. M. Servín, F.J. Cuevas, D. Malacara, J.L. Marroquin, R. Rodríguez-Vera: Phase unwrapping through demodulation by use of the regularized phase-tracking technique. *Appl. Opt.* **38**, 1934 (1999)
12. K. Itoh: Analysis of the phase unwrapping algorithm. *Appl. Opt.* **21**, 2470 (1982)
13. D.C. Chiglia, M.D. Pritt: Two-Dimensional Phase Unwrapping. Wiley Interscience (Wiley 1998)

Part II

Wavefront Sensors

12 Extended Hartmann–Shack Wavefront Sensor

B. Schäfer¹, K. Mann¹, and M. Dyba²

¹ Laser Laboratorium Göttingen
Hans-Adolf-Krebs-Weg 1, 37077 Göttingen, Germany

² MPI für Biophysikalische Chemie
Am Fassberg 11, 37077 Göttingen, Germany

Summary. A combination of a Hartmann–Shack sensor and a standard far-field measurement on one single detector is proposed. The technique is fast, manages without moveable parts, thus permitting a very compact design. It is not only suited for characterisation of the wavefront distribution, but may also be considered for determination of the important parameters beam width, beam divergence and beam propagation ratio M^2 of partially coherent laser beams. First results indicate that a fairly thorough beam characterisation including spatial coherence, propagation characteristics and beam quality can be achieved with this method.

12.1 Introduction

During the last decade the requirements on laser beam quality in scores of industrial applications, as e.g. photolithography or materials processing, have been scaled up considerably. In addition to beam power and, in some cases, spectral or polarization properties, the designer or operator most frequently needs information about the propagation characteristics, the propagation ratio M^2 and the coherence properties of the beam. The propagation characteristics or wavefront $w(x, y)$, which is, according to the ISO 15367-1 international standard [1], defined as the characteristic surface of the Poynting vector distribution $\mathbf{S}(x, y)$ weighted by the irradiance distribution $I(x, y)$:

$$\iint I(x, y) \left[\nabla_{\perp} w(x, y) - \frac{\mathbf{S}(x, y)}{|\mathbf{S}(x, y)|} \right]^2 dx dy \stackrel{!}{=} \min \quad (12.1)$$

carries detailed information about the beam aberrations, including the intrinsic ones as well as those introduced by the optical components along the beam path. It is therefore often needed if diffraction limited performance is desired. The M^2 value, on the other hand, measures the 4-dimensional volume occupied by the beam in phase space. It determines the minimum beam diameter achievable for a given numerical aperture, and is thus a measure of the beam quality, reaching a lower limit of unity for the TEM_{00} fundamental mode. The theoretical justification for the success of the beam propagation ratio as a widely accepted beam quality number traces back to the powerful concept of beam description by the 2nd order statistical moments [2]. The

latter permit a complete propagation by the well known matrix formalism of geometrical optics. According to its definition, M^2 is a true invariant of the beam within the framework of lossless paraxial optics. However, one cannot distinguish whether an M^2 value > 1 results from geometric aberrations and is thus correctable or is statistical in nature and associated with the finite spatial coherence length of the beam. This decision can only be made by virtue of some additional information, e.g. by a direct measurement of the mutual coherence.

However, even nowadays a comprehensive laser beam characterization remains quite challenging, especially if the state of coherence comes into play. Unfortunately, the standard tools for beam parameter estimation, namely Young's experiment or shearing interferometry for coherence measurements, as well as caustic measurements according to the ISO 11146 standard [3] need a couple of consecutive image recordings to work. Thus, real time operation and investigation of pulsed laser beams are very difficult to perform. This is even more evident for recent approaches utilizing the Wigner distribution function [4]. Although the latter permits an almost complete beam description, the experimental effort is huge, so industrial applications seem to be reserved to special cases.

12.2 Operation Principle of the Hartmann–Shack Sensor

The Hartmann–Shack (H–S) technique [5] (cf. Fig. 12.1), well established in fields like astronomy, lens testing or adaptive optics, is fast, robust, features white light capability and is equally well suited for coherent and partially coherent laser beams. It delivers the irradiance distribution as well as the wavefront of the beam from one single measurement, so there are no problems with pulsed lasers either. The Hartmann principle is based on a lens or pinhole array, which divides the incoming beam into a large number of $M \times N$ sub-rays indexed in the following by (i, j) . The intensity and position of the individual spots are monitored with a position sensitive detector

Table 12.1. Comparison of different methods for laser beam characterization regarding their suitability for determination of important beam parameters

Method \ Property	Diameter	Divergence	M^2	Wavefront	Coherence	Exp. Effort
Young experiment	–	–	–	–	X	high
Caustic (ISO 11146)	X	X	X	–	–	high
Wigner Distribution	X	X	X	X	X	high
Hartmann–Shack	X	X^a	X^a	X	–	slight
Ext. Hartmann–Shack	X	X	X	X	X^b	slight

^{a)} only coherent sources; ^{b)} only global coherence properties

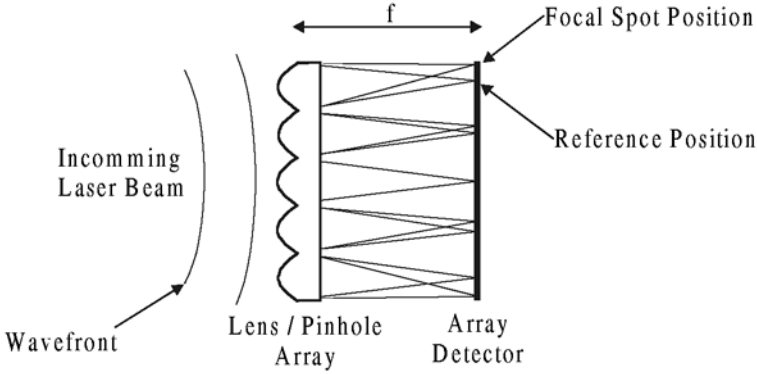


Fig. 12.1. Principle of the Hartmann–Shack sensor

placed at a distance f behind the array. Provided the intensity variation as well as the wavefront curvature across the sub-apertures can be neglected, the displacement of the spot centroid (x_{ij}^c, y_{ij}^c) with respect to a plane wave reference position (x_{ij}^r, y_{ij}^r) is a measure of the normalized local Poynting vector $\hat{\mathbf{S}}_{\perp} = (S_x, S_y)/|\mathbf{S}|$ and thus the local gradient $(\beta_{ij}^x, \beta_{ij}^y)$ of the wavefront $w = w(x, y)$ according to

$$\hat{\mathbf{S}}_{\perp} = \begin{pmatrix} \frac{\partial w}{\partial x} \\ \frac{\partial w}{\partial y} \end{pmatrix}_{ij} = \beta_{ij} = \frac{1}{f} \begin{pmatrix} x^c - x^r \\ y^c - y^r \end{pmatrix}_{ij}. \quad (12.2)$$

The only principle drawback of the H–S sensor is given by the fact that merely the time averaged wavefront can be sensed, which, however, carries no information about the beam coherence.

But this limitation can be overcome in a very convenient way by an additional far-field measurement, which delivers the true divergence and thereby reliable estimates of the second order angular moments of the beam. The key point then is, that one gets two independent estimates for the second order angular moments, one from the conventional H–S system and the second one from the far-field. Both estimates differ by the coherence term which can thus be determined [7]. It is then straightforward to obtain a measure of the global coherence length of the beam, based on focusability rather than interference fringe visibility as usual [7]. Moreover, it turns out that in the case of quasihomogeneous Gaussian sources, which are frequently used as model beams, both approaches give in fact identical results. It should, however, be emphasized, that for a general partially coherent beam the outcome of the combined H–S and far-field measurement is not sufficient for a reliable prediction of beam propagation beyond the second moment formalism. If a rigorous propagation is really needed, the more cumbersome methods mentioned above are superior, but most often the second moment based beam

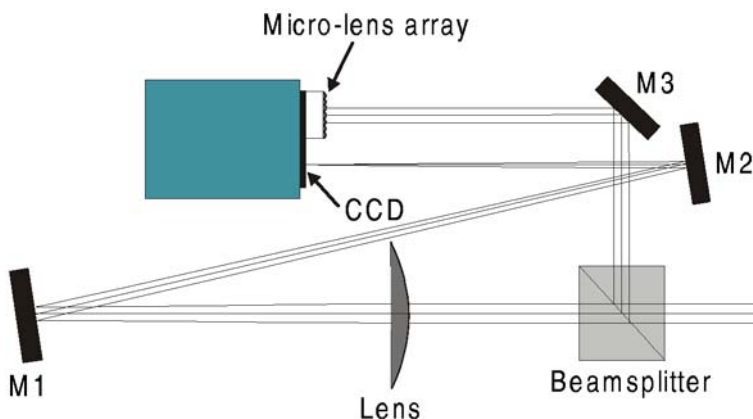


Fig. 12.2. Extended Hartmann–Shack system for simultaneous far-field, near-field and wavefront measurement

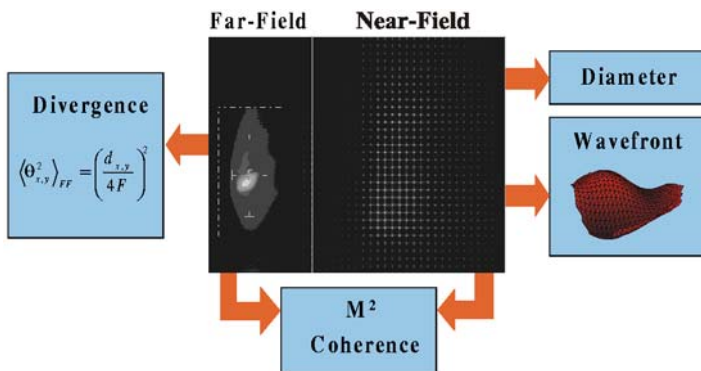


Fig. 12.3. Excimer laser recorded with the extended Hartmann–Shack sensor. The far-field distribution (*left*) enables the accurate determination of the beam divergence, whereas the Hartmann–Shack sensor (*right*) delivers beam diameter and wavefront. The combination permits the estimation of beam coherence and M^2

propagation appears to be completely adequate, meeting the practitioners requirements to a satisfactory extent. Obviously, the extended Hartmann–Shack approach described above, permits the determination of the complete 4×4 2nd moment beam matrix. The pure spatial moments are determined from the segmented near-field, the pure angular moments are obtained from the far-field and, at least, the mixed moments can be extracted from the local slopes of the wavefront. This is superior to the standard caustic approach, which delivers only nine out of ten independent elements of the beam matrix. The twisted phase parameter [2] remains undetermined unless several caustics including non spherical elements are formed.

Despite of its appealing theoretical properties, there is, however, one serious experimental problem faced to the beam description based on the 2nd moment concept, namely its high sensitivity to noise and to any non constant background intensity. Reliable results therefore require careful subtraction of a background image and a very high signal to noise ratio in order not to cut of the outer wings of the beam profile. This is even more demanding with the Hartmann–Shack sensor where only about 5% of the total detector area is illuminated. As a rule of thumb, to reach a certain accuracy level in the parameter estimation, the Hartmann–Shack sensor needs approximately 4–6 bits more dynamic range compared to the ISO 11146 standard approach. A second aspect solely associated with the Hartmann–Shack method is diffraction-induced crosstalk between neighboring sub-apertures, which leads to an erroneous estimation of the local wavefront slope. For steep beam profiles the errors of the beam divergence introduced by this effect can be as large as 30%. There are several possible ways to reduce crosstalk, apodisation of the microlens array, numerical deconvolution of the spot pattern and superlinear weighting within one sub-aperture. However, apodised microlens arrays are difficult to fabricate so commercial arrays of sufficient performance over a wide spectral range are still not available. On the other hand, deconvolution is rather time consuming and leads to satisfactory results only if the overlap between the spots remains moderate. Thus superlinear weighting seems to be the most effective reduction method, which has been confirmed experimentally and by extensive numerical simulations [8].

12.3 The Extended Hartmann–Shack Sensor

The new concept [6, 7] senses both the wavefront as well as the far-field measurement on a single CCD chip. It basically consists of a beamsplitter for dividing near- and far-field path. One part of the beam is directed onto a micro-lens array which covers approximately 2/3 of the detector area. The residual third is occupied by the far-field, which is produced by a plano-convex lens in the second path. The set-up can be almost as compact as a pure Hartmann–Shack system and does not contain any moveable parts. It enables a fairly complete beam characterisation including diameter, divergence, M^2 and coherence estimates of the beam. As a side effect, which applies to fully coherent beams as well, the accuracy in beam parameter estimation is considerable enhanced in comparison to a pure Hartmann–Shack sensor, mainly as a consequence of the improved spatial resolution of the far-field measurement.

12.4 An Example

The skill of the new sensor concept for laser beam characterization is demonstrated by means of an example representing a partially coherent source.

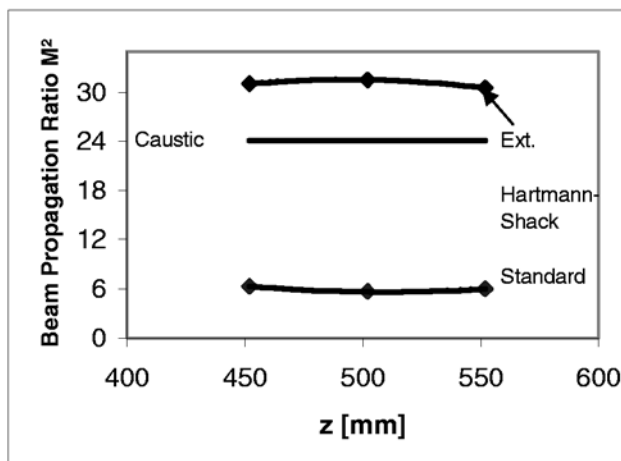


Fig. 12.4. Slow-axis beam propagation ratio of the KrF excimer laser recorded at 3 different positions along the beam axis, using the caustic measurement, the ordinary as well as the extended Hartmann–Shack sensor

Figure 12.3 shows the slow axis beam propagation ratio of a Lambda Physik Optex KrF-Excimer laser recorded at 3 positions along the beam axis. The reference caustic measurement yields $M^2 = 24$, whereas an M^2 value of only 6 is predicted by the ordinary H–S system. This tremendous difference arises as a result of the low coherence length of this source. The latter was estimated from the extended sensor to about $220\ \mu\text{m}$ [7], which is in satisfactory agreement with the results from direct measurements of the average coherence length, which were obtained from a Young experiment, yielding $260\ \mu\text{m}$. Finally, the extended H–S sensor predicts an M^2 of 31, which demonstrates the improved accuracy compared to the pure H–S sensor. The still significant difference in the M^2 values results from the limited number of subapertures, i.e. the spatial resolution of the H–S sensor, being $200\ \mu\text{m}$ for this particular array. A larger number of subapertures would certainly improve the accuracy.

The fast axis ($M^2 \sim 100$) measurements (cf. Fig. 12.5) show by and large the same picture. Now however, due to the smaller coherence length of only $120\ \mu\text{m}$, the absolute differences of the estimated M^2 -values are even larger. The standard sensor predicts $M^2 \sim 35$ whereas the extended sensor gives $M^2 \sim 100$ which is in close agreement to the reference caustic measurement.

12.5 Conclusion

The previous examples disclose the extended H–S sensor as a promising tool for laser beam characterization, delivering valuable coherence information which cannot be obtained with the standard ISO approach. Furthermore,

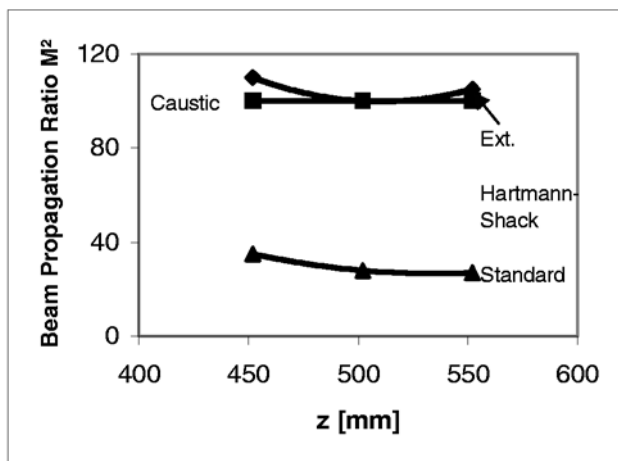


Fig. 12.5. Fast-axis beam propagation ratio of the KrF excimer laser recorded at 3 different positions along the beam axis, using the caustic measurement, the ordinary as well as the extended Hartmann–Shack sensor

accuracy comparable to the latter is accessible if a high spatial resolution of the H–S sub-system joins a CCD detector with sufficiently high dynamic range of at least 12bit, although both requirements are not fully exhausted at this stage. Thus, the extended H–S sensor may be regarded as a future supplement, or, in some cases, even a substitute to the standard ISO tools.

Acknowledgement

This work is supported by the Bundesministerium für Bildung und Forschung (BMBF) within the scope of the Eureka project CHOCLAB II (13EU0158)

References

1. ISO/CD 15367-1: Lasers and laser related equipment – Test methods for determination of the shape of a laser beam wavefront – Part I: Terminology and fundamental aspects
2. G. Nemes, J. Serna: The ten physical parameters associated with a full general astigmatic beam: A Gauss Schell-model. 4th International Workshop on Laser Beam and Optics Characterisation (LBOC), A. Giesen and M. Morin (eds.), 29, Munich 1997
3. ISO/FDIS 11146: Lasers and laser-related equipment – Test methods for laser beam parameters – Beam widths, divergence angle and beam propagation factor (1999)
4. B. Eppich: Measurement of the Wigner distribution function based on the inverse Radon transformation. In: L.W. Austin, A. Giesen, D.H. Leslie, H. Weichel

- (eds.): Beam Control, Diagnostics Standards and Propagation, Proc. SPIE **2375**, 261 (1995)
5. D.R. Neal, W.J. Alford, J.K. Gruetzner, M.E. Warren: Amplitude and phase beam characterization using a two-dimensional wavefront sensor. Proc. SPIE **2870**, 72 (1996)
 6. B. Schäfer, K. Mann: Characterisation of laser beams using a Hartmann–Shack wavefront sensor. 6th International Workshop on Laser Beam and Optics Characterisation (LBOC), edited by WLT, Munich 2001
 7. B. Schäfer, K. Mann: Determination of beam parameters and coherence properties of laser radiation by use of an extended Hartmann–Shack wavefront sensor, Appl. Optics **41**(15), 2809 (2002)
 8. B. Schäfer, K. Mann: Estimation of beam parameters and coherence properties of laser radiation by use of an extended Hartmann–Shack wavefront sensor. 7th International Workshop on Laser Beam and Optics Characterisation (LBOC), Proc. SPIE **4932**, 569 (2002)

13 High Resolution Wavefront Sensing

J.E. Oti, V.F. Canales, and M.P. Cagigal

Universidad de Cantabria, Departamento de Física Aplicada
Avda. Los Castros S/N, 39005 Santander, Spain

Summary. High resolution wavefront sensors are devices with a great practical interest since they are becoming a key part in an increasing number of applications like extreme Adaptive Optics. We describe theoretically a novel wavefront sensor, which basically consists of a telescopic system with a linearly increasing amplitude mask placed at the intermediate common focal plane. This sensor offers high resolution and an easy adjustment of the sampling and of the dynamic range. The parameters and performance of the new sensor are discussed, and a comparison with commonly used Hartmann–Shack sensors is carried out. Our sensor presents several advantages. Resolution is higher, and consequently a larger number of modes can be estimated for reconstructing the wavefront, and the dynamic range and sampling can be easily adjusted. Furthermore, we show that a proper election of the mask parameters allows an acceptable performance even in adverse photon noise conditions.

13.1 Introduction

In Adaptive Optics systems for very large telescopes, and especially in certain applications such as the search for exoplanets, a sensor with the highest resolution is required [1] In recent years, the development of low-cost devices allows the application of Adaptive Optics in other fields such as lasers, confocal microscopy or human vision [2–4], in which new kinds of sensors may result advantageous. Furthermore, there are other applications out of the scope of Adaptive Optics in which new wavefront sensing devices could be useful, too.

In this paper, we describe the Optical Differentiation (OD) wavefront sensor, which consists of a telescopic system with a mask at the intermediate focal plane. The first lens performs the Fourier transform of the incoming field, then it is multiplied by the mask, and Fourier-transformed again by the second lens. The mask amplitude increases linearly along a certain direction. The wavefront phase derivative is estimated from the detected light intensity. In practice, the sensor performs an optical differentiation process. Actually, a rotating filter can be used to provide the derivatives in two orthogonal directions.

First, we analyze the actual implementation of the sensor and the parameters that characterize the mask. The signal-to-noise ratio of the tech-

nique is obtained from these parameters and it is compared with that of the Hartmann–Shack (H–S). Then, the relationship between the size of the mask and the dynamic range is derived. Finally, a computer simulation is performed to evaluate the performance of both sensors. The main advantages of the new sensor are its high (and adjustable) spatial resolution, the easily adjusting of the dynamic range and that it is able to work with polychromatic sources [5]. Its main drawback is the energy loss due to the mask absorption. Nevertheless, it presents a SNR comparable to that of the H–S sensor provided a proper election of the mask parameters. Although there are other adjustable resolution sensors [6, 7], they present limitations that this sensor overcomes.

13.2 The Optical Differentiation Sensor

To describe the theoretical principles of the OD sensor, let us consider the electric field $E(x, y) = A e^{j\phi(x, y)}$, where A is the constant amplitude and $\phi(x, y)$ is the wavefront phase. The derivative of the wavefront in a particular direction will be performed using the Fourier transform (FT) properties. The arrangement consists of a pair of achromatic lenses forming a usual $4-f$ system and a mask M placed at the common focal plane of the lenses. The first lens performs the FT of the input field on the mask, whose amplitude linearly increases along the direction in which the derivative is to be estimated. The product of the transformed wavefront times the mask is then Fourier transformed again onto a detection system (CCD). Two separated measurements are required to obtain wavefront phase slopes series in two orthogonal directions.

Since the mask is the key element in the OD sensor it must be carefully analyzed. The masks that allow the differentiation along the x and y directions, M_x and M_y respectively, can be expressed as

$$\begin{aligned} M_x &= 2\pi b_r r_x + a = 2\pi b u_x + a \\ M_y &= 2\pi b_r r_y + a = 2\pi b u_y + a, \end{aligned} \quad (13.1)$$

where f the focal distance of the first lens and r_x and r_y represent real distances in the mask plane. The mask can also be expressed in terms of

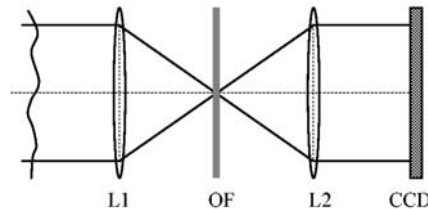


Fig. 13.1. Set-up of the OD sensor. OF is the amplitude mask for optical differentiation. L1 and L2 are achromatic lenses of equal focal length

the spatial frequencies of coordinates x and y in the pupil plane, u_x and u_y , where $b = \lambda f b_r$. In addition, a and b_r (or b) are two constant parameters that determine the mask behaviour.

When a mask of this kind is placed at the intermediate plane of a telescopic system, due to the differentiation property of the FT [8], the intensity at the CCD is related to the field derivative along the corresponding mask direction:

$$\begin{aligned} I_x(x, y) &= \left| \text{FT}^{-1} [\text{FT}(E(x, y)) \cdot M_x] \right|^2 = \left| -j b \frac{\partial E(x, y)}{\partial x} + a E(x, y) \right|^2 \\ I_y(x, y) &= \left| \text{FT}^{-1} [\text{FT}(E(x, y)) \cdot M_y] \right|^2 = \left| -j b \frac{\partial E(x, y)}{\partial y} + a E(x, y) \right|^2 \end{aligned} \quad (13.2)$$

Then, by substituting the field expression, the derivatives of the wavefront phase along orthogonal directions can be obtained from the intensities

$$\begin{aligned} \alpha_x &= \frac{\partial \phi(x, y)}{\partial x} = \frac{\sqrt{I_x/A} - a}{b} = \frac{\sqrt{I_x/A} - a}{b_r \lambda f} \\ \alpha_y &= \frac{\partial \phi(x, y)}{\partial y} = \frac{\sqrt{I_y/A} - a}{b} = \frac{\sqrt{I_y/A} - a}{b_r \lambda f} \end{aligned} \quad (13.3)$$

Note that the wavefront slope can be obtained as the product of the wavefront phase slope, $\alpha \times \lambda/2\pi$ and thus, it is independent on wavelength. It can be seen that the values of b_r and f control the dynamic range of the phase derivative estimate. In contrast with the H-S sensor [9], which is based on the measurement of a centroid position, this is a photometric sensor. Thus, the phase derivative is estimated at each pixel of the detector by comparing the intensity with that corresponding to a flat wavefront portion $I_0 = (aA)^2$. The wavefront phase is sampled by the pixels contained in the CCD illuminated area providing very high spatial resolution without limitations of the dynamic range.

This sensor can also be explained using a ray tracing picture. Note that, if achromatic lenses are used, each small area of the sensor entrance pupil is directly mapped in one area of the detection plane. In addition, parallel rays (wavefront regions with the same slope) will go to the same point at the filter plane, and thus, will suffer the same attenuation. The intensity at each area of the detection plane provides an average of the wavefront phase slope for the area. When using polychromatic sources, the sensor also provides an average over the whole source bandwidth.

The masks defined in (13.1) have a linearly increasing amplitude. In practice, these masks are an intensity filter with variable transmittance given by $(2\pi b_r r + a)^2$. For particular values of (a, b) the amplitude ranges from negative to positive values. In such cases, a second mask, consisting of a phase plate step function, is required for attaining the correct sign [8]. In this work, only amplitude filters are used. Finally, the size of the filter is also determined

by the values of the parameters a and b . Assuming that the maximum value of the mask is equal to one (in order to minimize the lost energy), its width can be derived as: $W = \lambda f(1 - a)/(\pi b)$, where it is assumed that the centre of the filter lies on the optical axis.

13.3 Signal-to-Noise Ratio for the OD Sensor

13.3.1 Photon Noise

From the expression of the slope α as expressed in (13.3) and using the standard error propagation formula to work out the variance, the SNR for photon noise can be written as

$$\text{SNR}_{\text{OD}} = \langle \alpha \rangle 2Ab = \langle \alpha \rangle \sqrt{n_{\text{OD}}} 2b, \quad (13.4)$$

where n_{OD} is the number of photons arriving at the corresponding area in the entrance pupil of the sensor and $\langle \dots \rangle$ means ensemble average.

To maximize the SNR, an actual filter should have a value of b as large as possible. This is carried out taking $a = 0.5$ and making the filter size as small as possible, although a compromise between the energy loss and the filter size is necessary.

13.3.2 Signal-to-Noise Ratio Comparison

We compare the SNR of the OD sensor with that of the Hartman–Shack sensor in the photon noise case. The corresponding SNR for the H–S can be expressed as $\text{SNR}_{\text{H-S}} = \langle \alpha \rangle d \sqrt{n_{\text{H-S}}} / (0.86\pi)$ [10, 11] where d is the diameter of the circular microlens. It is necessary to state that this equation, due to the approximations used to develop it [10, 11], only determine an upper limit to the SNR of the H–S.

The ratio between the SNR due to photon noise of both sensors is expressed as

$$\frac{\text{SNR}_{\text{OD}}}{\text{SNR}_{\text{H-S}}} = \frac{2b \cdot 0.86\pi \sqrt{n_{\text{OD}}}}{d \sqrt{n_{\text{H-S}}}} = \frac{0.0087 D_{\text{lens}} 0.86\pi}{d \sqrt{2}}, \quad (13.5)$$

where D_{lens} is the diameter of the lens used to evaluate the first Fourier transform, and b has been expressed in terms of the number of Airy rings covered by the filter, N_A ($W = 1.22 \cdot N_A \lambda f / D_{\text{lens}}$). In this expression the ratio $n_{\text{OD}}/n_{\text{H-S}}$ is set to $1/2$ because the light of the OD sensor must be split in two channels. A further analysis of the SNR ratio behaviour can be found in a previous work [12].

13.4 Dynamic Range

The range of wavefront phase slopes that can be measured also depends on the size of the filter, and, consequently, on b . Thus, the maximum slope that can be measured is $\alpha_M = (2\pi/\lambda) (W/2f) = 1/(2b)$. This relationship between the parameters of the mask and the wavefronts to be measured enables the election of the appropriate mask. Moreover, different masks can be implemented using a LCD. As a result, the dynamic range of the OD sensor can be easily adjusted. If we define the dynamic range as $DR_{OD} = 2\alpha_M$, we obtain that $DR_{OD} = 1/b$. It only depends on the parameters of the mask and not on the sampling of the wavefront. This implies that high dynamic range can be attained without loss of the spatial resolution.

13.5 Simulation and Comparison with the Hartmann–Shack

Once described the sensor characteristics, we will compare the OD sensor performances with that of the standard H–S sensor. We have seen that the main two advantages of the OD sensor are its high resolution and the possibility of easily adjusting the dynamic range. The main drawback is that the intensity mask absorbs part of the incoming energy.

We performed a simulation for comparing both sensors. Four hundred distorted wavefronts following Kolmogorov statistics with $D/r_0 = 1$ were generated using Roddier’s technique [13]. In this technique, the wavefront is decomposed into Zernike polynomials. The number of Zernike modes that we used in our simulation was $N = 560$, and the three first modes (piston, tip and tilt) are assumed to be corrected. The number of samples in the wavefront was $(\pi/4) \times 241 \times 241$. Then, the phase derivative was estimated both using a H–S sensor and our technique. In a first case, the sampling area was the same for both sensors, 80 areas in the whole pupil, in order to analyze them under the same conditions. Finally, the wavefront is reconstructed, so that a certain number, k , of coefficients is obtained from the wavefront slopes. The error in the whole process is estimated using the residual phase variance of the reconstructed wavefront, defined as

$$\sigma_{\text{rec}}^2 = \int_{\text{Pupil}} [\phi(\mathbf{r}) - \phi_{\text{rec}}(\mathbf{r})]^2 d\mathbf{r} \approx \sum_{i=1}^N [a_i - a_{i\text{rec}}]^2, \quad (13.6)$$

where a_i are coefficients of the corresponding Zernike polynomials, $a_i = 0$ for $i > k$. Figure 13.2 compares the residual variance obtained using the OD and the H–S sensor as a function of the number of reconstructed modes k . As expected, when the number of modes increases, the error in the reconstruction process decreases. The main conclusion is that the accuracy of our

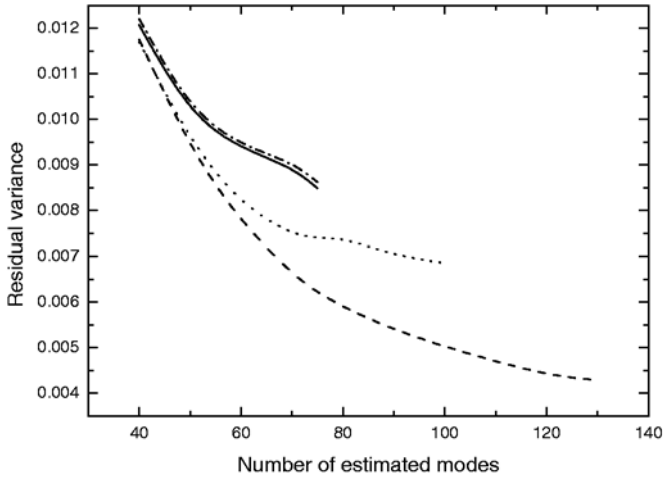


Fig. 13.2. Comparison of the residual variance obtained using the H-S (*dashed-dot curve*) and the OD sensor (*solid line*) as a function of the number of reconstructed modes k with 80 sampling areas. The behaviour of OD with a higher resolution is also shown (*dotted line*: 112 sampling areas, *long-dashed line*: 177 sampling areas). The values of the masks parameters are $a = 0.5$ and $b = 0.0013D/2$

technique is very similar to that of the HS sensor under the same conditions. However, our sensor is able to attain very high spatial resolution if necessary. Figure 13.2 also shows the residual variance when the OD sensor number of sampling areas is higher than that of the H-S sensor. In such a case, the OD sensor allows the estimate of higher order modes and provides better accuracy, especially if the number of modes to be estimated is high.

Finally, the proposed sensor is compared with the H-S sensor in low-light-level conditions. Photon noise affects the behaviour of both sensors and preserves them from attaining the accuracy shown in the previous analysis unless a high enough number of photons are available.

Figure 13.3 shows the residual phase variance of the reconstructed wavefront as a function of the number of photons that arrive at the wavefront sensor. The number of simulated wavefronts is 400 and $D/r_0 = 15$. The number of reconstructed modes is fixed and equal to 95 and both sensors are analyzed under the same conditions. As expected the residual phase variance decreases as the energy that reaches the sensor increases, and it saturates when the number of photons is high enough. Both sensors show similar behaviour despite the OD sensor presents slightly lower SNR in low-light-level conditions, because a part of the incoming energy is lost at the mask. However, when the resolution of the OD sensor is increased, the results even improve those given by the H-S sensor, especially if a higher number of modes are estimated, as shown in Fig. 13.3.

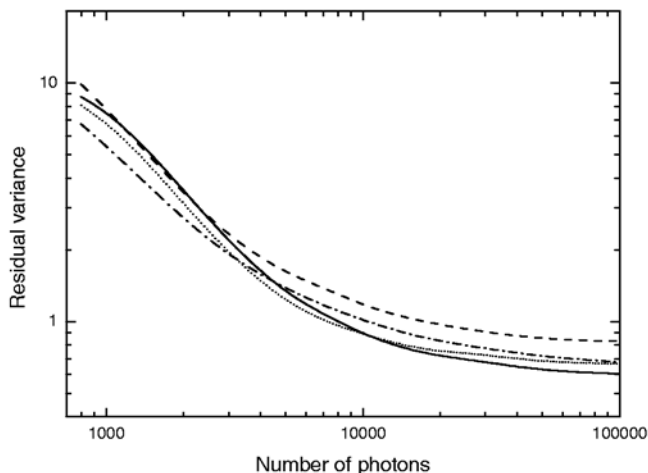


Fig. 13.3. Comparison of the residual phase variance of the reconstructed wavefront obtained using the H-S (*dotted-dashed curve*) as a function of the number of photons with 112 sampling areas and 95 estimated modes. The results of OC sensor with a higher resolution, 177 sampling areas, are also shown both for the same number of estimated modes (*dotted line*, 95 modes) and for a higher number of estimated modes (*solid line*, 120 modes). The value of the masks parameters are $a = 0.5$ and $b = 0.01 D/2$

13.6 Conclusions

We present a novel wavefront sensor consisting of a linearly increasing amplitude mask placed at the focal plane of a telescopic system. The parameters and performance of the OD sensor have been discussed, and a comparison with commonly used H-S sensors has been carried out. The OD sensor is able to work with polychromatic source and the dynamic range and sampling can be easily adjusted. This allows us to obtain high resolution, and consequently to estimate a large number of modes for reconstructing the wavefront. Furthermore, we have shown that a proper election of the mask parameters provides an acceptable performance even in adverse photon noise conditions.

Acknowledgement

This research was supported by Ministerio de Ciencia y Tecnología grant AYA2000-1565-C02.

References

1. V.F. Canales, M.P. Cagigal: Gain estimate for exoplanet detection with adaptive optics. *Astron. Astrophys. Suppl. Ser.* **145**, 445 (2000)
2. G. Vdovin: Micromachined membrane deformable mirrors. In: R. Tyson (ed.): *Adaptive Optics Engineering Handbook* (Marcel Dekker Inc., New York 1998)
3. M.A. Neil, M.J. Booth, T. Wilson: New modal wavefront sensor: a theoretical analysis. *J. Opt. Soc. Am A* **17**, 1098 (2000)
4. E.J. Fernandez, I. Iglesias, P. Artal: Closed-loop adaptive optics in the human eye. *Opt. Lett.* **26**, 746 (2001)
5. O. von der Lühe: Wavefront error measurement technique using extended, incoherent light sources. *Opt. Eng.* **27**, 1078 (1988)
6. E.N. Ribak: Harnessing caustics for wavefront sensing. *Opt. Lett.* **26**, 1834 (2001)
7. R. Ragazzoni: Pupil plane wavefront sensing with an oscillating prism. *J. Mod. Opt.* **43**, 289 (1996)
8. K. Iizuka: *Engineering Optics* (Springer, Berlin Heidelberg New York 1987)
9. M. Geary: *Introduction to Wavefront Sensors* (SPIE Press, Washington 1995)
10. R. Irwan and R.G. Lane: Analysis of optimal centroid estimation applied to Shack–Hartman sensing. *Appl. Opt.* **32**, 6737 (1999)
11. J. Primot, G. Rousset, J.C. Fontanella: Deconvolution from wavefront sensing: a new technique for compensating turbulence-degraded images. *J. Opt. Soc. Am. A* **7**, 1913 (1989)
12. J.E. Oti, V.F. Canales, M.P. Cagigal: Analysis of the signal-to-noise ratio in the optical differentiation wavefront sensor. *Opt. Express* **11**, 2783 (2003)
13. N. Roddier: Atmospheric wavefront simulation using Zernike polynomials. *Opt. Eng.* **29**, 1174 (1990)

14 Distorted Grating Wavefront Sensing in the Midwave Infrared

D.M. Cuevas, L.J. Otten, P. Harrison, and P. Fournier

Kestrel Corporation
3815 Osuna Rd. NE, Albuquerque, NM, 87109, USA

Summary. Kestrel Corporation has extensive experience using distorted grating wavefront sensors (DGWFS) in a number of applications. The DGWFS has previously been demonstrated in the visible range (400–700 nm) by Kestrel and others. An experimental system was built in a laboratory environment to show that the DGWFS could recover wavefront characteristics of a midwave infrared (MWIR) laser. This paper describes the theory of the DGWFS and the experimental procedures implemented to run the system with the MWIR laser. The sensitivity to the type of gratings employed will be addressed. The results of sensitivity, dynamic range and thermal noise measurements will be discussed.

14.1 Introduction

For the past several years Kestrel Corporation has been investigating a wavefront measurement technology based on the use of distorted gratings. Similar to a curvature sensor, a DGWFS measures intensity in two planes through which the wavefront propagates [1, 2]. The difference between these planes gives a measure of the axial intensity gradient. Consider the wavefront propagation of a wavefront between two planes, Fig. 14.1. Those regions of the wavefront that are concave or convex on the first plane converge, or diverge, respectively as they propagate toward the second plane. The local intensity on the second plane is therefore increased or reduced, compared to the first plane. A measurement of the intensity gradient along the optical axis provides indications of the local wavefront curvature. The technology that creates the multiple images is based on local displacement of lines in a diffraction grating used to introduce arbitrary phase shifts into wavefronts diffracted into the non-zero orders (the phase detour effect) [3–5]. A quadratic displacement function is used to alter the optical transfer function associated with each diffraction order such that each order has a different degree of defocus.

This modification produces a distorted grating, which allows it to serve as a beamsplitter producing simultaneous images of multiple object planes on a single image plane. In Fig 14.2, the zero order records an image of an object at infinity. The two pupil plane images (I1 and I2) required for the wavefront sensing are formed in the -1 and $+1$ orders. These images correspond to planes (A & C) equal distances either side of the pupil and have magnifications of equal magnitude, but opposite sign. Kestrel and others have

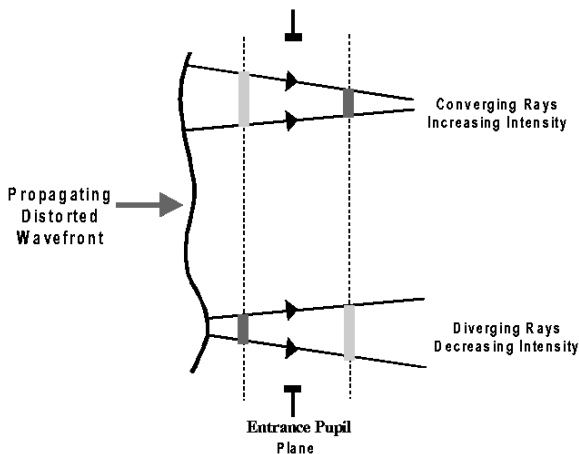


Fig. 14.1. Measurements made at two image planes with a known aberration are required for a phase diversity wavefront sensor

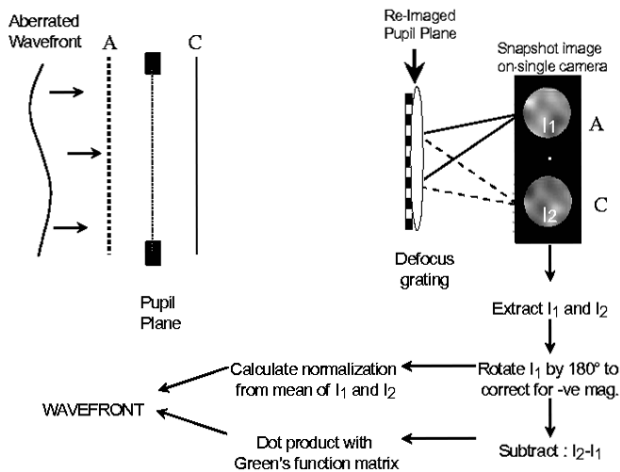


Fig. 14.2. Implementation of wavefront curvature sensing using a defocus grating

demonstrated the distorted grating wavefront curvature sensing non-iterative wavefront reconstruction technique in situations with high levels of scintillation [5–8].

14.2 Method

The objective of this research program was to demonstrate the feasibility of using a DGWFS as a MWIR wavefront measurement device. Theoretical

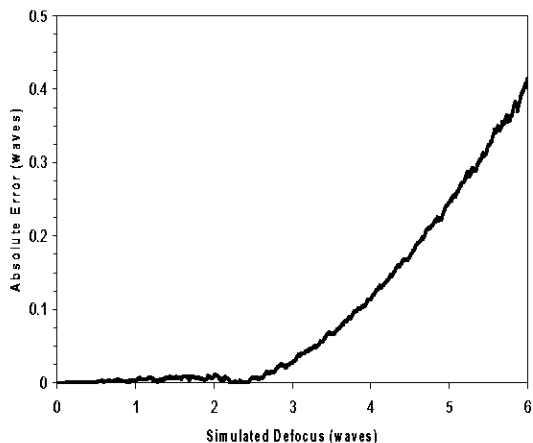


Fig. 14.3. Simulated wavefront sensor performance

analysis was used to determine the limitation of the concept and to define a baseline model for comparison to the laboratory demonstration. Laboratory experiments were then used to define the concept performance features and limitations.

The DGWFS model used for the visible bands was extended for operation at $3.39\ \mu\text{m}$ and was found to function satisfactorily. When there is defocus in the system, one order is proportionally slightly bigger than the other. To simulate the characteristics of the DGWFS in the MWIR, the order diameters for incremental defocus were calculated and used to make simulated raw images of the orders with the calculated diameters. These simulated raw images were then processed using the wavefront sensing software. The software was initialized with the appropriate MWIR parameters and a wavefront was successfully calculated. Using this technique, an analytical model of the MWIR wavefront sensor was produced and used to estimate the dynamic range and sensitivity of the system, as shown in Fig. 14.3. The analysis suggested that the wavefront sensor would be linear up to ± 2.5 waves of defocus (at $3.39\ \mu\text{m}$). Even though the system would be nonlinear after ± 2.5 waves the analysis predicted that the defocus would be predictable up to ± 10 waves of error for the specified grating. The sensitivity was predicted to be better than $\lambda/100$ through out this range.

For the experiment, an optical system was designed to validate the distorted grating wavefront curvature measurement technique. The system consisted of a 3.4 micron He-Ne laser, 25 : 1 beam expander, 1 : 1 relay, grating and imaging lens and an Amber 256×256 InSb MWIR detector, as shown in Fig. 14.4.

Three different gratings were tested. The first two were amplitude gratings, one on a quartz substrate; the other on glass. The third grating was

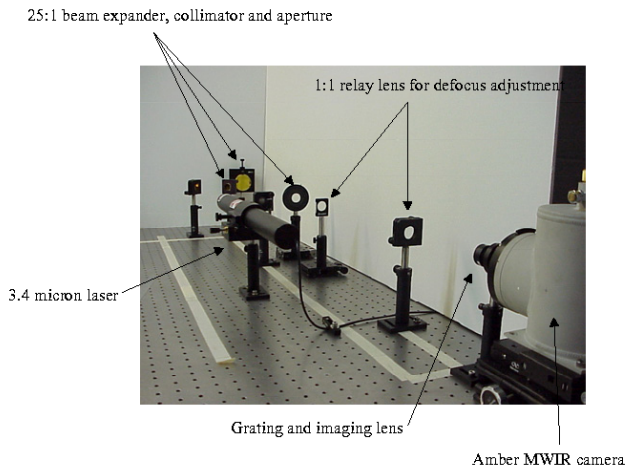


Fig. 14.4. Photo of the laboratory test set-up

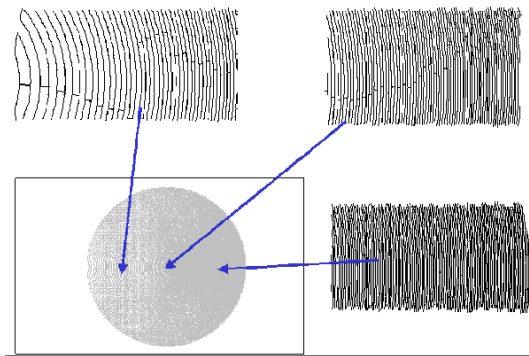


Fig. 14.5. Grating design for the ZnSe phase grating. Note how the period varies across the grating

a ZnSe phase grating. The design for the ZnSe phase grating is shown in Fig. 14.5.

The grating design was optimized for the $30\ \mu\text{m}$ pixel size Amber camera and a wavelength of 3.39 microns. The amplitude and phase gratings have the same power and nominal period. The amplitude gratings have a faster fabrication time so they were used to make the initial measurements with the experimental system. The phase grating was expected to have better performance than the amplitude gratings and was therefore tested and then compared to the amplitude gratings.

The performance characteristic measurements were defocus sensitivity, defocus dynamic range and influence of thermal noise. The dynamic range and sensitivity measurements use defocus, as this aberration could easily be

introduced into the system. Dynamic range and sensitivity were both determined by translating the first lens from the 1 : 1 relay (L_1); this translation introducing defocus. This defocus was plotted and the dynamic range determined by noting where the plot became nonlinear. By knowing the defocus dynamic range of the system, the limitation of the system to accurately detect defocus is also known. For the sensitivity measurements, L_1 was placed 4 mm away from its original location (x_0). This distance was chosen so that there was enough motion to detect the sensitivity of the system. The translation distance was then halved until L_1 approached the x_0 position. When L_1 was in its original position, there was no defocus remaining. The defocus coefficient was plotted as a function of position and the point at which there was no measurable change was used to determine the sensitivity. At the point where there was no more change in defocus from one position to another, the system could no longer detect the small change in defocus.

A fold mirror (M_1) was heated to demonstrate the effects of thermal noise. Data was taken when the mirror was at room temperature and at 10°C increments until it was 30°C above room temperature. By introducing thermal noise, the reaction to temperature fluctuation can be observed. Dynamic range, sensitivity and thermal effects were also used to compare the amplitude and phase grating performance.

14.3 Results

Data were manually processed using a program called File Wave. File Wave computes the shape of the wavefront from the difference matrix through a matrix multiplication with a pre-computed Green's function. Zernike coefficients values, as well as reconstructed wavefronts, are calculated by the software.

When L_1 was translated, approximately 4 waves of defocus were introduced before the translation stage limit was reached. After processing, the resulting defocus coefficients were plotted and compared to the theoretical values. The dynamic range data of the quartz amplitude grating and the ZnSe phase grating can be seen in Figs. 14.6 and 14.7 respectively. These data do not represent the limit for the amplitude gratings, due to the translation stage limitation. The dynamic range for both amplitude gratings is higher than 4 waves because the data is still linear at that point, but the phase grating became nonlinear at approximately 3.3 waves of defocus. Both gratings demonstrated a higher dynamic range than the predicted ± 2.5 waves of defocus.

Figures 14.8 and 14.9 show the defocus sensitivity data for the ZnSe phase grating and the quartz amplitude grating. The sensitivity for the quartz amplitude grating was $\lambda/50$, $\lambda/20$ for the glass amplitude grating and $\lambda/250$ waves for the ZnSe phase grating. Sensitivity can be found by locating the position on the graph where there is no longer a change in defocus with a

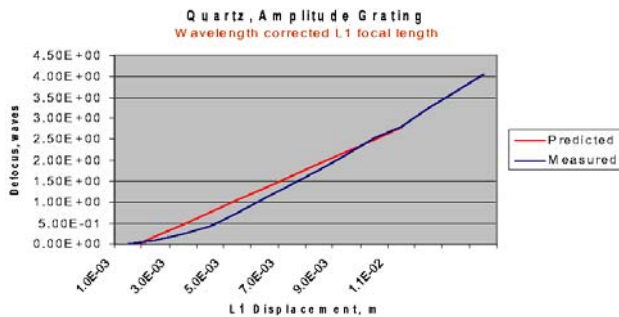


Fig. 14.6. Quartz amplitude grating dynamic range showing the predicted and measured values. Dynamic range of the amplitude grating is greater than 4 waves of defocus but could not be measured due to limitations from the translation stage

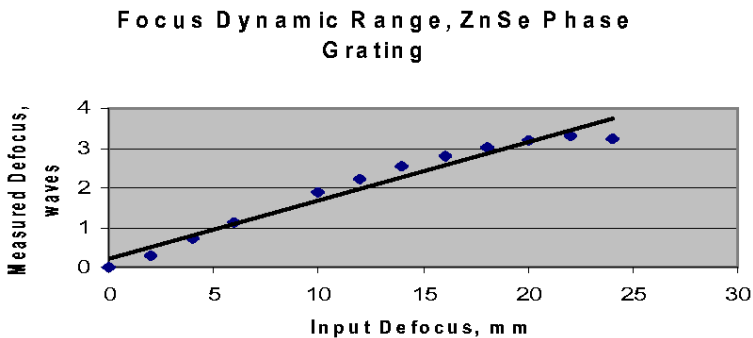


Fig. 14.7. Dynamic range of the ZnSe phase grating. The linear fit is for a perfect grating. This grating has a dynamic range of approximately ± 3.3 waves

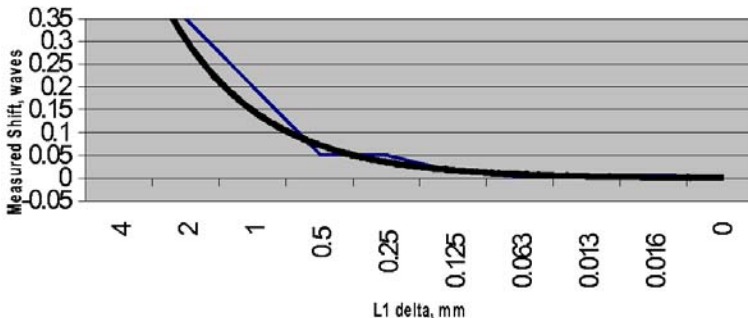


Fig. 14.8. Defocus Sensitivity with the ZnSe phase grating. A limiting sensitivity of approximately 0.004 waves was measured. The black line is the expected fit

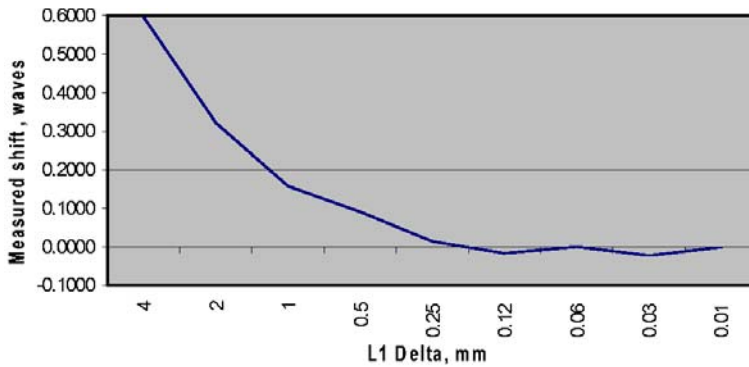


Fig. 14.9. Defocus Sensitivity of the Quartz amplitude grating. The limiting sensitivity of approximately 0.02 waves was measured

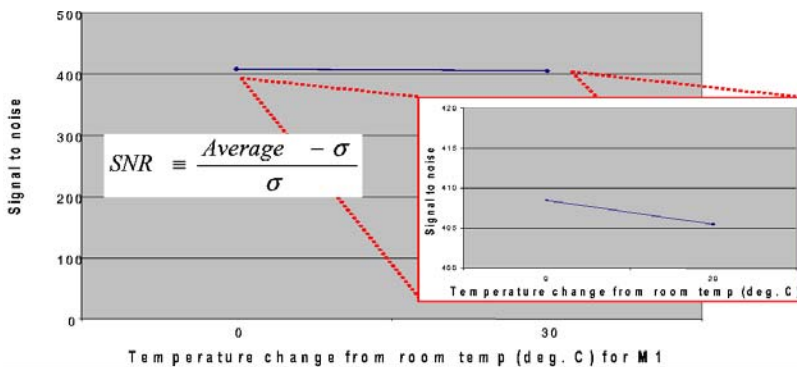


Fig. 14.10. Change in SNR as the temperature of M1 is changed. The insert is an enlargement of the curve to illustrate the small decrease as temperature is increased

change in position (the plot levels off). The phase grating was more sensitive than both amplitude gratings and better than the predicted sensitivity of $\lambda/100$.

The effect of thermal noise on the recovered wavefront manifests itself as noise in the measurement for both the amplitude and phase gratings. When the data was analyzed to determine the signal to noise ratio (SNR) there was only a very small change with the increase of temperature. SNR was defined as the average of the data minus the standard deviation (∇), divided by the standard deviation ($[Average-\sigma]/\sigma$). Figure 14.10 shows the measurements of the SNR as a function of M₁ temperature change for one of the amplitude gratings. The other amplitude grating and the phase grating showed similar results. Figure 14.11 shows the reconstructed wavefront when the mirror was at room temperature and when the mirror had been heated by 30°C. The wavefront when the mirror was heated 30°C did not significantly change from the wavefront at room temperature. The DGWFS was able to accurately

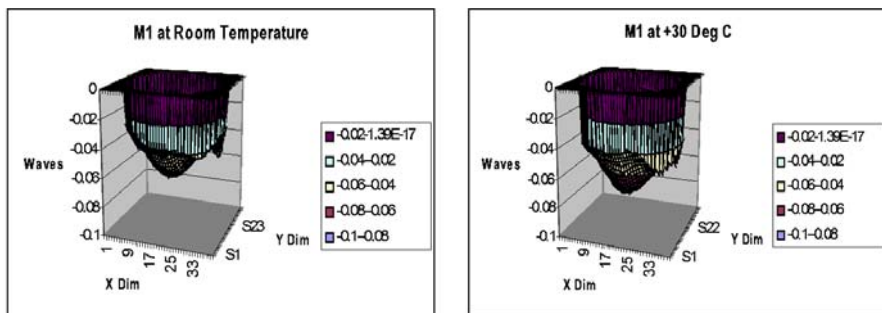


Fig. 14.11. Change in wavefront for a 30°C increase in the temperature of M1. All data are in waves

reconstruct the wavefront regardless of the temperature of the optics in the system.

14.4 Conclusion

Theoretical modeling and experimental data have shown that the distorted grating wavefront sensor can be successfully extended into the MWIR. Sensitivity and dynamic range were found to be predictable. More importantly, since the MWIR is in the thermal IR band, we noted that the DGWFS was insensitive to the temperature of the optical components used in the sensor. Testing of different MWIR compatible grating substrates indicated that the type of material had little effect on the quality of the data. However, there were notable differences between the sensitivity and dynamic range of similar geometry phase and amplitude gratings.

Acknowledgments

This work was sponsored by a Small Business Innovation Research contract from the United States Air Force's Research Laboratory, Air Force Material Command, Directed Energy Directorate, Contract F29601-02-C-0130, with Dr. Larry Weaver, the technical manager.

References

1. R.A. Gonsalves: Phase retrieval and diversity in adaptive optics. *Opt. Eng.* **21**, 829 (1982)
2. C. Roddier, F. Roddier: Wavefront reconstruction from defocused images and the testing of ground-based optical telescopes. *J. Opt. Soc. Am* **10**, 2277 (1993)
3. P.B. Blanchard, A.H. Greenaway: Simultaneous multi-plane imaging with a distorted diffraction grating. *Appl. Opt.* **38**, 6692 (1999)

4. P.M. Blanchard, A.H. Greenaway, L.J. Otten, I. McMakin: Chromatic properties and applications of distorted diffraction gratings. For submission to *Appl. Opt.* (1999)
5. L.J. Otten, P. Soliz A.H., Greenaway, M. Blanchard, G.S.H. Ogawa: 3-D cataract imaging system. In: *Proc. of the 2nd International Workshop of Adaptive Optics for Industry and Medicine*, Durham, UK, 1999
6. L.J. Otten, G. Erry, J. Lane, P. Harrison, S. Woods, M. Roggemann: Measurement of highly scintillated wavefronts. In: S. Restaino, S. Teare (eds.): *Proceedings of the 3rd International Workshop on Adaptive Optics for Industry and Medicine*. (Starline Printing, Albuquerque, NM 2002) pp.223–240
7. P. Harrison, G. Erry, S.C. Woods: A practical low cost wavefront sensor with real time analysis. In: S. Restaino, S. Teare (eds.): *Proceedings of the 3rd International Workshop on Adaptive Optics for Industry and Medicine* (Starline Printing, Albuquerque, NM 2001)
8. L.J. Otten, J. Lane, G. Erry, P. Harrison, J. Kinsky: A comparison between a Shack–Hartmann and a distorted grating wavefront sensor under scintillated propagation conditions. In: *SPIE Conference on Optics in Atmospheric Propagation and Adaptive Optics Systems*, Crete, Greece, 2002

15 Comparative Results from Shack–Hartmann and Distorted Grating Wavefront Sensors in Ophthalmic Applications

P. Harrison¹, G.R.G. Erry¹, P. Fournier¹, D.M. Cuevas¹, L.J. Otten¹, and
A. Larichev²

¹ Kestrel Corporation

3815 Osuna Road NE, Albuquerque, NM, 87109, USA

² M.V. Lomonosov Moscow State University, Center of Medical Physics
Leninskiye Gory, Moscow 119992, Russia

Summary. The aim of this work was to determine the relative performance of a Shack–Hartmann (SH) wavefront sensor and a distorted grating wavefront curvature sensor (DGWFS) when used to measure the aberrations in the human eye. Previous work carried out by Kestrel and others suggests that the DGWFS is able to successfully reconstruct wavefronts in severely scintillated conditions in which SH sensors typically fail to give a good reconstruction. The poor performance of conventional SH sensors in scintillated conditions prevents their use in ophthalmic aberrometers with human subjects who have medical conditions such as cataracts. This limitation substantially restricts the percentage of the population that can take advantage of emerging technology enabled by having accurate aberration data for the anterior segment. The SH sensor utilized has a novel dithered reference source which mitigates scintillation problems. However, the DGWFS potentially offers a simpler, lower cost and more robust solution.

15.1 Introduction

Conventional wavefront sensor technologies have limited performance in applications where wavefront reconstruction is required in conditions where amplitude fluctuations are significant. The measurement of aberrations in the human eye is one such application as the eye contains scattering sources which introduce such amplitude variations. These effects degrade the performance of conventional wavefront sensors. Scatter effects are present with all subjects, but are more pronounced in subjects who have certain conditions, such as cataracts. The inability to accurately reconstruct a wavefront for subjects with such conditions limits the proportion of the population for which aberrometry can be used as an ophthalmic diagnostic tool.

In an earlier study, the comparative wavefront reconstruction performance of two wavefront sensing technologies (SH and DGWFS wavefront sensors) was evaluated [1]. This study showed that the DGWFS technique [2,3], a combination of phase diversity [4] and wavefront curvature [5] wavefront sensing

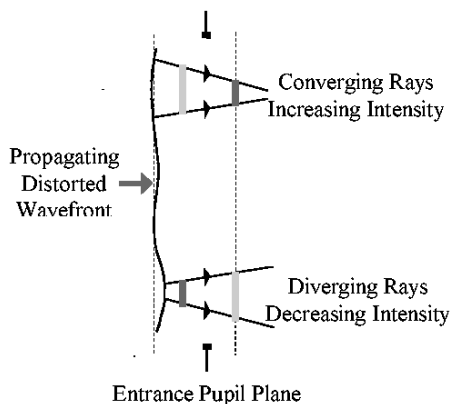


Fig. 15.1. Measurements made at two image planes with a known aberration are required for a phase diversity wavefront sensor

techniques, may have advantages when operating in scintillated conditions, or indeed other circumstances where amplitude variations are significant such as scatter [6].

In the phase diversity and wavefront curvature approaches, the intensity is measured in two planes through which the wavefront propagates, and the difference between the measured intensity patterns gives a measure of the axial intensity gradient. Solution of a differential equation, the Intensity Transport Equation (ITE), then provides a non-iterative solution to the wavefront reconstruction [7].

Investigated for a number of years, phase diversity requires the collection of two or more images of the intensity distribution in two spatially separated planes in the vicinity of the entrance pupil of the wavefront sensing instrument with a known wavefront aberration introduced between the images. These images must be measured in the time scale of the distortion being compensated, i.e. the sensing must be done while the disturbance is effectively stationary. A technique that can simultaneously measure the two intensity patterns is therefore essential.

In the DGWFS technique, the two image planes are located (usually symmetrically) either side of the entrance pupil for the wavefront sensor, as shown in Fig. 15.1. In this case, the known aberration introduced is therefore a defocus. The shape of the wavefront is computed from the intensity difference matrix through integration (i.e. a matrix multiplication) with a pre-computed Green's function. It is therefore critical that the multiple frames are accurately and consistently registered, the detector is well characterized and the introduced aberration is a controlled function.

This approach differs from conventional phase diversity analyses, which use information around the image plane and iterative wavefront reconstruction algorithms. By using planes situated either side of the pupil plane we are

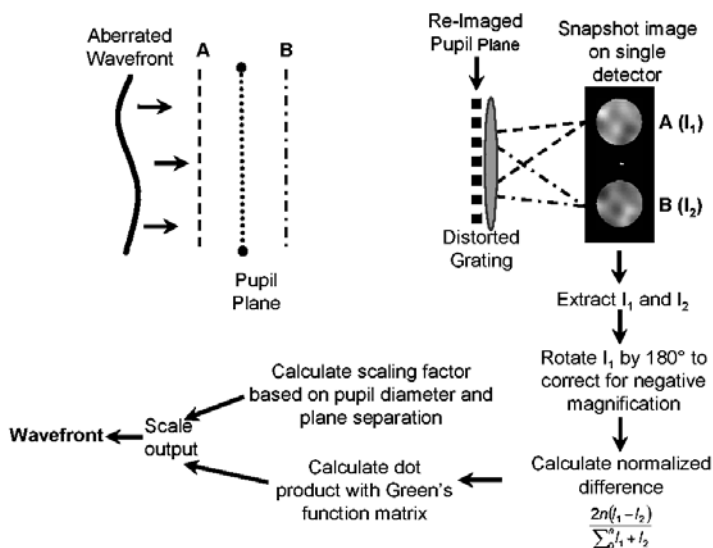


Fig. 15.2. Implementation of wavefront curvature sensing using a distorted diffraction grating

able to work with a linear relationship (the ITE). This technique is the basis for wavefront curvature sensing and needs only two image planes to calculate the wavefront, requiring no additional sensors. A novel use of boundary conditions means that we do not require separate sensors to estimate wavefront tilt at the pupil edge. It is these differences, which distinguish our approach from earlier attempts.

In order to image the two intensity planes simultaneously onto a single detector (preferable to using multiple detectors as the solution is physically more stable and has a lower cost as only a single detector and associated electronics are required) a quadratically distorted diffraction grating is used to introduce the required defocus (the amount of distortion determines the separation of the intensity planes and thus the sensitivity and dynamic range of the sensor), as shown schematically in Fig. 15.2.

The distorted grating technology is based on local displacement of lines in a diffraction grating, known as the phase detour effect, which introduces phase shifts into wavefronts diffracted into the non-zero orders [8, 9]. A quadratic displacement function is used to alter the optical transfer function associated with each diffraction order such that each order has a different degree of defocus. The resulting distorted grating acts as a beam splitter whilst producing simultaneous images of multiple object planes on a single image plane. The technique preserves the resolution of the input optics in each of the images and offers very accurate co-registration, i.e. a simultaneous multi-conjugate optical system.

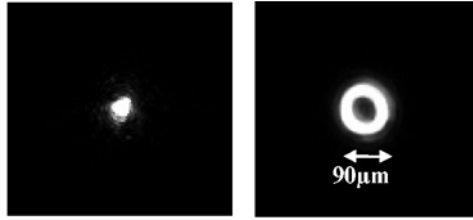


Fig. 15.3. Static (*top*) and dithered (*bottom*) reference spots

In the configuration shown in Fig. 15.2 (where the distance between lens adjacent to the distorted grating and the detector is equal to its focal length) the zero order records an image of an object at infinity. The two pupil plane images (I1 and I2) required for wavefront sensing are formed in the -1 and $+1$ orders. These images correspond to planes (labeled *A* and *B*) equal distances either side of the pupil and have magnifications of equal magnitude, but opposite sign.

The distorted diffraction grating itself can be manufactured as an amplitude or phase grating. Amplitude gratings can be quickly and cheaply fabricated, however their optical efficiency with respect to the -1 and $+1$ orders is low and the focused image of the object formed in the zero order, whilst useful in some applications, is very bright and compact. For this reason, phase gratings with top hat geometries are more often used, particularly for narrow wavelength band operations (for example when the source used is generated by a laser). In such cases the phase step used in the manufacture of the grating is chosen so as to maximize the flux directed into the $+1$ and -1 orders. The design parameters (level of quadratic distortion, nominal grating period and focal length of the imaging lens) and material used for manufacture of the distorted gratings are chosen to suit the application. Quadratically distorted gratings have been designed and manufactured for use at wavelengths varying from the visible to the mid-wave infrared [10].

The DGWFS has been shown to be relatively robust to amplitude variations as the amplitude variations are cancelled out during the calculation of the normalized difference (only intensity variations due to phase effects remain). In certain circumstances (primarily in scintillated conditions, but also where scattering effects are severe such as with human subjects suffering from cataracts) the local amplitude variation can be so severe that the local amplitude can drop to zero (or at least below the noise floor of the camera). As the DGWFS wavefront reconstruction has a low pass filtering effect, the resulting wavefront is smoothed over the region where the intensity has dropped to zero, whereas a conventional Shack–Hartmann sensor is unable to provide any wavefront reconstruction in the null region and complex post processing techniques are then required.

To improve the performance of the SH sensor in this application, a dithered reference beam was used [11, 12]. The spot projected onto the retina

of the subject is scanned in a circle, $90\ \mu\text{m}$ in diameter, at a rate of approximately 50 revolutions per second (the frame rate of the cameras is 30 frames per second), as shown in Fig. 15.3. The scanned spot size was selected to be smaller than the isoplanatic patch size for the human eye, which is typically on the order of a few tenths of a millimeter. As the projected spot is scanned, the beam passes through a slightly different part of the eye, and therefore passes through different scattering sources. As the beam scanned through multiple revolutions per frame, the effect of the scatter is therefore averaged out, substantially reducing the sensitivity of the SH sensor to scatter induced amplitude variations.

Previous work involving simultaneously recording wavefronts reconstructed by a Shack–Hartmann wavefront sensor and a DGWFS demonstrated that the DGWFS was able to successfully reconstruct a wavefront in conditions where the Shack–Hartmann failed due to severe scintillation. The aim of this work was to demonstrate that the performance of a Shack–Hartmann sensor can be improved for ophthalmic applications using a dithered source, and that the DGWFS is able to successfully reconstruct wavefronts without such modifications.

15.2 Methodology

In order to test our hypothesis, a dual wavefront sensor aberrometer system was constructed. A schematic representation of the aberrometer is shown in Fig. 15.4. The aberrometer consists of a Shack–Hartmann wavefront sensor with a dithered spot reference and a distorted grating wavefront sensor. The SH sensor is a self contained system, designed and constructed by Dr. Larichev’s group at Moscow State University whereas the DGWFS system was designed and constructed by Kestrel Corporation. The DGWFS was designed to interface to the SH system without modifying the later other than to allow for the mechanical connection of the systems. The two wavefront sensors see the same wavefront via the addition of a 50% beam splitter.

The aberrometer includes a number of optical features in addition to the wavefront sensors themselves to simplify use of the aberrometer and to increase its dynamic range. The first of these features is a scene camera with active illumination used to align the instrument to the subject’s eye. The scene camera itself is a simple grayscale video board camera (with the IR filter removed), interfaced to the TV input on the video card of the PC used to operate the SH system.

Illumination of the subject’s eye is provided by four low intensity LEDs operating at approximately $900\ \text{nm}$ with a $\pm 60\ \text{nm}$ bandwidth (clearly visible to the operator via the scene camera, but invisible to the subject). Alignment of the aberrometer is achieved using a pair of marker beams projected onto the front of the subject’s eye. These marker beams are projected from either side of the input of the aberrometer such that the beams overlap only when the

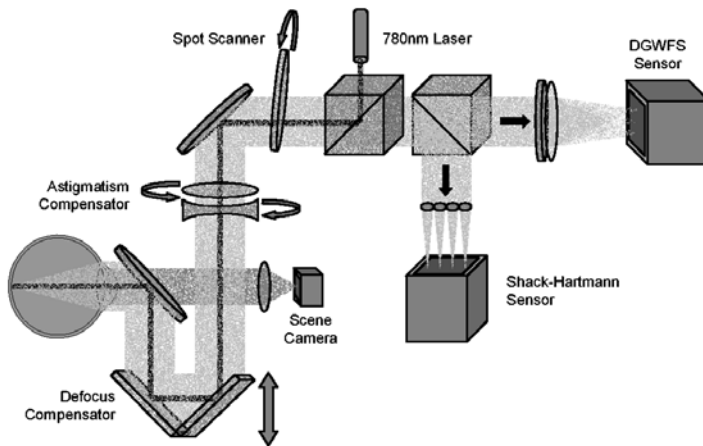


Fig. 15.4. Simplified schematic representation of the dual wavefront sensor aberrometer

subject is the correct distance from the aberrometer. The marker beams each project a circle with a V shape, the V being inverted in one beam relative to the other. When the beams overlap, they form a circle with a cross in the center. When the cross is centered on the subject's eye, the subject is positioned correctly relative to the instrument. The format of the marker beams and a typical scene camera image are shown in Fig. 15.5.

The most severe aberrations present in the human eye are defocus and astigmatism, which are found at strengths of up to ± 7 and ± 3 diopters respectively. If one were to design an aberrometer with sufficient wavefront sensor dynamic range to measure these aberrations, its sensitivity would be low. To allow a high sensitivity, defocus and astigmatism must therefore be removed from the wavefront presented to the wavefront sensors, or at least substantially reduced.

The dynamic range of the wavefront sensors implemented here is approximately ± 2 diopters for the SH and ± 1 diopter for the DGWFS (for defocus), so the defocus and astigmatism must be reduced below ± 1 diopter in this instrument. To compensate for the ophthalmic defocus, a prism on a moving stage is used (as shown at the lower left of Fig. 15.4). This prism is located between two lenses forming a 1 : 1 relay in the optical system (not shown in Fig. 15.4). When the prism is translated, the optical path length between the two lenses changes, thus introducing a defocus into the wavefront returned from the eye. The dynamic range of the defocus compensator implemented is -12 to $+16$ diopters and yields a typical residual defocus of less than 0.01 diopters.

During alignment of the dual instrument, it was found that a ghost reflection was introduced by the face of the defocus compensator prism perpendicular to the optical axis (although the prism was antireflection coated).



Fig. 15.5. Aberrometer alignment markers (*top* and *middle*) and typical scene camera image (*bottom*)

This caused some problems with the alignment of the wavefront sensors, so the prism was replaced by a roof-top mirror thereby eliminating the ghost reflection completely.

In order to compensate for astigmatism, a pair of cylinder lenses are used, which can be rotated relative to each other and about the optic axis of the aberrometer. The cylinder lenses have equal but opposite focal length and were manufactured as a pair and so are accurately matched. When the cylinder lenses are co-aligned, no astigmatism is introduced into the beam. When one lens is rotated relative to the other, the amount of astigmatism introduced increases. The angle of the astigmatism can be varied by rotating both cylinder lenses in the same direction. The dynamic range of the astigmatism compensator is greater than ± 6 diopters (we were unable to introduce more than ± 6 diopters of astigmatism to test beyond this range). The residual astigmatism is typically less than 0.01 diopters after compensation.

Previous work using a dithered reference beam was conducted using mirror mounted at a slight angle to the optic axis. It was found that this type of mirror based dithering mechanism can be very difficult to align. A reflective dither also requires quite a lot of space to implement and is optically inefficient as it requires a double pass through a beam splitter.

In this system, the reflective dither mechanism was replaced by a rotating circular glass wedge, as shown in the upper center of Fig. 15.4. As the wedge rotates, the tilt angle introduced into the transmitted beam rotates, thereby scanning the reference beam. The wedge was mounted at a slight angle to the optic axis, so that any ghost reflections from its surfaces did not reach the wavefront sensors. The beam returned from the eye also passes through the rotating wedge, thereby canceling the tilt introduced into the beam, so the SH spots and DGWFS intensity patterns are not scanned on their detectors. Note that the use of a transmissive dithering mechanism allowed single pass measurements to be made using the system, simply by removing the wedge.

The reference beam for the aberrometer is provided by a 780 nm laser diode, outputting $84\mu\text{W}$ (well within eye safety standards). The reference beam is projected at a small diameter into the eye such that it forms a small spot on the retina without passing through an extended region of the eye on the output pass. The aberrometer is therefore sensitive to all aberrations as

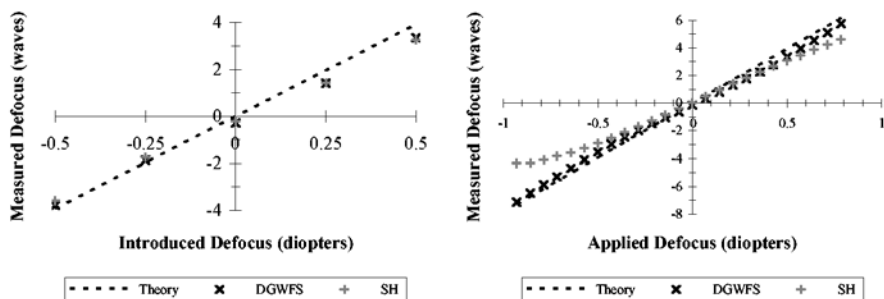


Fig. 15.6. Calibration data using single pass (*top*) and an artificial eye (*bottom*)

the wavefront sensing beam is only sensitive to aberrations in the eye on a single pass.

The camera used for the SH sensor is a 640×480 Hitachi model KP-F2A. This CCD camera is enhanced for IR operation as so has a high sensitivity at 780 nm. The DGWFS uses a Dalsa model CA-D1-0256T, selected as it allowed an existing distorted grating and data capture system to be used. Two computers are used to control the aberrometer and record data. One PC controls the aberrometer (defocus and astigmatism compensators, rotating wedge and scene camera active illumination) and records and processes the SH data. The second PC controls the Dalsa camera (which is synchronized to the Hitachi camera, allowing frame by frame comparison of the wavefront sensor outputs) and records the DGWFS data.

15.3 Results

Before the instrument was used with a human subject, the two wavefront sensors were characterized and their performance compared. The initial characterization was carried out using a collimated 7 mm diameter beam at 780 nm. Defocus was introduced by inserting ophthalmic test lenses into the collimated beam. This meant that the system was operated in a single pass configuration, reducing the complexity of some of the alignment. The results of this calibration (shown at the top of Fig. 15.6) showed that the two wavefront sensors agreed to a high precision (note that the results differ from the theory due to slight misalignment of the lenses used to introduce defocus).

A more rigorous calibration was then carried out using an artificial eye (a 5% reflectivity SpectralonTM hemisphere with a 6.5 mm diameter pupil and an 18 mm focal length lens) so that the wavefront sensors could be tested in double pass configuration using the onboard reference laser and the rotating wedge. The results of this calibration are shown at the bottom of Fig. 15.6. Note that the SH data disagrees with the theory and DGWFS data below approximately -0.5 diopters. This is due to a slight misalignment of the SH

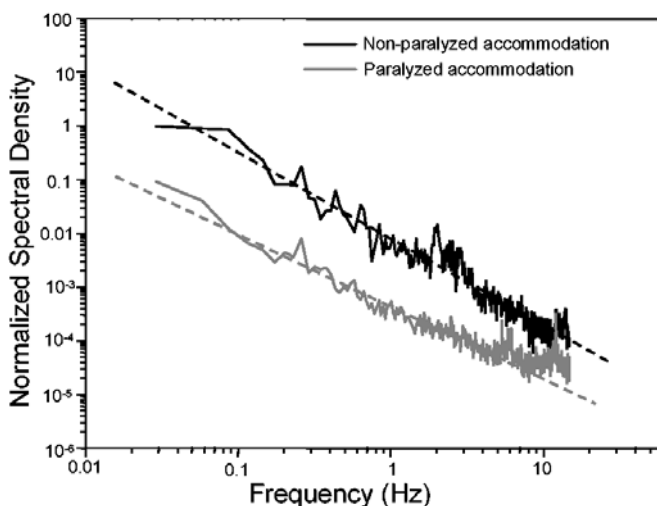


Fig. 15.7. Spectral analysis of aberration fluctuations in the human eye

optics and demonstrates the relative insensitivity of the DGWFS to misalignment.

Data were next gathered from human subjects using both wavefront sensors. Data was taken with the dithered reference operational and stationary for each subject so that, in addition to comparing the two wavefront sensors, the performance of the SH sensor with and without the dither could be determined.

There were some problems with the initial data captured using human subjects with the DGWFS and so it has not yet been possible to analyze this data. Data was successfully recorded using the SH sensor and has been subsequently analyzed.

Statistical analysis of SH data gathered from a single human subject with the dithered spot on and off has shown that the dithered spot does indeed improve the performance of the SH sensor. With the dithered reference switched on, a factor of 3 reduction in the RMS wavefront error has been consistently observed for the entire wavefront compared with measurements made with the dithered reference switched off or removed. A factor of 20 improvement in the measured centroid is observed for each individual Hartmann spot.

A similar effect could (in principle) be achieved by calculating a time averaged wavefront using a conventional SH sensor. To achieve a similar RMS wavefront error to that obtained with the dithered spot, a time average of 10 frames would have to be taken. However, spectral analysis of the SH data [11] has shown that the aberrations in the human eye fluctuate at a frequency of 15 Hz, as shown in Fig. 15.7, taking an average of 10 frames would prevent an aberrometer from seeing fluctuations beyond around 1.5 Hz.

15.4 Conclusions

A Shack–Hartmann and a distorted grating wavefront sensor were successfully integrated into an ophthalmic aberrometer for the first time. Calibration results have shown that the two wavefront sensors are well aligned and have sufficient dynamic range, when used in combination with defocus and astigmatism compensators, to measure expected ophthalmic aberrations. Initial data has shown a significant improvement in the performance of the SH sensor when a dithered reference source is used enabling measurements of dynamic aberrations not possible with a conventional SH sensor.

Work is continuing to gather further human subject data, including data from subjects suffering from ophthalmic conditions such as cataracts to test our original hypothesis that our techniques allow aberrometry to be used with a greater proportion of the population. Further work is being carried out to gather useful data using the DGWFS (the problems encountered are not thought to be fundamental).

Acknowledgements

This work was sponsored by a Small Business Innovation Research Program from the Department of Health and Human Services, National Eye Institute, contract number 1 R43 EY014518-01. We would like to thank Dr. Larichev and his team at Moscow State University for the help in alignment of the SH sensor and processing of the resulting data.

References

1. L.J. Otten, J. Lane, G.R.G. Erry, P. Harrison, L.D. Weaver, G. Martin: Comparison between a Shack Hartmann and a distorted grating wavefront sensor. In: *SPIE Optics in Atmospheric Propagation and Adaptive Systems V* (Crete, 2002)
2. P.M. Blanchard, D. Fisher, S. Woods, A.H. Greenaway: Phase diversity wavefront sensing using a distorted diffraction grating. *Appl. Opt.* **39**, 6649 (2000)
3. P. Harrison, S.C. Woods, G.R.G. Erry, A.M. Scott: A Practical Low Cost Wavefront Sensor with Real Time Analysis. In: *Proceedings of the 3rd International Workshop on Adaptive Optics for Industry and Medicine*, S.R. Restaino, S.W. Teare (eds.) (Albuquerque, NM, 2001)
4. R.A. Gonsalves: Phase retrieval and diversity in adaptive optics. *Opt. Eng.* **21**, 829 (1982)
5. C. Roddier, F. Roddier: Wavefront reconstruction from defocused images and the testing of ground-based optical telescopes. *J. Opt. Soc. Am.* **10**, 2277 (1993)
6. L.J. Otten, G. Erry, J. Lane, P. Harrison, S. Woods, M. Roggemann: Measurement of highly scintillated wavefronts. In: *Proceedings of the 3rd International Workshop of Adaptive Optics for Industry and Medicine*, S.R. Restaino, S.W. Teare (eds.) (Albuquerque, NM 2001)

7. S.C. Woods, A.H. Greenaway: Wavefront sensing by use of a Green's function solution to the intensity transport equation. *J. Opt. Soc. Am.* **20**, 508 (2003)
8. M. Li, A. Larsson, N. Eriksson, M. Hagberg, J. Bengtsson: Continuous-level phase only computer generated hologram realized by dislocated binary gratings. *Opt. Lett.* **21**, 1516 (1996)
9. P.M. Blanchard, A.H. Greenaway, R.N. Anderton, R. Appleby: Phase calibration of arrays at optical and millimeter wavelengths. *J. Opt. Soc. Am. A* **13**, 1593 (1996)
10. D.M. Cuevas, L.J. Otten, P. Fournier, P. Harrison: Distorted grating wavefront sensing in the mid-wave infrared. In: U. Wittrock (ed.): *Proceedings of the 4th International Workshop on Adaptive Optic for Industry and Medicine*, October 19–24, 2003, Münster, Germany (Springer, Berlin Heidelberg New York 2005)
11. A. Larichev, N. Ivanov, S. Iroshnikov, M. Gorbunov: Adaptive aberrometer for acuity measurements and testing. In: U. Wittrock (ed.): *Proceedings of the 4th International Workshop on Adaptive Optic for Industry and Medicine*, October 19–24, 2003, Münster, Germany (Springer, Berlin Heidelberg New York 2005)
12. G. Erry, J.L. Otten, A. Larichev, N. Irochnikov: A high resolution adaptive optics fundus imager. In: U. Wittrock (ed.): *Proceedings of the 4th International Workshop on Adaptive Optic for Industry and Medicine*, October 19–24, 2003, Münster, Germany (Springer, Berlin Heidelberg New York 2005)

16 Shack–Hartmann Sensors for Industrial Quality Assurance

J. Pfund, M. Beyerlein, and R. Dorn

Optocraft GmbH Optical Metrology
Hofmannstraße 118, 91052 Erlangen, Germany

Summary. The measurement of the deviations of a test sample from its ideal shape is the key to quality assurance in fabrication processes of the optical industry. Here, interferometers are often used as standard tools. However, in recent years Shack–Hartmann sensors have been introduced in various applications with competitive performance. We show two typical application examples, the null test of a sphere where the highest accuracy is obtained and a non null test of an aspherical surface. In the latter case the Shack–Hartmann sensor is superior to an interferometer due to its higher dynamic range.

16.1 Introduction

The quality of optical surfaces is typically measured and characterized using interferometric techniques. This requires a reference surface. Historically, mainly so called test glasses were used to provide this reference. The element under test was combined with a suitable test glass, leaving a small gap of air. After illumination with a spectrally narrow light source, this gap reflects the sum of the deviations of the tested surface and the test glass from their ideal shape as interference fringes.

Since the invention of the laser, contactless interferometry has gained more and more importance in metrology and production of optical components [1]. However, the general problem of mechanical stability of an interferometric set-up is so severe that in many cases more robust solutions are indispensable. The Hartmann sensor, or as a more modern version the Shack–Hartmann sensor [2], allows for a wavefront reconstruction without the necessity for a reference wave. This leads to a drastic increase in stability. On the other hand, wavefront errors introduced by optical elements outside the measurement or reference arm, that affect both object and reference wave simultaneously, no longer cancel out automatically. In that sense, a Shack–Hartmann sensor is not self referencing and often requires calibration.

Compared to phase shifting interferometry, the Shack–Hartmann sensor has the potential for a higher data rate as no moveable parts are necessary to shift the reference mirror to different positions.

Shack–Hartmann sensors sample the wavefront with a relatively small number of micro lenses, while in an interferometer the wavefront is sampled

by a larger number of CCD pixels. Therefore, for ultra high precision measurements with high spatial resolution, Shack–Hartmann sensors are typically outperformed by interferometric techniques.

When a wavefront with steep slopes is to be measured, the fringe density can become too high to allow for a successful evaluation of the fringe pattern. In Sect. 16.3, an example will be shown, where the high dynamic range of the Shack–Hartmann sensor allows one to reconstruct the wavefront when interferometric techniques fail.

Compared to interferometry, the Shack–Hartmann principle has a less severe requirement for the degree of spatial coherence. Even when the area of coherence is smaller than the area of the detector and it is no longer possible to clearly identify the wavefront of a coherent wave, one can still measure the directions of a bundle of light rays. This is an important property when, e.g., partially coherent laser beams have to be measured. Such a situation often occurs when optical elements for the UV have to be tested with 193 nm wavelength light.

A necessary requirement for a successful phase reconstruction using a Shack–Hartmann sensor is an unambiguous spot assignment. This typically requires that the spots remain inside their corresponding sub-apertures. However, when the local curvature is too large this condition is no longer fulfilled. Therefore, we use an extended spot assignment algorithm which leads to an increased dynamic range of the sensor and allows one to measure wavefronts with a minimum local radius of curvature $R_{\min} = 2 \cdot f_{\text{microlens}}$.

Below we show two examples for the application of a Shack–Hartmann sensor. The first example is an absolute test of a spherical surface. These experiments were made in direct comparison to an interferometric test to demonstrate the achievable precision of the Shack–Hartmann sensor. The second example is a non null test of an aspherical surface. For aspherical surfaces, the use of interferometric techniques often fails or is only possible with difficulty. This example demonstrates the high achievable dynamic range of a Shack–Hartmann sensor.

16.2 Absolute Measurement of a Spherical Surface: Comparison to Interferometry

The basic idea behind absolute methods is based on the combination of relative measurements. This will be shown here using the example of a Twyman–Green interferometer (Fig. 16.1). The surface under test is a concave mirror with a diameter $D = 42$ mm and a radius of curvature of $R = 60$ mm.

For a demonstration of the method let us consider the three positions of a spherical surface in the TWG-interferometer given in Fig. 16.2 and let us assume that in these three positions the surface interferograms have been evaluated resulting in wave aberrations $W_1(x, y)$ through $W_3(x, y)$:

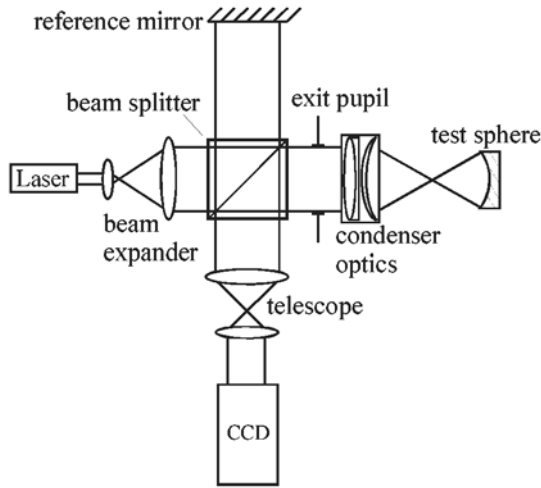


Fig. 16.1. Twyman Green set-up for sphericity testing

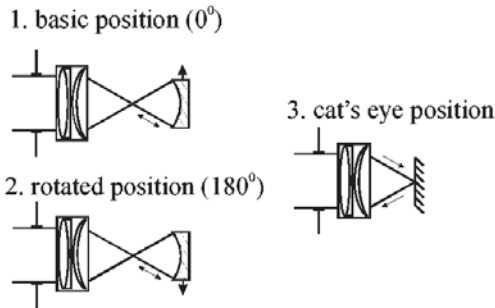


Fig. 16.2. Absolute sphericity test scheme relying on three relative measurements with a TWG

$$\begin{aligned}
 W_1(x, y) &= W_r(x, y) + W_c(x, y) + S(x, y) \\
 W_2(x, y) &= W_r(x, y) + W_c(x, y) + S(-x, -y) \\
 W_3(x, y) &= W_r(x, y) + \frac{1}{2} \times \{W_c(x, y) + W_c(-x, -y)\} . \quad (16.1)
 \end{aligned}$$

S symbolizes the wave aberrations introduced by the surface deviations (i.e., $S = 2\Sigma$), W_r the aberrations of the reference arm of the interferometer and W_c the aberrations introduced by the condenser optics necessary to match the wavefronts in the object arm with the surface to be tested.

From this the absolute surface deviations $\Sigma(x, y)$ can be derived [3]:

$$\begin{aligned}
 4 \times \Sigma(x, y) &= 2 \times S(x, y) \\
 &= W_1(x, y) + W_2(-x, -y) - \{W_3(x, y) + W_3(-x, -y)\} . \quad (16.2)
 \end{aligned}$$

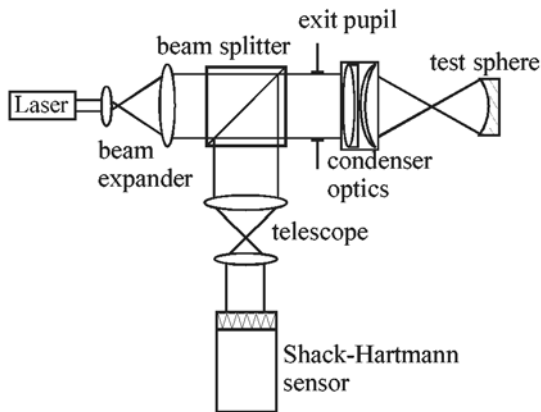


Fig. 16.3. Set-up for sphericity tests using a Shack–Hartmann sensor

The same philosophy can be applied to the Shack–Hartmann test which shall be explained by using Fig. 16.3.

Wavefront sensors provide the wave aberrations without the need for a reference wavefront. This has the advantage that the measurement is intrinsically more stable. The drawback is that wavefront errors introduced by optical elements outside the measurement or reference arm, which would therefore affect both waves simultaneously, no longer cancel out automatically. Here, this applies to the wave aberrations introduced by the beam expander $W_e(x, y)$, the beam splitter $W_s(x, y)$ and the telescopic system in front of the Shack–Hartmann sensor. Together with the remaining adjustment error of the SHS, these aberrations are labeled $W_t(x, y)$. The x, y -coordinate system shall be taken as that coinciding with the SHS array of micro-apertures. The aberrations introduced by the condenser optics and by the surface under test are labeled $W_c(x, y)$ and $S(x, y)$, respectively.

The following equations hold for the three positions indicated in Fig. 16.2 applied to the scheme of Fig. 16.3:

$$\begin{aligned}
 W_1(x, y) &= W_e(x, y) + W_s(x, y) + W_t(x, y) + W_c(x, y) + S(x, y) \\
 W_2(x, y) &= W_e(x, y) + W_s(x, y) + W_t(x, y) + W_c(x, y) + S(-x, -y) \\
 W_3(x, y) &= W_e(x, y) + W_t(-x, -y) + \frac{1}{2} \\
 &\quad \times \{W_c(x, y) + W_c(-x, -y) + W_s(x, y) + W_s(-x, -y)\} .
 \end{aligned}
 \tag{16.3}$$

From this set of linear equations the absolute deviations Σ of the spherical surface under test can be derived by using the following equation:

$$\begin{aligned}
 4 \times \Sigma(x, y) &= 2 \times S(x, y) \\
 &= W_1(x, y) + W_2(-x, -y) - \{W_3(x, y) + W_3(-x, -y)\} .
 \end{aligned}
 \tag{16.4}$$

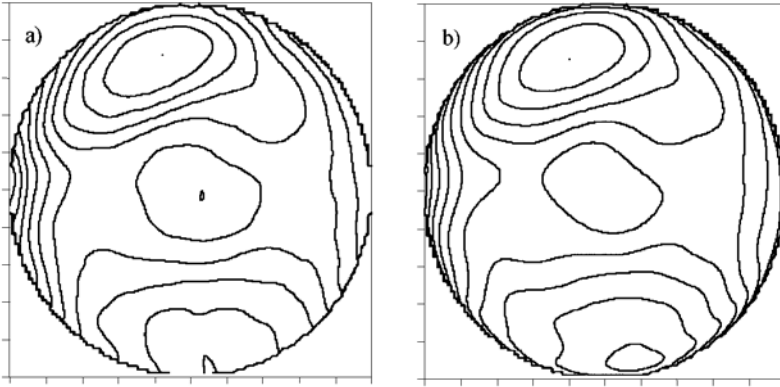


Fig. 16.4. (a) Contour line plot of the absolute deviations of a spherical surface measured with a TWG: $PV_{\text{TWG}} = 0.530\lambda$; $RMS_{\text{TWG}} = 0.086\lambda$; distance between two contours, $1/20\lambda$. (b) Contour line plot of the absolute deviations of the same spherical surface as in (a) but measured with a SHS: $PV_{\text{SHS}} = 0.556\lambda$; $RMS_{\text{SHS}} = 0.087\lambda$; distance between two contours, $1/20\lambda$

The absolute interferometric test has been carried out at BIFO with an existing TWG interferometer using the phase shifting technology and a software package enabling absolute tests due to (16.1) and (16.2). The same set-up and identical adjustments were used to measure the wave fields in front of the SHS. The absolute wavefront deformations due to the surface under test can be derived using (16.4) and (16.5).

In Fig. 16.4 the contour plots of the results of (a) an interferometric measurement and (b) a measurement with the SHS of a concave surface with a diameter of $D = 42$ mm and a radius of curvature of $R = 60$ mm are shown. The micro lenses of the Shack–Hartmann sensor had a pitch of $p = 150$ μm and a focal length of $f = 4$ mm.

There is a very good agreement in the root-mean-square values and the general shape for the two measurements. The relatively big difference in the peak to valley values ($\Delta PV = |PV_{\text{TWG}} - PV_{\text{SHS}}| = 0.026\lambda$) results from the different calculation methods for the wave aberrations W_i ($i = 1 \dots 3$). In the case of the Shack–Hartmann sensor a polynomial of degree $d = 20$ has been fitted to the discrete field of derivatives represented by the measured spot positions, whereas in the case of the interferometrical measurement the wave results from the phase shifting algorithm providing a much denser sampling of the surface shape.

16.3 Non-null Test of a Rotational Symmetric Asphere

Today the use of aspherical surfaces has been established in various optical systems. The main advantage of using aspherical components is the reduction

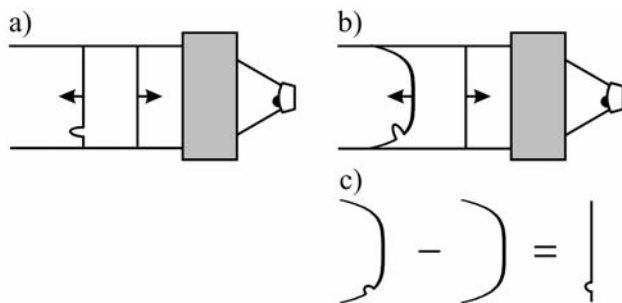


Fig. 16.5. (a) Test configuration for the null test of an aspherical surface. A computer generated hologram provides a wavefront which is phase conjugate to the surface under test. (b) Non null test of an aspherical surface. The beam shaping element provides a wavefront which matches the curvature of the vertex of the asphere. The reflected wavefront shows systematic deviations from a plane wave that have to be subtracted from the measurement to obtain the desired deviations of the surface of the sample

of the total number of elements together with an improvement of the image quality of the optical system. However, the production and the measurement process of aspherical surfaces is difficult, time consuming and costly. Therefore, there is a great need for a fast and flexible testing process, i.e., for testing prototypes or elements with no extreme quality demands.

Testing of aspheres is commonly carried out by using a so-called null corrector in the measuring arm of the test set-up. This null corrector lets the incoming light impinge perpendicularly onto the surface under test. In other words, the null corrector provides a wavefront which is phase conjugate to the ideal shape of the surface under test. In this case the wave aberrations of the reflected wavefront (Fig. 16.5a) are directly correlated to the deviations of the surface under test from its perfect shape, except for wave aberrations introduced by the manufacturing process of the corrector. The highest accuracy can be achieved in this constellation. For general aspheres a computer generated hologram (CGH) can be the best choice for a null corrector [4–6].

But one could wish to measure the surface deviations with a more general correction optics, when time and money for the fabrication of a CGH has to be saved. Typically, a high quality objective or condenser is used to generate a spherical wavefront. In this case one has to deal with very large systematic wave aberrations (Fig. 16.5b) which have to be subtracted from the measured wavefront in order to obtain the desired deviations of the surface under test from its ideal shape (Fig. 16.5c).

Therefore, compared to a null test situation, the optical system has to be capable to transmit a wavefront with a higher dynamics and the alignment and calibration process is more susceptible to systematic errors. Thus, non null tests are typically less accurate than null tests.

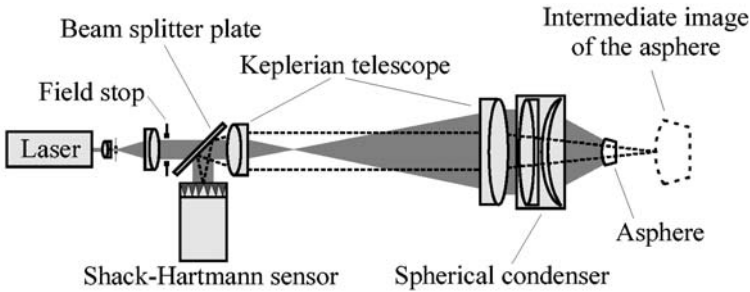


Fig. 16.6. Set-up for an absolute test of the surface of an aspherical lens

Here, we present experimental results of the measurement of a rotational symmetric asphere in a non null testing set-up. The theoretical analysis of this set-up has been published elsewhere [7], so we restrict our considerations to the discussion of the measurements. An interferometric measurement of the surface of the asphere was not possible, as the interferogram can only be evaluated in a vicinity of the centre (Fig. 16.7b).

16.3.1 Principle

In Fig. 16.6 the set-up is shown schematically. A collimated expanded laser beam is transformed into a spherical wavefront by a Fisba Optics μ -Lens objective which has a full aperture angle of 90° . The Keplerian telescope images the reflected wavefront via the beam splitter plate onto the micro lens array of the Shack–Hartmann sensor. The asphere under test is positioned such that the centre of the radius of curvature of the vertex is coincident with the focus of the objective. Therefore, in the ideal case the wavefront in the detection plane is plane in its centre and steeply aspherical at its rim (Fig. 16.7a). These systematic wave aberrations have to be subtracted from the detected wavefront to obtain the wave aberrations caused by deviations of the surface of the asphere from its ideal shape.

The systematic errors caused by the strong asphericity of the wavefront being transmitted by the optical set-up have been evaluated in [7]. In addition to the misalignment errors of the asphere relative to the spherical wavefront one has to deal with two main errors. First an error in the position of the detection plane, i.e., the plane of the micro lenses relative to the simulation (optical path difference error = OPD-error) and second an error in the imaging scale of the experimental set-up compared with the simulation (lateral magnification error = LM-error). For both errors functionals have been calculated which can be fitted to the measured wavefront and which account for the corresponding systematic error.

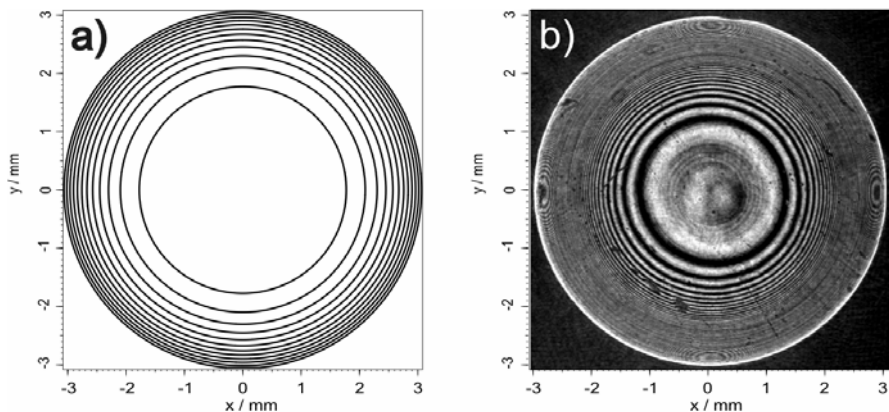


Fig. 16.7. (a) Ideal aspherical wavefront W_{ideal} . The peak to valley value is 39.98λ ; the wavefront difference between two contour lines is 5λ . (b) Measured interferogram. Only the central part can be evaluated as the fringe density of the outer part is too large to be clearly resolved by the detector

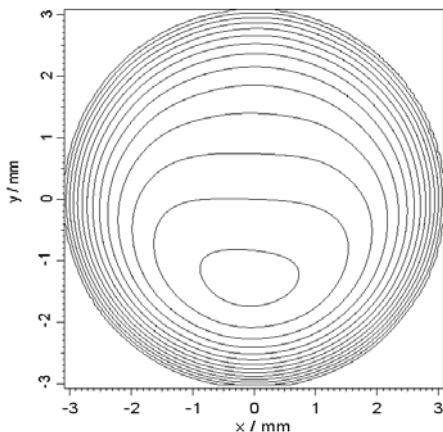


Fig. 16.8. Measured wavefront in the plane of the micro lenses. The peak to valley value of the wavefront is 42.92λ , the wavefront difference between two contour lines is 3λ

16.3.2 Experimental Results

The asphere which has been measured has a diameter of about 4.6 mm and a radius of curvature of 4.6 mm at the vertex. They are used for single-use cameras and are made from PMMA. For this kind of lenses a measurement sensitivity of $\lambda/4$ for the surface deviations has to be achieved. In Fig. 16.8 the measurement of the wavefront incident on the Shack–Hartmann sensor is shown. It has a peak-to-valley value of 42.92λ .

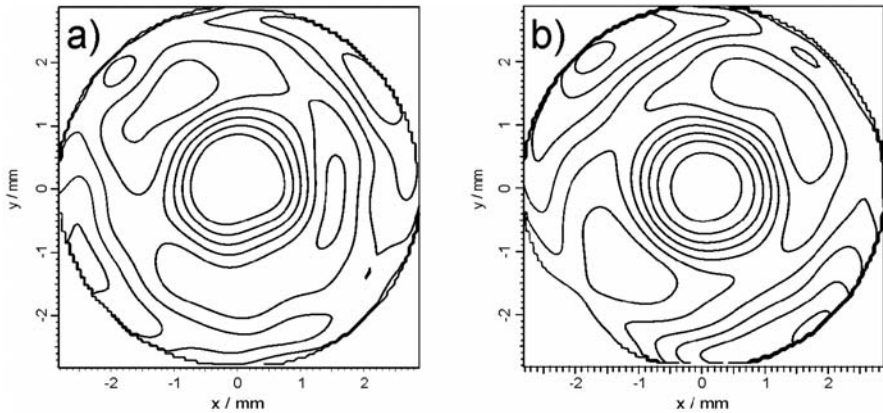


Fig. 16.9. Residual wave aberration 2Σ after correction for systematic errors and alignment errors. (a) 0-degree constellation: peak-to-valley value: 0.77λ , rms: 0.16λ , (b) 90-degree constellation: peak-to-valley value: 0.74λ , rms: 0.18λ . The wavefront difference between two contour lines is 0.1λ

After the systematic wave aberrations and the misalignment errors are removed from this wavefront, the residual wave aberration $S = 2\Sigma$ accounts for the deviations Σ of the asphere under test from its ideal shape (Fig. 16.9a). The peak-to-valley value of the residual wave aberration S is about 0.77λ . In the experiments one difficulty has been to prove that the calculated wave aberrations 2Σ are not feigned by errors in the testing set-up or by the algorithms used. Therefore, the asphere under test has been rotated by 90° about the optical axis. In Fig. 16.9b the residual wave aberrations measured in the 90° constellation are shown. Here the peak-to-valley value of the residual wave aberrations is about 0.74λ and the rotation of the symmetry is obvious.

16.4 Summary

We have demonstrated that a Shack–Hartmann wavefront sensor is suitable for industrial quality assurance tests and we have discussed the advantages and disadvantages compared to an interferometric test. Two typical application examples were presented. It was shown that in a null test configuration a suitable measurement and evaluation scheme for absolute tests leads to an accuracy comparable to an interferometric test. In a non null test situation the surface deviation of an asphere could be measured, which was not accessible with an interferometer. Although a non null test may only be suitable for applications where the intrinsically lower accuracy of a non null test can be tolerated, it offers the highest flexibility.

To optimize the results in an industrial quality test of optical elements, the geometry of the total measurement set-up has to be considered, rather than the performance of the wavefront sensor alone.

References

1. I. Ghozeil: In: D. Malacara (ed.): Optical Shop Testing (John Wiley and Sons, New York Chichester Brisbane Toronto 1978) pp. 323–349
2. B. Platt, R. Shack: Lenticular Hartmann Screen. *Opt. Sci. Center Newsletter* **5**, 15 (1971)
3. A.E. Jensen: *J. Opt. Soc. Am. (A)* **63**, 1313 (1973)
4. Y. Ichioka, A.W. Lohmann: Interferometric testing of large optical components with circular computer holograms. *Appl. Opt.* **11**, 2597 (1972)
5. T. Yatagai, H. Saito: Interferometric testing with computer-generated holograms: aberration balancing method and error analysis. *Appl. Opt.* **17**, 558 (1985)
6. J.E. Greivenkamp: Sub-Nyquist interferometry. *Appl. Opt.* **26**, 5245 (1987)
7. J. Pfund, N. Lindlein, J. Schwider: Nonnull testing of rotationally symmetric aspheres: a systematic error assessment. *Appl. Opt.* **40**, 439 (2001)

17 Single-Chip Neural Network Modal Wavefront Reconstruction for Hartmann–Shack Wavefront Sensors

T. Nirmaier¹, G. Pudasaini¹, C. Alvarez Diez¹, J. Bille¹, and
D.W. de Lima Monteiro²

¹ University of Heidelberg, Kirchoff Institute of Physics
Im Neuenheimer Feld 227, 69120 Heidelberg, Germany

² Delft University of Technology, EEMCS, Electronic Instrumentation Laboratory
Mekelweg 4, 2628 CD Delft, The Netherlands

Summary. We describe existing concepts for CMOS³-based Hartmann–Shack wavefront sensors and propose the next step for a further miniaturization of adaptive optics by integrating the modal wavefront reconstruction on chip. In conventional Hartmann–Shack wavefront sensing a CCD⁴ camera is placed on the focal plane of a microlens array. The spot pattern in the focal plane is captured, analyzed by image processing and the wavefront is often decomposed into orthogonal modes, usually expressed in coefficients of Zernike polynomials. The single-chip modal wavefront reconstructor would include all these processing steps in a single chip. We propose to use already existing CMOS-based wavefront sensor concepts and add a hardware artificial neural network for modal wavefront reconstruction.

17.1 CMOS-based Wavefront Sensors

Hartmann–Shack wavefront sensors are currently the most widely used wavefront sensors in astronomy, ophthalmology and laser beam control with adaptive optics (AO), basically because the absence of movable parts and the simplicity of data handling favor system operation in real time. Many of these applications require a frame rate of several hundreds of Hz to capture the complete bandwidth of aberrations. In ophthalmic applications, e.g. laser scanning retinal imaging aberrations are present up to several tens of Hz. Expensive scientific cameras with a large frame rate can be replaced by dedicated image sensors with on-chip determination of the positions of the focal spots.

A number of architectures for CMOS-based integrated wavefront sensors have been proposed, designed and tested in the last few years, each comprising different architectures, advantages and disadvantages. All of the proposed sensors use standard process technologies with no pre- or post-processing steps and passive pixels with photodiodes so far. The concept based on quad-cells has achieved a very good resolution (1 μm) at relatively high spot powers

³ Complementary Metal Oxide Semiconductor

⁴ Charge Coupled Device

[1] ($\mu\text{W}/\text{spot}$ range) and the concept based on the Winner-Take-All circuit [2] or a resistive-network of this circuit [3] has achieved a very good sensitivity ($0.1\text{ nW}/\text{spot}$ range), which is a necessary demand for ocular measurements. All sensors reported so far have achieved an intrinsic frame rate between 1 kHz and 4 kHz, which is fast enough for most applications.

A short description of the currently existing concepts can be found in Figs. 17.1–17.3. For a detailed analysis see also [4].

17.1.1 Limitations of Current CMOS-based Wavefront Sensors

Although standard CMOS technology is not optimized for photodetection, the CMOS wavefront sensors fabricated so far have proved that it is possible to achieve good light sensitivity for ophthalmic applications and good position resolution. By introducing design and conceptual changes we now try to have these two features on a single chip.

An important application of wavefront sensors are ophthalmic diagnostic instruments for ocular imaging, e.g. in laser scanning confocal microscopes for glaucoma detection. There are very strict safety limits for the application of laser radiation to the human eye. In the red and near-infrared the maximum applicable power is about 1 W per square meter, depending on national security regulations. Because the reflectivity of the human retina is only in the order of 1%, we can expect a single focal spot from a microlens array with dimension $400 \times 400\ \mu\text{m}$ to have an incident light power of only 1.6 nW. Because reported quantum efficiencies of photodiodes in standard CMOS process technologies lie between 10% and 70%, the circuitry has to deal with photocurrents in the range of a few or a fraction of nano amperes. This requires photodetectors with small dark current, sensitive read-out circuitry and special layout techniques.

One of the limitations of analog circuitry in CMOS technology is the mismatch of identically designed structures at different locations on the silicon die. In image sensors this results in fixed-pattern noise, which means, that uniform image results in non-uniform gray-scale values. The correlated double sampling technique has been developed for CMOS image sensors to cancel fixed-pattern noise. This technique is only available in integrating image sensors, while all presented concepts work in constant-current mode, where correlated double-sampling is not applicable.

Fixed-pattern noise can only be reduced by spatial averaging here. Dynamic noise components from thermal noise, photon and electron shot noise and other sources may be reduced though by adequate temporal filtering techniques, if the bandwidth of the wavefront sensor is large enough for the desired application.

In ophthalmic applications we are interested in the cancellation of ocular aberrations. The power spectral density of ocular wavefront aberrations falls with approximately 4 dB per octave up to $\approx 70\text{ Hz}$. The wavefront sensor should sample the wavefront with at least 140 Hz to allow some temporal

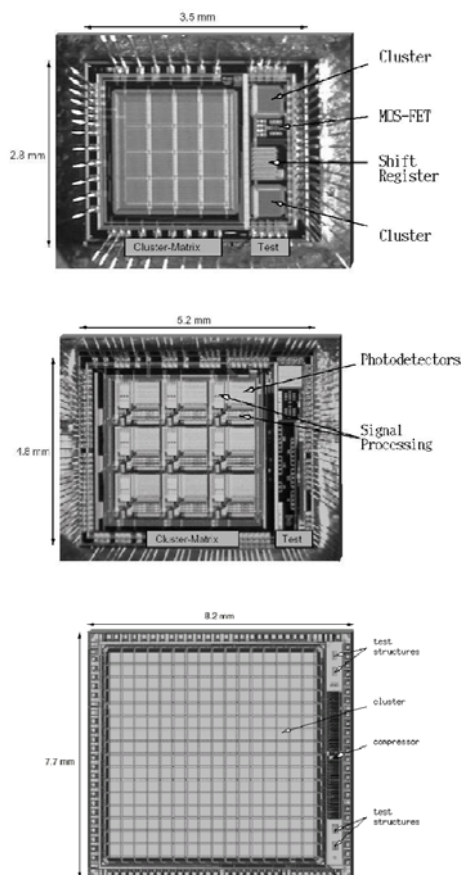


Fig. 17.1. The HSSX is the result of a series of prototypes, which has been started in 1998 for the use in ophthalmic AO. These sensors rely on the Winner-Take-All circuit as the PSD. The circuit detects the largest photocurrent from pixel rows and columns.

The first prototype contained 4×4 PSDs with 8×8 pixels each; n+/substrate photodiodes have been used here. This chip has been manufactured in the AMS $0.8\ \mu\text{m}$ technology and operated at $P > 50\ \text{nW}$ per spot and 1 kHz repetition rate. In order to increase the position resolution a second prototype has been built in the AMS $0.8\ \mu\text{m}$ BiCMOS technology which offers an additional vertical npn bipolar transistor with increased quantum efficiency. This chip consisted of a matrix of 3×3 PSDs with 10×10 pixels each.

The final version of this series, the HSSX consisted of 16×16 PSDs with 19×19 pixels each in AMS $0.6\ \mu\text{m}$ technology. In order to reach the desired frame rate of 1 kHz at $200\ \text{pW}$ per spot a special feedback mode has been implemented, which required the use of p+/nwell photodiodes. This wavefront sensor has been successfully used as an eye tracker using the reflection of the cornea. The photodetectors were not sensitive enough to measure the retinal reflection for ocular measurements

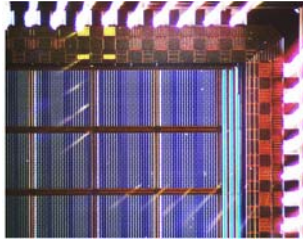


Fig. 17.2. The CeHSSA uses a resistive-ring network of Winner-Take-All circuits with pseudo-centroiding as a PSD. Fixed-pattern noise is decreased by the factor 2.4 with respect to the simple WTA circuit and the intrinsic bandwidth augmented to 4 kHz. This sensor allows random access to individual spot detectors. The sensor has been manufactured in the AMS 0.35 μm CMOS technology; n-well/substrate photodiodes have been used for the 21×21 pixels within each of the 8×8 PSDs

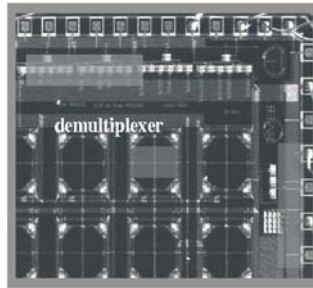


Fig. 17.3. The QC-WFS chip consists of 64 quad cells based on double-junction photodiodes. The photocurrents are transferred directed to the output nodes via multiplexed pixel-level switch sets. The four photodiode output signals are easily combined to yield the spot coordinates (x, y) .

This sensor is able to operate at a refresh rate of 3 kHz and the position resolution is good if enough light per spot is available (μW range). This sensor was fabricated in DIMES/TU-Delft in the framework of a standard 1.6 μm CMOS process

averaging or post-processing. The larger the final closed-loop bandwidth, the larger the fraction of aberrations that can be canceled out and the larger will be the Strehl ratio of the imaging system. In free-space terrestrial propagation and astronomy even kHz repetition rates are required. All presented CMOS-based sensors up to date fulfill the bandwidth requirements.

17.1.2 Wavefront Reconstruction

The measured data in the Hartmann–Shack sensor principle are the deviations of a focal spot from the optical axis of the lenslets in the lenslet array. These deviations are directly related to the local slope of the wavefront averaged over the area of the individual lenslet.

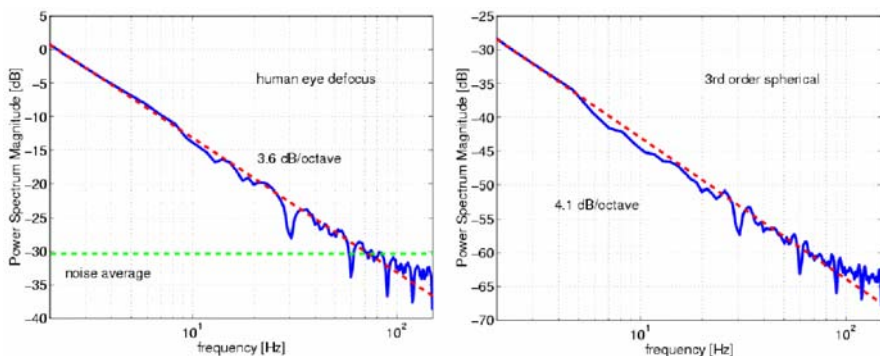


Fig. 17.4. Power spectrum density measurements of human eye ocular aberrations with the CeHSSA sensor, here defocus and 3rd order spherical aberrations are shown from [3]. The power spectrum falls with approximately 4 dB per octave up to about 70 Hz, where the noise level is reached

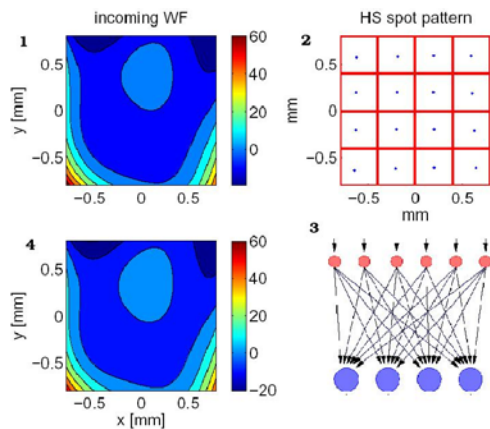


Fig. 17.5. Neural network training and performance evaluation without noise. An arbitrary complex wavefront is generated from random Zernike coefficients (upper left, contour plots in nm scale) and the spot positions are calculated (upper right). The position data is fed into a trained neural network (lower right), which estimates the Zernike coefficients for this data. The estimated coefficients are used to calculate the estimated wavefront (lower left) and the rms wavefront reconstruction error can be calculated

The most straightforward way of obtaining the wavefront from the local slopes is the zonal integration of the wavefront patches associated with local slopes. In general we are interested in global features of the wavefront, like defocus and astigmatism, which favors a decomposition of the wavefront in orthogonal polynomials, usually Zernike polynomials. The most straightforward way to obtain the coefficients for each Zernike polynomial is through the least-square approximation of measured slopes to Zernike derivatives in

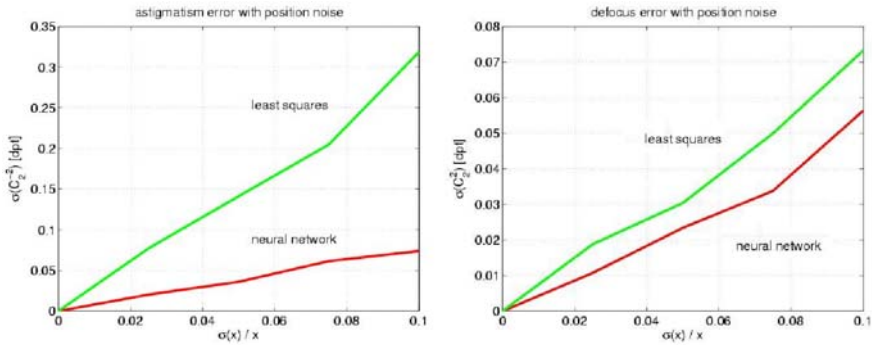


Fig. 17.6. Performance comparison between defocus and astigmatism measurements, evaluated from a Hartmann–Shack spot pattern with the Gaussian inverse and a trained neural network, in the presence of Gaussian position noise. The position noise is given as the percentage of the full dynamic range within the detector, here $400\ \mu\text{m}$

a reconstruction matrix. To obtain the solution it is necessary to invert the reconstruction matrix, which is usually done using Gaussian elimination, although more robust methods exist, like singular-value decomposition.

The ultimate fidelity of the reconstructed wavefront depends on two issues: the compatibility of the sampling-point density with the wavefront spatial frequency; and the presence of noise in the measurements of the spot deviations. The wavefront spatial resolution depends on the number of sampling areas (microlenses) used. For applications where only significant lower order aberrations are expected (e.g. defocus, tilt and astigmatism) a small number of position-sensitive detectors (PSDs), for instance 5×5 , will suffice. When using the least-squares approximation with Gaussian elimination for the reconstruction of the wavefront, the algorithm converges if twice the number of lenses is larger than the number of Zernike modes to be used in the reconstruction. However, the error in the spot-position determination (position resolution) propagates through the reconstruction algorithm and dictates the maximum number of modes that can be effectively used to yield a certain wavefront accuracy.

17.2 Technological Possibilities for Further Integration

While current AO systems are all mostly experimental and complicated to set-up and implement, a “black box” AO system to be simply put into the optical path of an imaging system is the desirable goal of our developments. Systems relying on CCD cameras with software image processing will probably never be miniaturized, because they require at least a host computer.

One of the possibilities for computing without a host computer is to use a high-performance, DSP-based controller board featuring the interface to an integrated CMOS-based wavefront sensor. This kind of small sized board (few square centimeters) can operate independently from a host PC allowing it to freely perform autonomous data acquisition, control functions and implementation of algorithms requiring floating point capabilities. This option could be perfect for a wide variety of applications requiring fast and small sized stand-alone systems with on-board processing, e.g. wavefront reconstruction and digital to analogue conversions. Such a system is suitable for interfacing our currently existing sensor as the wavefront reconstruction should be done off-chip. Nevertheless, if the applications require a host PC to perform other functions, one of the suitable PCI DSP cards available on the market can also be used.

In the next-generation integrated wavefront sensor, the wavefront reconstruction is aimed to be done on-chip. The data from the sensor can be read out by a micro-controller based stand-alone digital interface board. This system can be optimized for the desired real-time control applications in the closed loop AO. As most of the processing can be implemented on-chip, only data read out and bit-manipulation operations would have to be done on-board to provide the required control signals to drive an adaptive mirror.

17.2.1 Implementing Wavefront Reconstruction in Hardware

The complex mathematic floating point operations for the wavefront reconstruction by calculating the Gaussian inverse will probably not be feasible in a VLSI⁵ implementation. DSPs⁶ are often used in applications where fast floating point operations are required, but they require external hardware and programming. Further integration is often possible, where FPGAs⁷ are used instead of DSPs, but standard FPGAs cannot perform floating point operations.

The question arises how to implement wavefront reconstruction on a miniaturized system then. We propose to use hardware neural networks here. Neural networks have been used by Lloyd-Hart [5] on a software and transputer basis to sense and reconstruct the wavefront for a multi-mirror telescope. Implementation of neural networks in DSPs is possible, while most FPGAs cannot handle them. We propose to implement hardware neural networks which have been built and used successfully. In contrast to software implementations of neural networks they make use of the full parallel nature of the neural network and often use intrinsic transfer characteristics of MOSFET devices.

⁵ Very Large Scale Integration

⁶ Digital Signal Processor

⁷ Field Programmable Gate Array

17.3 Artificial Neural Networks

Neural networks are well capable of dealing with a number of signal processing tasks in AO, like wavefront analysis and control. Vdovin [6] performed simulations, where a neural network was trained to predict a vector of adaptive mirror signals from measured data from a curvature sensor. Brockie et al. [7] introduced a neural network predictor into the servo loop of an adaptive optics system in astronomy and achieved an increase in Strehl ratio. Neural networks evaluated in astronomy have been simulated in software with a very high computational load, which is contrary to the goal of miniaturizing an AO system on first sight. On the other hand, these systems do not make use of the original strength of neural networks, which is high parallelism, but rather simulate the functionality in software.

A multitude of possible neural network architectures, neuron types and learning algorithms exist. We present here the most straightforward approach for solving the wavefront reconstruction problem. A similar architecture has also been used by Sandler et al. [8] for phase-diversity telescope data. We start with an input data vector with $2n^2$ elements, representing the local slopes from a rectangular array with linear dimension n . The output data vector contains the k Zernike terms, which the neural network has to predict and we know, that a functional relation between the input and the output vector exists. Additional inputs could be a noise estimation in order to make the neural network more robust.

It is known that a two-layer feed-forward neural network with sigmoid input layer and linear output layer can be trained to approximate any multidimensional function with a finite number of discontinuities. A number of well established backpropagation learning algorithms exists for this kind of neural network.

The neurons in each layer of the neural network are identical and perform the simple operation

$$a = f(Wp + b),$$

with output a , input vector p , weight coefficient vector W and offset b . The transfer function f is sigmoid for the input layer and linear for the output layer. We first created the training vectors by starting with a set of random Zernike coefficients. From them we calculated the expected local slopes and spot deviations in the Hartmann–Shack sensor and used them as the input vector. Different training algorithms have been evaluated to learn the functional relationship between focal spot positions and Zernike coefficients, which from a practical point of view basically differ in the learning time. The algorithm most simple to understand is the gradient descent algorithm, which tries to minimize the difference between the output of the neural network and the training vectors by adjusting all weights in the neurons.

After training the neural network the *rms* wavefront reconstruction error has been evaluated in Monte-Carlo simulations and the values have been com-

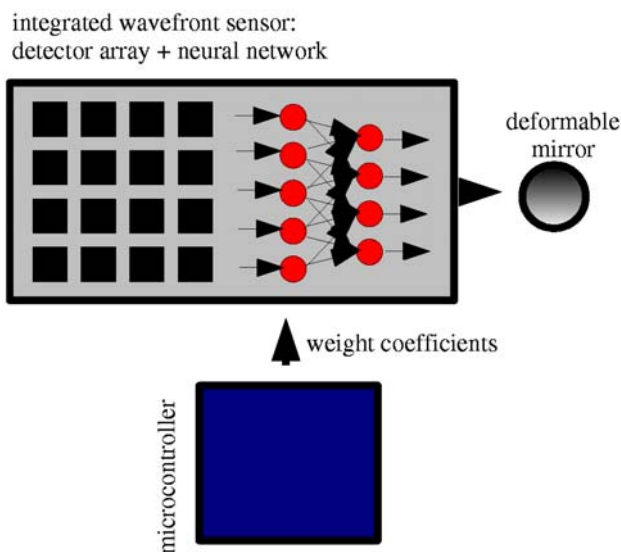


Fig. 17.7. Concept of a small AO system, without host computer. The positions of focal spots from a lenslet array are measured with a detector array. The position data serves as the input for a hardware neural network, with the weight coefficients set for modal wavefront reconstruction or driving of a deformable mirror. In order to make the neural network adaptable to different corrector devices, the predetermined weight coefficients are fed in by a micro controller

pared with results from a least-squares-fit with the same data, see Fig. 17.5 for a schematic of the procedure.

From this preliminary results we have seen that the neural network must be trained with noisy data, although training takes longer and may not reach the accuracy of the least squares solution. If trained without noise, the neural network reproduces the training vectors very well, but performs very poor, when noise is added. If trained well, the neural network may even outperform the analytical solution, see Fig. 17.6.

Instead of using spot positions for the input training vector, a slightly different architecture can use quad-cell photocurrents directly as the input data.

17.4 Proposed Single-Chip Approach

From all available neural network architectures the feed-forward network is easy to train and well-established, though a cellular neural network seems to be more adapted to the processing of detector array data.

Hardware implementations of neural network usually need full connectivity between all neurons in a layer, weight multiplication and storage elements.

Interconnection in large neural network is therefore a major problem in VLSI. For image processing tasks cellular neural networks have been used, where each neuron is only connected to its nearest neighbors.

In our case interconnection requirements are not that difficult to achieve, because we only need two-layers of some tens of neurons for a typical Hartmann–Shack sensor. Weight storage, either analog or digital, and weight update is a major obstacle for hardware neural networks. In our case this could be solved by determination of the rough weight coefficients in a software training environment and loading them to the chip through a micro controller. Updateable weight coefficients also allow adaptation to different corrector devices and make the neural network more robust against mismatch. Figure 17.7 shows a schematic of this hardware architecture.

17.5 Conclusions

Adaptive Optical systems are nowadays individually designed for each specific application; for each combination of wavefront sensor and corrector device a custom data acquisition and evaluation strategy and own driver procedures for the correcting device are developed. All processing and control steps are usually realized on computers in software, while the underlying problem of wavefront measurement and control is a functional relationship between the measured data and the required control signals for the wavefront corrector. The step of wavefront measurements according to the Hartmann–Shack sensor principle has been addressed recently by a number of specialized CMOS-based wavefront sensors, independently developed in Delft, Netherlands and Heidelberg, Germany. Image processing of the Hartmann–Shack spot pattern is performed from the output of position sensitive detectors in these devices.

Calculating a modal description of the wavefront and driving a deformable mirror still requires software processing of the spot position data. We propose to integrate a hardware neural network directly on the already existing CMOS-based wavefront sensors and perform the necessary operations for wavefront control on-chip. In a final version this would result in an AO system that does not require a host computer any more once the neural network is trained for the specific control problem.

We have shown that a two-layer neural network with a few tens of neurons is capable of calculating Zernike coefficients from Hartmann–Shack spot patterns. The output of the neural network can be used to drive a modal wavefront corrector or a deformable mirror; only the weight coefficients of the neural network have to be adapted to the corrector device. A micro-controller would be needed to provide the neural network with the appropriate weight coefficients, but no host computer. We will now investigate feasible hardware solutions for on-chip neural network wavefront measurement and control.

Acknowledgments

Thomas Nirmaier would like to thank Dr. D. Droste. D.W. de Lima Monteiro would like to thank Dr. G. Vdovin and STW (project: DOE.5375).

References

1. D.W. de Lima Monteiro, G. Vdovin, P.M. Sarro: High-speed wavefront sensor compatible with standard CMOS technology. To be published in *Sensors and Actuators A* (2004)
2. D. Droste, J. Bille: An ASIC for Hartmann–Shack wavefront detection. *IEEE J. Sol. State Circ.* **37** (2002)
3. T. Nirmaier, G. Pudasaini, J. Bille: Very fast wavefront measurements at the human eye with a custom CMOS-based Hartmann–Shack sensor. *Opt. Express* **11**, 2704 (2003), <http://www.opticsexpress.org/abstract.cfm?URI=OPEX-11-21-2704>
4. D.W. de Lima Monteiro, T. Nirmaier: CMOS technology in Hartmann–Shack wavefront sensing. In: U. Wittrock (ed.): *Proceedings of the 4th International Workshop on Adaptive Optics for Industry and Medicine*, October 19–24, 2003, Münster, Germany (Springer, Berlin Heidelberg 2005)
5. M. LLoyd-Hart, P. Wizinowich, B. McLeod, D. Wittman, D. Colucci, R. Dekany, D. McCarthy, J. Angel, D. Sandler: First results of an on-line adaptive optics system with atmospheric wavefront sensing by an artificial neural network. *Astrophys. J.* **390**, L41 (1992)
6. G. Vdovin: Model of an adaptive optical system controlled by a neural network. *Opt. Eng.* **34**(11), 3249 (1995)
7. R. Brockie, M. Wells, P. Gallan, G. Aitken: Predictors in the servo-loop of an AO system. *Adaptive Optical System Technologies*, Kona, Hawaii 1998. SPIE **3353**
8. D.G. Sandler, T.K. Barret, D.A. Palmer, R.Q. Fugate, W.J. Wild: Use of a neural network to control an adaptive optics system for an astronomical telescope. *Nature* **351**, 300

18 CMOS Technology in Hartmann–Shack Wavefront Sensing

D.W. de Lima Monteiro¹ and T. Nirmaier²

¹ Delft University of Technology, EEMCS. Electronic Instrumentation Laboratory
Mekelweg 4, 2628 CD Delft, The Netherlands

² University of Heidelberg, Kirchhoff Institute of Physics
Im Neuenheimer Feld 227, 69120 Heidelberg, Germany

Summary. We assess, in this paper, the use of CMOS technology (Complementary-Metal-Oxide-Semiconductor) for the fabrication of fast wavefront sensors based on the Hartmann–Shack technique. We briefly recapitulate the core of this technology and we point out its pros and cons with respect to the sensor performance. Focusing on fast operation, we compare conventional image sensors with custom layout approaches that make use of position-sensitive detectors (PSDs). We also present the results obtained with three different CMOS sensor concepts implemented so far:

Heidelberg1: $0.6\ \mu\text{m}$ – AMS – 16×16 -PSDs alternate – winner-take-all digital readout [1]

Heidelberg2: $0.35\ \mu\text{m}$ – AMS – 8×8 -PSDs chessboard-like – winner-take-all / resistive ring [2]

Delft1: $1.6\ \mu\text{m}$ – DIMES – 8×8 -PSDs quad cell – passive pixels [3,4]

The aim is to identify the practical capabilities of standard CMOS technology in wavefront sensing.

18.1 Introduction

As an alternative to the conventional CCD-camera approach, one can implement fast and yet cost-effective Hartmann–Shack wavefront sensors in the framework of the widely available standard CMOS technology, which offers the possibility to integrate photodetectors and reliable analog-digital circuitry on a single chip.

CMOS stands for *Complementary Metal-Oxide-Semiconductor* and is the most widely used microelectronics fabrication technology today. The ample market interest in this technology promotes continuous research and process improvement, rendering a good match between simulated and implemented circuitry. This technology is generic and largely accessible, it favors the integration of multiple electronic functions with a high yield and it intrinsically offers several photosensitive structures. CMOS imaging is a growing market that complements that of CCD imaging, i.e. it offers extended embedded functionality on a chip.

The Hartmann–Shack method is one of the most used wavefront sensing techniques; it is structurally simple and white-light compatible, it prompts

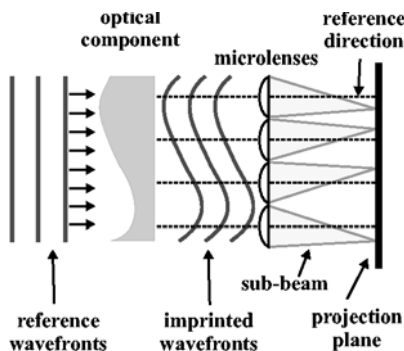


Fig. 18.1. In the Hartmann–Shack method the spot displacements on the projection screen represent the incoming arbitrary wavefront

straightforward data analysis and it has no 2π -ambiguity limitation. A microlens array samples an arbitrary wavefront and the light spots at the projection screen deviate from a reference grid according to the local slopes of the wavefront. Essentially, this method enables one to estimate the wavefront shape from the displacements of light spots. Figure 18.1 depicts the principle.

In optical shop testing, variations on this principle include, for example, Laser-Ray Tracing (LRT), in which a single laser beam scans an object under test at particular grid points and the *inverse* Hartmann test, in which small optical fiber heads project a few beams on the object surface, whose deviations upon reflection indicate the object quality. The projection screen in a Hartmann–Shack sensor is conventionally a CCD camera, which represents a bottleneck to fast operation. Although CCD technology is robust for imaging applications and capable of operation at very low light levels, inexpensive off-the-shelf CCD cameras offer limited frame rates usually reaching up to only 75 Hz. Besides, the fabrication processes are often proprietary and inopportune to custom designs. High-speed CCD cameras for scientific applications do exist, but they require a number of extra fabrication steps and architectural changes, which altogether push the costs far up.

Commercial CMOS cameras represent another choice. Several off-the-shelf models feature framing, which allows one to choose windows of interest within the imaging chip. This might increase the readout speed when one is interested in only a fraction of the total number of pixels available, however multiframing, as might be the case for the detection of largely spaced spots may involve a considerable frame transition time. Also, the diversity of photodetectors and circuitry layouts in CMOS makes datasheets tricky to analyze, and there is often a compromise between sensitivity, dynamic range and speed.

Recall that an imager, be it CCD or CMOS, is designed and intended to capture a scene, in which case a high density of pixels is often required. In the Hartmann–Shack method, we are ultimately interested in the positions of light spots, and the grabbed image is solely an intermediate step. There-

fore, the relatively slow image-processing step to perform the “centroding” calculations combined with the restricted camera frame rate limit the overall sensor speed. This suggests that we need to devise a custom layout in order to ensure operation at high repetition rates, and for this purpose, CMOS offers more flexibility.

18.2 Standard CMOS Technology

18.2.1 Technology Overview

The building blocks of this technology are the NMOS and PMOS field-effect transistors (MOSFETs) in silicon. The more advanced the CMOS process, the narrower the minimum achievable length of the gate. The gate length indicates the feature size of the technology, i.e., the minimum geometrical dimension reliably fabricated on chip. Feature sizes between $0.8\ \mu\text{m}$ and $0.18\ \mu\text{m}$ are industry standards today and the state-of-the-art is $0.13\ \mu\text{m}$.

From MOSFETs one can implement both digital and analog circuitry, making use of metal layers for interconnections. Capacitors, resistors and even inductors become possible by combining doped regions, insulating layers, metal layers and polysilicon layers appropriately. Photodetectors are intrinsically available in this technology. Using junctions between inversely doped regions and doped wells, one can implement not only photodiodes, but also phototransistors. However, the doping levels and junction depths are optimized for circuit operation rather than for photodetection. Figure 18.2 shows examples of possible photodetector structures.

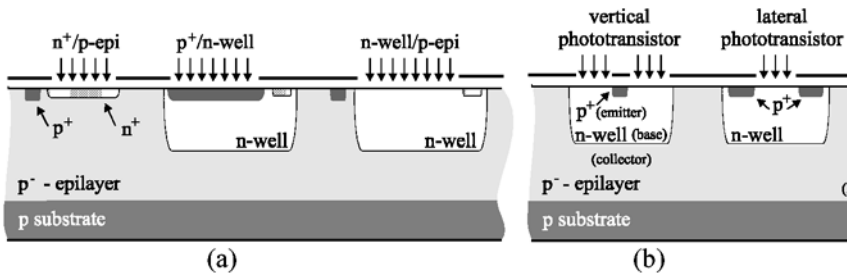


Fig. 18.2. Some photodetector structures available in standard CMOS technology: (a) photodiodes, (b) phototransistors

18.2.2 Limitations

Although CMOS represents a good choice for mixed-signal circuitry, it is not optimal for imaging, especially in a standard single-poly flow chart. Some of

the limitations are that there are no pinned and buried layers to minimize dark current; and multiple charge-packet transfer is not efficient because of the fixed doping profiles and the absence of overlapping polysilicon layers. Also, in a standard process line, there is no accurate control over the thickness of transparent dielectric layers, which makes them unpredictable for anti-reflection purposes.

As the trends migrate to submicron features, the disadvantages to photodetection increase, because in such processes the p - n junctions become shallower and the doping profiles become higher, resulting in thinner depletion layers. These two factors lead to a lower quantum efficiency for longer wavelengths (> 600 nm). The introduction of silicided drains/sources as well as silicided polysilicon layers impairs the penetration of incident light. Besides, the reduction of the supply voltages – and the disproportional scaling of the threshold voltages – constrain the signal swing, which in the analog domain can be detrimental. Moreover, the process costs for state-of-the-art processes increase drastically making them less convenient for small-scale custom devices. Besides, behavior of novel circuitry becomes less predictable because of insufficiently accurate model parameters due to additional physical phenomena affecting transistor operation.

For CMOS imaging, sub-micron feature sizes favor a high pixel density and a faster signal transfer, but they introduce more mismatches between transistors, which are translated as fixed-pattern noise and demand extra compensation circuitry. The increased number of dielectric layers in these processes results in high sidewalls around the photosensitive area affecting off-normal light incidence.

Nowadays, CMOS imagers with claimed CCD image quality have been reported [5,6]. They often use either four-transistor active pixels or customized steps with well-defined local doping profiles and highly doped pinned layers, or a combination of those.

18.3 CMOS Hartmann–Shack Wavefront Sensors

For a Hartmann–Shack wavefront sensor, two different approaches using CMOS technology can be considered: a *camera* or a *matrix of position-sensitive detectors* (PSDs). The basic difference between them is that a camera has a limited frame rate and requires image processing, whereas a matrix of PSDs (in which each PSD is associated with a light spot) renders almost direct information about the spot position and circumvents any image processing.

18.3.1 CMOS Imagers

A 2D imager consists of a densely packed array of adjoining pixels, whose main purpose is to capture an image by mapping a scene into a discrete dis-

tribution of light intensities. Obviously, a higher pixel density yields a better image reproduction. In a Hartmann–Shack wavefront sensor the camera is used to register a picture of the light spots projected with the microlens array. Each microlens is associated with a region on the chip, i.e., with a certain number of pixels $N \times N$, over which the spot is free to move without overlapping with the neighboring ones. The effective focal spot illuminates yet a smaller number of pixels, say $n \times n$, within that delimited region. One calculates the baricenter of the focal spot by using a simple centroiding (center of mass) formula or a pre-calibrated curve-fitting algorithm, which minimizes the discretization error. In both cases one can achieve subpixel resolution, which increases with the number of illuminated pixels $n \times n$ and with the array fill factor.

In assembling a Hartmann sensor, one should find an optimal compromise between the ratio of the spot size to the pixel size and the ratio between the microlens diameter and the spot size. The first ratio affects the resolution of the centroid calculation and the second ratio dictates the lateral range the spot is able to move (i.e., the maximum local wavefront tilt). The largest possible ratios are desirable, but practical limits are set by the choices of imaging-chip dimensions, pixel size and parameters of the microlens array (lateral size, pitch, fill factor and focal length). Conventional chip dimensions extend up to 15 mm and pixel sizes range from 5 μm to 20 μm , typically; the effective lateral size of the spot should preferably comprise at least 5 pixels. The maximum spot displacement depends on the focal length of the microlenses and on the magnitude of the wavefront aberrations. For a Hartmann–Shack wavefront sensor, color cameras are not recommended, especially if one is dealing with monochromatic light. The reason is that many color chips have a distribution of color filters on top of their pixels and the result of this color division is a reduction of the total resolution by at least a factor 3. Another source of centroiding error is the quantization noise, which is associated with the conversion of the pixel analog signal to an output digital signal with a given number of bits. The *rms* error is given by the voltage associated with the least-significant bit divided by $(12)^{1/2}$.

In principle, a CMOS imager can serve as a direct replacement for a CCD camera, with a number of important remarks we consider henceforth:

1. *Resolution and fill factor:* For the same resolution, the frame rate of a CMOS imager is usually higher than that of a CCD, and the price is lower. However, often the trade-off is the lower sensitivity and the reduced pixel fill factor, i.e., the pixel area usually consists of a photosensitive region plus appended pixel circuitry, contrasting to the full-frame or frame-transfer CCDs in which the photosensitive region occupies the whole exposed area (fill factor close to 100%). It is important to observe whether the CMOS chip has focusing microlenses deposited directly on chip, counteracting the lower fill factor, compared to a CCD;

2. *Dynamic range and mismatch*: Analog circuit elements have a direct influence on the camera output signals. CMOS cameras with a very high dynamic range usually make use of logarithmic pixels, which are very useful in low-light imaging but inconvenient for centroid detection. Several cameras offer the possibility to switch between logarithmic and linear modes. As regards noise, cameras with embedded circuitry for double sampling or correlated double sampling are able to effectively suppress spatial mismatches and to reset noise.
3. *Digital circuitry*: Pixel-level analog circuits are driven by either shift registers or digital demultiplexers, which are controlled by a clock and/or a digital address. Mono-chain shift registers address pixels in a fixed sequential manner, and therefore offer no extra flexibility compared to a CCD. On the other hand, imagers designed with either split shift registers or demultiplexers are, in principle, able to operate in fixed-framing mode or full-random-access mode, respectively. The first is useful if one wants to increase the readout speed of an off-the-shelf imager by addressing only a part of the chip. In some cases, multiple framing is possible, where several sub-areas can be defined on the chip. This can be convenient to track individual spots, eliminating the readout of obsolete dark pixels. However, the sequential readout and the switch time between frames slow down the operation. Demultiplexers offer full random access in the spatial domain and, depending on the pixel architecture, also in the time domain. This could readily reject dark pixels and promote longer integration times exclusively for faint spots. Yet, demultiplexers are not usually employed instead of shift-registers, both because they require a larger chip area and because the main goal of off-the-shelf imagers is to capture an image completely or partly, but not a spot, which makes full random access an unnecessary feature;
4. *Sensitivity*: Standard CMOS processes are not optimized for photodetection as discussed in Sect. 18.2.2. Most commercial CMOS imagers use the n^+/p -substrate photodiode (shallow junction), which enables a larger array density. But, the closer the junction is to the surface, the higher is the contribution of dark-current shot noise; the resulting signal upon a long integration time ends up being dominated by dark current. CMOS cameras with claimed CCD performance have their own enhanced and proprietary CMOS processes. The dark-current density in optimized processes can be as low as 50 pA/cm^2 (specialized CCDs $\approx 10 \text{ pA/cm}^2$). High-speed cameras require additional custom fabrication steps and are often manufactured in state-of-the-art processes, for which the smaller feature sizes result in smaller parasitic capacitances and larger operational bandwidth. However, the costs become much larger than for conventional processes, and the sensitivity becomes lower (Sect. 18.2.2).

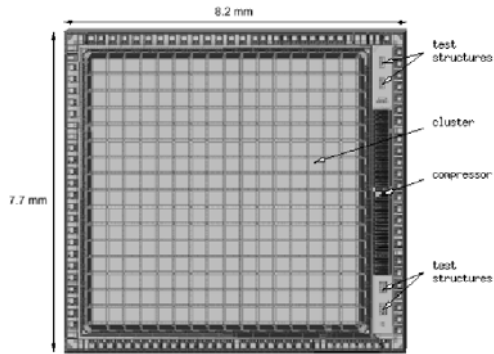


Fig. 18.3. Photo of the chip

technology	AMS 0.6 μm , <i>n</i> -well, double poly, double metal poly, double metal
chip size	7.7 \times 8.2 mm
photodetector	17.6 \times 17.6 μm pixels <i>p</i> + / <i>n</i> -well-photodiodes
PSD layout	alternate structure, 19 \times 19 pixels each (400 \times 400 μm)
array	16 \times 16 PSDs (orthogonal)
circuitry	Winner-Take-All circuit + daisy chain data transfer and data compression
spot detection	peak photocurrent, $P > 200$ pW/spot
readout	serial digital

18.3.2 CMOS Chips with Position-Sensitive Detectors

These chips comprise full custom designs for Hartmann(–Shack) sensors. Each design consists of a regular array of position-sensitive detectors (PSDs), signal-transfer and/or signal-processing electronics and digital control units (shift registers or demultiplexers). The main advantage of using PSDs is the nearly direct information about the positions of the spots, rendering image processing unnecessary. The three design approaches presented here were fabricated and tested, and they differ from each other in the feature size of the CMOS process used, the type of PSDs chosen and the spot-detection scheme.

Heidelberg 1 (HSSX)

The noise-free position resolution is equal to the pixel size due to the binary nature of the WTA circuit. After every millisecond the state of all PSDs is reset. The binary data is then transferred in a daisy-chain architecture to a data compressor unit for subsequent readout. The PSDs, which detect the position of the largest photocurrent, are linear over the whole dynamic range. The SNR is mostly limited by fixed-pattern noise.

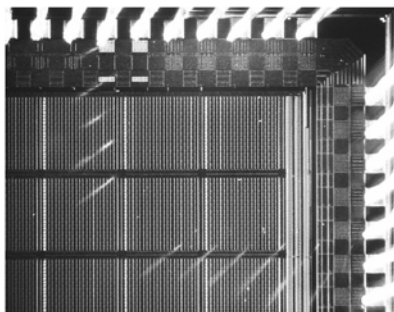


Fig. 18.4. Photo of a corner of the chip

technology	AMS 0.35 μm , <i>n</i> -well, double poly, double metal
chip size	4.1 \times 4.1 mm
photodetector	17.0 \times 17.0 μm pixels <i>n</i> -well/substrate-photodiodes
PSD layout	chessboard-like, 21 \times 21 pixels each (400 \times 400 μm)
array	8 \times 8 PSDs (orthogonal)
circuitry	resistive network of Winner-Take-All circuits + internal tristate data bus and multiplexed binary output
spot detection	pseudo-centroiding or peak photocurrent detection $P > 20 \text{ pW/spot}$
readout	16-, 32-, and 42-bit digital output modes

Heidelberg 2 (CeHSSA)

The position resolution is equal to the pixel size in the noise-free case. The sensitivity is better with respect to the *HSSX* (previous sensor) through the use of *n*-well/substrate photodiodes and a novel resistive-ring network of WTA circuits. Fixed-pattern noise is reduced by a factor of 2.4 through pseudo-centroiding with respect to peak photocurrent detection. After addressing a detector its data is stored in an internal tristate bus for subsequent parallel or 16-bit multiplexed readout.

Delft 1 (QC-WFS)

The position resolution is determined by the ratio of the spot size to the cell size, by the spot intensity profile and by the signal-to-noise ratio of the pixels. The geometrical arrangement of a quad-cell allows both spot-centroid detection and spot centering. The first is convenient when the sensor is used in diagnostic applications and the latter when it is used to drive a deformable mirror. Although the quad-cell response is only linear in its very center, the full response range is very well described by a sigmoidal function obtained in a calibration step.

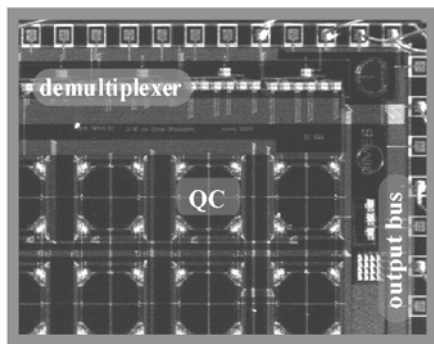


Fig. 18.5. Photo of a corner of the chip

technology (feature size)	DIMES: 1.6 μm , <i>n</i> -well single poly, double metal
chip size	10 \times 10 mm
photodetector	300 \times 300 μm pixels, double-junction photodiodes (<i>p</i> ⁺ / <i>n</i> -well/substrate)
PSD layout	quad cell, 2 \times 2 elements (600 \times 600 μm)
array	8 \times 8 PSDs (orthogonal)
appended circuitry	passive analog switch set per pixel + demultiplexer
spot detection	full spot centroiding
readout	8 analog outputs

18.4 Performance of the Custom Chips

The user of a Hartmann–Shack sensor often observes a few important characteristics: the spatial sampling density (# of spots), the operational speed, the wavefront-sensing accuracy (the minimum *rms* wavefront variation the sensor is able to detect) and the light sensitivity. They all depend on a number of other core parameters related either to the technology used, or to the design choices. For instance, the wavefront accuracy is associated intimately with the PSD position resolution, because the spot-position error propagates through the wavefront reconstruction algorithm affecting the reconstruction fidelity.

Heidelberg 1 (HSSX)

The position resolution is basically limited by the pixel size (17.6 μm) and fixed-pattern-noise (FPN), which depends on the spot size and on the frame rate. For very small intensities a feedback mode has been implemented with increased bandwidth at the expense of increased position noise. The chip features no random access to the individual detectors, but has a data compressor for the position data.

quantum efficiency		10% (680 nm)
operational frequency		1 kHz
position resolution: frequency/FPN		spot intensity
250 Hz	0.74 pixel	10 nW
1 kHz	1.85 pixel	1 nW

Heidelberg 2 (CeHSSA)

The influence of fixed-pattern noise was cancelled out to a large extent in this chip by using a modified topology for the Winner-Take-All circuit. The larger quantum efficiency and the reduced parasitic capacitance also increased the bandwidth and the sensitivity. The position resolution above ≈ 100 pW per spot is mostly limited by the pixel size ($17.0 \mu\text{m}$).

quantum efficiency		40% (680 nm)
operational frequency		4 kHz
position resolution: frequency / FPN		spot intensity
1 kHz	0.59 pixel	300 pW
1 kHz	1.25 pixel	30 pW

Delft 1 (QC-WFS)

In this chip, the position resolution depends on the process/pixel architecture through the signal-to-noise ratio. For passive pixels, the large pixel capacitance (50 pF), due to the large pixel size and the use of double-junction photodiodes, introduces considerable kTC noise, because of the photocurrent transferred through a switch. Reduction of this noise contribution is a solution for operation at lower light levels.

quantum efficiency		40% (630 nm)
		70% (680 nm)
operational frequency		3 kHz
position resolution/ wavefront accuracy		spot intensity ($\lambda = 633$ nm)
$10 \mu\text{m}$	$\lambda/10$	$2.5 \mu\text{W}$
$5 \mu\text{m}$	$\lambda/20$	$4 \mu\text{W}$
$1 \mu\text{m}$	$\lambda/50$	$10 \mu\text{W}$

18.5 Directions for Future Improvements

The first presented chip (*Heidelberg 1*) features high operational speed but does not offer random access to the PSDs. It also has a very good light sensitivity (nW range) but the position detection is based solely on the peak intensity of the spot, which limits the position resolution to the pixel pitch. The second chip (*Heidelberg 2*) represents an enhanced version of the previous one. It enables full random access, enhances the good light sensitivity to the sub-nW range and improves the position resolution (wavefront accuracy) by using pseudo centroiding with multiple peak detections. It is also able to operate at 4 kHz in the centroiding mode. This sensor is suitable for low-light operation but the position resolution still limits its use to low-order aberrations with relatively large magnitudes. The third presented sensor (*Delft 1*) offers full random access, very good position resolution (wavefront accuracy) but requires light levels in the μW range due to the high capacitive noise associated with the large pixels. Both chips (*Heidelberg 2* and *Delft 1*) still offer room for improvement, the first in terms of position resolution and the latter in terms of low-light operation.

Heidelberg 2

The basic limitation of wavefront sensors based on the Winner-Take-All circuit is the restricted resolution of the spot detection. The design goal with respect to sensitivity ($\approx 200\text{ pW}$ per focal spot) has been achieved with this sensor. The practical limit for the minimum pixel size (and position resolution) in the chosen CMOS process technology is $\approx 10\ \mu\text{m}$.

Though in the static case the position resolution is limited to the pixel size, this limit can be passed under in the dynamic case, by adequate temporal post-processing of the spot position time series [7], e.g. through adequate Kalman or other filtering techniques. A spatial resolution well below the pixel resolution can be achieved and no different chip architecture is required. On the other hand, it would be useful to increase the functionality of the sensor by adding a modal wavefront-reconstruction module directly on the chip. A possible implementation would be a hardware artificial neural network [8], which could provide a direct analog output signal for some low order aberrations, like tilt, defocus and astigmatism, useful for modal wavefront correctors. This could result in miniaturized AO systems, which do not need a host computer.

Delft 1

The goal is to improve the light sensitivity of this sensor by three orders of magnitude ($\mu\text{W} \rightarrow \text{nW}$ per spot), while keeping the good wavefront accuracy it already offers. The main limitation now is capacitive noise. Still preserving the benefits of the quad-cell architecture and the supra-micron fabrication

technology (1.6 μm), several measures can contribute towards this achievement: substitution of the double-junction photodiodes with n -well/ p -epi photodiodes, of passive pixels with active pixels, and of simple transimpedance amplifiers with capacitive shunted ones. The junction substitution leads to a capacitance one order of magnitude lower; active pixels ensure the decoupling of the photodiode capacitance from the line capacitance and enable the cancellation of fixed-pattern noise and kTC noise; and a properly designed shunted amplifier reduces the amplitude of the noise spectral density over the bandwidth of interest. These measures also improve the sensor intrinsic frequency.

18.6 Conclusions

CMOS-based wavefront sensors are growing mature and can be beneficial for a number of applications in industry and medicine, e.g., laser diagnostics, direct optical data links and ophthalmology. Off-the-shelf CMOS cameras can substitute the long-used CCD cameras for Hartmann–Shack sensors. However, the choice of an appropriate CMOS camera can be tricky; often, an improved speed performance results in lower resolution and/or sensitivity. The most important advantages of CMOS technology are its hospitality to custom designs and the possibility of implementation of reliable digital and analog circuits as well as photosensitive elements on a single chip. Therefore, the use of CMOS favors the development of custom wavefront sensors with embedded functionality.

The custom CMOS wavefront sensors developed so far are based on integrated matrices of position-sensitive detectors. This approach renders a faster readout of the spot centroids and circumvents the need for an image-processing step. The sensors independently developed in Delft (The Netherlands) and in Heidelberg (Germany) have also shown that CMOS-based solutions can offer both a good resolution and a good light sensitivity. We now try to combine these two characteristics on a single chip. In this paper we also presented some feasible approaches for further improvement of both sensors.

Acknowledgements

D.W. de Lima Monteiro is thankful to Dr. Gleb Vdovin, to the Dutch Technical Foundation (STW.DOE.5375) and to DIMES; T. Nirmaier would like to thank Dr. Dirk Droste and Prof. Josef Bille.

References

1. D. Droste, J. Bille: An ASIC for Hartmann–Shack wavefront detection. *IEEE J. Sol. State Circ.* **37**, 173 (2002)

2. T. Nirmaier, G. Pudasaini, J. Bille: Very fast wavefront measurements at the human eye with a custom CMOS-based Hartmann–Shack sensor. *Opt. Expr.* **11**, 2704 (2003)
3. D.W. de Lima Monteiro: CMOS-Based Integrated Wavefront Sensor (University Press, Delft 2002)
4. D.W. de Lima Monteiro, G. Vdovin: High-speed wavefront sensor compatible with CMOS technology. *Sensors Act. A* **109**, 220 (2004)
5. G. Meynants, B. Dierickx, D. Scheffer: CMOS active pixel image sensor with CCD performance. *Proc. SPIE* **410**, 68 (1998)
6. A. Krymski, N. Khaliullin, H. Rhodes: A $2e^-$ noise 1.3 megapixel CMOS sensor. *Proc. IEEE Workshop on CCDs and AISs*, Elmau, 2003, pp. 1–6
7. M. Wang, S. Saleem, N.F. Thornhill: Time series reconstruction from quantized measurements. *CPC6 Conference, Tucson, Symposium Series* **326**, 98 (2001) p. 448–452
8. J. Schemmel, F. Schürmann, S. Hohmann, K. Meier: An integrated mixed-mode neural network architecture for megasynapse ANNs. *World Congress of Computational Intelligence (WCCI2002)*, (2002)

19 Generalised Phase Diversity Wavefront Sensor

A.H. Greenaway¹, H.I. Campbell¹, and S. Restaino²

¹ Heriot-Watt University, Department of Physics, Riccarton
Edinburgh, EH14 4AS, UK

² Naval Research Laboratory, Remote Sensing Division, Code 721
Kirtland Airforce Base, Albuquerque, NM, USA

Summary. Phase-Diversity is an algorithm for reconstruction of wavefront phase from data corresponding to images of the input wavefront intensity on two planes normal to the direction of propagation and located at different positions along the axis of propagation. These planes are generally described as symmetrically placed about the image plane, but can equally well be symmetrically placed about the system input pupil. In this case the phase diversity algorithm becomes essentially the same as the wavefront curvature algorithm. For reconstruction of the wavefront phase the inverse problem is presented in terms of the differential Intensity Transport Equation and solved either iteratively or through use of Green's functions. Here we will explore what other aberrations, other than defocus, can be used in a generalised phase diversity wavefront reconstruction. The possible advantages of this approach will be considered.

19.1 Introduction

For control of an adaptive optical system it is not strictly necessary, and may even be detrimental, to reconstruct the input wavefront. A sufficient condition for satisfactory operation of an adaptive optical system is the ability to drive a wavefront modulator using a null sensor, where a control signal derived from a wavefront sensor system indicates the size, location and (preferably) the direction of the wavefront error. Thus, if the wavefront modulator is providing full correction of the input wavefront error, the control signal will be zero and the wavefront modulator will not be driven from its present position.

Phase-diversity [1] has historically been seen as an algorithm for reconstruction of wavefront phase from data corresponding to images of the input wavefront intensity on two planes normal to the direction of propagation and located at different positions along the axis of propagation. The approach taken is generally close to the “two-defocus” method used in microscopy [2] and operates with two close-to-focus images [3]. Although the data planes are generally described as symmetrically placed about the image plane, they can equally well be symmetrically placed about the system input pupil [4], in which case the phase diversity algorithm becomes essentially the same as the wavefront curvature algorithm [5].

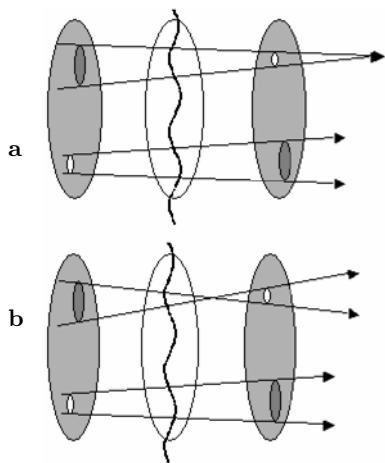


Fig. 19.1. Schematic showing the connection between the wavefront shape and intensity. (a) A concave wavefront propagating from left to right leads to a local increase of intensity. A convex wavefront leads to a decrease in the local intensity. In each case here the intensities recorded in the $+1$ diffraction orders represent the intensities on the ends of the cylinder. (b) Ambiguity can arise if the curvature is so severe that a focus point occurs within the volume sampled by the measurements. The upper part of each figure leads to the same intensity increase

For measurements on planes symmetrically spaced either side of either the image or the pupil planes, the intensity on the two measurement planes will be identical, and the difference between the images will be zero, if, and only if, the wavefront in the entrance pupil plane is a plane wavefront. The measurement of the difference between the intensity on the two data planes (the phase-diverse data) thus satisfies the requirements for a null sensor. If the input wavefront is distorted, the propagation between the measurement planes results in convergence (concave wavefront) or divergence (convex wavefront) and the resulting intensity difference between the measurement planes is indicative of the location, magnitude and direction of the wavefront curvature.

The data on the two image planes can be recorded in a variety of ways. One of the most convenient methods is the use of off-axis Fresnel lenses [6]. For reconstruction of the wavefront phase the inverse problem may be solved iteratively [7, 8] or presented in terms of the differential Intensity Transport Equation (ITE) and solved through the use of Green's functions [9] with the phase-diverse data providing an estimate of the axial derivative of the intensity. Assumptions imposed through use of the ITE involve uniformity of the input intensity in the entrance pupil, continuity in the wavefront phase and continuity of the first derivative of the wavefront phase [10].

At the expense of assumptions imposed on the uniformity of the input illumination, the current work on phase-diversity has progressed a long way

from the early electron microscope applications of the two-defocus technique and ITE-based approaches have demonstrated real-time data reduction with high (sub-nanometre) accuracy [11]. However, in all cases the two data sets are recorded under conditions where the wavefront is subject to a known defocus aberration between the two measurements. Some obvious questions that arise from this are:

- What, if anything, is unique about the defocus aberration used?
- Can equally satisfactory, or better, results be obtained using other aberration functions? If so, what generic properties should suitable aberration functions possess?
- Are the restrictions on the uniformity of the input wavefront necessary?
- Are there optimum aberration functions and does optimisation depend on *a priori* knowledge about the nature of the input wavefronts?
- Do the optimum aberration functions depend upon whether the intention is a null sensor for use in adaptive optics or a wavefront sensor for use in metrology or other applications?

In this paper we will begin to explore these general questions, which amount to a generalisation of the phase diversity approach, and show what properties the aberration function used should have in order to provide a null sensor. We will show that these functions are capable of encoding the sense and location of wavefront errors on heavily scintillated and discontinuous input wavefronts. Thus we will quantify the necessary and sufficient conditions required of aberration functions suitable for use in a generalised phase-diversity null wavefront sensor for adaptive optics applications. We will address here neither the question of optimisation of the aberration function nor the numerical reconstruction of the wavefront from the generalised phase-diverse data.

19.2 Analysis

19.2.1 Definitions

Let $\Psi(r) = |\Psi(r)|e^{i\varphi(r)}$ represent the complex amplitude distribution in the entrance pupil of an optical system, r being the co-ordinate in the pupil plane. If $\Psi(r)$ represents a plane wavefront, the phase satisfies $\varphi(r) = \text{constant}$. Any spatial variation in the wavefront phase represents a distortion, or aberration, that requires correction in an AO system.

To operate successfully as a null wavefront sensor in an AO system we require a device that produces an error signal if, and only if, $\varphi(r)$ is not constant. It is desirable that the error signal provides information that localises the wavefront error in r -space and indicates the sense in which correction should be effected (in the absence of such indication a multi-dither technique [12] is required to effect correction).

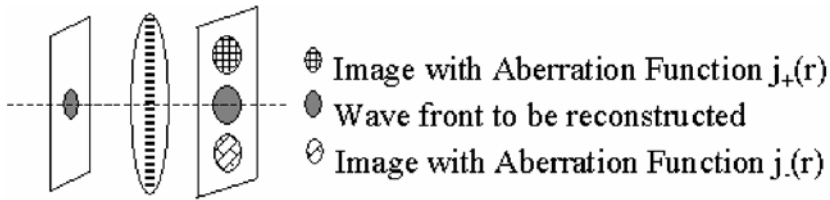


Fig. 19.2. Schematic showing the relationship between the wavefront to be reconstructed and the Aberration Function

Let $\Psi(\xi) = H(\xi) + A(\xi)$ be the Fourier transform of $\Psi(r)$, where $H(\xi)$ and $A(\xi)$ represent respectively the Fourier transforms of the real and imaginary parts of $\Psi(\xi)$. Clearly, $H(\xi)$ is Hermitian and $A(\xi)$ is anti-Hermitian. These symmetry properties will be required later. Thus,

$$H(\xi) = H^*(-\xi), \quad A(\xi) = -A^*(-\xi). \tag{19.1}$$

Let $F_{\pm} = R(\xi) \pm iI(\xi)$ be the Fourier transform of a filter function $f_{\pm}(r)$, which represents a complex function with which $\Psi(r)$ is convolved when forming an image of the system entrance pupil. The functions $R(\xi)$ and $I(\xi)$ are real-valued functions and the \pm indicates the use of two filter functions, in which the Fourier phase of the filter is reversed. In this work we are particularly interested in the necessary and sufficient conditions that constrain $R(\xi)$ and $I(\xi)$ in such a way that $f_{\pm}(r)$ are suitable filter functions to provide a null wavefront sensor for use in adaptive optics. The detected intensity function may thus be written

$$j_{\pm}(r) = \left| \int d\xi \Psi(\xi) F_{\pm} \xi e^{-i\xi r} \right|^2. \tag{19.2}$$

The physical relationship between these different functions is indicated schematically in Fig. 19.2.

19.2.2 The Difference Function $d(r)$

Substituting for F_{\pm} in (19.2), expanding and simplifying, the difference between the images formed using the two filter functions may be expressed

$$\begin{aligned} d(r) &= j_+(r) - j_-(r) \\ &= 2i \left[\int d\xi \Psi(\xi) I(\xi) e^{-ir\xi} \int d\xi' \Psi^*(\xi') R(\xi') e^{ir\xi'} \right. \\ &\quad \left. - \int d\xi \Psi(\xi) R(\xi) e^{-ir\xi} \int d\xi' \Psi^*(\xi') I(\xi') e^{-ir\xi'} \right]. \end{aligned} \tag{19.3}$$

This is a real-valued function, since the quantity in [] is a difference of two complex conjugates and is thus imaginary-valued, so

$$\begin{aligned} \frac{d(r)}{2i} &= \int d\xi [H(\xi) + A(\xi)] I(\xi) e^{-ir\xi} \int d\xi' [H^*(\xi') + A^*(\xi')] R(\xi') e^{ir\xi'} \\ &\quad - \int d\xi [H(\xi) + A(\xi)] R(\xi) e^{-ir\xi} \int d\xi' [H^*(\xi') + A^*(\xi')] I(\xi') e^{ir\xi'} . \end{aligned} \quad (19.4)$$

The *rhs* of (19.4) can then be expanded and the terms grouped into 4 separate expressions, which are equal to the *rhs* of (19.4) when summed:

$$\begin{aligned} &\int d\xi H(\xi) I(\xi) e^{-ir\xi} \int d\xi' H^*(\xi') R(\xi') e^{ir\xi'} \\ &- \int d\xi H(\xi) R(\xi) e^{-ir\xi} \int d\xi' H^*(\xi') I(\xi') e^{ir\xi'} \end{aligned} \quad (19.5)$$

$$\begin{aligned} &\int d\xi H(\xi) I(\xi) e^{-ir\xi} \int d\xi' A^*(\xi') R(\xi') e^{ir\xi'} \\ &- \int d\xi A(\xi) R(\xi) e^{-ir\xi} \int d\xi' H^*(\xi') I(\xi') e^{ir\xi'} \end{aligned} \quad (19.6)$$

$$\begin{aligned} &\int d\xi A(\xi) I(\xi) e^{-ir\xi} \int d\xi' H^*(\xi') R(\xi') e^{ir\xi'} \\ &- \int d\xi H(\xi) R(\xi) e^{-ir\xi} \int d\xi' A^*(\xi') I(\xi') e^{ir\xi'} \end{aligned} \quad (19.7)$$

$$\begin{aligned} &\int d\xi A(\xi) I(\xi) e^{-ir\xi} \int d\xi' A^*(\xi') R(\xi') e^{ir\xi'} \\ &- \int d\xi A(\xi) R(\xi) e^{-ir\xi} \int d\xi' A^*(\xi') I(\xi') e^{ir\xi'} . \end{aligned} \quad (19.8)$$

This expression for the difference between the two detected intensity functions is generally valid – no restricting assumptions have so far been made. We may now investigate under what conditions of symmetry these expressions individually, or summed, are identically zero.

19.2.3 Conditions for Operation as a Null Sensor

For filter functions with complex values we need to consider the odd or even symmetry of both the real and imaginary parts of the filter function.

Filter Function Must Be Complex

Unless both R and I are non-zero, all of the terms in (19.5–19.8) are identically zero $\forall \psi$. Thus $d(r)$ is identically zero for all input wavefronts and no error signal is generated from a non-flat wavefront.

This may be readily understood since, if the filter function is purely real, the filter function F_{\pm} is identical whatever the arithmetic sign, so the two images are identical. If the filter is purely imaginary, the change of arithmetic sign is lost by the modulus square operation that is an inevitable part of quadrature detection processes – and thus the two images are again identical.

Complex Filter Function: Even Symmetry

Suppose that both $I(\xi)$ and $R(\xi)$ are even functions of ξ . Consider the first expression (19.5). Since $H(\xi)$ is Hermitian and $I(\xi)$ is symmetric and real-valued, the product $H(\xi)I(\xi)$ is Hermitian. Thus the Fourier integral $\int d\xi H(\xi)I(\xi)e^{-ir\xi}$ is real-valued. The same is true of $\int d\xi' H^*(\xi')R(\xi')e^{ir\xi'}$. The second product of two integrals is term by term the complex conjugate of the first product. Thus expression (19.5), the difference between two complex conjugates, is always zero when both $I(\xi)$ and $R(\xi)$ are symmetric. Similarly (19.8) is always zero because each of the integrals reduces to a purely imaginary function. The product of these imaginary functions is real and the difference between the two complex conjugate terms is again always zero.

Thus the difference between the two images is the sum of (19.6) and (19.7) and can be written.

$$\begin{aligned} \frac{d(r)}{2i} = & \int d\xi H(\xi)I(\xi)e^{-ir\xi} \int d\xi' A^*(\xi')R(\xi')e^{ir\xi'} \\ & - \int d\xi A(\xi)R(\xi)e^{-ir\xi} \int d\xi' H^*(\xi')I(\xi')e^{ir\xi'} \\ & + \int d\xi A(\xi)I(\xi)e^{-ir\xi} \int d\xi' H^*(\xi')R(\xi')e^{ir\xi'} \\ & - \int d\xi H(\xi)R(\xi)e^{-ir\xi} \int d\xi' A^*(\xi')I(\xi')e^{ir\xi'}. \end{aligned} \quad (19.9)$$

In (19.9), for each pair of integrals one integral reduces to a real-valued function and the other integral to an imaginary-valued function. The first and fourth terms, also the second and third terms, are complex conjugate pairs and thus the rhs of (19.9) is imaginary valued or zero.

If either H or A is zero, or if $A = He^{i\varphi}$ with φ constant, (19.9) and thus $d(r)$, is zero. However, these conditions are exactly those under which the input wavefront is flat and a null sensor is required to produce a null output. Thus, if the filter function is complex with even symmetry, the difference between the two images formed using these filters forms a potentially useful null wavefront sensor. Note that the defocus filter may be expressed as $F_{\pm}(\xi) = \exp(\pm i\Delta\xi^2)$, a function with symmetric but non-scaled real and imaginary parts and one that thus fits the description given in this section.

Complex Filter Function: Odd Symmetry

Suppose that both $I(\xi)$ and $R(\xi)$ are odd functions of ξ . In (19.5) and in (19.8) the odd symmetry of the real functions R and I means that the products within the integrals in (19.5) have anti-Hermitian symmetry and those within (19.8) have Hermitian symmetry. Thus, although the arguments given are reversed for each term from those given in Sect. 19.2.3 (“Filter Function

Must Be Complex”’), both (19.5) and (19.8) are identically zero $\forall \Psi$. Thus $d(r)$ again reduces to (19.9). The arguments from Sect. 19.2.3 (“Complex Filter Function: Even Symmetry”) again hold, although the role of the terms is reversed, one term in each integral product is purely real and the other term purely imaginary. Thus a filter function with complex odd symmetry is potentially suitable for use as a filter function for wavefront sensing.

Complex Filter Function: Mixed Symmetry

Suppose that one of $I(\xi)$ and $R(\xi)$ is an even function of ξ and the other is an odd functions of ξ . In (19.5) the mixed symmetry will result in one integral in each product being purely imaginary and the other integral purely real (dependent on whether R or I is odd). In either case the product of the integrals is purely imaginary and (19.5) is imaginary or zero. An equivalent argument shows that (19.8) is imaginary or zero.

In (19.6) and (19.7) the mixed symmetry results in both integrals in each product being either purely real-valued or purely imaginary-valued. In either case each product reduces to a real-valued function and since the two integral products in each equation are complex conjugate pairs the equations (19.6) and (19.7) are zero $\forall \psi$. Thus the difference function between the two images can be expressed:

$$\begin{aligned} \frac{d(r)}{2i} = & \int d\xi H(\xi)I(\xi)e^{-ir\xi} \int d\xi' H^*(\xi')R(\xi')e^{ir\xi'} \\ & - \int d\xi H(\xi)R(\xi)e^{-ir\xi} \int d\xi' H^*(\xi')I(\xi')e^{ir\xi'} \\ & + \int d\xi A(\xi)I(\xi)e^{-ir\xi} \int d\xi' A^*(\xi')R(\xi')e^{ir\xi'} \\ & - \int d\xi A(\xi)R(\xi)e^{-ir\xi} \int d\xi' A^*(\xi')I(\xi')e^{ir\xi'}. \end{aligned} \quad (19.10)$$

Note, however, that expressions (19.5) and (19.8) are reliant on the interactions between H and the filter function, or on A and the filter function, and do not involve cross terms between H and A .

In (19.10) the mixture of odd and even symmetry will mean that in each integral product one integral will reduce to a purely real-valued function and the other integral to a purely imaginary-valued function. Thus each integral product will be purely imaginary valued. Since equations (19.5) and (19.6) are the difference of complex conjugates, (19.10) is imaginary valued or zero. For the result to be zero $\forall r$ at least one integral in each product must be zero. This is not possible with non-trivial inputs, since all terms are entire functions of exponential type. Thus such filters are liable to produce an error signal for any non-trivial input wavefront. Thus, filters with mixed symmetry produce are unsuitable for use as a wavefront sensor.

19.2.4 Sensing the Error Direction

We have established that the crucial term that encodes information about the wavefront aberrations is the sum of the cross terms in (19.9).

If the sense of the wavefront error is reversed, the arithmetic sign of $A(\xi)$ reverses because the phase of the wavefront will change arithmetic sign. This means that, for a wavefront error of given amplitude, the error signal [(19.9) for filter functions with complex even or complex odd symmetry] changes sign if the sense of the error is reversed. The wavefront sensor thus delivers an error signal that preserves information about the sense of the wavefront error. Note that, since the relationship between the error signal and the wavefront error is non-linear and periodic with wavelength (involving the balance between H and A in the description of the wavefront), this does not guarantee that the error signal can be inverted to find the wavefront shape. The analysis given does not guarantee that the arithmetic sign (nor indeed the magnitude) of the error can be deduced from the sign (or magnitude) of the error signal.

19.2.5 Localising the Wavefront Error

Returning to (19.9) we note that each of the integrals, when expressed as a function of r , appears in the form of a convolution of the Fourier transform of H or A with a Hermitian function related to the filter function. Without loss of generality, the location of the wavefront error can be identified with the position at which $a(r)$, the Fourier transform of $A(\xi)$, is non-zero ($a(r)$ is directly related to the phase distortion). The function with which the convolution takes place may or may not have a maximum at the origin. When it does not, the location of the non-zero component is, in some sense, localised at the point where $a(r)$ is non-zero, in the sense that it may be distributed around the position at which $a(r)$ is non-zero. When the intensities are recorded in pupil space this provides the localization required for a null wavefront sensor.

19.3 Implementation

Figure 19.3 is a suggestion for a Compact Adaptive Optics System (CAOS) based on Generalised Phase Diversity (GPD). This system uses Spatial Light Modulators (SLM's) to provide the wavefront modulation. SLM's offer one of the most attractive solutions for low-cost, low-voltage and low-volume modulators. Diversity is applied to the input wavefront in the grating and lens combination. The grating will contain the carefully selected filter (aberration) function that satisfies the necessary and sufficient conditions for a null wavefront sensor. The grating allows the source image (in the 0th order) and the phase diverse data (in the ± 1 orders) to be displayed on the same focal plane, which is where we would place a CMOS camera. The images in the

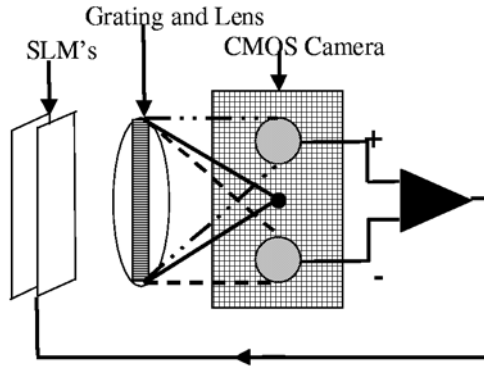


Fig. 19.3. Suggestion for a CAOS set-up

diffraction orders would then be subtracted to deduce the error signal and this information would be fed back to the modulators to adjust the correction of the incoming wavefront.

19.4 Conclusions

Necessary and sufficient conditions for aberration functions suitable for use in a generalised phase diversity null wavefront sensor have been developed. These show that a pair of aberration functions in which the aberrations are applied as a complex conjugate pair will satisfy the requirements for null wavefront sensing provided that the following conditions are met. First, that the aberration functions have complex Fourier transforms (both real and imaginary parts of the Fourier transform of the aberration point spread must be complex). Secondly, that the real and imaginary parts of the Fourier transform of the aberration function must both have even symmetry or both have odd symmetry (mixed symmetries are not allowed).

For filter functions constructed as described above, the deviation of an input wavefront from a plane wave will produce an error signal that is non-zero for nonflat wavefronts and zero for flat input wavefronts. The analysis also demonstrates that a change in the direction of deviation from a plane wave on the input wavefront will change the arithmetic sign of the error signal (showing that the sensor indicates the sense of the wavefront error). Further, the error signal is, in a mathematical sense, localised to the position of the error on the wavefront.

Acknowledgements

Much of the work contained in this paper was funded by the US Airforce Office of Scientific Research through the European Office of Aerospace Research and Development (EOARD) based in London. This work is part of a

larger collaborative programme, OMAM (Optical Manipulation And Metrology, based at Heriot-Watt University), funded by PPARC and dstl. We would also like to thank Dr. Sijiong Zhang for the simulations he has conducted to test the theory presented here.

References

1. R.A. Gonsalves: Phase retrieval and diversity in adaptive optics. *Opt. Eng.* **21**, 829 (1982)
2. D.L. Misell: An examination of an iterative method for the solution of the phase problem in optics and electron optics: I. Test calculations. *J. Phys. D: Appl. Phys.* **6**, 2200 (1973)
3. E. Barone-Nugent, A. Barty, K. Nugent: Quantitative phase-amplitude microscopy I. Optical microscopy. *J. Microscopy* **206**, 194 (2002)
4. P.M. Blanchard et al.: Phase-diversity wavefront sensing with a distorted diffraction grating. *Appl. Opt.* **39**, 6649 (2000)
5. F. Roddier: Curvature sensing and compensation: a new concept in adaptive optics. *Appl. Opt.* **27**, 1223 (1988)
6. P.M. Blanchard, A.H. Greenaway: Simultaneous multiplane imaging with a distorted diffraction grating. *Appl. Opt.* **38**, 6692 (1999)
7. F. Roddier, C. Roddier: Wavefront reconstruction using iterative fourier transforms. *Appl. Opt.* **30**, 1325 (1991)
8. N. Baba, H. Tomita, M. Noriaki: Iterative reconstruction method in phase diversity imaging. *Appl. Opt.* **33**, 4428 (1994)
9. M.R. Teague: Deterministic phase retrieval: a Green's function solution. *J. Opt. Soc. Am. A* **73**, 1434 (1983)
10. S.C. Woods, A.H. Greenaway: Wavefront sensing by use of a Green's function solution to the intensity transport equation. *J. Opt. Soc. Am. A Opt. Image Sci.* **20**, 508 (2003)
11. S. Djidel, A.H. Greenaway: Nanometric wavefront sensing. In: 3rd International Workshop on Adaptive Optics in Industry and Medicine (Starline Printing 2002)
12. F. Youbin, Z. Xuening, Y. Jiexiong: Research on the dynamics of a multidither adaptive optical system. *Opt. Eng.* **37**, 1208 (1998)

20 Generalised Phase Diversity: Initial Tests

S. Zhang, H.I. Campbell, and A.H. Greenaway

Heriot-Watt University, Department of Physics, Riccarton
Edinburgh, EH14 4AS, UK

Summary. Some early results demonstrating the performance of the Generalised Phase Diversity Wavefront Sensor were presented. In these computer simulations we would seek to validate the theoretical analysis that we have previously published and to explore the optimisation of the sensor for various forms of wavefront error. Consideration would be given to the extent to which optimisation that exploits *a priori* information about the wavefront decreases the chance to detect other wavefront characteristics.

20.1 Introduction

A recent paper [1] described the use of a distorted diffraction grating to image simultaneously multiple object planes on a single camera. The grating was distorted according to a quadratic function such that a different focal length could be associated with each diffraction order.

One specific application discussed in [1] was that of wavefront sensing for adaptive optics. Wavefront sensing using this method is, however, not just confined to the quadratic distorted grating. Our theoretical analysis (see the theory paper in this proceedings) for a null wavefront sensor has proved this point. Furthermore, numerical simulations in this paper have shown that other phase diversity filters can give superior performance to the defocus method by using *a priori* information about the wavefront to be sensed. We call this method generalised phase diversity.

In this paper we firstly used numerical experiments to test the theory for generalised phase diversity which was described in our theory paper, then numerically simulated generalised phase diversity wavefront sensing with different phase diversity kernels in addition to the defocused kernel.

The simulation algorithm for wavefront reconstruction used in this paper was the modified Gerchberg–Saxton algorithm [2] which can address both defocus and generalised phase diversity. The numerical simulations are encouraging and give indications that optimisation of the phase diversity wavefront sensor to make maximum use of *a priori* information about distortion is indeed feasible and can give superior performance to the defocus method. In general, the algorithm appeared to converge well if the SNR is better than about 30.

20.2 Description of AO System and Simulation Algorithm

20.2.1 Description of Compact AO System

Simulations relate to a compact adaptive optical system (CAOS) based on transparent wavefront modulators (e.g. liquid crystal SLMs) and phase diversity wavefront sensing, see theory paper Fig. 3. The rationale for CAOS is that a compact Adaptive Optical (AO) system, based on the use of DOEs, phase diverse wavefront sensing and transparent wavefront modulators, offers the potential for construction of AO systems with benefits such as

1. Minimisation of non common-path errors by combining the wavefront sensor data and the corrected image in a single focal plane with essentially no separation of the ‘science’ and wavefront sensing optical trains.
2. The ability of placing wavefront modulators conjugated to multiple planes in the object space whilst preserving a compact and robust optical train that would be particularly well-suited to multi-conjugate AO (MCAO).
3. Avoidance of the requirement for conventional optics, such as beam splitters and conventional bulk optical components for re-imaging conjugate planes, that increases the size and weight of the equipment.

In Compact AO System (CAOS), a DOE (with the appropriate filter function) is used to produce the phase diverse data and the image of the source onto a CMOS camera. We suggest the use of SLM’s (such as liquid crystals) for easily controlled modulation of the wavefront. In this design we have, as far as possible, made the propagation common path as we believe that this is the easiest way to build a compact system.

An imaging system is constructed with a diffractive optical element (DOE) positioned in the plane of the imaging lens. The DOE generates various diffraction orders $0, \pm 1, \pm 2, \dots$. By adjusting the phase amplitude, the DOE can be engineered to ensure that most of the radiation is concentrated into the orders $0, +1$ and -1 , thus higher diffraction orders will be ignored. Under some circumstances the target field may represent an image plane, in which case the zero diffraction order contains the AO-corrected image of the scene.

20.2.2 Necessary and Sufficient Conditions for a Null Wavefront Sensor

The necessary and sufficient conditions for a null wavefront sensor was described in detail in the theory paper. For completeness, we briefly mention here:

Sufficient Conditions

The difference between two aberrated diversity images (± 1 diffraction images) is null if the input wavefront is plane wave and non-null for non-plane wavefronts.

Necessary Conditions

The filter function must be complex. Mixed symmetries of the filter function must not be used.

20.2.3 Error Reduction Algorithm for Generalised Phase Diversity

The flowchart of the algorithm is shown in Fig. 20.1. In the simulations we assume that the amplitude on the pupil plane is unity. This means that scintillation effect is neglected. In later research we will discuss the scintillation

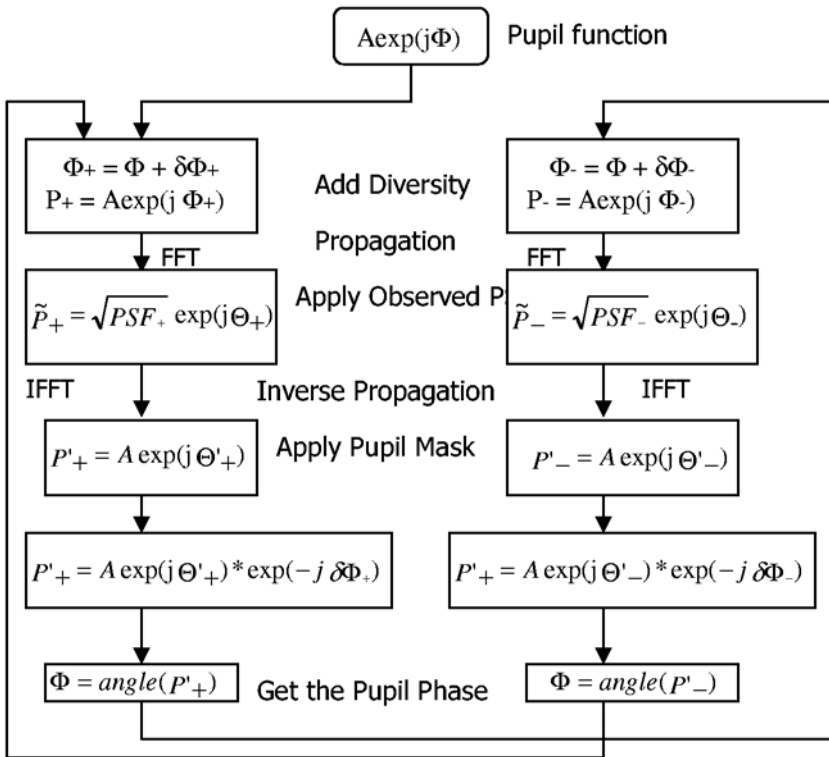


Fig. 20.1. Generalised phase diversity iterative-transform phase retrieval algorithm

effect. The phasor with unity amplitude, from which the wrapped phase is determined, is iteratively estimated as shown in Fig 20.1.

First we set an initial estimate of pupil plane phase Φ , which is taken as zero. Then a pupil function $P(x, y)$ is given by the product of the unity amplitude phasor with an aperture function $A(x, y)$, which is unity inside the aperture and zero outside it:

$$p = A \exp(j\Phi). \quad (20.1)$$

For the +1 order the known phase diversity $\delta\Phi_+$ is added to the initial phase estimate. The Fourier transform of the +1 order pupil function produces the complex amplitude distribution at the focal plane (We describe here use of image-plane data, but the analysis is equally valid for pupil-plane data):

$$P_+ = |P_+| \exp(j\Theta_+). \quad (20.2)$$

We replace the absolute amplitude with square root of the observed PSF_+ but keep the phase term of the derived complex amplitude distribution:

$$\tilde{P}_+ = \sqrt{PSF_+} \exp(j\Theta_+). \quad (20.3)$$

The inverse Fourier transform of the modified complex amplitude distribution gives the following expression

$$P'_+ = A \exp(j\Theta'_+), \quad (20.4)$$

which, multiplied by $\exp(-j\delta\Phi_+)$, will give the next estimate of the pupil function. Similar procedures are used for the -1 order phase diversity image.

The root-mean-square error between the observed intensity distribution and the calculated one generally decreases as the iteration proceeds. Here we define the root-mean-square error (RMSE) for intensity distribution as

$$RMSE = \frac{\sqrt{\sum(I_+ - \tilde{I}_+)^2}}{\sum I_+} + \frac{\sqrt{\sum(I_- - \tilde{I}_-)^2}}{\sum I_-}, \quad (20.5)$$

where I_+ and \tilde{I}_+ are the observed and calculated intensities for +1 order image, respectively, and I_- and \tilde{I}_- are the observed and calculated intensities for -1 order image, respectively.

20.3 Numerical Experiments for Validating the Null Wavefront Sensor Theory

Computer simulations have been undertaken with plane and non-plane input wavefronts and a range of phase diversity filter functions having the properties identified in Sect. 20.2.2. All input wavefronts used were smooth functions.

20.3.1 Plane Wave Input

Firstly, we deal with the plane wave input cases. Figure 20.2 shows simulation results with the plane wavefront input and the mixed symmetry phase diversity filter ($Z_2^0 + Z_3^{-3}$, defocus + astigmatism). In Fig. 20.2 the top left is the input wavefront, the top right is +1 order diffraction image intensity, the bottom left is the -1 order diffraction image intensity, and the bottom right is the intensity difference between +1 order and -1 order diffraction images. In Figs. 20.3–20.5, all pictures have the same meaning as Fig. 20.2. From the above results we can see that the intensity difference between +1 order and -1 order diffraction images is not zero for the plane wavefront input. So the mixed symmetry phase diversity filter is not feasible for a null wavefront sensor. This is just the necessary condition for a null wavefront sensor derived from the theory.

Figure 20.3 shows simulation results with the plane wavefront input and the even symmetry phase diversity filter (Z_2^0 , defocus). The simulation results show that the intensity difference between the +1 order and -1 order diffraction images is zero for the plane wavefront input. This is just the sufficient condition for a null wavefront sensor derived from the theory.

20.3.2 Non-plane Wave Input

Secondly, we deal with the non-plane wave input cases. Figure 20.4 shows the simulation result with the non-plane wavefront input and the even symmetry

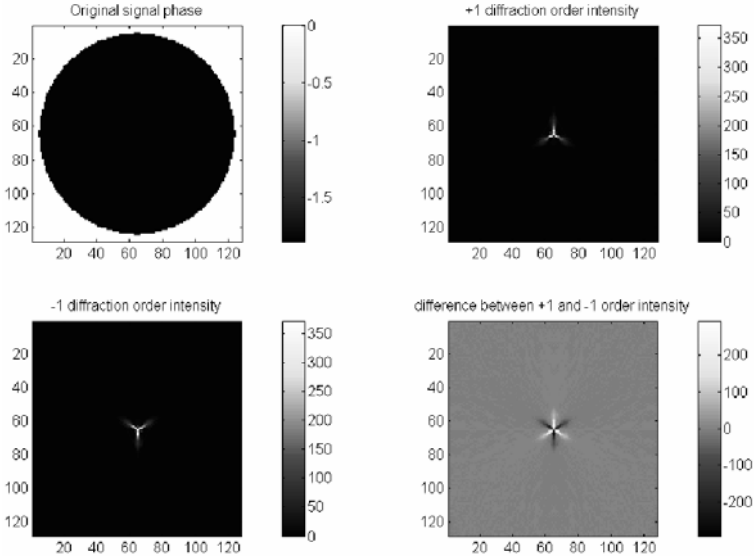


Fig. 20.2. Simulation result with the plane wavefront input and the mixed symmetry phase diversity filter

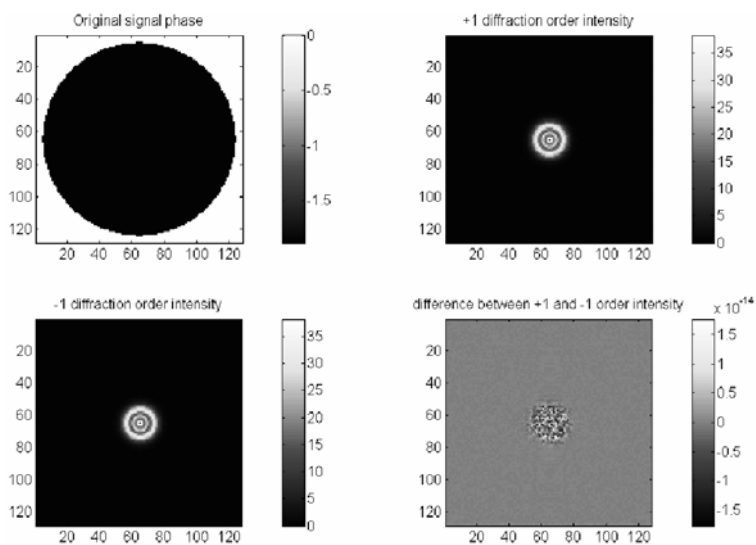


Fig. 20.3. Simulation result with the plane wavefront input and the even symmetry phase diversity filter

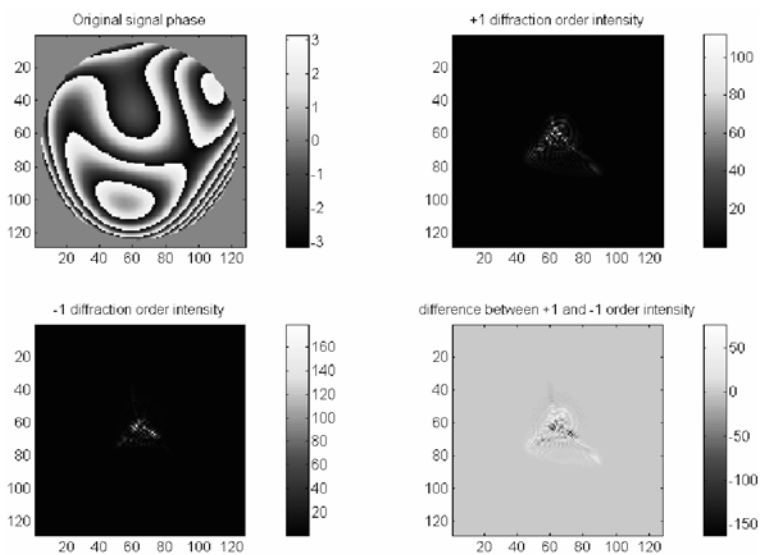


Fig. 20.4. Simulation result with the non-plane wavefront input and the even symmetry phase diversity filter

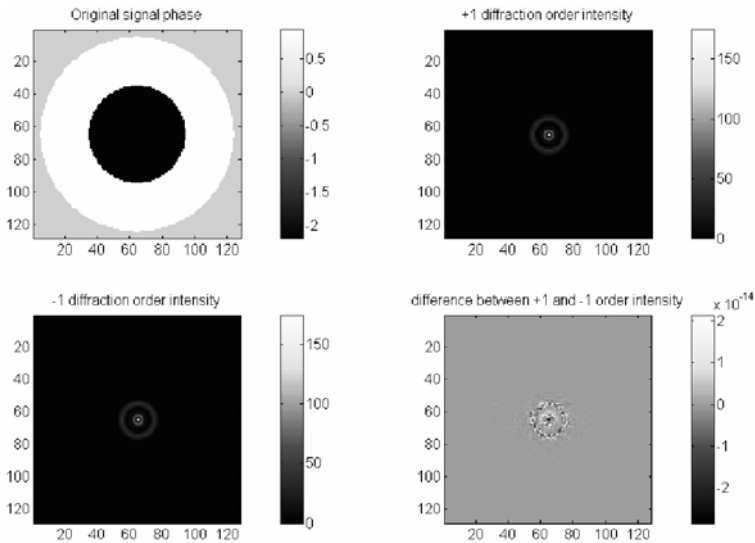


Fig. 20.5. Simulation result with the π step wavefront input and the even symmetry phase diversity filter

phase diversity filter (Z_{10}^0 , Zernike polynomial). From the simulation result we can see that the intensity difference between $+1$ order and -1 order diffraction images is non-zero for the non-plane wavefront input. This is just the sufficient condition for a null wavefront sensor derived from the theory.

Figure 20.5 shows the simulation results with a π step wavefront input and the even symmetry phase diversity filter (Z_2^0 , defocus). The simulation results show that the intensity difference between the $+1$ order and -1 order diffraction images is zero for this particular type of non-plane input wavefront. This is just one of the results derived from the theory. So there is ambiguity for a null wavefront sensor for these particular types of wavefront. This case is unimportant for astronomy but potentially important for metrology applications.

20.4 Simulation Results for Optimisation Using a Priori Information

In general it has been noted that the use of a phase diversity function other than defocus can be used to optimise the wavefront reconstruction where suitable *a priori* information is available. However, it is also noted that a poor choice of diversity function can lead to poor algorithm performance. Thus the choice of a symmetric phase diversity function appears generally beneficial if there is no *a priori* indication that the input wavefront is likely to be asymmetric. Thus, the use of symmetric phase diversity functions, such as defocus

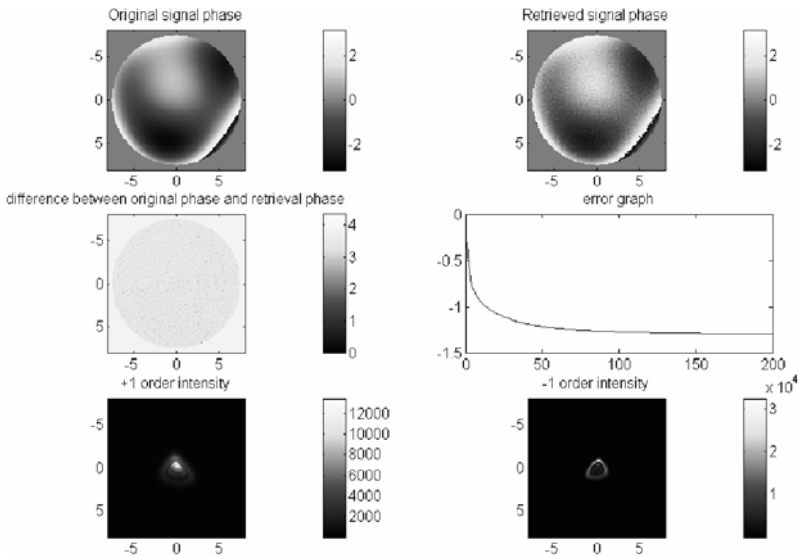


Fig. 20.6. Simulation result with the defocus phase diversity filter

(Z_2^0), spherical aberration (Z_4^0), etc. appear to offer the best choice when designing a wavefront sensor for application to wavefront sensing problems associated with atmospheric transmission. To our surprise the optimal diversity functions appear to be defocus (Z_2^0) and Z_{10}^0 . We can, at present, offer no logical explanation for the apparent superiority of these defocus functions over functions such as spherical aberration. Although the simulation results presented here use phase diversity functions consisting of pure Zernike terms, it should be noted that the combinations of terms having suitable symmetry properties are permissible providing that the appropriate symmetries are preserved.

In all our simulations, we used the signal to noise ratio (SNR) 30. The noise abides by Poisson distribution.

Figure 20.6 shows simulation results with the even symmetry phase diversity filter (Z_2^0 , defocus). In Fig. 20.6 the top left is the signal input wavefront, the top right is the retrieval phase using the error reduction algorithm, the middle left is the phase difference between original and retrieval phases, the middle right is the error graph (logarithm scale), and the bottom left and right are the +1 order and -1 order diffraction intensities, respectively. In Figs. 20.7 and 20.8, all pictures have the same meaning as Fig. 20.6. Figure 20.6 shows that the retrieved phase is pretty good.

Figure 20.7 shows simulation results with the spherical aberration phase diversity filter (Z_4^0). Clearly, the retrieved phase is not good. Figure 20.8 shows the simulation result with the Zernike polynomial Z_{10}^0 phase diversity filter. The retrieved phase is very good.

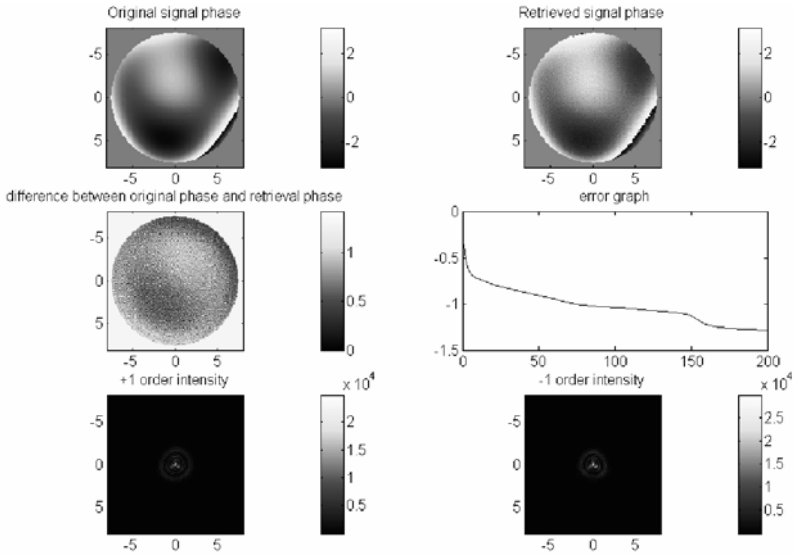


Fig. 20.7. Simulation result with the spherical aberration phase diversity filter

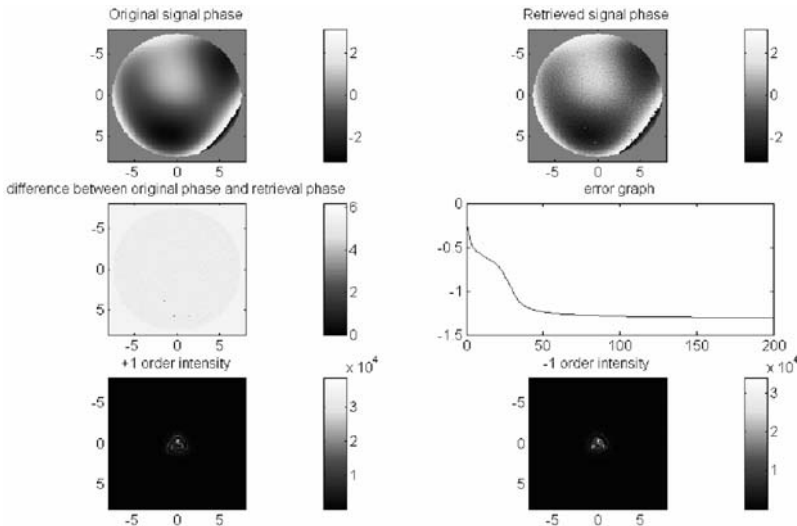


Fig. 20.8. Simulation result with the Z_{10}^0 phase diversity filter

Up to now we have retrieved the signal phase using three different phase diversities for a particular input wavefront. One obvious question is which phase diversity is more suitable to phase retrieval for this particular input signal. To answer this question we need to compare the error graphs for these three different phase diversity cases. Figure 20.9 shows that the error

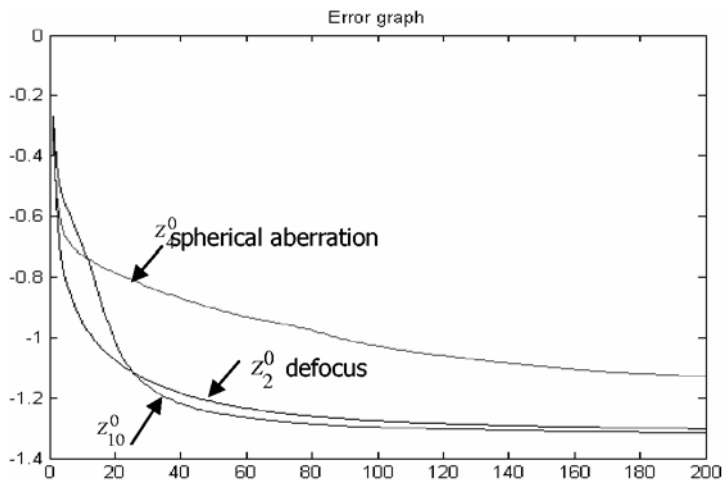


Fig. 20.9. Error graphs for the three cases

function with the phase diversity filter Z_{10}^0 is marginally better than defocus, although initial convergence is slower. However, this does illustrate that different diversity kernels can be used to achieve different results.

20.5 Conclusions

We used numerical experiments to validate the theory for the necessary and sufficient conditions for construction of a null wavefront sensor based on the principles of a generalisation of phase-diversity wavefront sensing. So far we have not found any deviations of numerical experiment results from theoretical results. Further we described generalised error reduction algorithm. Simulation results illustrated that the generalised wavefront sensor can be optimised to exploit *a priori* information in order to maximise the sensitivity of the wavefront sensor.

Acknowledgements

This work is supported by a PPARC Smart Optics Faraday grant.

References

1. P.M. Blanchard, A.H. Greenaway: Simultaneous multiplane imaging with a distorted diffraction grating. *Appl. Opt.* **38**, 6692 (1999)
2. N. Baba, K. Mutoh: Measurement of telescope aberrations through atmospheric turbulence by use of phase diversity. *Appl. Opt.* **40**, 544 (2001)

21 Prime Microlens Arrays for Hartmann–Shack Sensors: An Economical Fabrication Technology

D.W. de Lima Monteiro, O. Akhzar-Mehr, and G. Vdovin

Delft University of Technology, EEMCS, Electronic Instrumentation Laboratory
Mekelweg 4, 2628 CD Delft, The Netherlands

Summary. A Hartmann–Shack wavefront sensor consists basically of two elements: a microlens array and a photosensitive detector. This paper presents a technique to fabricate close-packed microlens arrays compliant to the sensor requirements. The method is based on bulk-silicon anisotropic etching and requires a single etch mask. We first etch a micromirror array in a KOH solution and use it later as a mold for the replication of microlens arrays. The elements in the fabricated microlens arrays feature excellent fit to a parabolic mirror surface, 100% optical fill factor, excellent parallelism of the optical axes and very high precision of the array pitch. The uniformity of the focal length of the microlenses is high (in the order of 5%) and the surface roughness – expressed in terms of wavefront – is of the order of 8–13 nm. This technology also enables simple single-mask fabrication of arbitrary aspherical optical surfaces.

21.1 Introduction

A microlens array in a Hartmann–Shack (H–S) sensor splits the incoming light beam into a number of sub-beams, which focus on an image plane (for instance a CCD or a custom CMOS imager [1–4]). The incoming wavefront can be estimated based on the positions of the light spots, which correspond to local wavefront tilts at the respective microlens apertures.

The number of lenses depends on the application and varies typically from 25–1000; orthogonally or hexagonal geometries are used to yield 100% fill factor; the optical axes and focal lengths should be uniform; the sagittal lies in the micrometer range and the total lateral size and focal length values usually extend from several to tens of millimeters.

Fabrication of these lenslet arrays often require costly and elaborate micro-optical technologies which translates into expensive samples. Although a set of microlens arrays with different geometries enables an H–S sensor to deal optimally with various wavefront magnitudes and spatial frequencies, the cost of such a set can dominate the price of the sensor.

We report on micromirror arrays fabricated in an inexpensive and simple bulk silicon micromachining technology that simply requires one mask and an anisotropic etchant (KOH:H₂O) [5]. We then use the etched structure as a mold for the replication of microlens arrays on polymer.

This technology also provides the means to realize micro-optical components with arbitrary profiles as reported in [6]. In later sections we explain the method and validate its assumptions with experimental results.

21.2 Parameters of the Microlens Array

There are some general issues that should be observed when designing a microlens array for an H-S sensor:

- *Optical Axes.* The parallelism of the optical axes over the array is very important in order to prevent crossing of sub-beams and therefore overlap of neighboring spots on the focal plane. Also, in H-S sensors based on position-sensitive detectors (PSDs) [1–4], this parallelism ensures that spots resulting from a plane wavefront fall in the center of the symmetrically layed PSD elements. In the technology we use, the optical axes are perfectly parallel because they only depend on the crystal orientation of silicon and can at most be affected by dislocations in the crystal lattice.
- *Microlens Position.* A high pitch precision of the designed array grid guarantees that the wavefront is sampled at the desired locations; this directly influences the reliability of the wavefront reconstruction. The accuracy in the position of the microlenses also yields a perfect match with the pixel array of the detector. Moreover, a high position precision enables one, in principle, to use a Hartmann–Shack sensor without a reference wavefront. In the presented technology the positions depend on the precision of the lithographic mask ($\approx 1\ \mu\text{m}$ in our case).
- *Fill Factor.* A close-packed array offers a better light-collection efficiency than a spaced array (or Hartmann mask) and minimizes sampling aliasing. Hexagonal and orthogonal grids are the more sensible options;
- *Number of Microlenses.* The optimal number depends on the application. It varies with the size of the pupil of interest, with the wavelength and with the spatial frequency of the aberrations [7]. Obviously, the higher the aberration order, the larger is the density of sampling apertures required.
- *Lateral Size.* It should preferably match with that of the imaging chip used, typically at most 10 mm.
- *Spot Diameter.* When an imager is used, the spot should be large enough to cover a number of pixels, so that the spot centroid can be calculated accurately. Currently, pixel sizes of off-the-shelf CCDs lie around $10\ \mu\text{m}$, and $50\ \mu\text{m}$ spots are a reasonable choice. An alternative to large spot sizes is to place the detector out of the focal plane, however this causes the centroid position to be dependent both on wavefront tilt and on the intensity profile over the aperture. In the case of custom detectors with position-sensitive elements [1–4], the spot size has to comply with the requirements of each particular detector.
- *Focal Length.* The optimal focal length depends on the magnitude of the wavefront aberrations. Short focal lengths are advisable for strong aber-

rations whereas long focal lengths guarantee higher sensitivity for mild aberrations. The focal lengths typically range from 10–50 mm. In the technology we use, the depth of field reaches several millimeters, which means that the spot size is almost invariable if the focal plane is moved within that range.

- *Grid Pitch.* The pitch should obey a compromise among the number of lenses in the array, the lateral size of the structure and the allowed distance between neighboring spots (to prevent spot overlap). The extent to which the spots move in the vicinity of the reference grid depend on the magnitude of the local wavefront tilts and to the focal length of the microlenses. Pitch values are usually between $200\ \mu\text{m}$ and $1500\ \mu\text{m}$.
- *Sagitta.* It is a consequential parameter that depends on the choices of pitch, grid geometry and focal length. Taking the figures above, the *sag* assumes values in the range between $0.5\ \mu\text{m}$ and $100\ \mu\text{m}$.

21.3 Fabrication Method

The fabrication method builds on the seldom known fact that, starting from a pyramidal pit, we can obtain a nearly spherical depression in the silicon bulk with *anisotropic* KOH (khalium hydroxide) etching [5]. We first etch an inverted pyramid through the opening in the oxide mask, then we strip the mask away and subsequently immerse the sample in the solution, which now favors the etching of the (411) crystallographic planes, whose etch rate is faster than that of the (111) planes. The (411) sidewalls evolve into another inverted pyramid, which successively changes into a rounded cavity as the etching progresses. Figure 21.1 illustrates this process.

The sagitta (s) of the cavity depends directly on the size of the initial opening in the mask (d_0): $s = \alpha d_0$, where α depends on the etch parameters and on the silicon orientation. The diameter of the cavity (D) depends on the total etch depth of the silicon sample (h) and on the size of the initial opening (21.1). The vertical profile of the cavity is only spherical for etch

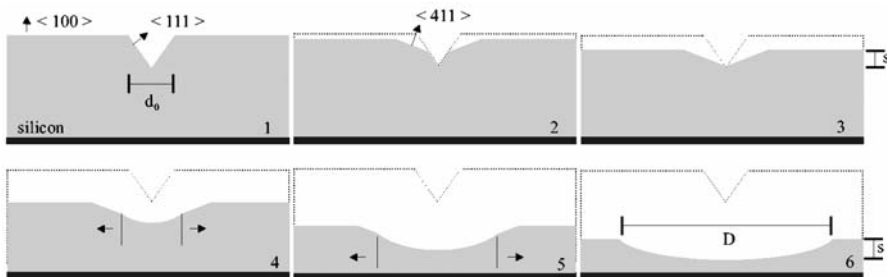


Fig. 21.1. Chart flow of a single-mask etching process to generate spherical depressions

depths larger than $2.5 d_0$.

$$D = 7.8h^{0.58}d_0^{0.42}. \quad (21.1)$$

21.4 Micromirror and Microlens Arrays

The extension from a single micromirror to a contiguous array is straightforward. We only need to design an oxide mask with openings arranged in a regular grid and then follow the process described in the previous section. When etching the sample, at a certain moment the edges of neighboring cavities overlap, resulting in well-defined sharp interfaces and uniform spherical bottoms (Fig. 21.2a).

For arrays with 100% fill factor, the diameter of each micromirror must be around 40% and 15% larger than the pitch for orthogonal and hexagonal grids, respectively.

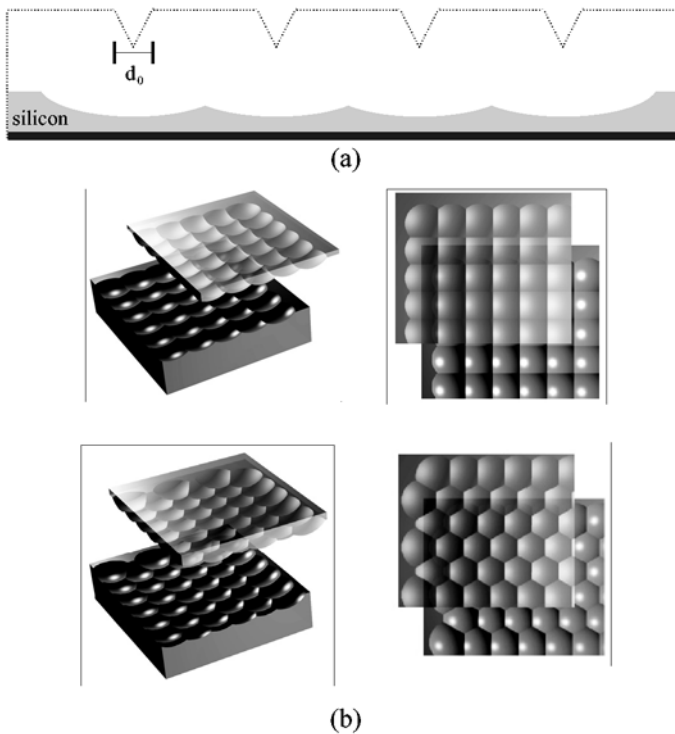


Fig. 21.2. (a) An array of isolated pyramidal pits evolves into a contiguous micromirror array when it is immersed in a KOH solution; (b) corner of microlens arrays replicated from the silicon mold

We fabricate a lenslet array by pressing a viscous polymer against the micromirror mold (Fig. 21.2b). Any wavefront aberration due to roughness present in the silicon template is reduced by a factor $1/(n - 1)$ in the lens profile, where n is the refraction index of the polymer.

The focal length (f) of the array elements is obtained from

$$f = 7.605 \frac{d_0}{\alpha(n - 1)} \left(\frac{h}{d_0} \right)^{1.16}. \quad (21.2)$$

The minimum achievable focal length is limited by the ratio $h/d_0 = 2.5$, which is an intrinsic requirement of this technology, and by the minimum effective mask opening d_0 . The maximum focal length depends on the wafer thickness and on d_0 as well. Focal length values ranging from 0.10–55 mm are achievable for a microlens ($1.4 \leq n \leq 1.6$) imprinted on a micromirror etched with a 33 wt% KOH solution, at 85°C, for a maximum etch depth of 400 μm and with a lithographic definition size of 1 μm . The normalized focal length of microlenses made with three different refraction indices is presented in Fig. 21.3a.

In a close-packed array the f -number ($F_{\#}$) of the elements depends on the normalized pitch (p/d_0) and on the array geometry; in the optimal situation the right-hand- and left-hand-side of (21.3) are equal.

Figure 21.3b shows how the optimal $F_{\#}$ varies with the normalized etch depth for a micromirror and for microlenses with different refraction indices. Here again the ratio h/d_0 determines the minimum $F_{\#}$. Hence, for the case of micromirrors the smallest value is $F_{\#} = 2.5$ and for the case of lenses $F_{\#} \approx 9.5$.

$$F_{\#} \geq \frac{1}{\alpha(n - 1)} \left(\frac{h}{d_0} \right)^{0.58}. \quad (21.3)$$

21.5 Results

We fabricated orthogonal and hexagonal micromirror and microlens arrays with a 100% fill factor by overlapping identical spherical sections laterally, as shown in the SEM pictures in Fig. 21.4. The arrays were etched in a 33 wt% KOH aqueous solution at 85°C. The orthogonal microlens array features 16×16 elements with a 450 μm pitch and $f = 50$ mm. The hexagonal microlens array features 127 elements with a 300 μm pitch and the focal length matches the designed value ($f = 17$ mm) to within 5%.

Figure 21.5 shows the stylo scan of one lens in the middle of the hexagonal array for two different etch depths. At 50 μm the mirrors boundaries do not touch each other and at 175 μm we notice the formation of sharp interfaces between adjoining mirrors, whose deviation from the spherical shape is better than 10 nm. The sagitta remains constant during the process.

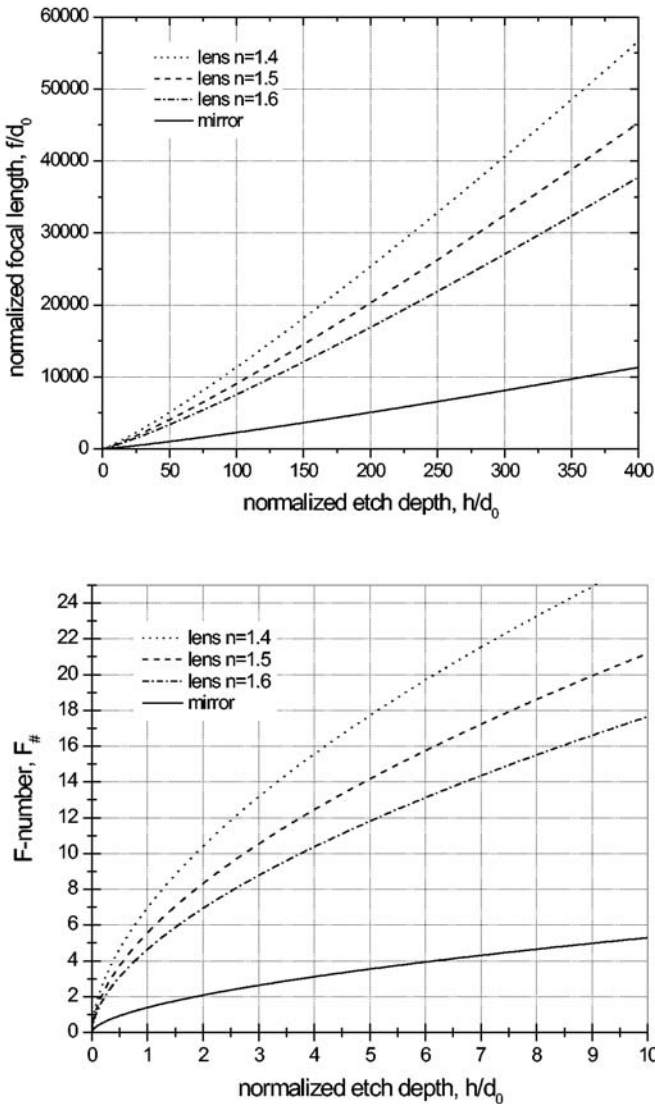


Fig. 21.3. (a) Focal length, normalized to d_0 , of microlenses with different refraction indices versus the normalized etch depth; (b) $F\#$ of the same microlenses as a function of the normalized etch depth

The *rms* surface roughness, at $175\ \mu\text{m}$, varies over the array in the range from 15–25 nm. Microlenses replicated using this template and with $n = 1.5$ introduce roughness-related wavefront deformations ranging from 8–13 nm, which correspond to Strehl ratios larger than 0.98 for $\lambda = 632\ \text{nm}$. We can see in Fig. 21.6 the interferometric pattern of the hexagonal microlens array

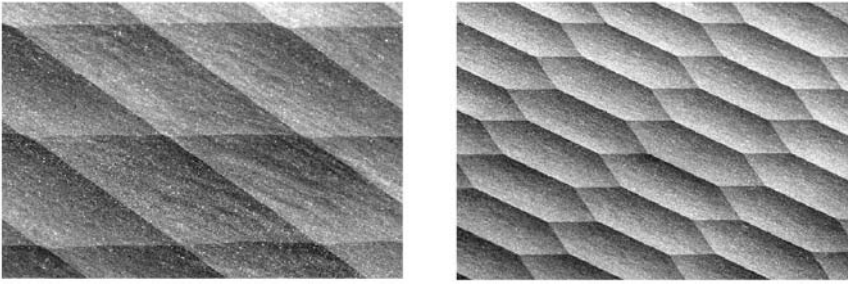


Fig. 21.4. SEM picture of parts of the orthogonal and hexagonal micromirror arrays fabricated with anisotropic etching of silicon. The sagittas are $1.2\ \mu\text{m}$ and $1.65\ \mu\text{m}$, respectively

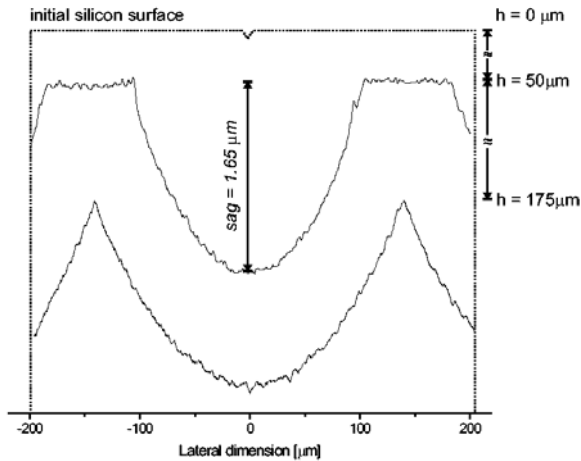


Fig. 21.5. Mechanical scan of a mirror in the middle of the hexagonal array for different etch depths ($h = 50\ \mu\text{m}$ and $175\ \mu\text{m}$) starting with a pyramidal pit with a $5\ \mu\text{m}$ base

and the corresponding focal plane image. The uniformity of the optical axes is high. Figure 21.6 also shows the theoretical and experimental intensity distributions for one of the focal spots, which has a diameter of approximately $85\ \mu\text{m}$.

The micromachining technology presented also allows us to manufacture arbitrary aspherical surfaces with lateral scales in the order of several millimeters and a profile depth in the order of several micrometers. The method consists in approximating a target surface by overlapping spherical depressions, each with specific depths. We demonstrated in [6] 1 and 5 mm aspherical phase plates reproducing defocus, tilt, astigmatism and high-order Zernike polynomials. This technology has a potential for serial production of reflective and refractive arbitrary aspherical micro-optical components.

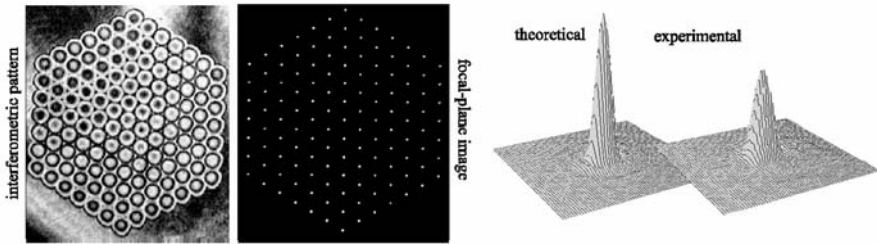


Fig. 21.6. Interferometric pattern of the hexagonal microlens array, the focal-plane image and the intensity distribution of one of the focal spots

21.6 Conclusions

We presented an inexpensive and straightforward method to fabricate prime microlens arrays for use as the sampling plane of Hartmann–Shack wavefront sensors. This technology relies on a subtle aspect of silicon anisotropic etching with a KOH solution, namely the evolution of a pyramidal pit into a spherical cavity when we etch the sample without the protecting oxide mask. We make use of this distinctive phenomenon to achieve 100%-fill-factor micromirror arrays starting from an orthogonal or hexagonal grid of pyramidal pits. Then, these structures serve as molds to imprint microlenses on a polymer layer.

The implemented structures match well the expected quality for use in the visible spectrum with highly spherical lenses featuring high optical-axis parallelism, precise microlens positions and focal lengths within 5% of the designed values. The range of achievable focal lengths goes from 0.10–55 mm (*minimum opening* = 1 μm and *maximum etch depth* = 400 μm), but the range can be extended when we use smaller lithographic feature sizes and/or thicker silicon wafers.

Also, the etching process presented can be used to fabricate arbitrary aspherical phase plates that reproduce Zernike polynomials. In this case, we approximate the surface profile with spherical cavities of different diameters and depths, which overlap laterally.

The flexibility and simplicity of this technology allied to the high quality of the produced structures and the possibility of serial production offer a promising alternative to the costly microlens arrays available today.

References

1. D.W. de Lima Monteiro, G. Vdovin, P.M. Sarro: High-speed wavefront sensor compatible with standard CMOS technology. *Sensors and Actuators A* **109**, 220 (2004)
2. D.W. de Lima Monteiro, G. Vdovin et al.: Integrated Hartmann–Shack wavefront sensor. *Proc. 3rd Adaptive Optics Conference for Industry and Medicine*, Albuquerque, USA (July 2001) p. 179–183

3. D. Droste, J. Bille: An ASIC for Hartmann–Shack wavefront detection. *IEEE J. Solid-State Circ.* **37**, 173 (2002)
4. T. Nirmaier, D. Droste, J. Bille: Hartmann–Shack sensor ASICs for real-time adaptive optics in biomedical physics. *Proc. 6th World multiconference on systemics, cybernetics and informatics*, **13** (2002) p. 280–284
5. D. Kendal et al.: Micromirror arrays using KOH:H₂O micromachining of silicon for lens templates, geodesic lenses, and other applications. *Opt. Eng.* **33**, 3578 (1994)
6. D.W. de Lima Monteiro, O. Akhzar-Mehr, P. Sarro, G. Vdovin: Single-mask microfabrication of aspherical optics using KOH anisotropic etching of Si. *Opt. Express* **11**, 2244 (2003)
7. G. Artzner: Microlens arrays for Shack–Hartmann wavefront sensors. *Opt. Eng.* **31**, 1311 (1992)

22 A Proposal for Wavefront Retrieval from Hartmann Test Data

V.M. Duran-Ramirez¹, D. Malacara-Doblado¹, D. Malacara-Hernandez¹, D.P. Salas-Peimbert², and G. Trujillo-Shiaffino²

¹ Centro de Investigaciones en Optica
Loma del Bosque 115, Leon, Gto, Mexico

² Instituto Tecnológico de Chihuahua
31310 Chihuahua, Chih., Mexico

Summary. In the classical Hartmann test analysis, the transverse aberrations are represented by small straight segments joining two consecutive measured points in the pupil. In the analysis presented in this paper we propose the wavefront to be synthesized by many nonflat functions whose domains are the squares defined by the square unit cell defined by an array of holes in the Hartmann screen placed at the exit pupil of the system. Two advantages of this method are that a higher precision in the wavefront retrieval is obtained and second that the local curvatures and astigmatism with their corresponding axes are obtained.

22.1 Introduction

The Hartmann test [1] is one of the simplest but most powerful tests to determine the wavefront shape of an optical system. It has been used for more than a century with great success. In the Hartmann test the wavefront is calculated from the transverse aberrations and represented by small square plane segments centered at each of the measured points in the pupil. In this paper we propose to synthesize the retrieved wavefront by many nonflat functions whose domains are the squares defined by the square unit cell defined by an array of holes in the Hartmann screen placed at the exit pupil of the system.

In the Hartmann test illustrated in Fig. 22.1, a screen with a rectangular array of holes, as in Fig. 22.2a, is placed near the entrance or exit pupil of the system under test. The square array of holes in the Hartmann screen is frequently defined with one of the holes being at the center of the screen. The wavefront deformations $W(x, y)$ are calculated from measurements of the transverse aberrations TA_x and TA_y . These aberrations and the wavefront deformations are related by the expressions

$$\frac{\partial W(x, y)}{\partial x} = \frac{TA_x(x, y)}{r} = \theta_x(x, y) \quad (22.1)$$

and

$$\frac{\partial W(x, y)}{\partial y} = \frac{TA_y(x, y)}{r} = \theta_y(x, y). \quad (22.2)$$

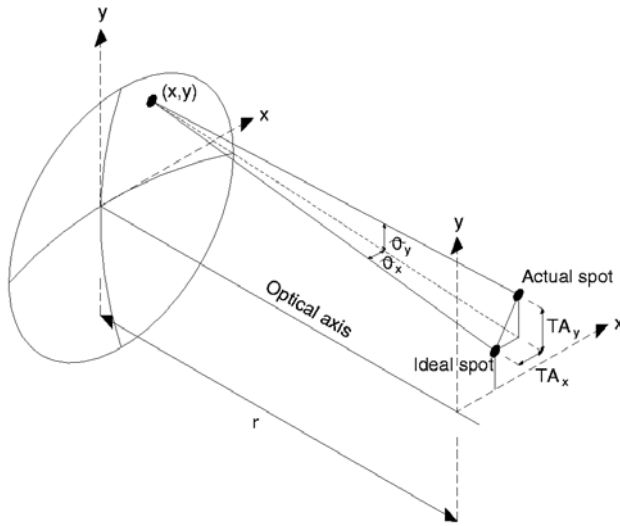


Fig. 22.1. Classical Hartmann test

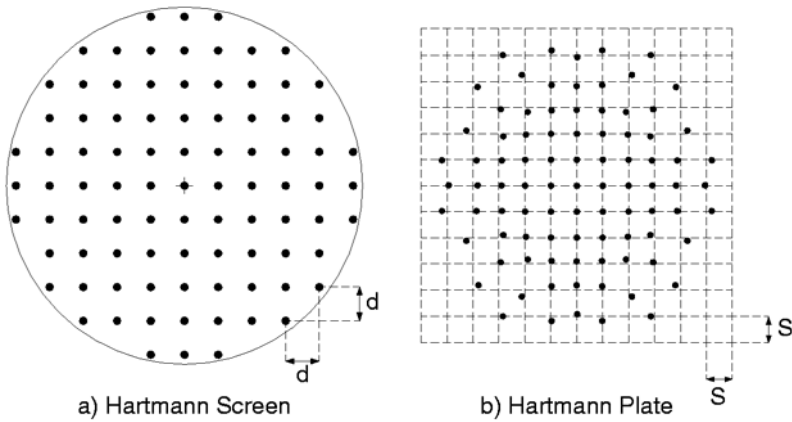


Fig. 22.2. (a) Hartmann screen and (b) Hartmann plate in the classical test

Here, r is the distance from the wavefront at the exit pupil to the Hartmann plate where the spots are recorded. The linear transverse aberrations are TA_x and TA_y and the angular transverse aberrations are $2x$ and $2y$. The wavefront is calculated by integration of the transverse aberrations being measured at the Hartmann plate shown in Fig. 22.2b.

In order to make possible the proper identification of the spots in the Hartmann plate it has to be located at a place displaced from the focus, frequently inside of focus, so that the light beams do not cross each other. This defocussing is specially important if the wavefront is aspherical. In that case the Hartmann plate has to be located outside of the caustic region.

This large defocusing introduces a large linear component in the transverse aberrations, which in turn produces a large spherical (quadratic) component in the calculated wavefront. To greatly reduce the effect of this defocussing the transverse aberrations can be measured not with respect to the optical axis, but with respect to the position that the measured spot would have if the wavefront had an ideal shape, as in a perfect optical system. Then, the calculated wavefront deformations are obtained with respect to a close reference sphere. If the perfect wavefront has a spherical shape, these reference points are the crossing points of a square array of lines with these crossing points near the Hartmann spots, as illustrated by the dotted lines in Fig. 22.2b. This array of reference lines that eliminates most of the defocussing being introduced can be found by calculating the average spot spacing and making it equal to the lines spacing S as follows:

$$S = \frac{1}{2K} \left(\sum_k \frac{\eta_x(n, m)}{n} + \sum_k \frac{\eta_y(n, m)}{n} \right), \quad (22.3)$$

where the first sum of all the K dots is for $n \neq 0$ and the second sum for $m \neq 0$, where η_x and η_y are the transverse aberrations measured from the optical axis and K is the total number of spots in the Hartmann plate. Then, the transverse aberrations TA_x and TA_y for each Hartmann spot n, m as measured from the ideal non-aberrated positions are

$$\begin{aligned} TA_x(n, m) &= \eta_x(n, m) - nS, \\ TA_y(n, m) &= \eta_y(n, m) - nS. \end{aligned} \quad (22.4)$$

22.2 Classical Hartmann Test

Since the measurements are made only at points in a rectangular array, in the classical Hartmann test the wavefront shape is found by an approximated trapezoidal integration of (22.1) and (22.2) writing

$$W(n, m) = \frac{d}{2r} \sum_{i=1}^n [TA_x(i-1, m) + TA_x(i, m)], \quad (22.5)$$

when scanning along the x -axis and

$$W(n, m) = \frac{d}{2r} \sum_{j=1}^m [TA_y(n, j-1) + TA_y(n, j)], \quad (22.6)$$

when scanning along the y -axis. Here, d is the separation between two consecutive holes in the Hartmann screen. Alternatively, expressions (22.5) and (22.6) can be written as

$$W(x_n, y_m) = W(x_{n-1}, y_m) + \frac{d}{2r} [TA_x(x_{n-1}, y_m) + TA_x(x_n, y_m)], \quad (22.7)$$

where $n = 0, \pm 1, \pm 2, \pm 3, \dots, \pm N$ and

$$W(x_n, y_m) = W(x_n, y_{m-1}) + \frac{d}{2r} [TA_y(x_n, y_{m-1}) + TA_y(x_n, y_m)], \quad (22.8)$$

where $m = 0, \pm 1, \pm 2, \pm 3, \dots, \pm M$.

It is possible to show that in this model the wavefront slope (transverse aberration) values along the small segment joining two consecutive holes in the x - and y -directions are given by

$$TA_x(x, y_m) = TA_x(x_{n-1}, y_m) + \left(\frac{TA_x(x_n, y_m) - TA_x(x_{n-1}, y_m)}{d} \right) x \quad (22.9)$$

and similarly, when integrating along the y -direction

$$TA_y(x_n, y) = TA_y(x_n, y_{m-1}) + \left(\frac{TA_y(x_n, y) - TA_y(x_n, y_{m-1})}{d} \right) y. \quad (22.10)$$

Thus, scanning these expressions we obtain

$$W(x, y_m) = W(x_{n-1}, y_m) + \left(\frac{TA_x(x_{n-1}, y_m)}{r} \right) x + \left(\frac{TA_x(x_n, y_m) - TA_x(x_{n-1}, y_m)}{2rd} \right) x^2 \quad (22.11)$$

and

$$\begin{aligned} W(x_n, y) &= W(x_n, y_{m-1}) + \left(\frac{TA_y(x_n, y_{m-1})}{r} \right) y \\ &\quad + \left(\frac{TA_y(x_n, y) - TA_y(x_n, y_{m-1})}{2rd} \right) y^2 \\ &= W(x_n, y_{m-1}) + \left(\frac{TA_y(x_n, y_{m-1})}{r} \right) y + \frac{c}{2} y^2, \end{aligned} \quad (22.12)$$

which are quadratic expressions and thus have a curvature c which is directly proportional to the slope of the linear segments. With these expressions the classical Hartmann test can be improved by calculating the wavefront at many points between the sampling positions for the Hartmann screen. As an example, let us observe the trapezoidal integration of a function $TA(x)$ and its wavefront in Fig. 22.3.

To find the wavefront deformations it is customary to begin the wavefront calculation at the center of the pupil where $n = 0$ and $m = 0$ with $W(0, 0) = 0$.

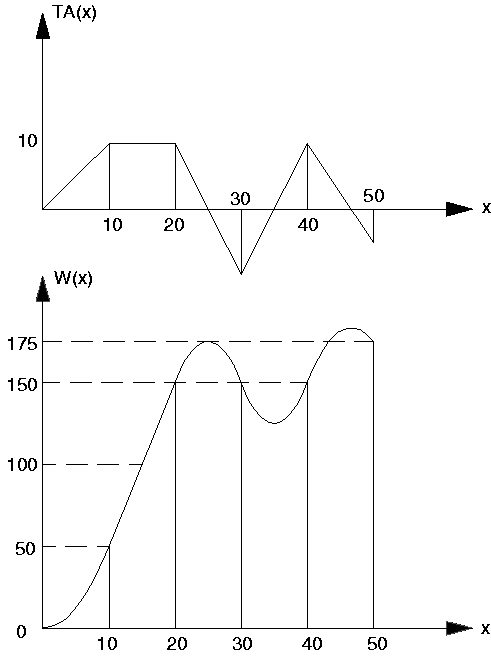


Fig. 22.3. Example of a trapezoidal integration of transverse aberration measurements

The classical integration method does not take advantage of all available information in the Hartmann plate. For example, the fact that slightly different results are obtained for the two integrations in orthogonal directions is not considered. The present common approach is just to take the average of these two measurements. Also, there is information on each square cell about a coma like term that is not taken into account in the trapezoidal integration method.

In this article we propose a more accurate method where the wavefront is synthesized by many non-flat functions whose domains are defined by the square array of holes in the Hartmann screen placed at the exit pupil of the system. The subscripts n and m assigned to each unit cell are those of its lower left corner as shown in Fig. 22.4.

The aberrations of the distorted wavefront at any unit cell n, m in the Hartmann screen are defined by

$$\begin{aligned}
 W_{nm}(x, y) = & A_{n,m} + B_{n,m}x + C_{n,m}y + D_{n,m}(x^2 + y^2) \\
 & + E_{n,m}(x^2 - y^2) + F_{n,m}xy + G_{n,m}(x^2 + y^2 - d^2)y \\
 & + H_{n,m}(x^2 + y^2 - d^2)x, \tag{22.13}
 \end{aligned}$$

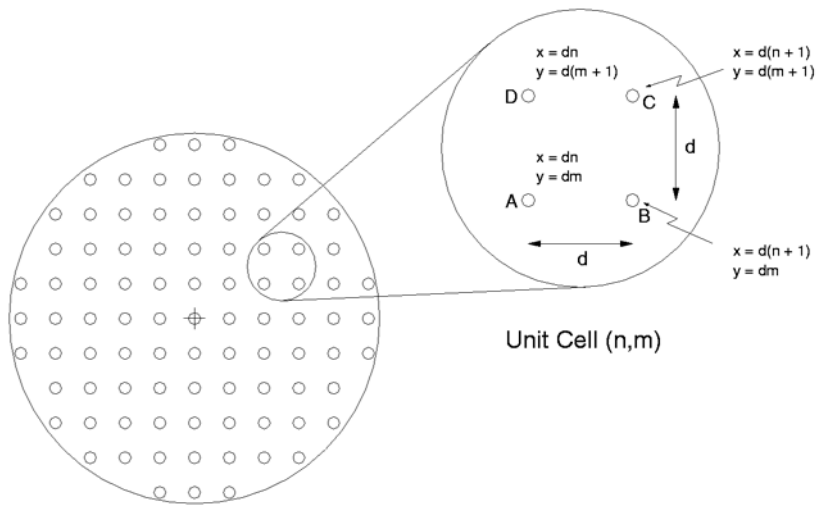


Fig. 22.4. A unit cell in a Hartmann screen

where the coefficients A, B, C, D, E, F, G and H represent

- A = constant or piston term,
- B = local cell tilt about the y -axis,
- C = local cell tilt about the x -axis,
- D = defocusing (local cell spherical deformation),
- E = astigmatism with axis at 0° or 90° ,
- F = astigmatism with axis at 45° ,
- G = coma along the y -axis,
- H = coma along the x -axis.

In this method being proposed still remains the problem that the wavefront curvatures are not continuous when going from one square cell to the next. Let us now consider the four Hartmann spots produced by the light beams passing through a unit square cell at the Hartmann screen in a similar manner to the method previously described by Malacara for a Hartmann test with only four holes [2]. The centroid (or center of gravity) of these four spots is not shifted by the presence by spherical aberration or astigmatism. Also, this centroid is not shifted by the presence of coma as defined here by adding the $-d^2$ term. It is only shifted by the two local wavefront tilts, displacing the four points system without changing their relative positions. These two local wavefront tilts can be produced by local wavefront deformations and by an axial displacement (defocusing) of the Hartmann plate.

Let us assume that the center of each unit cell of four points is the origin of coordinates for the wavefront function in that unit square. Then, the x components of the transverse aberrations are given by

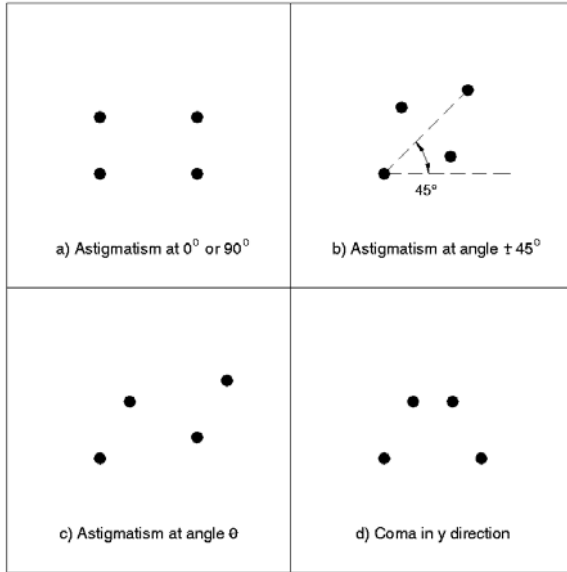


Fig. 22.5. Arrangements of the four Hartmann spots from a unit cell for some aberrations

$$\begin{aligned} \frac{\partial W(x, y)}{\partial x} &= \frac{TA_x}{r} = \phi_x \\ &= B + 2Dx + 2Ex + Fy + 2Gxy + H(3x^2 + y^2 - d^2), \end{aligned} \tag{22.14}$$

and the y components of these aberrations are given by

$$\begin{aligned} \frac{\partial W(x, y)}{\partial y} &= \frac{TA_y}{r} = \phi_y \\ &= C + 2Dy - 2Ey + Fx + G(x^2 + 3y^2 - d^2) + 2Hxy, \end{aligned} \tag{22.15}$$

where ϕ_x and ϕ_y are the angular transverse aberrations, measured from their corresponding ideal position on the square array of lines defined in the introduction and shown in Fig. 22.2b.

The configuration of the system of four spots depends on the aberration coefficients D, E, F, G, H and its global position depends on the tilt coefficients B and C . Summarizing, the center of gravity (average coordinates for the four spots) for each unit cell (see Fig. 22.5) has two properties of practical importance:

1. The position of this center of gravity of the four spots depends only on the values of the tilt coefficients $B_{n,m}$ and $C_{n,m}$ (modified by any defocusing of the Hartmann plate) and not any of the aberrations.
2. The aberrations for a unit square cell can be more easily calculated by shifting the system of four Hartmann spots from a unit cell, placing their center of gravity at the origin.

If there are no tilts the center of gravity of the four spots is located exactly at the ideal position for the spot corresponding to the center of the unit cell. However, the presence of the two tilts displace the center of gravity of these four spots from the ideal spot position for the center of the cell. Let us represent the x and y components of this displacement by $TAx_0(n, m)$ and $TAy_0(n, m)$.

Thus, the local tilt coefficients can be calculated by the deviation of the centroid from its ideal position, at the center of the corresponding square in the array of dotted lines shown in Fig. 22.2, obtaining

$$TAx_0(n, m) = B_{n,m}r = \frac{TA_{xA} + TA_{xB} + TA_{xC} + TA_{xD}}{4} \quad (22.16)$$

and

$$TAy_0(n, m) = C_{n,m}r = \frac{TA_{yA} + TA_{yB} + TA_{yC} + TA_{yD}}{4} \quad (22.17)$$

where the subscripts A, B, C, D correspond to each of the four holes at the unit cell being considered in the Hartmann screen, as in Fig. 22.4. TAx_0 and TAy_0 are the coordinates of the center of gravity of the four spots with respect to the center of the reference square array of dotted lines in Fig. 22.2b. The aberrations in the right hand of the expressions (22.16) and (22.17) are measured with respect to their ideal spot position in the corresponding corner at the rectangular array of reference dotted lines in Fig. 22.2b.

22.3 Conclusions

Summarizing, we have developed a new procedure to retrieve the wavefront shape using Hartmann test data with two important advantages. One of them is a greater fidelity and precision in the wavefront shape. The second advantage is that the local values of the curvature and the astigmatism and its axis are also obtained, which are quite useful in many ophthalmic and optometric applications.

Acknowledgments

The authors wish to thank to Consejo Nacional de Ciencia y Tecnología for the financial support.

References

1. I. Ghozeil: Hartmann and other screen tests. In: D. Malacara (ed.): Optical Shop Testing (John Wiley, New York 1992) pp. 367–396
2. D. Malacara: Testing and centering by means of a Hartmann test with four holes. Opt. Eng. **31**, 1551 (1992)

Part III

Laser Resonators and Laser Amplifiers

23 Use of Intracavity Adaptive Optics in Solid-State Lasers Operation at 1 μm

W. Lubeigt, P. van Grol, G. Valentine, and D. Burns

University of Strathclyde, Institute of Photonics
106 Rottenrow, Glasgow G4 0NW, Scotland

Summary. An intracavity 37-element deformable membrane mirror (DMM) has been used in order to control the transverse mode profile of a diode-pumped solid-state laser. Automatic spatial mode and output power optimisation of Nd:YVO₄ end-pumped and Nd:YAlO side-pumped lasers are demonstrated using a closed-loop genetic algorithm. Transverse mode and power optimisation of a diode-pumped, grazing incidence Nd:GdVO₄ laser has been performed successfully. The optimisation procedure featured a genetic algorithm ensuring the global maximum is attained. Using a Michelson interferometer with the DMM operating intracavity, the DMM was found to present negligible deformation when used with a power density of 115 W/cm² but noticeable deformation appeared with a power density of 1.25 kW/cm².

23.1 Introduction

Thermally induced optically-distorting effects are the main impediments to be overcome in developing high power solid-state lasers [1]. The problems of obtaining a good transverse mode oscillation from high average power lasers are related to the heat load induced by the high pump powers deposited into the gain medium [2]. Performance is degraded due to thermally induced birefringence and lensing in the gain material. Selection of birefringent host media or depolarization compensating laser cavity design [3] reduces the thermal birefringence problem, but inevitably the high heat load and the resultant thermal lens will restrict laser performance. The simple effects of the unaberrated spherical contribution of the thermal lens can be effectively reduced by good cavity design [4], however, the aberrating component cannot be compensated for in the same manner, and eventually leads to reduced efficiency and multi-mode oscillation as the heat load increases.

In this paper we present preliminary studies into the potential for spatial mode enhancement using an intracavity deformable membrane mirror (DMM) [5]. The mirror is operated in a computer controlled feedback scheme to enable self-optimisation of the spatial mode of the laser. Assessment of the technique with a higher pump power using a side-pumped Nd:YAlO laser cavity will also be discussed. Finally, on-going investigation on a high efficiency side-pumped, grazing incidence Nd:GdVO₄ laser will be presented.

Low-cost DMMs have recently been developed for use in astronomical and medical imaging [6]. The dynamic electronic control of the mirror shape combined with a detector of laser mode-quality, gives unique possibilities for real-time alignment and optimisation when complemented by a suitable computer controlled feedback loop.

23.2 Micro-machined Deformable Mirror

The 15 mm diameter, OKOTECH [7] deformable membrane adaptive optic (AO) mirror comprises 37 hexagonal actuators arranged in a hexagonal pattern [8]. An additional $12 - \lambda/4$ -layer dielectric mirror coating was deposited onto the aluminum coated silicon nitride membrane to provide high reflectivity ($> 99.9\%$) at 1064 nm. The maximum specified central surface deflection range was $8 \mu\text{m}$. Similar mirrors have been demonstrated at optical power densities of 2.6 kW/cm^2 (intracavity) and 11 kW/cm^2 (extracavity) without damage [9].

The actuators could be individually addressed via a personal computer using an in-house developed software package with a graphical user interface (developed using National Instruments' CVI Labwindows). We have developed a 40 channel high voltage mirror driver interfaced to the computer with the parallel port. It is noteworthy that the electrostatic transducers can only "pull" the membrane surface from its zero-bias state. The mirror may therefore require a pre-bias to meet the demands of some applications. The AO mirror was placed inside a protective mount behind a 1064 nm anti-reflection coated window to prevent deposition of dust on the membrane.

23.3 Optimisation Methods

23.3.1 Software Aperture

Automatic optimisation was performed through a closed-loop control scheme shown in Fig. 23.1. The modal output from the laser was assessed by integrating the pixel intensity within a selected "video aperture" drawn onto the webcam image of the laser beam profile.

23.3.2 Optimisation Algorithm

Hill-climbing Algorithm

The first optimisation scheme employed was demonstrated to work well for a simple laser arrangement. The optimisation procedure was based on a two stage "hill-climbing" algorithm, which by its nature can only locate a local maximum of the system dependent on the starting point (Fig. 23.2).

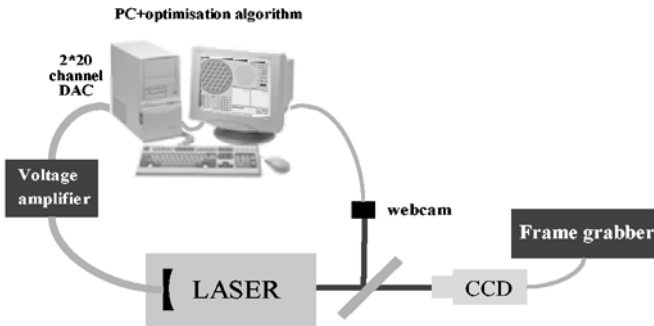


Fig. 23.1. Schematic of the closed loop feedback network used for the self-optimizing laser

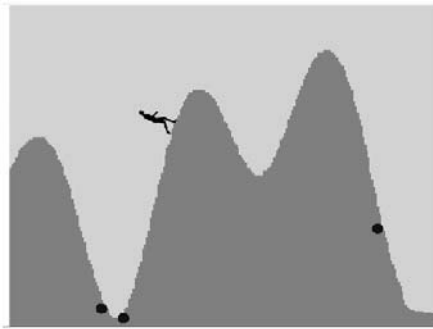


Fig. 23.2. Illustration of hill-climbing algorithm: the final solution is always the maximum most local to the initial starting point

The first “coarse” stage of the optimisation scheme involves increasing the applied voltage by 25 V steps from the 0 V start point. The actuator was set to the “best” voltage determined by the detector, i.e. the voltage corresponding to the maximum control signal value. This is evaluated for each of the 37 actuators in turn. This is then repeated N times, where N can be set by the user for optimal performance. Figure 23.3 outlines the coarse optimisation algorithm for one transducer.

Stage two of the optimisation, for “finer” adjustment of the mirror shape, was similar to the first but the transducer voltage was varied from -15 to $+15$ V about the previously set “best” value in 5 V steps. Again this was repeated for all actuators in turn, and could be reiterated M times.

The time taken for the whole optimisation procedure was variable, however, the results presented below were obtained for $N = M = 2$, took about 4 min to complete and are limited by the speed of the PC used during this initial assessment.

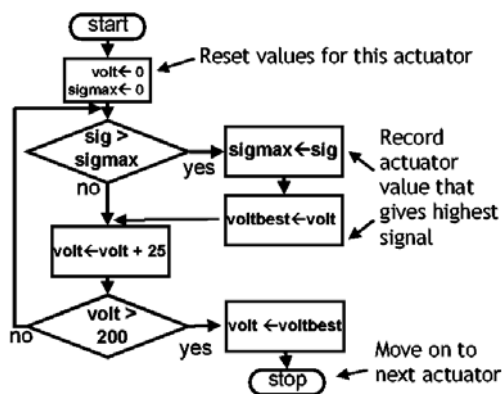


Fig. 23.3. Flowchart of the coarse step of the optimisation algorithm for one transducer

Genetic Algorithm (GA)

The genetic algorithm is an evolutionary algorithm [10]. It starts by producing a generation of N random membrane shapes or individuals whose fitness is assessed. The fitness function is derived from a video aperture recorded via a CMOS camera. The best individual is stored. The individuals produce a second generation dictated by the fitness parameter; the better their fitness, the more likely they have offspring. A one-point crossover is used and mutation can occur. The process is repeated for the new population. The number of generations, the crossover and mutation rate are set by the user. A hill-climbing iteration can follow the GA in order to ensure that the maximum value is reached but was not performed during our experiments. The use of the GA ensures that the global maximum of the fitness parameter is found. The GA loop is shown in Fig. 23.4.

It was found out that 40 generations of 40 individuals with a crossover rate of 85% and a mutation rate of 2% would ensure a final solution close to the global maximum. The whole process would take about 15 min.

23.4 Optimisation of a Low Power End-Pumped Nd:YVO₄ Laser

23.4.1 Laser Set-Up

For preliminary investigations into the use of an intracavity DMM to control the modal performance of an all-solid-state laser, the Nd:YVO₄ resonator of Fig. 23.5 was configured. The 150 mm focal length lens, used intracavity, ensured a large (≈ 7 mm diameter) spot on the adaptive mirror such that the beam area covered many actuators. Hence, the resolution of the beam/mirror

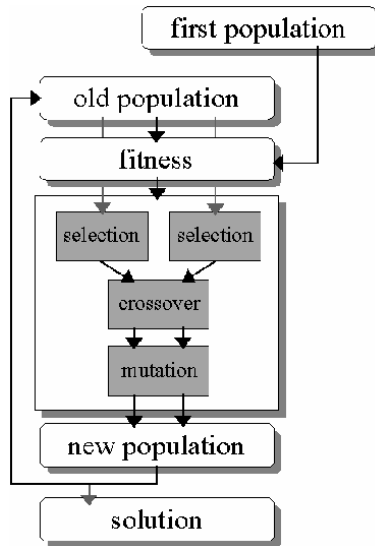


Fig. 23.4. Flowchart of the genetic algorithm

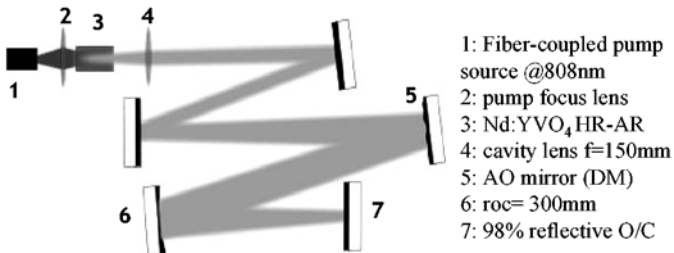


Fig. 23.5. Schematic of the Nd:YVO₄ laser cavity used to assess active transverse mode control

interaction was enhanced allowing a greater degree of optimisation to be performed. The resonator exhibited a small stability region that was spanned by the range of curvatures available with the adaptive mirror.

The gain medium was a 2 mm thick HR-AR coated Nd:YVO₄ crystal pumped using a 10 W fiber-coupled diode emitting at 808 nm. A 98% reflective mirror was used as the output coupler (M1) giving 120 mW output power when optimized with the AO mirror at 6 W pump power. Note that the laser was configured with the specific intention of assessing the potential of automated mode control, and the pump to laser extraction efficiency is low due to poor pump-laser mode overlap and lossy cavity components such as the intracavity lens.

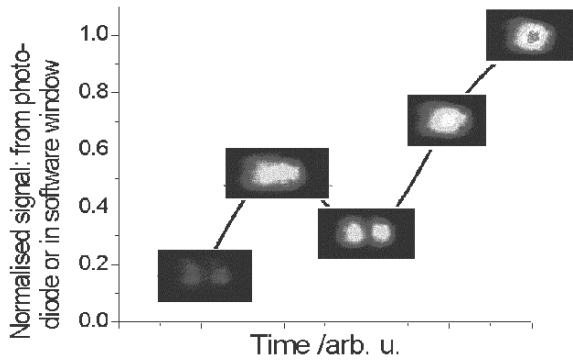


Fig. 23.6. Beam profiles from the Nd:YVO₄ laser and associated interference patterns recorded at various intervals during an optimisation sequence plotted as a histogram

23.4.2 Optimisation of Transverse Mode Profile

The first optimisation scheme was studied with a pump power of 6 W incident on the Nd:YVO₄ rod. The video aperture on the webcam supplied a “fitness” of the laser for the hill-climbing algorithm.

Whilst performing the optimisation procedure, the evolution of the output profile was recorded and is summarized in Fig. 23.6. Before optimisation, the output power from the laser was ≈ 20 mW and the oscillating spatial mode took the form of a TEM₀₁ profile. During the optimisation procedure, the transverse mode profile was observed to change substantially, especially when the central transducers were varied. The output mode profile converged rapidly towards the desired single-lobed profile after both stage 1 passes were completed. Stage 2 of the optimisation cleaned up the mode distribution further resulting in an accurate TEM₀₀ like transverse mode profile. Also as a consequence of the optimisation the average output power increased to 120 mW.

23.5 Optimisation of a Side-pumped Nd:YAIO Laser Using a Genetic Algorithm

23.5.1 Laser Set-Up

For further assessment of the technique, a side-pumped Nd:YAIO laser was set-up. The gain medium was a 15 mm long, Brewster cut Nd:YAIO crystal pumped by a laser diode stack. The configuration used ensured again a large spot (5 mm diameter) on the AO mirror. The absorbed pump power in the crystal was 35 W.

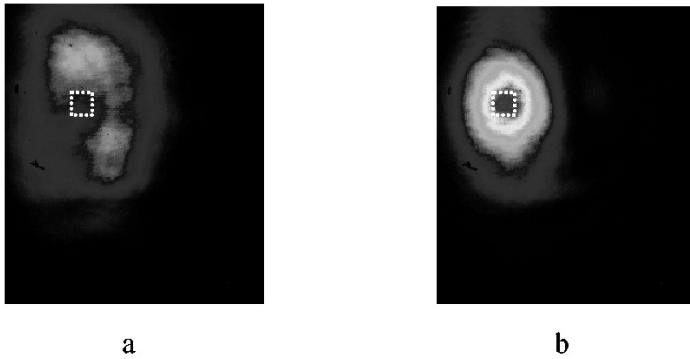


Fig. 23.7. Measured beam profile (a) before and (b) after optimisation using the genetic algorithm

23.5.2 Optimisation of Transverse Mode Profile

The optimisation scheme was studied with an absorbed pump power of 35 W in the Nd:YAlO slab. The video aperture on the webcam supplied a “fitness” of the laser for the hill-climbing algorithm.

The GA produced 40 generations of 40 individuals. The video aperture was positioned close to the centre of the initial mode (indicated by the small square in Fig. 23.7a). The optimisation procedure lasted approximately 10 min, and the result is shown in Fig. 23.7b. No significant change in the output power between the initial and final states of the laser was observed; however, during optimisation large fluctuations occur as the GA examines the search space of the DMM.

23.6 Optimisation of a Side-pumped, Grazing-Incidence Nd:GdVO₄ Laser Using a Genetic Algorithm

23.6.1 Laser Set-Up

The laser geometry (Fig. 23.8) featured a 22 mm long, 1% Nd-doped, antireflection coated, Nd:GdVO₄ crystal. The pump beam from a fast-axis collimated, 35 W diode laser bar line-focussed onto the Nd:GdVO₄ crystal was polarised parallel to the high absorbing *c*-axis.

As no cylindrical mode-matching cavity optics were used, at high incident pump power, the laser output was found to be highly multimode in the tangential plane (see Fig 23.9a). However, it is expected that the DMM will contribute some cylindrical mode-matching during optimisation. An intracavity 7× telescope was exploited in order to match the intracavity laser beam to the DMM and to enhance the effect of curvature of the mirror on

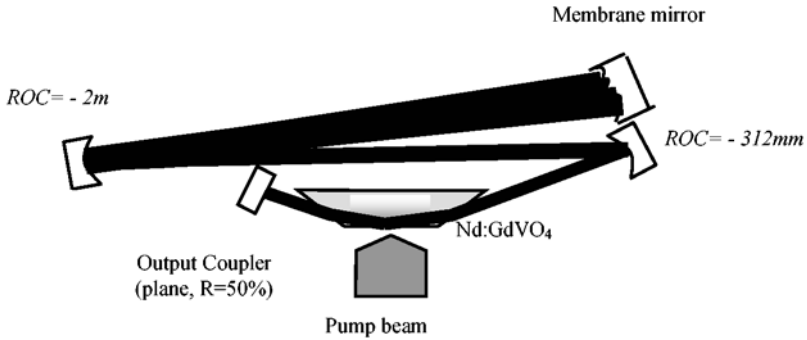


Fig. 23.8. Schematic of the intracavity AO controlled, grazing-incidence Nd:GdVO₄ laser

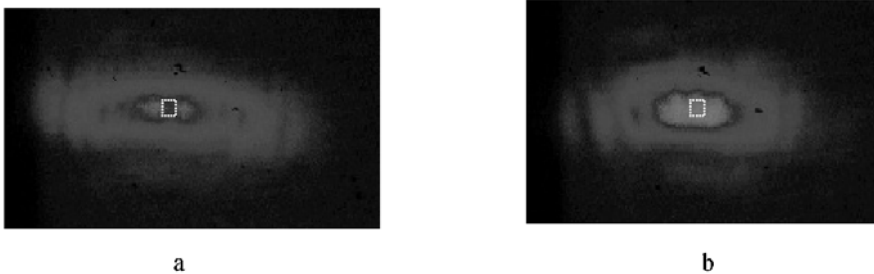


Fig. 23.9. Measured beam profile (a) before and (b) after optimisation using the genetic algorithm

the resonator stability. At a pump level of 30 W, multimode output powers of up to 8.5 W were recorded through the $R = 50\%$ output coupler.

23.6.2 Results

The results of an optimisation procedure to improve the free-running laser mode, where the output power was initially 8 W, are shown in Fig. 23.9. The video aperture was positioned close to the centre of the initial mode (indicated by the small square in Fig. 23.9a). The GA lasted approximately 10 min, and the result of this optimisation procedure is shown in Fig. 23.9b. Line scans through these profiles are presented in Fig. 23.10. No significant change in the output power between the initial and final states of the laser was observed. Again during optimisation, large fluctuations occurred as the genetic algorithm examined the search space of the DMM and a short delay was occasionally observed in the response of the laser output to changes in the mirror shape.

To further examine the properties of the laser, an intracavity slit was positioned to physically constrict the laser oscillation in the tangential plane.

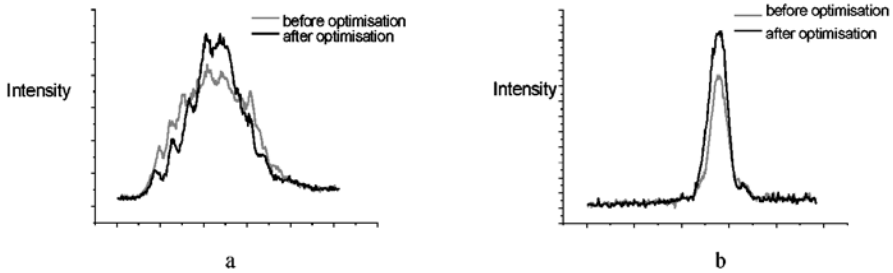


Fig. 23.10. Measured line scan through tangential plane (a) and saggital plane (b) before and after optimisation using the genetic algorithm



Fig. 23.11. Measured beam profile (a) before and (b) after optimisation using the genetic algorithm

Figure 23.11 details the initial and final states of the optimisation. After optimisation, it is evident that the beam quality was significantly improved to the circularly symmetrical mode profile shown in Fig. 23.11b. Accompanying this modal improvement the output power increased from 3.2 to 4.3 W.

23.6.3 Stability of the Membrane Intracavity

A Michelson interferometer was built in order to assess the stability of the membrane intracavity. With an intracavity power of 18 W corresponding to power density of 115 W/cm^2 on the membrane, the thermal induced mirror deformation observed when all actuators were set to 0 (Fig. 23.12a and b), and when all actuators were set to 200 V (Fig. 23.12c and d) was insignificant.

The 50% O/C was replaced by one of 1% to increase the intracavity power to 200 W giving a power density of 1.25 kW/cm^2 on the mirror. The membrane deformation was more important (Fig. 23.13). During the experiment, the front window was removed ensuring the distortion was due to the DMM alone. The time constant for thermal equilibrium to be reached by the DMM was about 10 s.

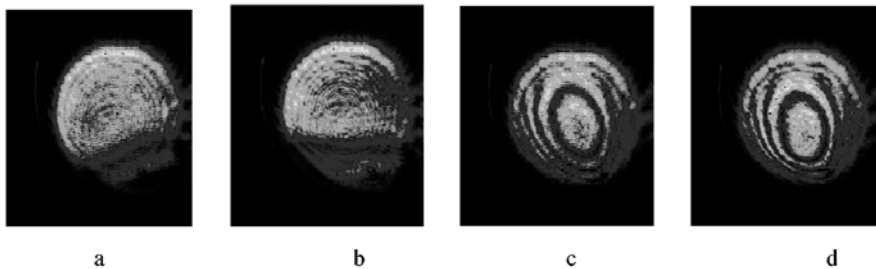


Fig. 23.12. Interferometer patterns recorded at 115 W/cm^2 when all actuators are set to 0 V (a) with laser off and (b) with laser on; when all actuators are set to 200 V (c) with laser off and (d) with laser on

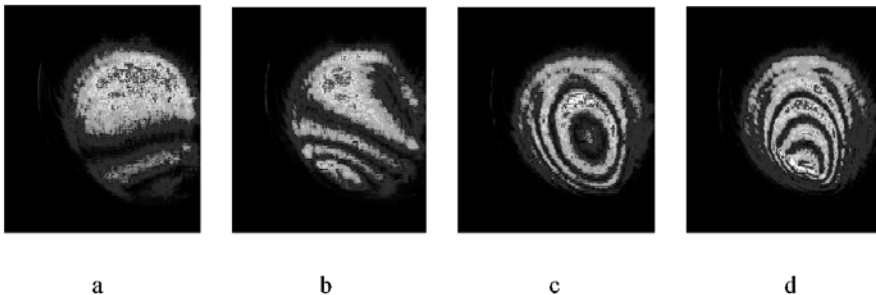


Fig. 23.13. Interferometer patterns recorded at 1.25 kW/cm^2 when all actuators are set to 0 V (a) with laser off and (b) with laser on; when all actuators are set to 200 V (c) with laser off and (d) with laser on

23.7 Conclusion

We have demonstrated automatic spatial mode control using an electronically addressed 37-element DMM inside an all-solid-state laser cavity. Two methods of optimisation have been assessed: (i) using a hill-climbing algorithm; (ii) using a genetic algorithm. Mode and power improvements have been observed for three different laser set-ups.

Initial investigations into the stability of the DMM when used intracavity have indicated significant thermal induced distortion with high intracavity fields of up to 200 W. Insignificant distortion was observed with intracavity fields of 18 W. As the lasers described here can operate with output couplers of up to $T = 80\%$, we expect DMMs to be suitable for use in laboratory based lasers up to about 50 W power levels. For modest power levels, this will cause an extra delay in the optimisation. For very high power lasers, the deformation observed will be the limiting factor for successful operation, not the mirror damage threshold. Further investigation is being performed in order to fully characterise this limitation.

References

1. J.M. Eggleston, T.J. Kane, K. Kuhn, J. Unternahrer, R.L. Byer: The slab geometry laser. I. Theory. *IEEE J. Quantum Electron.* QE-**20**, 289 (1984)
2. W. Koechner: *Solid-State Laser Engineering*. 5th edn. (Springer, Berlin Heidelberg New York 1999)
3. W.A. Clarkson, N.S. Felgate, D.C. Hanna: Simple method for reducing the depolarization loss resulting from thermally induced birefringence in solid-state lasers. *Opt. Lett.* **24**, 820 (1999)
4. D. Burns, G.J. Valentine, W. Lubeigt, E. Bente, A.I. Ferguson: Development of high average power picosecond laser systems. *Proc. SPIE* **4629**, 4629 (2002)
5. W. Lubeigt, G. Valentine, J. Girkin, E. Bente, D. Burns: Active transverse mode control and optimization of an all-solid-state laser using an intracavity adaptive-optic mirror. *Opt. Expr.* **10**, 550 (2002) <http://www.opticsexpress.org/abstract.cfm?URI=OPEX-10-13-550>
6. R. Tyson: *Principles of Adaptive Optics*. 2nd edn. (Academic Press, 1998)
7. Flexible Optical B.V., PO Box 581, 2600 AN, Delft, The Netherlands, www.okotech.com
8. G. Vdovin, P.M. Sarro, S. Middelhoek: Technology and applications of micro-machined adaptive mirrors. *J. Micromech. Microeng.* **9**, R8 (1999)
9. G. Vdovin, V. Kiyko: Intracavity control of a 200-W continuous-wave Nd:YAG laser by a micro-machined deformable mirror. *Opt. Lett.* **26**, 798 (2001)
10. K.F. Man: *Genetic Algorithms: Concepts and Designs* (Springer, Berlin Heidelberg New York 1999)

24 Intracavity Use of Membrane Mirrors in a Nd:YVO₄ Laser

P. Welp, I. Buske, and U. Wittrock

Fachhochschule Münster
Stegerwaldstr. 39, 48565 Steinfurt, Germany

Summary. 10 mm and 15 mm diameter adaptive membrane mirrors have been implemented into a Nd:YVO₄ laser. The laser performance has been investigated and compared to a similar laser without an adaptive mirror. While some membrane mirrors did not change the laser behaviour, several other membrane mirrors lead to a switching between transverse modes. With less than 3 kW/cm², the maximum intensity on the mirror membrane was small compared to a damage threshold of more than 144 kW/cm².

24.1 Introduction

A major problem for the realization of high-brightness operation in solid state lasers is heat generation in the active medium. Temperature gradients lead to thermal lensing and birefringence in the gain medium. These effects scale with pumping power [1]. While birefringence and low-order aberrations like defocus can be compensated by a proper design of the laser cavity, higher-order aberrations of the thermal lens cannot be corrected with standard optical components. Calculations and simulations, on the other hand, have shown that a reduction of thermo-optical aberrations drastically improves the laser performance [2,3]. Introducing additional aberrations with the opposite sign by means of an adaptive resonator mirror should be a way to compensate for the higher-order aberrations. First experiments with low-power lasers have been successful [4].

When scaling to higher powers and thus increasing the beam intensity on the mirror membrane, it has to be ensured that the adaptive mirror itself is stable and thus does not introduce any further disturbances into the resonator. To test this, the HR-mirror of a conventional Nd:YVO₄ laser has been replaced by an adaptive membrane mirror. The deformation of the membrane has been monitored during lasing and the performance of the laser with the adaptive mirror has been compared to the performance of the same laser without an adaptive mirror.

We furthermore discuss the use of a power-in-the-bucket sensor for beam quality measurements of lasers with intracavity adaptive mirrors.

24.2 Principle Layout of a Laser Containing an Adaptive Mirror

An adaptive optics closed-loop system in general consists of an adaptive optical element, a feedback signal dependent on the beam quality and a control system to control the adaptive element as a function of the feedback signal. An example of a closed-loop system with a power-in-the-bucket sensor is shown in Fig. 24.1.

A plane wavefront travels through an aberrated optical element (e.g. a pumped laser rod) and is distorted. When this distorted beam is focused, the diameter of its focal spot is larger than the respective diameter of the focal spot of the plane wavefront would be. A diffraction-limited aperture in the focal plane therefore leads to complete transmission of the non-aberrated wavefront, while the aberrated beam is partly blocked. The intensity measured behind the aperture is thus a measure for the quality of the beam. As a result, it can be used as feedback signal to control the adaptive element of the system. This beam quality sensor, which consists of a lens, an aperture and a photodiode, is called “power-in-the-bucket sensor”. Its feedback signal is a scalar quantity and thus does not give any information of the shape of the distorted beam. Therefore, different deformations of the adaptive mirror have to be tested for their influence on the beam quality. The mirror deformation then has to be optimized with an optimization routine, e.g. a genetic or a hill-climbing algorithm, [4, 5]. Figure 24.1 shows the steady state of the closed-loop system. The aberration imprinted onto the beam by the adaptive mirror just compensates the distortion due to the aberrated optical element. The wavefront is optimized.

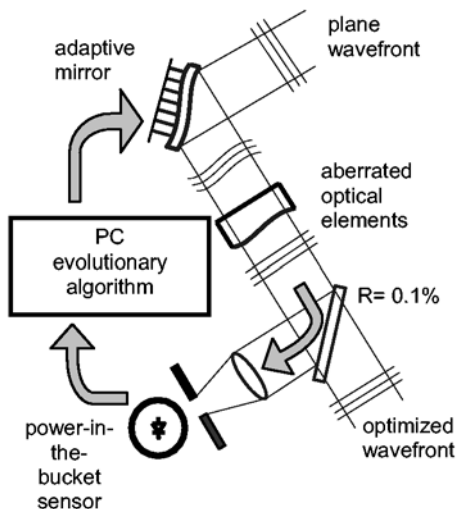


Fig. 24.1. Principle layout of a closed-loop adaptive system

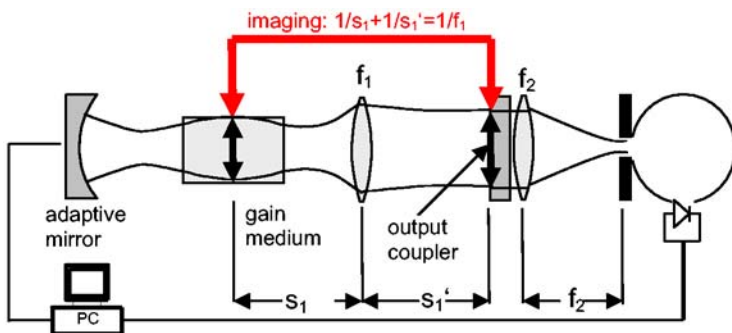


Fig. 24.2. Laser resonator with implemented adaptive mirror that is controlled by a closed-loop system. The diameter of the laser beam on the output coupler stays constant regardless of the deformation of the adaptive mirror

As the diameter of the focal spot of a lens is not just dependent on its focal length and on the wavelength of the beam, but also on the diameter and the phase of the beam at the lens, a power-in-the-bucket sensor is just able to measure correctly for a constant beam diameter at the lens. For the set-up shown in Fig. 24.1, this criterion is fulfilled when no defocus is added.

When setting up a laser with the power-in-the-bucket method, it has to be made sure that the beam diameter at the laser output coupler stays constant, regardless of beam quality. In other words, when the laser operates in multimode, the diameter of the output beam has to be the same as in singlemode operation. A laser resonator with constant beam diameter at the output coupler is shown in Fig. 24.2.

A lens inside the resonator images the center of the gain medium onto the output coupler. The gain medium is the limiting aperture of the resonator. As, on the other hand, the highest order – and thus largest – mode oscillating in the cavity always fills the gain medium completely, imaging the gain medium onto the output coupler ensures a constant beam diameter there. If the output coupler is flat, we also know that the waist of the output beam lies on the coupler. Figure 24.2 shows a laser resonator with an adaptive mirror that is controlled by a closed-loop system containing a power-in-the-bucket sensor.

24.3 A Membrane Mirror Implemented into a Nd:YVO₄-Laser

Before aberrations of a laser can be corrected with the set-up described above, it has to be made sure that the adaptive mirror itself does not introduce further disturbances into the resonator.

For our experiment we used membrane mirrors manufactured at Flexible Optical B.V. in Delft, Netherlands [6]. The 1 μm thick Silicon-Nitride membrane is coated with 12 dielectric layers for high reflectivity at 1064 nm. It

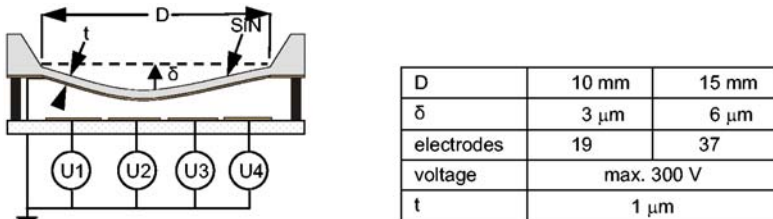


Fig. 24.3. Schematic drawing of the membrane mirrors and specifications of the tested mirrors

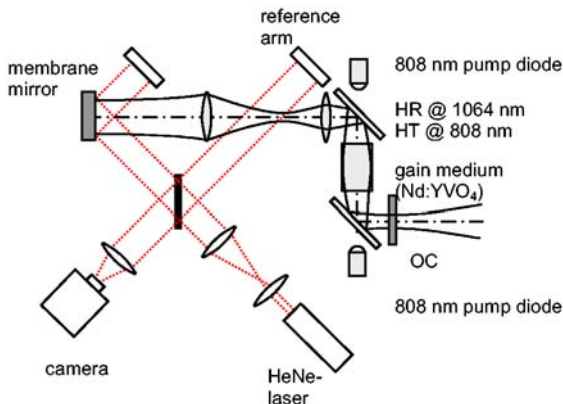


Fig. 24.4. VMc5 laser [2] with implemented membrane mirror and telescope. The deformation of the membrane is monitored with a Michelson interferometer

is actuated by electrostatic force from an array of electrodes. A schematic drawing and the specifications of the tested membrane mirrors are shown in Fig. 24.3. To get a first impression of the performance of these mirrors inside a resonator, the high reflective mirror of a commercial Nd:YVO₄-laser (VMc5, manufactured by TRUMPF Laser Marking Systems [7]) has been exchanged by a membrane mirror. In addition, a telescope has been inserted into the resonator to ensure a sufficient large beam diameter at the membrane mirror. The larger the beam, the more actuators are covered and can be used for optimization of the wavefront. A beam that is too large, on the other hand, would be influenced by the stiff mounting of the membrane. The ratio of beam to membrane diameter that is optimal for wavefront corrections has been reported to be 50–75% [8, 9]. With 5 mm, our beam diameter at the mirror membrane was smaller than this optimum. As shown in Fig. 24.4, a Michelson interferometer has been used to monitor the deformation of the membrane mirror.

First experiments have been done without applying voltage to the mirror membrane. The output power characteristic of the laser has been recorded for five smaller and three larger membrane mirrors. In addition, we once re-

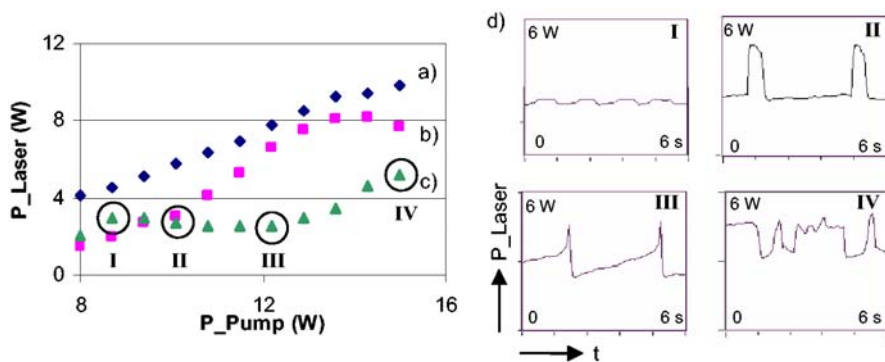


Fig. 24.5. Nd:YVO₄ laser VMc5 with implemented 1 : 5 telescope. Average laser output power versus pump power with (a) a conventional bulk HR-mirror, (b) membrane mirrors that did not lead mode-switching as HR-mirrors, (c) membrane mirrors that lead to mode-switching as HR-mirrors. (d) Output power of laser (c) versus time at pumping powers of (I) 8.5 W, (II) 10 W, (III) 12 W, (IV) 15 W

placed the membrane mirror by a conventional bulk mirror. Without applying voltage, some of the smaller membrane mirrors just caused a drop of laser output power compared to the laser with the conventional mirror (Fig. 24.5a–b). Apart from the drop, the output power characteristics of lasers with these membrane mirrors or with a conventional mirror are the same. The lasers run stable and have about the same beam quality. With some other membrane mirrors, a different output power function has been observed. Instead of going up with increasing pump power, the average output power of these lasers stays more or less constant for a wide pump range, before finally increasing (Fig. 24.5c). Unlike the other set-ups (Fig. 24.5a–b), these lasers do not run stable in one transverse mode, but show mode-switching above a certain pump power threshold. Below this threshold, these lasers oscillate stable in one mode. But when reaching the threshold, the lasers start switching between modes. With increasing pump power, the switching becomes faster and more unstable. Frequencies from 0.1–10 Hz have been observed. Laser output power recorded as a function of time gives a good impression of the switching behaviour, as different modes lead to different output power levels (Fig. 24.5d).

With the Michelson interferometer shown in Fig. 24.4 the deformation of the membrane mirror has been recorded before and during lasing. Without lasing, all our membrane mirrors – no matter whether they lead to mode-switching or not – show a small astigmatism term. Lasing always leads to additional focus and spherical aberration deformation of the membranes. These additional terms are due to heating of the membrane because of the lasing. Mode-switching occurs when the deformation of the membrane does not stay constant over time. The observations of the laser behaviour lead to the con-

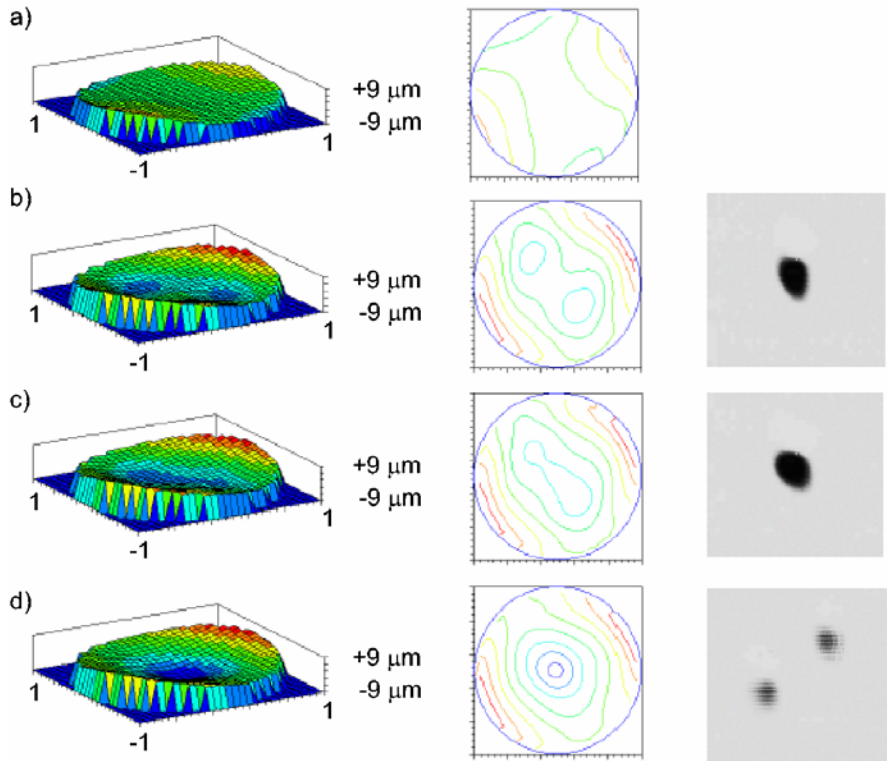


Fig. 24.6. Deformation of the 15 mm diameter mirror membrane and corresponding laser output (a) No lasing, (defocus: $0.12\ \mu\text{m}$, astigmatism: $0.69\ \mu\text{m}$, coma: $0.15\ \mu\text{m}$, spherical: $-0.11\ \mu\text{m}$) (b) 10 W pump power, 4.7 W output power, just after switching to the original mode (defocus: $0.70\ \mu\text{m}$, astigmatism: $0.79\ \mu\text{m}$, coma: $0.08\ \mu\text{m}$, spherical: $-0.10\ \mu\text{m}$), beam intensity on the membrane $\approx 2\ \text{kW}/\text{cm}^2$ (c) 10 W pump power, 4.7 W output power, just before switching away from the original mode (defocus: $0.72\ \mu\text{m}$, astigmatism: $0.79\ \mu\text{m}$, coma: $0.06\ \mu\text{m}$, spherical: $-0.47\ \mu\text{m}$), beam intensity on the membrane $\approx 2\ \text{kW}/\text{cm}^2$ (d) 10 W pump power, 2.4 W output power, just after switching to the mode (defocus: $0.86\ \mu\text{m}$, astigmatism: $0.67\ \mu\text{m}$, coma: $0.04\ \mu\text{m}$, spherical: $-1.09\ \mu\text{m}$), beam intensity on the membrane $\approx 1.4\ \text{kW}/\text{cm}^2$

clusion that this happens, when the deformation of the membrane exceeds the stability range of the mode that caused the deformation in the first place by heating the membrane up. This first mode becomes unstable and a second mode starts oscillating. Heating of the membrane still occurs, but as the intensity distribution of the now oscillating mode is different from the previous one, the deformation of the membrane changes as well.

An exemplary development of membrane deformations is shown in Fig. 24.6. When there is no voltage applied to the membrane mirror and the mirror is not under laser load, the main deformation of the membrane

is a small astigmatism term which is due to the mechanical support of the membrane. When lasing builds up in the resonator, defocus is added to the deformation. While – in our experiments – the amount of defocus stays more or less constant over time, even if mode-switching is observed, the spherical aberration term strongly increases with time. At a certain point, the deformation of the mirror membrane exceeds the stability range of the lasing mode. A different mode takes over. In Fig. 24.6d this second mode is not as intense as the original mode. The mirror membrane is thus able to return to its old shape until the resonator becomes stable for the original mode again. The original mode starts oscillating and the cycle starts once more. This cycle becomes more unstable and the switching between modes more frequent, the stronger the gain medium is pumped. This is due to the fact that, in our stronger pumped resonator, the intensity at the mirror membrane of most modes is high enough to cause additional deformations. In contrast to a lower pump level, there are less low intensity modes that allow the membrane to return to its old shape. Thus the switching between modes becomes more irregular.

The experiments described above have been done with a membrane mirror, where no voltage was applied. In order to suppress the observed mode-switching we applied offset voltages of 100–300 V to the mirror. Also the telescope inside the resonator was adjusted for each offset voltage level in order to optimize the resonator. But it was not possible to suppress or decrease mode-switching.

Five of the eight tested membrane mirrors lead to mode-switching. Among these were all three 15 mm diameter mirrors. Mode-switching occurred for pump powers above 9–10 W. Above pump powers of ≈ 13 W, two 10 mm diameter membrane mirrors showed mode-switching as well. Three other 10 mm mirrors did not cause any mode-switching until the maximum pump power of 15 W. This leads to the supposition that smaller membranes are more stable than larger ones. Of course, it is also possible that the dielectric coating of the small mirrors is just better than the coating of the large ones. But this is not likely as the eight mirrors are from various batches.

During all our experiments the maximum intensity on the mirror membranes was less than 3 kW/cm^2 which is small compared to their damage threshold of more than 144 kW/cm^2 [10].

24.4 Conclusion

First investigations on the intracavity use of deformable membrane mirrors show their sensitivity to the intensity of the incident light. With less than 3 kW/cm^2 , even intensities well below the damage threshold of the mirror ($> 144 \text{ kW/cm}^2$) can cause reversible deformations of the membrane – typically defocus and spherical aberration. Together with the dynamics of a laser resonator, this sensitivity can lead to mode-switching. Switching frequencies of 0.1–10 Hz have been observed. 10 mm diameter mirrors seem to be less

susceptible to mode-switching than 15 mm mirrors. It was not possible to suppress the switching by applying an offset voltage of up to 300 V. Deformations of the membrane due to the incident beam therefore seem to be the limiting factor for the intra-cavity use of deformable membrane mirrors rather than the damage threshold of the dielectric coating or the membrane. Investigations on these limitations will go on.

Acknowledgements

We are grateful to TRUMPF Laser GmbH + Co. KG for providing us with the Nd:YVO₄ laser.

References

1. W. Koechner: Solid-State Laser Engineering (Springer, Berlin Heidelberg New York 1992)
2. I. Buske, U. Wittrock: Simulations of optical resonators with aberrations. In: Proceedings of the 2nd International Workshop on Adaptive Optics for Industry and Medicine. G.D. Love (ed.) (World Scientific 1999) pp. 155–162
3. I. Buske, J. Hüve, U. Wittrock: Einflüsse von Aberrationen auf optische Resonatoren, presented at the Frühjahrstagung der DPG, Poster Q 31.5, Berlin (2001)
4. W. Lubeight, G. Valentine, J. Girkin, E. Bente, D. Burns: Active transverse mode control and optimization of an all-solid-state laser using an intracavity adaptive-optic mirror. *Opt. Expr.* **10**, 550 (2002)
5. I. Buske, H.-M. Heuck, J. Hüve, H. Zimer, U. Wittrock: Master-Oscillator-Power-Amplifier laser with adaptive aberration correction. *Proc. CLEO (Long Beach 2002)*
6. Flexible Optical B.V., www.okotech.com, PO Box 581, 2600 AN, Delft, The Netherlands
7. TRUMPF Laser Marking Systems, www.vectormark.com, Ausserfeld, 7214 Grüşch, Switzerland
8. E.J. Fernandez, P. Artal: Membrane deformable mirror for adaptive optics: performance limits in visual optics. *Opt. Expr.* **11**, 1056 (2003)
9. U. Wittrock, I. Buske, H. Heuck: Adaptive aberration control in laser amplifiers and laser resonators. In: *Laser Resonators and Beam Control VI*. A.V. Kudryashov, A.H. Paxton (eds.), *Proc. SPIE* **4969**, 122 (2003)
10. Development and applications of novel optoelectromechanical systems micro-machined in silicon – Final report II. EU Project LTR 31069 – MOSIS (2001)

25 Adaptive Optics for High-Power Laser Beam Control

A. Kudryashov, V. Samarkin, A. Alexandrov, A. Rukosuev, and V. Zavalova

Russian Academy of Sciences, ILIT, Adaptive Optics for Industrial and Medical Applications Group
Svyatoozerskaya 1, Shatura 140700, Russia

Summary. This paper presents an adaptive optical closed loop system with a bimorph mirror as a wavefront corrector and a Shack–Hartmann wavefront sensor to compensate for the aberrations of high power lasers. An adaptive system can correct for the low-order aberrations in the real-time – the frequency of corrected aberrations is less than 25 (30) Hz. The amplitude of such aberrations – about 7 microns. These parameters are mostly determined by the utilized Shack–Hartmann wavefront sensor. Number of corrected aberrations – up to 30th Zernike polynomial (excluding tip-tilt). We are presenting the results of the use of our adaptive system in several TW laser systems such as ATLAS, LULI and Beijing Institute of Physics.

25.1 Introduction

Contemporary adaptive optical systems are used to correct for the aberrations in astronomical telescopes – the aberrations of the light from the stars that passed through atmospheric turbulence. Such systems had to compensate rapidly changing high order aberrations to improve the vision of the objects and, in fact, not always the astronomical ones [1]. They are rather expensive (up to 1 million USD), large, and of course could not be used for commercial application in lasers and laser complexes. But the development of contemporary adaptive optical technique allows nowadays to believe that such systems could be used in various apparatuses, including lasers. In our Group we managed to design a commercially available adaptive optical system for laser beam control. As usually, such a system consists of a wavefront corrector – in our case, a bimorph deformable mirror, a wavefront sensor – Shack–Hartmann type of sensor, a control unit and software worked out in our Group. We already showed the successful use of our adaptive system in various types of high power lasers in different countries.

25.2 Wavefront Corrector

Of course, the key element of any adaptive optical system is the wavefront corrector. Moreover, the property of any adaptive optical system depends on the parameters of the used corrector. In case of correction for the aberrations

of the laser beams it is rather simple to suggest the main demands to the wavefront corrector:

- wide range of surface deformation;
- continuous reflective surface deformation to avoid any diffraction effects at the edges of subapertures;
- efficiency of reproduction of the wavefront aberrations;
- temperature stability of the surface flatness;
- possibility to conjugate with wavefront sensor;
- simplicity of producing and application;
- and, of course, low price.

From this point of view, bimorph mirrors are the most suitable correctors to be used in laser adaptive systems. It was shown that a semipassive bimorph mirror with 13 actuators effectively reproduces low order wavefront aberrations of large amplitudes [2]. For example, for this mirror theoretical precision (RMS) of reproduction of defocus is 0.3%, astigmatism – 0.7%, coma – 5% and spherical aberration – 6%. But a deformable bimorph mirror is not a standard optical element. It is relatively thin; it consists of several layers from different materials with different properties. There are no standard optical technologies to produce bimorph mirrors. Special methods of piezoceramics treatment and training, surface polishing, reflecting coating deposition and so on have to be developed to produce high quality bimorph correctors. Some applications of bimorph correctors in lasers and optical systems for imaging require a wide range of deformation and a high stability of the mirror surface. The traditional semipassive bimorph mirror consists of a glass, copper or quartz substrate firmly glued to a plate actuator disk made from piezoelectric ceramic (lead zirconium titanate, PZT) (see Fig. 25.1). Applying the electrical signal to the electrodes of the piezoceramic plate causes, for example, tension of the piezodisc. Glued substrate prevents this tension, and this result in the deformation of the reflective surface. To reproduce different types of aberrations with the help of such a corrector, the outer electrode is divided in several controlling electrodes having the shape of a part of a sector. The size as well as the number of such electrodes depends upon the number and the type of the aberrations to be corrected. In our work we usually used the geometry of the electrodes given in Fig. 25.2. The behaviour of the bimorph corrector (deformation of the surface W when the voltage is applied to the particular electrode) is well described by the following equation [3]:

$$D' \nabla^2 \nabla^2 W + (\rho_1 h_1 + \rho_2 h_2) \frac{d^2 W}{dt^2} = \frac{d_{31} \nabla^2 \tilde{E}(x, y) E_1 (2\Delta h_1 - h_1^2)}{2(1 - \nu)}, \quad (25.1)$$

$$D' = \frac{E_2}{1 - \nu^2} \left(\frac{\Delta_1^3}{3} + \frac{\Delta_2^3}{3} - \Delta_1^2 h_1 + \Delta_1 h_1^2 - \frac{h_1^3}{3} \right) + \frac{E_1}{1 - \nu^2} \left(\Delta_1^2 h_1 - \Delta_1 h_1^2 + \frac{h_1^3}{3} \right), \quad (25.2)$$

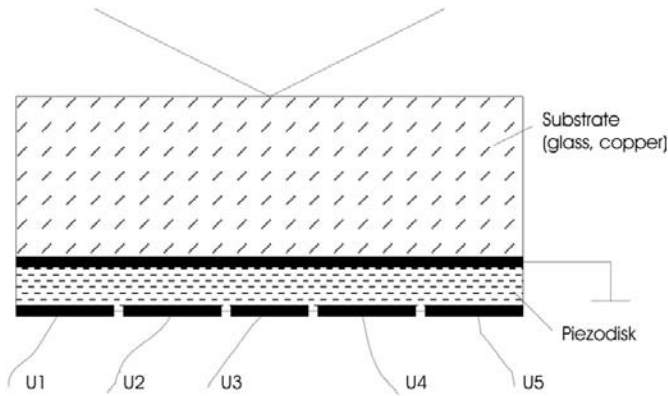


Fig. 25.1. Scheme of a semipassive bimorph corrector

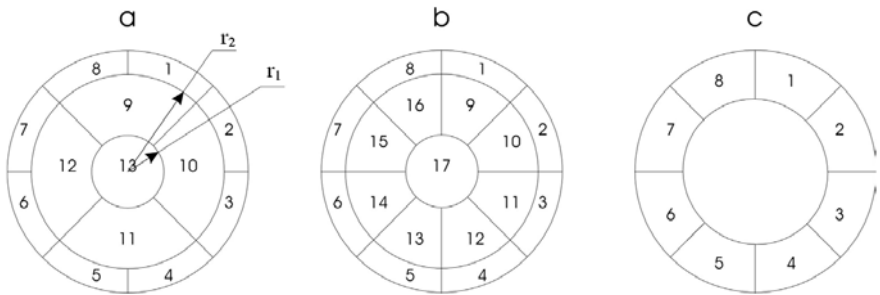


Fig. 25.2. Various schemes of the control electrodes on the surface of the piezodisk

$$\Delta_2 = \frac{E_2 h_2^2 + E_1 (h^2 - h_1^2)}{2(E_2 h_2 + E_1 h_1)}; \quad \Delta_1 = h - \Delta_2. \tag{25.3}$$

Here, h_1, h_2 – the thickness of a piezodisk, and substrate, E_1, E_2 – Young’s modulus of a piezodisk and substrate, h – total thickness of the mirror, ν – the Poisson ratios, d_{31} – transverse piezo modulus, $\tilde{E}(x, y)$ – the strength of the electric field applied uniformly to the given electrode. This equation was used to optimize radii r_1 and r_2 (Fig. 25.2) for the best correction of the low order aberrations such as coma, astigmatism, spherical aberration.

Several types of bimorph correctors were produced in the Adaptive Optics Group at IPLIT RAS. The technology of fabrication of such correctors was the following. A semipassive bimorph plate was heated in a furnace for 4–5 h at 80°C until the glue had completely hardened. The plate was then cooled in a refrigerator to remove any residual thermal deformations before being reheated in the furnace. This procedure was repeated four or five times. The quartz substrate was then polished to obtain an optical-quality surface (the deviation from sphere should not be greater than 0.1 μm) before a high reflectivity dielectric or metal coating (up to 99.8%) was deposited on its

Table 25.1. Main features of semipassive bimorph mirrors

Working aperture	40, 50 mm
Thickness of the mirror	3–5 mm
Number of actuators	8, 13, 18
Mirror quality	0.2 μ (P–V)
Stroke	7–15 μ
First resonance	2–7 kHz
Substrate material	Glass, quartz, copper

Table 25.2. RMS errors of several aberrations approximation by a 17-electrode bimorph corrector

Type of aberration	RMS error
Defocus	0.1%
Astigmatism	0.2%
Coma	3.0%
Spherical aberration	5.3%

surface. Conductors were then glued to the common and controlled electrodes. The corrector was inserted in a mounting at the back of which there was a connection to the control voltages. The main features of a semipassive bimorph corrector are shown in Table 25.1.

The static and dynamic characteristics of the mirrors were studied by an interference method. We used a Zygo Mark-3 phase-shifting interferometer. The sensitivity of the correctors was estimated from the displacement of the interference fringes at the center of the pattern when the voltage of 100 V was applied to all electrodes. The frequency of the first resonance of our correctors was in the range of 3–5 kHz. Table 25.2 presents the measured RMS errors of approximation of some low-order aberrations by a 17-electrode bimorph corrector.

Figure 25.3 presents various types of deformable bimorph mirrors we had manufactured in our Group and which we used in various types of laser systems.

25.3 Low-Cost Shack–Hartmann Wavefront Sensor

One of the demands of any optical system is its reliability and ability to work not only in the laboratory, but also under real conditions, so that every student could use it without breaking it. From this point of view the Shack–Hartmann wavefront sensor is the most suitable one to be included in an AO system. These kinds of sensors are widely used by astronomers or in medical research but in fact never were applied to control for a laser beam. One of the shortcomings of existing wavefront sensors is their relatively high

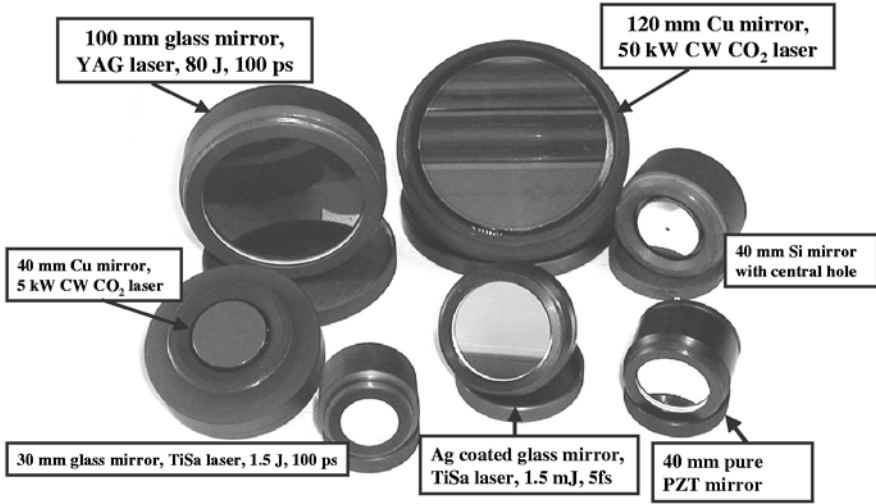


Fig. 25.3. Photo of various bimorph mirrors

price, which varies from \$25 000–\$60 000 or even to \$200 000 (it depends on the tasks and parameters of the system). In Russia we do not have any commercially available Shack–Hartmann wavefront sensor, though the attempts to fabricate it were made by different institutes and research groups. That is why we concentrated our efforts on developing our own low-cost version of the sensor.

25.3.1 Some Theory

The wavefront measurements by a Shack–Hartmann wavefront sensor (SHS) are based on the measurements of local slopes of a distorted wavefront $\partial\phi/\partial n$. So, the whole wavefront is divided in several subapertures by some phase plate or lenslet array and the deviation of the focal spot from some reference positions in each subaperture is measured. Figure 25.4 gives some idea about the work of the SHS. For the measurements a standard CCD camera is used.

The centroid position (x, y) of a focal spot is calculated as

$$x = \frac{\sum_{i=1}^m \left(\sum_{j=1}^n i I_{ij} \right)}{\sum_{i=1}^m \left(\sum_{j=1}^n I_{ij} \right)}, \quad y = \frac{\sum_{i=1}^m \left(\sum_{j=1}^n j I_{ij} \right)}{\sum_{i=1}^m \left(\sum_{j=1}^n I_{ij} \right)}, \quad (25.4)$$

where i, j are pixels of CCD, I_{ij} – optical intensity distribution.

The method of fast Fourier transfer was applied to determine the NX and NY (X and Y number of focal spots on the aperture) and the angle of

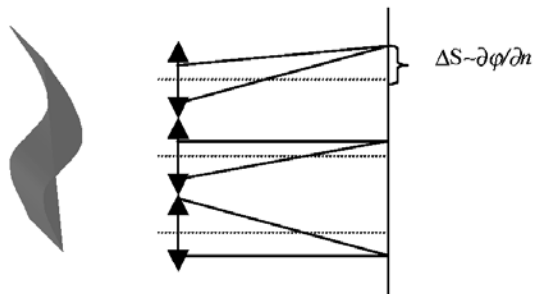


Fig. 25.4. Idea of SHS

hartmannogramme alignment relative to the boundary of the CCD camera matrix.

The phase function with some accuracy could be presented as the superposition of M orthogonal functions:

$$\phi(x, y) = \sum_{k=0}^M a_k F_k(x, y), \tag{25.5}$$

where x, y – coordinates of $NX \times NY$ spots, F_k – two-dimensional orthogonal function (Zernike polynomial, for example) and a_k – coefficients to be determined.

The local slope of the wavefront is obtained as

$$S^x = \sum_{k=1}^M a_k \frac{\partial F_k}{\partial x}, \quad S^y = \sum_{k=1}^M a_k \frac{\partial F_k}{\partial y}, \tag{25.6}$$

Or in matrix form:

$$\mathbf{S} = \mathbf{A}\mathbf{a},$$

where A – so-called gradient rectangular matrix with M columns and $2NX \times NY$ rows.

Therefore the coefficients a_k could be obtained by least-squares solution of $\min \|\mathbf{S} - \mathbf{A}\mathbf{a}\|^2$:

$$\mathbf{a} = \mathbf{B} \cdot \mathbf{S},$$

where

$$\mathbf{B} = (\mathbf{A}\mathbf{A}^t)^{-1}\mathbf{A}^t.$$

We use the method of Fast Fourier Transform of the input data from CCD to determine the NX and NY parameter of grid periodical structure of the



Fig. 25.5. Example of a hartmannogramme

spots image and the angle of the hartmannogramme arrangement relative to the boundaries of the CCD camera matrix.

It allowed, at first, to divide the whole area into the equal squares each containing an allocated individual spot. Secondly, it became possible to take into account the rotation of the lenslet array corresponding to the CCD. Third, the displacement of the grid borders with the reference to the CCD matrix boundaries was taken into account. Figure 25.5 gives the view of the standard image of the SHS picture on the CCD camera.

25.3.2 Experimental Set-Up and Computer Code

The experimental set-up of SHS for laser beam diagnostics is shown in Fig. 25.6. To synchronise the beam size of the incoming beam with the size of the CCD ($1/2''$) we suggest to use a simple lens. Of course in this case we would be able to determine the phase front up to defocus, but this does not harm the correct measurements of the rest aberrations of the beam.

The developed algorithm was tested by modelling the distortions of the wavefront with low order aberrations (with the noise and rotation of the lenslet vs. CCD matrix) of the hartmannogramms. The maximal time of complete processing by optimum algorithm was 18 ms. The obtained Zernike coefficient gave a good agreement with the predetermined. The accuracy of wavefront reconstruction was better than 0.7% (RMS) with added noise

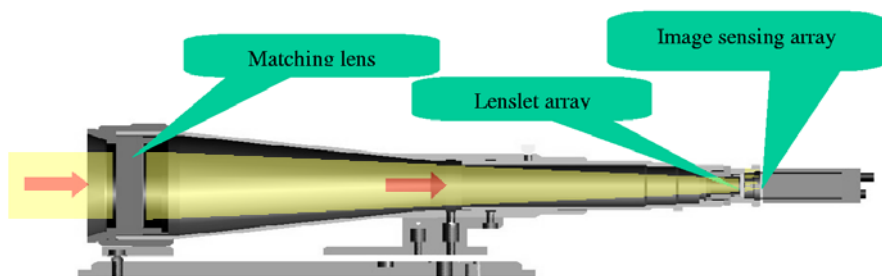


Fig. 25.6. Scheme of an experimental sample

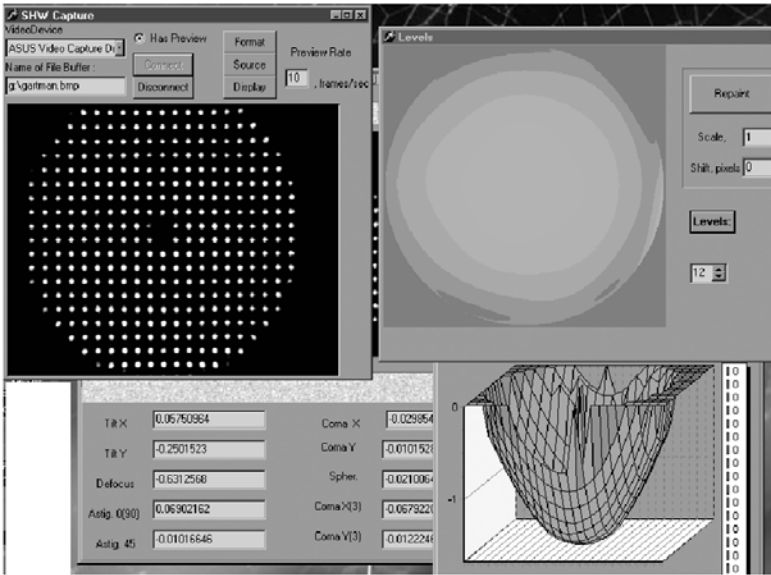


Fig. 25.7. User interface

(30 dB). The limited angle of lenslet rotation was ± 0.05 rad. The duration of the initial calibration stage is 1 s. Wavefront measurements were made with a bimorph mirror that produced time varying aberrations with the $P-V = 2 \mu$. From the reconstructed wavefront, various parameters such as peak-to-valley (P-V), root-mean-square (RMS), Zernike coefficients were calculated. As a CCD in our work we used WAT-103, and the framegrabber – Matrox Meteor II. The experimental sample of the SHS was able to analyse wavefront aberrations with the frequency of 25 Hz. The maximal P-V aberrations determinations are in the range of $\pm 8 \mu$. Sensitivity of the proposed SHS depends on the number of lenses on the aperture of the CCD window and for lenslet array 25×19 is about $\lambda/10$. Figure 25.7 provides the information about the user interface for the developed SHS.

25.4 Applications for High-Power Lasers

In this part we are going to give the examples of use of our adaptive optical system to correct for the radiation of some high-power pulsed lasers.

25.4.1 Adaptive Optics for ATLAS

For sure, we need to start from the experiment done on the ATLAS (Advanced Titanium:Sapphire Laser) facility at the Max-Planck-Institute of Quantum Optics, Garching, Germany – parameters of the laser pulse were – 1.5 J,

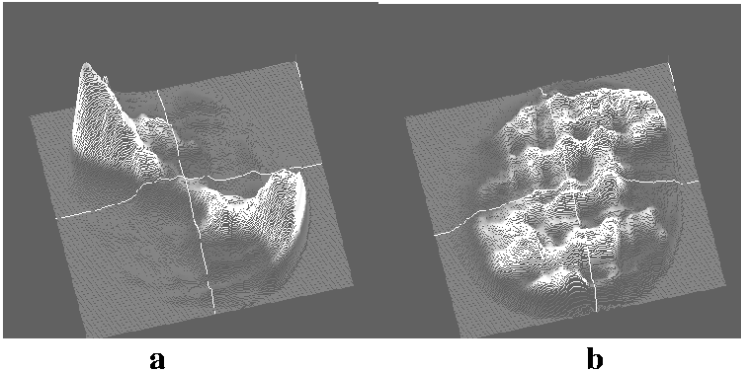


Fig. 25.8. Fluence profile before (a) and after (b) correction

790 nm and 130 fs and 10 Hz repetition rate. In order to clean a pulse from simultaneously present intensity profile modulations and wavefront aberrations, two deformable mirrors were needed. The first smoothens the intensity profile in a plane chosen downstream from the mirror. The second mirror located in this plane or close to it corrects the wavefront.

The first deformable mirror DM1 with an effective aperture of 30 mm and 17 electrodes arranged in two rings is placed in the beam line before the pulse makes the final transit through the amplifier and was placed before the compressor. The second deformable mirror DM2 with an effective aperture of 80 mm and 33 electrodes arranged in three rings is incorporated into the beam line shortly after the compressor. Both mirrors carry a high-reflective dielectric coating with a damage threshold of 1 J/cm^2 . When a plane mirror is used instead of DM1, the fluence profile in the compressor is double-peaked (see Fig. 25.8a) with a maximal energy density of 300 mJ/cm^2 at a pulse energy of 1.3 J. The use of DM1 effectively smoothens the fluence profile (see Fig. 25.8b). It turned out that the best electrode voltage settings can be manually found by trial and error rather quickly. This reduces the peak fluence to 90 mJ/cm^2 so that the pulse can be safely transmitted through the compressor up to a maximal output energy of 1.5 J.

The application of the second DM2 and the closed loop adaptive system with SHW remarkably improved the beam quality (Fig. 25.9) and also corroborated by performed neutron experiments in which solid deuterium targets were irradiated with ATLAS pulses. An increase in the neutron yield was observed by almost two orders of magnitude when wavefront-corrected pulses were used. It should be mentioned that the P-V of the initial aberrations to be corrected by the closed loop system was in the range of 7μ . The obtained Strehl ratio was close to 0.8 and the mean intensity inside the diffraction limited diameter is raised by more than a factor of ten from $\approx 10^{18}$ to $5 \times 10^{19} \text{ W/cm}^2$.

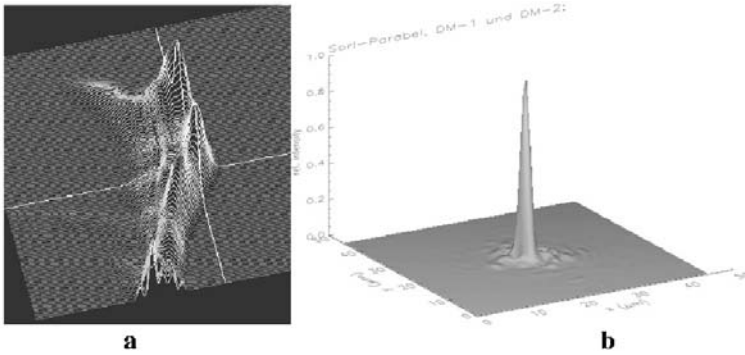


Fig. 25.9. Far field intensity distribution before (a) and after (b) correction

25.4.2 Adaptive Optics for LULI (Ecole Polytechnique, Paleseau, France)

The LULI 6×100 J laser is an in-line rod-amplifiers laser chain. A Nd:YLF oscillator delivers at a wavelength of $\lambda = 1053$ nm a train of temporally Gaussian pulses of 600 ps full width at half maximum (FWHM) duration. One of these pulses, selected by a Pockels cell, is amplified to about 50 J and split into 6 arms. Each beam is finally amplified to a maximum of 100 J with a beam diameter of 85 mm. The amplifier material is phosphate glass doped with Neodyme. The laser beams propagate over 30 m from the laser room to the experimental hall. Wavefront correction is applied to one beam, the interaction beam. It is focused on the plasma by a $f_1 = 500$ mm doublet. To monitor the far-field pattern of the interaction beam, we collect the transmitted beam after the focal point through a $\times 9$ telescope (two doublets: $f_2 = 250$ mm and $f_3 = 2200$ mm) associated with a $\times 4$ microscope objective. The images are recorded using a 12-bit CCD camera. Figure 25.10 presents the experimental set-up for close loop laser beam control. As a deformable mirror we used a 100 mm bimorph corrector with 31 electrodes placed in 3 rings. To measure the wavefront, two types of sensors were applied – SHS and

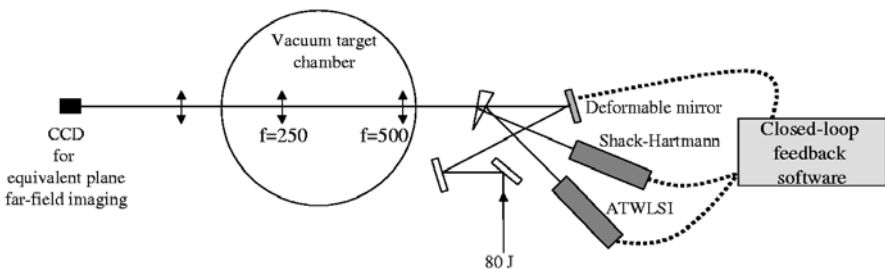


Fig. 25.10. Set-up of the wavefront correction

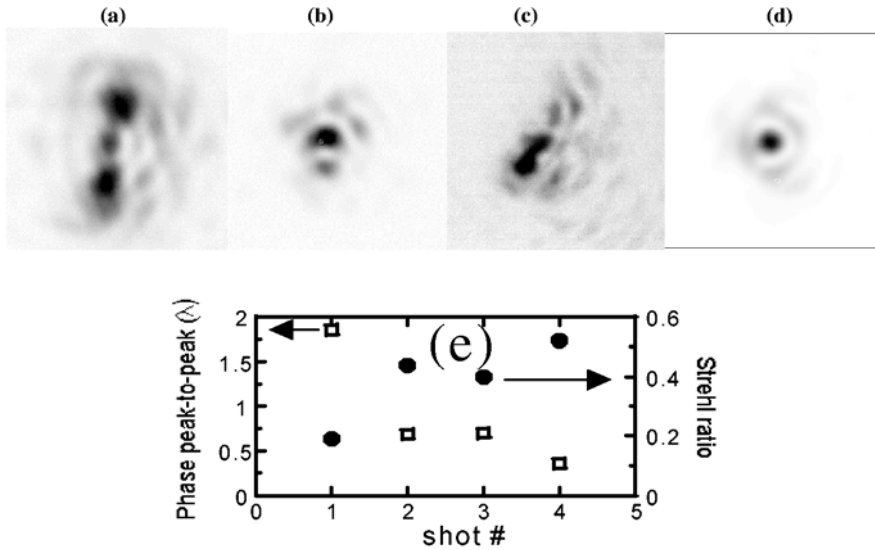


Fig. 25.11. (a–d) Far-field patterns of high-energy shots (50 J) during a converging sequence. (e) Corresponding evolution of the amplitude of the maximum wavefront phase distortion (*boxes*, left scale) and of the Strehl ratio (*filled circles*, right scale)

an achromatic three-wave lateral shearing interferometer (ATWLSI) [4]. The results of the laser beam correction are given on Fig. 25.11. The loop converges in less than four iterations, as shown in Fig. 25.11, where we display the wavefront phase and focal spot evolution along the convergence (starting from a mirror at rest) and we plot the evolution of the associated Strehl ratio and of the wavefront average P–V. Since the phase distortions of the laser chain are stable as long as it is fired at its nominal rate, the performances of the correction can be maintained for hours, once the convergence is achieved, by keeping the voltages that drive the deformable mirror fixed.

25.4.3 Adaptive Optics for Beijing Institute of Physics

The laser at the Institute of Physics in Beijing (China) had the following lasing parameters – output energy of the pulse – 0.2 J (expected 0.6 J), pulse duration – 50 fs, pulse rate – 10 Hz, output beam diameter – 35 mm (expected 50 mm). A deformable mirror was placed in the vacuum chamber right before the target chamber, while the SHS was put outside the vacuum chamber but after the deformable mirror (Fig. 25.12). In the experiment we used a 50 mm bimorph mirror with 31 control electrodes placed in three rings.

The results of the wavefront correction of such a laser are presented on Fig. 25.13. It is important to outline that the use of adaptive optics allowed us to improve the focusability of a femto second laser by a factor of 9.



Fig. 25.12. Experimental set-up of AO systems at the Chinese Institute of Physics

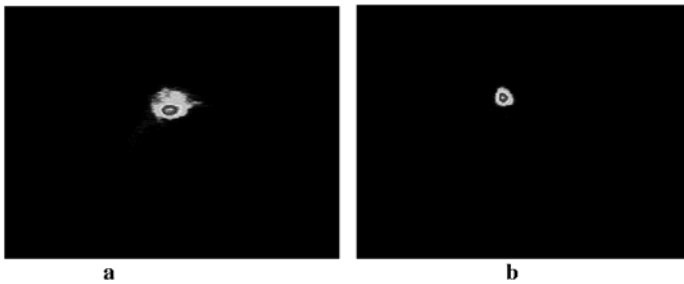


Fig. 25.13. Focal spot of the beam before (a) and after (b) correction. Increase of brightness more than 9 times

References

1. A. Kudryashov, H. Weber (eds.): Laser Resonators: Novel Design and Development. (SPIE Press 1999), 301 pp.
2. J.C. Dainty, A.V. Koryabin, A.V. Kudryashov: Low-order adaptive deformable mirror. *Appl. Opt.* **37**, 4663 (1998)
3. A.V. Kudryashov, V.I. Shaml'hausen: Semipassive bimorph flexible mirrors for atmospheric adaptive optics applications. *Opt. Eng.* **35**, 3064 (1996)
4. J.-C. Chanteloup, F. Druon, M. Nantel, A. Maksimchuk, G. Mourou: Single-shot wavefront measurements of high-intensity ultrashort laser pulses with a three-wave interferometer. *Opt. Lett.* **23**, 621 (1998)

26 Aberrations of a Master-Oscillator-Power-Amplifier Laser with Adaptive Optics Correction

I. Buske, H.-M. Heuck, P. Welp, and U. Wittrock

Münster University of Applied Sciences, Photonics Laboratory
Stegerwaldstr. 39, 48565 Steinfurt, Germany

Summary. Beam quality and efficiency of high-power solid state lasers are limited by aberrations of the active medium. The aberrations are due to temperature gradients in the laser crystals that in turn are due to the inevitable heat generation in the crystal. The aberrations lead to high diffraction losses of the laser resonator and reduced output power.

We use a birefringence-compensation scheme consisting of a relay-imaging telescope and a 90° polarization rotator to eliminate the stress-induced birefringence. In order to further improve the beam quality, the remaining aberrations of the thermal lens have to be eliminated. It is important to know the type and strength of the aberrations to determine the requirements of the adaptive mirror.

We present the investigation of aberrations in a MOPA cw-Nd:YVO₄/Nd:YAG laser system in which we employ an adaptive membrane mirror in order to compensate for the aberrations of the power amplifier. A genetic algorithm is used to control the adaptive mirror. A suitable power-in-the-bucket measurement behind a diffraction-limited aperture generates the beam quality signal for the feedback loop. The beam quality (M^2) is improved by a factor of 2.8.

26.1 Introduction

A main task of solid-state laser engineering is increasing the brightness of high power laser systems [1,2]. Here, brightness means the ratio of laser output power and beam quality parameter M^2 . The brightness of high-power solid state lasers is limited by aberrations of the active medium. Temperature gradients in the laser crystals cause a thermal lens with aberrations that in turn are due to the inevitable heat generation in the crystal. The aberrations lead to high diffraction losses of the laser resonator and reduced output power. The most important aberration in solid-state lasers results from thermal stress-induced birefringence. Inhomogeneous heat source density and inhomogeneous cooling, temperature dependence of thermal conductivity and laser cooling due to stimulated emission are other sources of aberrations. Analytical calculations and numerical simulations have shown that resonators with a good beam quality are very sensitive to aberrations. A reduction or compensation of thermo-optical aberrations dramatically improves the laser performance [3–5]. First experiments with low power lasers were done to compensate the aberration intracavity [6, 7].

In order to compensate the aberrations it is essential to know their type and strength. We investigated the aberrations of Nd:YAG laser rod which are pumped by cw arc-lamps and are used as laser amplifiers. The electrical pump power can be varied. The wavefront is measured by a Shack–Hartmann wavefront sensor and afterwards expanded in Zernike polynomial modes. The measured aberrations determine the requirements for the adaptive optical element. Deformable membrane mirrors [8, 9] as adaptive optical elements are suitable for high power lasers and low order aberration, even though they have a fairly limited stroke [10, 11].

Furthermore, we present additional measurements of a master-oscillator-power-amplifier (MOPA) cw-laser [12–14] in which we employ an adaptive membrane mirror in order to compensate for the aberrations of the power amplifier. With a suitable surface deformation of the mirror membrane we can pre-correct for the aberrations of the power amplifiers. Therefore, the pre-formed aberrations are afterwards compensated by the “real” aberrations of the Nd:YAG amplifier. A birefringence-compensation scheme [15, 16] consisting of a relay-imaging telescope and a quartz-rotator is used to cancel the depolarization of the two amplifiers. An adaptive optics closed-loop operation is built to optimize the beam quality by means of an optimization algorithm. The major advantage of this control technique is that the user neither has to know the strength of the aberrations, nor the required shape of the mirror surface. This simplifies the control loop, because the measurement of the wavefront distortion with a wavefront sensor is not necessary. The application of a genetic algorithm is leading to a fast search of an optimum in a very high parameter field. The genetic algorithm requires only a few seconds to find the optimum. Manually searching for the optimum voltage pattern would consume a lot of time. Genetic algorithm control is suitable for correction of static aberrations and slowly varying aberrations [17–19].

26.2 Measurements of Aberrations in Laser Crystals

26.2.1 Set-up

Figure 26.1 shows the layout for the measurement of the aberrations in Nd:YAG laser rods. The two laser rods are arc-lamp pumped. The thermal stress-induced birefringence of Nd:YAG crystals is compensated by a relay-imaging telescope and a quartz rotator located between the two laser rods. A HeNe probe laser with a different wavelength of 632.8 nm is required to avoid the influence due to the stimulated emission. The measurement wavelength for the Shack–Hartmann wavefront sensor is 632.8 nm. First the HeNe laser beam is focused by a lens to fit the beam propagation through the amplifier cavities. Then the HeNe laser is coupled into the Nd:YAG beam line through the high reflecting mirror for 1064 nm. The centre of the laser rods are relay-imaged by telescopes to the plane reserved for the adaptive mirror and to

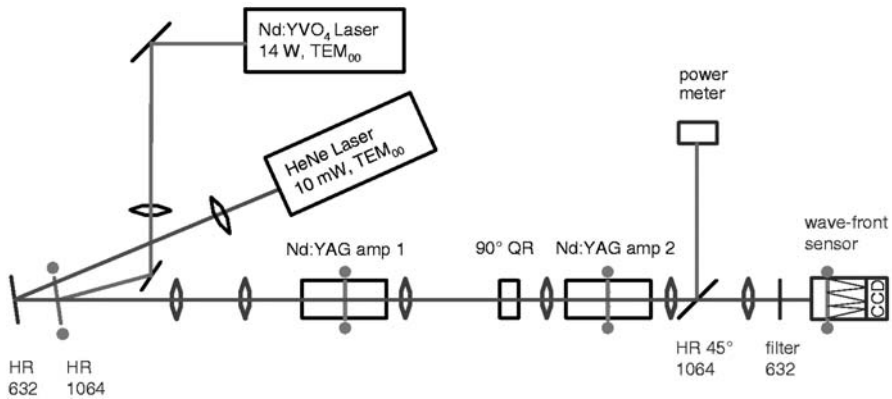


Fig. 26.1. Set-up for the measurement of the aberrations in the laser rods. A relay telescope between the two amplifiers and a 90° quartz rotator provides the birefringence compensation. The Nd:YVO₄ is amplified in the Nd:YAG rods and coupled out on a high reflecting mirror. The wavelength of the HeNe probe laser is the measurement wavelength for the Shack–Hartmann wavefront sensor

the plane of the Shack–Hartmann wavefront sensor. All corresponding relay planes are marked with circles. The quartz crystal rotates the polarization state of both wavelength 632 nm and 1064 nm at 90° . The Shack–Hartmann wavefront sensor is calibrated in the state of non-pumped amplifiers.

Additionally, a Nd:YVO₄ laser with TEM₀₀ mode and 14 W cw output power is integrated into the Nd:YAG beam line and amplified by the two Nd:YAG laser rods. The amplified laser beam is coupled out on a high reflecting mirror. This enables the investigation of the influence of laser cooling due to stimulated emission.

26.2.2 Measurement Results

In the state of a MOPA laser system the Nd:YVO₄ laser is amplified after the propagation through the Nd:YAG laser rods. A feature of Nd:YAG crystal is the thermal stress-induced birefringence under the condition of optical pumping. The results of birefringence are depolarization and a distorted wavefront, which in fact reduce the beam quality. With birefringence compensation, the depolarization decreases from 25–0.6%. Also, the optical power of the thermal lens is equal for the *s*- and *p*-polarization. A comparison shows that with birefringence compensation the M^2 value decreases by nearly a factor of 2. The total laser power stays constant at 90 W.

Afterwards, the aberrations of the Nd:YAG laser rods are measured by means of the HeNe probe laser. The first investigations are done with a non-operating Nd:YVO₄ laser. The Shack–Hartmann wavefront sensor expands the wavefront to Zernike polynomial modes up to the order of 10. In Fig. 26.2, the first 17 Zernike terms are plotted. The defocus term has the highest

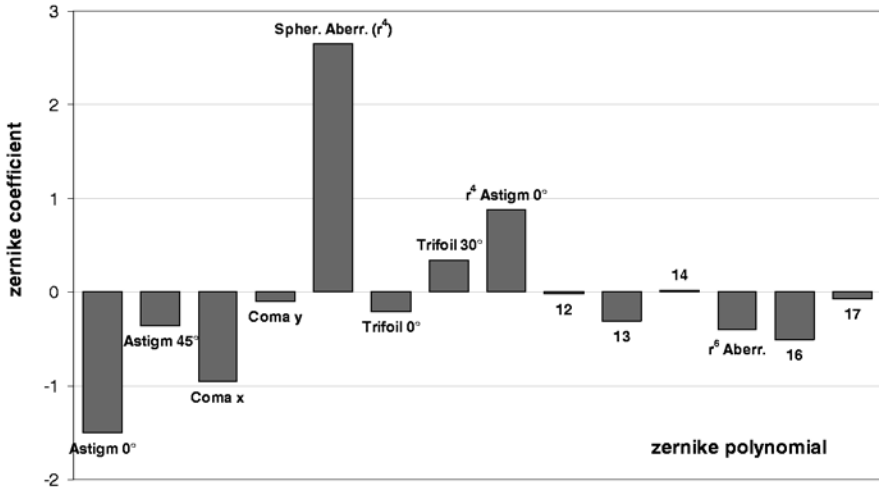


Fig. 26.2. The diagram shows the first 17 Zernike coefficients calculated from the measured wavefront after the laser amplification. The electrical pump power of the amplifiers was 31 kW. The defocus term with the highest Zernike coefficient of -33 is subtracted from the original measurement

Zernike coefficient of -33 . That is due to the strong thermal lens of the laser rods. In this example, the aberrations are measured with an electrical pump power of 31 kW. The defocus term was subtracted from the original measurement in the wavefront sensor software to resolve the residual aberration coefficients.

Four Zernike terms are especially high. They are astigmatism (Astigm 0°), second order astigmatism (r^4 Astigm 0°), coma x and spherical aberration (Spher. Aberr. (r^4)). The high astigmatism terms are caused by the orientation of the arc-lamps. All 4 arc-lamps are orientated parallel to the optical table in the same plane. Therefore the pump light distribution in the laser rod is not uniform. The outcome of this is a different heat power generation in the two planes of the laser rod which causes high astigmatism. Another important aberration term is the spherical aberration with a maximum Zernike coefficient of 2.7. Higher order Zernike terms have a coefficient less than 0.1. That is why in this case only the low order aberrations have to be compensated for an adaptive optics optimization.

Figure 26.3 shows the wavefront distortion of the Nd:YAG amplifiers pumped with an electrical pump power of 31 kW. The defocus term is subtracted. The residual wavefront aberration is drawn in 3-D. The peak-to-valley value is 6.5 waves. With a wavelength of the HeNe probe laser of 632 nm that corresponds to $4 \mu\text{m}$. One of the main Zernike terms is the spherical aberration with a coefficient of 2.7, but still just a fractional amount of only 8% of the high defocus term.

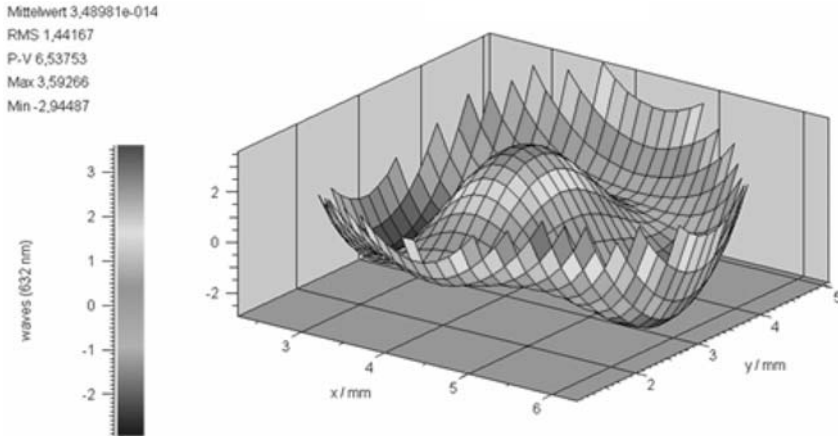


Fig. 26.3. Wavefront measured with a Shack–Hartmann wavefront sensor. The wavefront includes distortions of the Nd:YAG amplifiers pumped with an electrical pump power of 31 kW. The defocus Zernike term is subtracted. The peak-to-valley value is 6.5 waves corresponding to $4\ \mu\text{m}$

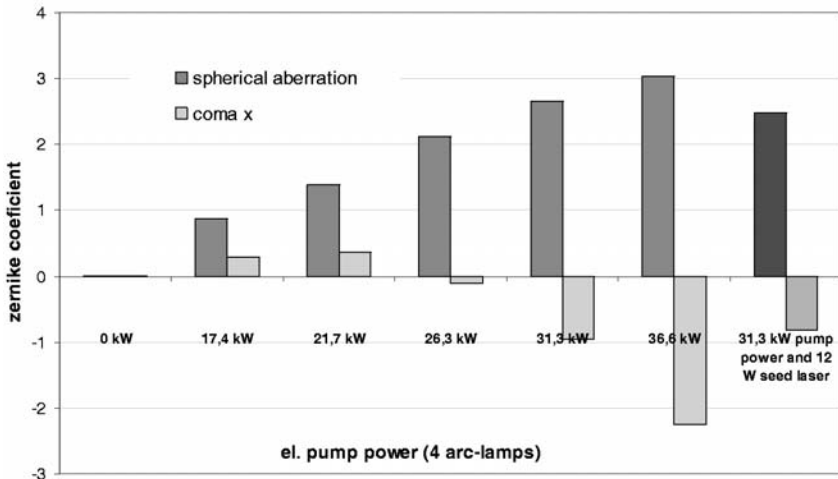


Fig. 26.4. The diagram shows the relation between the Zernike coefficients and the electrical pump power for the spherical and coma aberrations. The spherical aberration increases linear with the pump power. Meanwhile, coma x changes its sign at 24 kW pump power. The Zernike coefficients decrease slightly when the 12 W Nd:YVO₄ seed laser is operating due to the laser cooling process

The relation between the Zernike coefficients and the electrical pump power is printed in Fig. 26.4. Two of the main aberration types are investigated. The spherical aberration as the strongest aberration increases nearly linear with the pump power. But coma x is no longer linear and changes

the sign at 24 kW pump power. Other aberration terms with lower Zernike coefficients have a random behavior of their amplitude and sign during the variation of pump power. If the Nd:YVO₄ seed laser is running, the Zernike coefficients decrease slightly due to the laser cooling, a process of stimulated emission.

26.2.3 Requirements on Adaptive Mirrors

For a successful compensation of aberrations it has to be ensured that the adaptive optical element can produce the required wavefront. We used a deformable membrane mirror. For each electrical pump power of the laser rods the deformable mirror should establish the required deformation of the membrane. This deformation is calculated from the measurements above. Therefore, all Zernike coefficients are divided by 2 relating to the beam reflection. Also Zernike coefficients with an even-numbered radial order or angular frequency are inverted (e.g. defocus, astigmatism) due to usage of a relay-telescope.

Deformable membrane mirror show specific characteristics. Their dynamic behavior is like a low-pass filter and modes with an order higher than the number of actuators are not possible to generate. A telescope is often used to have the possibility of using adaptive mirrors with large diameters. The maximum deflection amplitude of a membrane mirror is proportional to the second of the membrane mirror diameter. In our set-up we apply a telescope. Therefore, the conjugated pupil is increased to 15.5 mm by a factor of 2.5. So we can use a 15 mm membrane mirror. The laser rod is 6.2 mm in diameter.

Figure 26.5 presents the required Zernike coefficients for the investigated MOPA system. The calculated Zernike coefficients are required in the plane of the adaptive mirror. Especially the strong spherical aberration term is difficult to generate with sufficient amplitude. Former investigations [10, 11] have shown that the deformable membrane mirror can only produce a spherical term in a range of 0.5 μm . From this, it follows that an optimization with a total compensation of the aberrations can not be expected in our MOPA laser system.

26.3 MOPA System with Closed-Loop Adaptive Optics

26.3.1 Set-Up

Figure 26.6 shows the set-up of our experiment. The master oscillator is a diode-pumped, almost diffraction-limited Nd:YVO₄ laser. The output power of 14 W is linearly polarized with a beam quality of $M^2 = 1.3$. This laser beam is projected onto the adaptive mirror. A 37 actuator deformable mirror was used with a maximum control voltage of about 250 V per actuator.

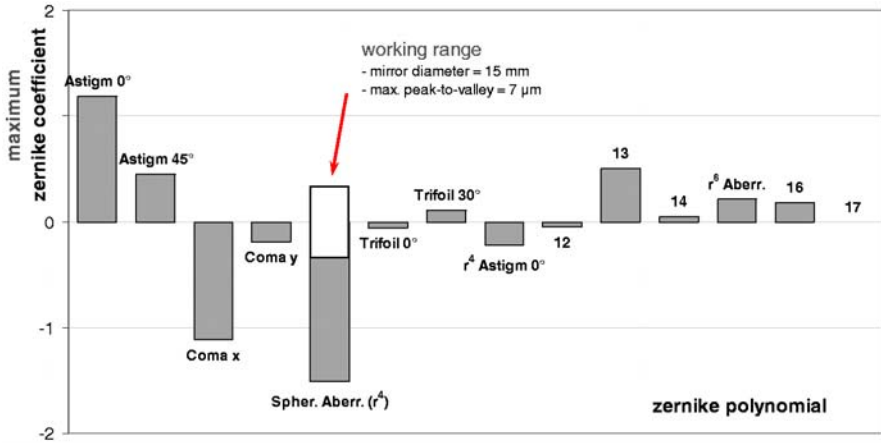


Fig. 26.5. Required Zernike coefficients of an adaptive optical element due to the aberrations caused by the Nd:YAG amplifiers. Maximum Zernike coefficients are determined for the working range of the amplifiers in the whole pump region. The maximal spherical aberration produced by the adaptive membrane mirror is not sufficient for optimal aberration compensation

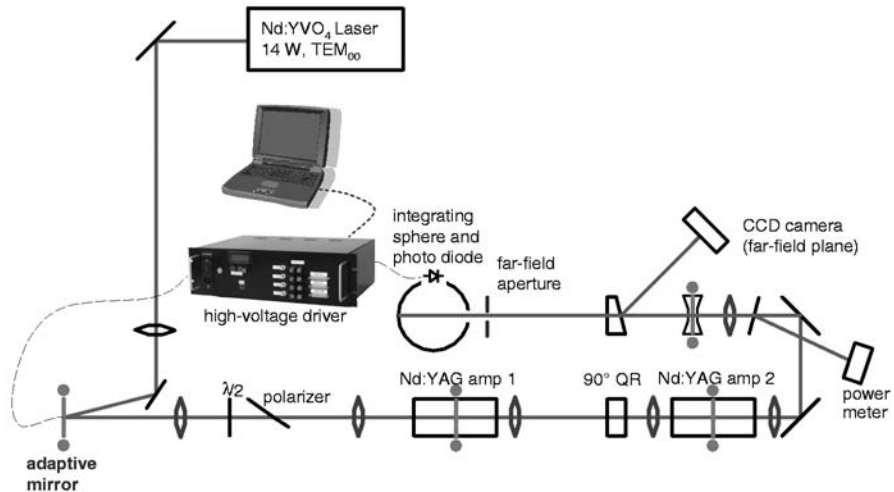


Fig. 26.6. Set-up for closed-loop adaptive optics operation. The plane of the adaptive mirror is defined as the near-field and is relay-imaged into the Nd:YAG amplifiers. The feedback signal for the optimization is measured with a photodiode behind the far-field aperture. The high-voltage driver (HVD-1) and a notebook with USB are used to calculate the optimum mirror shape by means of a genetic algorithm. The far-field intensity distribution is recorded with a CCD camera

With a suitable surface deformation of the mirror membrane we can pre-correct for the aberrations of the power amplifiers. We used a birefringence-compensation scheme consisting of the relay-imaging telescope with two $f = 229$ mm lenses and a quartz-rotator (90° QR) to eliminate the depolarization of the two amplifiers.

The plane of the adaptive mirror was relay-imaged into the amplifiers 1 and 2. We define the field on the adaptive mirror as the near-field. The far-field power-in-the-bucket measurement behind a diffraction-limited aperture is used to generate a beam quality signal. A CCD camera records the intensity distribution in the plane of the far-field aperture to visualize the optimization process online. Afterwards, the beam quality factor M^2 was determined by measuring the second moments of the intensity distribution in several planes of the caustic.

The control system [20] optimized the adaptive mirror deformation by means of a genetic algorithm. The main advantage of a genetic algorithm is the optimization of highly nonlinear systems using only one measured signal – the fitness signal. The general genetic algorithm was adapted to our specific problem. The fitness signal in our case was the power-in-the-bucket measurement.

The beam quality as a first approximation is proportional to the current of the photo diode in the integrating sphere. That means if the laser beam is diffraction-limited, the photo current reaches its maximum, and the applied voltage pattern at the electrodes produces the highest fitness signal. For all other patterns, the laser beam will not be diffraction-limited, therefore the transmitted power decreases, resulting in a lower fitness signal.

The optimum deformation of the membrane mirror can be acquired without knowledge of the real surface deformation. The algorithm automatically finds the pattern with the highest fitness respectively the best beam quality.

26.3.2 Experimental Results

First, we compensated for the most important effect of aberrations in laser crystals, the thermal stress-induced birefringence. The depolarization losses decrease to less than 0.6% in the compensated case. The birefringence compensated double-rod system behaves now like a single rod with twice the optical power, but without birefringence. With this method the beam quality can be improved in a first step. For the MOPA system the beam quality decreased from $M^2 = 8.1$ to $M^2 = 5$ at 90 W output power, a 40% improvement in beam quality.

In a second step the adaptive optics optimization process is started. In Fig. 26.7 (left hand side) the photo current as the fitness signal for the genetic algorithm is drawn during the optimization. The first region is characterized by the random voltage patterns applied to the mirror. In this operation mode the standard deviation of the fitness signals caused by the different mirror shapes is very high. The vertical lines label the sections of the iteration steps,

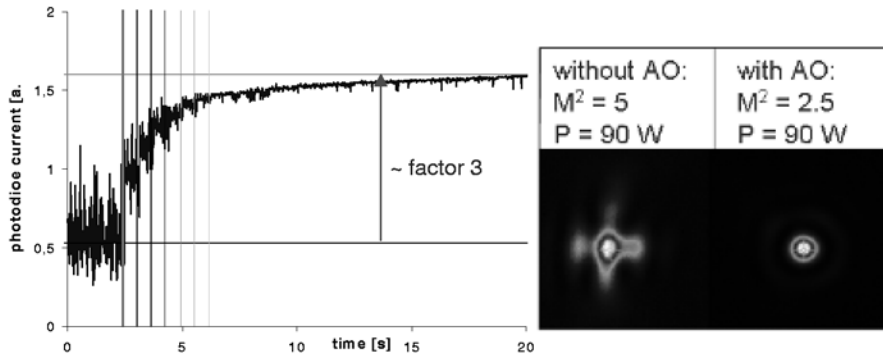


Fig. 26.7. On the left diagram the photo current as the feedback signal for the genetic algorithm is measured during the first 30 iteration steps. Vertical lines label the section of the iteration steps. The photodiode current improves by a factor of 3. The right figure shows the comparison between the far-field intensity distributions with and without adaptive optics optimization. With adaptive optics the beam quality M^2 is improved by a factor of 2 at 90 W laser output power

also known as generations. The optimization process requires about 20 iteration steps. The photodiode current improves from 0.6 to 1.7, a factor of 3 improvement.

On the right hand side, the comparison between the far-field intensity distributions with and without adaptive optics optimization is shown. Starting with the non-optimized beam the genetic algorithm searched for an optimum field distribution. That means an increase of power in the area around the center point. The near-field intensity distribution remains constant; therefore the beam quality is also optimized. With adaptive optics the beam quality M^2 is improved by a factor of 2 at 90 W laser output power. To check the repeatability of the genetic algorithm we restarted the optimization process 5 times. Former investigations [12] have shown the reliability of the algorithm.

26.4 Conclusion and Outlook

Aberrations of cw arc-lamp pumped Nd:YAG laser rods have been measured. Due to the strong thermal lens the highest Zernike coefficient is a defocus term. The strongest aberrations are low order aberrations with a total peak-to-valley of $4.1 \mu\text{m}$ at 31 kW electrical pump power. Four Zernike terms are especially high. These are astigmatism, second order astigmatism, coma x and spherical aberration with a peak-to-valley of around $3.4 \mu\text{m}$.

A near diffraction-limited closed-loop single-pass MOPA system with an output power of 90 W and an M^2 value of 2.5 was presented. The beam quality was improved by a factor of 2. We show that deformable membrane mirrors are suitable but not optimal for adaptive laser beam correction be-

cause of their poor ability to correct the spherical aberrations. Optimization based on the genetic algorithm is highly efficient to drive the deformable mirror in case of static or slowly-varying aberrations.

A Nd:YVO₄ laser resonator with adaptive optics compensation will be constructed. Additional investigations of adaptive mirrors are done to test the ability of intracavity application. A detailed analysis of different control algorithms for closed-loop systems is also in progress.

Acknowledgements

We are grateful to TRUMPF Laser GmbH + Co. KG for providing us with the Nd:YVO₄ laser.

References

1. W. Koechner: Solid-State Laser Engineering. 3rd edn. (Springer, Berlin Heidelberg New York 1992)
2. N. Hodgson, H. Weber: Optical Resonators (Springer, Berlin Heidelberg New York 1997)
3. N. Hodgson, H. Weber: Influence of spherical aberrations of the active medium on the performance of Nd:YAG lasers. *IEEE J. Quantum Electr.* **29**, 2497 (1993)
4. I. Buske, U. Wittrock: Simulations of optical resonators with aberrations. In: G.D. Love (ed.): Proceedings of the 2nd International Workshop on Adaptive Optics for Industry and Medicine (World Scientific, 1999) pp.155–162
5. I. Buske, J. Hüve, U. Wittrock: Einflüsse von Aberrationen auf optische Resonatoren. In: Frühjahrstagung der DPG, Poster Q 31.5., Berlin, 2001
6. W. Lubeight, G. Valentine, J. Girkin, E. Bente, D. Burns: Active transverse mode control and optimization of an all-solid-state laser using an intracavity adaptive-optic mirror. *Opt. Express* **10**, 550 (2002), <http://www.opticsexpress.org>
7. P. Welp, I. Buske, U. Wittrock: Intracavity use of adaptive mirror in Nd:YVO₄ and Nd:YAG laser. In: U. Wittrock (ed.): Proceedings of the 4rd International Workshop on Adaptive Optics for Industry and Medicine (Springer, Berlin Heidelberg New York 2005)
8. G.V. Vdovin, P.M. Sarro: Flexible mirror micromachined in silicon. *Appl. Opt.* **34**, 2968 (1995)
9. G. Vdovin, V. Kiyko: Intracavity control of a 200-W continuous-wave Nd:YAG laser by a micromachined deformable mirror. *Opt. Lett.* **26**, 1958 (2001)
10. L. Zhu, P.-C. Sun, D.-U. Bartsch, W.R. Freeman: Wavefront generation of Zernike polynomial modes with a micromachined membrane deformable mirror. *Appl. Opt.* **38**, 6019 (1999)
11. E.J. Fernandez, P. Artal: Membrane deformable mirror for adaptive optics: performance limits in visual optics. *Opt. Express* **11**, 1056 (2003), <http://www.opticsexpress.org>

12. I. Buske, U. Wittrock: Master-Oscillator-Power-Amplifier Laser with Adaptive Aberration Correction. In: S.R. Restaino, S.W. Teare (eds.): Proceedings of the 3rd international workshop on Adaptive Optics for Industry and Medicine (Starline Printing, 2002) pp.187–191
13. I. Buske, H.-M. Heuck, U. Wittrock: Master-Oscillator-Power-Amplifier Laser with Adaptive Aberration Correction. In: OSA Trends in Optics and Photonics (TOPS) **73**, Conference on Lasers and Electro-Optics, OSA Technical Digest, Postconference Edition (Optical Society of America, Washington DC 2002) pp.291–292
14. I. Buske, H.-M. Heuck, U. Wittrock: Adaptive Optics for Solid State Lasers. In: Europhysics Conference Abstracts. Vol.27E CS2-1-2-TUE, CLEO Europe 2003, Conference Digest (EPS, France 2003)
15. Q. Lü, N. Kugler, H. Weber, S. Dong, N. Müller, U. Wittrock: A novel approach for compensation of birefringence in cylindrical Nd:YAG rods. *Opt. Quantum Electr.* **28**, 57 (1996)
16. N. Kugler, S. Dong, Q. Lü, H. Weber: Investigation of the misalignment sensitivity of a birefringence-compensated two rod Nd:YAG laser. *Appl. Opt.* **36**, 9359 (1997)
17. D. Zeidler, S. Frey et. al.: Evolutionary algorithms and their application to optimal control studies. *Phys. Rev. A* **64**, 023420 (2001)
18. E. Schöneburg, F. Heinzmann, S. Feddersen: Genetische Algorithmen und Evolutionsstrategien: Eine Einführung in Theorie und Praxis der simulierten Evolution (Addison-Wesley, Bonn 1994)
19. D.E. Goldberg: Genetic Algorithms in Search, Optimization and Machine Learning (Addison-Wesley, 1989)
20. H.-M. Heuck, I. Buske, U. Buschmann, H. Krause, U. Wittrock: A novel micro-processor-controlled high-voltage driver for deformable mirrors. In: U. Wittrock (ed.): Proceedings of the 4th International Workshop on Adaptive Optics for Industry and Medicine (Springer, Berlin Heidelberg New York 2005)

27 Dynamic Aberrations Correction in an ICF Laser System

Y. Zhang, Z. Yang, C. Guan, H. Wang, P. Jiang, B. Xu, and W. Jiang

Chinese Academy of Sciences, Institute of Optics and Electronics
PO Box 350, Shuangliu, Chengdu 610209, PR China

Summary. The wavefront aberrations in inertial confinement fusion (ICF) laser system consists of static aberration such as material inhomogeneous, optical figure error and assemble error and so on, and dynamics aberration such as pumping induced thermal distortion, nonlinear effect induced index fluctuation and so on. Two Years ago, an adaptive optical system with 45 correction elements was established for the wavefront control of ICF laser system. And the static aberration correction had been realized. Recently this adaptive optical system has been used to correct the lamp pumping induced thermal distortion. For the nanosecond scale pulse laser output, the directly close-loop operation of adaptive optical system is impossible. So the pre-correction method of the wavefront control has been adopted. The dynamic thermal distortion pre-correction has been realized. The system also successfully corrected the compound aberration both of static and thermal aberration. This work would be helpful for shortening the operation period of the ICF laser system.

27.1 Introduction

In an ICF system, a high power laser pulse is transformed and focused on a target to initiate nuclear fusion reaction. The power density on focal plane is one of the most important performances. The wavefront aberrations existing in a laser beam will increase the focal spot size and decrease power density. These wavefront aberrations come from optical figuring errors of optical components and homogeneity problem of optical materials, optical components assembling errors, thermal distortion induced by pumping light and high power laser passing through, and turbulence in the optical path. At the Durham conference in 1999, we reported that an adaptive optical system was designed for the new ICF system project to correct the wavefront aberrations [1]. Later this adaptive optical system had been established and in 2001 we reported that this adaptive optical system was used to complete the static aberrations correction in our laboratory [2]. In this paper, we will give a description about some primitive experiments of the static aberration correction, and the dynamic aberration correction which induced from lamp pumping and compound aberrations both thermal distortion and static aberrations.

27.2 Adaptive Optical System

The block diagram of the inertial confinement fusion system is shown in Fig. 27.1. In the final ICF system, the correspondent adaptive optical system is integrated with it. The adaptive optical system consists of a 45-channel deformable mirror, two Shack–Hartmann wavefront sensors with 10×10 sub-apertures focal spots, a 45-channel high voltage amplifier and a wavefront control computer.

In Fig. 27.1, the laser pulse is generated and pre-amplified in the front-end laser system, then injected into the 4-pass slab main amplifier for further amplification. The deformable mirror and the Shack–Hartmann sensor I are located at the output end of the front-end system. The Shack–Hartmann sensor II is located between the end of the main amplifier and the frequency converting nonlinear optical crystals. It is used to measure the wavefront errors of the laser beam output from the main amplifier. The static wavefront aberration of the front-end laser and the pre-amplifier system can be corrected by closing the loop of the deformable mirror and the Shack–Hartmann sensor II by using the continuous or repeatable laser output come from the front-end laser oscillator. The dynamic wavefront errors of the main amplifier cannot be corrected in the laser pulse duration, but they can be recorded by the Shack–Hartmann sensor II. Through analyzing this recorded wavefront errors, the deviation data for pre-correction are obtained and are used to change the calibrated baseline of the Shack–Hartmann sensor II. Then by closing the loop between the deformable mirror and the Shack–Hartmann sensor II before the next laser shot, the dynamic wavefront error of the next shot can be compensated by the pre-correction of the deformable mirror and a flat wavefront of output laser beam can be obtained. The beam apertures (FWHM) of the pre-amplifier and the main amplifier are $70 \times 70 \text{ mm}^2$ and

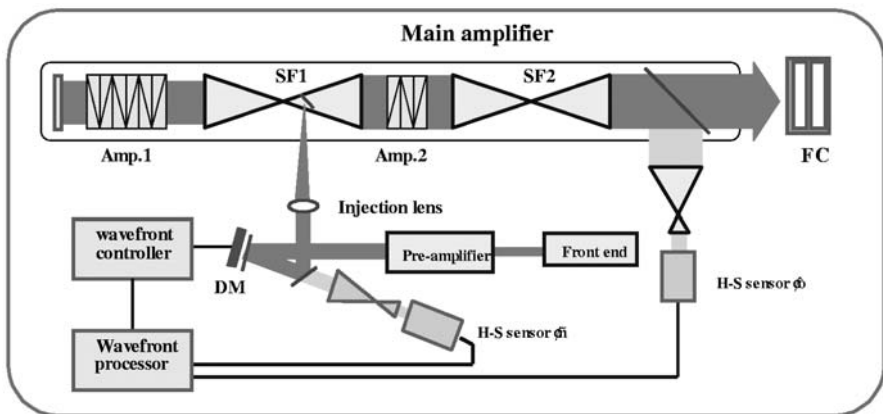


Fig. 27.1. The schema of the wavefront correction system

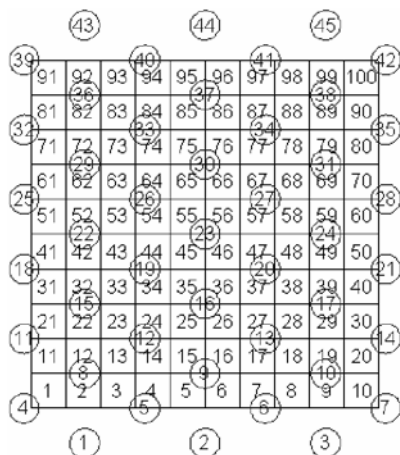


Fig. 27.2. The configuration of the actuators of the deformable mirror and sub-apertures of H-S sensor

$220 \times 220 \text{ mm}^2$ respectively. The output laser beam is sampled and condensed into $50 \times 50 \text{ mm}^2$ before it enters the Shack–Hartmann sensor II.

Several kinds of matched configuration between the actuators arrangement of the deformable mirror and the sub-apertures arrangement of the Shack–Hartmann wavefront sensor are compared to each other through computer simulations. Finally we chose one of them as shown in Fig. 27.2, because its correction ability is comparatively better, its reconstruction matrix has a relatively small condition number and a lower noise propagation factor [3].

We built a 45-channel deformable mirror for this system. The positions of all the actuators are shown in Fig. 27.2. The optical clear aperture of it is $70 \times 70 \text{ mm}$, the distance between the actuators is 15 mm and the dynamic range of each actuator is $\pm 3.5 \mu\text{m}$, as shown in Fig. 27.3.

Two Shack–Hartmann wavefront sensors are built for this wavefront control system. As shown in Fig. 27.1, the first Hartmann sensor was used to detect the wavefront aberrations that exist in the output laser beam from front-end laser system while the aberrations distribution of the whole system is needed for analysis. The second Hartmann sensor located at the output of the main amplifier was used to measure the static aberrations existing in the main amplifier and the dynamic aberration produced during the laser shot process. Except for the different optical apertures, the other parameters of these two sensors are the same. Both sensors use a 10×10 sub-apertures array with the same F -number. The measurement accuracy of the two sensors is about $\lambda/10$ at 1053 nm.

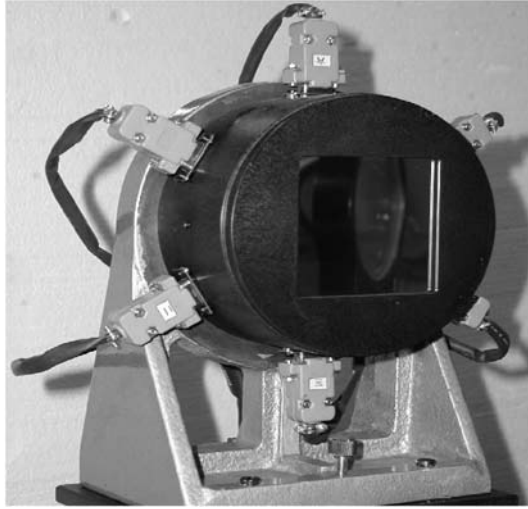


Fig. 27.3. 45 elements PZT deformable mirror

27.3 Experiments

At first, this system had been calibrated in our laboratory and a phase plate had been used to test the correction ability of this system [2]. Then this system was connected with the ICF laser system, as shown in Fig. 27.4.

Second step, the adaptive optical system was connected with the laser system. Before the correction system operated, the static and dynamic wavefront aberrations of the laser system were measured by those two Hartmann wavefront sensors. As shown in Fig. 27.5, the static aberration of the master amplifier is larger than the design tolerance of $\approx 8\lambda$ (1054 nm) in the preliminary state. It is obvious that there is a very big astigmatic aberration in the laser beam wavefront, the optical components in the main amplifier system need to be calibrated further. After further calibrating, the static aberrations of the master amplifier became small, as shown in Fig. 27.6.

After finely calibrating, the close-loop operation experiment for static aberrations correction had been performed. A pulse laser with 1 Hz and 100 mJ output coming from the front-end is used as a beacon, the static aberration was corrected by the closed loop operation between the deformable mirror and the Hartmann wavefront sensor II. After close-loop correction, the residual static aberration became small as shown in Fig. 27.7. So the adaptive optical system can correct the static aberrations in the laser system effectively.

Before correcting the thermal dynamic aberration, the dynamic aberrations in the master amplifier should be measured and analyzed. If the master amplifier is keeping in stable state after fine calibration, the measurement results show that the static aberrations keep in stable state also. The fluc-

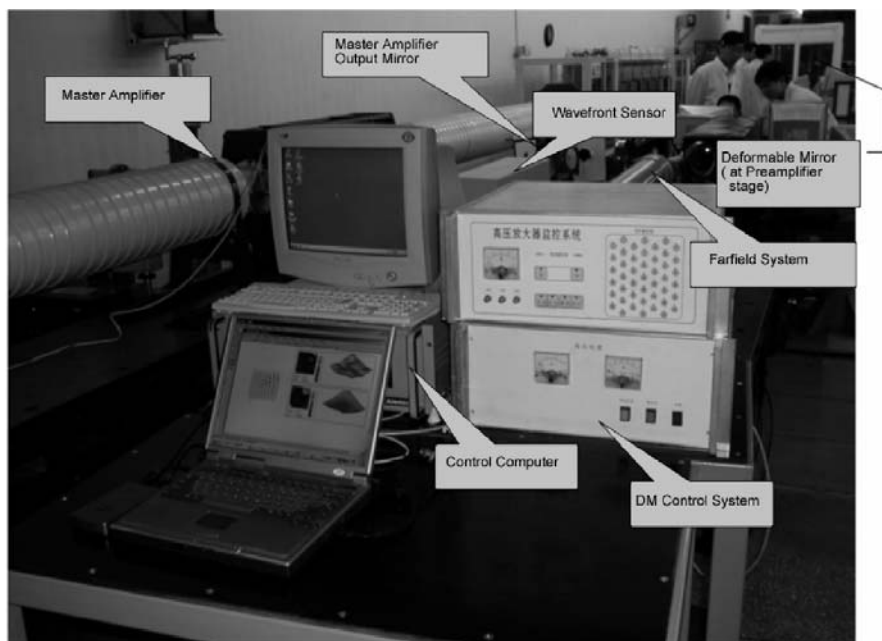


Fig. 27.4. The adaptive optical system connected with the laser system in experimental hall

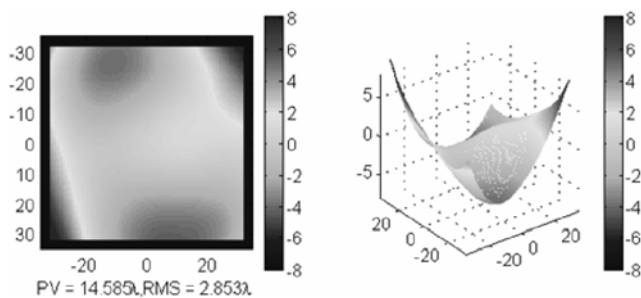


Fig. 27.5. The static aberration of master amplifier in laser system

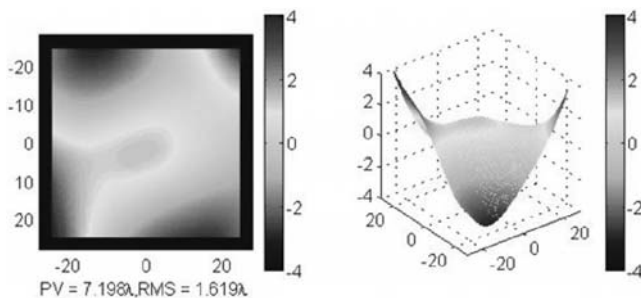


Fig. 27.6. The static aberration of master amplifier after carefully calibrating

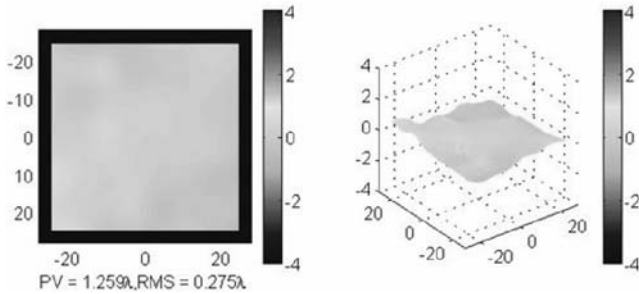


Fig. 27.7. The residual static aberration of master system after close-loop correction

tuation of the static peak-valley aberrations is kept in about $\pm 0.1\lambda$. So the static aberrations are measured in stable state without lamp pumping at first, then the mixture aberration is measured in lamp pumping condition, and last the dynamic aberration could be obtained by subtracting the static aberrations from that mixture aberration.

Because it is impossible to correct the dynamic aberration in a laser pulse via the method of close-loop directly, the pre-correction method had been adapted. Therefore the differences and correlation of dynamic aberrations between adjacent laser pulses is important for the correction result. Obviously, the result is so much the better the smaller the difference is. The difference also limits the correction ability of the pre-correction method. Figures 27.8a–c show that the dynamic aberration induced from lamps pumping at first shot in completely cold master cavity condition. These measurement results show that the biggest difference reached $\approx 0.6\lambda$ peak-valley error in different first shots. Because this difference is in the error tolerance, it implies that pre-correction method would operate effectively while laser system keep in cold cavity and stable state.

And the thermal dynamic aberration is a kind of slowly changing aberration, the different interval time laser pulse shots would have different residual thermal dynamic aberrations. This factor also affects on the correction result. Figure 27.9 shows the thermal dynamic aberration recovering process in natural condition. After laser shot in cold cavity condition 10 min later, the thermal dynamic aberration will recover $\approx 50\%$. To shorten the laser shots interval time would improve the operation efficiency of the ICF laser system. Too short shots interval time will have bigger accumulation residual thermal dynamic aberration in pre-correction way which aberration will degrade the power density on the focus plane. So it is a dilemma problem. A trade-off between efficiency and optical quality is needed. Further experiments would be necessary to find the optimal equilibrium point.

Figure 27.10 shows the thermal dynamic aberrations of adjacent laser pulse shots in 20 min interval time. The result shows that there is an $\approx 1.1\lambda$ difference in thermal aberration because of the thermal aberration accumula-

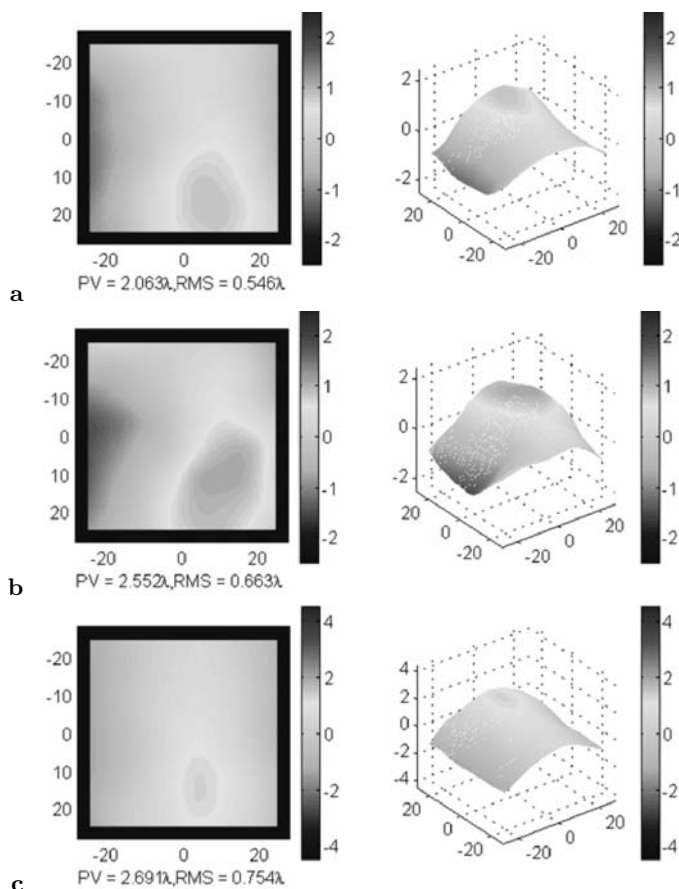


Fig. 27.8. The dynamic aberration induced from lamps pumping at first shot in completely cold master cavity condition

tion. And this difference part could not be compensated by the pre-correction method.

Based on the above works, the experiment for the thermal dynamic aberration compensating in the pre-correction way had been operated. At the first shot in cold cavity condition, the Hartmann sensor II grabbed the thermal dynamic aberration and sent it to the control computer. In a second step, the 45 elements deformable mirror (DM) generated the conjugation wavefront of this thermal aberration under the control of a computer, as shown in Fig. 27.11a. About 20 min later, the laser system shot the next laser pulse and its thermal aberration was measured, as shown in Fig. 27.11b. The residual thermal aberration is $\approx 1.4\lambda$ peak-valley which is slightly bigger than the $\approx 1.1\lambda$ difference between those shown in Fig. 27.10a and b. It means that the correlative thermal aberration between these adjacent shots had been

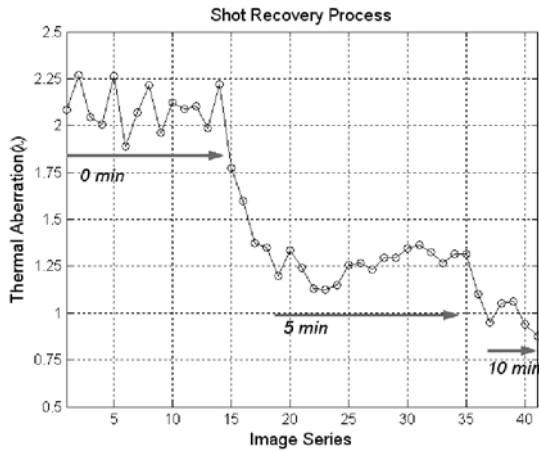


Fig. 27.9. The thermal dynamic aberration recovering process in natural condition

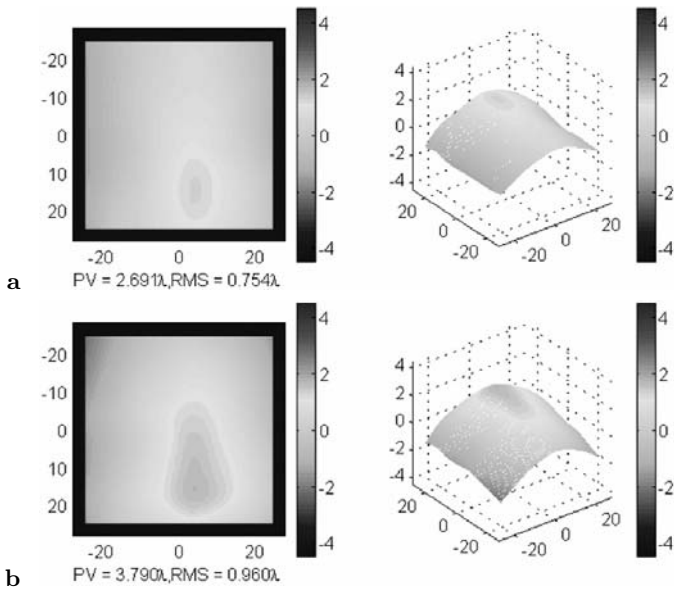


Fig. 27.10. (a) The thermal dynamic aberration of first shot in cold cavity condition. (b) The thermal dynamic aberration of second shot after 20 min interval time

compensated very well. Then the driving voltage on the DM was released and the Hartmann sensor II grabbed the thermal dynamic aberration of the third shot after next 20 min later, as shown in Fig. 27.11c. This thermal aberration is much bigger than that in cold cavity condition because of thermal accumulation effect. The third 20 min later, the driving voltage was added on

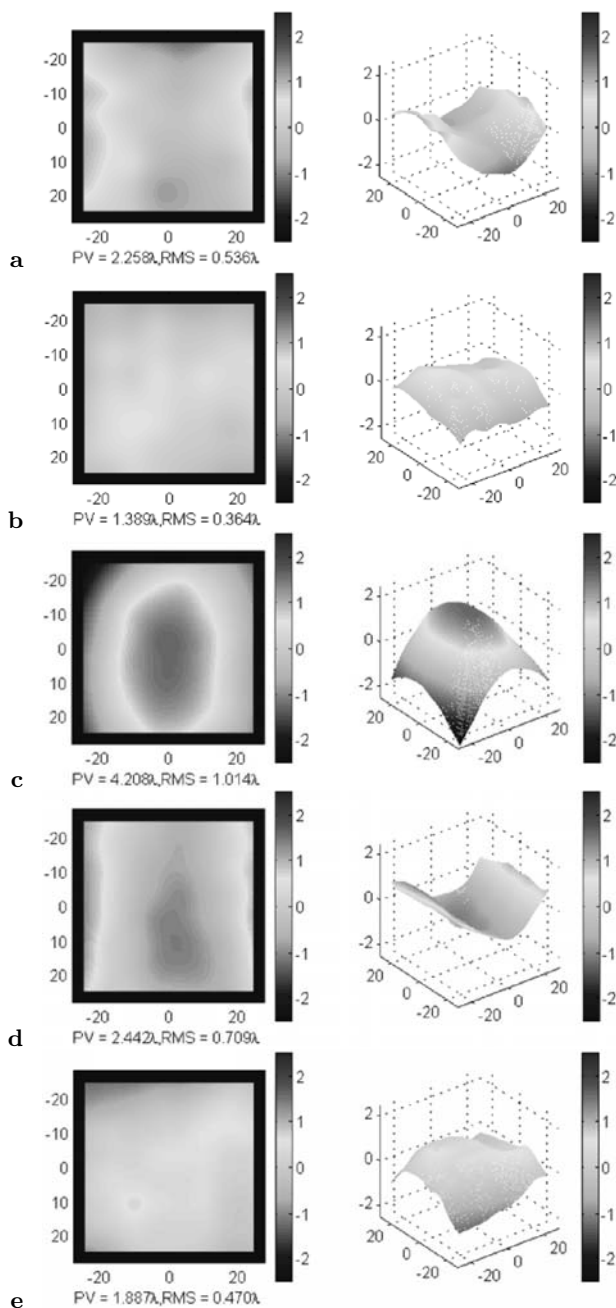


Fig. 27.11. (a) The conjugation wavefront of the thermal aberration generated by DM. (b) The thermal aberration in next shot after compensated by DM. (c) The thermal aberration in third shots without compensation. (d) The conjugation wavefront of the thermal aberration generated by DM. (e) The thermal aberration in next shot after compensated by DM

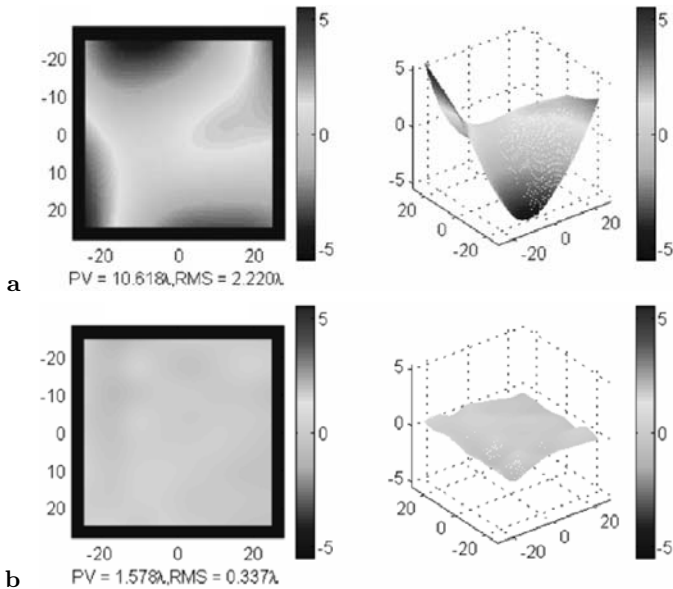


Fig. 27.12. (a) The static and thermal dynamic compound aberration. (b) The residual compound aberration after compensation

DM again and generated the conjugation wavefront as shown in Fig. 27.11d. The laser system shot again and its thermal aberration was measured, shown in Fig. 27.11e. This residual thermal aberration is bigger than that shown in Fig. 27.11b. From this experiment, it could be found that the thermal accumulation effect is the important one of the factors which have an affect on the compensation result. Based on the static aberration and the thermal dynamic aberration compensation experiments, the compound aberrations compensating experiment was undertaken. Before deformable mirror compensating, the static and the thermal dynamic compound aberration is shown in Fig. 27.12a. After compensating, the compound aberration is shown in Fig. 27.12b. This experiment demonstrates that this adaptive optical system can correct both static and thermal dynamic aberrations in the ICF laser system effectively.

27.4 Conclusions

A 45 elements adaptive optical system had been established for the static and thermal dynamic aberration compensating in the ICF laser system. The system compensated the static aberration of the ICF laser system successfully. For the thermal aberration compensation, the pre-correcting method operated effectively in an appropriated laser shot interval time condition. And the compound aberration of the static and thermal dynamic aberration was compensated successfully.

References

1. W. Jiang, Y. Zhang, H. Xian, C. Guan, N. Ling: A wavefront correction system for inertial confinement fusion. In: G.D. Love (ed.): Proceedings of the 2nd International Workshop on Adaptive Optics for Industry and Medicine (World Scientific 1999)
2. Y. Zhang, N. Ling, Z. Yang, H. Duan, S. Jiao, C. Guan, W. Jiang: An adaptive optical system for ICF application. Proc. SPIE **4494**, 96 (2001)

28 Adaptive Shaping of High-Power Broadband Femtosecond Laser Pulses

T. Witting¹, G. Tsilimis¹, J. Kutzner¹, H. Zacharias¹, M. Köller²,
and H. Maurer²

¹ Westfälische Wilhelms-Universität Münster, Physikalisches Institut
Wilhelm-Klemm-Str. 10, 48149 Münster, Germany

² Institut für Numerische und instrumentelle Mathematik
Westfälische Wilhelms-Universität Münster
Einsteinstr. 62, 48149 Münster, Germany

Summary. We demonstrate the implementation of a feedback controlled pulse shaping device in a femtosecond high-power Ti:sapphire laser system. The laser system consists of a mirror dispersion controlled oscillator and a multipass amplifier with a pairing double prism compressor. The system provides pulses with a duration of 30 fs and an energy of up to 1.2 mJ per pulse at 1 kHz repetition rate. The phase distorted output pulses are phase modulated with a high resolution spatial light modulator (SLM). The pulse shaper consists of an all-reflective zero-dispersion compressor equipped with a liquid crystal array. For adaptive compression of the amplified pulses a feedback loop is implemented. A two-photon process is used to monitor the temporal pulse characteristics. To achieve the shortest possible pulse an evolutionary algorithm controls the pulse shaper utilizing the two-photon signal as feedback. With this set-up transform limited pulses are achieved. Detailed investigations of algorithm parameters and their effect on convergence behaviour have been performed and are compared with the experimental findings.

28.1 Introduction

In the last years quantum coherent control in the field of laser matter interactions gained much interest [1–4]. It became possible to use pulse shaping devices to manipulate the spectral phase of femtosecond laser pulses [5] which can be used to imprint a phase onto excited wave packets of a molecule or of any other physical system. By utilizing a closed-loop arrangement including the pulse shaper and a non-deterministic optimization algorithm, which uses the output of the experiment as feedback, control of experiments became possible without knowledge of the system's Hamiltonian.

We present the implementation of a high resolution pulse shaping device which is capable of shaping high-power broadband femtosecond laser pulses. As a first application we used a two-photon experiment to adaptively compress phase distorted pulses to their transform limit. The settings of the optimization algorithm are examined by simulations of the experiment.

28.2 Experimental

28.2.1 Laser System

The passively soft aperture Kerr-lens mode-locked Ti:sapphire oscillator (Femtsource PRO, Femtolasers) is equipped with chirped mirrors to control the round trip dispersion in the cavity [6]. It delivers pulses with an energy of $E_{\text{osc}} \geq 2 \text{ nJ}$ per pulse and a spectral bandwidth of $\Delta\lambda_{\text{osc}} \geq 100 \text{ nm}$ (FWHM) at a repetition rate of 77 MHz. These pulses can externally be compressed to 12 fs using additional chirped mirrors. The amplifier system (OMEGA 1000, Femtolasers) is a Ti:sapphire multi pass amplifier operating at a repetition rate of 1 kHz [7]. For amplification the oscillator pulses are stretched to 10 ps by material dispersion in a SF57 glass block. After a 4-pass amplification a pockels cell is used to pick pulses with a repetition rate of 1 kHz. The remaining pulse is further amplified in a 5-pass amplification stage. After the last five passes the pulses have an energy of up to $E_{\text{amp}} \approx 1.2 \text{ mJ}$. The amplified pulses are compressed to $\Delta t \approx 30 \text{ fs}$ in a high-throughput folded pairing double prisms compressor. For additional compensation of the negative third-order dispersion mainly caused by the compressor prisms specially designed chirped mirrors are used for pre-compensation. However, the output pulses still show phase distortions and are non-transform limited. This is caused by un-compensated higher order dispersion in the laser crystal and other optical components in the amplifier system. The residual bandwidth of the pulses after amplification is $\Delta\lambda_{\text{amp}} = 45 \text{ nm}$ (FWHM). Assuming a Gaussian pulse profile the possible transform-limited pulse duration referring to this bandwidth is $\Delta t = 20.9 \text{ fs}$.

28.2.2 Pulse Shaping Device

Control of the phase and the amplitude of a femtosecond laser pulse cannot be implemented in the temporal regime due to the ultrafast timescale. Therefore the pulse is modulated in the spectral domain. An arbitrary modulation of the pulse spectrum $E_{\text{in}}(\omega)$ by a transfer function $H(\omega)$ leads to an output spectrum $E_{\text{out}}(\omega) = H(\omega)E_{\text{in}}(\omega)$. It is directly related to the temporal pulse characteristics $E_{\text{out}}(t)$ via a Fourier transform. Mainly three different types of devices for pulse shaping in the spectral domain have been implemented: acousto optic modulators [8], deformable mirror [9] and liquid crystal based systems. Acousto optic modulators have the disadvantage of a low damage threshold $I_{\text{d}} \approx 100 \text{ MW/cm}^2$ of the active material. Therefore they cannot be used for high-power pulses. Devices based on deformable mirrors have the disadvantage of a small number of driving actuators limiting the number of parameters for pulse modulation.

We have implemented a pulse shaping device based on a liquid crystal (LCD) array. The LCD array is inserted in the Fourier plane of an all-reflective zero-dispersion compressor in $4f$ arrangement. The scheme of the

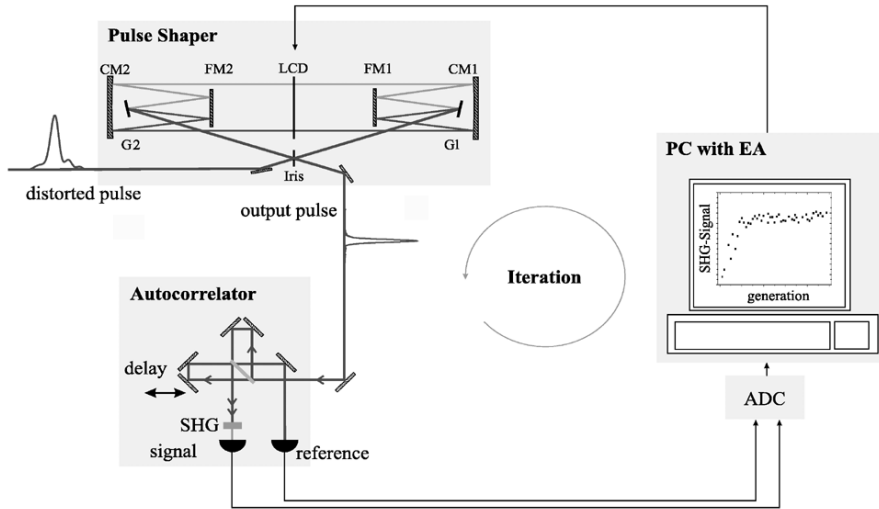


Fig. 28.1. Closed loop set-up for adaptive pulse compression

compressor is shown in Fig. 28.1. The pulse is dispersed by a gold coated holographic grating (G1) with 1200 lines/mm. A plane, dielectrically coated mirror (FM1) guides the spectrum to a cylindrical focussing mirror (CM1) with a focal length of $f = 300$ mm. The mirrors CM2 and FM2 and the grating G2 reverse the spectral fanning of the laser beam. The folded set-up minimizes aberrations [10]. In the Fourier plane a 640 pixel LCD-array (SLM-S 640/12, Jenoptik) is used to manipulate the spectral phase of the pulse leaving the amplitude unchanged. The mask has a size of 64×10 mm. The pixels have a width of $97 \mu\text{m}$ and are separated by $3 \mu\text{m}$ gaps. Due to the large active area and the high damage threshold of $I_d = 300 \text{ GW/cm}^2$ this device can be used to shape high-power pulses up to a peak power of 2 TW enabling pure phase control experiments in the high-power regime. It should be noted that the overall transmission of the device amounts to 60%.

28.2.3 Pulse Compression

As a first application of the pulse shaping device adaptive pulse compression is performed using an evolutionary algorithm (EA) controlled closed-loop arrangement including the pulse shaper and a two-photon experiment (Fig. 28.1). The laser pulses from the amplifier system are phase modulated by the pulse shaping device. The modulated pulse is detected by a nonlinear detector. The signal is digitized by a 16 bit analog-to-digital converter (NuDAQ PCI-9118HR, Adlink) providing the feedback for the optimization algorithm.

Computer-generated phase patterns are applied to the LCD array. A GaAsP photodiode (G1115, Hamamatsu) with a bandgap $E_{\text{gap}} \geq 1.55 \text{ eV}$

is used as a nonlinear detection device instead of frequency doubling in a nonlinear crystal [11]. The two-photon signal $I_{2\omega}$ is proportional to $|E(t)|^4$. Thus, the shorter the pulse duration the higher the electronic signal. Monitoring the diode signal and using it as feedback for the optimization algorithm allows the adaptive compression of the phase distorted pulses from the amplifier system. We additionally monitor the fundamental signal in order to be independent from laser pulse energy fluctuations. The optimization algorithm addresses phases to the mask and iteratively tries to optimize the outcome of the “SHG” experiment. After a few ten iterations the algorithm converges to the optimal phase settings. To check the results from the optimization runs, the temporal pulse characteristics before and after optimization are measured by interferometric autocorrelation with the same two-photon diode [12].

28.3 Optimization Algorithm

For optimization of the pulse shape an evolutionary algorithm is used [13]. These type of algorithm work without utilizing local attributes as continuity or differentiability of the objective function which can be either a mathematical term or a physical experiment. Evolutionary algorithms are a very robust tool for searching in large parameter spaces with many local extrema. Basically these algorithms make use of the biological principles of selection, recombination and mutation to find the global optimum of the objective function. The optimization procedure is based on the artificial evolution of populations which are comprised of a set of N individuals. Every individual consists of some variables (termed genes) which define a laser pulse modulation. The experimental outcome of every individual is determined as objective function and ranked by a nonlinear fitness function

$$f(n) = \frac{Nx^{n-1}}{\sum_{i=0}^{N-1} x^i}, \quad p(x) = (S - N)x^{N-1} + Sx^{N-2} + \dots + Sx + S,$$

with x given by the real solution of $p(x) = 0$. The parameter S denotes the selection pressure, i.e. the reproduction probability of the best individual in proportion to the average reproduction probability of a population. After measuring the objective function and ranking of all individuals of one population descendants are created by recombination of two individuals. The parents are selected with a probability according to their fitness values and recombined by intermediate recombination: The variables of the parents define two edges of a cuboid, wherein the variables x of the recombined individuals are chosen randomly. In order to explore the whole search space the algorithm introduces a mutation \tilde{x} of the variable x :

$$\tilde{x} = x + sM(b - a)2^{-16u}, \quad s \in \{-1, 1\} \text{ random}, \quad u \in [0, 1] \text{ random}.$$

The size of the mutation step of a variable x is randomly chosen and bound by the mutation range M , with a larger probability for small mutation steps and a lower probability for large mutation steps. The interval $[a, b]$ is the domain of the variable x . The mutation range M designates the largest possible mutation-step in proportion to the domain $[a, b]$ of the according variable x . In this way the new population is constructed completely by offspring, a cloning of individuals does not occur. Again the objective values of the population are determined and the whole procedure starts over again.

28.3.1 Simulation of the Experiment

In order to explore the performance of the evolutionary optimization algorithm we simulated the SHG experiment numerically. Starting point is a laser pulse defined by a discrete spectrum $E(\omega_j)$ with 640 frequency components, which represent the pixels of the phase modulator, and showing a Gaussian amplitude $A(\omega_j)$ with 45 nm bandwidth and a spectral phase $\phi(\omega_j)$:

$$E(\omega_j) = A(\omega_j)e^{i\phi(\omega_j)},$$

where

$$\phi(\omega_j) = \sum_{n=2}^5 \varphi_n \frac{(\omega_j - \omega_0)^n}{n!}, \quad j = 1, \dots, 640.$$

ω_0 denotes the center angular frequency of the laser pulse. As mentioned before the laser pulses from the amplifier are not transform limited, therefore we set the phase of the laser pulses ϕ_L with $\varphi_n = a_n \neq 0$ according to the coefficients determined from experiments. The phase modulation imposed by the pulse shaper is introduced by adding a phase $\phi_{\text{SLM}}(\omega_j)$. Consequently, the laser pulse after shaping assumes:

$$E'(\omega_j) = A(\omega_j)e^{i[\phi_L(\omega_j) + \phi_{\text{SLM}}(\omega_j)]}.$$

This simulation thus significantly extends an earlier analysis where only the second order Taylor coefficient φ_2 of the phase has been examined [14]. We tested two different approaches to parametrize the phase modulation ϕ_{SLM} . Either the phase ϕ_{SLM} is defined by a Taylor polynomial and the 4 coefficients $\varphi_n = b_n$, ($n = 2, \dots, 5$) or by a spline interpolation over 8 equally positioned grid points in the spectral domain.

In order to obtain the SHG intensity corresponding to a specific phase modulation by ϕ_{SLM} the modulated pulse $E'(\omega_j)$ is transformed to the time domain $E(t_j)$ by a Fast Fourier Transform routine [15] and integrated over time:

$$E(t_j) = \text{FFT}^{-1}(E'(\omega_j)) \quad \Rightarrow \quad I_{\text{SHG}} \propto \sum_{j=1}^{640} I^2(t_j) \propto \sum_{j=1}^{640} (|E(t_j)|^2)^2.$$

Finally, I_{SHG} is the objective function for the optimization algorithm. On a contemporary PC one optimization run with 30 individuals and extending to 150 generations takes a few minutes. This allows detailed studies of the effects of different algorithm parameters with significant statistics by averaging over 50 optimization runs for every algorithm parameter setting. Specifically, we analyzed the influence of the settings for the selection pressure S and the mutation range M on convergence behavior and speed.

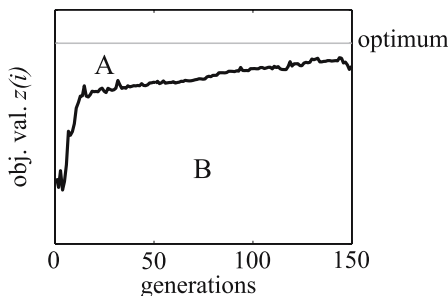
28.3.2 Algorithm Performance

To benchmark the results of the simulation two criteria are used to judge the optimization runs. The weighted sum σ describes the deviation of results $z(n)$ of N optimization runs to the known optimum z^* as a measure of convergence quality:

$$\sigma = \frac{1}{N} \sum_{n=1}^N \left(1 - \frac{z(n)}{z^*} \right)^2 .$$

The faster the results approach the global optimum z^* the smaller the deviation σ . Secondly, the area comparison criterion q judges the convergence speed:

$$q = \frac{A}{B} = \frac{\sum_{i=1}^I (z^* - z(i))}{\sum_{i=1}^I z(i)} .$$



The area comparison criterion q is defined as the ratio of the area A above to the area B below the graph of the best objective values $z(i)$ as indicated in the figure above. This area A is bound by the known global optimum value z^* . The faster the convergence the smaller the ratio $q = A/B$.

We tested several control parameters with 50 optimization runs each. It turned out that the mutation steps should be chosen not too small to allow a search of the whole search space. On the other hand they should not be too large to allow concentration of the search around the optimum. Reasonable values for the mutation range M are between 5 and 15% in relation to the domain of the according variable. The setting of the selection pressure is more sensitive and crucial for a good convergence. In Figs. 28.2 and 28.3 the results from the parameter studies are plotted.

The selection pressure, which designates the reproduction probability of the best individual in relation to the average probability, is found to be suit-

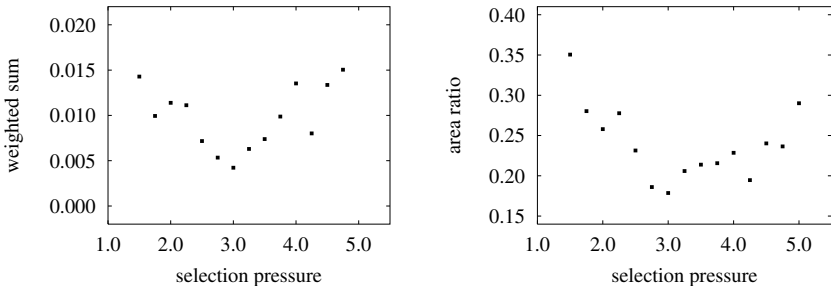


Fig. 28.2. Analysis of selection pressure at a mutation range of 0.05 for the Taylor phase parametrization

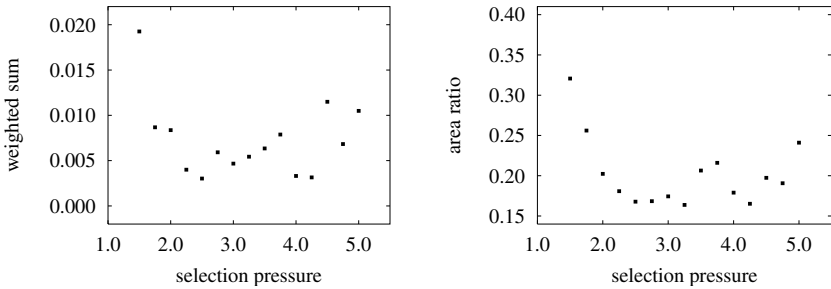


Fig. 28.3. Analysis of selection pressure at a mutation range of 0.05 for the spline phase parametrization approach

able in a range of 2.25–3.25. For a too low selection pressure S the search is less distinctive, thus leading to poor convergence which is revealed by both criteria. Decrease of selection pressure S down to 1 leads to random searching without any progress by evolution. On the other hand for a too large selection pressure S the algorithm’s search becomes stuck in local suboptimal solutions, which hardly can be left. In this case the optimization results become random according to the local optimum which is caught accidentally. Besides the optimal range of M , it can be deduced from the simulation results that the spline approach of phase parametrization leads to a better convergence, note the equal scaling on the ordinate axis in Figs. 28.2 and 28.3.

28.4 Experimental Results

For every optimization run the pulse characteristics are measured before and after the evolutionary optimization using an interferometric autocorrelation method. In Fig. 28.4 a typical measurement of the un-modulated input laser pulses is shown. The autocorrelation trace shows wings (marked by the ar-

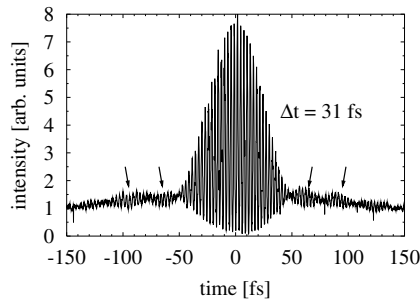


Fig. 28.4. Interferometric autocorrelation of the pulse before optimization

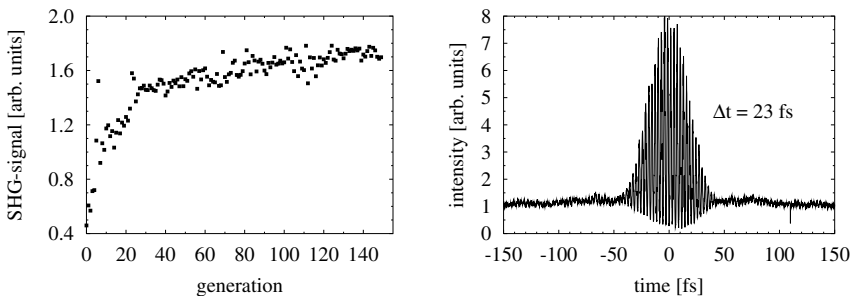


Fig. 28.5. (a) Evolution of the SHG intensity and (b) interferometric autocorrelation of the optimized pulse. The phase was parametrized by a Taylor-Series

rows) indicating the presence of a chirp. Thus the pulse before optimization is clearly not transform limited.

In the pulse compression experiments both approaches to describe the phase functions which are applied to the LCD modulator are compared. In case of the Taylor series we used the phase coefficients from quadratic to 5th order (b_2, \dots, b_5) as genes. The normalized two-photon intensity $I_{2\omega}/I_\omega^2$ is defined as objective function for the algorithm in order to be independent from laser pulse energy fluctuations. The signals from the diodes are integrated over 25 laser pulses after background subtraction. The algorithm uses 30 individuals, i.e. phase coefficient sets, for one population. The optimal parameters for the algorithm are set according to the results from the performance tests with the simulation.

In Fig. 28.5 the experimental results for an optimization run with Taylor parametrization of the applied phase are shown. The two-photon signal is normalized to the intensity with no phase correction by the SLM. After 40 generations of the algorithm the two-photon signal reaches a plateau-like regime followed only by minor improvements. The interferometric autocorrelation of the phase corrected pulses corresponding to the highest “SHG” signal found by the algorithm is shown in Fig. 28.5b. The pulse shows only

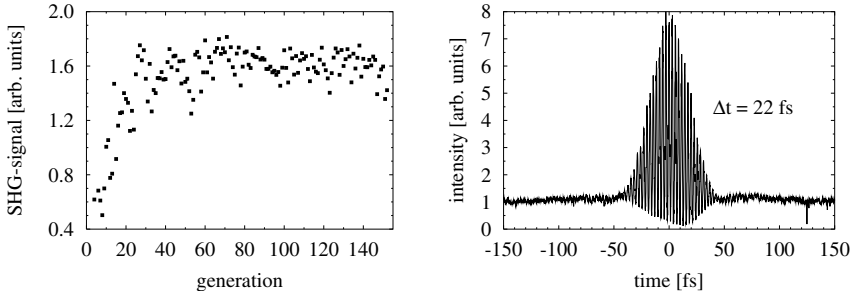


Fig. 28.6. (a) Evolution of the SHG intensity and (b) interferometric autocorrelation of the optimized pulse. The phase was parametrized by a spline-interpolation

small indications of a remaining chirp and the temporal width (FWHM) is measured to $\Delta t = 23$ fs.

The second type of phase parametrization was a spline interpolation. All other experimental parameters and the algorithm settings are kept the same as for the Taylor approach. The results are shown in Fig. 28.6. Again the two-photon signal increases fast over the first 30 generations followed by a plateau region. But the fitness does not increase further. This means that the algorithm converges faster to the global optimum compared to the Taylor coefficient optimization. The interferometric autocorrelation corresponding to the best “SHG” signal (Fig. 28.6b) again reveals a nearly transform limited pulse. The pulse duration Δt is reduced to 22 fs (FWHM) which is only 1.1 fs off the theoretical transform limit for a Gaussian pulse profile.

28.5 Conclusion

A high-resolution pulse shaping device has been implemented suitable for phase shaping of high-power femtosecond pulses. It can be used after the amplifier stage directly before the experiment enabling pure phase coherent control experiments. Two different approaches for the parametrization of the spectral phases on the LC pixels are compared. We have optimized the performance of the evolutionary algorithm by means of convergence speed and reproducibility using a numerical simulation of the two-photon experiment. The spline interpolation approach leads to a faster and better convergence which is verified in the experiments. This can be attributed to non-Taylor like phase distortions in the spectral phase of the amplified pulses and the weaker correlation between the optimization phase variables. However, we have managed to adaptively compress the phase distorted pulses from the amplifier system close to their transform limit utilizing a self-learning feedback loop.

Acknowledgements

We would like to thank G. Stobrawa (Institut für Optik und Quantenelektronik Jena) for valuable discussions and H. Pohlheim (Daimler-Chrysler AG) for help with the evolutionary algorithm. The authors are grateful to the Deutsche Forschungsgemeinschaft (DFG) for financial support within the Schwerpunktprogramm 1134 “Aufklärung transienter Strukturen in kondensierter Materie mit Ultrakurzzeit-Röntgenmethoden” under grant number Za 110 / 23-1.

References

1. R.S. Judson, H. Rabitz: Teaching lasers to control molecules. *Phys. Rev. Lett.* **68**, 1500 (1992)
2. J.J. Gerdy, M. Dantus, R.M. Bowman, A.H. Zewail: Femtosecond selective control of wave packet population. *Chem. Phys. Lett.* **171**, 1 (1990)
3. A. Assion, T. Baumert, M. Bergt, T. Brixner, B. Kiefer, V. Seyfried, M. Strehle, G. Gerber: Control of chemical reactions by feedback-optimized phase-shaped femtosecond laser pulses. *Science* **282**, 919 (1998)
4. B.J. Pearson, J.L. White, T.C. Weinacht, P.H. Bucksbaum: Coherent control using adaptive learning algorithms. *Phys. Rev. A* **63**, 0634121 (2001)
5. A.M. Weiner: Femtosecond pulse shaping using spatial light modulators. *Rev. Sci. Instr.* **71**, 1929 (2000)
6. A. Stingl, M. Lenzner, C. Spielmann, F. Krausz, R. Szipöcs: Sub-10-fs mirror-dispersion-controlled Ti:sapphire laser. *Opt. Lett.* **20**, 602 (1995)
7. M. Lenzer, C. Spielmann, E. Wintner, F. Krausz, A.J. Schmidt: Sub-20-fs, kilohertz-repetition-rate Ti:sapphire amplifier. *Opt. Lett.* **20**, 1379 (1995)
8. F. Verluise, V. Laude, Z. Cheng, C. Spielmann, P. Tournois: Amplitude and phase control of ultrashort pulses by use of an acousto-optic programmable dispersive filter: pulse compression and shaping. *Opt. Lett.* **25**, 575 (2000)
9. R. Bartels, S. Backus, E. Zeek, L. Misoguti, G. Vdovin, I.P. Christov, M.M. Murnane, H.C. Kapteyn: Shaped-pulse optimization of coherent emission of high-harmonic soft X-rays. *Nature* **406**, 164 (2000)
10. G. Stobrawa, M. Hacker, T. Feurer, D. Zeidler, M. Motzkus, F. Reichel: A new high-resolution femtosecond pulse shaper. *Appl. Phys. B* **72**, 627 (2001)
11. J.K. Ranka, A.L. Gaeta, A. Baltuska, M.S. Pshenichnikov, D.A. Wiersma: Autocorrelation measurement of 6-fs pulses based on the two-photon-induced photocurrent in a GaAsP photodiode. *Opt. Lett.* **22**, 1344 (1997)
12. J.-C. M. Diels, J.J. Fontaine, I.C. McMichael, F. Simoni: Control and measurement of ultrashort pulse shapes (in amplitude and phase) with femtosecond accuracy. *Appl. Opt.* **24**, 1270 (1985)
13. H. Pohlheim: Evolutionäre Algorithmen. Verfahren, Operatoren und Hinweise für die Praxis (Springer, Berlin Heidelberg New York 1999)
14. D. Zeidler, S. Frey, K.-L. Kompa, M. Motzkus: Evolutionary algorithms and their application to optimal control studies. *Phys. Rev. A* **71**, 023420 (2001)
15. W.H. Press, B.P. Flannery, S.A. Teukolsky, W.T. Vetterling: Numerical Recipes in C (Cambridge University Press, 1988)

29 Wavefront Measurement and Adaptive Optics at the PHELIX Laser

H.-M. Heuck¹, U. Wittrock¹, C. Häfner², S. Borneis², E. Gaul², T. Kühl²,
and P. Wiewior³

¹ Münster University of Applied Sciences, Photonics Laboratory
Stegerwaldstr. 39, 48565 Steinfurt, Germany

² Gesellschaft für Schwerionenforschung mbH
Planckstr. 1, 64291 Darmstadt, Germany

³ Julius Maximilian Universität Würzburg
97703 Würzburg, Germany

Summary. The PHELIX (Petawatt High Energy Laser for Heavy Ion Research) laser project has been initiated to build a high energy, ultra high power laser for research purposes in connection with the heavy ion accelerator of the GSI. The PHELIX laser should provide ns-pulses with an energy up to 5 kJ and, alternatively, fs-pulses reaching 1 petawatt with an energy of 500 kJ. Aberrations due to beam transport and due to the amplification process limit the focus ability and the intensity on the target. For the amplification of the fs-pulse, the CPA (chirped pulse amplification) technique is used. Distortions in the phase also entail longer pulses during the compression in the CPA process.

29.1 Introduction

Following the closure of the PHEBUS laser in France and the NOVA laser at the Lawrence Livermore National Laboratory (LLNL) [1] some of the beam lines were passed on to several research facilities around the world [2–4]. One of these facilities is the organisation for heavy ion research (GSI) in Darmstadt, Germany, where currently the PHELIX (Petawatt High Energy Laser for Heavy Ion Experiments) laser is build up with the 315 mm clear aperture NOVA disk amplifier in the main amplifier stage. The GSI is a laboratory that performs basic and applied research in physics using a heavy ion accelerator facility. With the heavy ion accelerator all elements can be accelerated up to 2 GeV per mass unit. The key aspects of research at the GSI are the nuclear and hadron physics, atom physics and plasma physics. Now, the PHELIX laser allows new experiments from the symbiotic use of an intense heavy ion beam and a very intense laser. Examples are X-ray spectroscopy, interaction of heavy ions with ionized matter, laser acceleration, and inertial fusion [5].

29.1.1 The PHELIX Laser

PHELIX is designed to be a versatile laser capable of supplying a few kJ, nanosecond-long pulses as well as petawatt level, femtosecond-long pulses to

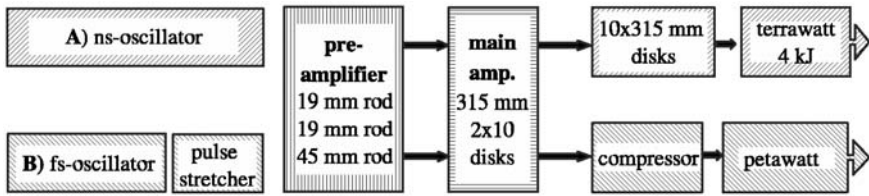


Fig. 29.1. Schematic overview of the PHELIX laser for the two options, the high energy option (a) and the high power option (b)

the experiments. Hence, PHELIX has two different front-ends both injecting an energy of 50 mJ into the same pre-amplifier. The ns-front-end (Fig. 29.1a) was built in cooperation with LLNL and is a copy of the NIF front-end. It consists of a Yb:silica fiber ring master oscillator followed by a fiber amplifier, and a flash-lamp-pumped glass regen amplifier. the fs-front-end (Fig. 29.1b) consists of a commercial Ti:Sa mode-locked oscillator (Coherent Mira), a stretcher, and a linear and ring Ti:Sa regen amplifier.

The laser pulse from the front-end is amplified in the pre-amplifier by two diameter = 19 mm Nd:Glass rod amplifiers and one diameter = 45 mm rod amplifier. In the entrance of the pre-amplifier a serrated aperture [6] defines an object-plane which is relay-imaged on the rods and in the end of the pre-amplifier on a diameter = 100 mm bimorph adaptive mirror. During the whole amplification the beam size is increased to reduce the fluence on the optics and to reduce nonlinear effects. After the pre-amplifier the beam is expected to a diameter of 280 mm and amplified by the main amplifier. The main amplifier is a double-pass amplifier and consists out of ten flash-lamp-pumped disks. One of the mirror holders in the main amplification chain, the retro-reflecting mirror holder, is modified to deform the mirror and to pre-correct for astigmatism. In the high energy option (Fig. 29.1a) the laser can be amplified again by ten disk amplifiers and reach with this optional booster an output energy of 4 kJ in 20 ns.

In option B the laser is compressed after the main amplifier in a vacuum grating compressor to achieve intensities on the order of 10^{21} W/cm² behind the focusing parabola.

29.2 Motivation for Adaptive Optics

Realizing very high energy and very high output power is one of the major tasks of this laser project. The limitation of the output power is the fluence of the laser on the optical components. If we want to increase the energy, we need to increase the beam diameter. This causes bigger and much more expensive amplifier disks, mirrors, gratings, and so on. On the other hand the beam quality is not good due to wavefront aberrations which are discussed

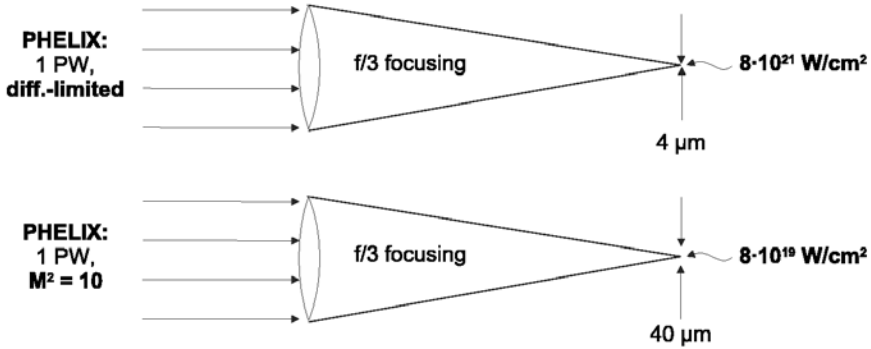


Fig. 29.2. With a plane wavefront the laser can be focused diffraction-limited with an $f/3$ focusing mirror to a $d = 4 \mu\text{m}$ spot. If the laser has aberrations, the reachable spot-size increases dramatically

later on. If we are able to increase the beam quality we get a higher brightness and consequently more energy and power onto the target.

29.2.1 Spatial and Temporal Brightness

We define the spatial brightness (29.1) with the M^2 -formalism. M^2 is a common used absolute measure for the quality of a laser beam [7]. Wavefront aberrations cause a higher M^2 value, which means that the far-field diameter increases and the encircled energy is far below its maximum [8] (Fig. 29.2)

$$B_{xy} = \frac{P}{M_x^2 M_y^2}. \tag{29.1}$$

Another important aspect that will affect the pulse length is the wavefront quality entering the compressor. This effect occurs only for the chirped pulse amplification in the high power option. The stretched pulse is compressed with two diffraction gratings. If the laser has aberrations these result in different path lengths between the two gratings in the compressor and in a longer pulse (Fig. 29.3) [9]. Equation (29.2) gives a modification for the brightness of fs-laser where Δt is the real pulse length and τ is the theoretical pulse length

$$B_{xyt} = \frac{P}{M_x^2 M_y^2 \Delta t / \tau}. \tag{29.2}$$

29.2.2 Repetition Rate

The repetition rate of the main amplifier is limited by the thermally induced long term aberrations after one first shot. The thermal recovery time of the main amplifier is about 10 h. This value is reported from the NOVA petawatt

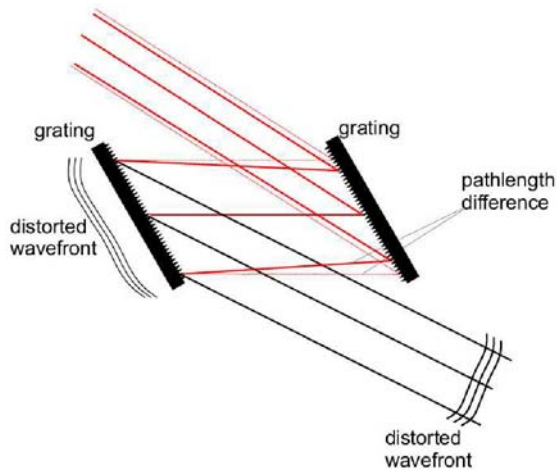


Fig. 29.3. Wavefront gradients regarded as localized pointing errors result in different path lengths of the laser through the compressor

laser chain in which the same disk amplifiers were used [10]. When the laser was fired after 7 h cooling delay, the peak power of the far-field was 6 times lower compared to a shot after 1.5 h cooling delay which was corrected by adaptive optics. This example shows that adaptive optics can improve the profitability of the PHELIX laser a lot. In our system we hide a repetition rate of 30 min with the help of adaptive optics.

29.3 Adaptive Optics of PHELIX

29.3.1 Types of Aberrations

The PHELIX exhibits mainly three different types of wavefront aberrations: static aberrations, pump shot aberrations and long-term thermal aberrations. Static aberrations arise from imperfections of the surfaces and misalignment of the optical components. Some optical components, e.g. relay telescope lenses, require a tilt to avoid ghost foci within the amplifier. The expected wavefront deformation is about 1λ without defocus [11]. Pump shot aberrations are caused by the inhomogeneous pump profile from the two flash lamp panels in the center of the laser disks and by the ASE heated edge cladding. This effect has been measured at LLNL for the 31.5 cm NOVA amplifiers to have $\pm 5 \mu\text{rad}$ of phase angle corresponding to a wavefront deformation of around 1.5λ [12]. The long-term thermal aberrations are not measured, yet. It is planned to measure the recovery time and thermal wavefront aberrations of PHELIX during the commissioning phase planned for 2004.

29.3.2 Deformable Mirrors at the PHELIX

To correct the aberrations described above we have implemented two adaptive mirrors in the PHELIX laser – an actively controlled bimorph mirror bought from the Russian Academy of Science and a static deformable HR-mirror in the main amplifier.

The bimorph mirror and the active control loop were installed into the pre-amplifier during last summer. The bimorph adaptive mirror consists of a dielectric coated glass substrate that is attached with its backside to a stack of two piezo disks. The piezo disks themselves are coated with 31 electrodes. The maximum achievable deformation of this mirror is about 6λ . The mirror is placed in the relay image plane of the laser rods and represents the object plane for the transport telescopes of the doublepass section in the main amplifier. This allows the mirror to correct the aberrations that arise in the pre-amplifier and, in the near future, to pre-correct for aberrations in the main amplifier. Behind a leaky mirror at the end of the pre-amplifier a Shack–Hartmann wavefront sensor is installed. With this wavefront sensor and an automatic control program, a closed-loop operation for the pre-amplifier was realized.

29.3.3 Control Algorithm

In the first step, the Shack–Hartmann sensor has to be calibrated with a plane wavefront. Therefore a diffraction limited pinhole was installed in front of the wavefront sensor into the last telescope to produce a plane wavefront. In the next step, the response of the mirror surface to an applied voltage at each individual mirror electrode was recorded. These responses can then be described by the so-called influence functions [13]. This set of functions is grouped into the influence function matrix M . Assuming that the process is linear, one obtains the mirror surface as the response to a given voltage vector \mathbf{V}

$$\mathbf{A} = M \cdot \mathbf{V}, \quad (29.3)$$

where \mathbf{A} is a vector which describes the mirror surface. This could be the deviations of spots from the referenced pattern of a Shack–Hartmann sensor or alternatively the coefficients of Zernike polynomials \mathbf{Z} of the mirror surface S according to

$$S = \mathbf{A} \cdot \mathbf{Z}.$$

Measuring the wavefront with the Shack–Hartmann sensor, the required voltages are calculated for the inverse mirror surface by inverting of (29.3)

$$\mathbf{V} = M^{-1} \cdot \mathbf{A}. \quad (29.4)$$

Because the matrix M is generally not square and the non-singularity of the matrix can not be guaranteed, the pseudo-inversion of the matrix M is built with the singular-value decomposing method (SVD).

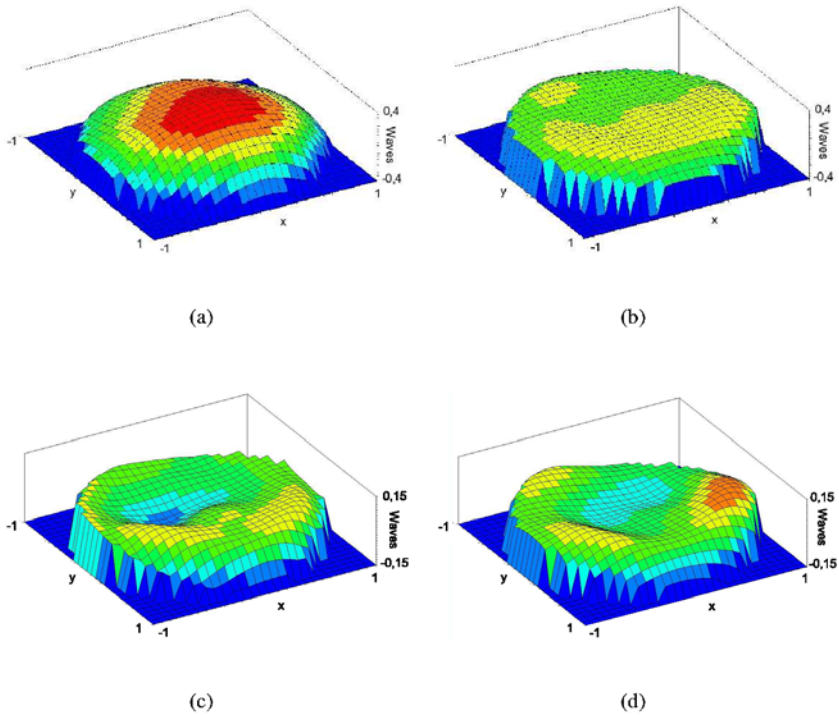


Fig. 29.4. Wavefront measured with a radial-shear interferometer after the pre-amplifier. (a) without and (b) with the closed-loop adaptive correction. The Strehl ratio increases from 0.3 to 0.9. In (c) and (d) the defocus term of (a) and (b) is removed

The SVD is useful because the eigen-modes of the mirror surface can be obtained and any surface can be described by a linear combination of these modes. This allows to compute the surface which is the best approximation to the desired surface.

29.3.4 Preliminary Experiments

After the calibration of the close-loop adaptive mirror set-up, we successfully demonstrated the optimization of the pre-amplifier. The laser was fired two times with a delay of 5 min between each shot to introduce thermal aberrations into the amplifier. During the second shot the wavefront was measured and inverse surface of the adaptive mirror was calculated. Figure. 29.4 shows the optical path difference over the entire surface for the adaptively controlled amplifier and for the free running system. The correction system proved to be capable of improving the Strehl ratio by a factor of three. But, as expected for the rod amplifier, the major part of the thermal aberrations is in the defocus term.

29.3.5 Static Deformable Mirror at the Main Amplifier

In addition to the actively controlled bimorph mirror in the pre-amplifier, the retro reflecting mirror of the double-pass amplifier can be deformed by four micrometer screws. This will allow the correction of astigmatism which is expected to be the major aberration when using the disk amplifiers. The concept was successfully demonstrated at the VULCAN laser in the Rutherford Appleton Laboratory [14].

29.4 Summary and Outlook

After completion of the double-pass section in 2004, the closed-loop adaptive optics will be extended to pre-correct for the disk amplifiers. The expected aberrations are in the magnitude of a few waves and appear mostly in the astigmatism term. With the actively controlled adaptive mirror and the static deformable mirror it should be possible to increase the repetition rate dramatically and concurrently increase the brightness.

References

1. Lawrence Livermore National Laboratory, 7000 East Ave., Livermore, CA 94550-9234, USA, <http://www.llnl.gov/str/Remington.html>
2. Central Laser Facility Rutherford Appleton Laboratory (CLF), Chilton, Didcot, Oxfordshire, OX11 0QX, UK, <http://www.clf.rl.ac.uk/>
3. Laboratoire pour l'Utilisation des Lasers Intenses (LULI), Ecole Polytechnique, Route de Saclay, 91128 Palaiseau cedex, France, <http://luli.polytechnique.fr/>
4. Gesellschaft für Schwerionenforschung mbH, Planckstr.1, 64291 Darmstadt, Germany, <http://www.gsi.de/phelix>
5. T. Kühl, J. Kluge et al.: Phelix Proposal Part A. Tech. Rep. <http://www-aix.gsi.de/phelix/>, Gesellschaft für Schwerionenforschung (GSI) (1998)
6. J.M. Auerbach, V.P. Karpenko: Serrated-aperture apodizers for high-energy laser systems. *Appl. Opt.* **33**, 3179 (1994)
7. A.E. Siegman: New developments in laser resonators. In: Conference on Optical Resonators, *Proc. SPIE* **1224**, 2 (1990)
8. I. Buske, H.-M. Heuck, U. Wittrock: Adaptive aberration control in laser amplifiers and laser resonators. In: Conference on Laser Resonators and Beam Control VI, *Proc. SPIE* **4969**, 122 (2003)
9. J. Collier, R. Allott, C.N. Danson, C.B. Edwards, S. Hancock, D. Neely, D.A. Rodkiss, I.N. Ross, T.B. Winstone, B.E. Wyborn: CPA Design Considerations for the Vulcan Petawatt Upgrade. Tech. Rep., Central Laboratory of the Research Councils (CLRC), Rutherford Appleton Laboratory (2000)
10. D.M. Pennigton, C.G. Brown, M. Kartz, M. Landon, M.D. Perry, G. Tietbohl: Production of High Intensity Laser Pulses with Adaptive Optics. Tech. Rep. UCRL-JC-133182 Abs, Lawrence Livermore National Laboratory

11. C. Haefner, K. Abdeli, J.C. Chanteloup, J. Collier, C. Danson, C. Edwards, J. Fuchs, E. Gaul, S. Hawkes, H.-M. Heuck, C. Hooker, J. Kluge, T. Kuehl, P. Neumayer, C. Reason, I. Ross, D. Ursescu, B. Wattellier, P. Wiewior, J. Zou: Aberration Compensation and Adaptive Optics in the PHELIX Laser. Tech. Rep., Gesellschaft für Schwerionenforschung (GSI) (2002)
12. J.E. Murray, H.T. Powell, G.F. Ross, J.D. Wintemute: Pump-induced beam steering in large aperture disk amplifiers. In: Annual Meeting Optical Society of America. OSA Technical Digest, Postconference Edition (Optical Society of America, Washington DC 1988)
13. C.J. Hooker, C.J. Reason, I.N. Ross, M.J. Shaw, N.M. Tucker: Progress in adaptive optics for laser beam phasefront control. Tech. Rep., Central Laboratory of the Research Councils (CLRC), Rutherford Appleton Laboratory (1997)
14. C. Hernandez-Gomez, J. Collier, S. Hawkes: Vulcan Intensity Increase by Wavefront Quality Improvement. Tech. Rep., Central Laboratory of the Research Councils (CLRC), Rutherford Appleton Laboratory (1998)

30 ISTC Projects from RFNC-VNIIEF Devoted to Improving Laser Beam Quality

F. Starikov and G. Kochemasov

Russian Federal Nuclear Center – VNIIEF
Sarov, Nizhny Novgorod Reg. 607190, Russia

Summary. Information is given about the Projects # 1929 and # 2631 supported by ISTC and concerned with improving laser beam quality and interesting for adaptive optics community. One of them, Project # 1929 has been recently finished. It has been devoted to development of an SBS phase conjugation mirror of super-high conjugation quality employing the kinoform optics for high-power lasers with nanosecond scale pulse duration. With the purpose of reaching ideal PC fidelity, the SBS mirror includes the raster of small lenses that has been traditionally used as the *lenslet* in Shack–Hartmann wavefront sensor in adaptive optics. The second of them, Project # 2631, is concerned with the development of an adaptive optical system for phase correction of laser beams with wavefront vortex. The principles of operation of modern adaptive systems are based on the assumption that the phase is a smooth continuous function in space. Therefore the solution of the Project tasks will assume a new step in adaptive optics.

30.1 Introduction

Phase conjugation (PC) at the stimulated Brillouin scattering (SBS) and adaptive optics (AO) are the well-known approaches for improving laser beam quality. They have their own advantages and disadvantages. PC at SBS allows to compensate the phase as well as amplitude distortions of the laser beams whereas AO corrects the phase distortions only. Advantages of PC in comparison with AO are in that it is inexpensive, does not require complicated optical alignment, enables self-adjustment of the system as a whole, and is characterized by prompt response. But in case of PC at SBS there is the SBS threshold problem in low energy laser systems, risk of appearing the non-linear parasitic processes in the SBS medium, and the impossibility to treat femtosecond laser pulses. At the same time AO is applied to short-pulse CPA lasers, and reflection of adaptive mirror is close to the unity.

In the present paper we report about two Projects supported by the International Science and Technology Center (ISTC). Both deal with improving laser beam quality. Though the finished Project # 1929 is concerned with PC at SBS, it will present some interest for adaptive optics community since the developed SBS mirror includes an original component, namely, a raster of small lenses used in many adaptive systems for wavefront sensing. The Project # 2631 has been just begun and directly deals with AO. It is de-

voted to development of AO system for phase correction of laser beams with wavefront vortex when the phase surface has a discontinuity in the form of a screw dislocation. Optical vortices are a very popular object of investigation now. Various transformations of vortex beams are studied in singular optics for potential applications in the communication systems and optical data processing. Along with this, optical vortices can play a negative role as well. This occurs, for example, under passing laser beams through turbulent atmosphere. Note that the principles of operation of modern AO systems are based on the assumption that the phase is a smooth continuous function in space. Therefore the solution of the Project # 2631 tasks will be a new step in adaptive optics.

30.2 ISTC Project # 1929: SBS Mirror for High-Power Lasers

A 3D simulation of PC at the direct focusing of the laser beam into the SBS cell has shown [1] that at linear SBS (near the threshold), when the reflection coefficient is $R \approx 1-5\%$, the PC quality is unsatisfactory, PC coefficient $h \approx 60\%$. Nearly ideal quality of PC with $h > 90\%$ occurs only at $R > 80\%$. Such high values of R may lead to considerable beam loads and rise of parasitic processes in the SBS medium (thermal and striction self-action, optical breakdown), which have a negative influence on the SBS process and may cause even its suppression. Hence it follows that an actual task is to obtain the quality of PC that is near to ideal in a wide range of pump powers including moderate reflection coefficients.

Therefore a more complicated SBS mirror [2] with a raster of small lenses and an angular selector was studied (Fig. 30.1). The transmission angle of the selector θ_{sel} exceeds the laser beam divergence θ_L . The laser intensity after passing through the raster has specific distributions in two zones. One of them is the focal region of the main focusing lens (zone I) where a discrete

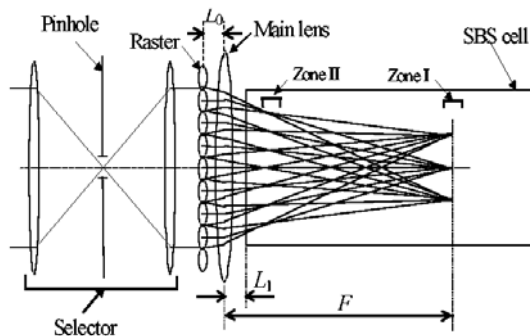


Fig. 30.1. Scheme of the SBS-mirror with a raster of small lenses

ordered picture is formed. Each peak of the picture has a structure of angular distribution of the beam incident on the raster. The angular distance between the peaks is $\theta_d = \lambda/d$. The values d and f are the size and the focal length of a small lens in the raster. Other specific distribution of the laser beam intensity occurs in the focal region of small lenses in the raster (zone II).

Calculations [3] have shown that the Stokes beam intensity distribution at the plane of the selector pinhole consists of a discrete set of peaks, an angular interval between which is θ_d that was observed in experiments as well. For ideal PC only a zero Stokes order of diffraction is required, coincident with the laser beam. Angular selection at the diaphragm plane removes higher orders of diffraction, thus increasing the PC quality. In work [3] a new effect of extremely low noising of the Stokes beam has been found. Its essence is that the angular selection of higher Stokes orders of diffraction allows nearly ideal quality of PC to be achieved at optimal geometry of the PC mirror. For this purpose the input window of the SBS cell must be located in a special intermediate region between zones I and II where quasi-light guide mosaic zones are formed with the periodic distribution of laser intensity. At optimal configuration of the PC mirror the PC coefficient is $h_{\text{sel}} > (90-95)\%$. To increase the transmission coefficient of the selector k_{sel} (a portion of the Stokes energy transmitted through the pinhole) the SBS cell must be located at a closer distance to the lens, so that zone I would be inside the cell. However, this increase of k_{sel} is followed by noticeable reduction of the PC quality after selection.

Experiments were conducted on a pulsed Nd laser facility consisting of a master oscillator and two amplifiers [4,5]. At the laser output a laser beam is formed with a wavelength $\lambda = 1.06 \mu\text{m}$, energy 1.5 J and duration 25 ns. The radiation energy at the second harmonic ($\lambda = 0.53 \mu\text{m}$) is about 300 mJ, the beam width of 0.8 cm. SBS was excited in the cell filled with a gas mixture of SF_6 and Xe. The partial pressure of SF_6 was 1.5 atm, the total pressure of the mixture was 28 atm, which gives SBS gain coefficient $g = 23 \text{ cm/GW}$, hypersound decay time $\tau = 5 \text{ ns}$. An 8-level kinoform raster of close-packed Fresnel lenses with lens size $d = 0.05 \text{ cm}$, focal lens $f = 10 \text{ cm}$ and the diffraction efficiency of 95% was used. To conduct experiments special SBS cells of ultra-high purity have been created. After mechanical and electrical polishing the height of micro-irregularities of inner walls and separate parts of the cell does not exceed $0.3 \mu\text{m}$. The use is made of copper and indium spacers. The design of the cells and their manufacturing technology allow the initial purity of a gas admitted into the cell to be preserved. A special system was manufactured for gas purification and its admission into the cell. Owing to this system it is possible to purify gases from mechanical impurities and fill the cells with mixtures at desired partial pressures. The system uses two stages of gas purification. In the developed system the use is made of filters allowing purification of gases from particles of a size higher than $0.1 \mu\text{m}$ with efficiency of $\approx 99.9999\%$.

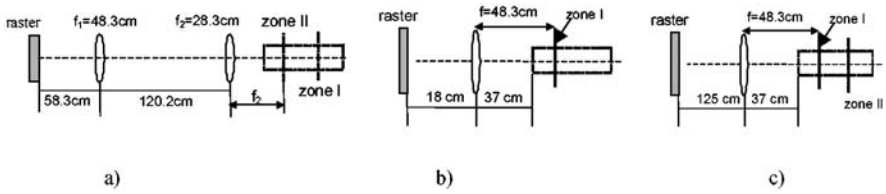


Fig. 30.2. SBS-mirror scheme for configurations “zone II+zone I” (a), “zone I” (b), “zone I+zone II” (c) in the SBS-cell

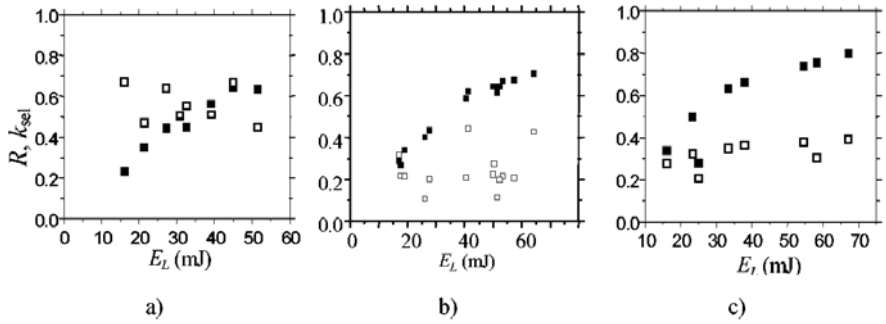


Fig. 30.3. Experimental dependence of reflection R (closed squares) and selection k_{sel} (open squares) coefficients for configurations “zone II+zone I” (a), “zone I” (b), “zone I+zone II” (c) in the SBS-cell

In calculations and experiments three configurations of the SBS mirror were considered (Fig. 30.2). In the first one the cell contained the both bright zones in the sequence II+I. In the second one the cell contains only zone I so that the region of quasi-waveguide zones is near the input window of the cell, which provides the highest PC quality [3–5]. In the third one image of zone II is situated in the cell behind zone I. Experimental and calculated dependences of the reflection coefficient R and the transmission coefficient of the selector k_{sel} on laser pulse energy in both SBS mirror configurations are in a good agreement with each other.

Experimental reflection R and selection k_{sel} coefficients are shown in Fig. 30.3. They are in close agreement with calculated data [4,5]. It is difficult to compare the calculation and the experiment according to the parameter h_{sel} due to impossibility of its direct measurement. We have measured the laser and Stokes energy distributions at the plane before the raster, i.e., in the near field. Figure 30.4 shows experimental dependences of a portion of energy in the circle of radius r for the laser and Stokes beams for three configurations of the SBS mirror. The laser and Stokes intensity distributions are obtained in the same laser flash with the help of two CCD cameras. One can see from Fig. 30.4a, that the SBS mirror configuration II+I gives a narrower Stokes radiation energy distribution if compared to laser radiation in

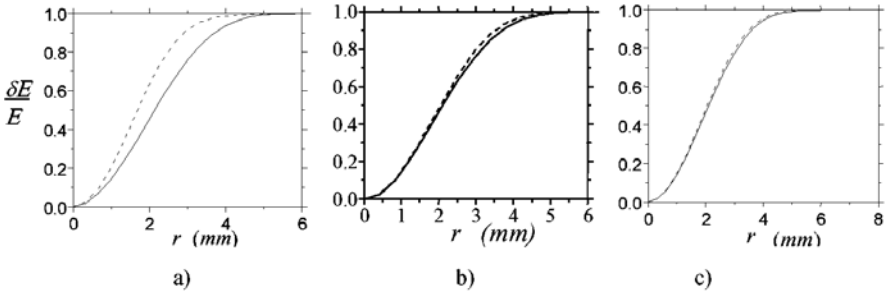


Fig. 30.4. Experimental dependence of a portion of energy in the circle of radius r in the near field for laser (solid lines) and Stokes (dotted lines) beams for configurations “zone II+zone I” (a), “zone I” (b), “zone I+zone II” (c) in the SBS-cell

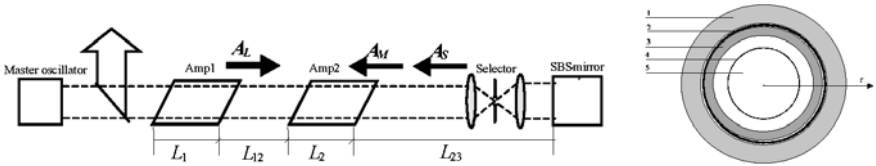


Fig. 30.5. Schematic of the EPDL with SBS mirror and transverse section of the amplifier: 1 external explosive, 2 amplifier casing, 3 internal explosive, 4 shock wavefront position, 5 working region

the near field, which is typical for PC far from ideal ($h_{sel} \approx 0.8$ in calculations). But the selection coefficient is rather large here (Fig. 30.3a). When the configuration contains only zone I, a close agreement is observed between the distributions of the laser and Stokes energies (Fig. 30.4b). This agrees with the calculated values $h_{sel} > 0.95$. But an excellent PC quality is achieved at low and unstable k_{sel} (Fig. 30.3b). In the SBS mirror configuration I+II [5] it is possible to increase and stabilize k_{sel} (Fig. 30.3c) at saving high PC quality (Fig. 30.4c). Further increase of k_{sel} in configuration I+II up to a level of k_{sel} in configuration II+I is possible by changing focal length of the main lens.

Below we present some results of application of the developed SBS mirror in the case of two very different laser systems. The first of them is a high-power explosively pumped photo-dissociation laser (EPDL). The EPDL is a MOPA double-pass laser system (see Fig. 30.5). In typical experiments [6] the laser amplifier stage consists of two amplifiers Amp₁ and Amp₂. The lengths of amplifiers are L_1 and L_2 , respectively; the distance between them is denoted as L_{12} . In the conducted experiments the typical values $L_1 = L_2 = 1$ m and $L_{12} = 20$ m were used. The distance L_{23} is sufficiently large and achieves several tens of meters to reduce the probability of damaging the optical elements of the selector and the diagnostic equipment by fragments formed during explosion.

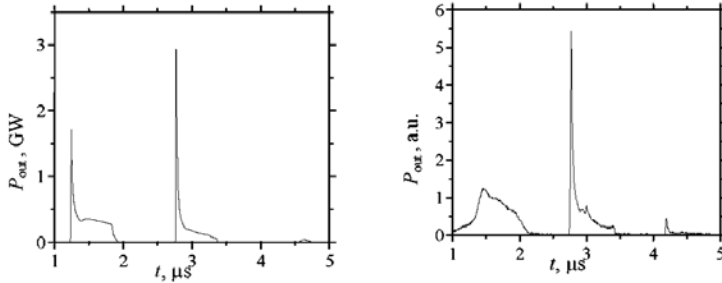


Fig. 30.6. Dynamics of output laser power in calculation (*left*) and experiment (*right*)

During the first pass through the channel the radiation wavefront becomes distorted due to optical nonuniformities in the active medium, aberrations of wide-aperture optical elements and atmospheric turbulence. Developed SBS mirror with the raster allows to solve the problem of PC quality. An optimal configuration of this SBS mirror was determined having unique properties if compared to the existing SBS mirrors. It stably produces a nearly ideal quality of PC (the PC coefficient is $\geq 95\%$) at any level of SBS saturation, i.e., at any reflection coefficient [4, 5]. In SBS mirrors of other types the high-quality PC is observed only at high reflection coefficients, which is often difficult to realize in experiment.

The EPDL experiments and 3D calculations were made for the laser mixture 25 Torr C_3F_7I +125 Torr Xe. The distance from the end of the second amplifier to the SBS cell was $L_{23} = 68$ m. The maximum diameter of the active region is 15 cm. The input intensity from the master oscillator equals 2 W/cm^2 .

The EPDL operates as follows. The power of laser radiation amplified during the first pass increases in time at the beginning of the pulse and as soon as it exceeds the threshold power of SBS, it begins to be reflected from the SBS mirror. The reflected Stokes radiation enters the amplifier where it begins to take off the population inversion and abruptly decrease the gain coefficient. In consequence, the laser radiation power becomes below the threshold and the SBS mirror stops reflecting. The gain coefficient grows again due to pumping and the conditions for laser radiation amplification once again become favorable. As a result a pulse-periodic regime is realized. Duration of each pulse of output Stokes radiation is close to the time of double pass of radiation through the whole system, whereas the pulse repetition rate depends on the pump growth rate.

The dynamics of the EPDL radiation power is shown in Fig. 30.6. The EPDL radiation energy is about 400 J, which agrees with the experiment [6]. If we take into account the complexity of the whole task, then we may say that the calculated dependence provides good simulation of the typical experimental data in Fig. 30.6.

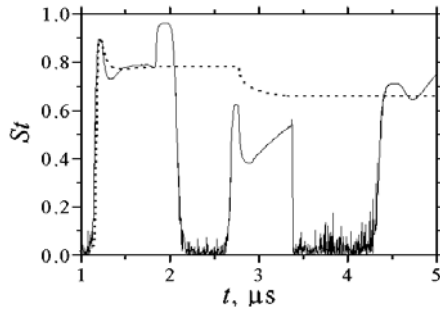


Fig. 30.7. Calculated dynamics of the instantaneous (*solid line*) and time-averaged (*dotted line*) Strehl number of output laser radiation

Figure 30.7 shows the dynamics of the Strehl number both instantaneous and average in time. The calculation shows that at a given EPDL geometry the average Strehl number does not exceed 0.7 which agrees with the best experiment data [6]. Even at ideal work of the SBS mirror because of its location far from the block of amplifiers the Stokes radiation is amplified in the medium that has undergone some changes in the distribution of optical non-uniformities.

The EPDL produces the brightness of about 10^{12} J/sr. Calculations show that the beam quality of the EPDL substantially depends on parasitic reflections of laser radiation from the ends of amplifiers and elements of the optical scheme. Reflection coefficient exceeding 10^{-7} considerably decreases the brightness of output radiation and lead to instability of laser parameters in the experiments. To reduce the harmful effect of parasitic reflections, it is needed to reduce SBS threshold, increase input intensity and the distance between the amplifiers.

The second example of the laser with the developed SBS mirror is a pulse-periodic Nd:YAG laser consisting of a master oscillator and an amplifier (Fig. 30.8). The master oscillator works under conditions of passive

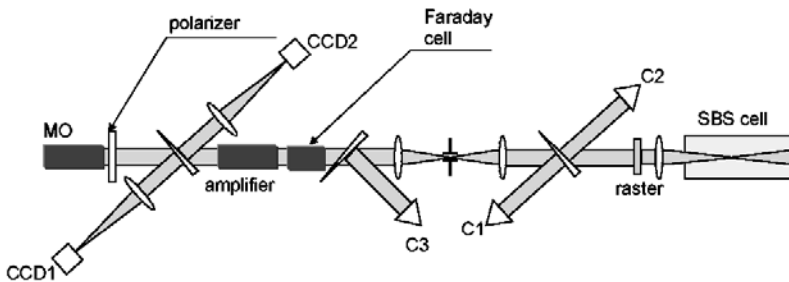


Fig. 30.8. Scheme of a pulse-periodic Nd:YAG laser

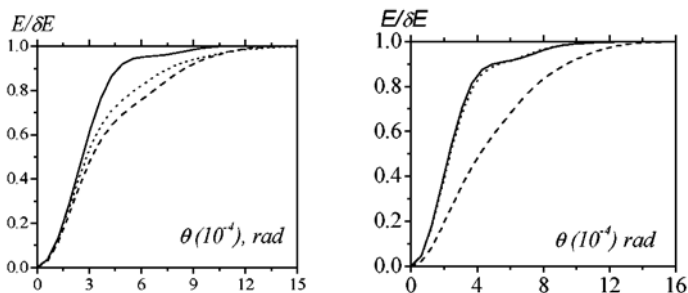


Fig. 30.9. Experimental angular distribution of laser radiation before (*solid line*) and after (*dashed line*) amplifier and selected Stokes radiation after amplifier (*dotted line*) in far field at nonoptimal (*left*) and optimal (*right*) configuration of SBS mirror

Q-switching and has the spectral line width 0.05 cm^{-1} , the pulse duration 40 ns.

An 8-level raster of diffraction lenses with the lens size of 0.1 cm and focal length 20 cm is used. In the SBS cell the bright zones have been situated in the sequence “zone I+zone II”. PC quality is measured by means of comparison of spatial energy distributions of laser and Stokes radiation in far field between the master oscillator and amplifier. The simultaneous registration of laser and Stokes patterns is conducted on the individual CCD cameras followed by determination of dependence of energy part in a circle of radius r against r . Experiments have shown that in the case of optimal calculation geometry the phase conjugation quality is close to an ideal (Fig. 30.9). As a result, the pattern of output radiation of pulse-periodic laser system completely coincide with the pattern of master oscillator radiation of diffraction divergence (Fig. 30.10). This situation is observed at 1 Hz frequency and not deteriorated in time. It should be noted that a special phase element has been additionally introduced in the amplifier stage in order to model a noticeable

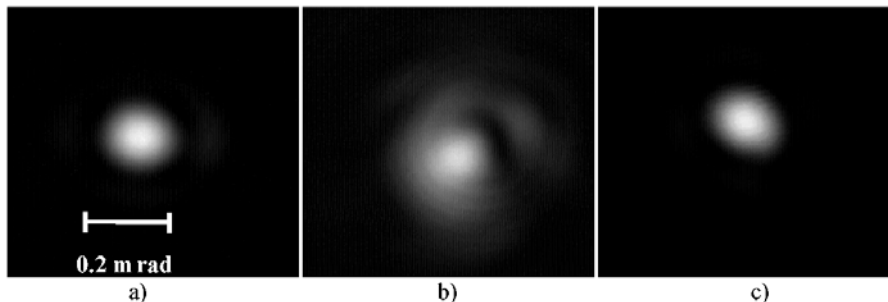


Fig. 30.10. Experimental far field patterns of laser radiation before (a) and after amplifier (b) and Stokes radiation after amplifier (c) at optimal configuration of SBS mirror

effect of thermal aberration in the amplifier. The ideal performance of the laser system has been achieved at relatively small (less than 20%) reflection coefficients and great selection coefficient (near to 95%).

30.3 ISTC Project # 2631: Adaptive System for Correction of Vortex Beams

The principles of operation of modern wavefront sensors and correctors are based on the assumption that the phase is a smooth continuous function in space. But when a laser beam passes a sufficiently long distance in the medium with relatively small-scale optical inhomogeneities, the optical field of the beam becomes speckled. Such fields are characterized by the presence of isolated points in the transverse plane, where intensity turns to zero, the phase is unknown, and the phase gradient integration over the closed contour surrounding such a point of branching gives different from zero circulation. These properties are the symptoms of strong wavefront distortions – screw dislocations. In addition to the name “wavefront dislocations”, which appeared due to similarity with the defects of the crystalline lattice. Fried [8] introduced the term “phase discontinuities” or “breaks of branching”. The appearance of dislocations indicates the mode of strong oscillations upon laser beam propagation in the inhomogeneous medium. Such features of laser beams can appear, for example, at ophthalmologic investigation of eye-ground in medicine, in the tasks of astronomy and optical communication.

The traditional methods of wavefront measurements in case of the above mentioned atmospheric and ophthalmologic tasks are in fact of no help. The sensors are not capable to restore the phase under the conditions of strong oscillations [9]. Already the experimental determination of the location of phase discontinuities itself brings about serious difficulties [10]. It is not an easy problem to develop effective algorithms for phase reconstruction under these conditions. Yet more complex is the task of creating the correctors of screw phase dislocations when the equiphase surface near the centers of dislocations is a helical (screw) structure. By the present moment there are no experimental results on compensation of phase distortions under conditions of strong oscillations. There is no information on creation of adequate wavefront correctors either. Recent publications are mainly devoted to creation of the theoretical basis of phase reconstruction [9, 11, 12], numerical evaluations of the operational efficiency of adaptive systems with complete or partial compensation of phase distortions [13, 14].

The Project #2631 is directed both to the theoretical solution of the problem of adaptive correction of beams with wavefront screw dislocations and to its experimental demonstration. A team of research workers has performed investigations connected with the laser beam propagation, development of adaptive systems, study of properties of wavefront dislocations [15–20].

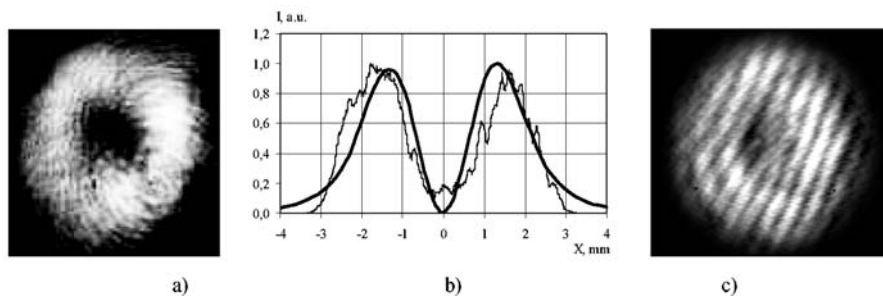


Fig. 30.11. Image of vortex beam (a), its section compared with calculated data (bold line) (b) and pattern of interference with plane wave (c)

For creation of effective algorithms and devices for compensation of phase singularities it is necessary to conduct experimental investigations in model conditions when wavefront dislocations are generated artificially by using special laboratory means. Generation of optical beams with the preset configuration of singularities is one of the main directions of research and applied activities presently in a new scientific direction – singular optics [21]. Thus, the first task of the Project will be the generation of laser beams with wavefront dislocation (Gauss–Laguerre modes). For this purpose, the computer-generated gratings and phase plates are to be used. The preliminary results obtained with the help of a computer-generated grating with a fork-like structure are shown in Fig. 30.11. The vortex is formed in the first diffraction order and detected experimentally in the interference pattern of the beam with an obliquely incident plane wave where the typical “fork” appears.

One of the key elements of the Project is to develop a theory for phase reconstruction from the measured wavefront slopes or optical field phase gradient. Such measurements are made with the help of Shack–Hartmann wavefront sensors or a shear interferometer. The theory takes into account differential properties of the vector field of slopes allowing this vector field to be presented as a sum of a vortex-free (potential) and a solenoidal component [15, 16]. Unlike works [9, 11], where similar representation was used for extending the capabilities of the existing phase reconstructors, the participants of the Project build their theory of phase reconstruction based on strict integral relations which connect a vortex-free (divergent) part and a solenoidal part of the wavefront slopes and the slope values on the contour limiting the entrance pupil. This Project conjectures detection of phase singularities and reconstruction of phase distribution on the basis of measurements of the Shack–Hartmann wavefront sensor. Thus, the second task of the Project is to create a wavefront sensor with using the kinoform rasters.

The signals generated by the wavefront sensor enter the correcting device—adaptive mirror. This mirror shall have a reflecting surface, the profile of which may change and satisfy in the amplitude of deformations, in the num-

ber of degrees of freedom, and in the frequency transmission band the requirements providing the preset efficiency of compensation of phase perturbations of optical radiation. For correction of a beam with wavefront dislocations we plan to investigate and develop adaptive systems on the base of bimorph and segmented (on basis of liquid crystal modulator) correctors. Thus, the third task of the Project is to create an adaptive mirror with an electronic system and new algorithms for the corrector control.

Within the framework of the final task of the Project, the work of the close-loop adaptive system including all afore said components will be demonstrated.

Acknowledgements

The present work was financially supported by ISTC within the framework of the projects #1929 and #2631.

References

1. F.A. Starikov et al.: Proc. SPIE **3930**, 12 (2000)
2. S.T. Bobrov et al.: Optika i Spectroscopia **62**, 402 (1987)
3. G.G. Kochemasov, F.A. Starikov: Optics Communications **170**, 161 (1999)
4. F.A. Starikov et al.: Proc. SPIE **4184**, 445 (2001)
5. F.A. Starikov et al.: Proc. SPIE **4353**, 202 (2001)
6. Y.V. Dolgoplov et al.: Izv. AN SSSR, ser. fiz. **58**, 35 (1994)
7. F.A. Starikov et al.: Proc. SPIE **5147**, 60 (2003)
8. D.L. Fried, J.L. Vaughn: Appl. Opt. **31**, 2865 (1992)
9. D.L. Fried: J. Opt. Soc. Am. A **13**, 2759 (1998)
10. E.-O. Le Bigot, W.J. Wild, E.J. Kibblewhite: Opt. Lett. **23**, 10 (1998)
11. W.W. Arrasmitth: J. Opt. Soc. Am. A **16**, 1864 (1999)
12. E.-O. Le Bigot, W.J. Wild: J. Opt. Soc. Am. A **16**, 1724 (1999)
13. B.V. Fortes: Atmospheric and Oceanic Optics **12**, 406 (1999)
14. M.C. Roggeman, A.C. Koivunen: J. Opt. Soc. Am. A **17**, 911 (2000)
15. V.P. Aksenov, V.A. Banakh, O.V. Tikhomirova: Appl. Opt. **37**, 4536 (1998)
16. V.P. Aksenov, Y.N. Isaev: Opt. Lett. **17**, 1180 (1992)
17. A.V. Kudryashov, V.I. Shaml'hausen: Opt. Eng. **35**, 3064 (1996)
18. J.C. Dainty, A.V. Koryabin, A.V. Kudryashov: Appl. Opt. **37**, 4663 (1998)
19. A. Kudryashov, H. Weber (eds.): Laser Resonators: Novel Design and Development. (SPIE Press, 1999)
20. F.A. Starikov, G.G. Kochemasov: Opt. Commun. **193**, 207 (2001)
21. M.S. Soskin et al.: Phys. Rev. A. **56**, 4064 (1997)

Part IV

Medical Applications

31 Adaptive Optical System for Retina Imaging Approaches Clinic Applications

N. Ling¹, Y. Zhang¹, X. Rao¹, C. Wang¹, Y. Hu¹, W. Jiang¹, and C. Jiang²

¹ Chinese Academy of Sciences, Institute of Optics and Electronics
PO Box 350, Shuangliu, Chengdu 610209, PR China

² E&ENT Hospital of Fudan University
Shanghai, PR China

Summary. We presented “A small adaptive optical system on table for human retinal imaging” at the 3rd Workshop on Adaptive Optics for Industry and Medicine. In this system, a 19 element small deformable mirror was used as wavefront correction element. High resolution images of photo receptors and capillaries of human retina were obtained. In recent two years, at the base of this system a new adaptive optical system for human retina imaging has been developed. The wavefront correction element is a newly developed 37 element deformable mirror. Some modifications have been adopted for easy operation. Experiments for different imaging wavelengths and axial positions were conducted. Mosaic pictures of photoreceptors and capillaries were obtained. 100 normal and abnormal eyes of different ages have been inspected. The first report in the world concerning the most detailed capillary distribution images cover $\pm 3^\circ$ by $\pm 3^\circ$ field around the fovea has been demonstrated. Some preliminary very early diagnosis experiment has been tried in laboratory. This system is being planned to move to the hospital for clinic experiments.

31.1 Introduction

The diffraction-limited high resolution image is pursued by both scientific research and applications. High resolution vivo human retina imaging has strong potential application in clinic ophthalmologic very early diagnosis. Since the first high resolution vivo human retina image was obtained via Adaptive Optics in Williams’s research group [1], many research groups have been engaged in this field. The one of the most important issues is to promote clinic application of this sophistic technology. In this respect, many things should be done. Of course, the system should have enough resolution that the photoreceptor cells and capillaries of about 3 micrometer can be clearly resolved. The system must be compact enough that it can be fitted with a table. The system should be easy to operate, such that the imaging area can be adjust both in transverse (focused at different off-axial position) and longitudinal (focused at different depths of retina) directions. The medical database of different ophthalmologic diseases based on this diffraction limited high resolution technology needs to be accumulated. The relative medical diagnosis standard of high resolution images should be established. The closed corporation between the technical aspects and medical physicians is expected.

In 1999 we developed a novel small deformable mirror with 19 elements and 20 mm clear diameter [2]. Based on this deformable mirror, in 2000, we developed an adaptive optical system for retina imaging, which was reported at the 3rd Workshop on Adaptive Optics for Industry and Medicine [3]. We realized high resolution imaging of photoreceptors and capillaries. The overall size of this set is $81 \times 47.5 \times 18.3$ cm.

In the demonstration experiment of this system we found that the correction capability is limited by the element number of the deformable mirror, only the first 9 Zernike wavefront errors can be corrected effectively. It is enough for a little application case, but in most cases the higher orders Zernike terms correction are desired also. It is also found that some operation aspects, such as transverse and longitudinal focusing should be improved. In 2001, a new adaptive optical system with a new 37 element deformable mirror was developed. In the last two years, experiments with this system have been conducted to verify its specifications. In this paper, the structure of this new adaptive system and some experimental results are reported.

31.2 37 Element Adaptive Optical System

The optical schematic is shown in Fig. 31.1. A commercial laser diode (LD) with output wavelength of 780 nm and output power of 10 mw has been used as the beacon. This kind of LD operates in a wide spectral bandwidth (about

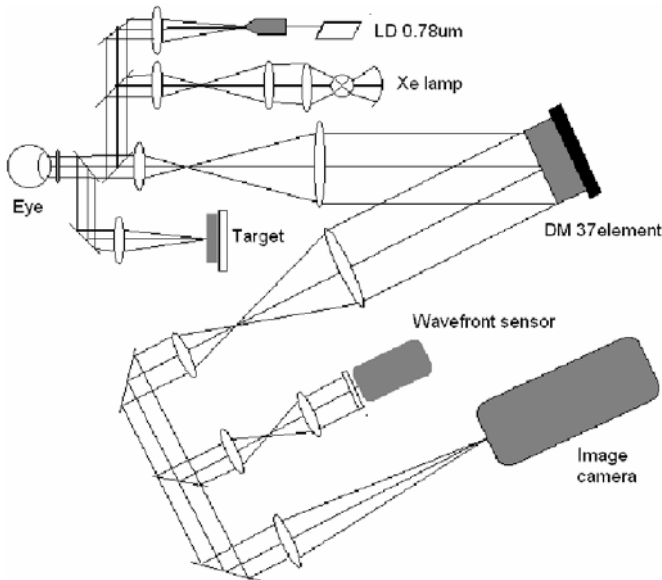


Fig. 31.1. Schematic of the table-top adaptive optics for human eye retina

10 nm) so it benefits to decrease the speckle effect and human eye is insensitive at wavelength of 780 nm. The output beam of beacon is collimated as a parallel light beam after passing through a spatial filter and the beam expander, reflected by mirror and beam splitter, and projected into human eye pupil.

The backward scattering light of beacon from the human eye retina exits through the eye pupil, passes through dichroic mirror, beam expander telescope, DM, beam condenser, mirror and beam splitter, and projects into the Hartmann wavefront sensor (WFS). The wavefront slope data measured by the WFS is acquired by a computer. By using the directed slope algorithm [4] and control algorithm the slope data are transferred directly to the control signals. The control signals are amplified by high-voltage amplifier and are used to drive the DM to realized close-loop control. After close-loop operations, the residual wavefront error approaches to the minimum and the system is stable, the computer triggers a flash lamp to illuminate the human eye retina. The illuminating light reflected from the retina propagates along the same optical path as the backward scattering light of beacon from retina, passes through the dichroic mirror and arrives to the imaging CCD camera.

In the 37 element AO system, there are some modifications. A target plate with an array of independently controlled light spots is used. When the inspected eye stares at a light spot, the eye rotates at a definite off-axis angle and the respective part of retina can be observed. The field of the target is $\pm 6^\circ$ by $\pm 6^\circ$. The imaging camera is mounted on a focusing mechanism. By adjusting the position of the camera, the structures at different layers of retina can be imaged at the imaging CCD of the camera. The CCD camera used in this system is DB512 of Princeton Instrument with 16 bit output. Its CCD sensor is back-illuminated and more sensitive than the PixCel 237 of SBIG with 12 bit output used in the 19 element system. Filters of different pass bands are used by which the imaging wavelength can be selected. Figure 31.2 shows this adaptive optical system for retina imaging. The overall size is $120 \times 57 \times 31$ cm, larger than the 19 element system, but still can be fit with an ordinary table.

Figure 31.3 shows the matching arrangements of actuators of the DM and subapertures of the WFS. 97 sub-apertures in 11 by 11 array and 37 actuators are used. The matching arrangements have been simulated to investigate the correction capability of wavefront error. In the simulation, given a Zernike mode with 1λ RMS, the wavefront slopes are detected by the subapertures of WFS and processed by the reconstruction algorithm to compute the control voltages at actuators of the DM. After multiplying with the influence functions of actuators, we can get the wavefront produced by the DM to correct the given wavefront. The difference between the given and produced wavefronts is the residual error of correction. The results are shown in Fig. 31.4. For comparison, the simulation results of the 19 element system are also included. As shown in the figure, the first 20 order Zernike modes could be corrected effectively and higher order mode would not be amplified during

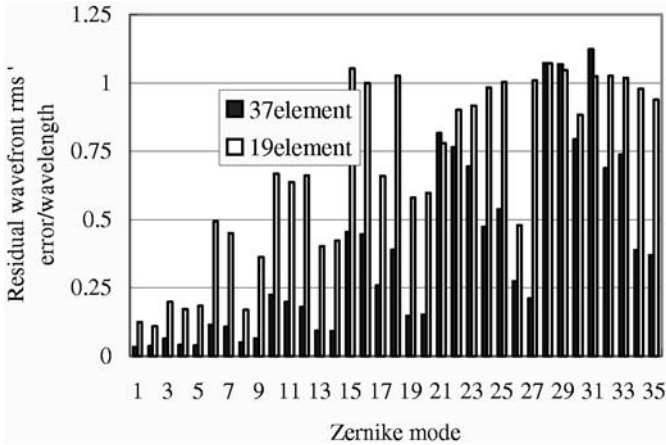


Fig. 31.4. Fitting rms error of two systems to the first 35 Zernike modes, given wavefront for each mode is 1 wavelength rms

31.3.1 Resolution and Residual Error

In the tests for resolution and residual error, an artificial eye was used. The artificial eye consists of a single lens and a glass plate with a rough surface located on the focus plane of the lens. The adaptive optical system is close-looped to correct the wavefront error of this artificial eye. The resolution after correction was tested. The light reflected by the mirror was focused at the imaging camera. The angular FWHM of the corrected focus spot is $1.2 f\lambda/D$ for $D = 6 \text{ mm}$ and $\lambda = 0.78 \mu\text{m}$ (in this test, the beacon light was focused and detected by imaging camera), corresponding to the resolutions of $2.6 \mu\text{m}$ at retina. For imaging wavelengths of 0.55 and $0.65 \mu\text{m}$, the resolution is higher.

The wavefronts before and after correction are shown in Fig. 31.5. The RMS wavefront error before correction is about 0.7λ , the main components are defocus, first and third order astigmatism, coma and spherical. After correction, the RMS wavefront errors are reduced to 0.11λ .

31.3.2 Imaging Wavelength and Longitudinal Focusing

Two wavelengths (0.55 and $0.65 \mu\text{m}$) were used for imaging. Results show that the contrast of $0.55 \mu\text{m}$ is better than that of $0.65 \mu\text{m}$. We chose $0.55 \mu\text{m}$ wavelength for imaging in most of the experiments.

For the artificial eye, when the system is close-looped, the imaging of the rough surface of the glass plate can be taken at a longitudinal position of the CCD camera. It is not necessary to readjust the position for different imaging wavelength. It means the longitudinal chromatic aberration of the imaging optics can be ignored. This position can be set as the origin of longitudinal adjustment. By adjusting the longitudinal position of the imaging camera,

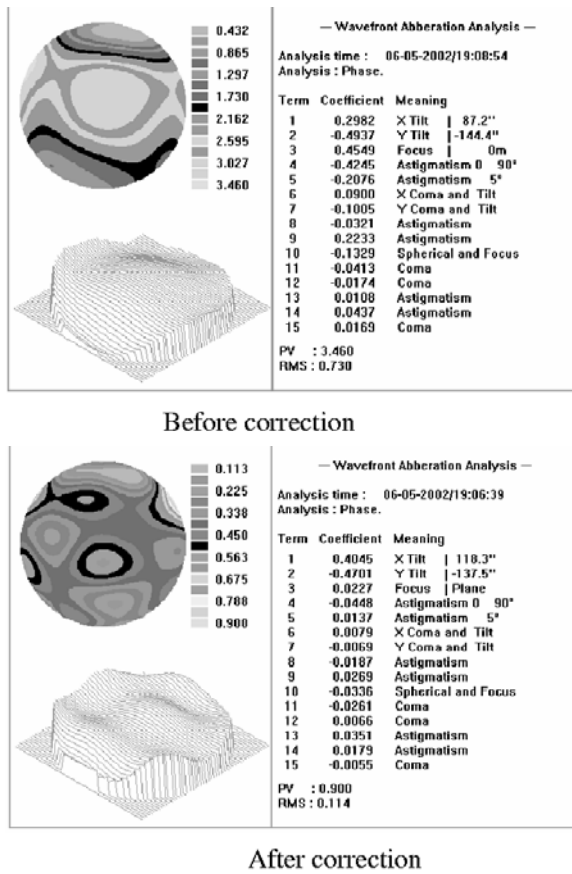


Fig. 31.5. Wavefronts before and after correction of the 37 element system tested with an artificial eye

Table 31.1. Camera position for imaging two layers of retina

Imaging wavelength	Photoreceptor	Capillary
0.55 μm	37 \approx 41 mm	23 \approx 25 mm
0.65 μm	21 \approx 25 mm	4 \approx 7 mm

the focusing layer in the retina can be adjusted. Two layers with structures of retina can be clearly imaged. One is the image of photoreceptors, the other is the image of capillaries. If we set the position of the CCD camera for imaging the glass plate of an artificial eye as the origin, the positions for clearly imaging the photoreceptors and the capillaries are listed in Table 31.1. From Table 31.1, the camera positions for clear imaging by two wavelengths are different. This is mainly due to the chromatic aberration of the eye. The

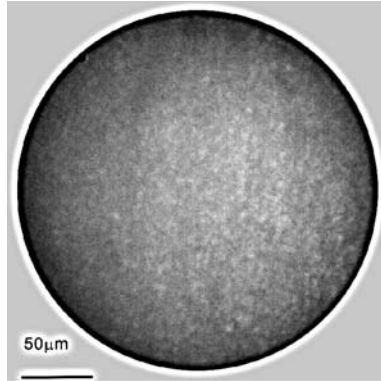


Fig. 31.6. Retina image without correction

displacement of camera for imaging the photoreceptors and the capillaries is $15 \approx 17$ mm. Considering the axial magnification, the distance of these two layers is $81\text{--}91 \mu\text{m}$.

31.3.3 Image of Photoreceptors

In the experiments of correcting wavefront error and high resolution imaging of living human eye retina, for alleviating the wavefront aberration changing, tropimide has been used to dilate the human eye pupil before correction experiment. For subject A, Fig. 31.6 shows the photograph of his retina in fovea before wavefront error correction, no details can be resolved. Figure 31.7 shows the photographs of retina image after correction at 3 different off-axis angles from fovea. The sizes of photoreceptors at these positions (00, 20 and 40 from fovea) are 3.3, 5.1 and 6.9 μm respectively. It shows that the nearer to the fovea, the denser the cell population and the smaller photoreceptor cell size.

31.3.4 The Most Detailed Capillary Distribution Image Around Vivo Human Fovea

About $81\text{--}91 \mu\text{m}$ from the layer of photoreceptors, there is a layer of capillaries, which can clearly be imaged by the AO system. The first report in the world concerning the most detailed capillary distribution images cover $\pm 3^\circ$ by $\pm 3^\circ$ field around the fovea of subject B was obtained in our experiment, as shown in Fig. 31.8. Figure 31.8 is the mosaic, every segment is a high resolution capillary photograph of corresponding part of retina. Figure 31.9 shows three segments of Fig. 31.8. The tube structure of the capillary and blood cells in the capillary can be resolved. The diameter of capillary in the right-bottom of Fig. 31.9a is $4.7 \mu\text{m}$. Figure 31.9 shows that there are no capillary at the center of fovea, which is coincident with the result of anatomy.

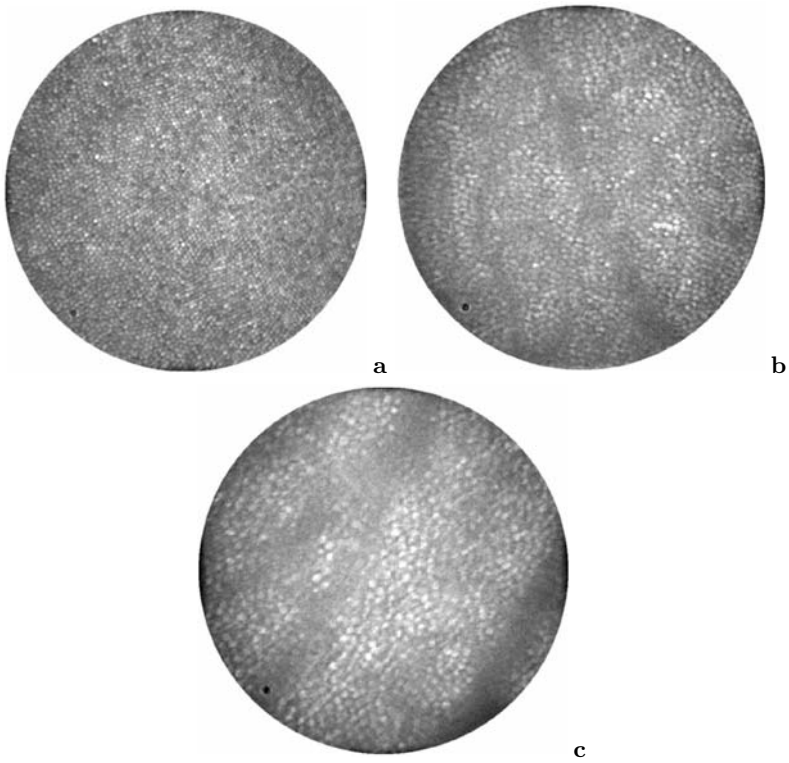


Fig. 31.7. Corrected image at fovea, cell diameter $3.3\mu\text{m}$ (a). Corrected image at 2° from fovea, cell diameter $5.1\mu\text{m}$ (b). Corrected image at 4° from fovea, cell diameter $6.9\mu\text{m}$

31.3.5 Some Preliminary Very Early Diagnosis Experiment in Laboratory

Several abnormal images of unhealthy eyes were taken in the experiments. For elderly it is frequently found that at the layer of capillary there are some white spot. Figure 31.10 shows two examples. Figure 31.11 are images of two layers of left eye of subject C. His eye was injured and very weak. The Snellen chart test is 0.2. Figure 31.12 shows an image of photoreceptor layer of the eye of a diabetic. There is a large black spot. Some details of unhealthy eye detected by the AO system are very small which could not be found by current clinic instruments. These results imply that this instrument offers potential applications for the very early diagnosis of some diseases which have effects on retina.

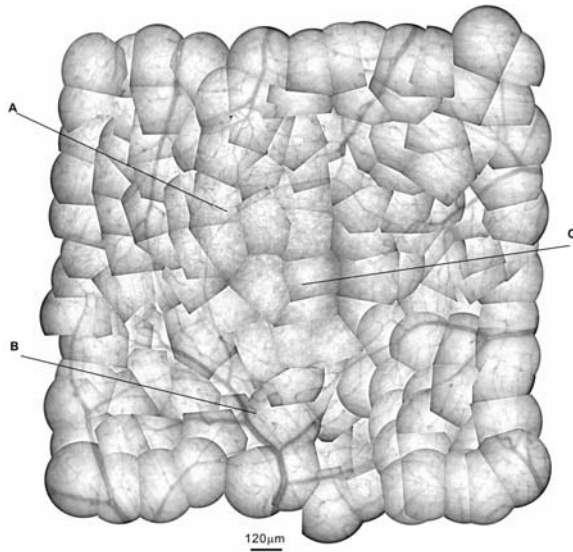


Fig. 31.8. Mosaic of capillary images around the fovea ($\pm 3^\circ \times \pm 3^\circ$)

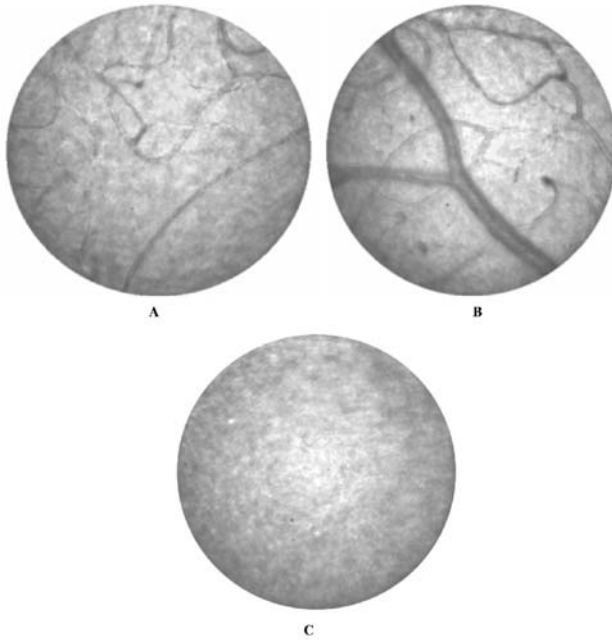


Fig. 31.9. Three enlarged segments in Fig. 31.8 (marked **A**, **B**, **C**). The tube structure and blood cells can be resolved. In the center of fovea (segment **C**), there are no capillaries

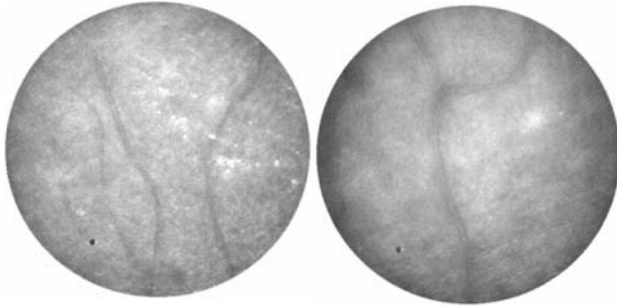


Fig. 31.10. Two examples of elder's eyes, white spots are found at the layer of capillary

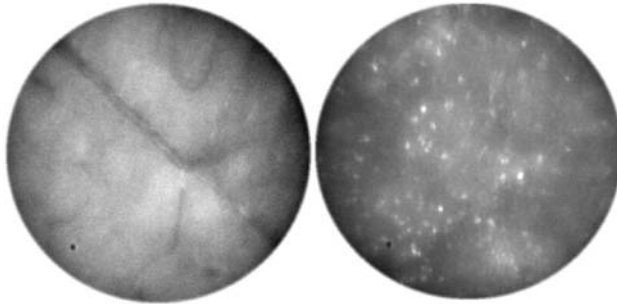


Fig. 31.11. The high resolution image in two layers of an abnormal vivo human retina

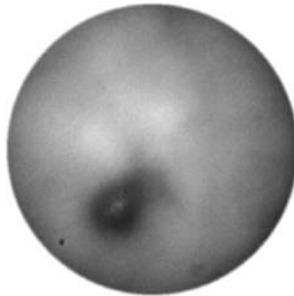


Fig. 31.12. A high resolution image of photoreceptor layer of the eye of a diabetic

31.4 Conclusion

The 37 element adaptive optical system for high resolution retina imaging has been built successfully. Comparing with the previous 19 element system, the 37 element system has much higher capability of wavefront correction. It can correct up to the first 20 Zernike modes. It also has more operation flexibilities. Experiments show it can clearly resolve the photoreceptors, cap-

illaries of human retina and small details at retina, which cannot be resolved by current clinic instruments. The first most detailed capillary distribution image around central fovea in vivo human retina has been obtained in the world. Some preliminary very early diagnosis experiment have been adapted in laboratory and these results imply that this instrument offers potential applications for the very early diagnosis of some diseases which have effects on retina. By cooperation with physicians, further more medical experiments for promoting clinic applications are desired.

References

1. J. Liang, D.R. Williams, D.T. Miller: Supernormal vision and high-resolution retinal imaging through adaptive optics. *J. Opt. Soc. Am. A* **14**, 2884 (1997)
2. N. Ling, X. Rao, L. Wang, et al.: Characteristic of a novel small deformable mirror. In: G.D. Love (ed.): *Proc. of the 2nd International Workshop on Adaptive Optics for Industry and Medicine*, Durham, 1999 (World Scientific, 2000) pp. 129–135
3. Y. Zhang, L. Ning, X. Rao, et al.: A small adaptive optical system on table for human retinal imaging. In: S.R. Restaino, S.W. Teare (eds.): *Proc. of the 3rd International Workshop on Adaptive Optics for Industry and Medicine*, Albuquerque, 2001 (Starline Printing, 2002) pp. 97–104
4. J. Wenhan, L. Huagui: Hartmann–Shack wavefront sensing and wavefront control algorithm. *Proc. SPIE* **1271**, 82 (1990)

32 Adaptive Optics to Simulate Vision with a Liquid Crystal Spatial Light Modulator

S. Manzanera, P.M. Prieto, J. Salort, E.J. Fernández, and P. Artal

Universidad de Murcia, Laboratorio de Óptica
Campus de Espinardo Ed. C., 30071 Murcia, Spain

Summary. Adaptive optics for the human eye has two main applications: to obtain high-resolution images of the retina and to produce aberration-controlled retinal images to simulate vision. We built an adaptive optics prototype specially designed for visual testing based on the use of a liquid crystal spatial light modulator (Hamamatsu X8267). The system consists of a measurement channel with switchable red (633 nm) or infrared (780 nm) illumination, a real time Hartmann-Shack sensor (25 Hz), and an additional channel allowing subjects to perform visual tasks in green light through the adaptive optics system. We tested the modulator, both as aberration generator and as corrector, first in an artificial eye and then routinely in different living eyes. This device has advantages in terms of effective stroke and mode independence allowing production and compensation of a larger range of aberrations than with other correcting devices. This opens new possibilities for visual applications of adaptive optics. However, a low temporal response and diffraction effects may be important drawbacks of the modulator for some particular applications. Examples of the performance of the system and a discussion of its limitations and potential for performing visual optics experiments will be presented.

32.1 Introduction

Deformable mirrors are the most common technology used for the active element in current Adaptive Optics systems. Although they offer advantages in terms of speed and phase smoothness, they also have important drawbacks like a limited stroke, inability to reproduce steep phase changes, and (usually) high price.

Liquid crystal phase modulators are an alternative to deformable mirrors for wavefront shaping or correction [1, 2]. The main advantage of this technology is the capability for reproducing abrupt phase maps, which additionally allows the use of wrapped phase representations, greatly increasing the device effective stroke. Also, they can profit from the advances in liquid crystal manipulation gained in other technological fields, to produce low cost devices in the near future. Among their drawbacks, the low speed is the most important. In addition, low efficiency and artifacts due to diffraction have been traditionally pointed out as major problems in liquid crystal modulators. However, these problems have been greatly reduced with a new type of modulators, basically consisting of an optically driven continuous sheet

of liquid crystal, which are not pixelated and, therefore, are claimed to be virtually diffraction-free.

In this work, a continuous liquid crystal spatial light modulator was evaluated as the active element in an adaptive optics system for Visual Optics applications. The device is a Hamamatsu X8267 Programmable Phase Modulator (PPM). Its performance as wavefront generator was checked by producing different amounts of single Zernike terms of increasing order. The generation quality was studied both by measuring the wavefront shape and by experimentally recording the point spread function images. The device capability as wavefront corrector was first checked in an open-loop compensation for an artificial eye. Finally, the device was used in a close-loop mode to correct the aberrations of a real eye in real time.

32.2 Apparatus

The Hamamatsu X8267 Programmable Phase Modulator consists of an optically-addressed liquid crystal spatial light modulator optically coupled to an intensity light modulator. The former is composed of a liquid crystal continuous layer, a light blocking layer and a photoresistive layer sandwiched between transparent electrodes. When an image of the desired phase map is displayed in the intensity light modulator, it causes the voltage between the electrodes to locally change, varying the effective refractive index and, consequently, inducing the associated wavefront distortion. Both elements are coupled through an optical system that removes pixelation. Therefore, the PPM is theoretically free from the diffraction patterns produced by the pixel structure associated to the typical electrically-addressed liquid crystal devices.

For this particular model, phase maps can be generated with XGA resolution (768×768 active pixels) over the 20×20 mm liquid crystal active area. The maximum optical path difference was around 1 wavelength for $\lambda \approx 700$ nm. Wrapped phase maps were displayed onto the PPM as images with the contrast manipulated to achieve the correct phase values for the wavelength in use.

The adaptive optics system (see Fig. 32.1) was based on a double-pass apparatus, previously used for applications in the human eye [3, 4], with the main objective of its use in Visual Optics experiments both for retinal imaging or to simulate vision. The illumination channel was either a 633-nm HeNe laser or a 780-nm diode laser as light source. The PPM was included in the measurement channel, which usually conveyed the light to the Hartmann-Shack (H-S) sensor used for measuring the system aberrations [5], including those of the eye. Alternatively, aerial images were recorded deflecting the light towards a CCD camera by means of a movable mirror that was inserted, when required, in front of the H-S sensor (dashed line). In order to use most of the active area of the PPM, a telescopic system was used to magnify the eye

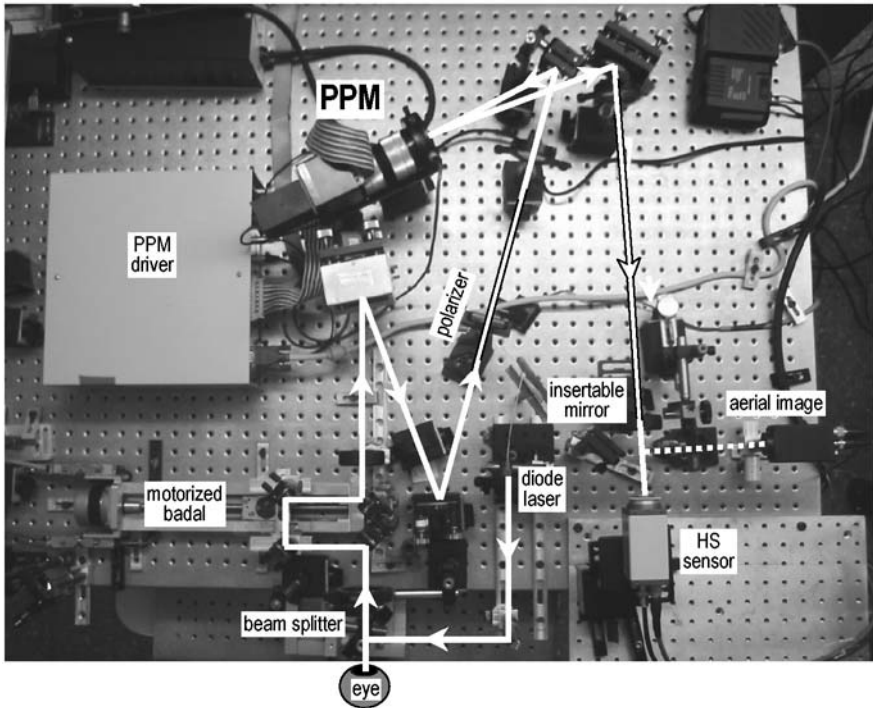


Fig. 32.1. Double pass adaptive optics apparatus used to test the PPM

pupil plane by a factor of 2.5 onto the PPM plane. With this magnification value, a 5.5 mm eye pupil corresponds to 13.8 mm on the PPM. This value was convenient since it allowed displacements of the phase map over the PPM to fine tune of the alignment with the eye's aberrations.

By construction, the PPM requires the use of linearly polarized light. This was achieved by means of a polarizer inserted in the measurement channel. The measurement channel also includes a motorized focus-corrector system. In this experiment, this system was used to induce known amounts of defocus for checking the PPM calibration.

32.3 Performance of the PPM as an Aberration Generator

The performance of the PPM as a phase generator was evaluated by producing different amounts of a single Zernike mode. We selected a vertical coma (term $Z_{3,1}(\rho, \theta)$ in the OSA standard ordering). Figure 32.2 shows the estimates for the Zernike coefficient ($C_{3,1}$) provided by the H-S sensor as a function of the input value together with the residual measured coefficients

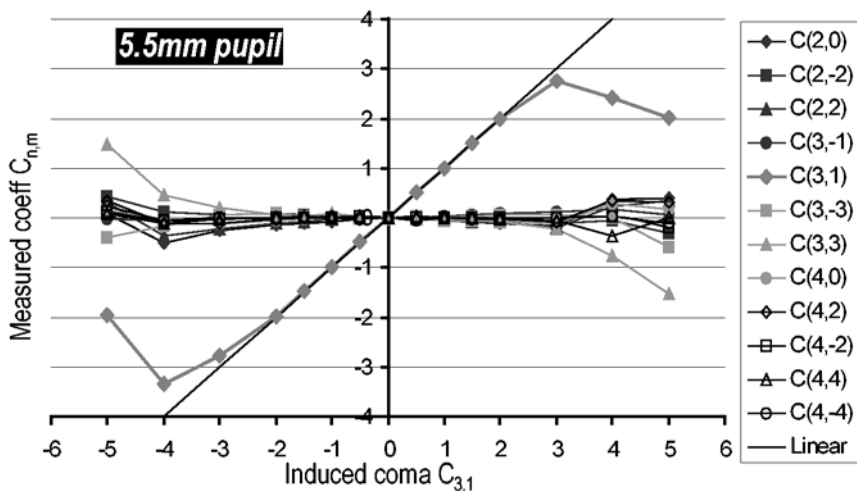


Fig. 32.2. Measured Zernike terms obtained when inducing different amounts of coma ($C_{3,1}$) with the PPM. All the coefficients are expressed in microns



Fig. 32.3. Experimental aerial images for pure Zernike coma induced with the PPM. *Left:* $C_{3,-1} = 1 \mu\text{m}$. *Right:* $C_{3,-1} = 3.25 \mu\text{m}$

for all the Zernike terms up to 4th order. For a wide range of values, these estimates are in very good agreement with the induced coma while negligible amounts of other terms are measured. For higher values, the linearity begins to fail and other terms start appearing in the measured wavefront. The coefficients are expressed in μm over a 5.5 mm pupil in the eye pupil plane.

As a further test, we recorded the double-pass images for an aberration-free artificial eye and for the induced coma values. Two of those images are shown in Fig. 32.3. For moderate values of coma inside the linear range of aberration generation, the double-pass image resembles quite well the expected shape. For higher values, the coma shape is still easily recognizable but a spurious peak appears in the paraxial image position. This peak is as-

sumed to be a 0-order diffractive artifact associated to the phase wrapping required by the PPM due to its limited phase stroke. The sources of this artifact may be residual pixelation effects, under-sampling problems in high phase slope areas, and/or failure to cover the whole 2π phase range. These diffraction problems might be reduced with a better calibration of the system or with a higher resolution device.

32.4 Aberration Correction in an Artificial Eye

The adaptive optics system was used to correct the aberrations of an artificial eye. In this case, a diode laser was used as light source. Figure 32.4 presents the original wrapped aberration over a 5.5 mm pupil, the associated PSF and the experimentally recorded double-pass image. The initial RMS was $0.62\ \mu\text{m}$. These images can be compared with those obtained with a single step correction, i.e., by displaying in the PPM the negative of Fig. 32.4 (left panel). The combined wavefront become virtually flat (RMS = $0.05\ \mu\text{m}$). Consequently, the PSF collapses to a very narrow peak, which corresponds to a high Strehl ratio. This improves the resolution of the double pass images, although only the second pass is being corrected. The two peaks that appear in the compensated image are due to the propagation modes of the optical fiber used to couple the diode with the system. When the adaptive optics is off, they are blurred by the ocular aberrations to a single broad peak (Fig. 32.4, right panel). Successive correction steps further reduce the RMS and increase the Strehl ratio, although visually the differences with Fig. 32.5 are hardly apparent.

This procedure corresponds to an open loop correction. Open-loop operation requires a high fidelity between the wavefront sensor outcome and the phase map finally produced by the active element. Deformable mirrors typically present non-linearities that force close-loop operation. On the contrary, these results prove the capability of the PPM to work open-loop or even in a single step.

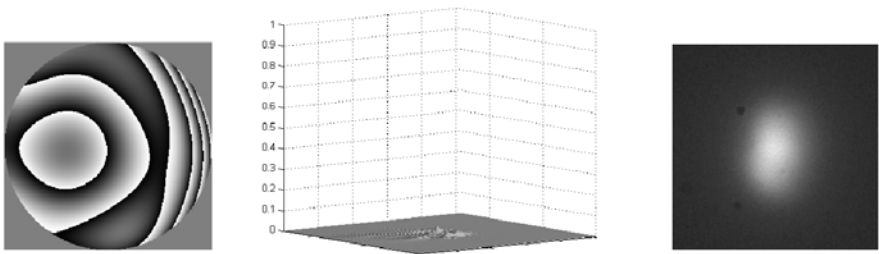


Fig. 32.4. Wave aberration (*left*), PSF (*center*), and aerial image (*right*) for the artificial eye with the adaptive optics OFF. The aberration RMS was $0.62\ \mu\text{m}$ and the Strehl ratio associated to the PSF was 0.03

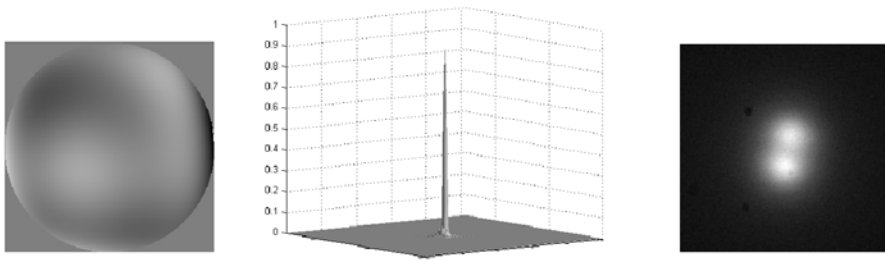


Fig. 32.5. Wave aberration (*left*), PSF (*center*), and aerial image (*right*) for the artificial eye with the adaptive optics ON after a single iteration (open-loop mode). The aberration RMS was $0.05\ \mu\text{m}$ and the Strehl ratio associated to the PSF was 0.90

32.5 Close Loop Aberration Correction in a Real Eye

As a final step of our testing of the performance of the PPM for Visual Optics applications, we performed a close-loop correction of a real eye. We modified our real time (25 Hz) H-S wavefront sensor control software in order to feed the PPM with the instantaneously measured aberrations. Due to the slow response of the modulator (around $1/4\text{s}$), we slowed the loop to work around 4 Hz.

Figure 32.6 shows the results of a close-loop correction experiment on a normal subject (one of the authors: PA male, natural viewing conditions, 5.5 mm artificial pupil). The RMS decreases from an initial value of $0.56\ \mu\text{m}$ to values around $0.1\ \mu\text{m}$ within 1 s. The Strehl ratio improves from an initial 0.028 to values as high as 0.81. Figure 32.7 shows examples of the evolution of the wave aberration and the associated PSF.

Both the asymptotic RMS value of around $0.1\ \mu\text{m}$ and the instabilities that can be noticed in both graphs in Fig. 32.6 are presumably due to the

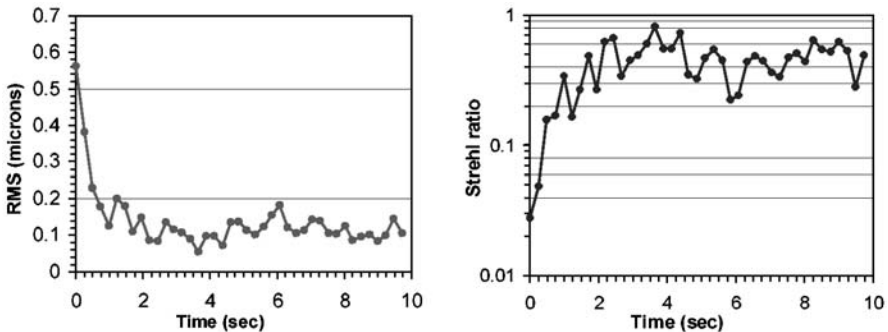


Fig. 32.6. Residual RMS (*left*) and associated Strehl ratio (*right*) for a 9.7 s run of close-loop aberration correction

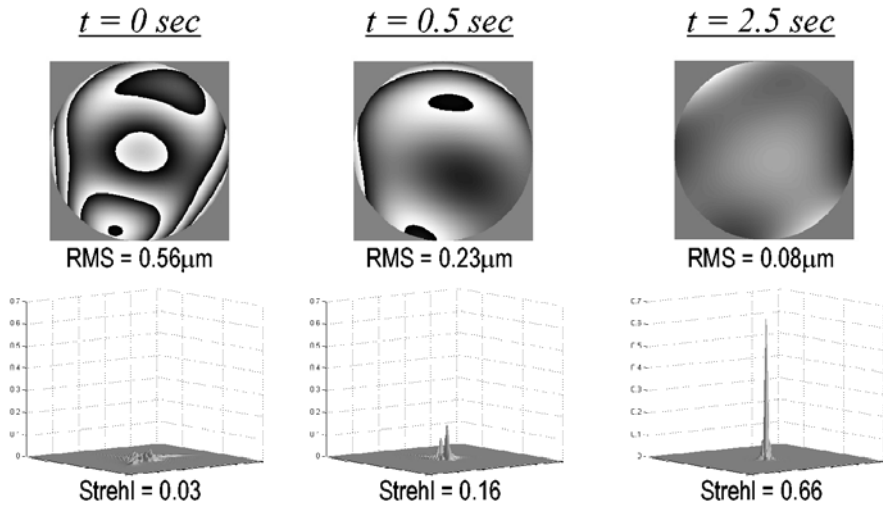


Fig. 32.7. Instantaneous wave aberration and associated PSF for three different instants through the close-loop correction on subject PA

dynamics of the ocular aberration [6] since they are not observed when a close-loop correction is applied to an artificial eye. This dynamics have been shown to have important spectral components up to 5 Hz, faster than the close-loop rate used. As a consequence of this dynamics, the close-loop tended to diverge unless an attenuation factor or gain between the measured aberration and the displayed phase map is used (0.3 for the present case). This is the ultimate responsible of the gradual behavior of the RMS in Fig. 32.6 at the beginning of the loop. For an artificial eye, where no gain is required, correction from Fig. 32.4 to Fig. 32.5 is achieved in around 1/4 s.

32.6 Conclusion

In this study, the Programmable Phase Modulator X8267 from Hamamatsu was tested as the active element of an adaptive optics system for Visual Optics applications, both as wavefront generator and corrector. The capacity of working with wrapped phase maps greatly increases the PPM effective stroke. The range of linear production of aberrations is larger than those typical in deformable mirrors. Besides there is virtually no cross-coupling inside this linear range. The PPM was tested as wavefront corrector in an artificial eye, reducing its aberrations to a negligible value in a single step. The high fidelity of the device for reproducing the intended phase map allows open-loop operation, typically impracticable with mirrors. Finally, a close loop correction was performed in a real eye. The slow temporal response of the modulator, which is probably its major drawback, imposed a reduction on

the aberration display rate to a value a little below the highest frequency of the relevant components of the ocular wavefront dynamics. As a consequence, the residual RMS after correction was higher than for the artificial eye case and the instability appeared in the correction loop. The latter effect was reduced by including a gain in the close loop, although this increased the convergence time. Nevertheless, the PPM proved to be capable of working as the active element in a close-loop adaptive optics system for the eye with an efficiency at least comparable to that achieved with low cost deformable mirrors.

Acknowledgements

This work was supported by the “Ministerio de Ciencia y Tecnología”, Spain, Grant BFM2001-0391.

References

1. G.D. Love: *Appl. Opt.* **36**, 1517 (1997)
2. F. Vargas-Martín, P.M. Prieto, P. Artal: *J. Opt. Soc. Am. A* **15**, 2552 (1998)
3. E.J. Fernández, I. Iglesias, P. Artal: *Opt. Lett.* **26**, 746 (2001)
4. E.J. Fernández, P. Artal: *Opt. Express* **11**, 1056 (2003)
5. P.M. Prieto, F. Vargas-Martín, S. Goelz, P. Artal: *J. Opt. Soc. Am. A* **17**, 1388 (2000)
6. H. Hofer, P. Artal, B. Singer, J.L. Aragón, D.R. Williams: *J. Opt. Soc. Am. A* **18**, 497 (2001)

33 Confocal Scanning Retinal Imaging with Adaptive Optics

I. Iglesias, B. Vohnsen, and P. Artal

Universidad de Murcia, Laboratorio de Óptica
Campus de Espinardo Ed. C., 30071 Murcia, Spain

Summary. We have developed a prototype of a confocal scanning laser ophthalmoscope that incorporates adaptive optics to correct for the wavefront aberrations of the eye and those induced by the optical system. Two corrector devices were tried out in the experiments: a membrane deformable mirror and a liquid crystal spatial light modulator. We obtained high-resolution images of different parts of the retina with and without the wavefront correction. We also explored alternative adaptive optics configurations to improve on the imaging performance of the system.

33.1 Introduction

Retinal imaging with the scanning laser ophthalmoscope (SLO) is limited by the aberrations of the eye, specially if large diameters of the eye pupil are used. The improvement of the images has previously been accomplished by incorporation of adaptive optics (AO) correcting with a Xinetics mirror in a reflective relay optics system [1]. However, one of the requirements to facilitate the widespread use of these techniques is to simplify the system and to reduce the cost of the components. With this aim we tested two relatively low cost correctors: a membrane deformable mirror (MDM) and a programmable phase modulator in a refractive relay optics scanning laser ophthalmoscope (AO-SLO) set-up.

33.2 Using an Electrostatic MDM in AO-SLO

The MDM (Flexible Optical, Holland) consists of a reflective mirror membrane ($\varnothing 15$ mm) hanging over an arrangement of 37 electrodes occupying a diameter of ≈ 7.5 mm. Details about the mirror characteristics can be found elsewhere [2–4]. To efficiently control the mirror, the area used must be less than the clear aperture but slightly more than the area covered by electrodes. In this work the $\varnothing 6$ mm at the eye pupil is transported to a $\varnothing 9$ mm on the mirror membrane.

The wavefront sensing is done using a Hartmann–Shack sensor consisting of a squared array of lenslets with 6.3 mm focal length and 0.6 mm pitch attached to an IR-enhanced CCD camera. The system has around 60 spots

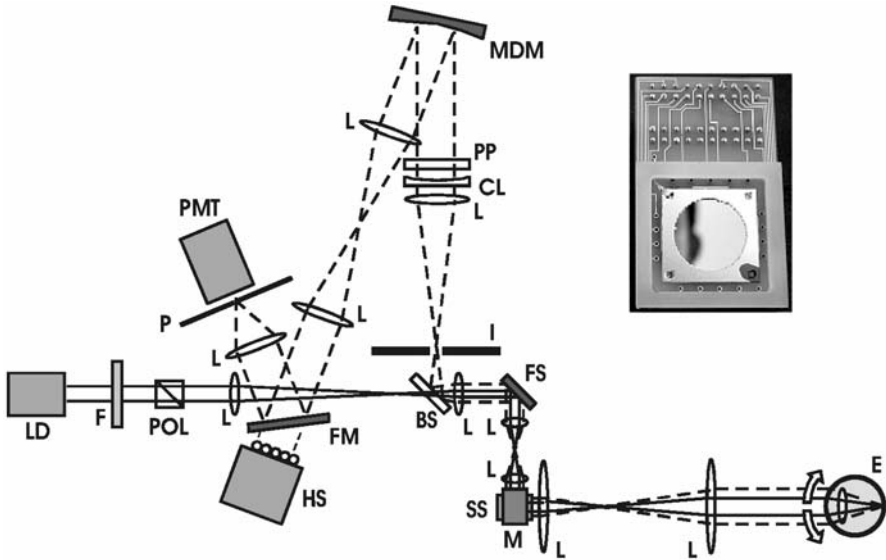


Fig. 33.1. Diagram of the AO-SLO system. The system consists of a laser diode (LD), fast (FS) and slow (SS) scanners, a photomultiplier tube (PMT), pinhole (P), neutral density filter (F), beam-splitter (BS), adjustable iris (I), mirror (M), flip mirror (FM), lenses (L), Phase plate (PP) and cylindrical lens (CL), polarizer (POL), Hartmann–Shack (HS), membrane deformable mirror (MDM). The inset shows a photo of the MDM

to determine the wavefront gradient when using the $\varnothing 6$ mm eye pupil to reconstruct the aberrations to 4^{th} order.

The configuration of the system is shown in Fig. 33.1. An IR diode laser is used to illuminate the eye. The beam power is reduced to maintain the illumination of the eye at around $100\mu\text{W}$; well below the safety levels for continuous viewing of a collimated beam at 785 nm [5]. The beam scanning is done using two galvanometric scanners (one of them resonant) in conjugate planes with the eye pupil. An important amount of the defocus of the eye is corrected by allowing the displacement of the lens nearest to the eye and the bite bar used to stabilize the head of the subject. The light reflected from the retina is de-scanned and redirected to the adaptive optics components using a beam splitter. The correction used for the acquisition of images is in this set-up static. Thus once the correct voltages for the mirror have been obtained in a closed-loop control scheme, the voltages are maintained and flip mirror is used to redirect the aberration-corrected light to the photomultiplier through the confocal pinhole. This is justified because the movements of the eye are small enough to have a relative stable aberration; normally well below the aberration of the uncorrected eye. The signal of the photomultiplier is digitalized to build images of 512×512 pixels at a frame rate – limited

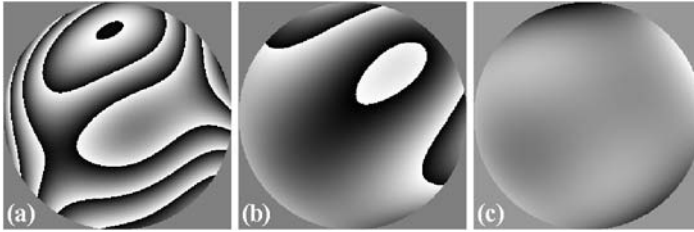


Fig. 33.2. (a) A sample of the aberration measured for $\varnothing 6.0$ mm at 4° eccentricity represented modulus 2π , (b) an example of the aberration once corrected the eye and the system with the phase plate and the cylindrical lens and (c) a sample after the close-loop correction

by the angular speed of the scanners – of 15 Hz. It must be noted that in this experiment the AO system only corrects the outgoing beam. In the incoming beam, the aberrations of the eye do not play a significant role due to the small beam diameter used ($\varnothing 2$ mm) [6].

A sample of the wave aberration map for the right eye and the system of one of the authors is shown in Fig. 33.2a. The Strehl ratio is 0.01. The values of the Zernike coefficients is shown in Table 33.1 column A. In addition we tested the ability of the MDM to generate different terms individually. Table 33.1 column B shows the results obtained. It can be observed that the MDM is not able to generate enough astigmatism, coma and in particular the spherical aberration. At this point it must be stressed that the MDM was not designed taking these special requirements into account. Nevertheless, the characteristics of this MDM were interesting enough to overcome its limitations by introducing into the system a spherical aberration phase plate and a cylindrical lens. The phase plate was mounted on a stage allowing lateral displacements and the cylindrical lens in a rotation stage. The position of the phase plate and the rotation of the cylindrical lens was set to minimize the aberration while using the HS sensor. The wave aberration obtained af-

Table 33.1. Zernike coefficients

	Coefficient	A	B	C	D
Defocus	a_4	0.123	± 0.5	0.181	-0.034
Astigmatism	a_5	0.276	± 0.4	0.155	0.076
"	a_6	-0.471	± 0.3	0.011	0.011
Coma	a_7	0.242	± 0.12	-0.061	-0.021
"	a_8	0.178	± 0.15	0.004	0.000
	a_9	0.134	± 0.12	0.081	0.017
	a_{10}	-0.004	± 0.20	0.091	0.034
Spherical	a_{11}	-0.187	± 0.05	-0.017	-0.024
	a_{12}	-0.001	± 0.07	0.001	-0.044

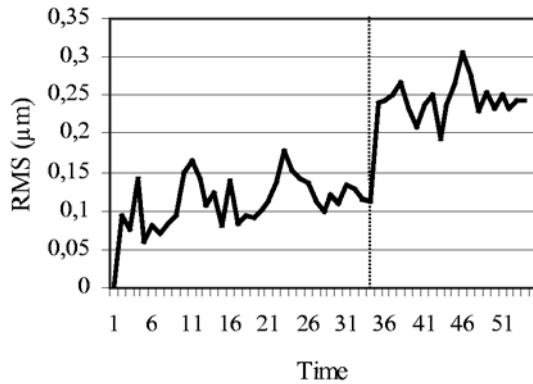


Fig. 33.3. Graph of the RMS variation with time (units of 0.12 s) when the MDM is on (data on the left of the division line) and off (on the right)

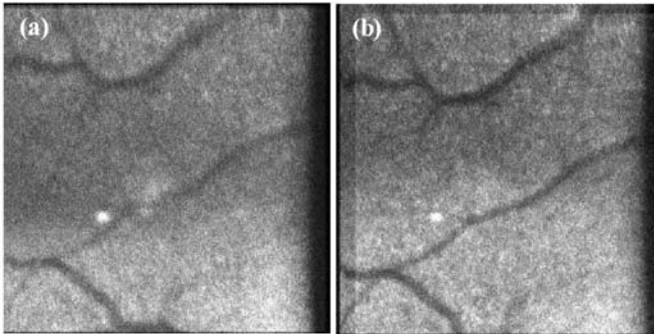


Fig. 33.4. Retinal images subtending $8 \times 8^\circ$ at 4° degrees eccentricity (a) without adaptive optics and (b) with adaptive optics

ter this procedure is shown in Fig. 33.2b and the corresponding coefficients in Table 33.1 column C. The Strehl ratio reaches now a value of ≈ 0.1 . With this modified system we operated the MDM in closed loop to minimize the residual aberration reaching the wavefront shown in Fig. 33.2c. The associate coefficients are presented in Table 33.1 column D. At this stage, the Strehl ratio oscillates around a value of 0.5. Figure 33.3 shows the variations on the RMS with and without the MDM correction. It should be mentioned that these experiments have been carried out without paralyzing the accommodation of the eye.

When comparing the images obtained without and with AO applied (Fig. 33.4) it becomes apparent that there is a significant improvement in image quality and contrast in the latter case. In all cases a confocal pinhole of $\varnothing 200 \mu\text{m}$ was used (corresponding to $\approx 75 \mu\text{m}$ at the retinal plane) and the approximate power reaching the photomultiplier was around 1 nW. To

increase the signal to noise ratio six images were averaged after calculation of the relative displacements by the use of a correlation algorithm.

33.3 Using a Programmable Phase Modulator in AO-SLO

In the next experiments a programmable phase modulator (PPM) from Hamamatsu (X8267 series) was used [7]. The device consists of an LCD with SVGA (1024×768 pixels) receiving signal from the computer. An internal laser illuminates (write light) the LCD acting as transmission mask (see inset on Fig. 33.5). The LCD plane is spatially filtered to reduce pixelation and conjugated onto a transparent photoresistive electrode layer, which creates a transversal spatial variation of voltage across a liquid crystal generating a phase mask. The liquid crystal is a parallel-aligned nematic where the molecules are arranged in the transversal plane. As voltage is applied across the liquid crystal, the molecules reorient. The amount of reorientation is proportional to the change in the index of refraction experienced by the readout light when its polarization state is linear and oriented parallel to the molecules orientation with the offset voltage. The maximum amount of phase change is slightly more than 2π for the wavelength used implying a modulus 2π wrapped wavefront correction.

Some modifications respecting the previous system were introduced to conjugate the $\varnothing 6$ mm eye pupil now on to $\varnothing 18$ mm PPM active area and

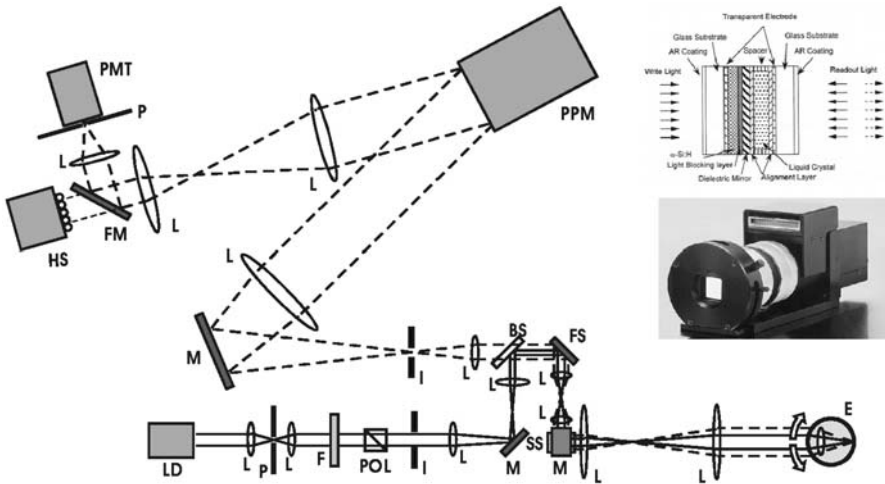


Fig. 33.5. Layout of the scanning laser ophthalmoscope with a programmable phase modulator (PPM). The system is similar to the one represented in Fig. 33.1. Inset shows the PPM active media layered structure (from Hamamatsu instructions manual) and a photo of the device

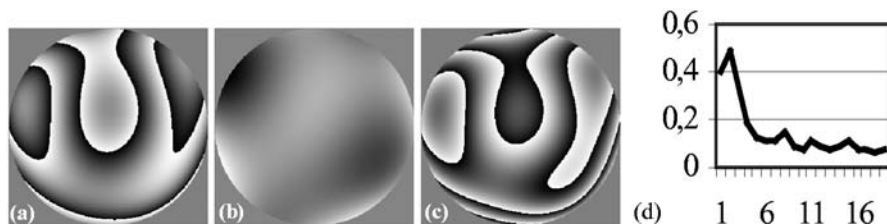


Fig. 33.6. (a) A sample of the aberration measured for $\varnothing 6.0$ mm at 4° eccentricity represented modulus 2π , (b) an example of the aberration once corrected with the PPM, (c) the gray scale image sent to the PPM through the SVGA computer port, (d) graph of the wave aberration RMS (μm) vs. time (units of 0.12s) in the closed-loop approach from (a) to (b)

to linearly polarize the beam entering the eye (see Fig. 33.5). No significant depolarization by the eye was observed and therefore no other polarizer is required in the exit path. The PPM is not a modal device as in the case of the MDM, so a careful alignment of the PPM is needed to match the controlled pupil with respect to the pupil on the HS in order to correct the aberration. In principle, a direct correction of the measured aberration is possible with the PPM. Nevertheless, better results were obtained by weighting the measure and using a closed-loop correction scheme at 4 Hz reaching a phase distribution better suited to compensate a given aberration than the direct measurement.

Figure 33.5a shows the measured aberration at 4° degrees eccentricity and, (b) the final result after 6 iterations. The Strehl ratio increases from 0.058 to 0.8. On panel (b) is the gray scale image used to correct the aberration and in (d) the evolution of the RMS with time.

We observed artifacts in the beam exiting the PPM that cannot be detected with the HS sensor but can affect the PSF of the system. Some of them are the presence of a first diffraction order generated by incompletely filtering of the LCD pixel structure, which increase as the demands in correction rise, inhomogeneities of the amplitude in the beam caused by the interfaces between differing phase domains in the liquid crystal and the presence of an unmodulated beam – together with the corrected one – reflected probably from the outer interface of the device. The detailed effect of such artifacts on the formation of retinal images must still be studied.

Figure 33.7 shows the retinal images obtained after averaging six shifted frames for two scanning areas in the same region. An image improvement was obtained with the corrected beam comparing Fig. 33.7a with 33.7b, specially notable are the results of $2 \times 2^\circ$ where it is possible to identify different cones. It is interesting to note that there is an excess of movement of the retina compared with the system speed that spreads the light coming back from the cones.

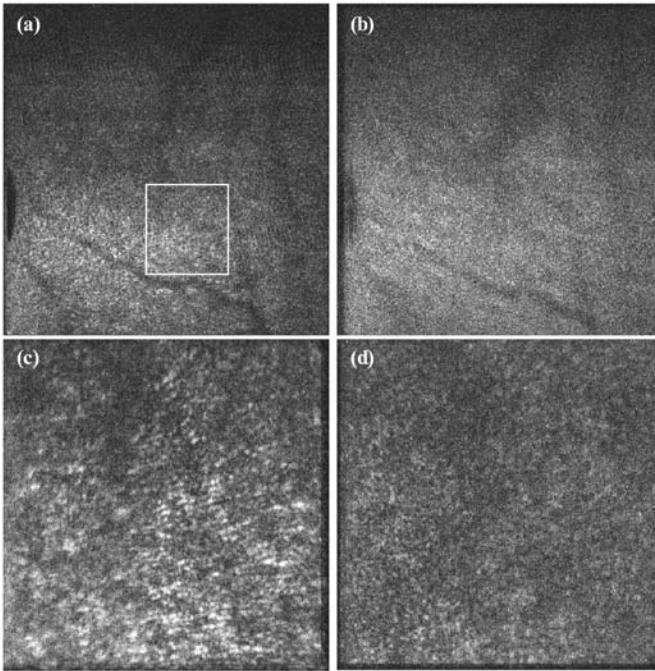


Fig. 33.7. Retinal images subtending $8 \times 8^\circ$ at 4° degrees eccentricity (a) with adaptive optics and (b) without adaptive optics, (c) a new scan subtending $2 \times 2^\circ$ of the area marked with a white square with correction and (d) without correction

33.4 Conclusions

In this contribution we have presented a new SLO prototype that incorporates relatively low-cost AO. First we used a phase plate and a cylindrical lens to reduce the RMS and the MDM to correct the residual aberration. In the second place we adapt the system to the use of a PPM, a device specially interesting for practical implementations of AO in imaging devices like SLO.

Acknowledgments

This work has been supported by Spanish Fondo de Investigación Sanitaria (FIS 01/1463), Ministerio de Ciencia y Tecnología (BFM2001-0391) and Marie-Curie fellowship HPMD-CT-2000-00052. We wish to thank Flexible Optical for providing a replacement of the MDM used in this work and acknowledge the help of José Salort for helping with software development.

References

1. A. Roorda, F. Romero-Borja, W.J. Donnelly III, H. Queener, T.J. Hebert, M.C.W. Campbell: Adaptive optics scanning laser ophthalmoscopy. *Opt. Express* **10**, 405 (2002)
2. E.J. Fernández, I. Iglesias, P. Artal: Closed-loop adaptive optics in the human eye. *Opt. Lett.* **26**, 746 (2001)
3. E.J. Fernández, P. Artal: Membrane deformable mirror for adaptive optics: performance limits in visual optics. *Opt. Express* **11**, 1056 (2003)
4. B. Vohnsen, I. Iglesias, P. Artal: Confocal Scanning Laser Ophthalmoscope with Adaptive Optical Wavefront Correction. *Proc. SPIE Int. Sec. Opt. Eng.* **4964**, 24 (2003)
5. American National Standard, *American National Standard for Safe Use of Lasers Z136.1-2000* (Laser institute of America, Orlando 2000)
6. P. Artal, R. Navarro: Monochromatic modulation transfer function of the human eye for different pupil diameters: an analytical expression. *J. Opt. Soc. Am. A* **11**, 246 (1994)
7. Y. Kobayashi, Y. Igasaki, N. Yoshida, N. Fukuchi: Compact high-efficiency electrically-addressable phase-only spatial light modulator. *Proc. SPIE Int. Soc. Opt. Eng.* **3951**, 158 (2000)

34 A High-Resolution Adaptive Optics Fundus Imager

G.R.G. Erry¹, L.J. Otten¹, A. Larichev², and N. Irochnikov³

¹ Kestrel Corporation

3815 Osuna Road NE, Albuquerque, NM, 87109, USA

² Lomonosov Moscow State University, Center of Medical Physics

M.V. Leninskiye Gory, Moscow 119992, Russia

³ M.V. Lomonosov Moscow State University, Faculty of Physics

Leninskiye Gory, Moscow 119992, Russia

Summary. The spatial resolution of retinal images is limited by the presence of time-varying aberrations present within the eye. A low-order adaptive optics system using a Shack–Hartmann wavefront sensor and a bimorph deformable mirror is described. Using a standard Hitachi video camera and a PC running Windows 2000, control of low-order aberrations within the eye can be achieved, enabling high resolution images to be obtained. The wavefront sensor employs a novel dithered reference technique to reduce speckle recorded in the hartmannogram. As a measurement of the residual errors within the image is known, it is possible to use post-processing techniques to further improve the resolution of the image. Example images of retinas taken with the system and then post-processed are shown, demonstrating the ability to calculate near diffraction-limited images. Data on the performance of the system are presented.

34.1 Introduction

A typical standard fundus imager is able to take images of the retina with a 20–30 μm resolution, which is mainly restricted by the comparatively poor optics with the subject's eye. It would be desirable to have a better resolution image of the retina enabling earlier diagnosis of such conditions as age related macular degeneration (ARMD) and diabetic retinopathy. One technique to overcome the aberrations in the eye is to use adaptive optics. By using such a system, if all the aberrations were corrected, then the limit would be the size of the eye's pupil. A typical dilated pupil for a human is approximately 8 mm, and using the Rayleigh criterion gives a diffraction limit of 3 μm .

Standard adaptive optics system could be used for such an imaging system. However, due to the complexity and expense of such devices, a lower cost and a system readily adapted to the clinical environment is required. As the single most expensive item in an AO system is the mirror, a relatively simple mirror is required implying that it will only correct the low-order aberrations. Although such a mirror will correct the major aberrations, to create a high resolution image further correction is necessary. By using deconvolution techniques on the recorded image, with knowledge of the residual aberrations

derived from the wavefront sensor it should be possible to improve the image further.

34.2 Hardware Considerations

34.2.1 Shack–Hartmann Sensor

As the eye does not have any natural beacons for a wavefront sensor it is necessary to inject light into the eye to form an artificial “guide star” on the retina. The easiest technique is to use a laser that is focused on the retina through the fundus imager. The drawback is that the laser is spatially coherent, so gives rise to speckle within the sub-images of the Shack–Hartmann sensor, Fig. 34.1.

To overcome the issue, a “dithered” reference spot can be used. By quickly rotating the spot in a circle on the retina it is possible to mitigate the problem. As the spot traverses the retina the speckle pattern recorded on the Shack–Hartmann sensor changes. By creating many different speckle realizations on the sensor during one integration period it is possible to effectively decohere the image, thus removing the speckle from the Shack–Hartmann image. The circle subscribed by the spot is of order of $200\ \mu\text{m}$, thus is well within the isoplanatic patch of the eye, but large enough that the speckle is averaged sufficiently to improve the accuracy of the recovered wavefront, Fig. 34.2.

For example, if a dithering technique is not used, then the error on the centroid in the Hartmannogram in Fig. 34.1 is approximately one wavelength,

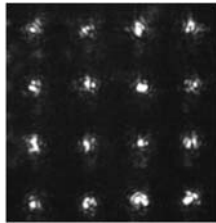


Fig. 34.1. A set of Shack–Hartmann spots without a dithered reference

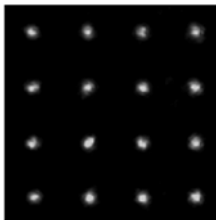


Fig. 34.2. A set of Shack–Hartmann spots with a dithered reference

whereas when the reference is dithered as in Fig. 34.2 then the error on the centroid is reduced to $1/20$ of a wavelength.

34.2.2 Deformable Mirror

Due to the large aberrations that can be present within a human eye, the overriding factor in choosing a deformable mirror is the maximum stroke. It is possible to see eyes that have in excess of 4 dioptres of error both in defocus and astigmatism. The mirror must have enough stroke to effectively remove aberrations of this magnitude. As the AO system has a complexity and cost constraint the mirror chosen was an 18 element bimorph deformable mirror, manufactured by Kudryashov. Due to the novel construction, the mirror has a stroke (for defocus) in excess of $9\ \mu\text{m}$, making it suitable for this application.

34.2.3 Illumination Source

The illumination source for the system has two purposes, firstly a continuous broad-band light is required to allow the operator to view the retina and align the subject to the equipment. Although the illumination does not have to give a good signal to noise ratio on the scene camera (the camera used for aligning the subject) it needs to allow the operator to easily identify major features (such as the macula and optic disk) to allow alignment.

The other light source required is used when the data image is taken. The light for this needs to be brighter to achieve a good signal to noise ratio on the camera, however this light can be flashed as it only needs to coincide with the integration on the data camera, typically about 50–100 ms to avoid blurring due to eye saccades. Due to the requirement for this light to be a known intensity when illuminating the eye, rather than switching the light directly a shutter technique is used to control the output from a continuous illumination source. This allows better control over the light, including the overall exposure of the eye and the length of time the eye is exposed to a high intensity beam.

Due to the shutter of the beam, it is required that the light be synchronized to the start of integration of the data camera. This is achieved by using a pulse sent from the light box to the camera, thus synchronizing the data collection to the light pulse from the light box. Again this needs to be under computer control to allow all the necessary steps of arming and triggering the light box to be easily controlled.

34.2.4 System Design

An optical layout of the system is shown in Fig. 34.3. A commercially available fundus imager (model KFG2) was used as the fore-optics to the adaptive optics system. Consisting of a laser diode of wavelength 780 nm, a tilted rotating mirror to introduce the dither, a deformable mirror and Shack–Hartmann

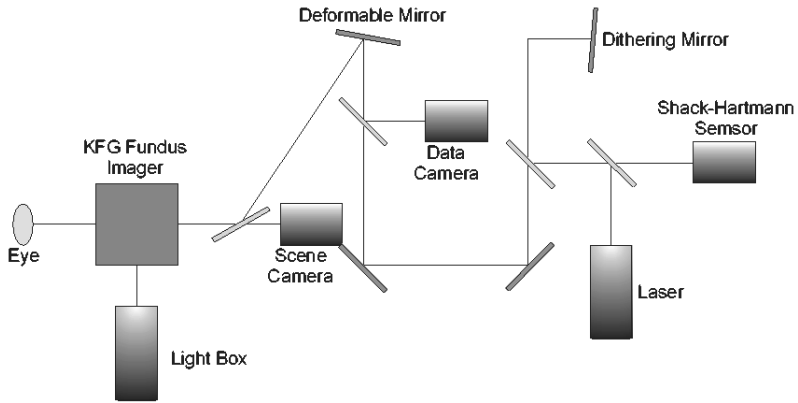


Fig. 34.3. Schematic of optics in the AO system

sensor. The other cameras are for aligning to the eye (scene camera) and a high resolution, large format Electron camera for taking the data image. The illumination is fiber-fed from the light box into the standard illuminating optics within the fundus imager.

34.2.5 Hardware Implementation

The system was constructed as seen in Fig. 34.4 and attached to the fundus imager.

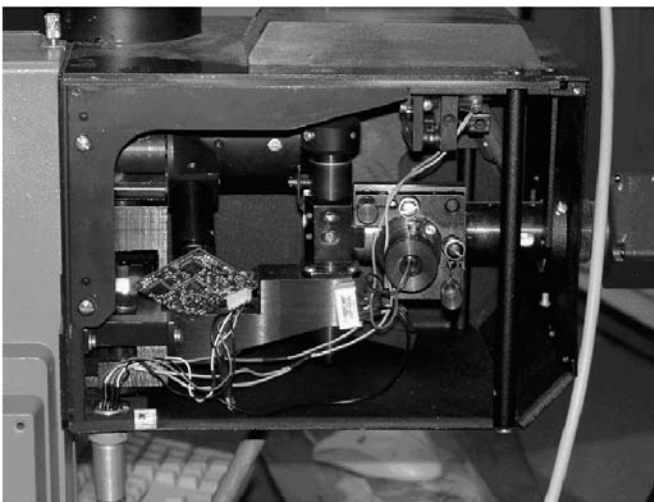


Fig. 34.4. An internal view of the AO system

34.3 Software Considerations

34.3.1 Control Loop

As with all adaptive optics system a control loop is necessary to take the information provided by the wavefront sensor and convert it into control signals for the deformable mirror. As the system does not require a high bandwidth, a standard PC running Windows 2000 is sufficient. The algorithms used are standard linear matrix multiplications derived from actuating each element of the mirror in turn, and calculating the influence on the wavefront sensor.

34.3.2 System Controller

Software is also required to control the system, particularly when timing the sequence of events to take an image. The system measures the rms error of the wavefront from the Shack–Hartmann sensor, and when below a preset level will trigger an image capture sequence. The data camera is set to wait for a signal event from the light box, the light box shutter closes on the exam lamp, and the control loop freezes the shape of the mirror (so when the data lamp is triggered the saturated Shack–Hartmann camera does not affect the wavefront correction.) The light box then opens the shutter to the data lamp, and triggers the data camera. After the required exposure time, the data lamp shutter is closed, and the image is read and recorded from the data camera.

34.3.3 Deconvolution Software

A further software task is that once the images are recorded, along with the residual wavefront aberration present when the image was taken, a deconvolution step is required. This consists of using a modified Weiner filter scheme, where an additional defocus is added to the optical transfer function used depending on the wavelength of the measurement used. This helps to compensate for the wavelength dependent different depths of reflection from the retina. The final, processed image is then stored for later analysis.

34.4 Results

34.4.1 Artificial Eye Tests

Test Hardware

Before any human testing was undertaken, it was necessary to calibrate and measure the performance of the AO system. For such experiments an artificial

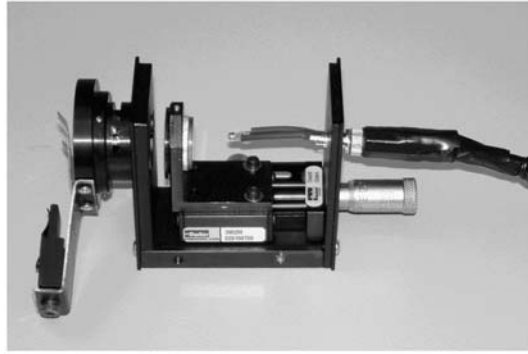


Fig. 34.5. An artificial eye

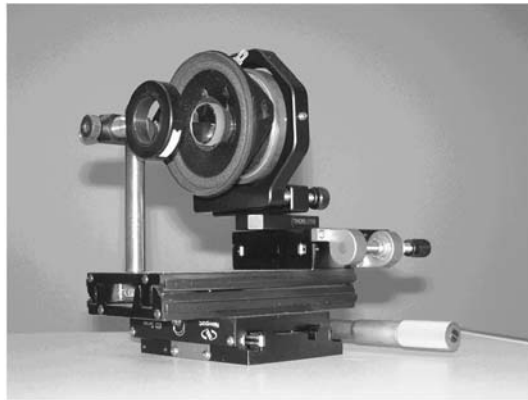


Fig. 34.6. A dynamic artificial eye

eye was constructed, that mimics the real eye, but has known (and variable) optical properties.

The eye consists of a front lens, and a bar chart attached to a fiber bundle. The front surface of the bundle is curved and the back surface is butted onto the bar chart. The fiber bundle projects the bar chart as a curved surface, thus giving a curved “retina” with known dimensions. The front lens acts as the imaging part of the eye giving it the correct optical power. The holder at the front of the eye allows known opticians lenses to be inserted into the system, allowing calibration and performance data to be collected, Fig. 34.5.

A second artificial eye was created to allow dynamic performance of the imager to be assessed, shown in Fig. 34.6. This eye uses a flat mirror mounted on a loudspeaker, with a lens providing the optical power. By controlling the loudspeaker with static or dynamic signals the amount of defocus within the eye can be controlled. This enables dynamic aberrations to be used whilst testing the system.

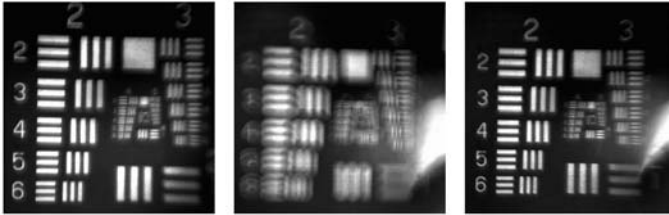


Fig. 34.7. (a) Image of bar chart without aberrations, (b) with 6D of defocus, (c) after correction

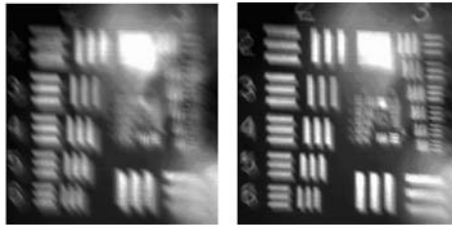


Fig. 34.8. (a) Image of bar char with 4D cylinder, (b) after correction

Static Test Results

The first set of measurements were taken using the static artificial eye and introducing known aberrations by using ophthalmic lenses. Figure 34.7 shows the results of a 6 dioptre defocus error before and after correction, and Fig. 34.8 shows results using a 4 dioptre cylindrical aberration. From these images it is immediately apparent that the AO system can easily correct errors of this magnitude.

Dynamic Test Results

A set of dynamic tests were then undertaken. By applying a known, measured sinusoidal signal to the dynamic artificial eye and measuring the output on the defocus actuator of the mirror, it was possible to calculate the phase difference between the two measurements at different frequencies. The result is shown in Fig. 34.9.

Whilst performing these measurements it was observed that the system began to resonate when the driving frequency was approximately 1 Hz. Additionally the 90° point, giving the effective bandwidth of the system was approximately 0.6 Hz. Such a low bandwidth implies that the AO system is removing the static aberrations, but virtually none of the dynamic aberrations.

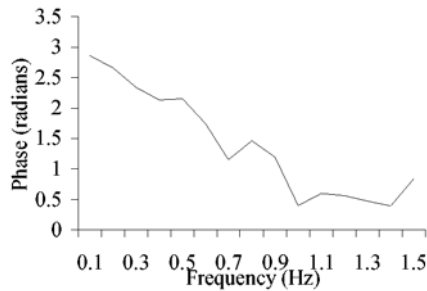


Fig. 34.9. Plot showing the change in phase between output and input as a function of frequency

34.4.2 Subject Tests

The system was then tested to ensure the illumination levels were within FDA safety levels. A variety of subjects were then imaged using the AO system.

Figure 34.10a shows a retinal image taken using a standard camera. The boxed section highlights an exudate which appears as a single white structure. Alongside there is evidence of a hemorrhage. Figure 34.10b is an image of the highlighted section taken with the AO system. This image clearly shows the exudate comprises many small structures, and the hemorrhage shows a vessel structure as the blood has been strewn along the nerve fiber layer, which is also clear in this image.

Figure 34.11 shows a “classic” image of the nerve fiber layer. The straight line in the right-hand portion is a fixation stick. The subject was asked to look directly at the point; hence the fovea is at the end of the stick.

Figure 34.12 shows the choroid layer. This image was taken with red light, giving more penetration into the retina. The random lines are choroidal vessels that carry blood to the outer part of the retina.

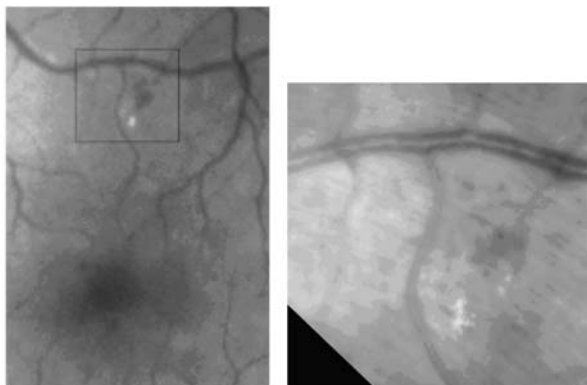


Fig. 34.10. (a) An image without AO. (b) The highlighted area with AO

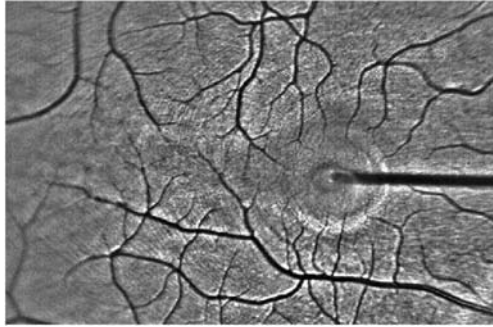


Fig. 34.11. The nerve fiber layer

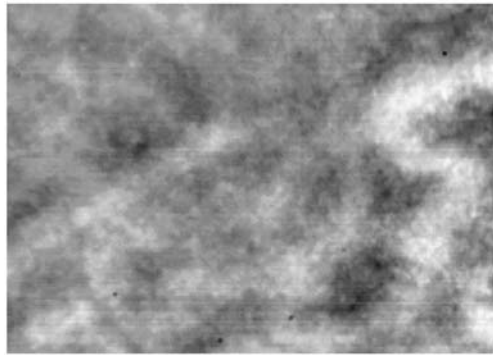


Fig. 34.12. The choroid layer

34.5 Conclusions and Future Work

A fundus imager that uses adaptive optics to improve the resolution of the acquire images was described. Using a dithered Shack–Hartmann wavefront sensor and a bimorph deformable mirror, the system showed resolutions approaching the theoretical diffraction-limit, governed by the pupil size. Although tests revealed several issues with the current device, work is now underway to produce a second prototype system that will correct these deficiencies and add functionality to the imager.

Acknowledgements

The authors wish to thank the NATO Science for Peace program for funding the development of the first unit, and the National Eye Institute for funding the development of the next unit.

35 Perceived Image Quality Improvements from the Application of Image Deconvolution to Retinal Images from an Adaptive Optics Fundus Imager

P. Soliz¹, S.C. Nemeth¹, G.R.G. Erry¹, L.J. Otten¹, and S.Y. Yang²

¹ Kestrel Corporation

3815 Osuna Road NE, Albuquerque, NM, 87109, USA

² Texas Tech University

Lubbock, TX, USA

Summary. *Aim:* The objective of this project was to apply an image restoration methodology based on wavefront measurements obtained with a Shack–Hartmann sensor and evaluating the restored image quality based on medical criteria. *Methods:* Implementing an adaptive optics (AO) technique, a fundus imager was used to achieve low-order correction to images of the retina. The high-order correction was provided by deconvolution. A Shack–Hartmann wavefront sensor measures aberrations. The wavefront measurement is the basis for activating a deformable mirror. Image restoration to remove remaining aberrations is achieved by direct deconvolution using the point spread function (PSF) or a blind deconvolution. The PSF is estimated using measured wavefront aberrations. Direct application of classical deconvolution methods such as inverse filtering, Wiener filtering or iterative blind deconvolution (IBD) to the AO retinal images obtained from the adaptive optical imaging system is not satisfactory because of the very large image size, difficulty in modeling the system noise, and inaccuracy in PSF estimation. Our approach combines direct and blind deconvolution to exploit available system information, avoid non-convergence, and time-consuming iterative processes. *Results:* The deconvolution was applied to human subject data and resulting restored images compared by a trained ophthalmic researcher. Qualitative analysis showed significant improvements. Neovascularization can be visualized with the adaptive optics device that cannot be resolved with the standard fundus camera. The individual nerve fiber bundles are easily resolved as are melanin structures in the choroid. *Conclusion:* This project demonstrated that computer-enhanced, adaptive optic images have greater detail of anatomical and pathological structures.

35.1 Introduction

A clinical retinal imaging system does not exist that provides the researcher and clinical ophthalmologist with high spatial (cellular features $5\ \mu\text{m}$), wavelength selectable, and moderately high (10 nm) spectral resolution images of the human retina over a wide field of view ($10\text{--}15^\circ$). We describe an imaging system that will give ophthalmic researchers and clinicians a diagnostic tool that presents an *in vivo* view into the fine retinal structures and that over-

comes many of the shortfalls of current high resolution imaging approaches. To realize this capability, we have integrated two key technical elements. First, we integrated into the AO fundus imager a means for filtering the source light at narrow spectral bands. Other research, including our own, has demonstrated the value of narrow band multispectral data in characterizing retinal features because it allows one to select the optimal wavelength(s) with which to observe specific anatomical features [1–3]. For example, by selecting near infrared wavelengths, the ability to image sub-retinal layers (e.g. retinal pigment epithelium (RPE), Bruch’s membrane, and choroid) has been demonstrated [2, 4]. The second element is our new approach to combining wavefront sensing and adaptive optics to measure and largely correct refractive errors due to inhomogeneities in the cornea, lens, and vitreous humor. The technology that we applied uses a post-detection image reconstruction that will remove high order aberration errors coupled to a new adaptive optics and wavefront sensing technique. The result is an approach that offers the promise of very high performance at a reasonable cost by reducing the complexity of the adaptive mirror and wavefront sensing elements.

High resolution digital retinal images, based on wavefront sensing and adaptive optics technology, may provide much greater detail of the retinal structures which could lead to more accurate diagnosis than retinal images collected with today’s clinical fundus camera. However, the challenge in producing a clear retinal image lies in the design of the imaging system that can reduce the large aberrations of the human eye and adjust for the photographer’s expertise in focusing the fundus camera. A technique that combines an advanced adaptive optical system and image post-processing algorithm has been shown to significantly improve the image quality [5]. The function of the former is to correct or suppress the aberrations while the latter to restore lost details resulting from the imaging system or introduced by inaccurate operations of the system, such as defocus, when the image is taken. The optical system has been designed to suppress low-order aberrations and enhance the precision of the wavefront measurement. Image post-processing mainly involves deconvolution by calculating the system function (here the optical transfer function (OTF)) from the data obtained by the Shack–Hartmann wavefront sensor.

35.2 The Adaptive Optics Fundus Imager

35.2.1 Optical Design

An AO fundus imager has been developed with our collaborators at Moscow State University [6–8] which integrates the AO system with a wavefront sensor, a reference illuminator and the required optics into a package that is suitable for wide clinical use (Fig. 35.1). Our design differed significantly from others who work in this area in that it has been integrated into a clinical

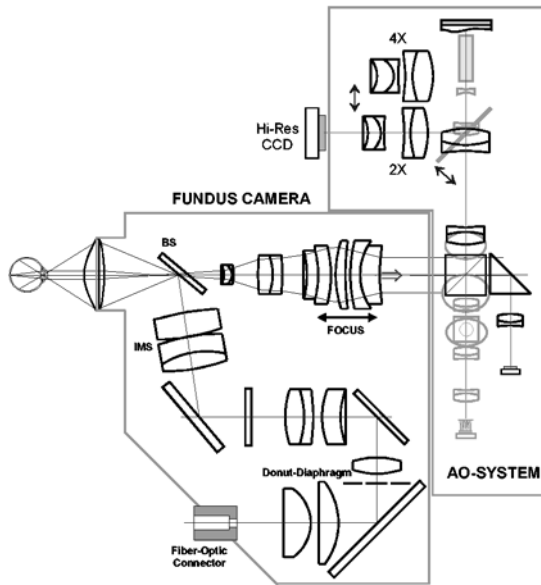


Fig. 35.1. An optical representation of the adaptive optics fundus imager. The layout is 60 by 40 by 15 cm, or the size of a standard fundus camera



Fig. 35.2. Photograph of AO fundus imager

fundus imager (Fig. 35.2) and does not require an extensive expanse of custom optics spread over a laboratory optical bench. Our research has clearly bridged the transition between physics and practicality and has indicated that the introduction of a high-resolution clinically usable fundus imager is feasible.

35.2.2 Wavefront Sensor and the AO Mirror

There are two major components to the AO fundus imager shown in Figure 35.1: the fundus camera (lower left portion of the diagram in Fig. 35.1) and the AO system (drawn on the upper right, Fig. 35.1). Within the AO system is the Shack–Hartmann wavefront sensor. A laser is focused and, in our approach, dithered onto the subjects retina and is distorted by the eye as it passes through the refracting elements and media in the eye. The lenslet array samples the existing wavefront by forming an array of images of the laser spot. The CCD camera images the lenslet laser spots. Displacements of the spots are used to calculate the wavefront aberration and to activate the deformable mirror (DM). The deformable mirror with its 18 activators compensates for the aberrations by introducing the conjugate of the measured aberrations. A high-resolution image is then recorded with the large format camera. The individual components are described below, as is the timing cycle for producing a high resolution, spectral image.

35.3 Image Deconvolution

35.3.1 Background

A significant departure from previous approaches to high-resolution retinal imaging is our separation of the image correction issues into a low order correction and a high order correction. AO imaging technology has been used successfully in astronomical application. There are, however, a number of differences between the astronomical implementation and the use of the technology for retinal imaging. For atmospheric corrections, the characteristic scale size, r_0 , is on the order of a few cm and the aperture, D , is on the order of several m for a D/r_0 of 50. The aberrations have a time constant of a hundredth of a second due to wind induced motion. In the eye, the aberrations have a scale size of approximately 2 mm and the aperture is limited to 9 mm for a D/r_0 of about 4 and a time constant related to the saccadic motions of the eye. Therefore, atmospheric corrections require much higher frequency corrections while the eye has larger low frequency corrections and a slower time scale. In our approach, a conventional AO system was used to measure and correct low order aberrations. This allows the use of a more modest cost AO mirror and associated electronics. A post image deconvolution technique is then used to correct the higher order terms.

To implement this hybrid approach, a deconvolution algorithm has been written for application to the images produced by AO fundus imager. The algorithm for deconvolution of the image uses information on the point spread function (PSF) of an optical system and its propagation path. The contribution of the convolution process is balanced with the AO technology to meet

the imaging requirements of the retina-related applications. This hybrid approach has been used with great success in astronomical imaging, where experimental demonstrations of improvements in resolution by a factor of two or more have been published [5, 9]. The concept is a cost-effective solution that lends itself to a clinical device. The first stage for low order aberration suppression uses an adaptive optics flexible mirror and control system that can be made with low bandwidth and simple, inexpensive components. The second stage, computer image deconvolution, is applied to the measured fundus image to remove distortions resulting from errors not corrected by the deformable mirror.

35.3.2 Wiener Filter

Post-processing of the image obtained from the fundus imaging system aims at improving the image quality by applying image processing techniques including, but not limited to, image deconvolution, with or without the data provided by the imaging system. Naturally, the investigation started by exploiting the information provided by the imaging system [6]. Direct deconvolution was performed by calculating the OTF derived from the Zernike coefficients, and then the image was restored by using the Wiener filter if the noise characteristic of the system was known otherwise, the pseudo-inverse filter.

With the Shack–Hartmann, the aberrations can be expressed as the summation of a set of Zernike Polynomials that are calculated from the wavefront measured by this device. The restored image can be found by a direct deconvolution from the Wiener filter as depicted in Fig. 35.3.

Where $G(u, v)$ is the Fourier transform of the blurred image, $F(u, v)$ is the restored image, and $H^*(u, v)$ is the complex conjugate of $H(u, v)$, $S_n(u, v)$ is

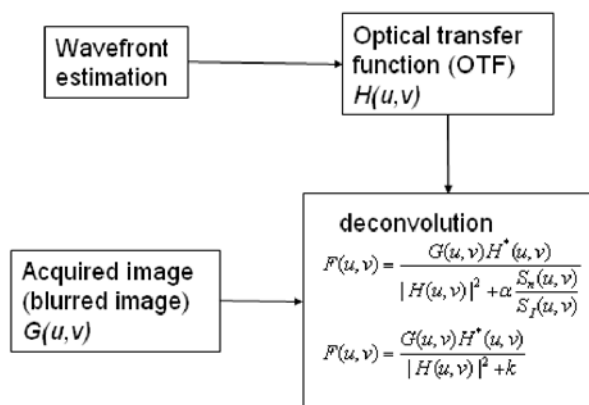


Fig. 35.3. Image restoration by direct deconvolution

the power spectrum of the noise, and $S_I(u, v)$ is the power spectrum of the image. α is a scaling parameter.

35.3.3 Self-deconvolving Data Reconstruction Algorithm (SeDDaRA)

The second step of the investigation was to estimate efficiency of the above direct deconvolution and to assess whether greater improvements can be achieved. To perform this task, the accuracy of the wavefront sensor is challenged by manually altering individual Zernike coefficients, thus the OTF, to see if the image can be improved. Lastly, other deconvolution approaches are also investigated assuming no information from the imaging system.

The SeDDaRA was selected for studying a deconvolution algorithm that does not depend on the measurement of the wavefront. SeDDaRA is a computationally efficient, non-interactive algorithm that requires little human interaction and does not explicitly require knowledge of $H(u, v)$. This algorithm has been described by Caron et al. [10].

35.4 Results

Ultimately, it is the observer who determines the most perceptually appealing deconvolution. The criteria for determining the best convolution results will be based on the diagnostic information that the image presents and/or the improved depiction of the natural structures, such as the nerve fiber layer or the clarity and contrast of the smallest retinal vessels. It is in these qualitative terms that the following deconvolved images are described.

35.4.1 Optic Disc

Figure 35.4 shows the optic disc of an individual with no known retinal or systemic disease. A region of interest centered around the optic disc was used to test the two approaches to the deconvolution. Figure 35.5b shows the results of the deconvolution based on the Wiener filter using the wavefront measurement and the image derived from the SeDDaRA (Fig. 35.5c).

Qualitatively, Fig. 35.5a shows a significant improvement in the presentation of the small retinal vessels on the optic disc over the original image given in Fig. 35.4b. The vessels appear to have more distinct edges. Similarly, the SeDDaRA deconvolved image in Fig. 35.5b also appears to have sharply defined edges. The SeDDaRA image in Fig. 35.5c, though possibly having sharper edges than Fig. 35.5b, it does not seem as natural in appearance. Both deconvolution algorithms have improved the sharpness and contrast of the natural structures in the optic disc.

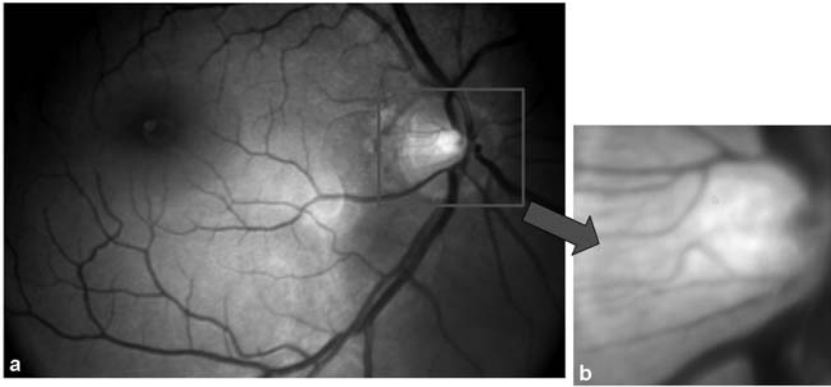


Fig. 35.4. (a) Retinal image of a right eye. Fovea is the dark region on the left. (b) The optic disc is bright object on the right and enclosed by the box in (a)

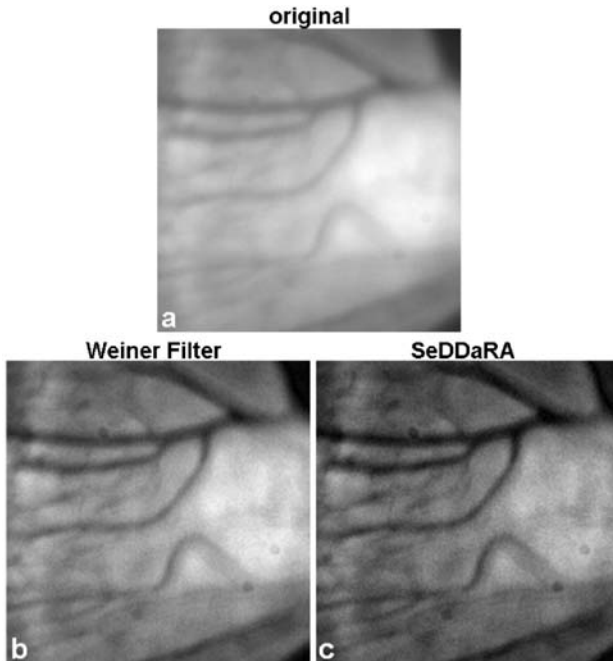


Fig. 35.5. (a) Original image deconvolved images based on (b) the Weiner filter and wavefront measurement and (c) the deconvolved image based on SeDDaRA

35.4.2 Nerve Fiber Layer (NFL)

Figure 35.6 shows an overlay of lines that represent the typical path of the nerve fiber layer that lies on the inner surface of the retina. In some images taken from standard fundus cameras, one often may observe patches of the

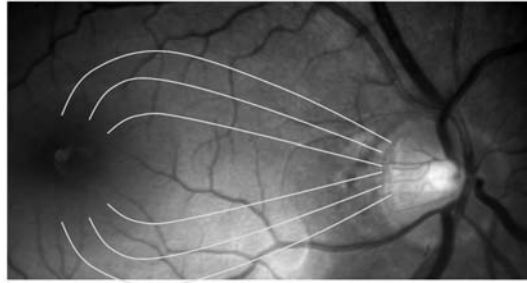


Fig. 35.6. Nerve fiber layer

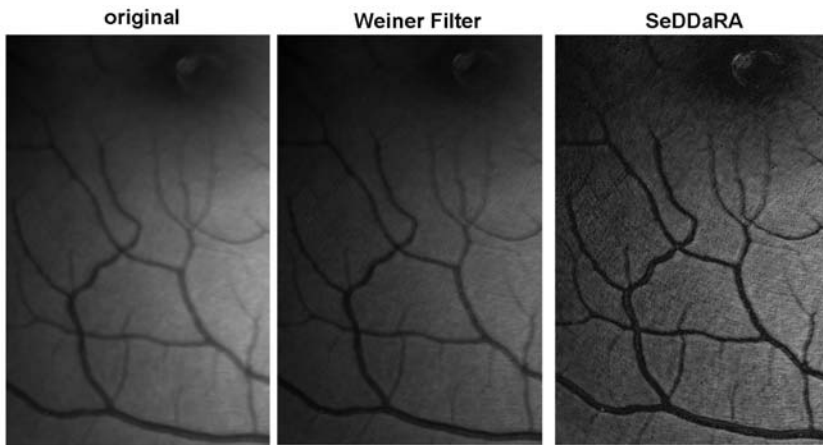


Fig. 35.7. Nerve fiber layer most apparent in the image processed with SeDDaRA

NFL in the green or blue channels of a color image. This is particularly true for younger subjects. Because of the limitation of the printed text, it is difficult to illustrate the effect of the deconvolutions in enhancing the NFL. The original full size image depicted in Fig. 35.7 clearly shows the sweeping pattern of the NFL that is illustrated in Fig. 35.6.

35.4.3 Retinal Vessels

The sharpness of the edges produced by the deconvolution algorithms is clearly portrayed in Fig. 35.8. Note the amplitude of the vessel depth, i.e. low reflected intensity, of each of the images. Though the SeDDaRA shows the greatest amplitude, it is at the expense of increasing the speckle noise in the image. Obviously, one would like to increase the edge sharpness and contrast without increasing the noise. However, this example illustrates the balance that must be achieved by the deconvolution algorithms.

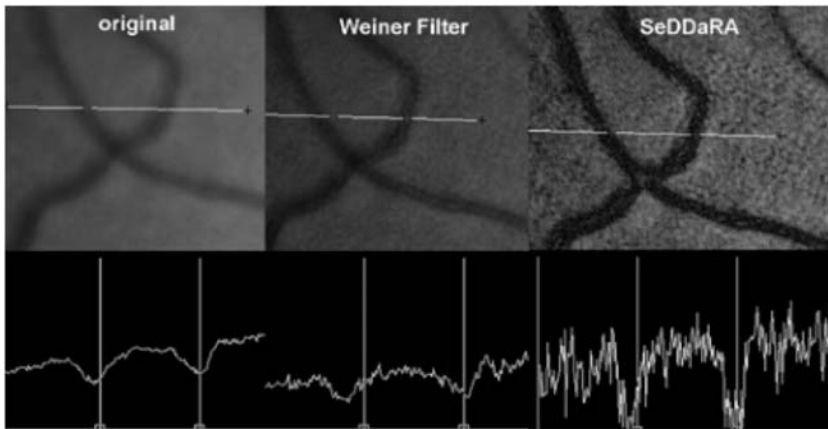


Fig. 35.8. Vessel cross sections. Both deconvolutions are increasing noise while improving contrast

35.5 Conclusions

Both deconvolution algorithms clearly demonstrate an improvement in the edge sharpness and contrast of the images that were processed. Because the free parameters that affect the sharpness and the noise in the processed images have not been fully explored, the results presented herein are preliminary. Quantitative metrics are being studied to allow one to assess the deconvolved images both quantitatively and qualitatively in order to assess the deconvolution alternatives more efficiently.

Acknowledgements

The authors wish to acknowledge funding support from the National Eye Institute (Grant #R43-EY12590), and NATO Science for Peace (Grant #974292). We are indebted to our collaborators at Moscow State University, Drs. Andrey Larichev and Nikita Irochnikov, who were instrumental in the development of the AO fundus imager.

References

1. P.W. Truitt, N. Magotra, P. Soliz: Spectral imaging of the human ocular Fundus. In: 21st Annual International Conference of the IEEE Engineering in Medicine and Biology Society, Atlanta, GA, 1999
2. P.W. Truitt, D.H. Hart, M.G. Wood, G.S.H. Ogawa, S.C. Nemeth, P. Soliz: Utility of high resolution spectral imaging for improved visualization and classification of retinal tissue in normal and age-related macular degeneration subjects. In: Association for Research in Vision and Ophthalmology (ARVO), Ft. Lauderdale, FL, 2000

3. F.C. Delori, K.P. Pflibsen: Spectral reflectance of the human ocular fundus. *Appl. Opt.* **28**, 1061 (1989)
4. A.E. Elsner, S.A. Burns, J.J. Weiter, F.C. Delori: Infrared Imaging of Sub-retinal structures in the human ocular fundus. *Vision Research* **36**, 191 (1996)
5. M.C. Roggemann et al.: Linear reconstruction of compensated images: theory and experimental results. *Appl. Opt.* **31**, 749 (1992)
6. A.V. Larichev, N.G. Irochnikov, P. Ivanov, A.V. Kudryashov: Deconvolution of color retinal images with wavefront sensing. In: *SPIE Photonics West*, San Jose, CA, 2001
7. A.V. Larichev, R. Ivanov, I. Irochnikov, S.C. Nemeth, A. Edwards, P. Soliz: High speed measurements of human eye aberrations with Shack–Hartman sensor. In: *Association for Research in Vision and Ophthalmology (ARVO)*, Ft. Lauderdale, FL, 2001
8. A.N. Simonov, A.V. Larichev, V.P. Shibaev, A.I. Stakhanov: High-quality correction of wavefront distortions using low-power phase conjugation in azo dye containing LC polymer. *Optics Comm.* **197**, 175 (2001)
9. M.C. Roggemann, E.L. Caudill, D.W. Tyler, M.J. Fox, M.A.V. Bokern, C.L. Matson: Compensated speckle imaging: theory and experimental results. *Appl. Opt.* **33**, 3099 (1994)
10. J.N. Caron, N.M. Namazi, R.L. Lucke, C.J. Rollins, P.R. Lynn: Build data restoration with an extracted filter function. *Opt. Lett.* **26**, 1164 (2001)

36 Adaptive Aberrometer for Acuity Measurements and Testing

A. Larichev¹, N. Irochnikov¹, and S. Gorbunov²

¹ M.V. Lomonosov Moscow State University, Faculty of Physics
Leninskiye Gory, Moscow 119992, Russia

² IPLIT RAS
Pionerskaya 2, Troick, Moscow region, 142092 Russia

Summary. We present the novel instrument combining the Shack–Hartman wavefront sensor, compensator of low order aberrations and bimorph adaptive mirror for high order aberration correction. We have tested the developed instrument in the clinical environment on human subjects. The measurement rate was 77 frames per second. The typical residual error of correction was between 0.1–0.15 microns per second. The wavefront can be reconstructed in form of up to 36 Zernike polynomials. Automatic low order aberration compensator allows introduction of spherical and astigmatic terms with amplitudes up to ± 15 D and ± 6 D correspondingly and accuracy of 0.05 D. An 18 electrode bimorph deformable mirror corrector makes it possible to model Zernike aberrations up to the 3-th order + Spherical aberration with RMS amplitudes up to 1 micron. The results of measurements were compared with clinical refraction and good correspondence was found.

36.1 Introduction

Several groups in the world are working under implementation of the systems for measuring and correction of the human eye aberrations. The Shack–Hartmann (SH) wavefront sensor consisting of micro-lens array (lenslet) and CCD camera seems to be most widely used for eye aberration measurements [1, 2]. Haro and Dainty proposed the original implementation of such a sensor where the reference point source is created by retinal fluorescence under laser radiation [3]. This sensor ensures true single-pass measurements of aberrations. Hamam introduced [4] a direct numerical method to reconstruct the aberration curve from SH image, without passing through a wavefront fit. The method does not require precise knowledge of the position of the pupil center of the eye.

Hofer et al. [5, 6] recently reported that they constructed a real-time (video-rate) SH wavefront sensor to measure the dynamic of eye aberration. They experimentally compared the quality of eye aberration correction in cases of static and dynamic control of a 37-electrode monolithic mirror. The Shack–Hartmann wavefront sensor used in experiments measured aberrations with the 30-Hz rate. The analysis showed that the dynamic compensation increases the Strehl ratio by a factor of three and contrast of observable photoreceptors by 33% compared to the static compensation.

Other techniques for eye aberration measurements, such as phase retrieval using double pass measurements of human eye PSF [7, 8] and laser ray tracing [9] also can be successfully applied for eye aberration measurements. However, such methods are respectively slow, and can be considered only for the measurements of steady eye aberrations.

The wavefront sensors based on Shack–Hartman technique are sensitive to the speckle modulation of the intensity distribution on the pupil plane. In the case of human eye and illumination and the coherent reference source the amplitude of modulation in the pupil plane is rather high and accurate measurement of the aberrations is possible only when temporal integration of Shack–Hartman picture is performed. This limits the temporal performance of the wavefront measurement. The application of the low temporal coherence reference source (like super-luminescent diodes) only partially improves the situation. The technical opportunity studying the temporal properties of the eye aberrations is appeared only recently [5, 10]. It has been shown that fluctuation in high-order aberrations have similar spectra dropping at a rate of approximately 4 dB per octave in temporal frequency. However, the origin of this fluctuations and dependence of the temporal properties on the action of cycloplegics are not known. That is why the further investigations of eye aberration properties are required.

It is known that the amplitude of eye aberrations decays sharply with the increase of their order number [11]. Low-order aberrations such as the defocusing, astigmatism, coma and spherical aberration have the maximum amplitude. Monolithic and membrane mirrors allow one to correct only for aberrations with relatively low amplitudes. In this connection, in experiments [6, 12, 13] the defocusing and astigmatism were compensated before the feedback closure by means of the additional lens optics. In paper [14], the possibility to use a 69-segment liquid crystal corrector for this purpose was examined. However, the authors failed to achieve a desirable effect and came to a conclusion that the dynamic range and the number of segments of a corrector should be significantly increased to compensate for real eye aberrations. Thus, the issue of optimal choice of a wavefront corrector for compensation of eye aberrations remains open.

There is another type of wavefront correctors yet not been used in adaptive compensation of human eye aberrations – modal deformable mirrors [15, 16]. Using a small number of control channels, such correctors allow a high-precision modelling of low-order aberrations with relatively high amplitudes. This property of such correctors corresponds to the statistical properties of phase distortions of the eye.

The response functions of modal correctors are non-localised: when applying the control voltage at any chosen electrode, the entire mirror changes its form. This fact substantially impedes the control of such a mirror.

In this paper, we introduce an adaptive system for compensation of human eye aberrations during measurements of the eye refraction and acuity. A human subject can look at the reference target through compensator and

bimorph mirror, thus the quality of vision and respectively subjective visual acuity can be determined. Applying certain control signal on the compensator and flexible mirror one can introduce different aberrations and study their influence on the subjective acuity. Particularly, in the closed loop model system is able to automatically generate best objective correction, which later on can be compared with subjectively obtained correction.

36.2 Methods

36.2.1 Experimental Set-up

In order to investigate the possibility of high-speed measurement and adaptive correction of the human eye aberrations the laboratory set-up was built. Figure 36.1 shows a photograph and the optical arrangement of the experimental set-up. The laser beam passes through the diaphragm with diameter 0.8 mm (not shown on the scheme). The diaphragm firstly reduces the power laser light delivered into the retina, and secondly reduces phase distortions which laser beam obtains before focusing on the retina, that is necessary to

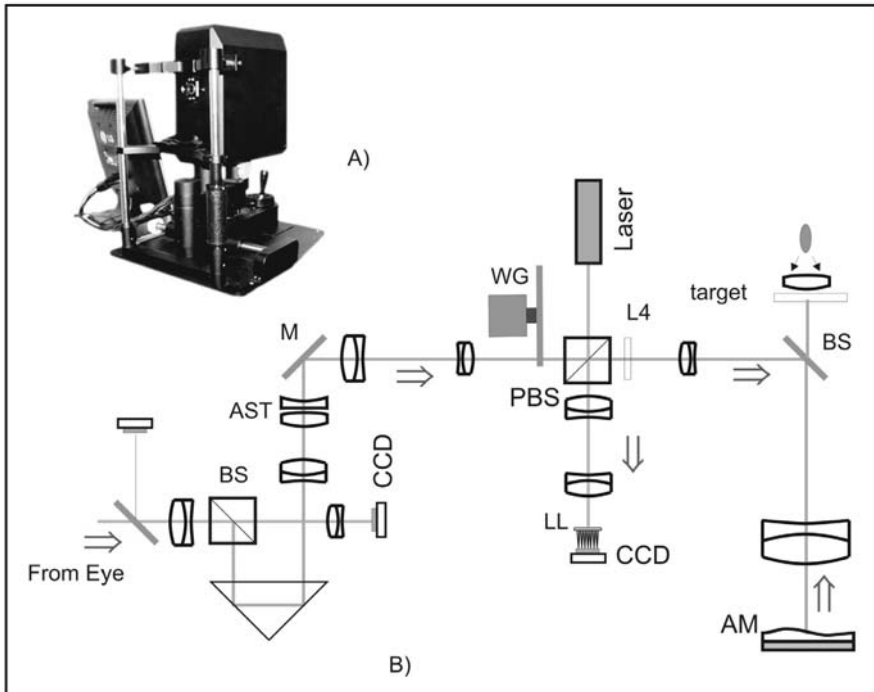


Fig. 36.1. External view (A) and optical scheme of aberrometer “Multispot250/A” (B)

obey single-pass measurement conditions. The laser light propagates through a polarized beam splitter (*PBS*), confocal lenses and a mirror *M*. The glass plate *WG* having wedge shape is mounted on the shaft of the DC motor. This unit is used for introducing an illuminating beam scanning on the retina. The diameter of laser beam on the cornea was 0.8 mm. The irradiance on the retina is lower than $30\ \mu\text{mW}$, approximately ten times less than the maximum permissible exposure according ANSI [17]. The lens of the eye focuses the laser beam and forms a reference point source on the retina. Reflected and scattered light propagates back through the system. A beam splitter *BS* separates polarized light reflected by the cornea from almost unpolarized scattered illuminating light. Compensators for defocus and astigmatism (*AST*) reduce 2nd order aberrations down to $\pm 1\ \text{D}$ and $\pm 0.1\ \text{D}$ for sphere and cylinder correspondingly. Confocal lenses expand laser beam to illuminate an adaptive mirror (*AM*). The surface of the mirror is conjugated with the pupil of the eye. Then an image of the adaptive mirror is formed on the lenslet array of the Shack–Hartmann wavefront sensor (*LL*). The adaptive mirror can be used for aberrations compensation. Each lenslet is $0.2 \times 0.2\ \text{mm}$ square and has 7 mm focal length. The lenslet array area illuminated by the system contains 15×15 active subapertures. Such wavefront sampling is close to optimum for typical human eye aberrations. The hartmanogram is registered by a progressive scan B&W CCD camera (*CCD*) with the maximum frame rate of 30 fps. Then an image is acquired by a PCI framegrabber that provided spatial resolution of 640×480 pixels. A beam splitter *BS* reflects a portion of the light to form conventional image of the pupil on CCD camera (*CCD*).

One of the most important problems that prevents the high accuracy and real-time operation of Shack–Hartman sensor with a human eye is the speckle structure of the reference laser beam reflected from the retina (Fig. 36.2a). Under such conditions the shape of the focal spots of the lenslet array becomes irregular (Fig. 36.2b). Consequently, the accuracy of the spot centers location is poor. That is why the wavefront estimation errors for the eye modal tend to be rather high (up to 1λ for set of measurements presented on Fig. 36.2a,b). The temporal integration of hartmanogram for the period of 60–100 s effectively suppresses speckle modulation due to eye movements [1]. However, such a regime is not suitable for real-time operation. The alternative solution is the usage of retinal luminescence under the laser beam illumination [3].

We propose another technique based on respectively high frequency scanning of the reference beam across the retina. As a result, the speckle pattern can be effectively averaged during the exposure time of the CCD camera (30 ms). Scanning patch should be rather small to lie within the isoplanatic region. In our experimental set-up we use a novel scanning system when a reference spot is rapidly moved around the 140-micron circle on the retina. For this purpose a glass plate is fixed on the rotating axis of the electric motor. Rotational frequency of the motor was 50 Hz. Figure 36.2c,d illustrates the results of the scanning procedure. As it is readily observable the shape of

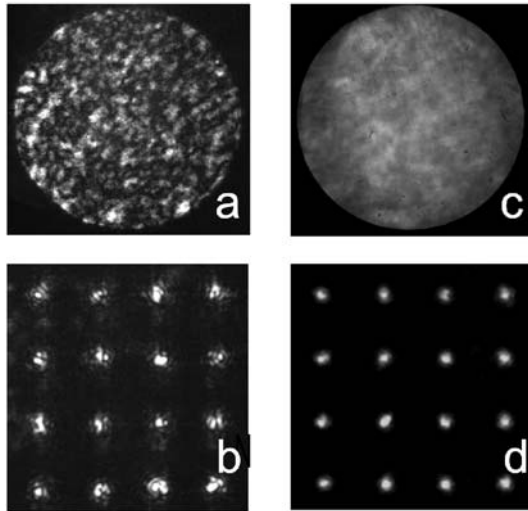


Fig. 36.2. Suppression of speckle patterns by retina scanning

focal spots is rather regular. The accuracy of wavefront estimation is $\lambda/25$. Another advantage of scanning across the retina is lower average intensity of the laser beam on the retina. Under our experimental conditions the average intensity is 10–15 times lower than without scanning.

36.2.2 Compensation of Model-Eye Aberrations

Characterization of the system was performed with the help of an eye-model. The model of an eye represents an objective with a focal length 20 mm and an eye-retina-imitating scatterer (a fibreglass plate with fibre diameter of $6\ \mu\text{m}$). The front facet of the plate had a concave spherical surface with the radius of curvature equal to the radius of the focal surface of the objective. This allowed us to achieve precise focusing on the entire surface of the plate. The laser beam passing through the objective was focused on the front face of the plate. Then, light propagated through the fibres, reflected from the mire, propagated in backward direction, and formed a reference source on the front facet of the plate. Phases of radiation emerging from different fibres were uncorrelated. The fibreglass plate was fixed to a micrometer positioning stage, which provided the longitudinal displacement with the positioning accuracy of $10\ \mu\text{m}$.

The performance of the adaptive system is demonstrated in Fig. 36.3. Here, the wavefront interferograms are shown in cases of open and closed feedback loop. To introduce phase distortions, the eyeglass lens of poor quality was placed in the plane of the artificial eye pupil at an angle to optical axis of the system. No preliminary compensation of defocusing by means of an adjustable refraction compensator was performed.

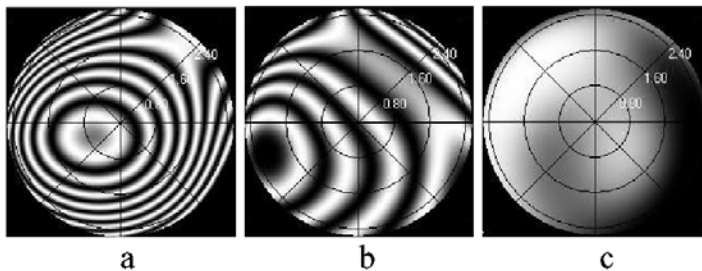


Fig. 36.3. Wavefront interferograms before compensation (a), before compensation, with compensated defocusing (b), and after compensation (c)

36.2.3 Compensation of Real-Eye Dynamic Aberrations

The eye pupil was preliminary dilated by mydriatic eye drops (Phenylephrine Hydrochloride, 2.5%) that do not paralyse accommodation. The patient's head was fixed by the face-holder of the aberrometer. All patients were instructed to look on a circled formed by the scanning laser beam (an infinitely far object). The reference laser beam does not pass through the adaptive mirror, thus deformations of the adaptive mirror did not influence the eye accommodation.

The eye aberrations were measured in real time, and the data were displayed on the monitor of the computer. As a preliminary to the feedback closure, the eye refraction and cylinder were compensated by means of corresponding compensators. The Zernike coefficients corresponding to the defocusing and astigmatism were reduced to the minimum value under these conditions. This allowed us to use the entire dynamic range of the adaptive mirror. After feedback closure, the compensation of eye aberrations was performed. Compensation was assumed successful when the residual root-mean-square error of the compensation σ was reduced below $0.15 \mu\text{m}$. However, in some cases, when aberration amplitudes exceeded the dynamic range of adaptive mirror deformations, we failed to achieve the satisfactory quality of suppression of phase distortions. Another, less common reason of poor-quality compensation was related to the low intensity level of the detected Hartmannogram, for example, due to the crystalline lens opacity.

An illustration of the adaptive compensation of eye aberrations is given in Fig. 36.4. Aberrations were detected for 10 s. The feedback loop was closed at the third second. No preliminary compensation of the defocusing was performed; therefore, the defocusing (curve 7) was the predominant aberration ($0.5 \mu\text{m}$) before the feedback closure. The following-in-magnitude aberrations were the astigmatism (curve 2) and coma (curve 3). Aberrations of the order, higher than spherical, were low and are not shown in Fig. 36.4. One can see from the presented dependences that the process of the adaptive compensation lasted about 1.5 s. The root-mean-square phase deviation σ decreased

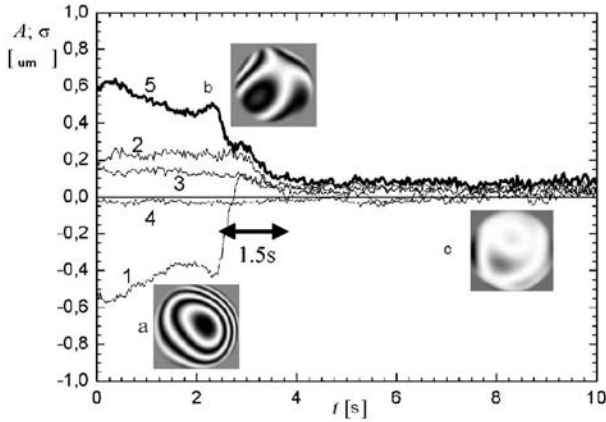


Fig. 36.4. Times dependences of aberration amplitudes A defocusing (1) total astigmatism (2), total coma (5), spherical aberration (4), and root-mean-square phase deviation σ (5). Aberration interferograms before compensation (a), before compensation, with eliminated defocusing (b), and after compensation (c)

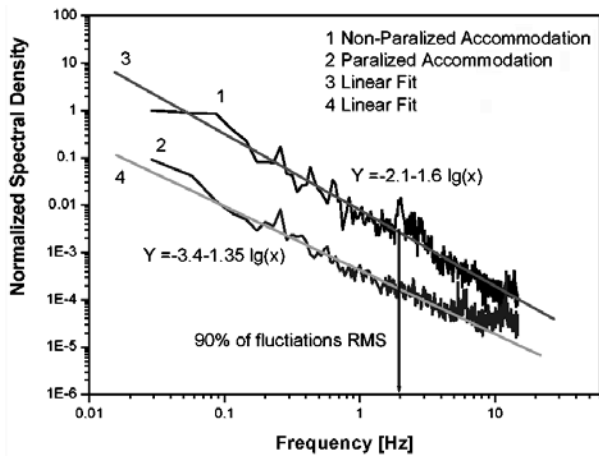


Fig. 36.5. Spectra of Zernike coefficient temporal fluctuations

under these conditions from 0.6 to 0.1 μm . The wavefront interferograms, written before and after the adaptive compensation, are shown in Fig. 36.4 as well. The interferogram of Fig. 36.4b corresponds to phase distortions before the feedback closure in the case of eliminated defocusing.

Figure 36.5 shows temporal spectra of fluctuations of Zernike coefficients for paralyzed and non-paralyzed eye. It may be shown that 90% of integral fluctuations is below the 2 Hz frequency. This means that, if the adaptive system response is less than 0.5 s, the system will compensate non-paralyzed eye fluctuations effectively.

36.2.4 System Latency and Usable Bandwidth

Total response system time is determined by at least two origins: system latency time and adaptive mirror nonlinearity, which requires several iterations for compensations.

System latency time may be estimated as a sum of CCD integration time, time of frame transfer from the CCD to the computer memory, processing time and mirror response time (Fig. 36.6). The latter is determined by the adaptive mirror construction and cannot be reduced. The processing time is generally proportional to the computer memory access rate and processor clock and may be slightly improved. For CCD dependent time is 75% of the total latency time, change for faster cameras, for example Philips FTF 1010 with 77 Hz, can dramatically (two times) improve the system performance.

However, the system response time depends on not only the latency time, but also the number of adaptive mirror control cycles, which in our case is about 5–7. There are two phenomena that influence the mirror response. At first, mirror response is nonlinear. Figure 36.7a illustrates that the nonlinear discrepancy is about $1.5\mu\text{m}$ in defocal RMS terms. At second, a hysteresis is observed on the dependence of mirror response. In our case it can obtain $0.65\mu\text{m}$ of defocus RMS (Fig. 36.7b). Both these features make control of adaptive mirror iterative that slow down the system response time. This may

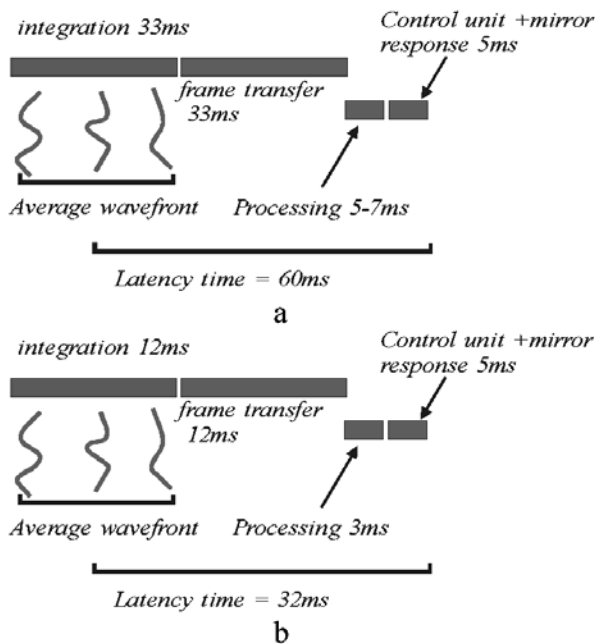


Fig. 36.6. System latency time for 30 Hz (a) and 77 Hz (b) CCDs

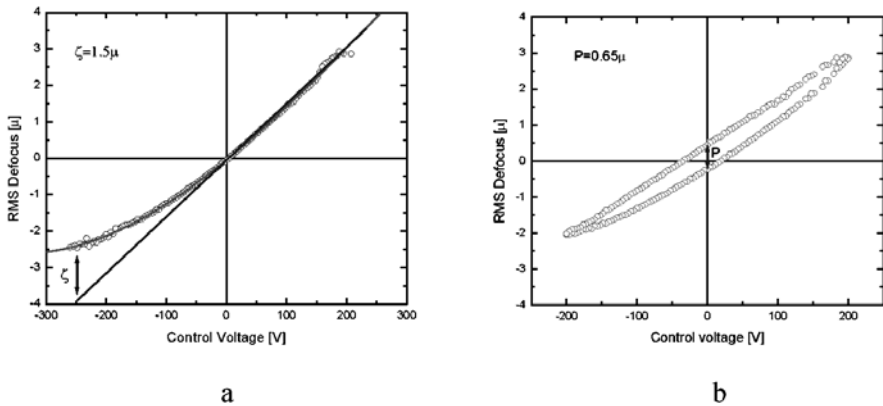


Fig. 36.7. Virgin (a) and hysteresis (b) curves of bimorph mirror

be avoided by developing of a special mathematical model for the adaptive mirror description.

Acknowledgements

We thank Kestrel Corporation (Albuquerque, US) for sponsoring our participation in AOIM-2003 conference.

References

1. J. Liang, D.R. Williams: Aberrations and retinal image quality of the normal human eye. *J. Opt. Soc. Am. A* **14**, 2873 (1997)
2. J. Liang, B. Grimm, S. Goels, J. Bille: Objective measurement of wave aberrations of the human eye with use of a Hartmann–Shack wavefront sensor. *J. Opt. Soc. Am. A* **11**, 1949 (1994)
3. L. Diaz Santana Haro, J.C. Dainty: Single-pass measurements of the wavefront aberrations of the human eye by use of retinal lipofuscin autofluorescence. *Opt. Lett.* **24**, 61 (1999)
4. H. Hamam: A direct technique for calculating the profile of aberration of the eye measured by a modified Hartmann–Shack apparatus. *Opt. Comm.* **173**, 23 (2000)
5. H. Hofer, P. Artal, B. Singer, J.L. Aragon, D.R. Williams: Dynamics of the eyes wave aberration. *J. Opt. Soc. Am. A* **3**, 497 (2001)
6. H. Hofer, L. Chen, G. Yoon, B. Singer, Y. Yamauchi, D.R. Williams: *Opt. Exp.* **8** 631 (2001)
7. P. Artal, I. Iglesias, N. Lo'pez-Gil, D.G. Green: Double-pass measurements of the retinal-image quality with unequal entrance and exit pupil sizes and the reversibility of the eye's optical system. *Opt. Soc. Am. A* **12**, 2358 (1995)
8. I. Iglesias, N. Lo'pez-Gil, P. Artal: Reconstruction of the point-spread function of the human eye from two double-pass retinal images by phase-retrieval algorithms: *J. Opt. Soc. Am. A* **15**, 326 (1998)

9. E. Moreno-Barriuso, R. Navarro: Laser Ray Tracing versus Hartmann–Shack sensor for measuring optical aberrations in the human eye. *J. Opt. Soc. Am. A* **6**, 974 (2000)
10. A. Larichev, P. Ivanov: Eye Aberrations with Shack–Hartman Sensor. [ARVO Abstract] *Invest. Ophthalmol. Vis. Sci.* **42**, 897 (2001)
11. A. Guirao, J. Porter, D.R. Williams, I.G. Cox: *Opt. Soc. Am. A* **19**, 1 (2002)
12. J. Liang, D.R. Williams, D.T. Miller: *Opt. Soc. Am. A* **14**, 2884 (1997)
13. E.J. Fernandez, I. Iglesias, P. Artal: *Opt. Lett.* **26**, 746 (2001)
14. F. Vargas-Martin, P. Prieto, P. Artal: *Opt. Soc. Am. A* **15**, 2552 (1998)
15. A.V. Kudryashov, V.I. Shmalhausen: *Opt. Eng.* **35**, 3064 (1996)
16. J.C. Dainty, A.V. Koryabin, A.V. Kudryashov: *Appl. Opt. LP* **37**, 4663 (1998)
17. *American National Standard for the Safe Use of Lasers*, ANSI Z136.1 (Laser Institute of America, Orlando, FL 1993)

Part V

Atmospheric Propagation

37 Adaptive Optics with Strong Scintillation and Optical Vortices for Optical Communication

C. Paterson and C.R. Walker

The Blackett Laboratory, Imperial College
London, SW7 2BW, UK

Summary. There is increasing interest in applying adaptive optics to beam propagation over long horizontal paths through the atmosphere for line-of-sight optical communications. Over longer optical paths phase aberrations give rise on propagation to intensity fluctuations (scintillation). Both scintillation and phase aberrations limit the performance of line-of-sight systems, being responsible for signal fade and placing a lower limit on the area of photodetectors at the receiver respectively. Beyond the weak regime of the Rytov approximation, dislocations or vortices appear in the waves. Linear gradient reconstructors used in adaptive optics fail in the presence of vortices since the underlying assumption that a wavefront can be represented as a single-valued function in Hilbert space is not valid. By decomposing the phase gradients of a wave containing vortices into a conservative dislocation-free component and a solenoidal component containing only the dislocations, the effect of the dislocations on adaptive optics is studied. We present modelling results of a study for using adaptive optics at both ends of a line-of-sight optical link in strong scintillation conditions. We assume that the systems are mutually ignorant but nevertheless they interact. The results show that both scintillation and phase are correctable simultaneously by use of phase-only compensation at each end of the link. The use of two interacting adaptive optics systems at either end of the link has interesting implications for control stability.

37.1 Introduction

It is well known that as spatially coherent beams propagate through the atmosphere, refractive index fluctuations associated with turbulence give rise first to phase aberrations in the beam and, over longer propagation paths, to intensity fluctuations or scintillation. Adaptive optics systems that can compensate these effects are of interest to applications such as line-of-sight optical communications. As the scintillation strength increases beyond the limits of the Rytov approximation ($\sigma_R^2 < 0.3$), screw wavefront dislocations or optical vortices, associated with zeros of intensity, start to appear in the beam [1]. Optical vortices present a number of difficulties for adaptive optics systems [2, 3].

Although gradient wavefront sensors can detect the presence of optical vortices, the linear least-squares wavefront reconstruction techniques commonly used in adaptive optics fail. Furthermore, continuous surface de-

formable mirrors cannot correct for optical vortices, which by their very nature do not have wavefronts that are continuous single valued but helical in structure.

37.2 Adaptive Optics and Optical Vortices

To analyse the problem in more detail, we shall consider least-squares reconstruction from a gradient field. The least-squares reconstruction technique can be expressed as finding the single-valued scalar potential ϕ_c , representing the phase or wavefront, that minimizes the square error over the pupil Ω

$$\varepsilon^2 = \iint_{\Omega} |\mathbf{E}(x, y) - \nabla\phi_c(x, y)|^2 dx dy, \quad (37.1)$$

where $\mathbf{E}(x, y)$ is the gradient field and $\nabla = i\partial/\partial x + j\partial/\partial y$ is the two-dimensional gradient operator. Any component of the vector field $\mathbf{E}(x, y)$ that is not consistent with the gradient of a scalar potential will result in an error. Only the conservative component of the field $\mathbf{E}(x, y)$ is reconstructed.

Figure 37.1 shows an example for a wave propagated beyond the distance for which the Rytov approximation is valid. The complex amplitude $U(x, y)$ was calculated using the beam propagation approach described later. From the complex amplitude the phase gradient field $\mathbf{E}(x, y)$ is calculated,

$$\mathbf{E}(x, y) = -i\Im \left[\frac{\nabla U(x, y)}{U(x, y)} \right] \quad (37.2)$$

and the least squares phase estimate reconstructed using (37.1). The difference between the estimated phase and the actual phase of the wave (Fig. 37.1c) illustrates the problem of the least-squares phase reconstruction. The significant errors are due to optical vortices in the wave, which contribute a solenoidal component to the gradient field. The assumption implicit in the least squares wavefront reconstructor, that the wavefront is a single-valued function in Hilbert space, is not valid. The solenoidal component is inconsistent with this assumption and is ignored by the least-squares phase reconstructor. However, a solenoidal potential representing this part of the gradient field can be estimated by minimizing the square error

$$\varepsilon_s^2 = \iint_{\Omega} |\mathbf{E}(x, y) - \nabla_{\perp}\phi_s(x, y)|^2 dx dy, \quad (37.3)$$

where $\nabla_{\perp} = i\partial/\partial y - j\partial/\partial x$ represents a vector rotated gradient operator [4]. Figure 37.1d shows this solenoidal potential. The peaks in the potential coincide with optical vortices; positive or negative peaks corresponding to opposite polarity vortices. The complete gradient field is the sum of the

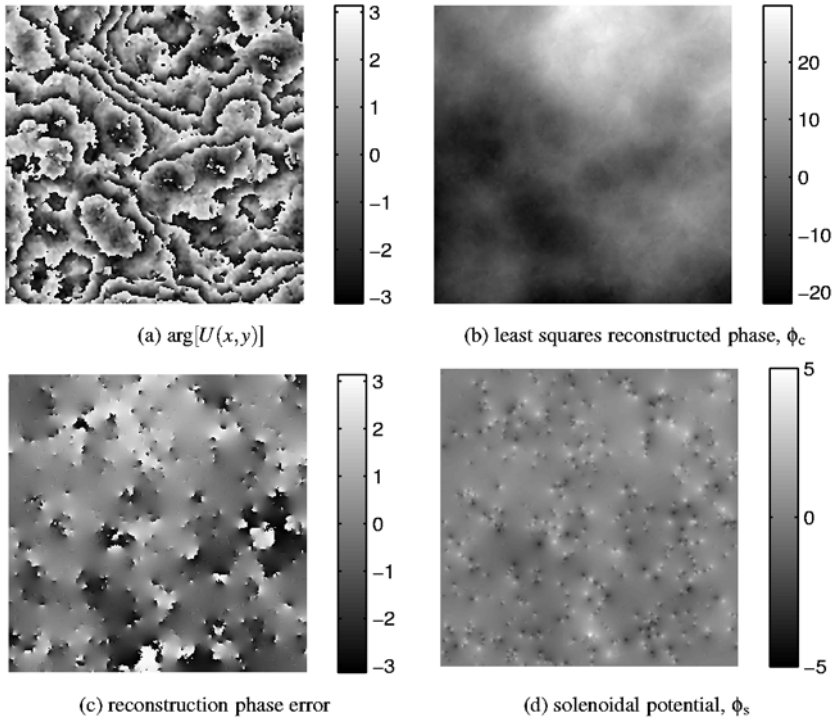


Fig. 37.1. Least-squares estimation from gradients of a wave containing optical vortices ($L = 2 \text{ km}$, $\lambda = 0.8 \mu\text{m}$, $C_n^2 = 10^{-14} \text{ m}^{-2/3}$, image size corresponds to $0.74 \times 0.74 \text{ m}$)

conservative and solenoidal components,

$$\mathbf{E}(x, y) = \nabla \phi_c(x, y) + \nabla_{\perp} \phi_s(x, y). \quad (37.4)$$

Propagation simulations were carried over a range of propagation path lengths. Uniform intensity plane waves at $z = 0$ are propagated to different distances through turbulence aberrations with Kolmogorov statistics and uniform refractive index structure function profile C_n^2 . The atmospheric propagation is modelled using a beam propagation approach based on the angular spectrum of plane waves. The turbulent volume is divided into layers sufficiently thin such that a weak geometrical phase approximation is valid for the layer. Each layer is then replaced by a phase screen at its midpoint. The beam is propagated between the phase screens using the angular spectrum of plane waves; at each phase screen the complex amplitude of the wave is multiplied by the complex transmission function of the phase screen. The propagation modelling parameters chosen were $\lambda = 0.8 \mu\text{m}$, and $C_n^2 = 10^{-14} \text{ m}^{-2/3}$, however, the results for different parameter values only vary according to the Rytov variance parameter,

$$\sigma_R^2 = 1.23C_n^2 \left(\frac{2\pi}{\lambda}\right)^{7/6} L^{11/6}. \tag{37.5}$$

The effect of ignoring the solenoidal component in an adaptive optical system was quantified by considering the properties of the wave after using least-squares continuous correction of the phase. The resulting complex amplitude after this correction is given by

$$U'(x, y) = U(x, y) \exp[-i\phi_c(x, y)] = |U(x, y)| \exp[(i\phi_s(x, y))]. \tag{37.6}$$

Figure 37.2 plots the mean residual RMS phase error (RMS error evaluated over a 0.74×0.74 m region of the wavefront, each point corresponding to an ensemble average of ten propagations). It can be seen that the RMS phase error is very small for short distances (< 1 km corresponding to $\sigma_R^2 \approx 0.43$), where the effect of vortices is negligible. Beyond about 1 km, vortices begin to have an impact and the RMS phase error rises. By 2.5 km the RMS phase error is close to the theoretical maximum of $\pi/\sqrt{3}$ for uniformly distributed random phase in the interval $[-\pi, \pi]$.

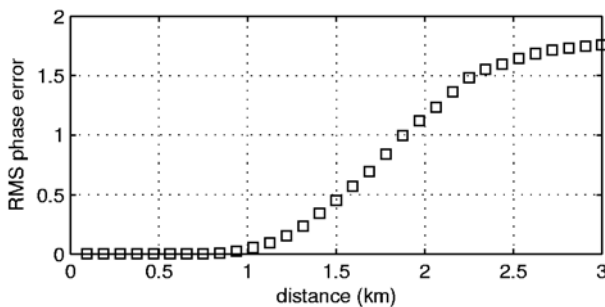


Fig. 37.2. Mean RMS phase error after least-squares continuous phase correction from gradients for plane waves propagated through uniform turbulence ($\lambda = 0.8 \mu\text{m}$, $C_n^2 = 10^{-14} \text{m}^{-2/3}$)

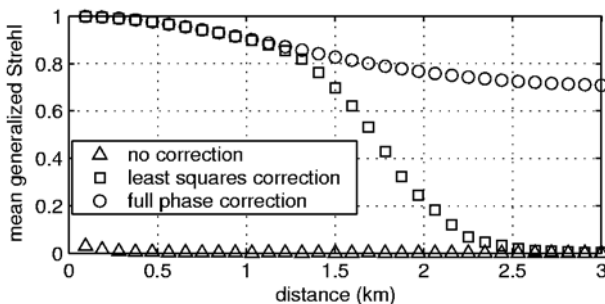


Fig. 37.3. Mean generalized Strehl S for propagation as per Fig.38.2 with no correction, least-squares continuous phase correction and full phase correction

A useful measure of the residual aberrations after correction is the Strehl ratio. A generalization for non-uniform intensity in the pupil is given by

$$S = \frac{|\iint_{\Omega} U(x, y) dx dy|^2}{\iint_{\Omega} |U(x, y)|^2 dx dy}, \quad (37.7)$$

which can be considered as the ratio of the on-axis intensities at the focus of a perfect lens for the wave $U(x, y)$ and for a uniform intensity plane wave of the same total power over the pupil Ω . It also gives an indication of the fraction of the received optical power that could be coupled into a single mode fibre in a communications link. This generalized Strehl reduces to the Strehl for uniform intensity input. Figure 37.3 plots the generalized Strehl after least squares continuous phase correction, full phase correction including the solenoidal component and no correction. For the full phase correction case, the generalized Strehl is high throughout; the reduction as the propagation distance increases is due solely to scintillation or intensity fluctuations across the pupil. The least-squares continuous correction performs as well over distances up to about 1 km at which point vortices start to appear and the generalized Strehl falls rapidly: beyond about 2.5 km it is comparable to that for no correction.

37.3 Dual Adaptive Optics

The use of adaptive optics to compensate both for scintillation effects and for phase aberrations over a bi-directional link is investigated. Phase correcting adaptive optics at a transmitter to reduce scintillation at a target or a receiver has previously been studied [5]. The basic principle is to measure the wavefronts for light that has travelled from the target to the transmitter through the aberrating volume, to apply the conjugate phase to the transmitted beam and rely on reciprocity of propagation. Here we shall investigate using two identical closed-loop adaptive optics systems, one at each end of a symmetric optical link (Fig. 37.4). Each of the two adaptive optics system consists of a receiver/transmitter telescope arrangement, a wavefront corrector (deformable mirror) and a wavefront sensor. Light from the far end of the link is collected by the telescope arrangement and relayed via the wavefront corrector to the signal receiver and the wavefront sensor. The wavefront

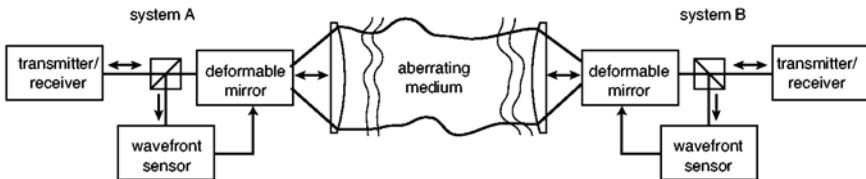


Fig. 37.4. Dual symmetric adaptive optics systems

sensor and corrector form a closed-loop adaptive optics system that is configured to correct for the phase aberrations on the received waves. However, since the outgoing transmitted beam also passes via the wavefront corrector, it gets the same wavefront modification as the received beam. In this way, the function of each adaptive optics system is both to correct phase aberrations on the received beam and to compensate for the scintillation on the transmitted beam.

A symmetric adaptive optical system has been modelled using the iterative method of projection on convex sets [6], in which only one system is permitted to operate at a given time, the systems effectively taking turns to correct. The parallel iterative approach we present here models the two systems as operating truly simultaneously. We model the function of each system as an independent control loop, although, since the two adaptive optics systems are operating at different points along on the same optical beams, there will be some feedback interaction between them. We refer to these systems as mutually ignorant, but interacting. In real adaptive optics systems, the response of the system is not instantaneous, but there is a latency between an aberrated wavefront being incident on the wavefront sensor, and a response to the aberration appearing on the wavefront corrector. It is assumed that the optical time of flight between the two systems is negligible, i.e., $L/c \ll \tau$, where L is the path length, c the speed of light and τ the time constant of one system. The closed loop systems are modelled as time-discrete iterative systems. In each iteration step, light is propagated simultaneously along both directions of the link. The received wavefronts are measured by the wavefront sensors and the wavefront correctors of both systems are updated together. We shall refer to this modelling as parallel iterative control.

Consider first the beam transmitted from one end of the link, A , propagating to the other end B . At a time t_1 , the complex amplitude at the telescope exit pupil of system A is given by

$$U_A(x, y; t_1) = U_0(x, y) \exp [i\Phi_A(x, y; t_1)] , \quad (37.8)$$

where $U_0(x, y)$ is the initial amplitude of the beam, which we take to be constant with time, and $\Phi_A(x, y; t_1)$ is the phase correction added by wavefront corrector A . The beam propagates through the atmosphere to the telescope pupil of system B , which, neglecting atmospheric absorption and scattering, can be considered as a linear unitary operation on the complex amplitude. Neglecting the finite time-of-flight (L/c), the complex amplitude of the beam received in the pupil of system B is then given by

$$U_B(x, y; t_1) = \mathcal{P}_{A \rightarrow B}[U_A(x, y; t_1)] , \quad (37.9)$$

where $\mathcal{P}_{A \rightarrow B}$ is the propagation operator from telescope pupils A to B , which is a function of the instantaneous turbulence refractive index variations. After correction by wavefront corrector B , the complex amplitude of the beam entering the wavefront sensor is given by

$$\begin{aligned}
U_{WS}(x, y; t_1) &= \mathcal{P}_{A \rightarrow B} [U_A(x, y; t_1)] \exp[i\Phi_B(x, y; t_1)] \\
&= \mathcal{P}_{A \rightarrow B} \{U_0(x, y) \exp[i\Phi_A(x, y; t_1)]\} \exp[i\Phi_B(x, y; t_1)],
\end{aligned} \tag{37.10}$$

where $\Phi_B(x, y; t_1)$ is the current phase correction applied by wavefront corrector B .

Similarly, the beam propagating in the reverse direction from B to A will have complex amplitude

$$U'_B(x, y; t_1) = U_0(x, y) \exp[i\Phi_B(x, y; t_1)] \tag{37.11}$$

in the exit pupil of system B , and upon reaching the wavefront sensor of system A ,

$$U'_{WS}(x, y; t_1) = \mathcal{P}_{B \rightarrow A} \{U_0(x, y) \exp[i\Phi_B(x, y; t_1)]\} \exp[i\Phi_A(x, y; t_1)]. \tag{37.12}$$

The phases of the two wavefront correctors are then updated according to the local wavefront sensor data,

$$\Phi_A(x, y, t_2) = \Phi_A(x, y, t_1) + gC [U'_{WS}(x, y; t_1)] \tag{37.13}$$

$$\Phi_B(x, y, t_2) = \Phi_B(x, y, t_1) + gC [U_{WS}(x, y; t_1)] \tag{37.14}$$

where C denotes the operation of the wavefront sensor and reconstructor, g is a loop gain parameter, determining how much correction is applied per iteration cycle and $t_2 = t_1 + \Delta t$, where Δt is the time interval between iteration steps. Since both beams are modified by both wavefront correctors, it can be seen that a change to one of the correctors will change the beams at the wavefront sensors at both ends of the link.

The atmospheric propagation (operator \mathcal{P}) is modelled with the beam propagation method already described. It is assumed that the propagation time is short enough that the turbulence aberrations are static during the propagation.

37.3.1 Static Turbulence Case

First the performance of the symmetric systems are investigated for the case of frozen, static turbulence aberrations. The wavefront correctors are initially set to be flat, and the initial beam profile $U_0(x, y)$ a uniform spherical wave converging to the centre of the telescope pupil of the other system. The parallel iterative control procedure is then applied with least-squares continuous phase wavefront reconstruction and correction as described above. To concentrate on the underlying principles, both the wavefront sensor and corrector are modelled as being ideal in the sense that the wavefront sensor measures gradients to arbitrary accuracy and the mirror gives zero fitting error. Figure 37.5 shows an example of the initial intensity and phase of the received

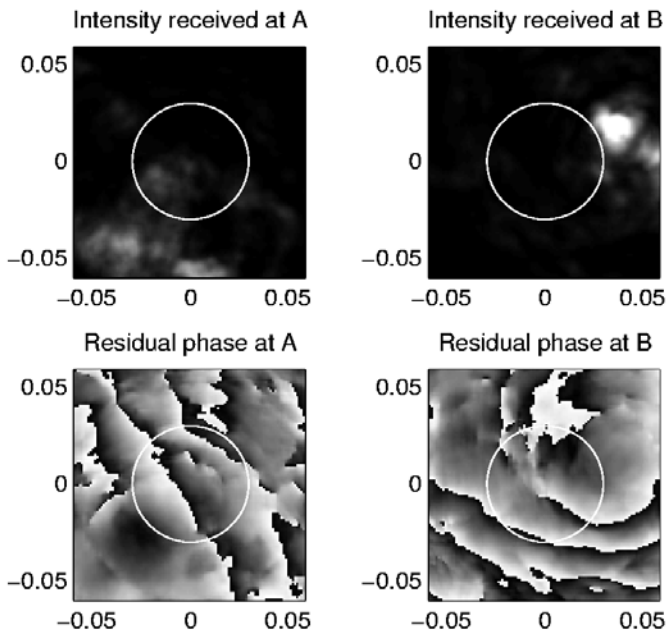


Fig. 37.5. Initial intensity and phase of waves received at each end of an optical link ($\lambda = 0.8\mu\text{m}$, $C_n^2 = 10^{-14}\text{m}^{-2/3}$, $L = 2\text{ km}$, $D = 60\text{ mm}$. Circles indicate the positions of the receiver telescope pupils)

waves at each end of the link before iteration begins. The optical wavelength is $\lambda = 0.8\mu\text{m}$, the refractive index structure constant $C_n^2 = 10^{-14}\text{m}^{-2/3}$ and the path length $L = 2\text{ km}$, which (using the weak turbulence formulae) give a Rytov number and Fried parameter for plane wave propagation of $\sigma_R^2 \approx 7.7$ and $r_0 \approx 8.8\text{ mm}$. The telescope pupil diameters are $D = 60\text{ mm}$, giving $\sqrt{\lambda L}/D \approx 1.5$. In this case the scintillation is considerable, with significant optical power falling outside of the optical pupils of the receiver telescopes.

Figure 37.6 shows the fraction of the total optical power falling inside the pupil of each receiver as the iterative control proceeds, for different values of the loop gain parameter g . For smaller gains, the received optical power increases significantly when the adaptive optics systems are iterated indicating that the systems are successfully reducing the effects of scintillation. When $g = -1$ the received optical power oscillates indicating overshoot in the correction at each iteration, caused by too large a gain. When $g = -1.5$, the combined systems are unstable. For a *single* linear correction system, a gain $g = -1.0$ would be optimal giving maximum correction in one iteration and the system would be stable for $0 > g > -2$. However, since two adaptive systems are independently and simultaneously attempting to correct correlated aberrations on the same beams (albeit at different planes along the

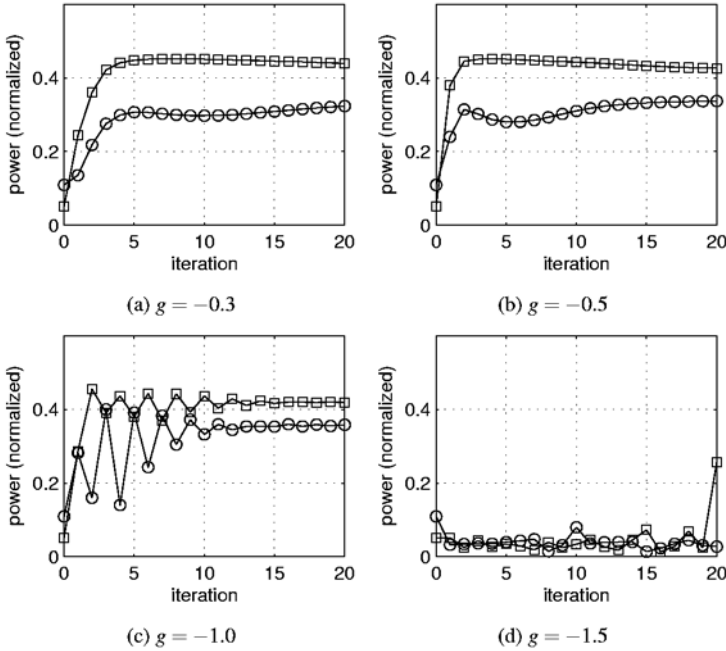
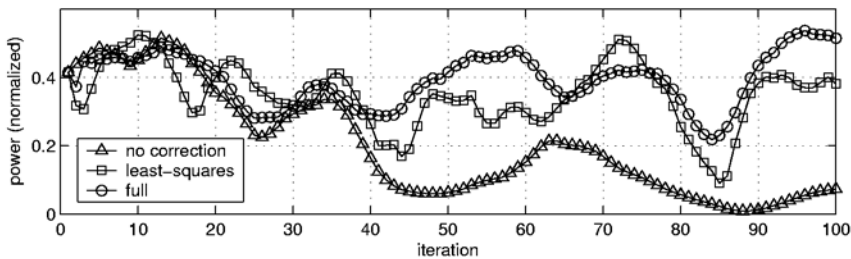


Fig. 37.6. Example plots of the fraction of the optical power falling inside the pupil of each receiver (circles *A*, squares *B*) against iteration for different loop gain parameters *g*

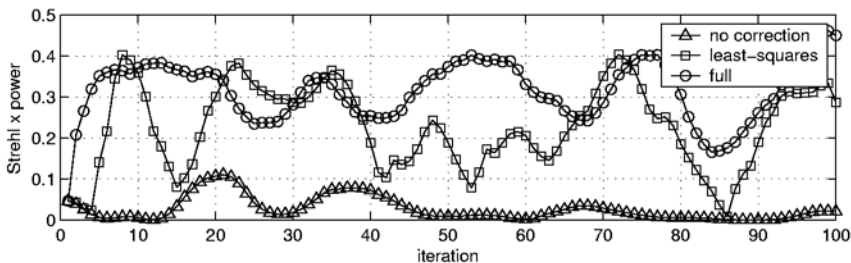
beam), the combined effective loop gains will be larger than that of a single system [7].

37.3.2 Dynamic Turbulence Case

The symmetric arrangement was also modelled for time varying dynamic turbulence. In this case, the same modelling process is followed as above, but after each iteration the turbulence phase screens are also adjusted. The evolution of the turbulence is modelled according to the Taylor frozen flow: the phase screens making up the turbulent volume are translated across the pupil by a constant distance Δx per iteration (giving an effective wind speed of $v = \Delta x / \Delta t$, where Δt is the time interval corresponding to one iteration). Figure 37.7 shows an example of the temporal evolution of (a) the total normalized power falling inside one of the telescope pupils and (b) the generalized Strehl S of the received beam $U'_{WS}(x, y, t_i)$ after correction by the local wavefront corrector ($\Delta t = r_0 / 4v$, $C_n^2 = 5 \times 10^{-14} \text{m}^{-2/3}$, where r_0 is the Fried parameter value calculated from the weak turbulence formulae.) Plots are given for least squares continuous phase correction, for full phase correction (both conservative and solenoidal components) and for no



(a) normalized optical power



(b) on-axis power, (received optical power \times generalized Strehl S) of the beam $U'_{WS}(x, y, t_i)$

Fig. 37.7. Plots of the received optical power and the generalized Strehl with dynamic Taylor turbulence ($g = -0.6$, $C^2 = 5 \times 10^{-14} \text{m}^{-2/3}$, $L = 2 \text{ km}$, $D = 60 \text{ mm}$, $\Delta t = r_0/4v$)

adaptive correction. It is seen that both types of wavefront correction give significant increase in the total received power and reduction in the residual phase aberration on the received beam, with the full phase correction method performing better.

37.4 Conclusions

The impact of optical vortices on adaptive optics systems based on least-squares wavefront reconstruction has been investigated. The presence of optical vortices gives rise to errors in the least-squares continuous phase reconstructor. The performance of the least-squares continuous wavefront reconstructor falls off over a relatively short transition range (as the propagation distance increases from a distance for which $\sigma_R^2 \approx 0.5$ to about twice that distance). We have presented a model for a dual adaptive optics system suitable for a bi-directional line-of-sight optical link, consisting of two symmetrically arranged adaptive systems operating simultaneously. Modelling shows that using the two systems together requires smaller individual loop gains than would be possible for a single system. Modelling of the systems with dynamic turbulence indicates that such an arrangement can in principle significantly reduce both scintillation and phase errors, with benefits of increased optical

power efficiencies across the link, and improved optical coupling efficiencies into single mode optical fibres or point detectors. Preliminary results indicate that correction of the complete phase, including the solenoidal components gives larger improvements, but that for the relatively small optical diameters modelled, least-squares correction can still give significant improvement.

Acknowledgements

The authors gratefully acknowledge the support of the Royal Society (through the University Research Fellowship scheme) and the UK PPARC.

References

1. V.V. Voitikhovich, D. Kouznetsov, D.K. Morozov: Density of turbulence-induced phase dislocations. *Appl. Opt.* **37**, 4525 (1998)
2. N.B. Baranova, A.V. Mamaev, N.F. Pilipetsky, V.V. Shkunov, B.Y. Zeldovic: Wavefront dislocations – Topological limitations for adaptive systems with phase conjugation. *J. Opt. Soc. Am.* **73**, 525 (1983)
3. D.L. Fried, J.L. Vaughn: Branch cuts in the phase function. *Appl. Opt.* **31**, 2865 (1992)
4. E.O. Lebigot, W.J. Wild: Theory of branch-point detection and its implementation. *J. Optical Soc. Am. A-Opt Image Sci. Vis.* **16**, 1724 (1999)
5. C.A. Primmerman, T.R. Price, R.A. Humphreys, B.G. Zollars, H.T. Barclay, J. Herrmann: Atmospheric-compensation experiments in strong-scintillation conditions. *Appl. Opt.* **34**, 2081 (1995)
6. J.D. Barchers, D.L. Fried: Optimal control of laser beams for propagation through a turbulent medium. *J. Opt. Soc. Am. A-Opt. Image Sci. Vis.* **19**, 1779 (2002)
7. J.D. Barchers: Closed-loop stable control of two deformable mirrors for compensation of amplitude and phase fluctuations. *J. Opt. Soc. Am. A-Opt. Image Sci. Vis.* **19**, 926 (2002)

38 Wavefront Measurement over an Extended Horizontal Path Using a Wavefront Curvature Sensor

J. Burnett, S. Woods, A. Turner, and A. Scott

QinetiQ Ltd., Malvern Technology Centre
St Andrews Road, Malvern, Worcs WR14 3PS, UK

Summary. This paper reports on the results of wavefront curvature sensor measurements over horizontal paths of 66 m and 4 km. The wavefront curvature sensor used has been developed at QinetiQ and is based on the use of a quadratically distorted diffraction grating to enable the simultaneous recording of two symmetrically separated planes about the entrance pupil of a telescope. The measurements allow us to characterize the spatio-temporal nature of the wavefront errors and therefore enable us to estimate the wavefront sensor (WFS) and deformable mirror (DM) requirements for the development of an adaptive optic system (AOS). For the 66 m path the dynamic range and frame-rate of the WFS camera was found to be adequate to drive the AOS, although the software based control resulted in intermittent performance. The data for the 4 km path suggested that the frame-rate of the WFS camera was at least a factor of 3 slower than would be necessary to either drive the AOS or make any detailed conclusions about the spatial analysis.

38.1 Introduction

This paper reports on the use of a wavefront curvature sensor, developed at QinetiQ, to make wavefront measurements over horizontal paths of 66 m and 4 km. The measurements are used to help define the spatio-temporal requirements for an adaptive optics system (AOS) for improved imaging or free space communication applications. A closed-loop AOS was implemented using software control on a Pentium II PC and the use of relatively cheap commercially available devices.

Wavefront curvature sensing makes use of the Intensity Transport Equation (ITE) that describes how the wavefront phase affects the intensity distribution across the wavefront as it propagates. By measuring the difference between two intensity distributions symmetrically placed about either the image plane or the pupil plane (both geometries are conjugates of each other) one can estimate the curvature of the wavefront. These wavefront curvature measurements can in turn be used to determine wavefront phase by solving the ITE [1].

A practical implementation of this technique has been demonstrated through the use of a distorted diffraction grating, referred to as an IMP[®] (Image MultiPlex) grating by its inventors. The grating makes it possible

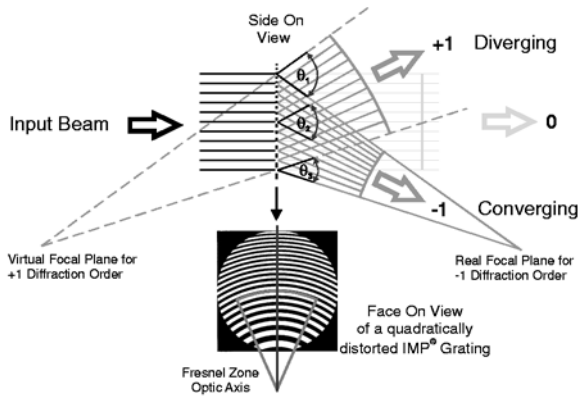


Fig. 38.1. Illustration of an off-axis Fresnel zone plate to create two beam paths with equal but opposite amounts of optical power

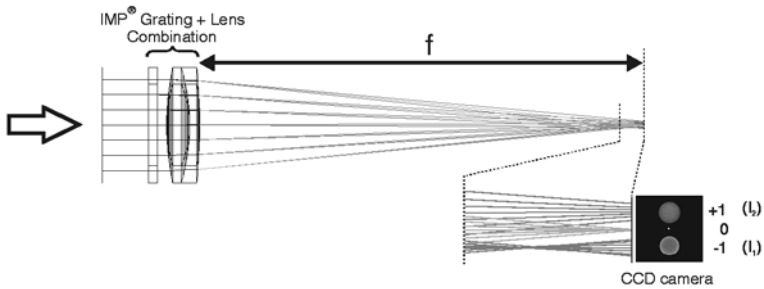


Fig. 38.2. The combination of an IMP[®] grating and an imaging lens will produce three spatially separated beams, one corresponding to the image plane and the other two corresponding to the intensity distribution on either side of the image plane

to simultaneously record on a single 2-dimensional detector array two intensity distributions symmetrically positioned about the pupil plane of an optical system. This technique eliminates the need for complex optics or the synchronisation of multiple cameras [2,3].

The IMP[®] grating technique is illustrated in Fig. 38.1 and 38.2. The grating can be considered as that part of a Fresnel zone plate (FZP) whose focal axis is laterally displaced from the optic axis of the imaging system. The variation of the grating period as a function of the radius of curvature of the annular rings of a FZP is such that all rays, due to a plane wavefront incident on the grating, that diffract into the -1 order or $+1$ order will have a common point of real or virtual convergence respectively. For such a grating the ± 1 diffracted orders represent two beams separated in angle and with equal but opposite amounts of optical power. Their angular separation is inversely proportional to the grating period at the centre of the aperture and

the optical power is dependent on the rate at which the grating period varies radially from the FZP optic axis.

If this grating is now combined with a lens at the re-imaged pupil plane of the telescope, as shown in Fig. 38.2, then the zero-order beam will correspond to the image plane and the nonzero orders will correspond to the intensity distributions I_1 and I_2 as illustrated.

Once the two data sets I_1 and I_2 have been simultaneously recorded they can be processed to reconstruct the wavefront phase. A recently developed method [4] for doing this very efficiently is the use of a Green's function solution to the ITE. The Green's function solution provides a matrix through which the wavefront curvature data can be transformed into wavefront phase.

38.2 Description of the System

38.2.1 Optical Layout

The optical system used to record the wavefront data and for adaptive correction is illustrated in Fig. 38.3. The telescope is a 280 mm-diameter $f10$ Celestron C-11. A single-mode fibre (SMF) fed $f10$ reference beam is used for alignment and calibration of the AOS. Two narrow field-of-view (NFOV) cameras are used to simultaneously monitor the uncorrected and corrected image scene (only the "corrected" NFOV image plane camera is shown in the figure, although a beam-splitter placed in the collimated beam before the first fold mirror is used to direct light to an 'uncorrected' NFOV camera). Tip-tilt control can be implemented as shown, although we currently use two orthogonally controlled galvanometer mirrors.

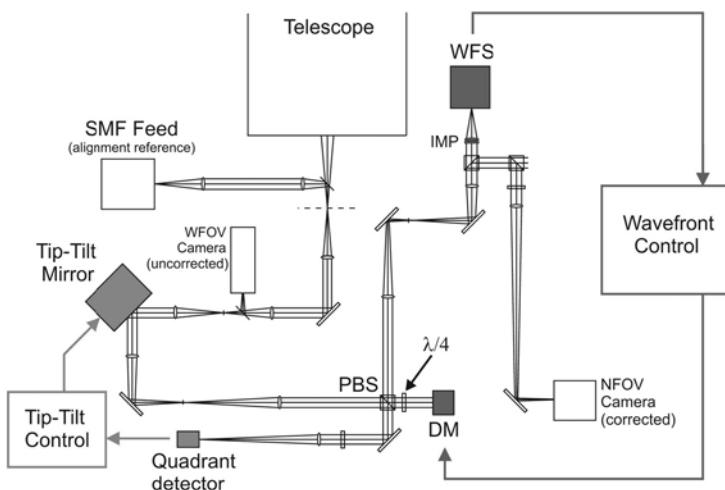


Fig. 38.3. Optical layout used for wavefront data gathering and adaptive correction

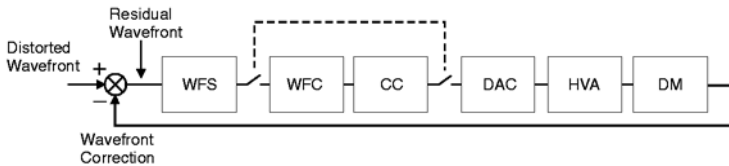


Fig. 38.4. Closed-loop block diagram for the AOS

The DM is a 15 mm diameter, 37-element OKO Technologies electrostatically controlled membrane mirror. The telescope pupil is re-imaged to a 10 mm diameter beam at the DM.

38.2.2 Closed-loop Control

The current AOS is implemented on a PC platform (Pentium II, dual processor, 800 Mhz, Windows 2000). The control software is written in Visual C++ and uses the Microsoft Foundation Classes (MFC) for Input–Output control and user interface. The complete closed-loop system can be described with the block diagram in Fig. 38.4 and the three main elements of the system are discussed below.

WFS (Wavefront Sensor) consists of an IMP[®] grating/lens combination, a Dalsa CCD camera and framegrabber. Images are integrated by the CCD camera at a fixed frame-rate of 736 fps. Each frame, consisting of 128×128 8-bit digital values, is readout and stored by the framegrabber until requested by the AOS application software. The wavefront sensing data is restricted to two 40×40 patches.

WFC (Wavefront Computer) This is part of the AOS application code that requests image data from the framegrabber and subsequently processes the data to provide a vector of 37 values that correspond to the voltage increment required to update the DM shape and therefore correct for the residual wavefront error detected at the WFS.

CC (Control Computer) The 37 values determined by the WFC need to be applied to the DM in such a way that the conjugate of the distorted wavefront is synthesised at the DM. It is the CC's function to manage this integration process in such a way that an accurate and stable synthesis of the wavefront is formed at the DM.

The AOS closed-loop algorithm was developed as a simple pure integrator described by the following equation:

$$\mathbf{V}_k = K_I \mathbf{v}_k + \mathbf{V}_{k-1}.$$

The vector \mathbf{V}_k represents the 37-voltage values output to the DM for the k -th integration step. These values are determined by taking the previous DM

voltage values and incrementing them by the values \mathbf{v}_k , scaled by the integration factor K_I . The values \mathbf{k}_k are determined by multiplying the curvature measurements with a pre-calibrated control matrix.

The n -values $\mathbf{v}_{(n)}$ are determined from the m -measurements \mathbf{p}_m and the pre-calibrated control matrix $\mathbf{D}_{(n \times m)}^*$, which is the pseudo-inverse of the optical interaction matrix $\mathbf{D}_{(m \times n)}$, which defines the sensitivity of the WFS measurements to the DM deformations.

The calibration step involves the use of an ideal local reference source that projects an un-aberrated reference image of the primary pupil of the telescope through the optical system. A predefined voltage is applied to each of the n -actuators of the mirror in turn such that the measurements $\mathbf{p}_{(m)}$ correspond to the n -th actuator influence function for the system, i.e. the n -th column of the interaction matrix $\mathbf{D}_{(m \times n)}$. The interaction matrix is then inverted using singular value decomposition (SVD) to give the pseudo-inverse $\mathbf{D}_{(n \times M)}^*$, the control matrix:

$$\underbrace{\mathbf{p}_{(m)} = \mathbf{D}_{(m \times n)} \mathbf{v}_{(n)}}_{\text{Calibration}} \implies \underbrace{\mathbf{v}_{(n)} = \mathbf{D}_{(n \times m)}^* \mathbf{p}_{(m)}}_{\text{Control}} .$$

Provided the optical system is not subsequently altered then this calibration needs only to be computed once.

38.3 Results: 66 m Path

38.3.1 Pixel Saturation

Since wavefront curvature sensing relies on measuring the intensity distribution across the propagating beam profile it is important that the dynamic range of the wavefront-sensing camera is sufficient to be able to measure the full range of intensity fluctuations. In practice this is difficult to achieve with an 8-bit camera and there was always some level of pixel saturation. For the 66 m path data we determined that pixel saturation only occurred on average at a rate of 1.26 pixels per frame and therefore not deemed to be significant. It was also apparent that the majority of pixels had rather low values, with 90% of them having a digital value less than 32. Thus most of the data is recorded with a resolution of only 5 bits.

38.3.2 Spatial Correlation

Two sets of data covering a time period of 6.8 s each (5000 consecutive frames at a frame-rate of 736 fps) were recorded and the wavefronts analysed. The mean phase variance for each data set was calculated, and an approximate value for the Fried parameter, r_0 , obtained from the formula $r_0 \approx D \langle \varphi^2 \rangle^{-3/5}$,

where D is the telescope pupil diameter (280 mm). The Fried parameter represents the effective diameter of the telescope pupil in terms of resolution, i.e. any increase in diameter beyond this value offers increased light gathering capability but no further increase in angular resolution.

The phase variance was calculated with the tip/tilt component of the wavefront removed. This gives values that correspond to short-exposure imaging, in which image jitter is unimportant (since the image motion is effectively “frozen” by the short integration time). These values are also appropriate for considering an imaging system with adaptive tip/tilt control but no other wavefront correction. The corresponding values for r_0 for the two data sets were 48 mm and 63 mm.

The number of actuators required on the deformable mirror can be determined from the Fried parameter according to $N = (D/r_0)^2$. For the two sets of 66 m data this gives $N = 33$ and $N = 20$. Thus, the 37-element mirror currently in the system should be capable of correcting these wavefronts.

38.3.3 Temporal Correlation

The wavefront sequences were analysed to determine the rate of decorrelation of the wavefronts. This was done by calculating the mean RMS phase differences between wavefronts separated by one frame, then two frames, and so on. That is, we calculate

$$a_n = \frac{1}{N-n} \sum_{i=n}^N \left(\frac{1}{m} \sum_{j=1}^m (\varphi_{i,j} - \varphi_{(i-n),j})^2 \right)^{1/2},$$

where N is the number of wavefronts in the sequence, n is the frame delay, m is the number of wavefront “pixels” and $\varphi_{i,j}$ is the wavefront phase in frame i , pixel j .

Of particular interest is the time taken for the mean RMS phase difference to reach 1 rad. This is a measure of the atmospheric correlation time, and indicates the required frame-rate of the WFS camera to effectively drive an AOS. The data over the first 40 frames (54 ms) is shown in Fig. 38.5, and was found to be a good fit to a power-law curve. From this data we can see that the RMS phase difference reaches 1 rad after a time delay of 4 frames (5.4 ms).

38.3.4 Closed-Loop Performance

Given the favorable results outlined for the 66 m path wavefront measurements there should be a reasonable chance that a closed-loop AOS can be successfully implemented over this range. We were able to demonstrate closed-loop performance as described below. Performance was characterized using the two NFOV cameras, operating at 25 fps. The AOS was always operated

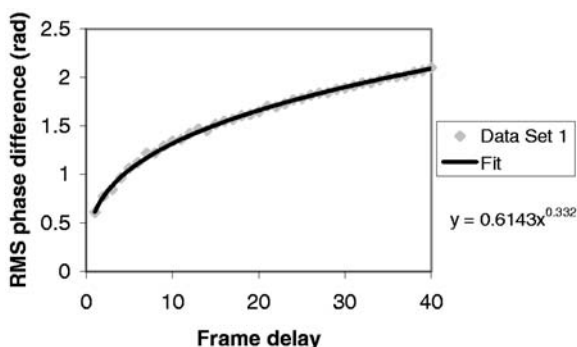


Fig. 38.5. Temporal decorrelation of RMS phase error as a function of frame delay for the 66 m path data

with the aid of a laser diode beacon (635 nm @ 1 mW) mounted at the end of the 66 m path. Video data was taken with the laser beacon and single video frames are shown in Fig. 38.6. The same video data was also time averaged over periods of 4.7 s and is shown in Fig. 38.7.

Data was also recorded with a standard chrome-on-glass USAF resolution chart mounted with the laser diode beacon projected through a central hole. Blocking filters are used to filter out the laser light from the white-light illuminated target of the resolution chart, hence the black patch at the center of the scene, as shown in Fig. 38.8. An interference filter is used at the WFS so that only light from the laser beacon is used to drive the AOS.

Simultaneous images of the uncorrected and corrected resolution chart are shown in Fig. 38.8. For comparison a diffraction-limited image is also shown on the left. The MTF cut-off for the imaging cameras is nearly 16 mm^{-1} , which corresponds to somewhere between Elements 5 and 6, Group 2. With the AOS switched off one can make out on average Element 3, Group 0, corresponding to a spatial frequency of 3 mm^{-1} at the camera. With the AOS operating this is improved by a factor of 2 such that Element 3, Group 1 can be resolved.

One of the main problems with a software-based implementation of the AOS, however, is that the control of the application can be intermittently interrupted by the PC operating system, which leads to intermittent instability of the closed-loop performance.

38.4 Results: 4 km Path

38.4.1 Pixel Saturation

For the 4 km data pixel saturation occurs, on average, at a rate of 50 pixels per frame, i.e. affecting 8% of the curvature data. As with the 66 m data, it

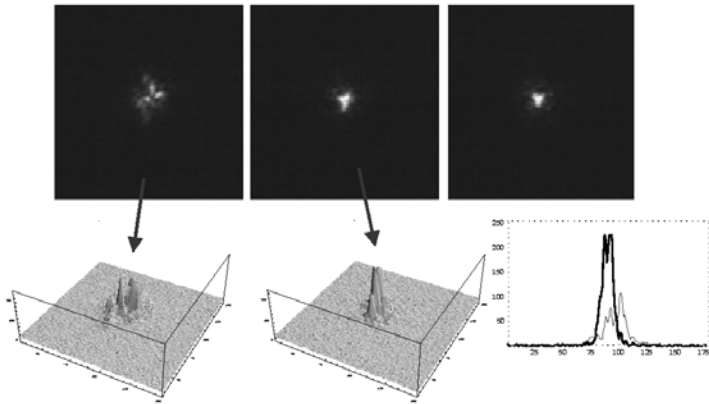


Fig. 38.6. Single video frame data. (*Left*) uncorrected frame, (*middle*) frame 80 ms after AOS switched on, and (*right*) typically good frame showing near convergence to the diffraction limited PSF (see left-hand image in Fig. 38.7)

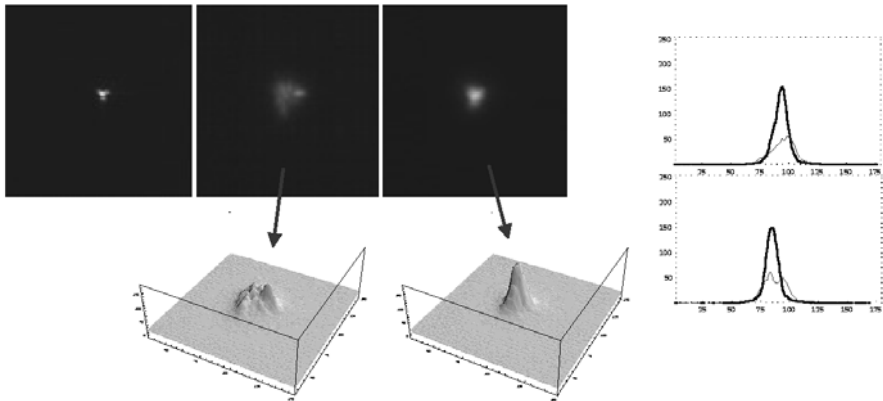


Fig. 38.7. Time average images. (*Left*) PSF of optical system using local laser reference source, (*middle*) 4.7 s time average with AOS switched off, and (*right*) 4.7 s time average with AOS switched on

is also apparent that the majority of pixels have rather low values, with 80% of them having a digital value less than 32. Thus most of the data is also recorded with a resolution of only 5 bits.

38.4.2 Spatial Correlation

Despite the higher pixel saturation values that occur for the 4 km data we also analysed the data as in Sect. 38.3.2 to try and estimate the scale of spatial de-correlation. For the same reasons as discussed in Sect. 38.3.2 the tip-tilt

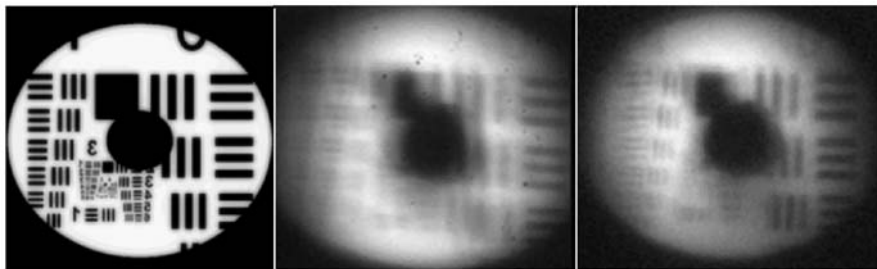


Fig. 38.8. (*Left*) theoretical diffraction limited image, (*Middle*) uncorrected image, and (*right*) corrected image

component of the wavefront data was removed. The estimated values of r_0 for six data sets varied from about 36 mm to 53 mm.

At first sight these results suggest that the spatial scales are not significantly dissimilar to those for the 66 m path results, which is contrary to what one would expect. The interpretation of this data however needs to take into account the limitations of curvature sensing and the frame-rate (and hence integration time) of the WFS camera used. It is demonstrated in the next section that the frame-rate used was insufficient for keeping up with the temporal evolution of the wavefront. The integration time for individual frames will most likely not correspond to the short-exposure limit and therefore some spatial averaging will inevitably filter out higher spatial structure.

38.4.3 Temporal Correlation

As with the 66 m path data we also determined the RMS wavefront phase difference as a function of frame delay. The results for six data sets are shown in Fig. 38.9. The solid lines represent fits to an exponential function of the form $a(1 - \exp(-bn))$, where n is the frame delay.

It is clear that the atmospheric decorrelation time is significantly shorter over the 4 km path than over the 66 m path. The wavefronts are almost completely decorrelated after a time delay of 5 frames (7 ms). In particular, the RMS phase difference reaches 1 rad after a time of just 0.3 frames, or 0.4 ms. This implies that the current WFS camera frame-rate is not fast enough to achieve the near diffraction limited imaging condition of < 1 rad RMS phase error in the closed AO loop.

38.5 Conclusions

The work reported here describes progress towards developing a system for capturing wavefront curvature data over a short (66 m) and a long (4 km) horizontal range. The intended applications for this work, such as improved

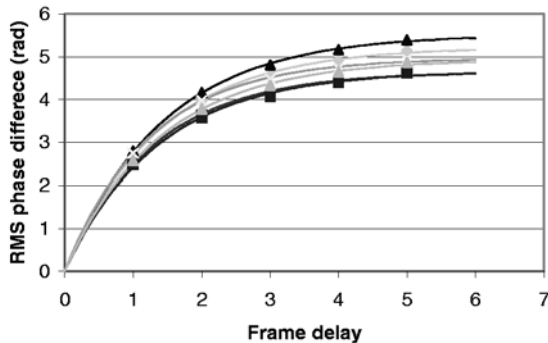


Fig. 38.9. Evolution of wavefront phase error with temporal delay (number of frames) for six data sets

imaging and optical communication links, require adaptive control and therefore based on our curvature WFS we also report on preliminary investigations as to the implementation of such an adaptive control system.

As a result of this work there have arisen a number of issues that need to be addressed before we progress with the development of an improved system. The first of these issues is that of pixel saturation. It is clear that we need an increase of at least a factor of 4 in the dynamic range of the wavefront intensity distribution measurements. It is also apparent that the frame-rate of the WFS camera needs to be increased by at least a factor of 3. For adaptive control it is also evident that our current software based system introduces too many instabilities due to the interaction of the PC operating system.

Acknowledgements

The authors would like to thank Gavin Erry and Paul Harrison (both now at Kestrel Corporation, USA) for their involvement in the early development of the AOS software and wavefront analysis software used in this study. We would also like to acknowledge the assistance of Steve Stone and David Benton for their work on implementing the current tip-tilt control system. Finally we acknowledge the support and funding for this work through the MoD Corporate Research Programme C/SEW/N03508.

References

1. F. Roddier: Curvature sensing and compensation – A new concept in adaptive optics. *Appl. Opt.* **27**(7), 1223 (1988)
2. P.M. Blanchard, A.H. Greenaway: Simultaneous multiplane imaging with a distorted diffraction grating. *Appl. Opt.* **38**(32), 6692 (1999)

3. P.M. Blanchard, D.J. Fisher, S. Woods, A.H. Greenaway: Phase-diversity wavefront sensing with a distorted diffraction grating. *Appl. Opt.* **39**(35), 6649 (2000)
4. S. Woods, A.H. Greenaway: Wavefront sensing by use of a Green's function solution to the intensity transport equation. *J. Opt. Soc. Am. A* **20**(3), 508 (2003)

39 The Detection of Atmospheric Tip-Tilt and its Program Construction in Lunar Laser Ranging

G. Rui and X. Yaoheng

Yunnan Observatory, National Astronomical Observatories, CAS

Summary. Based on the fact that the returned photon numbers are too low in Lunar Laser Ranging (LLR) and the new method that effects of atmospheric tip-tilt are considered, the two algorithms for computation of atmospheric tip-tilt, absolute difference and cross correlation, are investigated. Programs are applied to the extended target of the lunar surface. The atmospheric tip-tilt is computed in different conditions, the best algorithm is selected. A new method is put forward to reduce the time in atmospheric tip-tilt computing, and the possibility on real-time compensation in Lunar Laser Ranging is positive.

39.1 Introduction

As known to all, the most difficulty in lunar laser ranging is that the returned photon numbers are few because of many reasons, so the LLR basically belongs to sub-single photon detection. In order to increase returned photon numbers, the article [1] proposed a new idea that it introduces the real-time compensation technique of atmospheric tip-tilt on the LLR, and all factors that affect the returned photo numbers are analyzed and discussed at current technique condition in Yunnan observatory laser ranging system. The aim of this article is to find the best algorithm based on the data.

39.2 Algorithm of Extended Source Target

39.2.1 Cross-Correlation Algorithm (CC)

Consider a time series $I_1(x, y), I_2(x, y) \dots I_n(x, y)$ of two dimensionally resolved images taken from a small interesting part of lunar surface, x and y are the spatial coordinates [2]. To measure the relative displacement between $I_1(x, y)$ and $I_n(x, y)$, we calculate the normalized spatial cross correlation function $C(\delta_x, \delta_y)$ as a function of spatial lag δ_x, δ_y :

$$C_{1n}(\delta_x, \delta_y) = \frac{\iint I_1(x + \delta_x, y + \delta_y) I_n(x, y) dx dy}{[\iint I_1^2(x, y) dx dy \iint I_n^2(x, y) dx dy]^{1/2}}. \quad (39.1)$$

In this case, the image I_1 serves as a reference image with which all other images are compared. $C_{1n}(\delta_x, \delta_y)$ has a strong maximum at the lag for which

the structures in both match optimally, and then we can calculate the relative displacement of the two images. Consider the data taken with CCD, another form of (39.1) is used:

$$C_{1n}(\delta_x, \delta_y) = \frac{\sum_{x=0}^{M-1} \sum_{y=0}^{M-1} I_1(x, y) I_n(x + \delta_x, y + \delta_y)}{\left[\sum_{x=0}^{M-1} \sum_{y=0}^{M-1} I_1^2(x, y) \sum_{x=0}^{M-1} \sum_{y=0}^{M-1} I_n^2(x + \delta_x, y + \delta_y) \right]^{1/2}}. \quad (39.2)$$

Suppose the size of CCD and the live images are $N \times N$ pixels, the size of interesting window of the reference image is $M \times M$ pixels. Following the computation of the algorithm, the position (X_{\max}, Y_{\max}) is determined with subpixel precision using a parabolic interpolation.

$$X_{\max} = \delta x_{\max} + \frac{1}{2} \times \frac{C(\delta x_{\max} - 1, \delta y_{\max}) - C(\delta x_{\max} + 1, \delta y_{\max})}{C(\delta x_{\max} + 1, \delta y_{\max}) + C(\delta x_{\max} - 1, \delta y_{\max}) - 2C(\delta x_{\max}, \delta y_{\max})}, \quad (39.3)$$

$$Y_{\max} = \delta y_{\max} + \frac{1}{2} \times \frac{C(\delta x_{\max}, \delta y_{\max} - 1) - C(\delta x_{\max}, \delta y_{\max} + 1)}{C(\delta x_{\max}, \delta y_{\max} + 1) + C(\delta x_{\max}, \delta y_{\max} - 1) - 2C(\delta x_{\max}, \delta y_{\max})}. \quad (39.4)$$

39.2.2 Absolute Differences Algorithm (AD)

This method determines the displacement between two images by computing the sum of the absolute values between them and selecting the minimum.

$$D(\delta_x, \delta_y) = \sum_{i=0}^{M-1} \sum_{j=0}^{M-1} |I_{\text{ref}}(i + \delta_x, j + \delta_y) - I_{\text{live}}(i, j)|. \quad (39.5)$$

M is the size of the reference window, also we can acquire the position (X_{\min}, Y_{\min}) with subpixel precision using a parabolic interpolation. Then the relative displacement of the two images can be calculated.

$$X_{\min} = \delta x_{\min} + \frac{1}{2} \times \frac{C(\delta x_{\min} - 1, \delta y_{\min}) - C(\delta x_{\min} + 1, \delta y_{\min})}{C(\delta x_{\min} + 1, \delta y_{\min}) + C(\delta x_{\min} - 1, \delta y_{\min}) - 2C(\delta x_{\min}, \delta y_{\min})}, \quad (39.6)$$

Table 39.1. Comparison of the two algorithms

Algorithm	Sum of real number	Multiply of real number	Square of real number
Cross correlation	$M^2 (N - M + 1)^2$	$M^2 (N - M + 1)^2$	$(N - M + 1)^2$
Absolute difference	$M^2 (N - M + 1)^2$	Nil	Nil

$$\begin{aligned}
 Y_{\min} &= \delta y_{\min} + \frac{1}{2} \\
 &\times \frac{C(\delta x_{\min}, \delta y_{\min} - 1) - C(\delta x_{\min}, \delta y_{\min} + 1)}{C(\delta x_{\min}, \delta y_{\min} - 1) + C(\delta x_{\min}, \delta y_{\min} + 1) - 2C(\delta x_{\min}, \delta y_{\min})}.
 \end{aligned}
 \tag{39.7}$$

39.2.3 Algorithm Comparison

The two algorithms are discussed in article [2, 4, 5], what we care for most is the computation time. There is a time delay about 2 ~ 3 ms between image data sampling and servo control signal computing [5, 6]. if the delay is too large, the effect of real time compensation will not be very good. The calculation in cross correlation algorithm is a great quantity of sum of square and multiply. Table 39.1 gives the comparison of the two algorithms in calculation [1].

From Table 39.1 we can see that the calculation of absolute difference algorithm is minimum when M and N are bigger than 16, it is just the sum of real number, so absolute difference algorithm may be more effective for atmospheric tip-tilt calculating.

39.3 Data Sampling and Program Construction

The lunar data were collected by Yunnan observatory’s 1.2 m telescope with a field of view of $3' \times 3'$ on March 2003. A time series of digitized images are obtained with a two-dimensional CCD camera with 128×128 pixels, the size of each pixel is 16×16 microns, the image acquisition rate is 419 s^{-1} , and 2000 images are obtained in each time series. What should be pointed out is the limitation of the telescope status and the CCD sensitivity; the data we obtained are not the best. The flat-field of the CCD is not considered, but some useful results are obtained. The two algorithms programs are built in C language, an image with different interesting fields and different size can be chosen for the reference image window, and an arbitrary image can be chosen for the reference image.

39.4 Algorithm Analyzing on Lunar Data

In order to compensate the atmospheric tip-tilt in LLR, it must be computed accurately and real-time. Then, what size of the reference image and which algorithm will be adopted are the problems that we must deal with. In view of this problem, different algorithm and different size of the reference window will be researched and be selected the best. The size of 8×8 pixels, 16×16 pixels and 32×32 pixels of the reference windows are used respectively in the two algorithms. Then the comparisons of them are given out. The data we adopt are the moon surface near the Apollo 15 reflector. In the following figures, each pixel is corresponding to 0.45 arcsec, the time interval between two continuous figures is 2.4 ms. 100 figures are compared with the first one with the two algorithms of different size of reference window in Figs. 39.1 and 39.2, for simple we just show the tilt in x -direction. It can be seen that the absolute difference algorithm is more sensitive than the cross correlation algorithm because the calculated tilt signal is more real when the size of reference window is 8×8 pixels.

The different r_0 is calculated by (39.8) in Table 39.2 [1]

$$\langle \rho_c^2 \rangle \approx \frac{10.22 \cdot Z^2}{k^2 r_0^{\frac{5}{3}} D^{1/3}}. \quad (39.8)$$

Z is the distance from earth to lunar, k is the wave number, $\lambda = 0.532 \times 10^{-6}$ m, D the diameter of the telescope, ρ_c is the short-term beam wander on moon, it can be calculated by the tip-tilt we detected.

According to the r_0 in Table 39.2, values that are calculated by absolute difference algorithm when the sizes of reference window are 16×16 pixels and 32×32 pixels are quite close to the local average value detected by adaptive optics system. Although the value when the size of reference window is 32×32 pixels (14×14 arcsecs) seems to be good, it will take much time, and it will be above the limit of isoplanatic angle (about 10 arcsecs). So we can conclude that the tip-tilt can be obtained more accurately with absolute difference algorithm when the size of the reference window is 16×16 pixels.

Table 39.2. $r_0(m)$ at different algorithm and different reference image size

Size of window	Absolute difference	Cross correlation
8×8	0.001	0.0003
16×16	0.096	0.053
32×32	0.117	0.051

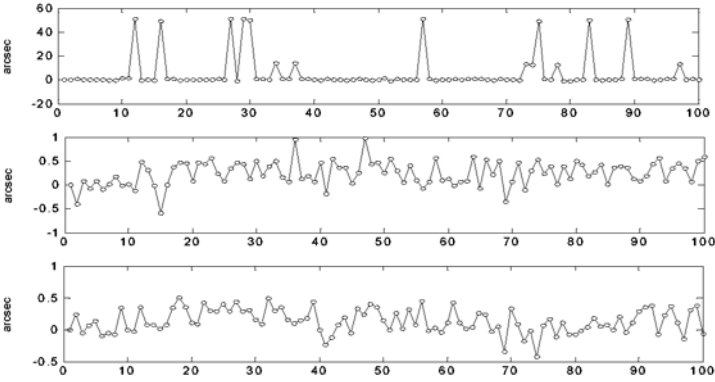


Fig. 39.1. Tilt in x -direction with different window size (8×8 , 16×16 , 32×32) absolute difference

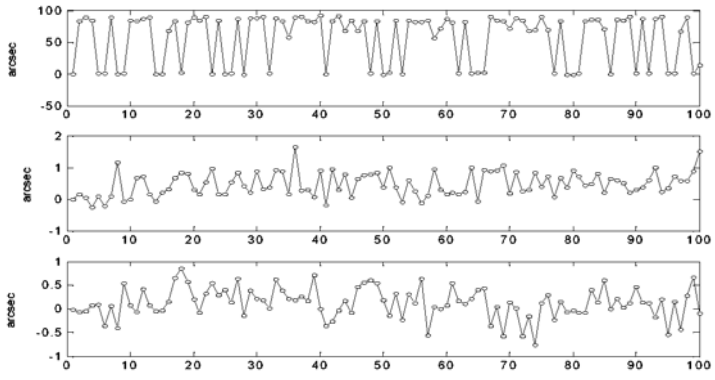


Fig. 39.2. Tilt in x -direction with different window size (8×8 , 16×16 , 32×32) cross correlation

39.5 Probability of Real Time Compensation

The size of live image is 128×128 pixels, corresponding to 58×58 arcsecs of the lunar surface, so the computing time is too large, about 300 ms, these make the real time compensation hard. Consider the fact that the atmospheric tip-tilt is about several arcsecs, and needs to be calculated in real-time, it is necessary to find the optimal computation area just near the reference window, namely let the size of the live image be smaller. This would decrease operating time enormously. We discover that it is enough for extending 5 pixels around the position of the reference window in the live image to compute the atmospheric tip-tilt; the time used for one image is less than 4 ms. It is enough for real time compensation. The following two figures are the results we computed 2000 images in x -direction in the two ways as discussed above, it can be seen that they are the same, so our idea and work are significant.

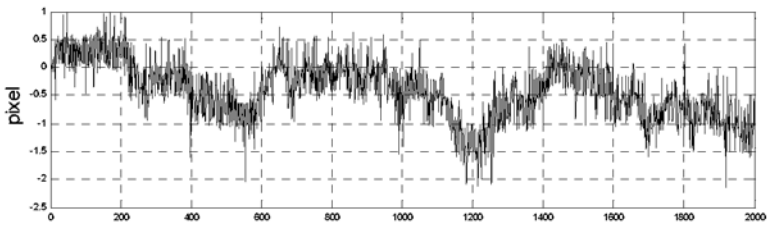


Fig. 39.3. Tilt calculated when the size of live image is 128×128

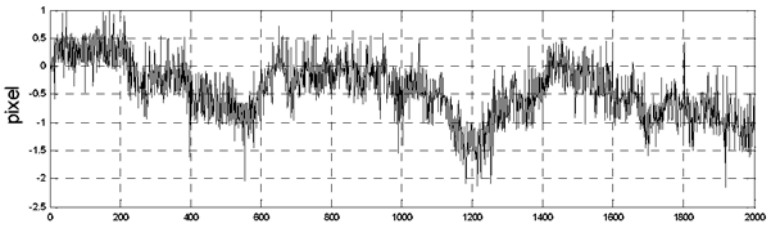


Fig. 39.4. Tilt calculated when the size of live image is 26×26

39.6 Conclusion

According to our job, the real-time atmospheric tip-tilt can be obtained accurately and effectively from an extended lunar surface with absolute difference algorithm when the size of the reference window is 16×16 pixels. In order to meet the time requirement of real time compensation, a new idea to decrease the computing time is proposed, and the feasibility of atmospheric turbulence compensation in LLR is proved. We will continue our research.

Acknowledgements

Authors are greatly thanks to the friendly help of Rao Changhui, Zhou Weichao, Zhang Xuejun of the Institute of Optics and Electronics, Chinese Academy of Sciences, Zhang Yuncheng, Zheng Xiangming, Jin Zhenyu, Xue Li of Yunnan Observatory, National Astronomical Observatories, Chinese Academy of Sciences.

References

1. X. Yaoheng, F. Hesheng: Applications of adaptive optics in lunar laser ranging. *Proc. SPIE* **4839**, 88 (2002)
2. O. Von Der Lühe: A study of a correlation tracking method to improve imaging quality of ground-based solar telescope. *Astron. Astrnoms* **119**, 85 (1983)
3. D.I. Barnea, H.F. Silverman: A class of algorithms for fast digital image registration. *IEEE Transaction on Computers* **C-21**(2), (1972)

4. O. Von Der Lühe, A.L. Widener, T.R. Rimmele et al.: Solar feature correlation tracker for ground-based telescope. *AA* **224**, 351 (1989)
5. E. Ballesteros, M. Collados, A. Bonet et al.: Two-dimensional high spatial resolution solar spectroscopy using a correlation tracker. I. Correlation tracker. Description. *AA Suppl. Ser.* **115**, 353 (1996)
6. M. Collados, I. Rodriguez, E. Ballesteros et al.: Two-dimensional high spatial resolution solar spectroscopy using a correlation tracker. II. Maps of spectral quantities. *AA Suppl. Ser.* **115**, 367 (1996)
7. D.I. Barnea, H.F. Silverman: A class of algorithms for fast digital image registration. *IEEE Trans. Comp.* **C 21**(2), 179 (1972)

Author Index

- Akhzar-Mehr, O. 197
Alexandrov, A. 237
Archer, N. 9
Artal, P. 317, 325
- Beyerlein, M. 141
Bhattacharya, N. 83
Bille, J. 151
Borneis, S. 283
Braat, J.M. 83
Burnett, J. 377
Burns, D. 217
Buschmann, U. 73
Buske, I. 73, 229, 249
Byer, R. 53
- Cagigal, M.P. 111
Campbell, H.I. 177, 187
Canales, V.F. 111
Carr, E. 53
Cuevas, D.M. 119, 129
- de Boer, M. 61
de Lima Monteiro, D.W. 151, 163, 197
Diez, C.A. 151
Doelman, N. 61
Dorn, R. 141
Duran-Ramirez, V.M. 207
Dyba, M. 103
- Erry, G.R.G. 129, 333, 343
- Fernández, E.J. 317
Fournier, P. 119, 129
Fraanje, R. 61
- Gaul, E. 283
Gorbunov, S. 353
Greenaway, A.H. 177, 187
- Griffith, M. 9
Guan, C. 261
- Häfner, C. 283
Hain, M. 35
Harrison, P. 119, 129
Heuck, H.-M. 73, 249, 283
Hinnen, K. 61
Hu, Y. 305
- Iglesias, I. 325
Irochnikov, N. 333, 353
- Jiang, C. 305
Jiang, P. 261
Jiang, W. 261, 305
Jung, I.-W. 53
- Knittel, J. 35
Kochemasov, G. 291
Köller, M. 273
Krause, H. 73
Krishnamoorthy, U. 53
Kudryashov, A. 237
Kühl, T. 283
Kutzner, J. 273
- Larichev, A. 129, 333, 353
Laycock, L. 9
Ling, N. 305
Loktev, M. 17, 25, 45
Lu, P. 53
Lubeigt, W. 217
- Malacara-Doblado, D. 207
Malacara-Hernandez, D. 207
Mann, K. 103
Manzanera, S. 317
Maurer, H. 273

- Nemeth, S.C. 343
Nirmaier, T. 151, 163
- Oti, J.E. 111
Otten, L.J. 119, 129, 333, 343
- Paterson, C. 365
Peter, Y.-A. 53
Pfund, J. 141
Prieto, P.M. 317
Pudasaini, G. 151
- Rao, X. 305
Restaino, S. 177
Richter, H. 35
Rowe, D. 9
Rui, G. 389
Rukosuev, A. 237
- Salas-Peimbert, D.P. 207
Salort, J. 317
Samarkin, V. 237
Schäfer, B. 103
Scott, A. 377
Solgaard, O. 53
Soliz, P. 343
Soloviev, O. 91
Somalingam, S. 35
Starikov, F. 291
- Trujillo-Shiaffino, G. 207
- Tschudi, T. 35
Tsilimis, G. 273
Turner, A. 377
- Valentine, G. 217
van Grol, P. 217
Vdovin, G. 3, 17, 25, 45, 61, 91, 197
Verhaegen, M. 61
Vohnsen, B. 325
Vuelban, E.M. 83
- Walker, C.R. 365
Wang, C. 305
Wang, H. 261
Welp, P. 229, 249
Wiewior, P. 283
Witting, T. 273
Wittrock, U. 73, 229, 249, 283
Woods, S. 377
- Xu, B. 261
- Yand, Z. 261
Yang, S.Y. 343
Yaoheng, X. 389
- Zacharias, H. 273
Zavalova, V. 237
Zhang, S. 187
Zhang, X. 45
Zhang, Y. 261, 305

SPRINGER PROCEEDINGS IN PHYSICS

- 50 **Magnetic Properties of Low-Dimensional Systems II**
New Developments
Editors: L.M. Falicov, F. Mejía-Lira,
and J.L. Morán-López
- 51 **The Physics and Chemistry of Organic Superconductors**
Editors: G. Saito and S. Kagoshima
- 52 **Dynamics and Patterns in Complex Fluids**
New Aspects
of the Physics–Chemistry Interface
Editors: A. Onuki and K. Kawasaki
- 53 **Computer Simulation Studies in Condensed-Matter Physics III**
Editors: D.P. Landau, K.K. Mon,
and H.-B. Schüttler
- 54 **Polycrystalline Semiconductors II**
Editors: J.H. Werner and H.P. Strunk
- 55 **Nonlinear Dynamics and Quantum Phenomena in Optical Systems**
Editors: R. Vilaseca and R. Corbalán
- 56 **Amorphous and Crystalline Silicon Carbide III, and Other Group IV–IV Materials**
Editors: G.L. Harris, M.G. Spencer,
and C.Y. Yang
- 57 **Evolutionary Trends in the Physical Sciences**
Editors: M. Suzuki and R. Kubo
- 58 **New Trends in Nuclear Collective Dynamics**
Editors: Y. Abe, H. Horiuchi,
and K. Matsuyanagi
- 59 **Exotic Atoms in Condensed Matter**
Editors: G. Benedek and H. Schneuwly
- 60 **The Physics and Chemistry of Oxide Superconductors**
Editors: Y. Iye and H. Yasuoka
- 61 **Surface X-Ray and Neutron Scattering**
Editors: H. Zabel and I.K. Robinson
- 62 **Surface Science**
Lectures on Basic Concepts and Applications
Editors: F.A. Ponce and M. Cardona
- 63 **Coherent Raman Spectroscopy**
Recent Advances
Editors: G. Marowsky and V.V. Smirnov
- 64 **Superconducting Devices and Their Applications**
Editors: H. Koch and H. Lübbing
- 65 **Present and Future of High-Energy Physics**
Editors: K.-I. Aoki and M. Kobayashi
- 66 **The Structure and Conformation of Amphiphilic Membranes**
Editors: R. Lipowsky, D. Richter,
and K. Kremer
- 67 **Nonlinearity with Disorder**
Editors: F. Abdullaev, A.R. Bishop,
and S. Pnevmatikos
- 68 **Time-Resolved Vibrational Spectroscopy V**
Editor: H. Takahashi
- 69 **Evolution of Dynamical Structures in Complex Systems**
Editors: R. Friedrich and A. Wunderlin
- 70 **Computational Approaches in Condensed-Matter Physics**
Editors: S. Miyashita, M. Imada,
and H. Takayama
- 71 **Amorphous and Crystalline Silicon Carbide IV**
Editors: C.Y. Yang, M.M. Rahman,
and G.L. Harris
- 72 **Computer Simulation Studies in Condensed-Matter Physics IV**
Editors: D.P. Landau, K.K. Mon,
and H.-B. Schüttler
- 73 **Surface Science**
Principles and Applications
Editors: R.F. Howe, R.N. Lamb,
and K. Wandelt
- 74 **Time-Resolved Vibrational Spectroscopy VI**
Editors: A. Lau, F. Siebert, and W. Werncke
- 75 **Computer Simulation Studies in Condensed-Matter Physics V**
Editors: D.P. Landau, K.K. Mon,
and H.-B. Schüttler
- 76 **Computer Simulation Studies in Condensed-Matter Physics VI**
Editors: D.P. Landau, K.K. Mon,
and H.-B. Schüttler
- 77 **Quantum Optics VI**
Editors: D.F. Walls and J.D. Harvey
- 78 **Computer Simulation Studies in Condensed-Matter Physics VII**
Editors: D.P. Landau, K.K. Mon,
and H.-B. Schüttler
-